Design, development and validation of tubular constructs for regenerative medicine

Thèse en cotutelle
Doctorat en génie des matériaux et de la métallurgie

Nele Pien

Université Laval
Québec, Canada
Philosophiæ doctor (Ph. D.)

et

Ghent University
Gent,Belgique

Résumé

Les lésions, les maladies et les dysfonctionnements des organes tubulaires représentent un défi unique pour les bio-ingénieurs et les cliniciens. Une approche multidisciplinaire doit être appliquée pour réussir à développer des organes fonctionnels issus de l'ingénierie tissulaire (TE). Dans la recherche actuelle concernant la fabrication d'organes tubulaires fonctionnels, il manque un lien qui se concentre sur la corrélation entre (i) les exigences mécaniques et biologiques de la conception de l'échafaudage dictées par la structure anatomique et les fonctions physiologiques, (ii) le processus de fabrication (y compris la sélection des matériaux et la technique de traitement) et (iii) les propriétés mécaniques et biologiques résultantes de l'organe tubulaire TE développé. Par conséquent, le présent doctorat vise à relever certains des défis actuellement rencontrés dans l'ingénierie tissulaire et la médecine régénérative, et plus particulièrement dans la réparation des tendons et la modélisation des parois vasculaires. À cette fin, des biomatériaux spécifiques ont été conçus et caractérisés, et de multiples techniques de fabrication des biomatériaux ont été évaluées.

Dans une première partie de cette thèse, des nouveaux polymères polyvalents photoréticulables à base d'uréthane (AUP) ont été développés, ainsi que leur mise en œuvre comme matériaux de départ pour le développement d'échafaudages tubulaires. Parce que chaque tissu a ses propres exigences mécaniques et biologiques, et parce que chaque technique de traitement a ses propres défis spécifiques, une boîte à outils de AUPs a été proposée. Des AUPs basés sur un backbone de poly(éthylène glycol) (PEG) et un backbone de poly(ε-caprolactone) (PCL) avec différentes masses molaires ont été synthétisés. Les AUPs ont montré une large gamme de propriétés physiques et mécaniques, couvrant les propriétés de nombreux tissus et les rendant idéales pour la médecine régénérative d'un point de vue mécanique. En outre, les AUPs développés ont permis une réticulation UV efficace à l'état solide, ouvrant la voie à diverses possibilités de techniques de fabrication, notamment l'électrospinning en solution (SES), l'impression 3D par extrusion (3DP) et l'électrowriting en fusion (MEW).

Une des possibilités de technique de fabrication mentionnées ci-dessus se trouve dans le MEW. Actuellement, l'un des défis associés à l'utilisation du MEW est la disponibilité limitée de matériaux compatibles. Par conséquent, dans cette thèse de doctorat, la MEW a été étudiée en tant que technique de fabrication émergente pour transformer les AUPs développés en constructions tubulaires avec une architecture prédéfinie et présentant des propriétés mécaniques réglables.

Une deuxième technique de fabrication choisie pour évaluer le potentiel des AUP développés est le SES. L'une des applications biomédicales possibles des constructions tubulaires en médecine régénérative est la réparation des tendons. Afin de surmonter les défis actuellement rencontrés dans la réparation des

tendons, une combinaison d'une approche mécanique (par la conception du matériau et de l'échafaudage) et biologique (par des médicaments anti-adhésion et anti-inflammatoires) a été proposée dans cette thèse.

Une autre application possible des constructions tubulaires en médecine régénérative peut être trouvée dans le domaine de la TE vasculaire. Dans cette thèse, l'utilisation d'un échafaudage synthétique tubulaire comme renfort pour des modèles à base de collagène a été exploitée dans le but d'obtenir les propriétés mécaniques requises pour la modélisation de la paroi vasculaire. Trois techniques de fabrications différentes (SES, 3DP et MEW) ont été évaluées pour le développement du renfort tubulaire en polymère.

Outre l'utilisation d'un échafaudage de renforcement synthétique pour obtenir des propriétés mécaniques supérieures dans les modèles de parois vasculaires à base de collagène, une autre approche consiste à maintenir l'intégrité structurelle des échafaudages par réticulation chimique, physique ou enzymatique. Par conséquent, dans la deuxième partie de cette thèse, un collagène photoréticulable aux propriétés ajustables a été développé et comparé à l'étalon-or de la TE, à savoir la gélatine modifiée par le méthacrylamide. La distribution de fragments photoréticulables sur un squelette protéique peut affecter le comportement de réticulation d'un biomatériau, et donc aussi ses propriétés mécaniques et biologiques. Une connaissance approfondie à cet égard est essentielle pour les biomatériaux exploités dans l'ingénierie tissulaire et la médecine régénérative, afin de permettre la transposition de nouveaux biomatériaux fonctionnalisés du laboratoire au chevet du patient, compte tenu des contraintes réglementaires. C'est pourquoi l'analyse protéomique a été évaluée comme un outil permettant de mieux comprendre les modifications des biopolymères photoréticulables.

Les recherches menées dans le cadre de cette thèse ont permis d'élargir la variété de biomatériaux, mais ont également permis de mieux comprendre certaines exigences critiques concernant la conception des biomatériaux, la technique de fabrication ainsi que les propriétés mécaniques et biologiques de l'échafaudage.

Abstract

Injury, diseases and malfunctioning of tubular organs represent a unique challenge for bioengineers and clinicians. A multidisciplinary approach needs to be applied to successfully develop functional tissue engineered (TE) organs. In the current research regarding the regeneration of functional tubular organs, there is a missing link that focuses on the correlation between (i) the mechanical and biological requirements of the scaffold design dictated by the anatomical structure and physiological functions, (ii) the fabrication process (including material selection and processing technique) and (iii) the resulting mechanical and biological properties of the developed tubular TE organ.

Therefore, the current PhD focuses on addressing some of the challenges currently encountered in tissue engineering and regenerative medicine, and more specifically, in tendon repair and vascular wall modeling. To this end, specific biomaterials were designed and characterized, and multiple biomaterial processing techniques were evaluated.

In a first part of this PhD thesis, novel versatile photo-crosslinkable urethane-based polymers (AUPs) were developed, along with their implementation as starting materials for the development of tubular scaffolds. Because each tissue has its own mechanical and biological requirements, and because each processing technique has its own specific challenges, a toolbox of AUPs was proposed, taken into account the challenges and requirements while synthesizing and formulating the AUPs. AUPs based on a poly(ethylene glycol) (PEG) backbone versus a poly(ε-caprolactone) (PCL) backbone with different molar masses were synthesized (i.e. AUP PEG2k, 20k; AUP PCL530, 2k, 10k and 20k). The developed PEG- and PCL-based AUPs showed a broad range in physical and mechanical properties, covering the properties of many tissues and rendering them ideal for regenerative medicine from a mechanical perspective. Moreover, the developed AUPs enabled efficient UV-crosslinking in the solid state, paving the way towards various processing opportunities, including solution electrospinning (SES), extrusion-based 3D printing (3DP) and melt electrowriting (MEW).

One of the above-mentioned processing opportunities can be found in MEW. At present, one of the challenges associated with the use of MEW is the limited availability of compatible materials. Therefore, in this PhD thesis, MEW was investigated as an emerging fabrication technique to process the developed AUPs into tubular constructs with a predefined architecture and exhibiting tunable mechanical properties.

A second processing technique that was selected to evaluate the processing potential of the developed AUPs is SES. One possible biomedical application of tubular constructs in regenerative medicine can be found in tendon repair. In order to overcome the challenges currently encountered in tendon repair (i.e.

insufficient mechanical properties along with adhesion and inflammatory issues), a combination of a mechanical (by material and scaffold design) and biological approach (by anti-adhesion and anti-inflammatory drugs) was proposed in this PhD thesis.

Another possible application of tubular constructs in regenerative medicine can be found in the field of vascular TE. In this PhD thesis, the use of a tubular, synthetic scaffold as reinforcement for collagen-based models was exploited with the aim to achieve the required mechanical properties for vascular wall modeling. Three different processing techniques (i.e. SES, 3DP, and MEW) were evaluated for the development of the tubular, polymeric reinforcement.

Apart from using a synthetic reinforcement scaffold to achieve superior mechanical properties in collagen-based vascular wall models, another approach includes maintaining the scaffolds's structural integrity by chemical, physical or enzymatic crosslinking. Therefore, in a second part in this PhD thesis, a photo-crosslinkable collagen (COL-MA) with tunable properties was developed and benchmarked against the gold standard in TE, being methacrylamide-modified gelatin (GEL-MA). The distribution of photo-crosslinkable moieties onto a protein backbone can affect a biomaterial's crosslinking behavior, and therefore also its mechanical and biological properties. A profound insight in this respect is essential for biomaterials exploited in tissue engineering and regenerative medicine to enable translation of novel, functionalized biomaterials from bench to bedside, given regulatory constraints and the need for perfectly defined and reproducible biomaterials. Therefore, proteomic analysis was evaluated as a tool to gain next level insights in photo-crosslinkable biopolymer modifications.

The research conducted in this PhD thesis resulted in the expansion of the biomaterial portfolio, but also provided greater insight into some critical requirements regarding biomaterial design, the fabrication process, and the scaffold's resulting mechanical and biological properties.

Table of contents

List of figures

Figure 7.9. Coverage of the identified and quantified peptides on the sequence of COL1α1 and COL1α2 for the samples of COL BS from both digestions. Green areas show the protein sequence coverage. Yellow areas show the non-covered parts of the protein.

Figure 7.10. The protein 3D-conformation of the COL1α1 (a) and COL1α2 (b) proteins modelled with I-TASSER in the cartoon view showing helices (red), sheets (yellow), loops (green), and lysine residues in the structure (magenta). The same models shown in the solvent surface accessibility view for COL1α1for one side (c) and 180° turn around Y-axis site (e), and COL1α2 for one side (d) and 180° turn around Y-axis site (f), showing the protein accessibility surface (green), unmodified lysines on the surface (magenta), modified lysine (cyan) and the RGD sequences at the surface (orange). Close-ups of the protein COL1α2 showing (g) the grouped RGD sequences (orange, indicated with arrow) and proximity of the modified lysines (cyan) and (h) the buried unmodified lysines (magenta, indicated with arrow).

List of tables

List of abbreviations

^{1}H-NMR	proton nuclear magnetic resonance spectroscopy
3D(B)P	three-dimensional (bio)printing
AA	amino acid
ATR	attenuated total reflection
AUP	acrylate-endcapped urethane-based polymer precursors
BAO	bioartificial organs
BHT	butylated hydroxytoluene
Ca-AM	calcein-acetylmetoxyester
CE	crosslinking efficiency
COL-MA	methacrylamide-modified collagen
CS	chondroitin sulphate
CVD	cardiovascular diseases
Đ	polydispersity
DC	degree of conversion
DMEM	Dulbecco's Modified Eagle's Medium
DMT	dimethyl terephthalate
DS	degree of substitution
DSC	differential scanning calorimetry
EC	endothelial cell
ECM	extracellular matrix
EQ	equivalents
FB	fibroblast
FDA	US Food and Drug Administration
FDM	fused deposition modeling
FTIR	fourier-transform infra-red spectroscopy
G'	storage modulus
G"	loss modulus
GEL-MA	methacrylamide-modified gelatin
GF	growth factor
GF	gel fraction
GPC	gel permeation chromatography
H3PO4	phosphoric acid
HA	hyaluronic acid
HDF	human dermal fibroblast

hFB	human fibroblast
HPLC	high-performance liquid chromatography
HR-MAS	high resolution-magic angle spinning nuclear magnetic resonance
HUVEC	human umbilical vein endothelial cell
IPDI	isophorone diisocyanate
KCl	potassium chloride
M_n	number average molar mass
M_w	weight average molar mass
MALDI	matrix-assisted laser desorption/ionization
MeAnH	methacrylic anhydride
MEW	melt electrowriting
MM	molar mass
MMP	matrix metalloproteinase
MS	mass spectrometry
MSC	mesenchymal stem cell
MTS	(3-(4,5-dimethylthiazol-2-yl)-5-(3-carboxymethoxyphenyl)-2-(4-sulfophenyl)-2H-tetrazolium)
MWCO	molecular weight cut-off
NAP	naproxen
NaOH	sodium hydroxide
OEOacr	monoacrylated oligo(ethylene oxide)
OPA	ortho-phthalic dialdehyde
PBS	phosphate buffered saline
PCL	poly(ε-caprolactone)
PEG	poly(ethylene glycol)
PGA	poly(glycolic acid)
PHB	poly(hydroxybutyrate)
pH	potential of hydrogen
pHEMA	poly(hydroxyethyl methacrylate)
pI	isoelectric point
PI	propidium iodide
PLA	poly(lactic acid)
PLGA	poly(lactic-co-glycolic acid)
PP	polypropylene
PTZ	phenothiazine
PU	polyurethane
PVA	poly(vinyl alcohol)

PVDF	poly(vinylidene fluoride)
RCPhC1	recombinant collagen peptide
RGD	Arginine-Glycine-Aspartic acid (Arg-Gly-Asp) tripeptide
RM	regenerative medicine
RGR	relative cell growth rate
ROS	reactive oxygen species
SES	solution electrospinning
SOTA	state-of-the-art
SMC	smooth muscle cell
SUC	solvent uptake capacity
TCP	tissue culture plastic
TE	tissue engineering
TEBV	tissue engineered blood vessels
TERM	tissue engineering and regenerative medicine
TGA	thermogravimetric analysis
TOF	time-of-flight
TPP	triphenylphosphite
UV	ultraviolet
vTE	vascular tissue engineering

Acknowledgements

I am grateful to have had the chance to meet and collaborate with wonderful people along the way. I would like to write some words to everyone that has crossed my path in these past 6 years (or longer) and that has helped in reaching this PhD finish line.

First and foremost, I would like to thank my supervisors, Peter Dubruel, Sandra Van Vlierberghe and Diego Mantovani for giving me this amazing opportunity. I started this journey as a master thesis student in the PBM group under the supervision of Peter and Sandra, and learned about the challenges in the multidisciplinary area of tissue engineering. This sparked my interest and triggered my motivation to continue with a PhD in the PBM group. Within the first months of my PhD, that I had started on a joint project between ULaval and UGhent, Diego offered me the opportunity to also be part of his team at the LBB lab, in Quebec. And so, I became a joint-PhD student. I would also like to thank Diego for believing in my potential to be granted a Vanier Scholarship and to help me through the application, this allowed me to continue my PhD a couple of years longer. I am grateful for the knowledge, experience, guidance and encouragements throughout this project, as well as for the great freedom in planning and following different research ideas. Thanks to them, I have had the chance to come into contact with different research groups, to present at conferences, to set up new collaborations and to have various research stays abroad.

I would like to thank the members of the examination committee for the time and efforts put in reading and reviewing my manuscript, and for their constructive comments that helped me in further improving this PhD manuscript.

I would like to acknowledge the financial support of the FWO for the first part of my PhD, and the Vanier Canada Graduate Scholarship for the final 3 years of my PhD.

I would like to express my deepest gratitude to the PBM group. I am grateful to my (ex-) colleagues for the amazing times that we have had in the past 6 years. I enjoyed the Friday afterworks, the (pool) parties, the conferences, the team buildings, the coffee breaks, the BBQs, the karaoke nights, … But I also like to thank them for their help and support in the lab, it was not always easy being a biomedical engineer in a chemistry lab. Maxime and Jasper, thank you for being the funniest colleagues I could ever imagine, for your friendship, and for the nice time at PBM and outside PBM. I do hope that we will have our old-timer meeting soon. Babs, Coralie and Nathan, the many coffee breaks, the jokes and sarcasm, the BBQs, the holidays toghether and the (pool) parties, I enjoyed every minute of it. Also to Lana, who has become a fixed value when it comes to (short) holidays in Spain to say hi to my grandparents, for her singing talent, for the kayaking trips in Ghent, for the Easter Mondays in the lab, for coming over to the far Dendermonde for NYE, BBQs and

drinks. Also many thanks to Annemie, Lara, Geert-Jan, Liesbeth, Arn, JP, Tom, Aysu, Veerle, Manon, Agi, Jasper D, Lenny, Lobke, Evelien, Laurens, Quinten, Lauren, Anna, Marguerite, Kristyna, Shraavya, Elly and the whole PBM group from the last 6 years, for always being available whenever I had questions, for your company during the breaks, and for your help in sending packages all over the world when I was in Canada.

And of course, I would also like to thank the whole LBB group. Thank you for welcoming me each year as if I had never left for 8 months (or longer). Daniele, for the supervision and the guidance in the Quebec life when I first arrived in Canada. Francesco, for your training, help and support in the lab, in reviewing my (written) work in detail, for always being available when I had questions and for introducing me to Ninkasi. Dimi, for being there at the start of my PhD, for introducing me to the LBB lab, and in how to learn to work with cells and with the bioreactor. Sara, for being an amazingly positive colleague who was always smiling and for a very efficient collaboration in the lab and in writing our review. Dali, for being the best oompaloompa, for helping me through some stressful months, for willing to spend a huge number of hours in the lab together and to make the 16h-days in the lab not too bad. Rafa, Müge, Vale, my gang, I loved our team meetings, lunches and coffee breaks, but even more our drag queen brunches and the multiple dinner dates (and parties) that we had, you girls are amazing. Pascale, thank you for being an indispensable member of the LBB lab and for being my number one supporter when Rouge et Or had a game. Sergio, my dear Mexican friend, thank you for always being there for a talk, for a beer (or two), for some chicken wings and for our weekly dinner dates, for the good laughs and the mental support. And also thank you to Sergio L, Sam, Gab, Masoud, Linda, Leticia, Samira, Souhila, Maria and all the other colleagues from the LBB lab for the nice group atmosphere and in making my research stays in the LBB an amazing experience.

I would like to specifically thank Tim Courtin (NMR), Veerle (PBM), Theo, Joris, Davy, Mario and Tim (Centrale Werkplaats) for the technical support and their creativity in solving problems. In addition, I would like to express my gratitude to Karien, Carine, Shana, Christel, Queenie, Veerle and Paul for their help with my (sometimes very complex) administration and sending packages around the world.

I would like to acknowledge my collaborators: Ian Peeters, Prof. Lieven De Wilde and Prof. Ann Martens for our joint-project on the tendon repair including the co-supervision of Liesbet and Ynse, the *ex vivo* sheep tendon testing and the *in vivo* evaluation of our repair constructs in rabbits; Michael Bartolf-Kopp and Dr. Tomasz Jüngst (fmz lab, Würzburg) for their very warm welcome in Germany, for the fruitful weeks of research and amazing times during this research stay including the many lunches, coffees and walks, and for the efficient writing, working and keeping in touch after my research stay; Marguerite Meeremans and Prof. Catharina De Schauwer for being utmost enthusiastic in agreeing to a last-minute supervision in the final part of Ynse's thesis, for the detailed corrections and feedback on articles and reviews and for their help whenever I had a question or needed a "dummyproof" explanation; Victor Chausse Calbet and Prof. Marta Pegueroles (Barcelona) for their positive reply to the proposed joint-project and the quick delivery of

3D printed scaffolds; Hubert Krzyslak and Prof. Pablo Pennisi for their help, supervision and feedback in our review on muscle, tendon and nerve repair; Dr. Fabrice Bray and Prof. Christian Rolando for the many hours spent explaining how proteomics works until I (think I) finally understood and for always smiling and being positive during our meetings, writing periods and revisions; Dr. Johannes Hackethal and Prof. Heinz Redl (Vienna) for their warm welcome in Austria, and for making my first research stay abroad very interesting and educational; Margot Vansteenland and Prof. Bruno De Meulenaer for sharing their expertise and for training me in the analysis of amino acid compositions.

Next, I would like to acknowledge the support from my friends and rugby family. Firstly, my Rouge et Or teammates, for making me feel at home and for giving me the best souvenirs possible from my stays in Quebec. I loved our training moments, our dinners and (themed) parties, and being part of this team. I've been seeing some of you in Dendermonde, in Europe and outside of Europe, and I have been missing all of you from the moment I left Quebec. Juji, a huge shoutout to you and your parents for "adopting" me into your family, and for literally giving me a home and more importantly, for making me feel at home. Secondly, my teammates from my rugby team in Dendermonde, for being there to train, gym and party together, and for the friendships. And thirdly, to my Belsevens family, for always being there when times were a bit more difficult, for your understanding, and for your encouragements throughout my PhD and especially, for all the tournaments we've played worldwide. The perseverance and hard-working needed in rugby, also helped in accomplishing my PhD studies. Clearing my head at our training sessions was sometimes the only way "not to think about my PhD". In particular, Hanne Boedt, for being my bestie, for the hours we have been training in the gym (and our "psychological sessions"), for the travels, and for the many good souvenirs.

A big shoutout to Joke, Silke, Shari and Loes, who have been and still are the best housemates one can wish for. The list of good moments is too long to explain here, but you know them. I enjoy(ed) coming home and being able to talk, cook, eat, watch movies, go to training, chill in the sun, … And that is mainly thanks to you. It would not have been / be my home without you guys. Loes and Shari, the past couple of months have been stressful, but I could always count on a hug (or a drink, whatever seemed best at the time) and your friendship and support. I would also like to thank Hanne, who was there for me in the good and the stressful moments. Thank you for helping me through these past months, for dealing with my stress-me and breakdowns, for your support and patience, for always believing in me, and for offering me a good distraction when needed, I couldn't have asked for a better motivation to complete this PhD.

And last but not least, I would like to thank my family and in particular, my sister (for the PhD survival kit), my brother, my parents and my grandparents for always believing in me and in doing so, helping me in pursuing my dreams. I am grateful to have you as my family.

Nele Pien, 19th May 2022

Preface

This research project is a joint-PhD project between Ghent University (Belgium) under supervision of Prof. Peter Dubruel and Prof. Sandra Van Vlierberghe (Polymer Chemistry and Biomaterials research group, PBM), and Laval University (Canada) under supervision of Prof. Diego Mantovani (Laboratory of Biomaterials and Bioengineering, LBB). This work was partially supported by the Flanders Research Foundation (Fonds Wetenschappelijk Onderzoek, FWO) and by a Vanier Canada Graduate Scholarship (2019-2022).

As first author of these articles, I conducted their design, validation and writing in collaboration with co-authors as indicated below:

Chapter 1 - Introduction

This chapter serves as an introduction to tubular organs in the human body, their diseases and malfunctions, the current treatment options and regenerative medicine as a viable solution. The PhD objectives are outlined in a final part of this chapter. Parts of this chapter have been published in/submitted as:

N. Pien, S. Van Vlierberghe, P. Dubruel, D. Mantovani. Hydrogels, Processing Techniques and Vascular Tissue Engineering. RSC Biomaterial science. Book series: Biomaterials Science Series, Injectable Hydrogels for 3D Bioprinting. EPUB eISBN: 978-1-83916-398-2, DOI: 10.1039/9781839163975-00207. Published: JUL 2021, Impact Factor: 6.183.

N. Pien, S. Palladino, F. Copes, G. Candiani, P. Dubruel, S. Van Vlierberghe, D. Mantovani. Tubular bioartificial organs: From physiological requirements to fabrication processes and resulting properties. A critical review. Cells, Tissues, Organs. DOI: 10.1159/000519207. Published: AUG 2021, Impact Factor: 2.481. Peer reviewed.

N. Pien, S. Shastry Kallaje, H. Krzyslak, C. De Schauwer, D. Mantovani, S. Van Vlierberghe, P. Dubruel, P. Pennisi. Repair of skeletal muscle, tendon and nerves by tissue engineering: A review of additive manufacturing techniques to meet the structural and functional requirements. In preparation.

Chapter 2 - Design and development of photo-crosslinkable acrylate-endcapped urethane-based precursors

This chapter describes the synthesis and characterization of a series of acrylate-endcapped urethane-based polymers (AUPs). The synthesis and physico-chemical characterization of the AUPs described in this chapter was done by N. Pien, except for the high resolution-magic angle spinning nuclear magnetic resonance (HR-MAS ^{1}H-NMR) spectroscopy measurements, which were performed by J. Delaey (UGent)

using the facilities of Prof. J. Martins (UGent). The processing and application of the developed AUPs will be discussed in other chapters: AUP PCL20k processing by melt electrowriting in Chapter 3; AUP PCL530 and AUP PCL2k processing by solution electrospinning for tendon repair in Chapter 4. The work done by co-authors of the listed publications was on the processing and application and will be described in the corresponding chapters. Parts of this chapter (on the synthesis and characterization of the AUPs) have been published in/submitted as:

N. Pien μ, I. Peeters μ, L. Deconinck, L. Van Damme, L. De Wilde, A. Martens, S. Van Vlierberghe, P. Dubruel, A. Mignon. Design and development of a reinforced tubular electrospun construct for the repair of ruptures of deep flexor tendons. Materials Science and Engineering: C, Volume 119, 111504. DOI: 10.1016/j.msec.2020.111504, Published: SEP 2020, Impact Factor: 7.328. Peer reviewed.

N. Pien, Y. Van de Maele, L. Parmentier, M. Meeremans, A. Mignon, C. De Schauwer, I. Peeters, L. De Wilde, A. Martens, D. Mantovani, S. Van Vlierberghe, P. Dubruel. Design of an electrospun tubular construct combining a mechanical and biological approach to improve tendon repair. Journal of Materials Science: Materials in Medicine, DOI: 10.1007/s10856-022-06673-4, Published: MAY 2022, Impact Factor: 3.896. Peer reviewed.

N. Pien μ, M. Bartolf-Kopp μ, J. Delaey, L. Parmentier, L. De Vos, D. Mantovani, S. Van Vlierberghe, P. Dubruel, T. Jüngst. Melt electrowriting of a photo-crosslinkable poly(ε-caprolactone)-based material into tubular constructs with predefined architecture and tunable mechanical properties. Macromolecular Materials and Engineering, DOI: 10.1002/mame.202200097, Published: MAY 2022, Impact Factor: 4.367. Peer Reviewed.

Chapter 3 - Melt electrowriting as an emerging processing technique for the development of tubular constructs with a predefined architecture

This chapter describes the processing of an AUP PCL20k precursor (synthesis and characterization, see Chapter 2) using melt electrowriting. The MEW processing was conducted by N. Pien in collaboration with M. Bartolf-Kopp within the fmz lab at Würzbürg University (Germany) under the supervision of Dr. T. Jüngst (during a 5-week research stay of N. Pien at fmz). The mechanical evaluation of the developed tubular constructs was executed by N. Pien at the fmz lab, whereas the physico-chemical characterization of the AUP material and the developed MEW constructs was conducted at PBM (UGent). The HR-MAS ^{1}H-NMR spectroscopy measurements discussed in this chapter were performed by J. Delaey (UGent) using the facilities of Prof. J. Martins (UGent). The GPC measurements and the *in vitro* biological evaluation were performed by L. De Vos (UGent) and L. Parmentier (UGent), respectively. Data processing and analysis was done by N. Pien. This chapter has been submitted as:

N. Pien μ, M. Bartolf-Kopp μ, J. Delaey, L. Parmentier, L. De Vos, D. Mantovani, S. Van Vlierberghe, P. Dubruel, T. Jüngst. Melt electrowriting of a photo-crosslinkable poly(ε-caprolactone)-based material into tubular constructs with predefined architecture and tunable mechanical properties. Macromolecular Materials and Engineering, DOI: 10.1002/mame.202200097, Published: MAY 2022, Impact Factor: 4.367. Peer Reviewed.

Chapter 4 - Design and development of a reinforced tubular electrospun construct for flexor tendon repair

This chapter describes the application of two AUP precursors for flexor tendon repair (synthesis and characterization, see Chapter 2), i.e. AUP PCL530 and AUP PCL2k. The AUPs were processed into tubular constructs using solution electrospinning. This project was conducted in collaboration with I. Peeters (University Hospital Ghent). This chapter is based on the work of L. Deconinck and Y. Van de Maele as part of their master thesis, supervised by N. Pien and A. Mignon. The *ex vivo* and *in vivo* testing was performed by I. Peeters under the supervision of Prof. L. De Wilde and Prof. A. Martens (Faculty of Veterinary Medicine, UGent). The *in vitro* biological evaluation was performed by L. Van Damme, L. Parmentier and M. Meeremans (UGent). This chapter has been published in/submitted as:

N. Pien μ, I. Peeters μ, L. Deconinck, L. Van Damme, L. De Wilde, A. Martens, S. Van Vlierberghe, P. Dubruel, A. Mignon. Design and development of a reinforced tubular electrospun construct for the repair of ruptures of deep flexor tendons. Materials Science and Engineering: C, Volume 119, 111504. DOI: 10.1016/j.msec.2020.111504, Published: SEP 2020, Impact Factor: 7.328. Peer reviewed.

I. Peeters μ, N. Pien μ, A. Mignon, L. Van Damme, P. Dubruel, S. Van Vlierberghe, D. Mantovani, V. Vermeulen, D. Creytens, A. Van Tongel, S. Schauvliege, K. Hermans, L. De Wilde, A. Martens. Flexor tendon repair using a reinforced tubular, medicated electrospun construct. Journal of Orthopaedic Research. DOI: 10.1002/jor.25103, Published: MAY 2021, Impact Factor: 3.494. Peer reviewed.

N. Pien, Y. Van de Maele, L. Parmentier, M. Meeremans, A. Mignon, C. De Schauwer, I. Peeters, L. De Wilde, A. Martens, D. Mantovani, S. Van Vlierberghe, P. Dubruel. Design of an electrospun tubular construct combining a mechanical and biological approach to improve tendon repair. Journal of Materials Science: Materials in Medicine, DOI: 10.1007/s10856-022-06673-4, Published: MAY 2022, Impact Factor: 3.896. Peer reviewed.

Chapter 5 - Design and development of a reinforced vascular wall model

This chapter describes the application of synthetic polymers processed into tubular constructs for the development of a reinforced collagen-based vascular wall model. Three different processing techniques were used for the fabrication of the tubular constructs, i.e. solution electrospinning, 3D printing and melt

electrowriting. The MEW processing was performed by N. Pien during a research stay in the fmz lab at Würzbürg University (Germany) under the supervision of Dr. T. Jüngst. The 3DP processing was conducted by V. Calbet at Biomechanics and Tissue Engineering group at Universitat Politècnica de Catalunya (Spain) under the supervision of Prof. M. Pegueroles. The mechanical and biological experiments were performed in collaboration with D. Di Francesco during a research stay at the LBB lab at ULaval (Canada) under the supervision of Dr. F. Copes and Prof. D. Mantovani. The SEM imaging was conducted by Dr. P. Chevallier (LBB lab). The data reported in this chapter will be submitted as an article which is in preparation:

N. Pien, D. Di Francesco, F. Copes, M. Bartolf-Kopp, V. Chausse Calbet, P. Chevallier, M. Pegueroles, T. Jüngst, S. Van Vlierberghe, P. Dubruel, D. Mantovani. Polymeric reinforcements for collagen-based vascular wall models: Influence of the processing technique on the final mechanical and biological properties. In preparation.

Chapter 6 - Design and development of photo-crosslinkable biopolymers with tunable mechanical properties

This chapter describes the methacrylamide modification of collagen bovine skin. The amino acid composition analysis was performed in collaboration with M. Vansteenland, under the supervision of Prof. B. De Meulenaer (Department of Food Safety and Food Quality, UGent). The *in vitro* assays were conducted by N. Pien during a research stay at the LBB lab (ULaval, Canada), under the supervision of Dr. D. Pezzoli. This chapter has been published as:

N. Pien, D. Pezzoli, J. Van Hoorick, F. Copes, M. Vansteenland, M. Albu, B. De Meulenaer, D. Mantovani, S. Van Vlierberghe, P. Dubruel. Development of photo-crosslinkable collagen hydrogel building blocks for vascular tissue engineering applications: a superior alternative to methacrylated gelatin? Materials Science and Engineering: C, Volume 130, 112460, DOI: 10.1016/j.msec.2021.112460, Published: OCT 2021, Impact Factor: 7.328. Peer reviewed.

Chapter 7 - Proteomics as a tool to gain next level insights into photo-crosslinkable biopolymer modifications

This chapter describes proteomics as a tool to identify and localize photo-crosslinkable moieties in the biopolymer's amino acid sequence and within its 3D structure. The proteomics analysis was conducted in collaboration with MSAP (Université de Lille, France) by Dr. F. Bray. The 3D modeling was performed by Dr. T. Gheysens. This chapter has been published as:

N. Pien, F. Bray, T. Gheysens, L. Tygat, C. Rolando, D. Mantovani, P. Dubruel, S. Van Vlierberghe. Proteomics as a tool to gain next level insights into photo-crosslinkable biopolymer modifications. Bioactive Materials, DOI: 10.1016/j.bioactmat.2022.01.023. Published: JAN 2022, Impact Factor: 14.593. Peer reviewed.

Introduction: Biomaterials and processing techniques for the fabrication of tubular constructs serving regenerative medicine

This chapter serves as an introduction to tubular organs in the human body, their diseases and malfunctions, the current treatment options and regenerative medicine as a viable solution. The PhD objectives are outlined in a final part of this chapter. Parts of this chapter have been published in/submitted as:

N. Pien, S. Van Vlierberghe, P. Dubruel, D. Mantovani. Hydrogels, Processing Techniques and Vascular Tissue Engineering. RSC Biomaterial science. Book series: Biomaterials Science Series, Injectable Hydrogels for 3D Bioprinting. EPUB eISBN: 978-1-83916-398-2, DOI: 10.1039/9781839163975-00207. Published: JUL 2021, Impact Factor: 6.183.

F. Copes, N. Pien, S. Van Vlierberghe, F. Boccafoschi, D. Mantovani. Collagen-based tissue engineering strategies for vascular medicine. Frontiers Bioengineering and Biotechnology, Volume 7, Issue 166, DOI: 10.3389/fbioe.2019.00166, Published: JUL 2019, Impact Factor: 5.890. Peer reviewed.

N. Pien, S. Palladino, F. Copes, G. Candiani, P. Dubruel, S. Van Vlierberghe, D. Mantovani. Tubular bioartificial organs: From physiological requirements to fabrication processes and resulting properties. A critical review. Cells, Tissues, Organs. DOI: 10.1159/000519207. Published: AUG 2021, Impact Factor: 2.481. Peer reviewed.

N. Pien, S. Shastry Kallaje, H. Krzyslak, C. De Schauwer, D. Mantovani, S. Van Vlierberghe, P. Dubruel, P. Pennisi. Repair of skeletal muscle, tendon and nerves by tissue engineering: A review of additive manufacturing techniques to meet the structural and functional requirements. In preparation.

1.1 Introduction

Bioengineering is a discipline in which engineering principles are applied to biological systems and biomedical technologies. One of the main goals of bioengineering is to reproduce, repair, or recapitulate tissues and organs, or their functions. In bioengineering, geometries are directly inspired by anatomy, while properties closely follow physiological functions. From an anatomical point of view, there are five fundamental levels of organization in the human body, from the simplest one to the most complex: (i) the cellular level, (ii) the tissue level, (iii) the organ level, (iv) the organ-system level, and (v) the organism level [3]. Each tissue is a complex structure composed by multiple cell types immersed in multiple sets of proteins dispersed in an extracellular matrix (ECM) [4]. The cells in a tissue work together in an orchestrated manner to accomplish specific functions. An organ is made of various types of tissues, and intrinsically, of several types of cells. Each organ is characterized by complex structural, mechanical, and motility patterns responsible for one or more specific physiological functions [5,6].

Diseases, injuries, and malfunctions of one (or more than one) of the organs affect and decrease the patient's quality of life, and in the worst case, lead to death [7]. The type of clinical treatment depends on the severity of the injury, the type of disease, and the medical history of the patient. As a first option, drug therapy and/or other non-invasive therapeutic treatments are privileged. However, when the progression of the disease advances, surgical intervention, including tissue transplantation or substitution, is unavoidable. Current transplantation and substitution techniques are based on the use of (i) autologous, or (ii) heterologous tissues, or (iii) synthetic prostheses, but these do not always represent a viable option [8,9]. Substitution or transplantation of autologous tissues is not possible in case of previous harvesting and/or pathological degenerative conditions. As for heterologous tissues, the main limitation is a shortage of suitable and available tissues [4,5,7,10]. In the past decades, synthetic prostheses were developed in the hope of tackling the above-mentioned shortcomings. However, there is an important mismatch between anatomical and mechanical requirements, and other issues can be found in the required biological properties and long-term expected patency [9]. Therefore, although organ shortage is already addressed by reparative [11–13] (through implants, artificial organs and devices) or regenerative [14] (cell-containing structures or cell-based therapies) medicine, clinical complications still limit the success of the implantation. In an attempt to improve this success rate and increase the overall clinical performance, tissue engineering and regenerative medicine (TERM) aim to restore the functional and structural properties of diseased or damaged tissue, while maintaining and/or improving tissue performance [15]. Different approaches have been explored, all relying on the use of cells, scaffolds, or their combination [5,8,16]. Through further process engineering, the resulting constructs are expected to mimic the structure (i.e. the internal architecture) and the complex cellular microenvironment of native tissues [4,17]. Bioartificial organs (BAOs) constitute the expected outcome of designing and developing functional organs from regenerative medicine (RM) strategies. In order to be able to mimic the native organs to the greatest extent possible, researchers have

to look in detail into the anatomical hierarchy of tissues [18] and their biological and mechanical properties [4,19–21].

Atala *et al.*, 2012 [22] have proposed four levels of classification according to a defined scale of increasing complexity: (i) flat tissue structures, (ii) tubular structures, (iii) hollow, non-tubular, viscous structures, and (iv) complex solid organs. Despite the available knowledge (both on the engineering and the biology side) and the accessible technologies (both the standard and the more advanced ones), there are still plenty of challenges in designing and developing more complex structures. Therefore, this chapter will point out the current situation considering these challenges and can hopefully open a new path for future studies. More precisely, this chapter will focus on the second group, namely the tubular structures.

The second group can be further subdivided into (i) non-hollow and (ii) hollow tubular structures. Skeletal muscles, tendons, and nerves belong to the category of non-hollow tubular structures. Skeletal muscle could be considered a special case within this group, because the muscle consists of tubular cells (the muscle fibers) arranged hierarchically in cylindrically shaped bundles (the muscle fascicles) [23,24]. The respiratory, digestive, urinary, and circulatory system [3,9] can be placed in the category of hollow tubular organ systems. Their main function is to transport fluids, metabolites, and gases from, to, and through organs [5,22].

To engineer these tubular systems, biomaterials are processed into a tubular structure that is used as such or combined with cells and allowed to mature *in vitro*, before implantation. Various processing techniques to fabricate tubular constructs have already been proposed [9]. Such processing techniques can be grouped into (i) conventional and (ii) advanced techniques. Some examples of conventional laboratory techniques are gas foaming, moulding, solvent casting, and a few others. More advanced techniques, for reproducible results and adapted to clinical transfer, include three-dimensional (bio)printing (3D(B)P), solution electrospinning (SES), and melt electrowriting (MEW) [6,9,25,26]. Each of them has its own pros and cons - they will be discussed here below - which will influence the resulting properties of the fabricated tubular construct. Likewise, the choice of the processing technique depends on the specific requirements for which each BAO has been designed for. These biological and mechanical requirements depend, in their turn, on the anatomical hierarchical structure of the different tissues and on the physiological functions related to the anatomy of a specific organ. Consequently, there is an underlying correlation between (i) the requirements to match the restoration of the physiological functions, (ii) the various processing techniques to fabricate a tubular construct and (iii) the obtained properties of the fabricated construct.

In this chapter, the development of functional tubular constructs from biomaterials and/or cells will be described (as depicted in the flow chart, Figure 1.1). More specifically, the hierarchical anatomical structure of the non-hollow and hollow tubular organs will be described (section 1.2), together with the complex

physiological functions and the mechanical and biological requirements of each one. Then, the diseases and malfunctions of tubular tissues will be described (section 1.3), followed by the current treatment options (section 1.4). The state-of-the-art (SOTA) of the biological model (section 1.5.2), the biomaterial selection (section 1.5.3) and the manufacturing process to develop tubular constructs (Section 1.5.4) will be discussed as well. In the final part, the clinical translation potential (section 1.5.5) and the perspectives of regenerative medicine (section 1.5.6) will be discussed.

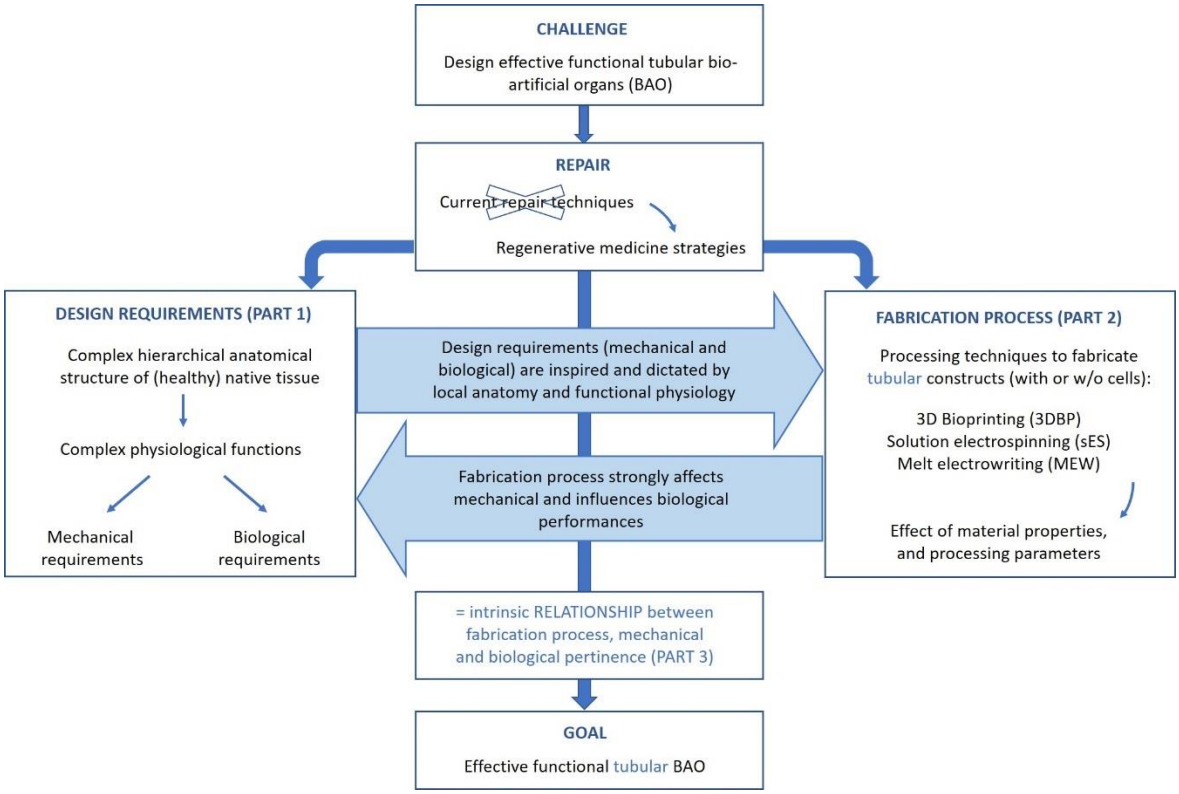

Figure 1.1. Flow chart. Part 1: Requirements dictated by anatomical and physiological concerns. Part 2: Strategies for the fabrication of tubular constructs for the regeneration of tubular organs. Part 3: Relationship between the process, cells, mechanical and biological performance.

1.2 The anatomical structure and physiological functions of tubular organs

a. Non-hollow tubular system: Tendon

Tendons are passive, relatively inelastic structures which have as main function to effectively transmit force from muscle to bone and enable body movement [1,27]. However, specific tendons, such as the human Achilles tendon or the equine superficial digital flexor tendon, have additional functional specializations that allow energy storage [28–30].

Tendons are highly organized structures consisting of parallel oriented collagen fibers (mainly collagen type I) embedded in an extracellular matrix (ECM). This ECM is composed of proteoglycans, glycoproteins, and elastin [27]. Figure 1.2 shows the hierarchical structure of the tendon, in which collagen fibers assemble into

subunits of increasing diameter. First, three collagen molecules form a triple helix (i.e., tropocollagen). Subsequently, five tropocollagen units form a microfibril, which are linked together to form a fibril. Depending on the functional role of the particular tendon, the diameter of these fibrils can range from 10 to 150 nm [1,31]. Different fibrils are grouped into fibers (i.e. primary bundle) and these are joined together in the fascicle (i.e. secondary bundle). Between the primary and secondary bundles, the endotenon is present, a cell-rich layer that facilitates sliding between fibers and/or fascicles. These fascicles are bundled together to form the tertiary bundles, which are surrounded by the epitenon (i.e., the fibrous sheath containing blood vessels and tracts for the nerves and lymphatics) and form the entire tendon [32]. Finally, the epitenon may be surrounded by a membrane or synovial sheath that facilitates smooth gliding of the tendon towards surrounding structures [31]. It ensures minimal friction and preserves the position of the tendon during muscle contraction.

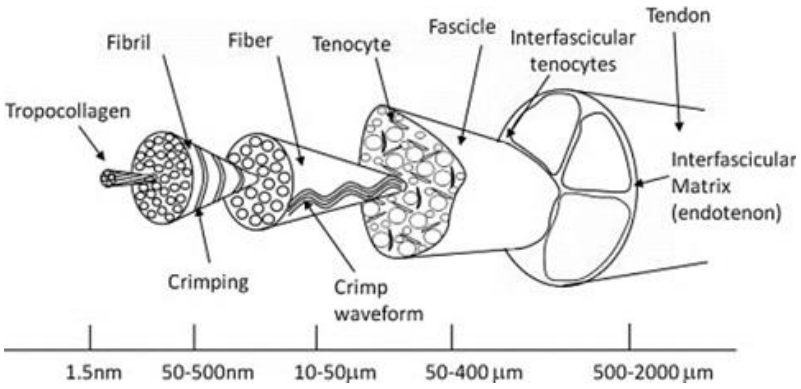

Figure 1.2. Schematic hierarchical structure of a tendon with subunits of increasing diameter (from 1.5 nm to 500-2000 μm). From the smallest subunit onwards, the tendon consists of: (i) collagen molecules or tropocollagen, (ii) fibrils, (iii) fibers, (iv) fascicles composed of tenocytes, and (v) interfascicular matrix or endotenon [1].

The main component of tendons is water, which accounts for 55 to 70% of the tendon's wet mass [1]. Collagen molecules count for 60 to 85% of the dry mass of tendons [1]. While tendons are predominantly composed of type I collagen (more than 95%), the endotenon is primarily composed of type III collagen (less than 5%) [32,33]. Collagen is produced and secreted by specialized fibroblasts (i.e., tenocytes) located in the tendon. These fibroblasts are arranged in a layered composition and parallel orientation, which maximizes tensile strength [31]. When subjected to tensile stress, tenocytes stretch along the collagen fibrils in the form of longitudinal arrays [34]. In addition, they produce the ECM and assist with the orientation of the newly synthesized fibrils [35]. Furthermore, they control the degradation and remodeling processes of the ECM structure, which illustrates the continuous interaction between the tenocytes and the ECM [35]. Blood supply is also very important, although it is not as abundant present as in muscle and bone. Blood accounts for only 1 to 2% of the ECM [34]. Blood supply is directly related to metabolic activity, which means it is essential and even increased during the healing process after an injury. Furthermore, tendons have a very rich neural network and are often innervated by the muscles to which they are connected or by the local cuticular nerves [34]. The sensory innervation of tendons is of particular interest when considering tendinopathies and tendon repair [36].

b. Hollow tubular system: Blood vessel

As introduced above, requirements for TERM applications are defined considering the organ anatomy and physiology. The wall of the five hollow, tubular organs is composed of different layers. In general, four layers can be distinguished including (i) mucosa, (ii) submucosa, (iii) muscularis externa, (iv) adventitia and/or serosa layer (Figure 1.3, left) [3], however, in some tubular systems, the submucosa and mucosa layer act as one layer (and thus only three layers are distinguished). A comparison between the basic layers of each tubular system (i.e. trachea, esophagus, intestines, urethra and ureter, and blood vessels) is shown in Figure 1.3. These four layers consist of various cell types and ECM, which are organ specific. Each kind of cell and ECM component has a specific role to perform individually, but also as a multi-layered structure in its whole, in such a way that they enable the physiological functions of the tubular organ.

The vascular wall architecture is highly complex and imparts unique biomechanical properties, challenging the development of vascular wall models that can withstand the pulsatile nature, high pressure and high flow rate of the bloodstream. The arterial wall is a three-layered structure composed of an intima (i.e. mucosa and submucosa), media (i.e. muscularis externa) and adventitia (Figure 1.3) [37]. Each layer exhibits specific histological, biochemical, and functional characteristics. Therefore, each layer contributes in a unique way to maintain the vascular homeostasis and to regulate the vascular response to stress or injury. In addition to the structure and composition of the vascular wall, another important aspect when developing a model of the vascular wall is the physiology and the functions of these different layers (*vide infra*, Table 1.1).

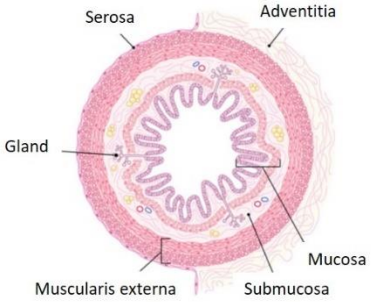

	Trachea	Esophagus	Intestines	Urethra and ureter	Blood vessels
Mucosa	Pseudostratified ciliated epithelium	Pluristratified, squamous epithelium, lamina propria and muscularis mucosa	Simple epithelium, lamina propria and muscularis mucosa	Epithelium and lamina propria	Epithelium (endotelium)
Submucosa	Connective tissue with seromucous glands	Connective tissue with branched tubular glands	Connective tissue with glands		
Muscularis externa	Smooth muscle and connective tissue reinforced with hyaline cartilage	Alternation of smooth and striated muscle cells	Connective tissue with peristaltic smooth muscles	Inner longitudinal and outer circular muscle layer	Connective tissue with smooth muscle
Adventitia and/or serosa		Connective tissue	Vascularized connective tissue	Connective tissue	Connective tissue

Figure 1.3. Anatomical structure of hollow tubular organs. Left: General structure of hollow tubular organs (Image adapted from UNIFAL-MG, Histologia interatva, https://unifal-mg.edu.br). Right: Comparison of the wall structure of the trachea, esophagus, intestines, urethra, ureter, and blood vessels.

Before 1980, studies addressing the control of vasomotor tone (i.e. action of vasodilation or vasoconstriction) mainly focused on the tunica media. In the late 1970s, it became evident that the tunica intima also played an important role in vasomotor responses [38]. Only recently, the tunica adventitia has been studied as a potential contributor to vascular function.

The tunica intima, composed of a mono-layer of endothelial cells (ECs), is in direct contact with the blood and therefore has a critical role in all aspects of tissue homeostasis [39–41]. Its main function is to provide structural integrity of the blood vessel by forming a smooth, friction-reducing, semi-permeable membrane. The endothelial cells are a significant contributor to the regulation of vasomotor tone, under the influence of physical and chemical factors originating from the lumen or from surrounding tissues [41]. Endothelial cells produce and release vasodilator (e.g. nitric oxide and prostacyclin) and vasoconstrictor substances (e.g. endothelin and platelet-activating factor) [41]. Next to this, the ECs are not only involved in fibrinolysis and thrombolysis but they also play a role in coagulation, inflammatory and immunological processes (including platelet activation, adhesion and aggregation, leukocyte adhesion and smooth muscle cell (SMC) migration and proliferation) [39,41].

The tunica media mainly consists out of elastin, collagen and SMCs. Elastin functions primarily as an elastic reservoir and distributes stress homogenously throughout the wall and onto the collagen fibers. The function of the vascular smooth muscle is to produce 'active tension' under vasomotor stimulation and thus to alter the total tension in the wall and change the diameter of the lumen [40,42]. The vascular SMC is activated by the sympathetic nervous system when vasoconstriction (and increase in blood pressure) is required. Changes in vascular diameter depend on the contractile activation and interaction of actin with myosin in vascular smooth muscle cells [40,43]. In addition to this, the vascular SMC synthesizes and organizes the complex and unique ECM that defines the mechanical properties of the vascular wall [43]. In this context, the vascular SMC monitors the changing tensional forces within the wall and adjusts the ECM matrix accordingly [44]. Wagenseil *et al.* stated that achieving and maintaining the functional elastic modulus may be the main physiological regulator of ECM gene expression in the vessel wall [44].

As the outer layer of the vascular wall, the tunica adventitia mainly acts as a protective and supportive layer [44]. However, Stenmark *et al.* describe the tunica adventitia as the most complex compartment of the vessel wall, that can act as a biological central processing unit that integrates key regulators of the vessel wall function [45]. Moreover, the resident adventitial cells (i.e. fibroblasts, immune cells and progenitor cells) are often the first to be activated and play a key role in the modulation of vascular tone and the restructuring of the vessel wall [38,45]. In response to vascular stresses (including hormonal, inflammatory and environmental stresses), adventitial fibroblasts undergo functional changes that include proliferation, differentiation, production of ECM proteins and adhesion molecules, and the release of reactive oxygen species (ROS), growth factors and matrix metalloproteinases (MMPs) [46,47]. The latter directly affect the tunica media SMC tone and growth [45].

1.3 Diseases and malfunction of tubular tissues

a. Non-hollow tubular system: Tendon

Two partially oval/round tendons that rupture most often, are the Achilles tendon and the deep flexor tendons. Tubular tendons respond equally to tensile loads with parallel collagen patterns. In addition, the cross-sectional area is proportional to the maximum isometric force of the muscle [34]. The Achilles tendon provides a connective tissue link between the gastrocnemius and soleus muscles and the *os calcaneus*. The two main blood vessels supplying the Achiles tendon, are the posterior tibial artery that supplies both the proximal and distal sections, and the peroneal artery that supplies its middle section [30,48]. The Achilles tendon is innervated mainly by the sural nerve, with minor contributions from other smaller branches of the tibial nerve [30]. It is the strongest and thickest tendon in the human body. As such, force measurements have shown that the tendon is loaded with up to 9 kN during running, which is 2.5 times the body mass. The Achilles tendon is the best example of an energy storage tendon as it centralizes the force of different muscles [34]. The deep flexor tendons extend from the forearm through the wrist and across the palm, providing flexion to the fingers [33]. This is in contrast with the extensor tendons, which provide extension to the fingers. The flexor tendon structure of the hand consists of the tendinous extensions of the flexor muscles of the forearm which attach to the small bones of the thumb and fingers. In addition, the deep flexor tendons are subjected to greater flexion during movement and are therefore typically surrounded by a vascularized synovial sheath [49]. The presence of synovial fluid compensates for the limited vascular supply compared with other tendons (such as the Achilles tendon) [50]. In addition, synovial cells are present in this tendon sheath and provide lubrication to reduce friction during movement and loading, which supports the tendon to glide smoothly and efficiently [32,33,35].

Tendon injuries are painful, persistent, and can significantly affect the quality of life of patients who had inadequate healing or unsuccessful treatment [51]. More than 4 million cases of tendon injuries are reported annually worldwide [52]. Tendon injuries to the hand, in particular, are amongst the most common tendon disorders in the human body. Typically, flexor tendon injuries of the hand account for a significant proportion of trauma emergencies, affecting one in 2700 people each year [50]. The hand, as a performing unit of the human body, is essential in daily life, including sport activities and occupations [53]. For this reason, the tendons of the hand are often subjected to chronic overuse and ruptures. These injuries can have a significant impact on hand function. Early treatment with optimal recovery is critical to prevent permanent dysfunction [54].

b. Hollow tubular system: Blood vessel

Cardiovascular diseases (CVDs) are the leading cause of mortality worldwide, responsible for over more than 17.9 million deaths annually. Moreover, in the European region, 48% of all deaths are caused by CVDs (Figure 1.4) [2]. Cardiovascular diseases are disorders of the heart, vascular diseases of the brain and diseases of blood vessels. They can be divided into two main groups: i) CVDs due to atherosclerosis, ii) other CVDs. Ischaemic heart disease or coronary artery diseases (e.g. heart attack), cerebrovascular disease (e.g. stroke), and diseases of aorta and arteries including hypertension and peripheral vascular disease can be listed into the first group. On the other hand, congenital heart disease, rheumatic heart disease, cardiomyopathies and cardiac arrhythmias are examples of other CVDs.

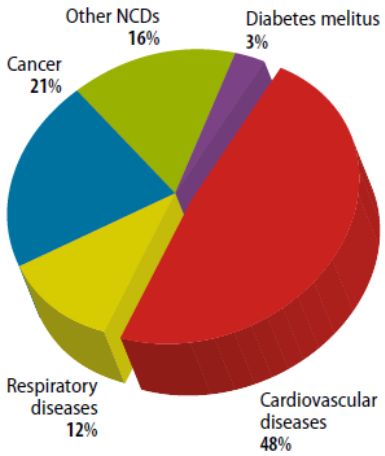

Figure 1.4. Distribution of global non-communicable diseases (NCDs) by cause of death for both sexes. This figure is obtained from World Health Organization, Global Atlas on CVD prevention and control [2].

Atherosclerosis is known as the underlying disease mechanism in blood vessels that results in coronary heart disease and cerebrovascular disease. It is responsible for most of CVDs, indirectly causing half of the deaths in the Western world. Atherosclerosis is a complex pathological process that takes place in the walls of the blood vessels [2]. The development mechanism of atherosclerosis is not yet completely understood but is believed to occur in progressive steps: i) the endothelium is injured, ii) lipids accumulate and oxidize in the tunica intima, iii) smooth muscle cells proliferate and a fibrous caps forms, and iv) the plaque becomes unstable. The presence of plaques not only stiffens the artery wall which in turn, results in hypertension (i.e. chronically elevated blood pressure), but it also constricts the vessel and causes the arterial walls to tear and ulcerate [55]. Various factors promote the process of atherosclerosis, including behavioral risk factors (i.e. tobacco use, physical inactivity, unhealthy diet, harmful use of alcohol), metabolic risk factors (i.e. raised blood pressure, raised blood sugar, raised blood lipids, overweight and obesity) and other risk factors (i.e. poverty and low educational status, advancing age, gender, inherited genetic disposition, physiological factors) [2,56]. These factors play a key role in the disease mechanism of atherosclerosis and need to be lowered to prevent heart attacks and strokes.

1.4 Current treatments of diseased or injured tubular tissues

a. Non-hollow tubular system: Tendon

Current surgical interventions include suture techniques (with needle and thread) or replacement tissue (i.e., biological and synthetic grafts) to repair tendon injuries. To date, none of these methods offer a long-term solution because of the significant drawbacks limiting their success. Repaired tendons do not regain their full functionality and strength [57–59]. Ideally, a healing response should be induced at the injured tendon

ends consisting of a repair site with low friction and minimal volume [33]. Adhesions are a frequently observed complication after tendon injury [60] as a result of the non-organized collagen production during the first phase of the healing process. Due to this scar tissue formation, injured tendons heal slowly, and a long recovery period is often required. In addition, inflammation plays a critical role in tendon injury and healing [61]. When surgical material is used, a strong inflammatory reaction might be triggered with inflammatory cells being attracted to the injured site. Following these inflammation and adhesion processes, the repaired tendon will be unable to regain its original mechanical properties, including ultimate tensile strength and elasticity. The latter illustrates how challenging it remains to realize regeneration instead of repair and restore the original mechanical properties of tendon by preventing the formation of adhesions and inflammation.

b. Hollow tubular system: Blood vessel

CVDs are mostly preventable although certain individuals are at a higher risk for CVD development as a direct result of a genetic predisposition. Nevertheless, the number of deaths caused by CVDs continues to increase mainly because preventive measures are inadequate [2]. Treatments for CVDs vary according to the affected body part and the medical history of the patient. In a first phase, medical drug therapy is often recommended in combination with lowering of some risk factors (e.g. smoking, unhealthy lifestyle). Yet, for many people these measures are not enough, and a surgical approach is needed. Balloon angioplasty and (drug releasing) stents will be deployed. Angioplasty is a technique that is based on a minimal surgical invasion to widen narrowed (i.e. stenosis) or obstructed arteries or veins. Even though angioplasty temporarily clears the blood vessel lumen, restenosis often occurs. Therefore, very often, angioplasty is combined with the insertion of a stent. A stent is a metal or plastic lumen-shaped structure that is inserted into the newly dilated vessel to keep the vessel open after the surgical intervention. However, when the disease is too advanced, angioplasty and stenting are not sufficient and other measures should be taken. General strategies in the surgical treatment of severe lesions include bypassing the obstructed vascular segments. Specific examples include coronary artery bypass grafting (CABG), or major arterial reconstruction procedures (i.e. aortic reconstruction of peripheral bypass) with autologous, synthetic or cryopreserved materials [62].

Given the limitations in available or suitable autologous vascular grafts (i.e. lack of tissue donors, previous harvesting or anatomical variability) and the higher complication rate with currently used synthetic materials (i.e. rejection, compliance mismatch), the search for a truly ideal conduit continues [62–65]. In this context, tissue engineering and biomaterial design have gained increasing interest for vascular graft application and in the development of *in vitro* models [11,66].

1.5 Tissue engineering and regenerative medicine as a viable solution

1.5.1 Principle of tissue engineering and regenerative medicine

To overcome the challenges encountered in currently employed treatments, and moreover, to improve success rates and enhance overall clinical performance, research has focused on tissue engineering (TE) and regenerative medicine (RM) approaches. The main goal of TERM is to develop methods to regenerate, repair, or replace damaged or diseased cells, tissues, or organs while maintaining and/or improving their performance [24,67]. This multidisciplinary research area combines expertise from developmental biology, materials science, cell biology, engineering and medicine.

To regenerate, repair, or replace a damaged tissue, it is critical to understand the macro- and microstructural architecture and functions of the tissue. Regardless of the complexity of the tissue being repaired, TERM approaches typically involve various combinations of biomaterials, cells, and bioactive compounds that are processed into a construct that attempts to mimic the functional unit of the tissue [68–71]. This chapter focuses on advances in TERM, which enable efficient repair of non-hollow and hollow tubular structures including tendon and blood vessel. Given recent advances in additive manufacturing technologies (section 1.5.3), the approach of this chapter is to describe how anatomical structure and function should serve as the basis for efficient 3D design that considers both micro and macro aspects of these tissue types.

a. Non-hollow tubular system: Tendon

A particular challenge in tendon TE approaches is the fabrication of constructs with suitable mechanical properties. Tendons are stiff and resilient structures that have a high tensile strength: they can stretch up to 4% before damage occurs [30]. They have also high anisotropic mechanical properties: they ensure that the tendon is stiff along its long axis and can withstand its predominantly uniaxial loading environment by transmitting muscle forces along the length of the tendon to the skeleton. Actin and myosin are present in resident tenocytes, while the tendon itself may also have an inherent contraction-relaxation mechanism to regulate force transmission [30]. Gomes *et al.* have listed some values on the mechanical properties of tendons [1], that are also described in Table 1.1.

Besides the micro- and macrostructure of the tendon, the biochemical and cellular structure should be taken into account as well in order to achieve its physiological functions. An overview of the anatomical key points, the physiological functions and the mechanical as well as biological requirements for the construct design is described in Table 1.1.

b. Hollow tubular system: Blood vessel

The four main factors to be considered in order to develop a successful vascular wall model are: i) a scaffold that can support the cells, ii) an appropriate cell population, iii) the right biomolecules (such as growth

factors), and iv) physical and mechanical stimuli to influence the proper development of the construct [72]. The cellular composition within each layer of the vascular wall is described above (section 1.2.b). The mechanical properties of the vascular wall include i) a highly resilient wall where a large proportion of energy input during systolic inflation will be recovered by elastic recoil, ii) low hysteresis (i.e. low energy lost during the inflation-deflation cycle) and iii) nonlinear elasticity characterized by stiffening with increasing pressure to protect the wall from rupture [44]. Thus, one of the key factors in the development of a physiologically-functional vascular wall model is elasticity. This property allows arteries to absorb pressure waves that come with every heartbeat. In close relation to this, contractility can be seen as another key function of arteries, that is controlled by the autonomic nervous system.

Human coronary arteries have a compliance of 4.5 - 6.2% change in diameter for a pressure increase from 80 to 120 mmHg, a burst pressure of 2031 - 4225 mmHg, a maximum stress of 1.44 ± 0.87 MPa, a maximum strain of 0.54 ± 0.25 and a physiological elastic modulus of 1.48 ± 0.87 MPa [64,73–79]. However, it should be noted that these characteristics depend on the applied mechanical testing set-up and protocols. Therefore, some variation on data can be found in literature. Moreover, the mechanical properties of blood vessels also vary depending on their location in the human body and their function, as has been described in more detail in the work of Awad *et al.* [80] and Camasao *et al.* [79]. As an example, in the work of "Mc Donald's Blood Flow in Arteries", reported values on the pressure-strain elastic (Peterson) modulus (E_p) of human arteries range between [52-118] kPa, depending on the type of artery and the age of the patient [78]. This can be translated to incremental (~ Young's) elastic modulus by taken into account the diameter and the thickness of the blood vessel. As an example, for the abdominal aorta of a human aged 27 years old (diameter of 13.2 mm and thickness of 1.59 mm) [78], an E_p of 52 kPa corresponds to an incremental elastic modulus of 216 kPa. These reported values are much lower than data described in other references, where elastic moduli of 1 MPa are reported [64,73–77]. This should be considered when comparing the mechanical properties of the engineered artery and the healthy human artery. An overview of the anatomical key points, the physiological functions and the mechanical as well as biological requirements for the construct design can be found in Table 1.1.

c. Summary of design requirements defined by the anatomy and physiology of the tissue

The design requirements for TERM applications are defined considering the anatomy and physiology of the organ in question (section 1.2). Each organ has a typical hierarchical structure and is composed of different cell types and a tissue-specific ECM. Each cell type and ECM component has a specific task to perform, both individually and as part of the overall structure, so that they enable the physiological functions of the organ in question. These important anatomical points and physiological functions in turn lead to very specific mechanical requirements (MR) and biological requirements (BR) that should be considered in the design of the constructs (i.e., the tubular structure comprising biomaterials and/or cells). In addition, it is crucial to investigate the correlations that exist between (i) the anatomy and hierarchical structure, (ii) the physiological

function and the (iii) mechanical and (iv) biological properties of the tissue. Table 1.1 provides an overview of these four important factors for tendons and for blood vessels. This table forms the basis for the following sections, which focus on the correlation of these factors in a current review of strategies to guide tendon repair and vTE.

Table 1.1. Anatomical key points, physiological functions and mechanical and biological requirements per system.

	Anatomical key points	Physiological functions	Construct design: Mechanical requirements (MR)	Construct design: Biological requirements (BR)	References
Musculoskeletal system (Tendons)	- Highly organized connective tissues consisting of parallel orientated collagen fibers embedded within an extracellular matrix (containing cells, proteoglycans, glycoproteins and elastin). - Three collagen molecules form a triple helix (i.e. tropocollagen), five tropocollagen entities constitute a microfibril, that in turn form a fibril, fibrils are grouped into fibers (primary bundle) and then assembled into a fascicle (secondary bundle), with an endotenon in between these two layers, and fascicles are bundled together to form the tertiary bundle, surrounded by the epitenon. - The tendon cells are tendon-specific stem cells and specialized fibroblasts or tenocytes.	- Store elastic energy (through reversible stretching of collagen molecules). - Withstand large forces and assure effective load transmission between muscle and bone. - Act as a buffer by absorbing external forces to limit muscle damage. - Support to the stability of the joints.	Strongly dependent on the type of tendon and the exerted load. 1. It should have appropriate mechanical properties (general): max. strengths [13 - 300] MPa, elastic modulus [4 - 8] GPa, strain and modulus at failure [6 - 50]% and [0.065 - 8] GPa. Deep flexor tendons: Young's modulus [3.1 - 5.0] MPa, ultimate stress 4 MPa, ultimate strain [4 - 10]% and tendon toughness [1000 - 4500] J/kg . 2. It should allow the crimping mechanism to stretch and recoil: protects the collagen fibers and relevant stress-strain properties (up to 8-10% before macroscopic failure). 3. It should show appropriate levels of fiber sliding and degree of rotations (depending on the type of tendon). Should not show any gap formation in the repair zone.	1. It should mimic the hierarchical organization and fiber orientation. Remodeling of the tendon: tenocytes produce collagen and thus play a role in the crimping mechanism and collagen fiber deformation; use of bioactive components and mechanical stimulation to guide the remodeling. 2. A limited blood supply is very important for metabolic activity; and innervation. 3. Minimal scar formation (minimal adhesion formation and inflammation) during healing.	[1,36,81–88]
Circulatory system (Blood vessels)	- Arteries: D = [5-10] mm and T = 1 mm, veins: D = [5-20] mm and T = 0.5 mm. - It consist of 3 layers: (1) **tunica intima**, most inner layer, in direct contact with blood, that consists of 1 layer of endothelial cells aligned in the direction of the blood flow and an underlying basal lamina, (2) **tunica media**, composed out of different layers of mostly circularly arranged smooth muscle cells in an ECM of collagen, elastin and proteoglycans, (3) **tunica adventitia**, composed of a dense network of collagen fibers that include fibroblasts and fibrocytes, this layer is infiltrated with nerve fibers, lymphatic vessels, and sometimes a network of elastic fibers and the vasa vasorum. - The tunica media is separated from the tunica intima and tunica adventitia by an **internal and external elastic lamina.**	- Arteries: carry blood away from the heart, veins: carry blood towards the heart. - 3 layers: repairing, remodeling and maintaining the blood vessel structure and function (i.e. transport of oxygen, nutrients, hormones and cellular waste products throughout the body). - **Tunica intima**: critical role in tissue homeostasis, thrombo-resistant barrier to enable laminar blood flow, regulates transport of substances across endothelium, controls vessel tone, platelet activation, adhesion and aggregation, and leukocyte adhesion. - **Tunica media**: regulates circulatory dynamics by providing contractile and relaxation response, and muscle tone, produces 'active tension' under vasomotor stimulation, alters the total tension, synthesizes and organizes ECM of the vascular wall. - **Tunica adventitia**: reinforces the vessel and enables anchoring to surrounding tissue, prevents vessel rupture and pulsatile deformation, responds to vascular stresses.	1. It should not leak. 2. It should withstand physiological pressures; Should be non-linear elastic, characterized by stiffening with increased pressure to protect the vessel wall from rupture (elastic modulus: [0.2-2] MPa, burst pressure: [2031-4225] mmHg, compliance: [4.5 - 6.2]% for a pressure increase from 80 to 120 mmHg, max. stress: [1-2] MPa, max. strain: [0.25-0.75]). 3. It should be highly resilient, a large proportion of energy input during systolic inflation should be recovered by elastic recoil; Should induce low hysteresis during inflation - deflation cycle.	1. It should consist of a smooth, friction-reducing and semi-permeable membrane (i.e. endothelium, tunica intima) that is in contact with blood; Should be non-thrombogenic. 2. It should also mimic the tunica media and tunica adventitia. 3. It should respond to vasomotricity.	[41,43,44,62,63,73,76,78,79,89–102]

1.5.2 The biological model: Cells and bioactive compounds

As highlighted in the previous sections, cells play an important role in the regeneration of damaged tissue. Therefore, cells are very often used as part of repair strategies, in combination with materials, or as a cell-based therapy. Depending on the type of tissue to be repaired or regenerated, specific cells are selected to achieve the appropriate physiological functions. For tendon repair, mainly tendon-specific stem and progenitor cells have been investigated in combination with autologous tenocytes and/or other co-cultures [103], which have been shown to increase collagen production and restore 3D collagen structure for both cell therapy treatments and 3D scaffolds [70,104]. Straightforwardly, the application of vascular cells (i.e. ECs, SMCs and FBs) is of great importance for vTE, and has been evaluated over the years [105]. In the simplest form, mono-culture systems using only one vascular cell type have been studied [106–108]. These systems were too simplified and were only useful to help understanding the main mechanism of only one cell type. Therefore, the use of mono-culture systems has evolved to the use of more complex, co-culture systems combining multiple human vascular cell types [109,110]. It is important to study the different populations of cells and evaluate their interactions in order to understand the mechanisms underlying tissue establishment and physiology [111,112]. In case of vascular wall modeling, the three different vascular cell types (i.e. ECs, SMCs and FBs) combined into a (triple) co-culture system would help in gaining insight into their interactions and in the development of functional tissue. Co-culture systems enable the development of more complex and more accurate conditions for vascular wall modeling. In addition, an approach employing a scaffold in combination with co-culture systems not only challenges the effect of cell-cell interactions but also the one of cell-biomaterial interactions.

In addition to cells, bioactive compounds have also been evaluated for tissue engineering applications. Bioactive compounds, including growth factors (GF), cytokines and signaling molecules play an important role in the healing and repair of a damaged tissue. Growth factors have the capability to amplify the healing response by enhancing cell recruitment, proliferation, differentiation as well as ECM synthesis at the repair site [113]. For example, fibroblast GFs (FGF) are a family of cell signaling proteins that promote the growth of tenogenic progenitor cells, resulting in histological and biomechanical improvement of the repaired tendon [114]. Other GFs that have been used in tendon repair include transforming GF-β (TGF-β), vascular endothelial GF (VEGF), platelet-derived GF, and insulin-like GF [1]. The role of GF in tendon regeneration has been described by Randeli *et al.* [115], in which the various GFs as well as platelet-rich plasma for the different tendinopathies are discussed in detail. In vascular TE, similar growth factors and cytokines have been exploited including MCP-1, platelet-derived growth factor (PDGF), VEGF, FGF, and TGF-β [96,98,116]. In addition to the importance of including GFs, it is critical that the correct GFs (and their precise ratio) are upregulated at the correct time during the various stages of the healing process, resulting in an increase in cellularity and tissue volume [117]. For a more detailed discussion of the use of bioactive compounds in tendon repair and vascular TE, we refer the reader to the reviews by Gomes *et al.* and Bianchi *et al.* [1,70], and Yancopoulos *et al.* [116], respectively.

Pharmacologically active compounds and drugs have been also employed in TERM approaches. In tendon repair, both anti-adhesive and anti-inflammatory drugs have been introduced into drug-eluting structures to efficiently enhance tendon regeneration [118–121]. Antibacterial drugs have also been studied in this area [122].

1.5.3 The material selection: Synthetic and natural materials in TERM

Biomaterials have been used for over 20 years in tissue engineering and regenerative medicine to enhance tissue repair and to support transplantation of cells and/or growth factors [123]. While initially "inert" biomaterials were developed that elicit minimal immune response upon implantation, the emphasis has shifted in recent years to polymers, hydrogels, and other materials that can function as bioactive matrices [124]. Based on their chemical structure or nature, biomaterials for TE can be broadly classified into different categories (i.e. synthetic versus natural materials). Each of these categories has advantages and disadvantages (Table 1.2), and both types can be combined to take advantage of the benefits.

Table 1.2. Overview of the advantages and disadvantages of the use of synthetic and natural materials.

	ADVANTAGES	DISAVANTAGES
SYNTHETIC MATERIALS	High reproducibility [125,126]	Missing biochemical cues [125]
	Simple quality control process [125]	Poor long term patency [72,127]
	Lower cost, unlimited supply [72,125,128]	Compliance mismatch [127]
	Mechanical properties can be tuned more effectively [72,125,128,129]	Thrombogenicity [72,127]
	Control of shape, architecture and chemistry [4,126]	Cytotoxicity (of degradation products) [72]
NATURAL MATERIALS	Biochemical cues for cell attachment and proliferation [125]	Often require crosslinking step to become insoluble in aqueous-based solutions [125]
	Non-toxic degradation products [125]	Limited processability and mechanical strength [4]
	Low immune response [125]	Batch-to-batch variability [130]

a. Synthetic polymers

Synthetic polymers are widely used as biomaterials for scaffolds because of their ease of fabrication, high reproducibility, control of shape, architecture, and chemistry, versatility of processing techniques, and effective tunability of mechanical properties [131–133]. Moreover, synthetic polymers are not associated with the risk of transmitting diseases. However, these materials generally do not have great bioactive

characteristics [134,135]. Synthetic polymers used for tissue engineering and regenerative medicine include (i) polyesters such as poly(ε-caprolactone) (PCL), poly(lactic acid) (PLA), poly(glycolic acid) (PGA), poly(lactic-co-glycolic acid) (PLGA) and poly(hydroxybutyrate) (PHB), (ii) polyurethanes (PU), (iii) poly(ethylene glycol)s (PEG), (iv) poly(vinyl alcohol)s (PVA), and (v) poly(hydroxyethyl methacrylate) (pHEMA) [117,136–139].

A first major group of synthetic polymers includes the aliphatic polyesters (Figure 1.5). Polyesters are thermoplastic polymers that have a hydrophobic structure and are generally biodegradable through the hydrolytic cleavage of their ester linkages. The synthesis of polyesters occurs through ring opening polymerization (chain growth) or a stepwise polymerization, depending on whether a cyclic lactone monomer or the corresponding α-hydroxyl acid monomer or derivatives thereof are used. The production method influences the molar mass which in turns affects the degradation time, i.e. the ring opening polymerization results in a higher molar mass characterized by a longer degradation time and vice versa [140–142]. Degradation occurs mostly through hydrolysis of the ester linkages within the backbone, resulting in an acid and an alcohol end group [143]. The produced acid accelerates biodegradation due to autocatalysis occurring during hydrolysis [144]. The degradation time frame is in the order of weeks to years, which should be considered for the degradation requirements depending on the specific biomedical applications.

Poly(lactic acid) (PLA) and poly(glycolic acid) (PGA). The chain growth polymerization of lactide or the stepwise polymerization of lactic acid leads to the polyester PLA [145]. Similarly, PGA is the result of the stepwise polymerization of glycolic acid or the chain growth polymerization of glycolide. PGA has a crystallinity of 45-55% and is not soluble in most common organic solvents. The polymer possesses a high melting point of 220-225°C and a glass transition temperature of 35-40°C [146]. It exhibits excellent mechanical characteristics with a tensile strength of 60-100 MPa, an elongation at break of 1.5-20% and an elastic modulus of 6-7 GPa [141,147]. PLA elongation at break is in the range of 2.5-6% and is characterized by a tensile strength of 21-60 MPa and an elastic modulus of 0.35-3.5 GPa [147]. However, the PLA mechanical characteristics depend on the isomer proportion of the monomers D-lactide and/or L-lactide, determining the crystallinity. Disadvantageous properties of PLA include brittleness and poor thermal stability [146]. The chemical structures (Figure 1.5) show that PLA is less polar and thus more hydrophobic compared to PGA resulting in a slower degradation rate. The additional methyl side group in PLA makes the structure more resistant towards hydrolysis due to the hydrophobicity and steric hindrance effect [146]. PLA completely degrades in a saline environment at 37°C over a period of 3-5 years, strongly depending on its morphology, crystallinity and composition. Half of its tensile strength is lost in these conditions after 6-12 months. PLA degradation products inside the human body after hydrolysis are α-hydroxylic acid, converted into the citric acid cycle before being excreted [148]. On the other hand, PGA loses 50% of its strength after 2 weeks and 100% after 4 weeks inside the

body. The material is completely degraded and absorbed after 4-6 months [149]. The fast PGA degradation rate yielding acidic products is another reason for the limited use of pure PGA implants, although it is used in biodegradable suture applications [146]. An intermediate degradation time can be obtained by combining the properties of PLA and PGA in the copolymer poly(lactic-co-glycolic) acid (PLGA) with a ratio depending on the intended application lifetime [148]. These polymers are widely applied as biodegradable biomaterials inside the human body. Examples include surgical suture thread applications with resorption of the thread when the wound has sufficiently healed, drug delivery applications and their use as scaffold material.

Poly(ε-caprolactone) (PCL) is synthesized by chain growth polymerization of the relatively low cost ε-caprolactone (CL) monomer using a catalyst or by the step growth polycondensation reaction of caproic acid. This biodegradable hydrophobic polyester dissolves in a wide range of organic solvents. The low melting point of 60-65°C accommodates straightforward processing of the polymer. The degradability depends on the crystallinity and molar mass. PCL starts to lose strength after 2-4 years [150]. The degradation time can be tuned by copolymerization of CL with e.g. lactide or glycolide. Degradation products of PCL hydrolysis are eliminated as metabolized components from the body [148,151,152]. PCL can reach a tensile strength up to 20.7-42 MPa with a particularly flexible elongation at fracture of 300-1000% and an elastic modulus of 0.21-0.44 GPa [140,146–148]. Semi-crystalline PCL degrades slower than amorphous PLA or PGA because it is less likely for water to penetrate the more hydrophobic and more stable semi-crystalline PCL structure. Due to these interesting properties, the polymer is used in various tissue engineering applications, as well as in wound dressings and drug delivery systems [148].

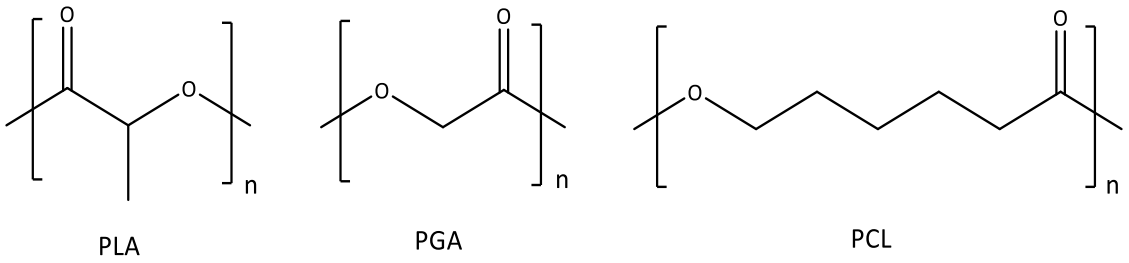

Figure 1.5. Overview of commonly used aliphatic polyesters in regenerative medicine: poly(lactic acid) (PLA), poly(glycolic acid) (PGA) and poly(ε-caprolactone) (PCL).

A second major group of synthetic polymers applied in TERM includes polyurethanes (PUs). This is mainly thanks to their excellent mechanical properties along with biocompatibility [153,154]. PUs can be composed of different building blocks or segments that allow synthesis of tailor-made materials, thereby providing the possibility to obtain a great variability of properties (Figure 1.6). Their versatile nature enables their use in several domains such as biomedical, construction, automotive applications, etc. Typically, PU is synthesized by a polyaddition reaction. Components required for this type of reaction include polyols (soft segment), chain extenders and diisocyanates (hard segment). Conventional polyols can be polyesters or polyethers

(including PEG, PLA, PCL-diol or other polymers with pendant hydroxyl groups such as PVA), whereas both aliphatic as well as aromatic diisocyanates can be used for PU synthesis. Usually, low molar mass molecules with either hydroxyl or amine end groups function as chain extenders [155]. It should be noted that the use of isocyanates often involves the generation of toxic degradation products [156]. Therefore, only aliphatic diisocyanates are used for the synthesis of urethane-based biomaterials for biomedical applications (for example isophorone diisocyanate, hexamethylene diisocyanate, L-Lysine ethyl ester diisocyanate). Alternatively, research has been focusing on the synthesis of non-isocyanate-based polyurethanes (NIPU), based on the reaction of polycyclic carbonates and polyamines [157–159].

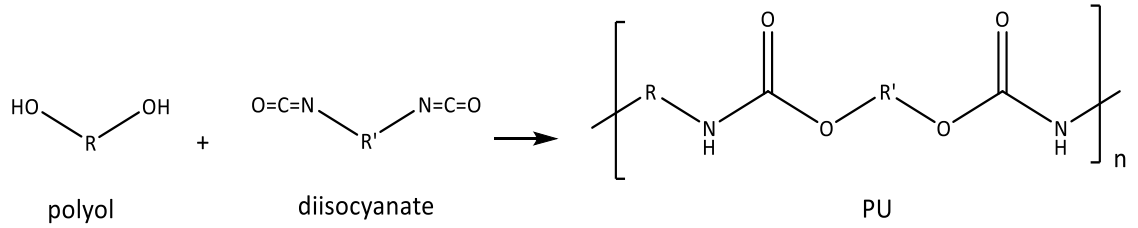

Figure 1.6. Basic reaction scheme for the synthesis of urethane-based polymers.

Degradable polymers such as aliphatic polyesters including PLLA, PLGA, PCL, and PHB or polyurethane-based materials are most commonly used for tendon repair [1,70] and for vascular TE [160,161]. These degradable polymers generally have better long-term biocompatibility than non-degradable materials such as poly(tetrafluoroethylene) (ePTFE) and poly(ethylene terephthalate) (PET), as they degrade over several months to physiological metabolites that are effectively excreted from the body [1,70].

A third major group of synthetic polymers includes poly(ethylene glycol) (PEG)-based hydrogels (Figure 1.7, left). PEG hydrogels have already been used in a wide variation of biomedical applications due to their non-toxic and non-immunogenic character. Moreover, the US Food and Drug Administration (FDA) approved the use of different PEG-based hydrogels for various clinical purposes (including PEG hydrogels for controlled drug release, protease-sensitive degradable PEG hydrogels, etc.) [162,163]. PEG is bio-inert to a number of biological components found in the human body including proteins and does not exhibit cell-adhesive properties [164]. PEG-based hydrogels can be easily modified to control the mechanical properties or to make the hydrogels more biomimetic. Surface modifications can be performed to improve the biocompatibility of their hydrogel surface. Furthermore, PEG polymers can be crosslinked to form hydrogels by several methods including for example the photopolymerization of (meth)acrylate-endcapped PEG macromonomers. Other methods use block copolymers of PEG to improve control over the degradation kinetics. Besides linear PEG macromers, also PEG-based dendrimers have been developed due to their ability to control the branching degree and thus the structural hydrogel properties and their degradation rate [134,135,164–167].

A fourth major group includes poly(vinyl alcohol) (PVA)-based hydrogels (Figure 1.7, middle). These hydrogels can be formed by crosslinking through chemical, irradiation-based or physical mechanisms.

Crosslinking can be based on the formation of acetal linkages in the presence of difunctional crosslinking agents, or covalent bonds can be formed using electron beam or gamma irradiation. These methods are advantageous because they do not use chemical crosslinking agents, which are in most cases toxic and therefore, to be avoided. However, an important drawback is that crosslinking methods based on electron beam or gamma irradiation do not allow cell encapsulation and concomitant cell survival. On the other hand, physical crosslinks can be formed during freeze-thaw cycling or can result in the formation of crystallites during annealing and dehydration [168]. PVA hydrogels are often modified in order to provide a greater biochemical similarity to native tissue and to improve their properties towards cell encapsulation [134,166].

Another important and widely applied synthetic polymer is poly(hydroxyethyl methacrylate) (pHEMA) (Figure 1.7, right). The properties of this hydrogel depend, among others, on the method of synthesis, polymer content, degree of crosslinking, temperature and final application environment. The synthesis of pHEMA can be carried out by crosslinking using UV-irradiation, and/or in the presence of a crosslinking agent and a good solvent [169]. This class of hydrogels (pHEMA and its derivatives) show moderate to poor swelling properties compared to others, e.g. PVA and PEG hydrogels [11]. Some of the main characteristics of pHEMA are its inertness to normal biological processes, resistance to degradation, permeability to metabolites, not being absorbed by the body, biocompatibility, ease of sterilization without damage, and the possibility to be prepared in a variety of shapes [11,134].

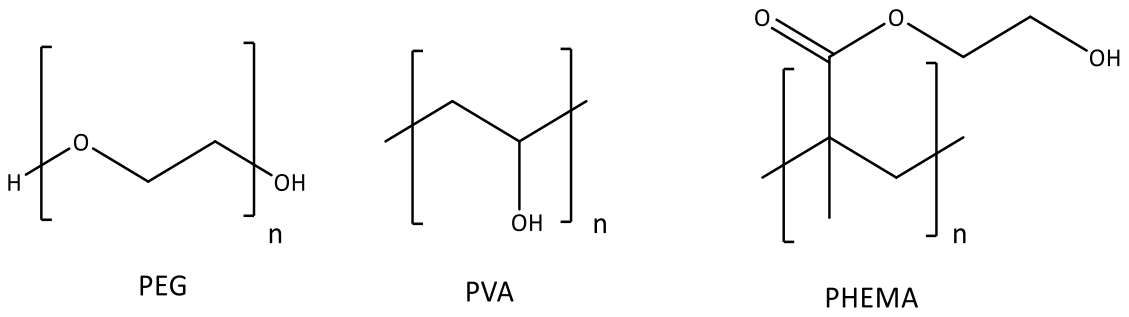

Figure 1.7. Chemical structure of poly(ethylene glycol) (PEG), poly(vinyl alcohol) (PVA) and poly(hydroxyethyl methacrylate) (pHEMA).

However, the use of synthetic materials also has some limitations, including lack of biochemical cues, poor long-term patency and compliance, and possible toxic degradation products [170–172].

b. Natural polymers

Natural polymers can mainly be derived from proteins (including collagen, gelatin, elastin, fibrin, silk) and from polysaccharides (including alginate, cellulose derivatives, hyaluronic acid, chondroitin sulphate, chitosan) [135,173,174]. Some selected natural polymers are shown in Figure 1.8.

Many natural polymers originate from various components found in the mammalian ECM including collagen, hyaluronic acid and fibrin. Other natural materials find their origin in non-mammalian sources. Some

examples include alginate and agarose, found in marine algae and chitosan prepared from arthropod exoskeletons [134,166]. Advantages of natural materials include high biocompatibility and bioactivity in combination with a low toxicity. Due to the presence of endogenous factors, these materials promote many cellular functions [134,164,167]. Their low immune response, non-toxic degradation products and the presence of biochemical cues make them highly efficient biomaterials for biomedical applications. However, in general they present limited processability and lack mechanical strength [4].

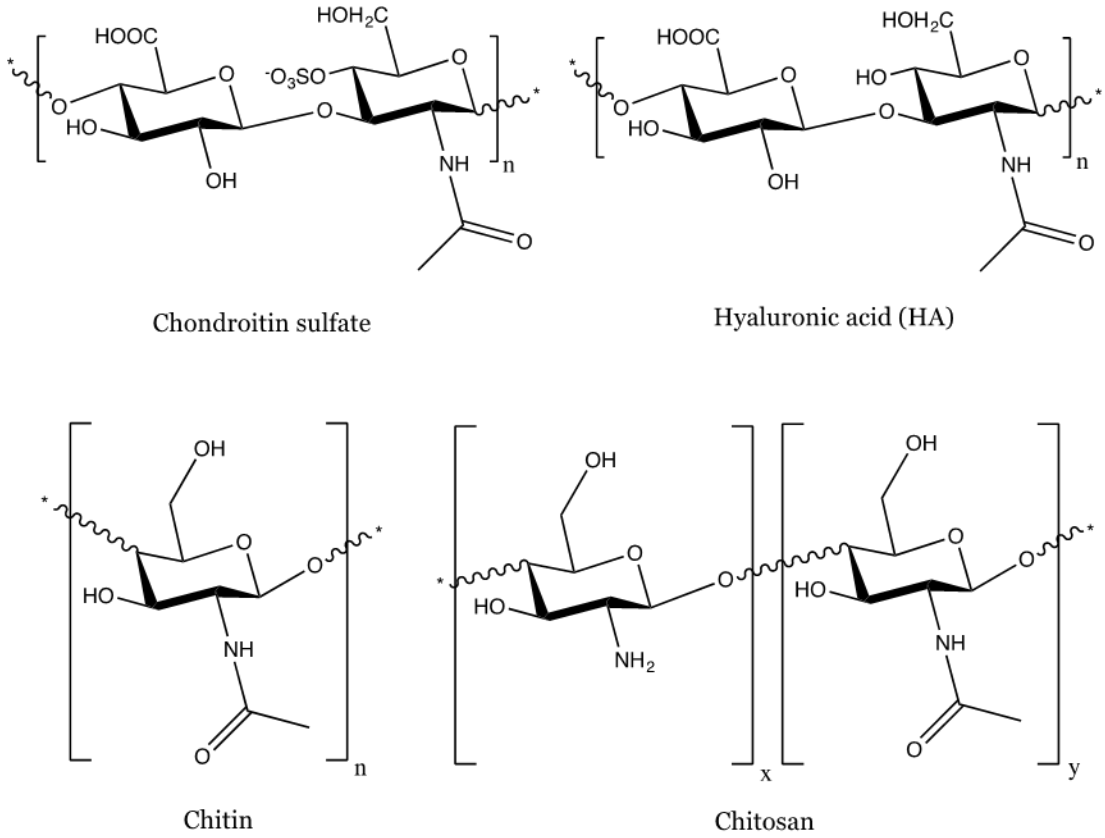

Figure 1.8. Examples of biomaterials from natural origin.

Alginate and agarose are used in TE due to their easy gelation process and cell encapsulation possibilities [166]. Alginate forms a gel via ionic crosslinking, whereas agarose can be formed into a gel following a thermal process. The properties of alginate depend on the type of marine algae resource, which strongly influences cell adhesion and hydrogel stiffness. As alginate gels under mild conditions, it is an attractive biomaterial for cell encapsulation [134]. The cell-interactive properties can be improved by coupling cell-interactive peptides or growth factors [174]. The degradation of alginate hydrogels is based on ion exchange. Agarose is non-degradable, which is a limitation for most tissue engineering purposes demanding degradation when new tissue is formed [135,175].

Chitosan is prepared by partially deacetylating chitin that can be found among other in the shells of crabs and shrimp (Figure 1.8, bottom) [174,176]. Interestingly, the properties of chitosan are highly pH-dependent. In an acid environment, the polymer is water-soluble and positively charged, whereas in a more basic

environment, a gel-like precipitation occurs [174]. At physiological pH, chitosan is neutral and hydrophobic and forms a hydrogel based on various gelation interaction mechanisms [135,174]. Chitosan degrades by lysosomes through hydrolysis and can therefore be degraded in the human body [134]. Moreover, degradation kinetics depend on the degree of acetylation and on the hydrogel properties (e.g. crystallinity) [166].

Hyaluronic acid (HA, Figure 1.8, top right) is a glycosaminoglycan (GAG) composed of repeating disaccharide units that are present in different tissues throughout the body including skin and cartilage [134]. It is involved in cell differentiation and ECM organization. HA can be chemically crosslinked to form a hydrogel, but ionically crosslinked HA has also been studied [177–179]. Degradation of HA is activated by cell-secreted hyaluronidase. Interestingly, HA can stimulate chondrogenesis due to their cell surface receptors. Moreover, HA can be prepared by microbial fermentation, thereby eliminating the risk of transmitting animal pathogens [135,166,174,175].

Chondroitin sulphate (CS, Figure 1.8, top left) is a GAG composed of alternating sugars (i.e. N-acetyl-D-galactosamine and D-glucuronic acid). CS can consist of over 100 individual sugars, each of which can be sulphated in variable positions and quantities. It is an important structural component of cartilage. Its main function in cartilage is withstanding compression. Other properties include binding and modulation of growth factors, cytokines and protease inhibitors [180]. However, since natural CS is water-soluble, chemical crosslinking is required when applied for biomedical applications [174].

Collagen is the most abundant protein present in the human body (i.e. 30%). Different types of collagen exist, with its most abundant form in the extracellular matrix being type I collagen [181]. Collagen hydrogels can form a gel without the use of chemical modifications. However, the collagen hydrogel is then characterized by weak mechanical properties [181]. These can be enhanced by synthesis methodologies such as chemical crosslinking or crosslinking through a temperature or UV trigger [134,175]. Different crosslinking techniques (chemical and physical) have been evaluated in literature [182]. The hydrogel degrades naturally by enzymatic cleavage of proteins such as collagenase [166,175]. Collagen hydrogels are attractive materials for cell growth due to the many cell-signaling domains present in their constitution. Cell-interaction can further be improved by incorporation of specific peptides and/or growth factors [174].

Gelatin is a biopolymer formed by hydrolysis of collagen. It is used in tissue engineering and a wide variety of other applications due to its unique gelation properties, its non-immunogenic character and biomimetic properties. Gelatin gel formation is mediated by a thermal process and is based on the formation of physical crosslinks [175,183]. Two types of gelatin (type A or type B gelatin) can be distinguished, depending on the applied extraction process from collagen. This process has an influence on the physico-chemical properties of the gelatin types. An acidic treatment leads to type A gelatin, whereas alkaline hydrolysis yields type B

gelatin. Type A gelatin possesses an isoelectric point (pI) around 9, whereas the type B variant has a pI around 5 [184,185]. Interestingly, gelatin shows a sol-gel transition around 37°C. At this temperature, gelatin dissolves in aqueous medium. Therefore, gelatin should be crosslinked to prevent dissolution at body temperature [174,175,183]. Most chemical crosslinking methods are irreversible. Reversible hydrogels can be realized for example, through crosslinking by disulphide bond formation. Their reversible character offers potential to act as cell carriers [183].

Elastin is a protein component of the ECM and is abundant in organs that involve stretching and recoil, including blood vessels, ligaments and tendons, elastic cartilage, lungs and skin [174]. It is comprised of approximately 800 amino acid residues [186] and is synthesized from tropoelastin, which is water soluble, non-glycosylated and highly hydrophobic. Elastin hydrogels are typically obtained by crosslinking tropoelastin solutions under physiological conditions [186]. Hydrogel crosslinking can be achieved through numerous enzymatic, chemical and irradiation methods. The structural stability, elastic resilience, and bioactivity of tropoelastin, combined with the capacity of self-assembly, make this protein a highly desirable candidate for biomedical applications [186,187].

Fibrin is a protein found in the blood and plays an important role in the blood clotting process. This greatly reduces the risk towards a foreign body reaction. Furthermore, fibrin shows excellent adhesion to the surrounding tissue [188]. The protease thrombin induces cleavage of fibrinogen that in turn initiates the formation of a fibrin network. One limitation of fibrin hydrogels is their poor mechanical properties [166,175]. Values of the elastic moduli range from 0.1 to 1500 Pa, depending on the clot structure and physiological conditions as reported by Weisel *et al.* [189].

Further details on the types and properties of natural materials used for the fabrication of scaffolds for regeneration of tendons [1,58,190] and blood vessels [63,187,191–195] have been described in literature and are not further discussed in this chapter. The use of collagen for vTE has been described in more detail in Chapter 4, 5 and 6.

c. Hybrid materials

Because of the intrinsic limitations of each group of materials mentioned above, research has focused on hybrid materials in which the advantages of natural and synthetic materials are combined. The combination of natural and synthetic materials results in higher cell affinity, low immune response, and excellent biocompatibility of natural materials, together with the superior (tunable) mechanical properties and control over shape, architecture, and structure of synthetic polymers [131]. Combining two or more polymers can be done simply by mixing, but also by advanced processing techniques. Research has been devoted to processing through coextrusion or coaxial pressure/electrospinning heads, where the core and sheath (and

even more than one layer of the sheath) can be made of two or more different materials. Other possible combinations include post-processing steps for coating.

As an example for tendon repair, Heidari *et al.* [196] have described the fabrication of hybrid scaffolds (i.e., PCL and GEL-MA) by co-electrospinning or by a coating step after processing. In this way, the mechanical properties are improved compared to using a pure gelatin-based hydrogel, while maintaining good cell adhesion properties. For vascular tissue engineering, mostly PCL has been exploited as a synthetic polymer in combination with natural polymers including collagen [197,198], elastin [199], and gelatin [200–202].

d. Photo-crosslinkable biomaterials: crosslinking mechanisms and the use of photo-initiators

One of the approaches to develop materials with precise structural control and tailored mechanical properties is photo-induced polymerization resulting in crosslinked networks [203,204]. The general mechanisms associated with photo-crosslinking include chain-growth mechanisms, step-growth mechanisms or photo-mediated redox crosslinking reactions [205–207] (Figure 1.9). The latter will not be further described herein, but can be found elsewhere [205].

Chain-growth polymerization, such as free-radical polymerization of (meth)acrylate-functionalized monomers, is (currently) the most frequently used method for 3D bioprinting of photo-crosslinkable constructs [206,208]. Advantages include straightforward material handling, consisting of material dissolution and the addition of a suitable photo-initiator (*vide infra*) prior to crosslinking. There is no need for any additional crosslinker. A drawback associated with this polymerization mechanism is that a more heterogeneous network is formed as a result of a spatially inhomogeneous crosslinking density [209]. In addition, the crosslinking mechanism is prone to oxygen inhibition due to rapid radical scavenging by oxygen molecules. This is undesirable when targeting cell encapsulation and also influences reaction reproducibility. Moreover, chain-growth polymerization typically requires more energy and more photo-initiator compared to step-growth polymerization.

In order to crosslink a polymer via free-radical polymerization, the polymer must initially be functionalized with two or more photo-crosslinkable functionalities such as double bonds (e.g. acrylates or methacrylates). Polymers that possess hydroxyl or amine groups (e.g. PEG, PCL-diol, gelatin) can be easily modified with double bonds by reacting them with (meth)acryloyl chloride or (meth)acrylic anhydride [210]. After modification with photo-crosslinkable functionalities, a photo-initiator is added. The photo-initiator creates free radicals upon absorption of a photon from the incident radiation, typically in the ultraviolet (UV) or visible range. The generated free radicals are highly reactive towards the double bonds and initiate the chain-growth polymerization. Specifically, radicals propagate through unreacted double bonds (e.g., methacrylates, acrylates, acrylamides) [205]. This process of propagation is ultimately concluded when termination occurs.

As an alternative for chain-growth polymerization, step-growth crosslinking mechanisms have also gained considerable attention recently [206]. A step-growth mechanism typically occurs between two complementary reactive groups. Some examples are thiol-ene photoclick, thiol-Michael addition and Diels-Alder click [209]. The thiol-ene photoclick reaction has emerged as a powerful method in tissue engineering applications due to their increased control over the crosslinking mechanism, particularly in comparison to free-radical chain-growth polymerization. The thiol-ene reaction involves light-mediated orthogonal reactions between multifunctional macromers that are endcapped with norbornene functionalities and sulfhydryl-containing linkers, in the presence of low amounts of photo-initiator [211]. This type of polymerization is not susceptible to oxygen inhibition, exhibits lower radical concentrations and is characterized by faster reaction rates compared to chain-growth polymerization [205]. Drawbacks include the necessity of a multi-functional, thiolated crosslinker present in the reaction mixture which can be susceptible to cross-reactivity with other thiols. Also, step-growth polymers generally exhibit lower storage moduli than their chain-growth counterparts [209].

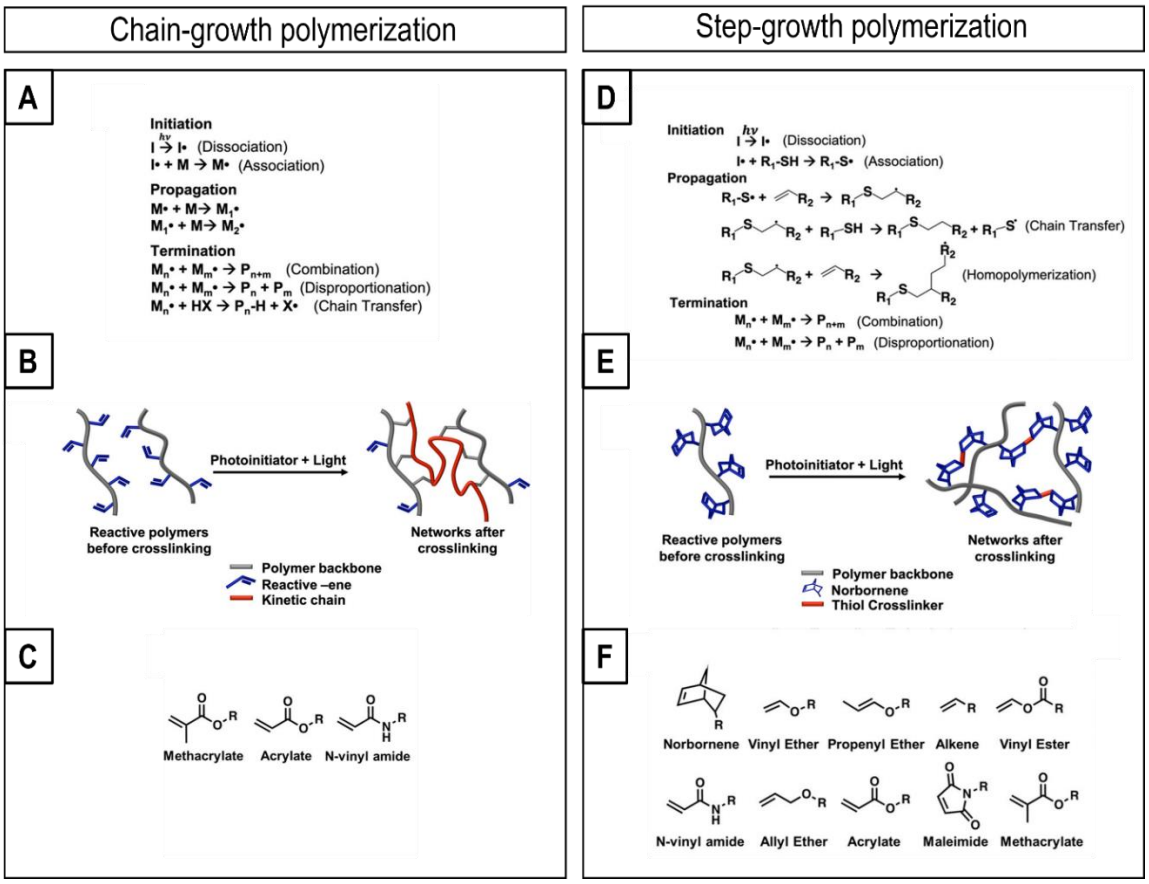

Figure 1.9. Chain-growth versus step-growth polymerization. (A) General mechanism for the chain-growth polymerization, (B) Schematic of crosslinking of polymers containing reactive groups through chain-growth polymerization, (C) Common functional groups employed in free-radical chain polymerization, (D) General mechanism of step-growth polymerization based on thiol-ene crosslinking, (E) Schematic of crosslinking of polymer chains containing reactive groups through thiol-ene reaction, (F) Common 'ene' groups employed in thiol-ene reactions. Figure adapted from [205].

When using light-based crosslinking mechanisms, typically a photo-initiator (PI) is required to initiate the crosslinking reaction. Selecting a suitable photo-initiator is imperative to ensure a desirable polymerization rate and to achieve optimal functionality to serve biomedical applications [212]. Several key characteristics should be considered when selecting a photo-initiator, including its absorption spectrum, molar extinction coefficient, water solubility (important in case of water-soluble polymers), stability and ability to produce free radicals [212]. The type of PI and the duration and exposure to light can affect the cell viability and photoinitiation efficiency [207].

In general, photo-initiators can be classified according to their activation behaviour into Norrish Type I and Norrish Type II photo-initiators [209]. The Norrish Type I PIs are typically characterized by photocleavage into different smaller molecule radical species and are usually active in the UV-region [209].

The most broadly used photo-initiator for tissue engineering applications is Irgacure 2959 (1-[4-(2-hydroxyethoxy)-phenyl]-2-hydroxy-2-methyl-1-propane-1-one) which is characterized by moderate water solubility, low cytotoxicity and minimal immunogenicity [212]. However, its low initiation efficiency and low molar extinction coefficient in the UV-A spectral range have motivated the search towards alternative photo-initiators that exhibit enhanced efficiency and biocompatibility such as lithium phenyl-2,4,6-trimethylbenzoylphosphinate (LAP) [213]. LAP has a superior water solubility and a much higher molar extinction coefficient (i.e.218 M^{-1} cm^{-1}) at 365 nm compared to Irgacure 2959 (i.e. 4 M^{-1} cm^{-1}), hence allowing more light to be absorbed at this wavelength [205]. This leads to a higher initiation rate and subsequent polymerization rate. Similar to Irgacure 2959, LAP has been applied in a range of bioinks and bioresins that undergo either free-radical chain polymerization or thiol-ene crosslinking, and also both in extrusion-based and lithography-based bioprinting [205].

1.5.4 The manufacturing process: Fabrication of tubular constructs

Regeneration of non-hollow and hollow tubular tissues should focus on structural cues to promote cell adhesion, proliferation, and spatial alignment. On the other hand, cell-biomaterial interactions and the mechanical and architectural impact (i.e., roughness, stiffness, porosity, orientation) of the material and/or scaffold on the cells are also important factors to consider. Thus, in addition to the selection of materials, cells and bioactive components, the processing technique also plays an important role in the required and resulting mechanical and biological properties of a construct.

Within the additive manufacturing techniques for processing biomaterials to serve tissue engineering and regenerative medicine needs, 3D (bio) printing (3D(B)P), solution electrospinning (SES), and melt electrowriting (MEW) have emerged as promising methods for fabricating tissue constructs suitable for the repair and regeneration of tubular tissues. Each of these fabrication techniques has specific advantages and

limitations that should be considered when scientists seek to repair or regenerate damaged tissue (section 1.5.4.d).

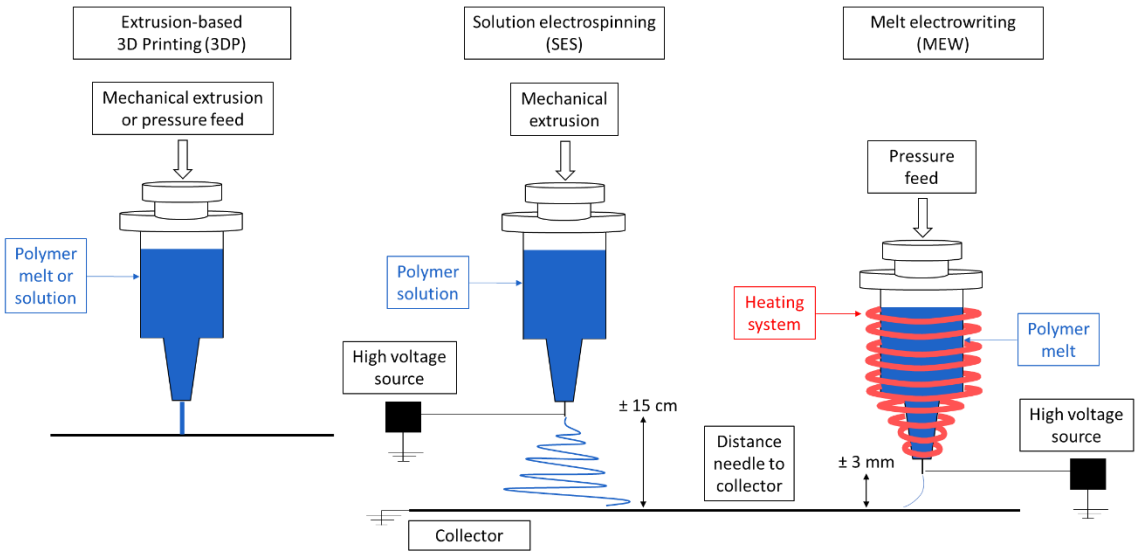

Figure 1.10. Schematic overview of the set-up of three-dimensional (bio) printing (3D(B)P), solution electrospinning (SES) and melt electrowriting (MEW) for biomaterial processing.

a. Introduction to the three-dimensional bioprinting process

3DBP is a fabrication method that, starting from a computer-aided design (CAD) model, creates a 3D construct in a layer-by-layer fashion [214]. As the 'bio' term suggests, it involves biologically derived materials and/or cells [215]. This technique allows the creation of constructs made of multiple materials and cell types in the same process, following a design-specific distribution. 3DBP techniques are usually classified into three categories, depending on the working principle of the layer-by-layer deposition process. They can be distinguished in (i) extrusion-based (Figure 1.10, left), (ii) inkjet-based, and (iii) laser-assisted bioprinting. For detailed information on the working principles of each bioprinter type, the authors suggest the reviews of Holland *et al.*, 2018 [9], Jeong *et al.*, 2020 [216], Murphy *et al.*, 2014 [214], and Van Hoorick *et al.*, 2019 [209].

Many advantages have been reported in literature on the 3DBP technique. One of them is the precise control at the micrometric scale of the biomaterial deposition. This allows to obtain a controlled porosity, in terms of both geometry and size, and to accurately mimic the physiological structure of the native organs [217]. Moreover, the possibility to combine multiple materials and cell types in the same process, with specific arrangements, allows to overcome the limitations of conventional fabrication techniques and it brings TERM closer to the complexity of native tissues. Finally, despite not yet used in clinical practice, in a future perspective, 3DBP will allow the fabrication of patient-specific BAOs, starting from the patient's medical images (e.g. magnetic resonance imaging) [218]. This customization would improve the technology readiness level (TRL) of regenerative medicine.

However, the formulation of biomaterials and cell components responding to the bioprinting requirements is the main challenge of this technique and the final construct accuracy strongly depends on it [219]. Additional drawbacks are (i) the possible cellular damage due to the stress applied during the process, and (ii) the use in some cases of temperatures or light wavelengths incompatible with cell survival.

b. Introduction to the solution electrospinning process

SES is a versatile processing technique that relies on the application of a high voltage electrical force to enable the production of micro- and nano-scale fibers from a polymer solution and deposit these fibers on a suitable collector. The high voltage (within a range of several kV, typically between 5-20 kV) generates electric charges on the polymer solution. These electric charges accumulate on the polymer surface until they eventually overcome the surface tension and form a Taylor cone. This results in an electrically charged polymer jet that is drawn from the tip of the Taylor cone and stretches in the electric field towards the oppositely charged collector such as a plate, a rotating mandrel, etc. As the polymer moves towards the collector, the solvent evaporates, and the jet solidifies, forming solid micro- and nanoscaled fibers. A schematic representation of the SES process and the different elements constituting the SES set-up are illustrated in Figure 1.10, middle. A detailed description of the fundamentals of SES can be found in the book of Bosworth *et al.*, 2011 [220].

Various factors influence the SES process, including solution parameters (i.e. polymer concentration and molar mass, solution viscosity and conductivity, surface tension, solvents), process parameters (i.e. applied voltage, flow rate, collecting electrode, needle tip-to-collector distance, diameter of the needle tip), and environmental parameters (i.e. temperature, humidity). All these factors have been described in detail by Ibrahim *et al.*, 2020 [221] in a review on electrospun polymeric nanofibers, and will not be discussed further in this introduction.

The main advantage of using SES as a processing technique for TERM is the production of fibrous networks that resemble those of the natural ECM in terms of hierarchical organization and properties. Other advantages include the high surface-to-volume ratio of the fibers, high aspect ratio, tunable porosity, flexibility to tailor surface properties, and the possibility to produce fibers from a large variety of materials. Electrospun scaffolds are known to provide a good microenvironment for cell adhesion, proliferation, and differentiation [222,223].

Even though the SES process has been known since the 1930s, it gained renewed interest in the last decades due to the inception of advanced electrospinning set-ups (e.g. side-by-side ES and coaxial ES). These advanced set-ups have the ability to produce scaffolds with multiple layers, made of multiple materials, with gradients, with fiber alignment, with multiphasic fibers, with core-shell fibers, with drug-loaded

fibers, etc. [224–227]. Therefore, it has been extensively used in research focusing on the development of scaffolds for various TERM applications [66,120,228–232].

c. Introduction to the melt electrowriting process

The MEW process is similar to SES, except that in MEW a polymer melt is used instead of a polymer solution [233,234]. Therefore, an extra heating system to heat up the polymer is needed in the MEW set-up (Figure 1.10, right). As in SES, an electrostatically ejected jet is drawn as a polymer jet which then cools down and solidifies either in air or on the collector. A low variation in fiber diameter can be obtained due to the high viscosity and low charge of these polymer melts. In combination with a moving collector, the MEW process enables (i) to directly write a 3D scaffold, and (ii) the rational design of scaffolds with control over pore size and pore interconnectivity [235]. More specifically, MEW allows to fabricate scaffolds with high reproducibility using a computer-controlled layer-by-layer approach (like fused deposition modelling technologies including 3DBP). In other words, MEW fibers can be precisely deposited to generate constructs with predefined architectures [236]. Another advantage of MEW compared to SES is that it has no solvent evaporation and thus, toxicity issues associated with solvents can be avoided [237–239].

The MEW technique and its use in TERM applications have already been extensively reviewed by Afghah *et al.*, 2019 [240], Dalton *et al.*, 2013 [241], and Muerza-Cascante *et al.*, 2015 [237]. The most recent literature has been summarized last year by Robinson *et al.*, 2019 [242], and will therefore not be described in detail in this introduction. In addition to the optimization of general processing parameters, research has also focused on the optimization of the MEW process with the aim to fabricate tubular constructs (and thus, on the fabricating process onto a rotating mandrel). For more details on MEW onto rotating mandrels, and the MEW design parameters of tubular constructs for TERM applications in general, the authors would like to refer to the work of Brown *et al.*, 2015 [238], Ibrahim *et al.*, 2019 [243], Jungst *et al.*, 2015 [244], McColl *et al.*, 2018 [245], Paxton *et al.*, 2019 [246].

d. Strengths, weaknesses, opportunities, and threats (SWOT)

Each one of the presented fabrication techniques has specific advantages and limitations that should be considered when scientists want to develop a BAO. Strengths, weaknesses, opportunities, and threats of each technique are summarized in Figure 1.11 in a parallel SWOT analysis.

Figure 1.11. Strengths, weaknesses, opportunities and threats (SWOT) of the 3 advanced processing techniques discussed in this review. 3DBP, 3D bioprinting; SES, solution electrospinning; MEW, melt electrowriting.

1.5.5 Clinical translational potential of tubular constructs processed by 3DBP, SES and MEW

As previously stated, in a scenario in which heterologous organ transplantation is burdened by the shortage of donor tissue and currently available synthetic grafts show issues in terms of biological and mechanical properties (especially on the long term), bioengineered artificial tissues certainly represent a viable solution. The development of physiologically relevant tubular tissues for regenerative medicine purposes can be used to correct defects, restore functions, or substitute damaged tissues in patients suffering from life-threatening conditions [9].

Tissue engineering-based constructs, in their journey from the lab bench to clinical use, are subjected to strict regulation. The European Medicine Agency (EMA) and the FDA are closely working together in many areas, streamlining efforts, sharing best practices and aiming to avoid duplication to promote human and animal health [247,248]. The FDA is a centralized agency that oversees the drug development process in a single country, whereas the EMA is a reviewing body that manages the process within Europe. As stated by the U.S. FDA, the process of development for new medical products and devices can be divided in 5 stages: 1) discovery and concept, 2) preclinical research, comprehensive of *in vitro* and *in vivo* testing, and prototype, 3) pathway to approval, 4) FDA device review and 5) FDA post-market device safety monitoring [U.S. Food and Drug Administration]. SES and 3DBP to design, develop and optimize tubular organs have already been reported, while MEW, despite its novelty, is rapidly gaining attention in this field.

The current advanced TERM strategies (such as 3DBP, SES, and MEW) are still affected by some limitations that impeach their successful translation into clinic. Despite the promising results and achievements obtained in the past years, the produced devices are still hampered by a mismatch in functionality (both at the mechanical and biological level) with the native tissues they are intended to substitute [9]. Hunsberger *et al.*, 2016 [250] reported that major drawbacks in the clinical transfer of advanced TERM strategies are related to the precise mapping of cells in the developed tissues (their placement, organization, phenotype and function), reliable sources for cells, immunosuppression, prosthetic tissue integration with the host and vascularization.

Finally, these new technologies evolve in a specific and precise regulatory structure allowing the scaling-up and marketing of tubular BAOs [9,251]. Although regulatory processes may appear to limit their development, which might be true in some cases, it should also be noted that this constitutes a unique moment for regenerative medicine specialists, including scientists, engineers, industrials and clinicians, to seed the basics of future regulations.

Regulating a new BAO is a long and complex procedure, which requires time, investment and collaborations. On the one hand, the International Standards Organization (ISO) must be involved, mainly because quality control will require testing and evaluation of the final products. ISO is open to extend and add new standards, specific to testing and assessing the mechanical performance, the stability, and the degradability of tubular BAOs. On the other hand, contrarily to what is (sometimes) mentioned in some manuscripts, FDA does not approve biomaterials, nor processes. The FDA is responsible for protecting public health by regulating medical devices (and a panoply of other industrial products, including drugs, tobacco products, food for humans and animals, cosmetics, and radiation-emitting electronic products). Future commercialised BAOs, after having been developed and fully tested in laboratories, must be proven safe and effective to FDA's satisfaction before companies can market them in the interstate American commerce. Future manufacturers must also prove they are able to make the product according to federal quality standards. The FDA does not develop or test products before approving them. Instead, FDA experts review the results of laboratory (*in vitro*), animal (*in vivo*), and human preclinical and clinical testing done by the manufacturers. If FDA grants an approval, it means the agency has determined that the benefits of the product outweigh the known risks for the intended use. FDA, and all other country-specific regulatory bodies, will require to be convinced that the proposed BAOs will not present risks for its population. An interesting example is constituted by the recent effort between FDA and the National Institute of Standard Technology, for the collaboration on standards development activities supporting innovation and translation of regenerative medicine products [252]. Standards development can accelerate product development cycles and broaden market opportunities in innovative fields such as regenerative medicine. Standardization provides a forum for the convergence of diverse scientific approaches; standardized approaches to address common scientific challenges can enable broader application of innovative products without stifling continuing innovation. Standardization efforts made by national standards regulatory bodies, industry, and academia can lead to

international harmonization and global marketing of regenerative medicine products. Regulation and standardization, together have the potential to speed up this important field: high-quality output is dependent on continuous input from the large community of stakeholders, and coordination of standards efforts may facilitate the development and the translation of regenerative medicine products, such as BAOs.

Despite the above considerations, the advancements achieved at the preclinical level by the above-detailed strategies, and the rapid development of processing we witnessed in the last decade, foresee that the gap separating them from the clinic will shortly be filled. In particular, the clinical translational potential of 3DBP of degradable scaffolds with living (including autologous) cells is unique and very high. 3DBP clinical translation would open the era of personalized medicine. For example, from medical images acquired from the patient during the preoperative diagnostic phase, a 3DBP-personalised process could be implemented for developing the required BAO to regenerate the diseased tissue or organ. If on one side this constitutes a confined application, it is on the other side important to highlight the high impact that this would have in some specific clinical cases. The clinical translation potential of SES and MEW for polymeric scaffolds (not-cellularized at the time of implantation but able to attract and interact with a patient's surrounding cells all along the implantation time) will be in high demand for local and long-term support for tubular BAOs partially affected by localized diseases (i.e. cancers, or inflammatory processes).

1.5.6 Perspectives of regenerative medicine for repair and regeneration of tubular organs

Injury, diseases and malfunctioning of tubular organs represent a unique challenge for bioengineers and clinicians. A multidisciplinary approach needs to be applied to successfully develop functional bioartificial organs. The main efforts in addressing the challenge are summarized in the following key points:

i. The mechanical and biological requirements should be the dictating factors during the design phase of a BAO, being the key point to address the anatomical structure and physiological functions. This is true for all tissues and organs, but it is particularly challenging in the case of tubular ones, due to the complex hierarchical structure;
ii. Construct cellularization is a key point for replacing diseased or damaged tissues and organs. On the one hand, 3DBP enables the incorporation of cells directly in the construct. On the other hand, SES and MEW rely on post-processing seeding or on cell migration and infiltration after implantation. In both cases, cell integration and cell-mediated remodeling are fundamental for a successfully outcome of engineered BAOs;
iii. The main advanced techniques for the fabrication of tubular BAOs are 3DBP, SES, and MEW. Although they are not all at the same level of technological maturity, they all have the potential for clinical translation. While 3DBP presents the unique advantage to process materials and cells together, this also raises the question of which cell source to use to ensure the best outcome. Autologous outsourcing of cells looks like an attractive possibility, but its clinical feasibility for personalized medicine remains low, due to possible auto-contamination issues, regulatory

processes, and ethical concerns. 3DBP, SES, and MEW all present unique advantages to process materials leading to high reproducibility at the micrometric level, nano- and micro-fibres production mimicking the ECM, and precise spatial deposition at fibre level, respectively;

iv. In the current research on the fabrication of functional tubular BAOs, there is a missing link that focuses on the correlation between (i) the mechanical and biological requirements of the construct design dictated by the anatomical structure and physiological functions, (ii) the fabrication process and (iii) the resulting mechanical and biological properties of the developed tubular BOA. Even though the development of functional tubular BAOs using the presented processing techniques is still at the preclinical level, the advancements in the last decade look promising and speculate great potential for clinical translation.

1.6 Aim of the PhD thesis

The current thesis focuses on addressing some of the challenges currently encountered in tissue engineering and regenerative medicine, and more specifically, in tendon repair and vascular wall modeling. To this end, specific biomaterials were designed and characterized, and multiple biomaterial processing techniques were evaluated.

In **Chapter 2**, the synthesis and characterization of photo-crosslinkable acrylate-endcapped urethane-based polymer precursors (AUPs) are described. AUPs based on a poly(ethylene glycol) (PEG) backbone and on a poly(ε-caprolactone) (PCL) backbone with different molar masses will be synthesized. By varying the constituting building blocks, polymers with tunable properties will be developed and the final properties of their crosslinked networks will be investigated.

In **Chapter 3**, melt electrowriting will be investigated as an emerging fabrication technique to process the developed AUPs into tubular constructs with a predefined architecture and tunable mechanical properties. The MEW processing potential of AUPs and the properties of the developed tubular constructs will be evaluated by physico-chemical and biological assays.

Chapter 4 focusses on the application of AUPs for tendon repair. The processing potential of the selected AUPs into tubular constructs will be investigated using solution electrospinning. In order to overcome the challenges currently encountered in tendon repair (i.e. insufficient mechanical properties and adhesion and anti-inflammatory issues), a combination of a mechanical (by material and scaffold design) and biological approach (by anti-adhesion and anti-inflammatory drugs) will be proposed. The developed tubular constructs will be physico-chemically and biologically characterized. Moreover, the developed tubes will be evaluated in an *ex vivo* sheep tendon model and an *in vivo* rabbit model.

One of the most important limitations of natural polymers in TE applications includes their inferior mechanical properties. Their viscoelastic properties are often unsatisfactory, limiting their use in TE applications. For example, in vascular TE, the mechanical properties of collagen-based constructs are unable to withstand the high pressures and stresses encountered in the blood vessel. Therefore, in an attempt to overcome this limitation, the next 2 chapters will explore different approaches to reinforce a collagen-based vascular wall model.

In **Chapter 5**, three different processing techniques (i.e. solution electrospinning, three dimensional printing and melt electrowriting) will be studied for the development of a tubular, (synthetic) polymeric reinforcement construct for vascular wall modeling. The effect of the processing technique on the resulting mechanical and biological properties of the reinforced vascular wall model will be evaluated.

A second approach explores the functionalization of collagen. **Chapter 6** focusses on the development of photo-crosslinkable collagen with tunable properties. The developed photo-crosslinkable collagens will be evaluated for their physico-chemical and biological properties, and their potential use towards vascular wall modeling will be described.

In **Chapter 7**, proteomic analysis will be evaluated as a tool to gain next level insights into photo-crosslinkable biopolymer modifications. ^{1}H-NMR spectroscopy and a colorimetric assay (i.e. OPA assay) will be used as conventional techniques for the analysis of modified biopolymers, and proteomics will be investigated as a stand-alone or as a complementary technique to these conventional techniques. Moreover, the photo-crosslinkable moieties will be localized in the 3D model of the biopolymer.

In **Chapter 8**, general conclusions are described while addressing the perspectives towards future research.

Chapter 2: Design and development of photo-crosslinkable acrylate-endcapped urethane-based precursors

This chapter describes the synthesis and characterization of a series of acrylate-endcapped urethane-based polymers (AUPs). The synthesis and the physico-chemical characterization of the AUPs described in this chapter was done by N. Pien, except for the high resolution-magic angle spinning nuclear magnetic resonance (HR-MAS ^{1}H-NMR) spectroscopy measurements, which were performed by J. Delaey (UGent) using the facilities of Prof. J. Martins (UGent). The processing and application of the developed AUPs will be discussed in other chapters: AUP PCL20k processing by melt electrowriting in Chapter 3; AUP PCL530 and AUP PCL2k processing by solution electrospinning for tendon repair in Chapter 4. The work done by co-authors of the listed publications was on the processing and application and will be described in the corresponding chapters. Parts of this chapter (on the synthesis and characterization of the AUPs) have been published in/accepted as:

N. Pien μ, I. Peeters μ, L. Deconinck, L. Van Damme, L. De Wilde, A. Martens, S. Van Vlierberghe, P. Dubruel, A. Mignon. Design and development of a reinforced tubular electrospun construct for the repair of ruptures of deep flexor tendons. Materials Science and Engineering: C, Volume 119, 111504. DOI: 10.1016/j.msec.2020.111504, Published: SEP 2020, Impact Factor: 7.328. Peer reviewed.

N. Pien, Y. Van de Maele, L. Parmentier, M. Meeremans, A. Mignon, C. De Schauwer, I. Peeters, L. De Wilde, A. Martens, D. Mantovani, S. Van Vlierberghe, P. Dubruel. Design of an electrospun tubular construct combining a mechanical and biological approach to improve tendon repair. Journal of Materials Science: Materials in Medicine, DOI: 10.1007/s10856-022-06673-4, Published: MAY 2022, Impact Factor: 3.896. Peer reviewed.

N. Pien μ, M. Bartolf-Kopp μ, J. Delaey, L. Parmentier, L. De Vos, D. Mantovani, S. Van Vlierberghe, P. Dubruel, T. Jüngst. Melt electrowriting of a photo-crosslinkable poly(ε-caprolactone)-based material into tubular constructs with predefined architecture and tunable mechanical properties. Macromolecular Materials and Engineering, DOI: 10.1002/mame.202200097, Published: MAY 2022, Impact Factor: 4.367. Peer Reviewed.

μ : Authors contributed equally.

2.1 Résumé

Dans cette chapitre, des nouveaux polymères polyvalents photoréticulables à base d'uréthane (AUP) ont été développés, ainsi que leur mise en œuvre comme matériaux de départ pour le développement d'échafaudages tubulaires. Parce que chaque tissu a ses propres exigences mécaniques et biologiques, et parce que chaque technique de traitement a ses propres défis spécifiques, une boîte à outils de AUPs a été proposée. Des AUPs basés sur un backbone de poly(éthylène glycol) (PEG) et un backbone de poly(ε-caprolactone) (PCL) avec différentes masses molaires ont été synthétisés. Les AUPs ont montré une large gamme de propriétés physiques et mécaniques, couvrant les propriétés de nombreux tissus et les rendant idéales pour la médecine régénérative d'un point de vue mécanique. En outre, les AUPs développés ont permis une réticulation UV efficace à l'état solide, ouvrant la voie à diverses possibilités de techniques de fabrication, notamment l'électrospinning en solution (SES), l'impression 3D par extrusion (3DP) et l'électrowriting en fusion (MEW).

2.2 Abstract

In this chapter, new versatile photocrosslinkable acrylate-endcapped urethane-based polymers (AUPs) were developed, as well as their implementation as starting materials for the development of tubular scaffolds. Because each tissue has its own mechanical and biological requirements, and because each processing technique has its own specific challenges, a toolbox of AUPs has been proposed. AUPs based on a poly(ethylene glycol) (PEG) backbone and a poly(ε-caprolactone) (PCL) backbone with different molar masses were synthesized. The AUPs showed a wide range of physical and mechanical properties, covering the properties of many tissues and making them ideal for regenerative medicine from a mechanical perspective. In addition, the developed AUPs enabled efficient solid-state UV crosslinking, paving the way for various possibilities of fabrication techniques, including solution electrospinning (SES), 3D extrusion printing (3DP) and melt electrowriting (MEW).

2.3 Introduction

Given the complexity of the human body, recent advances in biomaterial design have been directed towards the development and synthesis of novel polymers with properties tailored towards specific TERM applications [253]. Although natural polymers have demonstrated the potential advantage of supporting cell function and adhesion, there are a few limitations (including inferior mechanical properties and fast degradation rates) with regard to their use in biomedical applications [254,255]. Conversely, synthetic polymers have the advantage that they (i) are more reproducible, (ii) offer tuneable physico-chemical properties, and (iii) show a straightforward processability and bio-inertness compared to natural polymers [141,154,256].

One of the approaches to develop materials with precise structural control and tailored mechanical properties is photo-induced polymerization resulting in crosslinked networks [203,204]. Photo-crosslinking is an attractive technique to create tuneable crosslinked polymer networks as it offers temporal and spatial control over the reaction [257,258]. In addition, it is a cost-efficient technique that can easily be implemented for polymer processing techniques including electrospinning and additive manufacturing by means of *in situ* or post-processing curing. The properties of the resulting scaffolds can be controlled spatio-temporally by adjusting the concentration of the polymer, the amount and type of the photo-crosslinkable functionalities, the type and concentration of photo-initiator, the wavelength, the light intensity and the exposure time [259,260]. The general mechanisms associated with photo-crosslinking include chain-growth mechanisms, step-growth mechanisms or redox-based reactions [205–207]. Chain-growth polymerization, such as free-radical polymerizations of (meth)acrylate-functionalized monomers, is (currently) the most frequently used method for 3D bioprinting of photo-crosslinkable constructs [206,208]. As an alternative to chain-growth polymerization, step-growth crosslinking mechanisms including thiol-ene click chemistry have also raised considerable attention recently [206].

Efficient crosslinking of conventional photo-reactive precursors relies on the mobility of the reactive groups and is generally addressed from the liquid state [261]. This usually implies that the processing and UV-irradiation require the use of molten or dissolved polymers. This renders conventional photo-crosslinkable polymers hard to process into well-defined geometries using processing techniques such as extrusion-based 3D printing, which are important for their functional properties in tissue engineering and regenerative medicine.

In this chapter, previous work executed within the PBM research group addressing the above-mentioned issue involving the design of a novel photo-crosslinkable precursor, is applied as starting point. The precursor is an acrylate-endcapped urethane-based polymer (AUP) composed of different building blocks (*vide infra*), that exhibits excellent solid-state photo-reactivity owing to its molecular design. Herein, we extend the portfolio of solid-state photo-crosslinkable AUPs through variations in the polymer backbone and

its molar mass, constituting the AUP backbone. A series of AUPs was synthesized and characterized, with the aim to design polymers that exhibit tailorable physical properties to serve a wide range of tissue engineering and regenerative medicine applications.

2.4 Materials and methods

2.4.1 Materials

Poly(ethylene glycol) with an average molar mass (MM) of 2000 or 20000 g·mol^{-1}, poly(ε-caprolactone) diol with an average MM of 530 or 2000 g·mol^{-1}, isophorone diisocyanate (IPDI), triphenylphosphite (TPP), phenothiazine (PTZ), phosphoric acid (H_3PO_4), dimethyl terephthalate (DMT), ethylene glycol and stannous octoate were purchased from Sigma-Aldrich. Bisomer PEA6 and bismuth neodecanoate were obtained from GEO Specialty Chemicals and Shepherd, respectively. Butylated hydroxytoluene (BHT) was purchased from Innochem GMBH, and chloroform and toluene were obtained from Chem-Lab. TPO-L was purchased from Lambson.

2.4.2 Synthesis of acrylate-endcapped urethane-based poly(ethylene glycol) precursors

A schematic representation of the synthesis scheme for the PEG-based AUPs is shown in Figure 2.1. Two different acrylate-endcapped urethane-based PEG precursors were synthesized exploiting poly(ethylene glycol)s (PEG) with molar masses of 2000 and 20000 g·mol^{-1}. Prior to the synthesis of the AUP precursors, the PEGs were vacuum dried under a N_2 blanket. Subsequently, the weak basicity content was quantified by titration and phosphoric acid (H_3PO_4) was included to neutralize the small fraction of the weak basicity content in PEG. Butylated hydroxytoluene (BHT, 500 ppm)) was added as radical scavenger. The synthesis of AUP occurred through a two-step process. The reactions were carried out in bulk for PEG with a MM of 2000 g·mol^{-1}, and (dry) toluene was used as a solvent to decrease the viscosity of the reaction mixture for PEG with a MM of 20000 g·mol^{-1}.

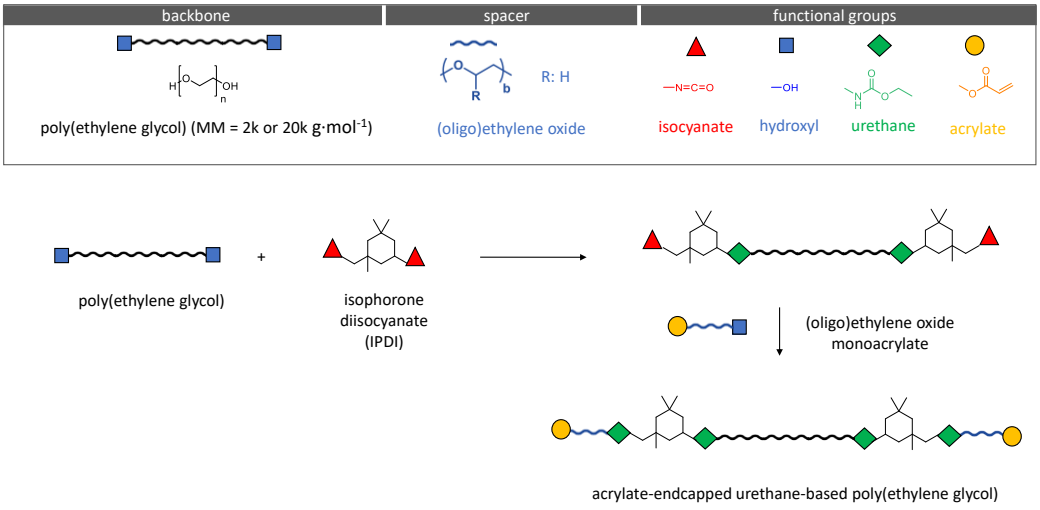

Figure 2.1. Schematic representation of the synthesis route performed for the PEG-based AUP precursors.

In a first step, PEG with a molar mass of 2000 and 20000 g·mol^{-1} was linked to isophorone diisocyanate (IPDI) in a 1:2 stoichiometric ratio. The reaction between the hydroxyl groups of PEG and the isocyanates was catalysed by the addition of 300 ppm bismuth neodecanoate which is followed by an exothermal reaction in a temperature range between 80 and 90°C. The urethane formation reaction then proceeded at 75°C. Potentiometric isocyanate titration allowed to monitor the progress of the urethane formation. A degree of conversion of 50% after the first reaction step was aimed at, corresponding with an NCO value of 0.82 meq·g^{-1}(i.e. ± 3.5% NCO-content). When the NCO value reached this theoretical value, the acrylated oligomeric ethylene oxide (6 units) (OEOacr) was added dropwise upon exposure to air in the presence of 300 ppm bismuth neodecanoate. Next, the temperature was raised to 80°C. The reaction progress was monitored by measuring the NCO value via potentiometric titration. The reaction proceeded until the NCO content reached a value of 0.02 meq·g^{-1} (i.e. < 0.10% NCO content). In case no titration system is available (or in case a solvent was used), the NCO content should be determined qualitatively via FT-IR spectroscopy. The reaction should be proceeded until no absorption band is observed at 2270 cm^{-1}, indicating that the NCO groups of IPDI have reacted completely. Phenothiazine (PTZ, 500 ppm) and triphenyl phosphate (TPP, 500 ppm) were added as stabilizers, and the reaction product was cooled to room temperature. Subsequently, if a solvent was used, the AUP was precipitated in 50/50 v/v% n-pentane/diethylether (10x excess) and filtered and/or the AUP was transferred into a plastic container and stored in the fridge.

2.4.3 Synthesis of acrylate-endcapped urethane-based poly(ε-caprolactone) precursors

For the synthesis of the PCL-based AUPs, a slightly modified synthesis route was applied. To this end, the endcap was synthesized in a first step and consecutively, this endcap was reacted with the PCL diol backbone. The PCL diol with a MM of 530 and 2k was purchased, whereas the PCL diol with a MM of 10k and 20k was synthesized as described below (section 2.2.3.b).

(a) Endcap synthesis. First, 1 equivalent of IPDI was added to 1.2 equivalents of OEOacr. The reaction proceeded at T = 65°C for 2 h, after which the temperature was increased to 75°C and the reaction proceeded during 1 h 15 min. The synthesized endcap is further abbreviated as IPDI-OEOacr.

(b) PCL diol 10k and PCL diol 20k synthesis. The monomer (ε-caprolactone, 50 g, 483 mmol), catalyst (stannous octoate, 4 g, 10 mmol), solvent (dry toluene, 160 mL) and initiator (ethylene glycol, 312 mg, 5 mmol) were added to a flame-dried Schlenk vial in an Argon-glovebox. The mixture was subjected to three freeze-thaw cycles. The Schlenk vial was placed in an oil bath at 100°C while stirring and allowed to react for 24 h. The synthesized PCL diol was exploited as backbone for the acrylate-endcapped urethane-based polymer in a one-pot synthesis. Before usage, toluene was dried by refluxing over sodium in the presence of benzophenone. ε-Caprolactone was purified by vacuum distillation over CaH_2, while ethylene glycol was purified by vacuum distillation and stannous octoate was used as received.

(c) Acrylate-endcapped urethane-based polymer synthesis. Next, acrylate-endcapped urethane-based PCL was synthesized by dissolving 2 equivalents of IPDI-OEOacr in dry toluene in a 1:1 w:v ratio and adding the solution to the PCL diol backbone together with 300 ppm catalyst (stannous octoate). The resulting mixture was allowed to react overnight at T = 75°C under inert atmosphere. Then, the reaction mixture was precipitated in a 10-fold excess of cold hexane. The resulting precipitate was filtered and washed with hexane and dried in vacuo for 24 hours. A schematic representation can be found in Figure 2.2.

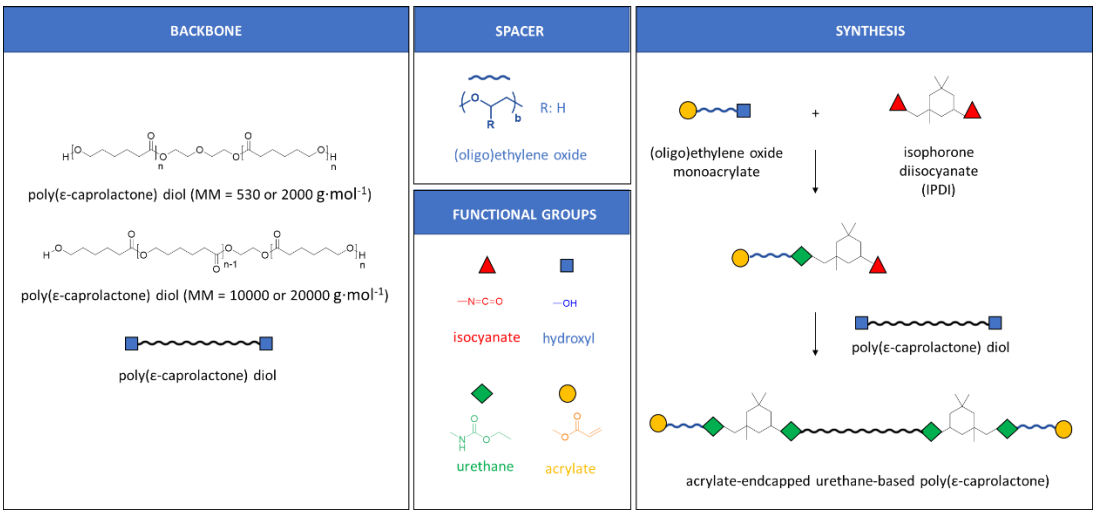

Figure 2.2. Synthesis of an acrylate-endcapped urethane-based polymer (AUP) constituting a poly(ε-caprolactone) backbone, an (oligo)ethylene oxide spacer and a monoacrylate endgroup.

2.4.4 ^{1}H-NMR spectroscopy to determine the chemical structure, the acrylate content and the polymer molar mass

Proton nuclear magnetic resonance (^{1}H-NMR) spectroscopy enabled to determine the acrylate content, as well as the MM of the backbone and of the developed AUP precursor. A fixed value of 10 mg AUP precursor, combined with the standard dimethyl terephthalate (DMT, 10 mg), was dissolved in 1 mL deuterated chloroform. An NMR spectrometer (Bruker Avance 400 MHz) was used to obtain the spectrum. Analysis of the obtained spectra was performed using the MestreNova software whereby a baseline correction, based on the Whittaker Smoother method, was carried out. The acrylate content was calculated using Equation (2.1). The MM of the backbones and AUP precursors were determined by equations (2.2) and (2.3) (for PEG-based AUPs) and equations (2.4) and (2.6) (for PCL-based AUPs), respectively.

$$MM_{acrylate\ content} = \frac{I_{\delta=5.83-6.4ppm}}{I_{\delta=8ppm}} \cdot \frac{N_{\delta=8ppm}}{N_{\delta=5.83-6.4ppm}} \cdot \frac{W_{DMT}}{MM_{DMT}} \cdot \frac{1000}{W_{AUP}} \quad (2.1)$$

PEG-based AUPs:

$$X = \frac{\left(N_{acrylate} \cdot \frac{I_{3.4-4.0ppm}}{I_{5.8-6.4ppm}} \cdot \frac{N_{5.8-6.4ppm}}{N_{3.4-4.0ppm}}\right) - N_{SEO}}{\frac{MM_{PEG\ backbone}}{MM_{EO}}} \quad (2.2)$$

$$MM_{AUP\ PEG} = 2 \cdot MM_{Bisomer\ PEO6} + MM_{IPDI} + X \cdot (MM_{IPDI} + MM_{PEG\ backbone}) \quad (2.3)$$

With:

$I_{\delta= 3.4 - 4.0\ ppm}$ = integral of signal of the methylene protons

$I_{\delta= 5.83 - 6.40\ ppm}$ = integrals of the signal of the protons part of the acrylates

$N_{\delta= 3.4 - 4.0\ ppm}$ = number of protons in 1 EO unit (= 4)

$N_{\delta= 5.83 - 6.40\ ppm}$ = number of acrylate protons per acrylate endgroup (= 3)

$N_{acrylate}$ = number of acrylates per AUP (= assumed to be 2)

N_{SEO} = number of EO repeating units in spacers of AUP (= 12)

$MM_{PEG\ backbone}$ = MM of PEG backbone used for the synthesis (g·mol^{-1})

MM_{EO} = MM of 1 EO unit (g·mol^{-1})

PCL-based AUPs:

$$MM_{PCL-backbone} = \frac{I_{\delta=2.3ppm}}{N_{\delta=2.3ppm}} \cdot \frac{N_{\delta=4.3ppm}}{I_{\delta=4.3ppm}} \cdot MM_{CL\ unit} + MM_{EO} \quad (2.4)$$

$$DS\ [\%] = \frac{\left(\frac{I_{\delta=5.83-6.4ppm}}{N_{\delta=5.83-6.4ppm}}\right)}{\left(\frac{I_{\delta=4.3ppm}}{N_{\delta=4.3ppm}}\right)} \cdot 100\% \quad (2.5)$$

$$MM_{AUP\ PCL} = MM_{PCL-backbone} + 2 \cdot \frac{DS}{100} \cdot (MM_{IPDI} + MM_{Bisomer\ PEO6}) \quad (2.6)$$

With:

$I_{\delta= 2.3\ ppm}$ = integral of signal of the protons from the repeating unit of CL

$I_{\delta= 5.83 - 6.40\ ppm}$ = integrals of the signal of the protons part of the acrylates

$I_{\delta= 8.00\ ppm}$ = integral of the signal of the protons from the aromatic ring in DMT

$I_{\delta= 4.3\ ppm}$ = integral of signal of the protons from the ethylene glycol initiator

$N_{\delta= 2.3\ ppm}$ = number of protons from the repeating unit of CL (= 2)

$N_{\delta= 5.83 - 6.40\ ppm}$ = number of acrylate protons per AUP molecule (= 6)

$N_{\delta= 8.00\ ppm}$ = number of protons in the benzene ring of DMT (= 4)

$N_{\delta= 4.30\ ppm}$ = number of protons in the ethylene glycol initiator (= 4)

MM_{DMT} = 194.186 g·mol^{-1}; $MM_{CL\ unit}$ = 114.16 g·mol^{-1}; MM_{EO} = 60.05 g·mol^{-1} (for AUP PCL10k and 20k) or 104.1 g·mol^{-1} (for AUP PCL530 and 2k); MM_{IPDI} = 222.3 g·mol^{-1}; $MM_{Bisomer\ PEO6}$ = 336 g·mol^{-1}

2.4.5 Chemical structure analysis by Fourier-transform infra-red (FTIR) spectroscopy

FTIR spectroscopy analysis was conducted on an FTIR spectrometer (PerkinElmer Frontier FTIR mid-IR combined with a MKII Golden Gate set-up equipped with a diamond crystal from Specac) operating in Attenuated Total Reflection (ATR) mode. AUP spectra were recorded in the range of 700 - 4000 cm^{-1} exploiting 8 scans using PerkinElmer Spectrum Analysis Software.

2.4.6 Determination of the thermal properties using thermogravimetric analysis (TGA) and differential scanning calorimetry (DSC)

Thermal stability was investigated by thermogravimetric analysis (TGA) (TA Instruments, Q50). First, the material pan was pyrolyzed to remove remaining impurities. Next, the material (10 mg) was heated following a pre-programmed method of equilibration at 35°C, heating at a rate of 10°C·min^{-1} up to 600°C and cooling until equilibration at 350°C. The software (TA Universal Analysis) registered the mass loss evolution as a function of temperature.

The thermal properties of the AUP precursors were determined using conventional differential scanning calorimetry (DSC) (TA instruments, Q2000 DSC, Zellik, Belgium). 4-6 mg samples were placed into Tzero aluminum DSC pans and subsequently sealed using an aluminum Tzero lid. The samples were then placed into the device furnace and equilibrated at 45°C prior to the start of the analysis. An initial heating cycle was applied to erase the thermal history of the samples by heating up the precursors up to 100°C at a controlled rate of 10°C·min^{-1}. Next, the precursors were cooled down to 20°C at a controlled cooling rate of 5°C·min^{-1} and equilibrated at 20°C for 10 minutes. Next, the samples were heated again up to 100°C at a controlled rate of 10°C min^{-1}. The DSC thermograms recorded during the cooling and heating cycles were plotted as a function of temperature.

2.4.7 Determination of the solvent uptake capacity, the gel fraction and the crosslinking efficiency of crosslinked AUPs

Cylindrical samples (D: 8 mm) were punched out from 1 mm thick crosslinked AUP sheets after 30 min of UV-crosslinking (λ = 365 nm, 10 mW·cm^{-2}). Every sample was first weighed in its dry state (W_i) and then placed in a 6-well plate and immersed in an excessive volume of ultrapure water (for PEG-based AUPs) or chloroform (for PCL-based AUPs). Following this, the samples were incubated at 20°C for 72 hours. After removal of the excess water or chloroform, the mass of the samples in swollen state was determined (W_s). Next, samples were dried, and the mass of the dried samples was recorded (W_f). The measurements were performed in sixfold. The solvent uptake capacity (SUC) and gel fraction (GF) were calculated using equations (2.7) and (2.8), respectively.

$$Solvent\ uptake\ capacity\ (SUC)[-] = \frac{(W_s - W_f)}{W_f} \tag{2.7}$$

$$Gel\ fraction\ (GF)[\%] = \frac{W_f}{W_i} \cdot 100\% \tag{2.8}$$

The crosslinking efficiency (CE) was assessed by high resolution magic angle spinning (HR-MAS) ^{1}H-NMR spectroscopy on a Bruker Avance II 700 spectrometer. The spectrometer contains a HR-MAS probe which was equipped with a ^{1}H, ^{13}C, ^{119}Sn and gradient channel. The spinning rate was set at 6 kHz. The freeze-dried samples were placed in a 4 mm zirconium oxide MAS rotor with Kel-F disposable inserts (50 µL). Next, 30 µL $CDCl_3$ was added to let the samples swell. Finally, the samples were homogenized prior to the measurement. A Kel-F cap was used to close the rotor. For the calculation of the crosslinking efficiency (CE) from the NMR spectra [262] using Equation (2.9), the ethylene oxide peaks were chosen as reference peaks since they represent groups that do not participate in the crosslinking reaction.

$$CE\ [\%] = \frac{\left(\frac{I_i}{I_{ri}} - \frac{I_e}{I_{re}}\right)}{\left(\frac{I_i}{I_{ri}}\right)} x\ 100\% \tag{2.9}$$

With:

I_i = integration of the acrylates before crosslinking (5.83-6.4 ppm)

I_{ri} = integration of the reference peak (EO) before crosslinking (3.55-3.65 ppm)

I_e = integration of the acrylates after crosslinking (5.83-6.4 ppm)

I_{re} = integration of the reference peak (EO) after crosslinking (3.55-3.65 ppm)

2.4.8 Evaluation of the mechanical properties of crosslinked AUP samples

The UV-crosslinked AUP samples (100 wt% initial precursor concentrations) were cut into dogbone-shaped samples (1 mm thickness, 30 mm gage length, 4 mm width). Next, the tensile properties of the crosslinked AUP dogbone-shaped samples were determined at room temperature using a universal testing machine (Tinius Olsen) equipped with a 500 N load cell. A preload force of 0.3 N was applied and the specimens were tested at a cross-head velocity of 10 mm·min^{-1}. Young's moduli were calculated from the initial slope of the stress-strain plots on 4 replicates.

2.4.9 Rheological measurements on crosslinked AUP discs

The UV-crosslinked AUP samples (100 wt% initial precursor concentration) were cut into disks (D = 14 mm, thickness = 1 mm). Storage (G') and loss moduli (G") of the AUP samples were determined via an Anton Paar Physica MCR 301 rheometer using a parallel-plate set-up (top plate diameter: 15 mm) as a function of

the frequency (0.1-100 Hz). During the tests, the normal force was kept at 0.8 N to ensure contact between the measuring system and the sample. The tests were performed at a strain (<0.5%) which was within the linear viscoelastic region of the samples, predetermined by the strain-controlled oscillatory tests (data not shown). The rheological measurements were done in triplicate.

2.5 Results and discussion

2.5.1 Synthesis of acrylate-endcapped urethane-based polymers

The developed AUPs are constituted of different building blocks: (i) a backbone, (ii) urethane linkers, (iii) spacer units and (iv) crosslinkable endgroups (Figure 2.2 and 2.3). By varying these building blocks, AUPs with tunable physico-chemical properties can be developed. Physical properties of the AUPs including solvent uptake capacity, hydrophilicity, degradation rate and mechanical properties are mainly determined by the backbone selection. The urethane linkers also contribute to the physical properties of the AUPs by improving the toughness and because they act as a linker between the backbone and the spacer units [263]. The latter provide additional mobility to the photo-crosslinkable endgroups and are key for the solid-state crosslinking kinetics [261]. The photo-crosslinkable endgroups enable the formation of a covalently crosslinked network upon UV-irradiation. Variations in chemistry of the AUP building blocks enable the development of AUPs with diverse physico-chemical properties and thus, the development of AUPs for specific biomedical applications.

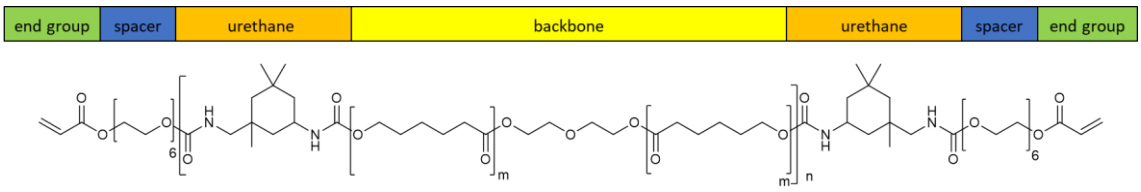

Figure 2.3. Schematic overview of the building blocks of the acrylate-endcapped urethane-based polymers (AUPs). The example is an AUP with poly(ε-caprolactone) backbone (MM = 2000 g·mol^{-1}, m=8, n=1-3).

The schematic overview in Figure 2.3 represents the chemical structure of one of the AUPs synthesized in this PhD research and shows the constituting building blocks. Herein, both poly(ethylene glycol) (PEG) and poly(ε-caprolactone) (PCL) were exploited as backbone of the AUP precursor. The PEG backbone was selected for its hydrophilicity and excellent biocompatibility. For some applications, the biodegradability of the material plays an important role, and hence, PCL was also evaluated as backbone of the AUP precursors. Moreover, the use of PCL as backbone will also result in materials with a higher Young's modulus, which could potentially be used for hard TE applications. Isophorone diisocyanate (IPDI) was chosen as diisocyanate resulting in the urethane linkers upon reaction with OH-functionalities. As a spacer group, an oligo(ethylene oxide) of six repeating ethylene oxide units was selected for its flexible nature, facilitating the polymerization rate in the solid state. Acrylates were used as photo-crosslinkable groups due to their intrinsic photo-reactivity [257]. As an alternative to changing backbone chemistry, another option to

obtain AUP precursors with different mechanical properties or tunable (bio)degradation, is to design for example, an PEG-based AUP with multi-acrylate endcaps or with caprolactone spacers instead of ethylene oxide units, respectively.

Herein, we targeted the development of a series of AUP precursors leading to biocompatible materials with a broad range of physical properties, by adjusting the type of polymer in the backbone as well as by varying the backbone's molar mass. By varying the backbone, AUPs with different crosslink densities and hence physical properties including mechanical properties can be developed. These can subsequently serve different TERM applications.

AUP precursors with a PEG backbone (MM = 2k and 20k g·mol^{-1}) and a PCL backbone (MM = 530, 2k, 10k and 20k g·mol^{-1}) were synthesized following the synthesis route described in the M&M section (sections 2.4.1 and 2.4.2, respectively). The final PEG-based (AUP PEG2k, AUP PEG20k) and PCL-based (AUP PCL530, AUP PCL2k, AUP PCL10k, AUP PCL20k) AUP precursors were characterized for their structural characteristics (section 2.5.2), and for the physical properties of their resulting crosslinked networks (section 2.5.3). The AUP PEG2k precursor will serve as benchmark for the newly developed AUP precursors throughout the present research.

2.5.2 Characterization of AUP precursors

(a) Chemical structure verification using Fourier-transform infrared (FTIR) and proton nuclear magnetic resonance (^{1}H-NMR) spectroscopy

The chemical structure of the developed AUP precursors was analyzed via Fourier-transform infrared (FTIR) and proton nuclear magnetic resonance (^{1}H-NMR) spectroscopy. In addition, via the latter technique, the acrylate content, the molar mass of the backbone and the molar mass of the AUP precursor were determined.

The FTIR spectrum revealed the characteristic absorption bands corresponding to N-H stretching (3330 cm^{-1}), the amide I (1720 cm^{-1}) and the amide II (1540 cm^{-1}) band confirming that the urethanization reaction successfully proceeded throughout the synthesis . The spectrum of the final AUP precursor (Figure 2.4.A and B) also confirmed the complete conversion of the isocyanate groups (i.e. disappearance of the peak corresponding to -N=C=O at 2260 cm^{-1}) that react with the hydroxyl moieties of the backbone and those of the end-capping agents. The absorption bands at 1635 cm^{-1} and 810 cm^{-1} correspond to the C=C stretch and the =CH_2 out-of-plane deformation of the acrylate groups [264]. The connection of the flexible, monoacrylate spacer to the backbone using a diisocyanate linker enables great mobility of the reactive groups, and exhibits excellent solid-state photo-reactivity [261,264]. An overview of the FTIR spectra of the developed PEG- and PCL-based AUP precursors is presented in Figure 2.4.

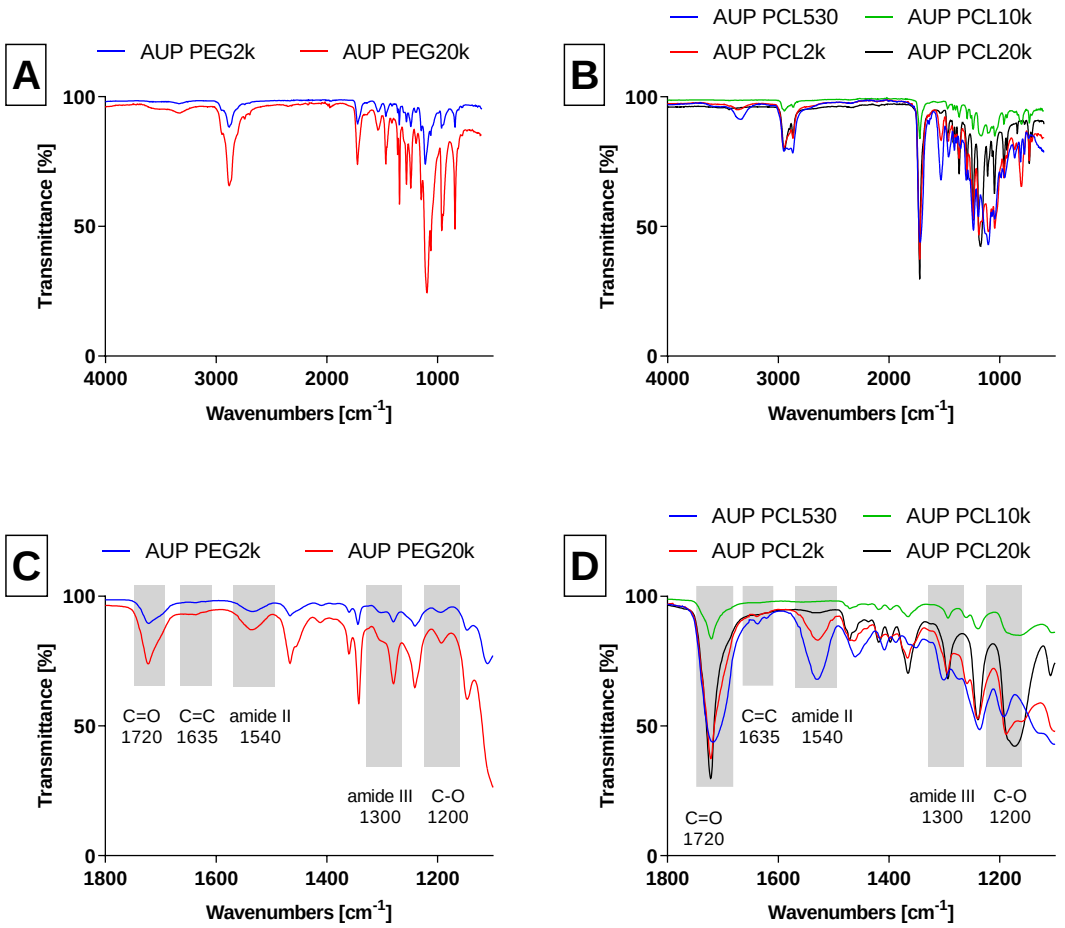

Figure 2.4. FTIR spectra of: (A) poly(ethylene glycol)-based AUPs, (B) poly(ε-caprolactone)-based AUPs, (C) and (D) region 1100-1800 cm^{-1} for PEG-based and PCL-based AUPs.

In addition to the qualitative FTIR analysis, ^{1}H-NMR spectroscopy was performed to reveal information on the chemical structures of the developed AUP precursors. The exact acrylate content can be quantified by adding a specific amount of suitable standard into the precursor solutions prior to ^{1}H-NMR spectroscopy. In this work, we used dimethyl terephthalate (DMT) as a standard compound to determine the acrylate content in the AUP precursors. The equation for the calculation of the acrylate content can be found in section 2.4.3, and the peaks of interest for the calculations are indicated in Figure 2.5.A. In addition to the acrylate content, ^{1}H-NMR spectroscopy also enabled the calculation of the molar masses of the backbones and the developed AUPs (*vide infra,* Table 2.1).

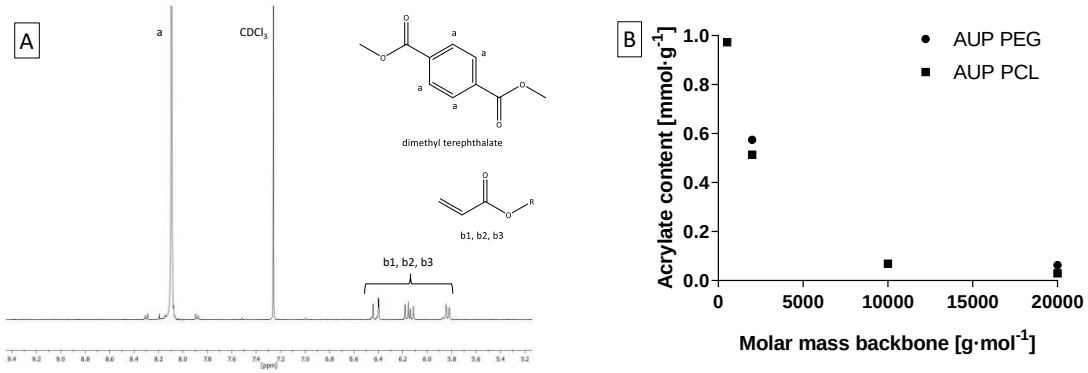

Figure 2.5. (A) Example of an ^{1}H-NMR spectrum (AUP PEG2k) showing the characteristic peak of the dimethyl terephthalate (DMT) standard, the deuterated chloroform (CDCl3) and the acrylate groups. (B) Experimentally determined acrylate content of the developed PEG- and PCL-based AUP precursors (based on ^{1}H-NMR spectra), as a function of the backbone's molar mass.

Figure 2.6.A shows an example of the ^{1}H-NMR spectrum of a synthesized PCL diol with a targeted molar mass of 20000 g·mol^{-1}. The characteristic peaks of the PCL diol are indicated in the spectrum. Figure 2.6.B shows the ^{1}H-NMR spectra of the PCL-based AUPs with the different backbone molar masses. These showed a first indication of the increase in concentration of acrylate functionalities for decreasing molar masses of the backbone. The experimentally determined acrylate content was calculated from the ^{1}H-NMR spectra and can be found in Table 2.1. The acrylate content is plotted as a function of the molar mass backbone in Figure 2.5.B. An exponential decrease in the acrylate content was observed for increasing MM of the backbone. More specifically, increasing the MM of the PCL backbone from 530 to 20000 g·mol^{-1} resulted in a decrease in acrylate content from 0.983 mmol·g^{-1} to 0.036 mmol·g^{-1}, respectively. The same trend was observed for the PEG-based AUPs, showing a decrease from 0.593 mmol·g^{-1} to 0.061 mmol·g^{-1} for the AUP PEG2k and the AUP PEG20k, respectively. These experimentally determined values were found to be lower than the calculated theoretical acrylate content values. As an example, for the AUP PCL2k, the theoretical acrylate content versus the experimental acrylate content is 0.642 mmol·g^{-1} versus 0.512 mmol·g^{-1}, respectively. The differences in these values can result from the differences in targeted and obtained MM of the developed AUP, which will be discussed in more detail in the next paragraphs.

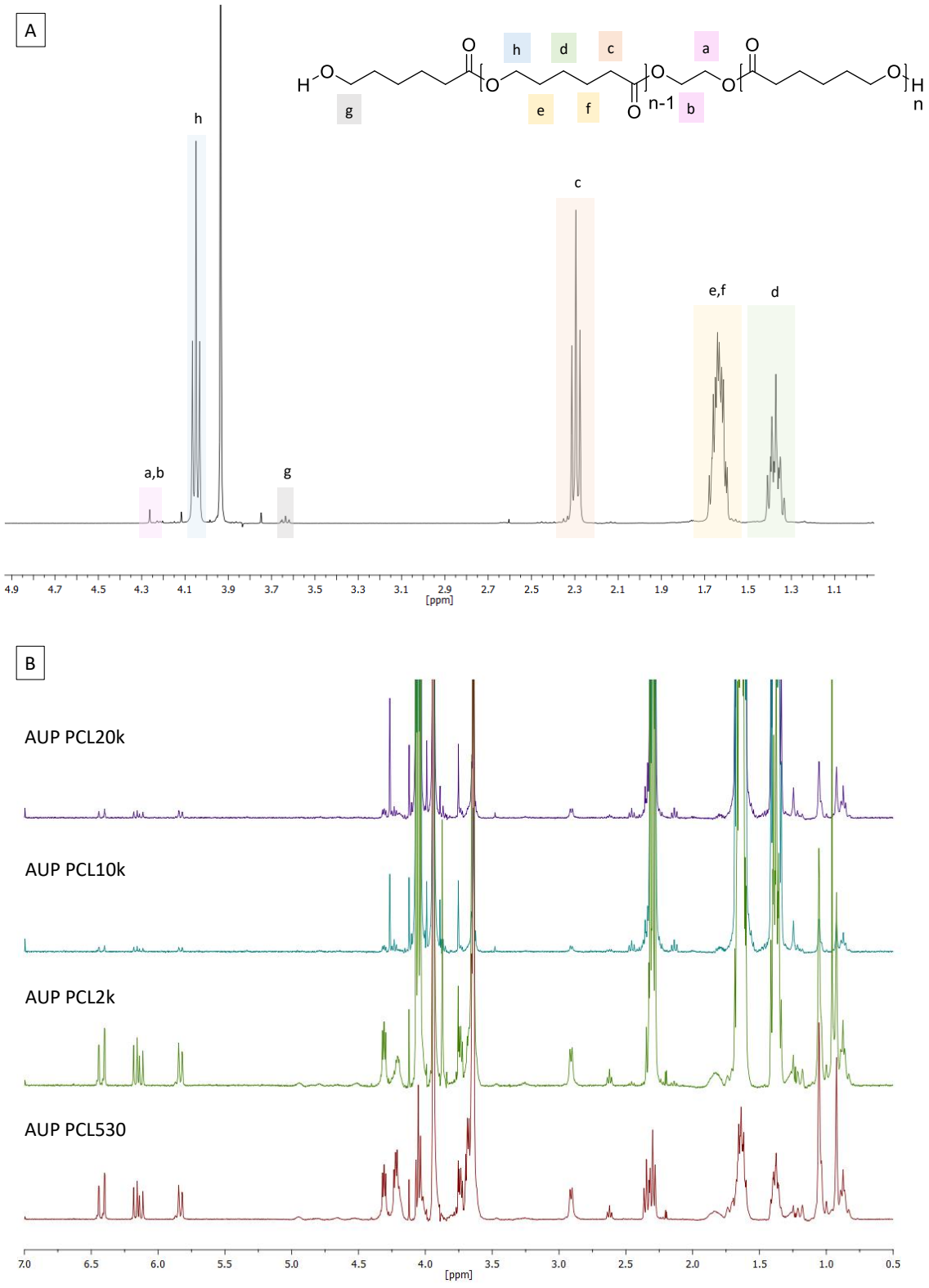

Figure 2.6. (A) Example of the ^{1}H-NMR spectrum of the synthesized PCL diol with a targeted molar mass of 20000 g·mol^{-1} and characteristic groups. (B) ^{1}H-NMR spectra of the PCL-based AUPs with varying backbone molar masses (AUP PCL530, 2k, 10k and 20k).

Table 2.1. Acrylate content, molar mass of backbone and molar mass of the developed AUPs with PEG and PCL backbones of different molar masses.

	AUP PEG2k	AUP PEG20k	AUP PCL530	AUP PCL2k	AUP PCL10k	AUP PCL20k
Acrylate content [mmol·g^{-1}]	0.593	0.061	0.983	0.512	0.064	0.036
MM backbone [g·mol^{-1}]	2000	20000	585	2402	12663	26168
MM AUP [g·mol^{-1}]	3284	31464	1652	3393	13698	27076

As evidenced quantitatively via a ^{1}H-NMR study, increasing the backbone molar mass resulted in a decrease in the concentration of acrylate functionalities (Table 2.1). The latter will strongly influence the curing kinetics and the physical properties of the resulting crosslinked networks including the solvent uptake capacity and the mechanical properties (*vide infra*). It is anticipated that the decreasing acrylate content will lead to a lower crosslink density and therefore lead to a higher solvent uptake capacity and a lower stiffness of the crosslinked AUPs.

In addition to the acrylate content, also the MM of the backbone and of the final AUP precursors were determined (Table 2.1). A linear correlation was observed between the MM of the AUPs as a function of the MM of the backbone, both for the PEG-based and the PCL-based AUPs. The linearity was expected, because the MM of the other groups (total of IPDIs and monoacrylated oligo(ethylene oxide)) was included as a constant value in the MM, resulting in a linear correlation (see also equations in section 2.4.4). For the PEG-based AUPs, the final MMs of the AUPs were found to be approx. 1.6 times higher than the MMs of the backbones. This could be explained by the imperfect selectivity of the catalyst [265]. The bismuth neodecanoate catalyst shows a slightly higher selectivity towards the secondary isocyanate, due to steric hindrance of the primary isocyanate caused by the methyl substituents in IPDI [265,266]. However, due to an imperfect selectivity, also some primary isocyanate groups could react during the 1st reaction step (see 2.2.1) [265,266]. Hence, this could lead to the formation of repeating PEG-IPDI units along with an increase in the average MM of the AUP. For the PCL-based AUPs with a lower MM backbone, the MM of the IPDI (MM of 222.3 g·mol^{-1}) and the monoacrylated oligo(ethylene oxide) (MM of 336 g·mol^{-1}) were predominant in the equation (section 2.4.3) leading to 2.8 and 1.4 times higher MM for the resulting AUP compared to the MM of the backbone. For AUP PCL10k and PCL20k, the high MM of the backbone was predominant over the MM of the monoacrylated endcaps, hence resulting in smaller differences between the backbone's MM and the resulting AUP's MM.

(b) Determination of the thermal properties of the developed AUP precursors

Considering the fact that the construct will be introduced into the human body, it is critical to evaluate at which temperature range the newly developed polymer remains stable. Moreover, the developed materials will be processed using extrusion 3D-printing and melt electrowriting. These techniques require the thermal

stability of the selected material at the elevated processing temperatures, as well as suitable melt viscosities and sufficient chain entanglements. The thermal stability and properties of AUPs were evaluated with TGA and DSC analysis, respectively. From TGA analysis, the degradation onset points were determined. In addition to the degradation onset point, the 5% and 50% mass loss were also recorded. From DSC analysis, the melting temperature, the crystallization temperature and the glass transition temperature were obtained. An overview can be found in Table 2.2.

Table 2.2. Overview of the data obtained with TGA and DSC analysis of the developed AUPs with PEG and PCL backbones of different molar masses.

	AUP PEG2k	**AUP PEG20k**	**AUP PCL530**	**AUP PCL2k**	**AUP PCL10k**	**AUP PCL20k**
T at 5% weight loss [°C]	276.99	346.07	263.35	289.06	214.76	227.22
T at 50% weight loss [°C]	385.43	387.25	362.44	389.31	270.62	276.93
Degradation onset point [°C]	361.74	367.22	319.81	355.08	240.56	256.27
Melting T [°C]	35.43	58.10	-	37.25	51.98	53.64
Enthalpy [J·g^{-1}]	64.26	127.90	-	38.80	64.97	67.86
Crystallization T [°C]	-5.06	45.33	-	-15.29	26.41	30.42
Enthalpy [J·g^{-1}]	48.51	146.8	-	20.57	66.31	71.25
T_g [°C]	-30.03	-47.76	-39.44	-53.61	-48.81	-47.54

The TGA analysis indicated that a 5% mass loss occurred between [215 - 346°C], whereas complete degradation did not occur below 300°C. As an example, for the AUP PCL2k, complete degradation was observed at 425°C. This is in accordance with other PCL-based materials as they appear to be stable up to 380°C and completely degrade around 410°C [267]. The degradation onset points were located between [241 - 367°C]. The PEG-based AUPs showed a similar degradation onset point (around 360°C). For the PCL-based AUPs, a PCL2k backbone showed the highest degradation onset point (355°C), whereas the PCL10k and PCL20k precursors had a degradation onset at temperatures around 250°C. For polymer processing through 3D printing and melt electrowriting, there is thus no degradation risk upon exposure to elevated processing temperatures.

The cooling cycle of the DSC thermograms indicated a dynamic crystallization exotherm for all materials, except for AUP PCL530. For the latter, no crystallization nor a melt peak were detected in the DSC thermograms, whereas a glass transition peak could be observed at -40°C. It can thus be stated that the AUP PCL530 is an amorphous polymer. As anticipated, the melting T and crystallization T and corresponding enthalpies increase with an increasing molar mass of the backbone (see Table 2.2) as a consequence of the increased tendency of higher MM polymers towards the formation of a crystalline phase [268–270]. In the heating cycle, a melting temperature below 60°C was observed for all AUP precursors. Both the T_m and the T_g of the developed PCL-based AUP precursors are slightly lower compared to those

of pure PCL (i.e. T_m = 60°C and the T_g = -60°C) [271,272]. This could be explained by the plasticizing influence of the oligo(EG) spacer in the AUP precursors.

2.5.3 Physical properties of crosslinked AUPs

For the determination of the physical properties of the crosslinked AUPs, the samples were molten at 60°C between two glass plates (covered with a Teflon sheet for easy release of the crosslinked film) separated by a silicone spacer of 1 mm thickness, and UV-irradiated at room temperature for 30 minutes (UV-A, λ = 365 nm, 10 $mW \cdot cm^{-2}$).

(a) Determination of the solvent uptake capacity, gel fraction and crosslinking efficiency

The physico-chemical properties of the crosslinked AUP precursors were assessed by means of a gel fraction (GF) and solvent uptake capacity (SUC) assay (Figure 2.7) as well as HR-MAS ^{1}H-NMR spectroscopy to determine the absolute crosslinking efficiency (CE). For the PEG-based materials, the GF and SUC tests were performed in water, whereas for the PCL-based materials, this was also done in chloroform.

Table 2.3. Gel fraction [%], solvent uptake capacity [-] and crosslinking efficiency [%] of the developed AUPs with PEG and PCL backbones of different molar masses as obtained from HR-MAS measurements.

	AUP PEG2k	**AUP PEG20k**	**AUP PCL530**	**AUP PCL2k**	**AUP PCL10k**	**AUP PCL20k**
Gel fraction [%]	93.4 ± 0.8	93.3 ± 0.5	96.7 ± 2.0	97.6 ± 0.7	57.7 ± 1.0	49.2 ± 0.3
Solvent uptake capacity [-]	1.9 ± 0.1	23.1 ± 0.3	1.7 ± 0.1	4.7 ± 0.1	25.1 ± 0.8	59.5 ± 1.6
Crosslinking efficiency [%]	90.2	91.3	94.5	91.8	60.6	49.8

The solvent uptake capacity is depending on the volume fraction of the polymer, the polymer-solvent interaction parameters, the molar mass between crosslinks and the crosslink density. The solvent uptake capacity for hydrogel-like materials such as the PEG-based AUPs was assessed in water. As anticipated, an increase in backbone MM (from 2k to 20k) resulted in a 10-fold increase in water uptake capacity (Table 2.3, Figure 2.7.A). This is caused by a decreased density of crosslinking points, leading to a higher water uptake capacity. Variations in water uptake capacity lead to networks with different mechanical strengths and diffusion rates towards e.g. ions, drugs and nutrients through the hydrogel network [273]. Given the potential application of the AUPs in tissue engineering and regenerative medicine, and thus in the human body, the SUC of PCL-based AUPs was also performed in water (as a simplification of the body's physiological fluids). The water uptake capacity of PCL-based AUPs was anticipated to be negligible due to the hydrophobic character of PCL [120,264]. The SUC assay in water resulted in negligible values for AUP PCL530, 10k and 20k, and a very limited water uptake capacity of 0.14 ± 0.05 for AUP PCL2k, confirming this statement. The slightly higher values for AUP PCL2k could be due to an interplay between an increase

in hydrophobicity and a decrease in network density. The SUC assay was also performed in chloroform (see Table 2.3 and Figure 2.7.B) as suitable solvent for the PCL-based materials to obtain information on the crosslink density. An increase in SUC from the lower MM to the higher MM AUPs was observed. Again, this is due to a decreased crosslink density.

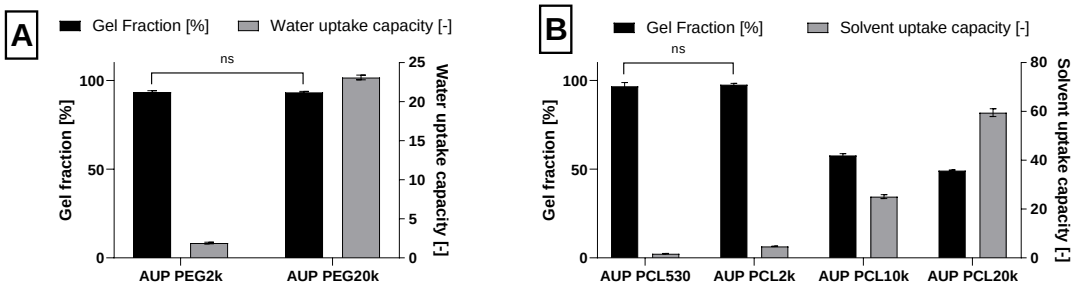

Figure 2.7. Gel fraction and solvent uptake capacity of the developed AUPs: (A) PEG-based AUPs in water, (B) PCL-based AUPs in chloroform. Non-significant differences between groups are indicated, while the other groups are significantly different with p < 0.0001.

The gel fractions represent the fraction of a material that remains incorporated within the network after removal of the non-crosslinked part of the network by incubating the crosslinked material in the appropriate solvent (i.e. water for the PEG-based, versus chloroform for the PCL-based AUPs). A high GF is a first indicator for an efficiently crosslinked network. This can then further be confirmed and quantified by HR-MAS ^{1}H-NMR spectroscopy. For the PEG-based AUPs (2k and 20k) and for the low MM PCL-based AUPs (530 and 2k), very high gel fractions were obtained (>90%). In accordance with the high GFs, also degrees of acrylate conversion exceeding 90% were obtained for these 4 AUP precursors. This implies that almost all acrylates have reacted during crosslinking and that the crosslinked networks maintained their network integrity, leading to the formation of stable, insoluble networks. However, the GFs of the higher MM AUP PCLs (10k and 20k) were found to be significantly lower compared to those of the other AUP networks. This can be due to the low acrylate content in these AUP precursors, leading to a less efficient crosslinking. HR-MAS data also confirmed this, indicating degrees of conversion (crosslinking effiencies) of approx. 60.6 and 49.8% for AUP PCL10k and 20k, respectively. It should be noted that these assays were performed in the absence of a photo-initiator to evaluate the solid-state crosslinking ability of the AUP precursors as such. Addition of photo-initiator is expected to lead to higher GFs and CEs, and thus a more efficient crosslinking, especially for these higher MM AUP PCLs.

(b) Evaluation of the mechanical properties of crosslinked AUP samples

The mechanical properties of the crosslinked precursors were evaluated via rheology and via tensile testing. Rheology is a useful tool to determine the viscoelastic properties of polymeric materials. Here, oscillatory shear tests were performed for gathering information on the viscoelastic behavior of crosslinked AUPs. To this end, a frequency sweep was performed in the linear viscoelastic range of the materials, where the

moduli are independent of the applied strain. The applied frequency sweep in the range of 0.1-10 Hz enables the determination of the storage modulus G', the loss modulus G" and the frequency dependence of the viscoelastic properties. For tensile testing, dogbone-shaped crosslinked films were fixed between the two clamps of the tensile tester and stretched at a constant velocity until break, while the force is being measured. The applied force and extension result in a stress-strain plot that enables the calculation of the Young's modulus, ultimate stress and strain at the break of a material [274]. An example of a stress strain curve of AUP PCL2k can be found in Figure 2.8.A, whereas Figure 2.8.B shows the storage and loss modulus in function of the frequency.

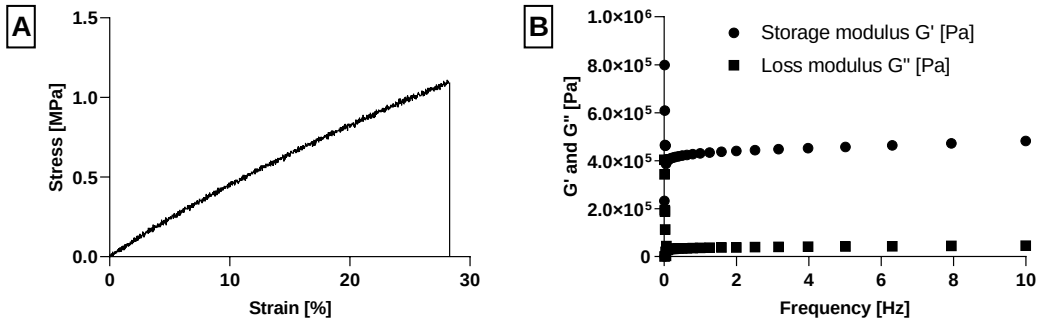

Figure 2.8. Evaluation of mechanical properties on crosslinked AUPs. Example of AUP PCL2k (A) stress strain curve (tensile testing) and (B) storage and loss modulus (rheological measurements).

An overview of the obtained mechanical data is shown in Table 2.4 and Figure 2.9. Storage moduli were approx. a 10-fold higher than the corresponding loss moduli, indicating a well-established crosslinked network. The rheological measurements on crosslinked PEG-based AUP discs revealed a decrease in storage modulus G' and loss modulus G" upon increasing the backbone's MM. This is due to a decreasing crosslink density with increasing AUP MM. For the PCL-based AUPs, AUP PCL2k indicated a slightly higher storage modulus G' of 417.45 ± 35.70 kPa compared to the higher MM AUP PCLs, however no statistically significant differences were obtained ($p > 0.05$). It was anticipated that an increase in MM would lead to a decrease in storage modulus (due to a decreasing crosslinking density). However, as discussed below in more detail, the chain entanglements and crystallinity also affect the storage and Young's modulus of a material, and thus a counterbalancing effect between decrease in crosslink density and increase in crystallinity.

Table 2.4. Ultimate stress, elongation at break and Young's modulus values (from tensile testing), and storage G' and loss moduli G" (from rheology measurements) for the developed AUPs with PEG and PCL backbones of different molar masses.

	AUP PEG2k	**AUP PEG20k**	**AUP PCL530**	**AUP PCL2k**	**AUP PCL10k**	**AUP PCL20k**
Ultimate stress [MPa]	0.40 ± 0.07	0.09 ± 0.01	1.28 ± 0.23	1.50 ± 0.28	12.51 ± 1.56	13.23 ± 1.17

Elongation at break [%]	14.13 ± 2.28	59.75 ± 7.16	17.75 ± 3.13	12.60 ± 7.96	7.34 ± 1.84	5.67 ± 1.16
Young's modulus [MPa]	2.99 ± 0.23	0.22 ± 0.05	8.72 ± 0.55	5.68 ± 0.23	243.44 ± 16.66	321.44 ± 21.23
Storage modulus G' [kPa]	119.25 ± 31.46	7.05 ± 1.67	-	417.45 ± 35.70	343.59 ± 48.68	387.81 ± 27.47
Loss modulus G" [kPa]	12.15 ± 0.88	1.25 ± 0.16	-	31.26 ± 5.43	69.36 ± 9.98	48.71 ± 7.08

The higher initial acrylate concentration in the lower MM AUPs should result in the formation of a more densely crosslinked network, and thereby also in a higher stiffness (Figure 2.9). As anticipated, a higher Young's modulus was observed for AUP PEG2k (2.99 ± 0.23 MPa) compared to AUP PEG20k (0.22 ± 0.05 MPa), which is indicative for an increased stiffness. Similarly, the ultimate stress was found to be higher for the lower MM backbone precursor (i.e. AUP PEG2k). In contrast to the ultimate stress and Young's modulus, the elongation at break increased from 14.13 ± 2.28% for AUP PEG2k to 59.75 ± 7.16% for AUP PEG20k as a result of the increase in MM (Figure 2.9.A).

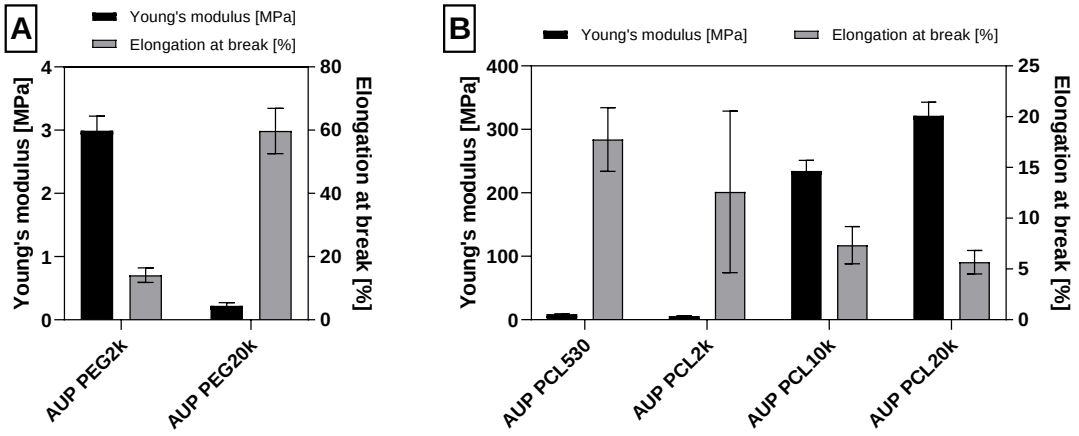

Figure 2.9. Young's moduli and elongations at break of the developed AUPs: (A) PEG-based, (B) PCL-based.

A similar trend was observed for AUP PCL530 compared to AUP PCL2k (Table 2.4), where a higher Young's modulus was observed for AUP PCL530 (8.72 ± 0.55 MPa) compared to AUP PCL2k (5.68 ± 0.23 MPa). However, for the higher MM PCL backbones, the trend inverted: AUP PCL10k and 20k showed an increased stiffness (i.e. higher Young's modulus) and a more brittle structure (i.e. low elongation at the break) upon increasing the MM of the backbone. Moreover, the developed AUP PCL20k indicated a higher maximum force and ultimate stress, and a lower corresponding strain when compared to the lower MM AUP counterparts (AUP PCL530 and 2k). Based on these results, it can be concluded that in case of PCL-based AUPs, from a certain MM of the backbone, an increase in MM mainly leads to stronger but less flexible materials. In addition, the increase in MM of the PCL diol backbone can also influence the crystallinity of the

AUP. It is hypothesized that the effect of the higher MM leading to an increased crystallinity and more chain entanglements and thus increased mechanical strength, is overcoming the reduced crosslinking ability due to the lower acrylate content for AUP PCL20k compared to AUP PCL530 or 2k. This hypothesis is based on similar observations as reported by Grosvenor *et al.* [275]. They observed an increased Young's modulus and tensile strength when increasing the MM of PCL, up to a certain point whereafter it started decreasing again, and concluded this was due to crystallinity and chain entanglements [275]. Moreover, based on the DSC data (section 2.5.2b) [276], the crystallinity (in %) increased with increasing MM backbone. Indeed, a crystallinity of 15%, 48% and 51% was obtained for AUP PCL2k, AUP PCL10k and AUP PCL20k, respectively.

2.6 Conclusions

Tuning the physical properties of a material would enable its successful application in specific tissue engineering and regenerative medicine fields. In this chapter, a series of acrylate-endcapped urethane-based polymers based on PEG- or PCL backbones with varying MMs was synthesized and characterized. The structural and thermal properties of the non-crosslinked precursors were analyzed. FT-IR and ^{1}H-NMR spectroscopy confirmed the chemical structure of the developed AUPs, and the latter technique indicated that AUPs with differences in acrylate content, backbone MM and AUP MM were synthesized. Determination of their thermal properties confirmed that the developed materials are processable at elevated temperatures without exhibiting degradation which is important for processing techniques such as extrusion 3D printing and melt electrowriting. The physical properties of the crosslinked AUPs revealed that by varying the backbone type (i.e. PEG or PCL) and/or the backbone MM (i.e. 530 g·mol^{-1} to 20 kg·mol^{-1}), AUPs with a wide range of physico-chemical characteristics can be obtained. For the PEG-based materials, an increase in solvent uptake capacity was observed with increasing MM (i.e. 1.9 ± 0.1 for AUP PEG2k versus 23.1 ± 0.3 for AUP PEG20k). For the PCL-based materials, the hydrophobic character of the PCL material led to almost no swelling. The developed AUPs showed Young's moduli ranging from 0.22 ± 0.05 to 321.44 ± 21.23 MPa, elongations at break between 7.34 ± 1.84 and 59.75 ± 7.16%, and ultimate stresses between 0.09 ± 0.01 and 13.23 ± 1.17 MPa. This indicates a potential application range of the developed AUPs to reconstruct various tissues or to construct medical devices. Potential applications can be found in the regeneration of, for example, skeletal muscle (Young's modulus of 0.3-3 MPa), blood vessels (1-2 MPa), tendons (0.5-1.5 GPa) [76,277,278].

Chapter 3: Melt electrowriting as an emerging processing technique for the development of tubular constructs with a predefined architecture

This chapter describes the processing of an AUP PCL20k precursor (synthesis and characterization, see Chapter 2) using melt electrowriting. The MEW processing was conducted by N. Pien in collaboration with M. Bartolf-Kopp within the fmz lab at Würzbürg University (Germany) under the supervision of Dr. T. Jüngst (during a 5-week research stay of N. Pien at fmz). The mechanical evaluation of the developed tubular constructs was executed by N. Pien at the fmz lab, whereas the physico-chemical characterization of the AUP material and the developed MEW constructs was conducted at PBM (UGent). The HR-MAS ^{1}H-NMR spectroscopy measurements discussed in this chapter were performed by J. Delaey (UGent) using the facilities of Prof. J. Martins (UGent). The GPC measurements and the *in vitro* biological evaluation were performed by L. De Vos (UGent) and L. Parmentier (UGent), respectively. Data processing and analysis was done by N. Pien. This chapter has been published in:

N. Pien [μ], M. Bartolf-Kopp [μ], J. Delaey, L. Parmentier, L. De Vos, D. Mantovani, S. Van Vlierberghe, P. Dubruel, T. Jüngst. Melt electrowriting of a photo-crosslinkable poly(ε-caprolactone)-based material into tubular constructs with predefined architecture and tunable mechanical properties. Macromolecular Materials and Engineering, DOI: 10.1002/mame.202200097, Published: MAY 2022, Impact Factor: 4.367. Peer Reviewed.

[μ] : Authors contributed equally.

3.1 Résumé

L'électrowriting en fusion (MEW) est une technique de fabrication additive électro-hydrodynamique qui gagne en importance ces dernières années. Ceci est principalement dû à la capacité de MEW à produire des constructions définies avec des éléments de l'ordre du micron à partir de polymères fondus. Ces constructions sont très pertinentes pour les applications biomédicales. Une configuration spécifique du MEW permet même d'imprimer des constructions tubulaires qui sont utilisées pour créer des structures tubulaires de petit diamètre. Le petit nombre de matériaux compatible est l'un des obstacles qui limitent l'application plus large du MEW en biomédecine. Pour pallier cet obstacle, dans ce chapitre, un polymère à base d'uréthane (AUP), basé sur poly(ε-caprolactone) (PCL) avec une masse molaire de 20000 $g \cdot mol^{-1}$ (AUP PCL20k) comme matériau de base, est synthétisé et utilisé pour le MEW.

3.2 Abstract

Melt electrowriting (MEW) is an electro-hydrodynamic additive manufacturing process that is gaining more prominence in recent years. This is mainly due to the ability of MEW to produce defined constructs with elements in the micron-range from polymer melts. These constructs are highly relevant for biomedical applications. A specific configuration of MEW even enables printing tubular constructs which are utilized to create small diameter tubular structures. The small pool of processable materials is one of the bottlenecks that limit wider application of MEW in biomedicine. To alleviate this obstacle, in this chapter, an acrylate-endcapped urethane-based polymer (AUP), based on poly(ε-caprolactone) (PCL) with a molar mass of 20 000 $g \cdot mol^{-1}$ (AUP PCL20k) as backbone material, is synthesized and utilized for MEW. ^{1}H-NMR and FT-IR spectroscopy confirm the successful modification of the PCL backbone with photo-crosslinkable acrylate end groups. Initial printing experiments of AUP PCL20k reveal limited printability but the photo-crosslinking ability is preserved throughout the process, allowing the material to be crosslinked after MEW processing. To improve printability and to tune the resulting mechanical properties of the developed constructs, the AUP PCL20k material is blended with commercially available PCL (ratio AUP PCL20k:PCL of 80:20, 60:40 and 50:50). Print fidelity improves greatly for blends of 60:40 and 50:50. Blending enables tailoring mechanical properties of the constructs and the resulting properties are in the range of relevant blood vessels for transplantation surgeries. The crosslinking ability of the material allows even the pure AUP PCL20k to be manipulated after processing and shows a significant difference in mechanical properties of the 80:20 blend before and after post-processing crosslinking. An *in vitro* cell compatibility assay using human umbilical vein endothelial cells (HUVECs) also demonstrates the non-cytotoxicity of the newly synthesized material and its blends.

3.3 Introduction

Melt electrowriting (MEW) is an emerging high-resolution, direct-writing additive manufacturing technique that is based on the deposition of an electro-hydrodynamically stabilized molten polymer jet onto a collector [279]. While conceptually comparable to the widely known principle of electrospinning, MEW offers the advantage of precisely depositing fibers in a well-defined pattern, allowing for intricate geometries to be realized [280]. In addition, a distinct advantage over conventional 3D printing (3DP) techniques, such as fused deposition modeling (FDM), is the smaller fiber diameter (i.e. 0.8-30 µm) [236] that can be achieved with MEW [281].

At present, one of the challenges associated with the use of MEW is the limited availability of compatible materials [282]. The ideal material should not only be efficiently processable via MEW (i.e. low melting point, slow thermal/hydrolytic degradation, rapid solidification), but should also fulfill the requirements of the intended application. In the field of regenerative medicine, this implies that the final construct should elicit biocompatibility and cell-biomaterial interactions, have a controllable biodegradation rate and tunable mechanical properties that strongly depend on the requirements of each individual tissue [141,159]. Additionally, bioactive compounds bound to the surface or a controlled release from the biomaterial is favorable to generate an ideal growth environment for cells [283,284]. Generally, thermoplastic polymers are chosen for MEW as they are processable above a certain temperature, and solidify upon cooling [285]. Most polymers used for MEW have a high molar mass (MM), implying an increasing degree of chain entanglements, which is improving jet stability during the MEW process [286]. The current gold standard used in MEW is poly(ε-caprolactone) (PCL). This is mainly due to its semicrystalline and biodegradable properties, low melting temperature and rapid solidification, and the U.S. Food and Drug Administration (FDA) approval for multiple clinical applications [287]. However, it also has the drawback of being a hydrophobic polymer, featuring a high elongation at break but overall low elastic properties [288]. Due to this, PCL is attractive for biomedical applications including scaffolding and drug releasing material [289], but is still lacking the ideal mechanical endurance to sustain tensile stress without plastic deformation to be the ideal material for applications in regenerative medicine [290,291].

To overcome the limitations of conventional PCL, blending has been used to modify and also enhance the properties of the material [291]. Ideally, a blend should improve upon the favorable characteristics of a material while reducing the unwanted attributes of the educts. Several different materials from synthetic to organic have been used in the past to achieve more biocompatible or mechanically comparable blends with tissue models [291]. Problematic for the blending process are occurrences where the materials are not homogeneously mixing, leading to a phase separation or inhomogeneous distribution of the blended materials within the compound [292].

A different approach to the challenge has been investigating the processability of other thermoplastic polymers, including commercially available polypropylene (PP) and poly(vinylidene fluoride) (PVDF) [293], as well as polymers specifically synthesized for MEW processing. Examples are the $(AB)_n$-type segmented copolymers, poly(2-oxazoline)s (POx), UV-crosslinkable polymers like poly(L-lactide-co-ε-caprolactone-co-acryloyl carbonate) (poly(LLA-ε-CL-AC)) [290], and PCL-based blends [282,287]. Despite those efforts, materials that enable printing constructs with tailorable mechanics and optimal mechanics for biomedical application are scarce. In addition, material blends that feature good results with MEW are prepared using solvents, hampering a transition into biomedical applications.

An interesting class of recently developed materials are acrylate-endcapped urethane-based polymers (AUP). One of their main benefits is that they can be designed by varying the different constituting building blocks [294,295]. Among other things, this enables the tunability of the mechanical properties of the developed material. Another key advantage of the AUP material is that it enables crosslinking in solid state [264]. In the past few years, AUP materials have been synthesized to serve various processing techniques and biomedical applications. For each specific application, the building blocks were selected in such a way that the material's properties would correspond to the application's requirements [120,121,296–298]. Initially, the AUP materials were based on a poly(ethylene glycol) (PEG) backbone in order to attain hydrogel-like properties [294,295]. These PEG-based AUPs have been processed successfully by 3D printing and electrospinning and have been used for meniscus tissue engineering (TE) and as wound dressings [296–298]. Next, AUPs with other backbones (e.g. PCL), exhibiting a variation in constituting building blocks (i.e. varying the spacer and end groups) were reported. To date, AUPs based on a PCL backbone with a MM of 2000 $g \cdot mol^{-1}$ have been evaluated in 2-photon polymerization processing [264] and for tendon repair [120,121].

Initially, MEW was established on planar collectors, but meanwhile, it has transitioned towards the fabrication of three-dimensional tubular geometries [244,299] as various applications in regenerative medicine rely on such structures (including blood vessels, urethra and ureters, intestine, nerve etc.) [300]. Therefore, research has been devoted towards the elaboration of methods to improve the design and fabrication of tubular scaffolds by exploiting specialized printer set-ups and mandrel collectors [244,299]. In this regard, the advantages of MEW (onto a rotating mandrel collector) offer great potential as they enable the generation of predefined architectures with high resolution, high porosity (i.e. > 87%) [301] and interconnectivity due to the small fiber diameters. Especially, adaptable mechanical scaffold properties resulting in flexibility and scaffold compliance would further advance applicability of melt electrowritten structures for applications in regenerative medicine like vascular grafts but, to date, materials used in tubular MEW are even more limited as those used with planar collectors [244].

To explore the potential of MEW as a processing technique to develop tubular scaffolds with a predefined architecture and tunable mechanical properties, we demonstrate a straightforward synthesis route for the development of an AUP material with a PCL backbone possessing a photo-crosslinkable moiety at each end and its processability with MEW. We show that post-process crosslinking has a significant impact on the mechanical properties of the constructs produced by MEW compared to "commonly used" non-crosslinkable PCL. Blending of functionalized AUP PCL and non-modified PCL enables tailoring mechanical properties as well as improving printing behavior. Both materials as such, blends with unmodified medical grade PCL, and the MEW processed tubular constructs are evaluated with respect to their physico-chemical properties. In addition, the cytocompatibility of the developed constructs is determined by an *in vitro* assay.

3.4 Materials and methods

3.4.1 Material synthesis and characterization

An acrylate-endcapped urethane-based polymer with a PCL backbone of 20000 $g \cdot mol^{-1}$ (AUP PCL20k) was synthesized following the synthesis protocol described in Chapter 2 (Section 2.4). The AUP PCL20k was physico-chemically characterized, as described in Chapter 2 (Section 2.5).

3.4.2 Material processing using melt electrowriting

(a) Material selection for MEW processing

For the blended materials, an automated micro-compounder system (MC 5, Xplore Instruments BV) was utilized. To the blends, 2 mol% TPO-L as photo-initiator was added with respect to the amount of AUP PCL20k material in the blend or pure batch of material. The following ratios have been realized by compounding at 85°C for 30 min at 50 rpm: (1) AUP PCL20k, (2) AUP PCL20k:PCL 80:20, (3) AUP PCL20k:PCL 60:40, (4) AUP PCL20k:PCL 50:50, and (5) PCL (Purac Purasorb PC 12, 1.18 $dl \cdot g^{-1}$ density, 80 $g \cdot mol^{-1}$).

(b) Device and processing parameters

Tubular constructs of AUP PCL20k or PCL, as well as blends of the two materials were processed with a custom-made melt electrowriting device with a cylindrical and interchangeable collector (diameter of 3 mm). The motorization is based on an Aerotech axis system (PRO115) and uses the A3200 (Aerotech) software suite as coding and machine operating interface. A modified code has been developed similar to previous work [245] to move the collector in translational as well as rotational directions to allow precise fiber placement onto a steel mandrel in predetermined winding angles. For the extrusion of materials, polypropylene cartridges and 22G flat tipped needles (Nordson EFD) were used in all experiments. Printing parameters were optimized for each individual blend of material and maintained throughout the experimental process.

The following predefined specifications were chosen for tubular construct generation: the length of the construct was set to 11.56 mm, the number of fiber layers on top of each other was set to 20, the angle at which the fibers are aligned in relation to the longitudinal axis (winding angle) was 70°, and the number of turning points (pivot points) of the construct was 8. Further description of the printing variables can be found in the work of McColl et al. [245].

3.4.3 Tubular construct characterization

(a) Photo-crosslinking of developed tubular constructs

A post-processing UV treatment was performed on the developed AUP PCL20k/PCL tubular constructs by ultraviolet (UV-A) irradiation at 2 x 5 $mW \cdot cm^{-2}$ (Philips TL 0W/08 P8 T5/BLB lamps in the holder of Bi-Sonic Technology Corp.; model 8B-230 HB; 250 - 450 nm range) for 30 minutes [120].

(b) Visualization of the tubes' micro- and macro-architecture

The tubular constructs were analyzed using a SEM device (Crossbeam CB 340 SEM, Carl Zeiss) for evaluation of the fiber diameter and the general fiber morphology. Videos to illustrate the mechanical behavior of the different AUP PCL20k/PCL blend tubular constructs have been recorded on a mirrorless interchangeable-lens camera (Nikon Z 4, Nikon Corporation) with a macro-lens (AF Micro-Nikkor 200 mm 1:4D IF-ED, Nikon Corporation).

(c) Physico-chemical characterization of the tubular constructs

- *Determination of gel fraction, solvent uptake capacity and crosslinking efficiency of the developed tubular constructs*

Crosslinked tubular constructs were weighed (Wi). Next, the tubular constructs were incubated in deionized water for 24h at room temperature and weighed in the swollen state (Ws). Then, the tubular constructs were removed, dried and weighed again (Wf). The SUCs and GFs were determined using Equations (2.7) and (2.8) (see Chapter 2), respectively.

The crosslinking efficiency (CE) was assessed by high resolution magic angle spinning (HR-MAS) ^{1}H-NMR spectroscopy on a Bruker Avance II 700 spectrometer. The spectrometer contains a HR-MAS probe which was equipped with a ^{1}H, ^{13}C, ^{119}Sn and gradient channel. The spinning rate was set at 6 kHz. The freeze-dried samples were placed in a 4 mm zirconium oxide MAS rotor with Kel-F disposable inserts (50 µL). Next, 30 µL $CDCl_3$ was added to let the samples swell. Finally, the samples were homogenized prior to the measurement. A Kel-F cap was used to close the rotor. For the calculation of the Degree of Conversion (DC) from the NMR spectra [262] using Equation (2.9) (see Chapter 2), the ethylene oxide peaks were chosen as reference peaks since they represent groups that do not participate in the crosslinking reaction, nor does this peak overlaps with the peaks of the blended virgin PCL.

- *Influence of melt electrowriting on the molar mass of the material*

The number average molar mass (M_n), the weight average molar mass (M_w) and the polydispersity (Đ) were determined by conventional gel permeation chromatography (GPC) using polystyrene standards (Agilent Technologies, weight average molar mass range: 580 – 1 930 000 g·mol^{-1}). The polymers were dissolved (10 mg·mL^{-1}) in chloroform (Biosolve, analytical grade) and filtered through a membrane with a 0.45 mm pore size. The analyses were performed by liquid chromatography (Alliance Waters 1515 isocratic pump with Waters 717plus Autosampler and Waters 2414 Refractive Index Detector) equipped with PLGel Mixed-D polystyrene divinylbenzene GPC columns (353 PSI). The sample components were separated by the GPC columns based on their molecular size in solution and detected by a refractive index detector.

- *Evaluation of mechanical properties of the developed tubular constructs by uniaxial tensile testing*

To determine the mechanical properties of the fabricated tubular constructs, a customized fixation setup on a dynamic mechanical testing device (ElectronForce 5500, TA Instruments) was used. The sample mounting construction allowed two metal pins to be introduced into the luminal cavity of the constructs and applied radial tensile force during the testing procedure (Figure S3.1). Samples were measured in a 100-cycle waveform setup with a peak displacement of 18% strain in reference to the inner tube diameter. Evaluation of the construct measurements has been done after initial hysteresis subsided and the peak force stabilized over several cycles. Pull to failure quantification used the identical setup and displaced the construct over a distance of 10 mm, equivalent to 330% strain. Both non-UV treated, and UV-treated tubular MEW constructs have been evaluated in triplicate.

(d) Biological evaluation of the tubular constructs using human umbilical vein endothelial cells

The biocompatibility of the various materials (AUP PCL20k, PCL and their combinations 50:50, 60:40 and 80:20) was evaluated through indirect contact *in vitro* biological assays. Human umbilical vein endothelial cells (HUVECs) (Lonza) were cultured under standard incubator culture conditions (37°C, 5% CO_2) with supplemented endothelial cell growth medium-2 (EGM-2) (Promocell) additionally supplemented with 1% Pen/Strep (Sigma). Medium was changed every 2-3 days. The cells were split until a confluency of 80-90% and used at passage 5.

The MEW tubes were sterilized through incubation in 70 v/v% EtOH for 24 hours with a change after 12 hours. Subsequently, the samples were exposed to UV-C irradiation for 2 hours followed by incubation at 37°C in culture medium at a concentration of 1.125 ml·mg^{-1} of material during 1, 3 and 7 days. Short-term component leaching was then evaluated on seeded cells both in terms of cell viability as well as cell proliferation.

To this end, 10 000 HUVECs were seeded into a well of a 96-well plate. The cells were allowed to attach for 24 hours awaiting the addition of the medium in contact with the manufactured tubes for 1, 3 or 7 days.

This test was performed in triplicate. Cells seeded on tissue culture plastic with the addition of standard supplemented EGM-2 medium was included as reference.

HUVEC cell proliferation was assessed through an MTS (3-(4,5-dimethylthiazol-2-yl)-5-(3-carboxymethoxyphenyl)-2-(4-sulfophenyl)-2H-tetrazolium) (Abcam) assay which was applied in a 20 v/v% ratio with culture medium to the cells. Reduction of the component into its formazan dye by the HUVECs during 2 hours of incubation at 37°C in the dark enables the quantification of metabolic activity through absorbance measurements at 490 nm (BioTek Instruments, EL800 Universal Microplate Reader with GEN5 software).

A live-dead viability assay was performed through the addition of 0.2 v/v% calcein-acetylmetoxyester (Ca-AM) (Sigma) and 0.2 v/v% propidium iodide (PI) (Sigma) in phosphate buffered saline (PBS). The cells were visualized after 10 min of incubation in the dark with a fluorescence microscope (Olympus IX81 with software Xcellence Pro) with a green fluorescent protein (GFP) filter for living cells and a texas red (TxRed) filter for dead cells.

3.4.4 Statistical analysis

All data were analyzed using GraphPad Prism 8.0.2. A one-way or two-way ANOVA test was performed followed by a Tukey post-test. The symbols representing the different significant levels are indicated on the graphs (i.e. ns = $p > 0.05$; * = $p \leq 0.05$; ** = $p \leq 0.01$; *** = $p \leq 0.001$).

3.5 Results and discussion

To successfully engineer a specific tissue model, research is focusing on material design and advances in processing. A combination of the emerging technology of MEW and the design of novel materials provides a promising approach for the fabrication of mechanically adjustable tubular constructs for applications in regenerative medicine. Herein, we hypothesize that our photo-crosslinkable PCL-based polymer is a suitable material feedstock to be applied in MEW. The presence of photo-crosslinkable moieties in the AUP and the possibility to easily blend with conventional PCL enables fine-tuning of material properties. A physico-chemical characterization was performed, before evaluating the material's potential for the use in in MEW of tubular constructs. In addition, the tubular samples were analyzed with respect to physico-chemical and biological properties after fabrication. A schematic overview of the research conducted in this study is visualized in Figure 3.1.

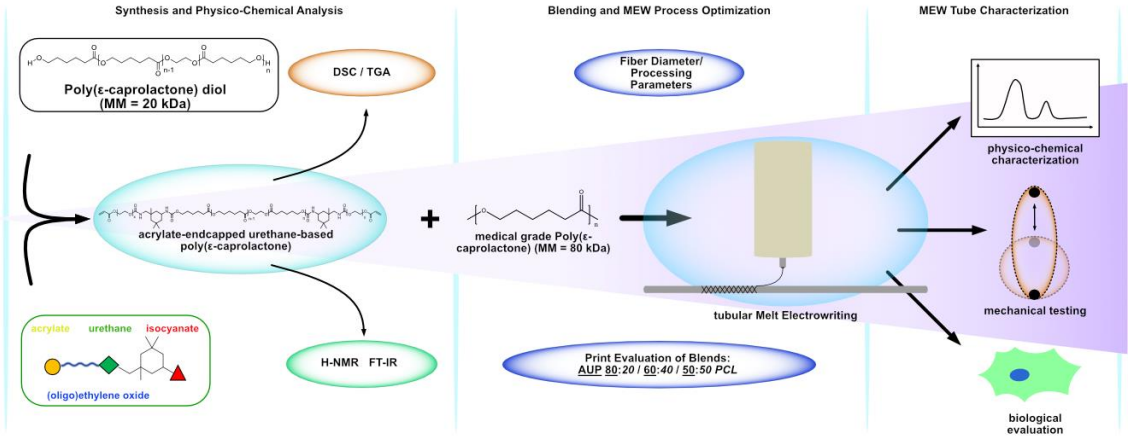

Figure 3.1. Experimental overview of the synthesis and process evaluation.

3.5.1 Synthesis and physico-chemical analysis

There are some key requirements to consider when designing a material for MEW. One important aspect includes the melting and glass transition temperature which enable processing of the material in a molten state. Ideally, the material is easily processable above its melt temperature due to reduced melt viscosity, lacks pronounced thermal degradation and is rapidly solidifying after processing [285]. These properties can be achieved by a sufficiently high molar mass [302] so that enough chain entanglements are present which result in viscoelastic melt properties that improve processing via MEW and help generating a stable jet [286].

As described in the introduction, AUPs are a class of materials that can be designed by varying the constituting building blocks (Chapter 2, Figure 2.2). With respect to the material requirements of MEW, an AUP with a PCL backbone of a higher molar mass (MM = 20000 $g \cdot mol^{-1}$) compared to previously reported PCL-based AUPs (MM = 530 and 2000 $g \cdot mol^{-1}$) [120,264] was synthesized. In addition to the higher MM aiming at improving the material's MEW processing potential, the acrylate endgroups enable crosslinking of the developed constructs after processing. The structural and physico-chemical characterization of the developed AUP PCL20k precursor can be found in Chapter 2.

Upon tensile testing, the crosslinked AUP PCL20k showed an ultimate force of 70.97 ± 10.73 N, a maximum stress of 13.23 ± 1.17 MPa with a corresponding strain of 5.67 ± 1.16%. The stress-strain relationship indicated a Young's modulus of 321.44 ± 21.23 MPa. When comparing the developed AUP PCL20k to commercially available PCL, a similar maximum stress (13.58 ± 0.83 MPa), a higher maximum strain (10.62 ± 1.18%), and a 16-fold lower Young's modulus (18.90 ± 5.15 MPa) was observed for the non-modified PCL. This implies that both materials will lead to tubular constructs with different mechanical properties after MEW processing. Moreover, it offers tuneability in mechanical properties when both materials are blended in different ratios as will be demonstrated later in this chapter.

3.5.2 Blending and MEW process optimization

After characterization of the developed PCL-based AUP (MM = 20000 g·mol^{-1}, AUP PCL20k), the potential for its application as MEW processable material was considered. The key processing parameters for MEW include i) mass flow rate, ii) collector speed, iii) electric field, and iv) melt temperature. Viscosity and conductivity of the fluid define the properties of the molten polymer and need to be considered when choosing process conditions [242]. It should also be stated that upon changing one of these key process parameters, the other parameters will also be influenced, and thus a proper optimization of all parameters in different combinations is required. The process parameters were adjusted until a suitable setting could be elaborated to achieve constant material flow and construct layering.

After achieving a stable material processing parameter set, the construct specifications were tested and optimized. Following predefined specifications were chosen for tubular construct generation: the length of the construct was set to 11.56 mm, the number of fiber layers on top of each other was set to 20, the angle which the fibers are aligned in relation to the longitudinal axis (winding angle) was 70°, and the number of turning points (pivot points) of the construct was 8. Further description of the printing variables can be found in the work of McColl *et al.* [245].

A printability evaluation of the pure AUP PCL20k material revealed vastly different characteristics compared to commercially available, non-modified PCL. The developed AUP PCL20k was more prone to electrical discharge phenomena, known as arcing, at a higher incidence than regular PCL. This was compensated by reducing the applied voltage and by increasing the printhead distance to the collector. Overall, it was difficult to retain fiber morphology directly after printing, resulting in fiber merging and fusion, requiring lower melt temperatures to allow quicker solidification of the material. This slow solidification characteristic also manifested in very inhomogeneous fibers as well as attraction between the previously placed fibers and newly deposited, causing deviations from the programmed printing path. Nevertheless, it was possible to create constructs that resembled the programmed geometry (Figure 3.2).

To improve the printing properties of AUP PCL20k, blending with non-modified PCL was performed. This enables combining the favorable printing behavior of medical grade PCL with benefits of the developed photo-crosslinkable AUP PCL20k material. It is assumed that the higher molar mass of PCL improves printability and fiber deposition while AUP PCL20k enables modification of the material´s mechanical properties via photo-crosslinking. In MEW, combining different materials is usually performed by mixing those in a dissolved state. Such an approach has already been undertaken in studies like the one by Hochleitner *et al.* [303,304] where blending of polymers to create a co-polymer for MEW was applied in order to alter the material properties. Toluene was utilized as a solvent to generate the blend. In contrast, blending was performed using a compounder to physically mix the PCL and AUP PCL20k to create a blend of materials in this study. To evaluate how much PCL was needed to improve printing properties of AUP

PCL20k and the resulting mechanics, several ratios with different composition of AUP PCL20k:PCL were chosen (80:20 and 60:40). Furthermore, a blend of 50:50 was added as previous studies with AUP have shown beneficial electrospinning behavior using this material ratio [120]. Materials were blended for 30 minutes at 85°C and afterwards transferred into printing cartridges. Melt viscosity and shear rate were recorded during blending, allowing for an initial evaluation of the blends and planning of process parameters. Lower viscosities usually require adaptation towards less material flow (reduced voltage / pressure) or faster collector speeds to properly distribute the material to achieve straight and homogeneous fibers [286]. Table 3.1 illustrates the printing parameters chosen to process the blends. Overall, printability of the blends increased with higher ratios of PCL within the blend. A sweet spot could be reached at 60:40 where the fiber morphology and fiber diameter variation were already very comparable to commercial PCL. The blend with a 50:50 ratio showed a similar result. A slight increase in fiber diameter of 4-5 µm was the most pronounced difference between the 60:40/50:50 blend and pure PCL. The 80:20 ratio still showed increased fiber merging and required adjustments of printing parameters. Overall processability of AUP PCL20k with MEW is possible, and with the blending of AUP PCL20k and commercial PCL, a beneficial printing behavior could be demonstrated.

Table 3.1. MEW printing parameters for the different materials processed. Veff = effective velocity, dm = distance to mandrel, ZHS (Z-Axis Height Shift) = strand layer height. Fiber diameter as measured on SEM images. Melt viscosity and shear rate of the materials and material blends as obtained by compounding at 50 rpm, T = 85°C and t = 30 min. ± indicates the standard deviation.

Material	Temperature [°C]	Pressure [bar]	Voltage [kV]	V_{eff} [mm·min^{-1}]	d_m [mm]	ZHS [µm]	Fiber diameter [µm]	Melt viscosity [kPa·s]	Shear rate [kN·m^{-2}]
AUP PCL20k	70	0.55	5.5	511	4.5	15	66.70 ± 34.22	0.26	4.1
80:20	80	0.60	4.4	707	3.5	17	36.21 ± 6.74	0.28	4.2
60:40	89	0.60	4.4	707	3.5	17	18.81 ± 1.76	0.32	5.1
50:50	89	0.60	4.4	707	3.5	14.5	17.02 ± 1.43	0.34	5.6
PCL	89	0.65	5.8	500	3.55	14.5	13.46 ± 0.23	0.35	5.7

An overview with representative images of each blend-ratio-group is depicted in Figure 3.2. The images were taken as a basis for the evaluation of the fiber diameter of the different blends, an integral value to assess the quality of MEW-processed materials [305]. A clear trend is visible regarding scaffold morphology: the scaffolds become more amorphous and inconsistent in their fiber distribution and overall structure when more AUP PCL20k is present in the material, with the most prominent effect observed in the pure AUP PCL20k sample. This effect can also be correlated with the increase in fiber diameter and the homogeneity

of the produced fibers (PCL 13.46 ± 0.23 µm, AUP PCL20k 66.7 ± 34.22 µm). The scaffolds made with pure AUP PCL20k and the ones with an AUP PCL20k:PLC ratio of 80:20 led to fiber morphologies which started to lose their clear appearance as single fibers stacked on top of each other. This is clearly visible at the crossover points of deposited fibers (Figure 3.2, 3rd column). With higher amounts of AUP PCL20k (ratios of 80:20 and higher), fibers begin to merge with each other as soon as they are stacked, indicating a slow solidification of the material after extrusion. Adjustments to the printing temperature were necessary to fabricate the structures (Table 3.1). The cause of this effect can potentially stem from a thermodynamically different behavior of AUP PCL20k compared to PCL. It is hypothesized that a combination of factors including the differences in melt viscosity and shear rate (Table 3.1), which were found to be lower for AUP PCL20k (0.26 kPa·s) compared to PCL (0.35 kPa·s), and the slightly lower melting temperature of AUP PCL20k (T_m = 53.96°C) compared to PCL (T_m = 60°C) can foster the effect of fiber fusing.

To quantitatively illustrate the difference between the mechanical properties of the printed constructs made with varying AUP PCL20k:PCL ratios, a manual compression test has been conducted (Supplementary video). Clearly visible is the increasing stiffness and resistance to compression for increased AUP PCL20k content compared to pure PCL, indicating the effective alteration of the material properties after processing, and successful post-processing crosslinking of the materials. The pure AUP PCL20k sample is not able to withstand the compression and breaks immediately while the blends all remain undamaged.

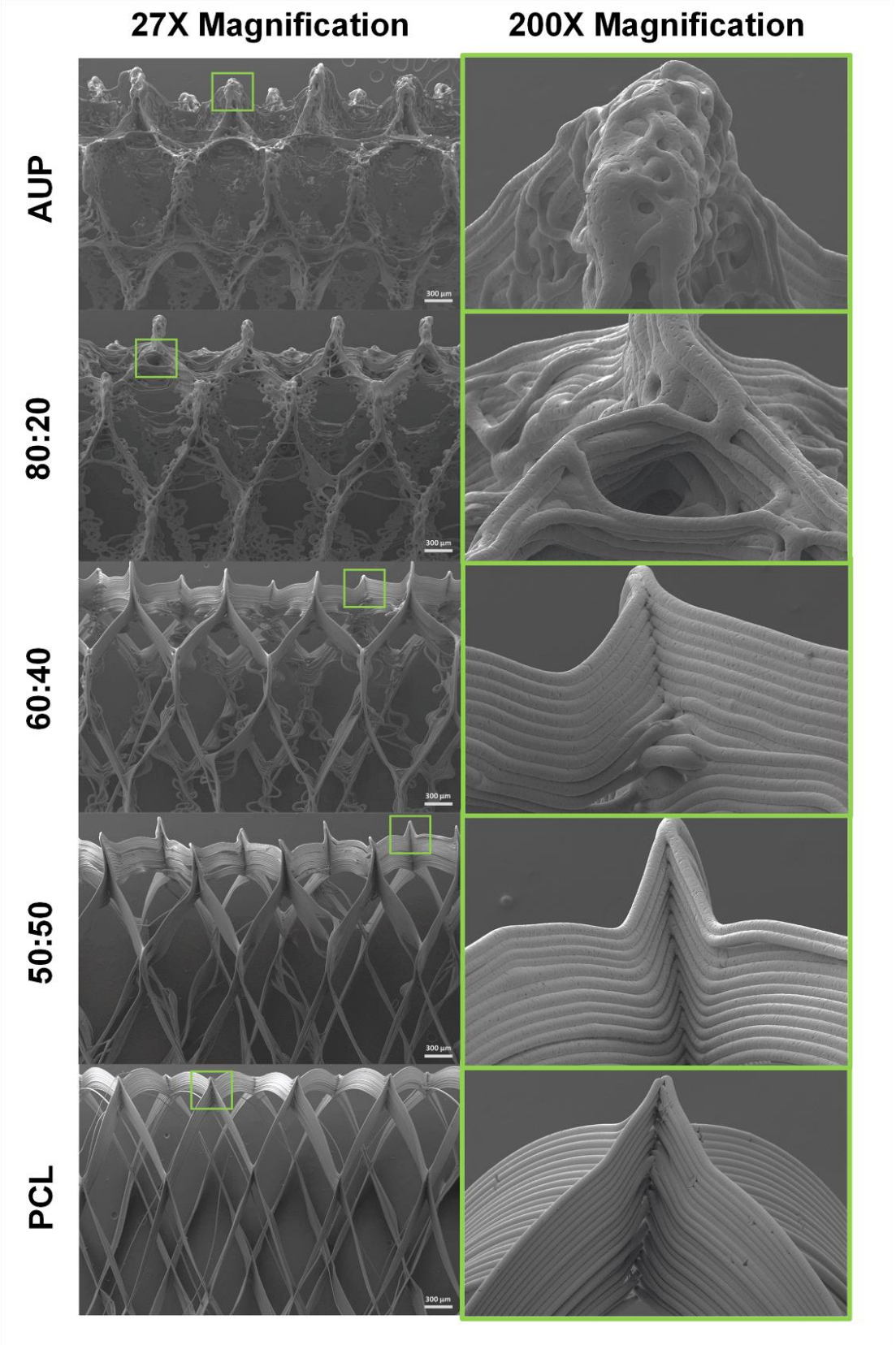

Figure 3.2. SEM images of the MEW processed tubes of PCL and AUP PCL20k, as well as the selected blends of AUP PCL20k at 27X and 200X magnification. The green boxes indicate the location of the 200X magnification on the SEM image with 27X magnification.

3.5.3 MEW tube characterization

(a) Physico-chemical characterization

- *Determination of gel fraction, solvent uptake capacity and crosslinking efficiency of the developed tubular constructs.*

The gel fractions of the tubes made by MEW from AUP PCL20k, PCL and their blends all exceed 95% (Table 3.2). For pure AUP PCL20k, a GF of 98.4 ± 2.5% was obtained, giving a first indication that processing with MEW did not influence the material's ability to crosslink effectively. This implies that almost no leaching out of potential non-crosslinked material constituting the developed tubes will occur when applied in tissue engineering. In addition, the material's ability to crosslink was confirmed by calculating the percentage of consumed acrylate groups (i.e. crosslinking efficiency, CE) obtained from HR-MAS ^{1}H-NMR spectroscopy indicating a crosslinking efficiency (CE) of 79.9% (Table 3.2). Moreover, the data showed that the CE clearly decreased with a decrease of AUP PCL20k in the blend. For the 50:50 and 60:40 blends, a CE lower than 50% was obtained, implying an incomplete conversion of the available reactive groups. The 50:50 blend only possessed a CE of 35.4%, which is due to the limited number of crosslinkable moieties.

For applications that rely on the mechanical properties of the constructs, it is important that the solvent uptake capacity (SUC) of the developed tubes is as low as possible to avoid excessive swelling of the construct to ensure that the scaffolds do not lose their shape and structure during cell culture. In accordance with the SUC of pure, non-printed AUP PCL20k (i.e. 0.93 ± 0.25 before processing), similar values were obtained for the processed AUP PCL20k tubes (i.e. 1.30 ± 0.42) (ns. $p > 0.05$). Very small SUC (< 1.30 ± 0.42) was obtained for the developed MEW tubes, independently of the blend ratio. As anticipated, for pure PCL constructs, shape and structure were perfectly maintained after contact with water as demonstrated by high GF and low SUC during a timeframe of 24 h.

Table 3.2. Gel fraction (GF), solvent uptake capacity (SUC) and crosslinking efficiency (CE) of AUP PCL20k, AUP PCL20k:PCL blends and PCL.

Material	GF		SUC		CE
	[%]	SD	[-]	SD	[%]
AUP PCL20k	98.4	2.5	1.3	0.4	79.9
80:20	97.4	0.9	0.9	0.1	69.0
60:40	95.4	1.6	0.2	0.1	49.6
50:50	99.0	5.9	0.1	0.1	35.4
PCL	100.0	0.0	0.3	0.1	-

- *Influence of melt electrowriting on the molar mass of the material*

As anticipated, the GPC measurements confirmed that the MEW processing technique did not influence the molar masses of the AUP PCL20k and PCL (Table 3.3). For AUP PCL20k, the number average molar mass (M_n) was around 23072 g·mol^{-1} and the weight average molar mass (M_w) was around 31504 g·mol^{-1} (with a Đ < 1.5) which corresponds to the MM that was determined using ^{1}H-NMR spectroscopy (i.e. 27076 g·mol^{-1}). The GPC measurements indicated a MM of the commercially available PCL was similar to that reported in the technical sheet of the supplier (MM of 120000 g·mol^{-1}). Depending on the AUP PCL20k:PCL ratio in the blend, both the M_n and M_w increased with an increasing PCL content in the blend. This was as expected because of the higher MM of PCL compared to AUP PCL20k. The differences in MM of the different blends have an influence on the printing parameters and optimization (as discussed in section 3.5.2) as well as on the mechanical properties of the developed tubes (*vide infra*). It was also observed that the polydispersity increased when more PCL was blended in, moreover, Đ was higher in all blends compared to Đ of both the pure AUP PCL20k and pure PCL. This confirmed that the observed distribution of the blends is less uniform (Đ = 1) upon blending in more PCL. The Đ of pure AUP PCL20k, PCL and the blend with a ratio of 80:20 could still be defined as moderate, whereas a Đ of more than 2 as is the case for 60:40 and 50:50 could be defined as a broad polydisperse distribution.

Table 3.3. Determination of the Mn, Mw and polydispersity (Đ) of AUP PCL20k, PCL and their blends, before and after MEW processing, using gas permeation chromatography. Mn = number average molar mass, Mw = weight average molar mass and Đ = polydispersity index determined via GPC analysis.

Material	M_n [g·mol^{-1}]		M_w [g·mol^{-1}]		Đ [-]	
	Before	After	Before	After	Before	After
AUP PCL20k	23072	22127	31504	30684	1.37	1.39
80:20	23652	25107	45920	45231	1.94	1.80
60:40	30226	32129	61354	64347	2.03	2.00
50:50	26369	34531	78038	72411	2.96	2.10
PCL	76946	65520	130381	108820	1.69	1.66

- *Mechanical properties of MEW tubes*

To investigate the mechanical properties of the fabricated tubular constructs, unidirectional mechanical tests were performed. The constructs were analyzed by a dynamic radial tensile experiment over a cycle count of 100 at a strain of 18% to simulate conditions close to those that blood vessel experience during physiological conditions [79,306–308]. Further, a series of pull to failure tests has been conducted to evaluate the behavior of the constructs under elevated influence of tensile force.

The graphs depicted in Figure S3.6 show the plots for representative samples of the different material blends of AUP PCL20k and PCL as well as the pure samples as force per displacement before and after UV-

induced post-process crosslinking of the acrylates within AUP PCL20k containing samples. Figure 3.3 A-B depicts stress/strain plots of the different samples. The graphs are also depicted in a larger version (easier to read) in Annex 1 – Chapter 3 in Figure S3.4 and S3.5. Young's moduli, peak force and retained force were calculated according to a method described in literature for the analysis of radially tested tubular constructs and are shown in Figure 3.3, C-F [309]. All samples, except the pure, non-crosslinked AUP PCL20k samples which broke apart during the first cycle, could be tested. Interestingly, the crosslinked AUP PCL20k samples did not break during the first cycle but only started to break over the course of the testing protocol. Even though the force reduced at each cycle, a minimal force was maintained at the end of 100 cycles (Figure S3.7).

Evaluating the maximum tensile stress exhibited by the constructs (Figure 3.3 F) revealed the rather brittle nature of the AUP PCL20k material. Successive increase in the amount of blended PCL into the compounded materials elevated the levels of ultimate tensile stress close to the values recorded for pure PCL. The 50:50 blend showed no significant difference compared to pure PCL regarding stress at break. On the one hand, AUP PCL20k showed a very small overall value in the amount of force required for a break of the construct. This might arise due to the overall fragile constructs and the testing protocol, which was set up to displace at slightly higher velocities than compared to the cyclic evaluation, leading to a more pronounced failure of the constructs early on. On the other hand, this reinforces the benefit of blending the material with PCL to attenuate this material characteristic. Figure 3.3 B depicts representative curves recorded during the pull to failure test. It is noticeable that the higher amount of PCL leads to the characteristic plastic deformation of PCL at elevated stresses before reaching a plateau of stagnant force increase where the material is undergoing a ductile failure behavior. Higher amounts of AUP PCL20k lead to a more brittle failure behavior of the material.

A clear trend is visible with respect to the declining amount of peak force depending on the amount of AUP PCL20k present in the blends. The highest recorded value was observed for the UV-crosslinked pure AUP PCL20k group (Figure 3.3 D). The only significant difference when comparing UV-treated versus non-UV treated values (within one blend) could be recorded for the 80:20 blend samples ($p < 0.0001$). The high content of AUP PCL20k within this blend enables a more effectively crosslinked network, due to increased acrylate group interaction, that leads to an increased mechanical strength. This is in agreement with the HR-MAS data (see Table 3.2), where a crosslinking efficiency of more than 50% was found for the 80:20 blend, and below 50% for the 60:40 and 50:50 blends.

The Young's moduli exhibit comparable trends as described for the peak force. The only significant difference between non-crosslinked and crosslinked samples is present in the 80:20 blend group (Figure 3.3 C) ($p < 0.0001$). When comparing Young's moduli with values from literature, the blended samples all range in the relevant window of 2 - 4 MPa which corresponds to average values from human saphenous

vein (1.77 ± 1.2 MPa), radial artery (3.68 ± 2.05 MPa) and coronary artery, which are in the range from 1.5 [73,76] to 4 MPa [310], depending on the specimen and test protocol used. With that, the blending allowed the manufactured constructs to be closer to human blood vessels regarding their Young's modulus, whereas constructs made only from PCL do not reach these ranges. As anticipated, the differences in mechanical properties of the pure AUP PCL20k and PCL (as discussed in section 3.5.1) also lead to differences in mechanical properties of the developed tubular constructs based on the different materials. By blending and varying the blend ratio, this resulted in achieving a range of Young's moduli in between the higher Young's modulus of the AUP PCL20k and the lower Young's modulus of the PCL, and thus tuneability in mechanical properties.

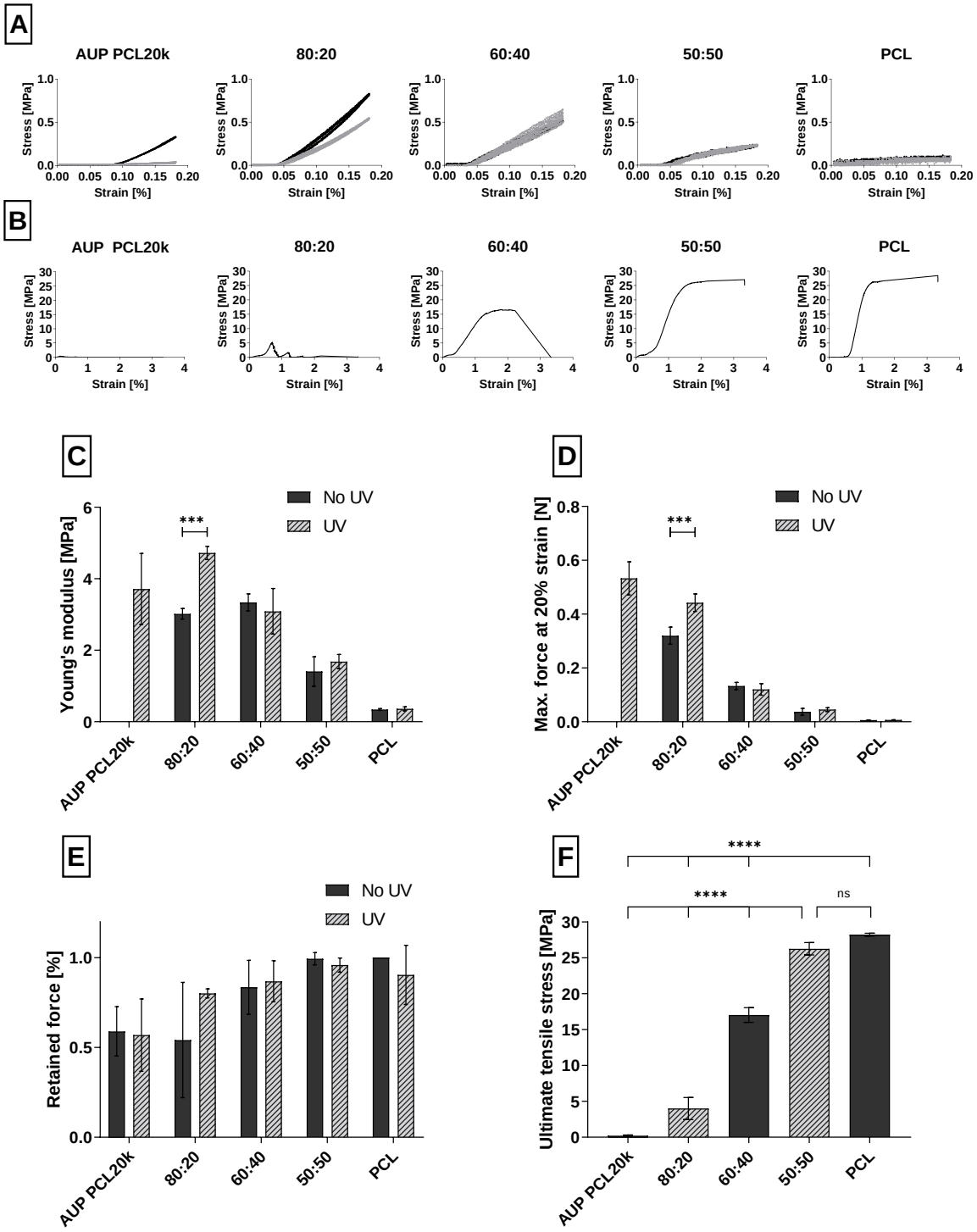

*Figure 3.3. Mechanical evaluation of tubular constructs: (A)-(B): Stress [MPa] versus strain [%] plots obtained from a single construct via uniaxial tensile testing data on MEW processed tubes (AUP, AUP:PCL ratios of 80:20, 60:40 and 50:50, and PCL): (A) Representative graphs of cyclic radial tensile testing after initial hysteresis resided. Compared are constructs with (black) and without (gray) post-processing UV irradiation. (B) Representative graphs of pull to failure testing. Constructs were pulled to 330 % strain to elucidate their failure point. (C)-(F) depict mean and SD values of mechanical data analysis: (C) Young's moduli [MPa]. (D) Max. force at 20% strain [N]. (E) The mean retained force [%], calculated by the difference of force at the beginning and at the end of measurement. (*** = $p < 0.0001$). (F) Ultimate stress [MPa] of the developed MEW tubes (after UV crosslinking) in AUP PCL20k, PCL and their blends (80:20, 60:40, 50:50) as obtained from uniaxial tensile testing until failure. (****: $p < 0.0001$, ns: $p > 0.05$).*

The graphs for all groups show very narrow hysteresis loops, indicating very little plastic deformation over the course of the cyclic measurement. A closer look at the peak force for all samples during 100 cycles (Figure 3.3 E) reveals a decline of peak force values during cycling testing. The decline can be attributed to the internal material properties, adjusting to the external tensile force until an equilibrium between fiber extension and orientation according to the applied force is reached [311,312]. Due to the crosslinked network, the amount of AUP PCL20k in the blend corresponds with a higher force decay over the course of the 100 cycles, while a higher PCL ratio shows little to no decay [313].

Regarding differences between non-UV and UV-treated samples, only the 80:20 group shows a 32% difference in peak force between the start and end of the measurement (Figure 3.3 D). This can be caused by the very brittle nature of the AUP PCL20k material that leads to breaking within the sample at the beginning of the measurement, resulting in an overall lower force, while the formed crosslinked bonds allow the material to withstand the applied tensile force better. The 50:50 blends perform best regarding force retention as well as having a noticeable increase in Young's modulus compared to pure PCL. Relevant observations for potential application in vascular regeneration or replacement are the small hysteresis loops shown during the testing, especially as the investigated displacement area is larger than physiological values for cyclic extension during systole of comparable small diameter blood vessels [308]. Additionally, there is only a very small decay of force over the whole 100 cycles of tensile testing. These results indicate the potential for long term mechanical dilatation and that the constructs are suited to withstand physiological stresses.

(b) Biological evaluation

The *in vitro* biocompatibility of the developed MEW tubes was evaluated via an MTS assay and Ca-AM/PI staining. To this end, human umbilical vein endothelial cells (HUVECs) were assessed on days 1, 3 and 7 after indirect contact with the materials, which is a common evaluation for testing of biocompatibility [314,315]. The rationale behind the choice of HUVECs as cell type is because one of the potential applications of the developed MEW tubes is their function as a reinforcement in *in vitro* vascular models. In blood vessels, endothelial cells, in the experimental evaluation represented by HUVECs, together with fibroblasts and smooth muscle cells form the majority of cell types present in vasculature [316] and therefore a logic option to test herein for their viability after exposure to the constructs.

Following the ISO 10993-5:2009(E), a biomaterial and its leaching components are non-cytotoxic if the viability is above 70% [317]. As indicated in Figure 3.4 A, the HUVEC viability at day 1, 3 and 7 remained well above 70% for AUP PCL20k, PCL and their blends (i.e. > 95%). The live/dead staining images can be found in Supplementary Information (Figure S3.8). In addition, an excellent metabolic activity was observed (Figure 3.4 B). Thus, it can be concluded that the developed MEW tubular constructs do not show any

cytotoxicity towards the HUVECs and could be further evaluated for their use as reinforcements constructs in vascular tissue engineering applications.

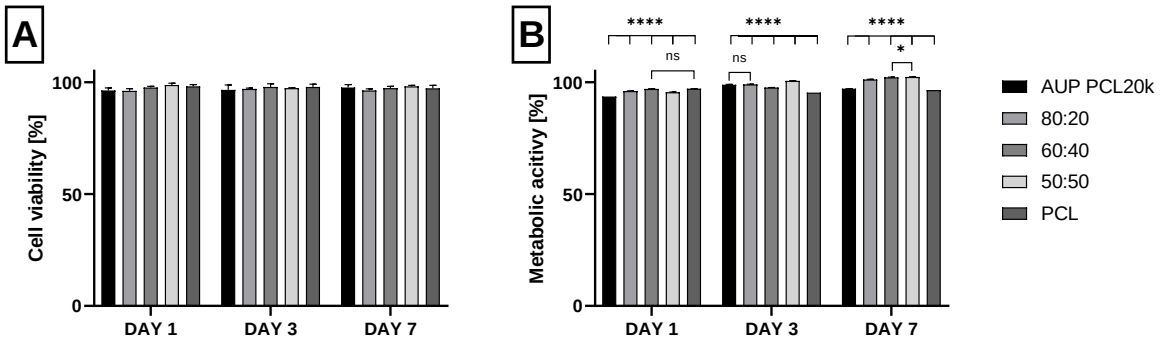

*Figure 3.4. In vitro biocompatibility assay using human umbilical vein endothelial cells on day 1, 3 and 7: (A) cell viability. (no significant differences, $p < 0.05$); (B) metabolic activity. (**** = $p < 0.0001$ between all groups per day except if indicated with another symbol: ns = $p > 0.05$ or * = $p < 0.05$).*

3.6 Conclusions

In conclusion, this chapter presents the application of an acrylate-endcapped urethane-based polymer (AUP PCL20k), synthesized with a straightforward synthesis route to introduce photo-crosslinkable moieties to a PCL backbone, for MEW of tubular constructs with adaptable mechanical properties. Processing with MEW did not result in degradation of the material and the photo-crosslinking capacity was preserved. Blending with commercially available PCL helped improving fiber morphology and homogeneity. At the same time, altering the mechanical properties of the created construct by adjusting the blend ratios was possible. This enables tailor-made construct characteristics for different applications and their corresponding specific mechanical requirements. *In vitro* assay using HUVECs revealed non-cytotoxic behavior of the AUP PCL20k material demonstrating its relevance in biomedical applications.

Chapter 4: Design and development of a reinforced tubular electrospun construct for flexor tendon repair

This chapter describes the application of two AUP precursors for flexor tendon repair (synthesis and characterization, see Chapter 2), i.e. AUP PCL530 and AUP PCL2k. The AUPs were processed into tubular constructs using solution electrospinning. This project was conducted in collaboration with I. Peeters (University Hospital Ghent). This chapter is based on the work of L. Deconinck and Y. Van de Maele as part of their master thesis, supervised by N. Pien and A. Mignon. The *ex vivo* and *in vivo* testing was performed by I. Peeters under the supervision of Prof. L. De Wilde and Prof. A. Martens (Faculty of Veterinary Medicine, UGent). The *in vitro* biological evaluation was performed by L. Van Damme, L. Parmentier and M. Meeremans (UGent). This chapter has been published in/accepted as:

AUP PCL2k:

N. Pien μ, I. Peeters μ, L. Deconinck, L. Van Damme, L. De Wilde, A. Martens, S. Van Vlierberghe, P. Dubruel, A. Mignon. Design and development of a reinforced tubular electrospun construct for the repair of ruptures of deep flexor tendons. Materials Science and Engineering: C, Volume 119, 111504. DOI: 10.1016/j.msec.2020.111504, Published: SEP 2020, Impact Factor: 7.328. Peer reviewed.

I. Peeters μ, N. Pien μ, A. Mignon, L. Van Damme, P. Dubruel, S. Van Vlierberghe, D. Mantovani, V. Vermeulen, D. Creytens, A. Van Tongel, S. Schauvliege, K. Hermans, L. De Wilde, A. Martens. Flexor tendon repair using a reinforced tubular, medicated electrospun construct. Journal of Orthopaedic Research. DOI: 10.1002/jor.25103, Published: MAY 2021, Impact Factor: 3.494. Peer reviewed.

AUP PCL530:

N. Pien, Y. Van de Maele, L. Parmentier, M. Meeremans, A. Mignon, C. De Schauwer, I. Peeters, L. De Wilde, A. Martens, D. Mantovani, S. Van Vlierberghe, P. Dubruel. Design of an electrospun tubular construct combining a mechanical and biological approach to improve tendon repair. Journal of Materials Science: Materials in Medicine, DOI: 10.1007/s10856-022-06673-4, Published: MAY 2022, Impact Factor: 3.896. Peer reviewed.

μ : Authors contributed equally.

4.1 Résumé

Les lésions des tendons de la main représentent un problème clinique majeur et peuvent réduire considérablement la qualité de vie des patients. Dans cette étude, une solution ciblée pour la réparation du tendon fléchisseur a été développée en combinant une approche mécanique et biologique. À cette fin, deux nouveaux polymères à base d'uréthane (AUP) ont été synthétisés en constituant différents backbones (c'est-à-dire du poly(ε-caprolactone) avec une masse molaire de 530 ou 2000 $g \cdot mol^{-1}$, PCL530 et PCL2k) et leurs propriétés physico-chimiques ont été caractérisées (voir Chapitre 2). Dans ce chapitre, des constructions de réparation tubulaires ont été développées en utilisant l'électrofilage (électrospinning en solution, SES) du matériau AUP avec du naproxène et de l'acide hyaluronique incorporés (c'est-à-dire des composés anti-inflammatoires et anti-adhésion, respectivement), et avec une tresse tubulaire comme renforcement mécanique. Les constructions de réparation de l'AUP à base de PCL ont été comparées à des constructions de réparation en PCL.

4.2 Abstract

Hand tendon injuries represent a major clinical problem and might dramatically diminish a patient's life quality. In this study, a targeted solution for flexor tendon repair was developed by combining a mechanical and biological approach. To this end, two novel acrylate-endcapped urethane-based polymers (AUPs) were synthesized constituting different backbones (i.e. poly(ε-caprolactone) with a molar mass of 530 or 2000 $g \cdot mol^{-1}$, PCL530 and PCL2k) and their physico-chemical properties were characterized (see Chapter 2). In this chapter, tubular repair constructs were developed using electrospinning of the AUP material with incorporated naproxen and hyaluronic acid (i.e. anti-inflammatory and anti-adhesion compounds, respectively), and with a tubular braid as mechanical reinforcement. The developed PCL-based AUP repair constructs were benchmarked against PCL repair constructs. Tensile testing of the repair constructs using *ex vivo* sheep tendons showed that the developed repair constructs fulfilled the required mechanical properties for tendon repair (i.e. minimal ultimate stress of 4 MPa), with an ultimate stress of 6.4 ± 0.6 MPa and 8.36 ± 0.57 MPa for the AUP PCL530 and PCL2k-based repair constructs, respectively. Moreover, *in vitro* biological assays showed that the developed repair tubes and the incorporated bioactive components were non-cytotoxic. In addition, when equine tenocytes and mesenchymal stem cells were co-cultured with the repair tubes, an increased production of collagen and non-collagenous proteins was observed. The developed AUP PCL2k repair constructs were also evaluated in an *in vivo* rabbit model (40 New Zealand rabbits) and benchmarked against the gold standard in tendon repair, i.e. Modified Kessler suture repair. The electrospun AUP PCL2k repair constructs showed similar strength as the Modified Kessler technique. Macroscopically, a significantly different adhesion pattern was observed at the suture knots, either centrally or peripherally, depending on the technique. Histologically, a qualitative assessment showed good to excellent repair at the tendon repair site, irrespective of the applied technique. AUP PCL530 was developed with the aim to design an electrospun repair construct without the need of the reinforcement layer. Even though superior mechanical properties were obtained for the AUP PCL530 compared to AUP PCL2k (Young's moduli of 2.5 ± 0.9 versus 0.6 ± 0.2 MPa, respectively), the construct still required the reinforced layer for application in tendon repair. In conclusion, this novel AUP PCL repair constructs in which a mechanical approach (fulfilling the required mechanical properties) was combined with a biological approach (incorporation of bioactive compounds), showed potential as flexor tendon repair application.

4.3 Introduction

Tendon injuries are painful and persistent, and can significantly reduce quality of life for patients in which insufficient healing is observed or which were treated unsuccessfully [51]. Hand tendon lesions in particular represent one of the most frequent tendon disorders in human [50]. The hand, being the human executing body unit, is crucial during daily life, especially when considering sport activities and professional life [53]. As such, chronic overuse injuries and ruptures in the hand are frequently observed. A considerable part of trauma emergencies typically involves flexor tendon lesions of the hand, affecting one in 2700 people each year [50]. These injuries might have a significant impact on hand function and thus quality of life. Therefore, early treatment with optimal recovery is indispensable to prevent permanent dysfunction [54].

The healing capacity of tendon lesions mainly depend on the type of injury, the physical activity and age of the patient, and also on the inflammatory response following injury [318]. Whereas relatively minor tendon traumas may primarily regenerate, complicated tendon traumas, and more specifically complete ruptures or transections, result in the formation of scar tissue. The mechanical properties of this scar tissue are impeded when compared to the original tendon tissue, which often results in pain and poor functionality. Damaged tendons heal slowly, and repair often requires a long recovery period. In these cases, surgical interventions are inevitable.

Current surgical interventions rely mostly on suturing techniques or on the use of tendon grafts (i.e. autografts, allografts, xenografts and synthetic grafts) [52,319,320]. The current state-of-the-art in surgical techniques still includes suturing the injured tendon ends together, which requires a non-degenerated tendon with regeneration potential [57,321]. Surgical repair using sutures is known to minimize scar tissue formation, increase the rate of collagenization and avoid the presence of non-tendinous tissues between the two ends of a tendon. Despite a successful surgical tendon repair, however, tendon adhesions are typically observed after tendon injury, both with the surrounding tissue and between tendon and tendon sheath [60,322]. These adhesions emerge from the non-organized scar tissue. A second limitation of the suturing techniques is the need for a splint to (at least partially) immobilize the tendon during rehabilitation [323,324]. This is important to protect the surgical repair and to prevent reinjury. Third, the insertion of a material during surgery often elicits a strong inflammatory response, with inflammatory cells being attracted to the injury site. In this respect, drug-releasing systems limiting adhesion and the inflammatory response have gained interest. The ability of hyaluronic acid (HA) and naproxen (Nap) to promote gliding and to counter adhesion formation around the repair complex, has been reported in literature [121].

The ideal technique of (flexor) tendon recovery should induce a healing response at the damaged tendon ends and to generate a repair site with low friction and minimal bulk, resulting in less inflammation and less adhesions (biological approach) [33]. Additionally, an optimal mechanical strength is required for tendon repair to fulfill the minimal needs of a healing tendon (i.e. mechanical approach). For an optimal repair of hand tendons, the minimal bearing stress of the construct should be approximately 4 MPa [82,319]. Both the mechanical and biological approach are essential when developing a construct for tendon repair. However, current state-of-the-art mostly

focusses on one approach, either mechanical or biological, rather than combining both [325–330]. Moreover, considering the biological approach, it is remarkable that often only one biological issue (such as adhesion) is evaluated in order to enhance tendon repair [122,331–333]. As such, a strong challenge in tendon repair remains in order to tackle adhesion, inflammation, and mechanical strength all together.

In the present chapter, a repair construct was developed representing an optimal and controlled healing environment with minimal inflammation reactions and adhesions to the surrounding tissues. To this end, both a mechanical and a biological approach were combined in a tubular electrospun repair construct. Firstly, as a mechanical approach, a novel acrylate endcapped urethane-based crosslinkable precursor (AUP), constituting a 530 g·mol^{-1} or 2000 g·mol^{-1} poly(ε-caprolactone) (PCL) backbone, was synthesized and characterized. To fabricate a tubular construct for tendon repair, electrospinning (ES) was elaborated as a processing technique. Subsequently, the developed repair construct was tested with regard to multiple mechanical requirements by means of tensile testing. More precisely, mechanical properties of the developed constructs using *ex vivo* sheep tendons were evaluated. Furthermore, a degradation study on the developed repair constructs was performed as well. The developed PCL-based AUPs repair constructs were benchmarked against PCL repair constructs.

Secondly, in the biological approach, the proposed design aimed to provide a controlled drug release to avoid adhesion and inflammation. Therefore, both naproxen and hyaluronic acid were incorporated in order to gradually release the pharmaceutical components at the injured site. *In vitro* biological assays using human fibroblasts (hFBs) were assessed to test the cytocompatibility of the developed repair constructs. Moreover, to evaluate the potential supportive effect of the construct on tendon healing, collagen production was evaluated in an indirect co-culture of equine tenocytes and mesenchymal stem cells (MSCs) with the repair construct.

Finally, the developed AUP PCL2k repair constructs were evaluated for tendon repair in an *in vivo* study in forty white New Zealand rabbits. The developed repair constructs were compared with the gold standard being the modified Kessler suture. The performance of the repair techniques was evaluated by biomechanical tensile testing, macroscopic evaluation, and histological analysis.

4.4 Materials and methods

4.4.1 Material synthesis and characterization

The PCL-based AUP precursors were synthesized following the protocol described in Chapter 2 (section 2.4). In this study, a AUP PCL530 and a AUP PCL2k were developed based on a PCL backbone with a molar mass (MM) of 530 g·mol^{-1} and 2000 g·mol^{-1}, respectively. For the methods and protocols regarding the characterization of the AUPs, we refer to Chapter 2. The chemical structure of the developed materials was determined by ^{1}H-NMR spectroscopy, the thermal properties through TGA and DSC while the following physico-chemical properties were also determined: solvent uptake capacity, gel fraction, crosslinking efficiency and viscoelastic properties.

4.4.2 Material processing using solution electrospinning

(a) Solution parameters

The ES solutions, i.e. PCL (reference), AUP PCL530 (i.e. AUP PCL530:PCL blend in a 50:50 mass ratio) and AUP PCL2k (i.e. AUP PCL2k:PCL blend in a 50:50 or 25:75 mass ratio), were constituting a polymer concentration of 16 wt% in chloroform. The photo-initiator, ethyl (2,4,6-trimethylbenzoyl) phenyl phosphinate (TPO-L), was applied in a quantity of 2 mol% relative to the acrylate content to facilitate crosslinking in the post-electrospinning step.

To enhance tendon repair, active compounds were incorporated in the electrospun constructs. These additional components were included in the polymer solution (PCL or AUP:PCL blends) prior to ES. Based on literature [118,119,122,334,335], the addition of an anti-adhesion and an anti-inflammatory component (i.e. HA, 1 wt% and Nap, 1.5 wt%) was pursued.

(b) Device processing parameters

The in-house manufactured electrospinning set-up is composed of a high voltage source (Glassman High Voltage, Inc.; model series EL50P00, high voltage DC power), a motion controller (CWFW Ghent University) and a motor-driven syringe pumping system (New Era Pump Systems, Inc.; model Single Syringe Pump NE-300). The applied processing parameters (i.e. voltage: 15-20 kV, flow rate: 0.5-8.5 $mL \cdot h^{-1}$ and needle-to-collector: distance 18-21 cm) were varied within the ES process and an optimal set of parameters was selected subsequently. For the AUP PCL530 blend: voltage of 18 kV, flow rate of 1.5 $mL \cdot h^{-1}$ and needle-to-collector distance of 18 cm. For the AUP PCL2k blend: voltage of 15 kV, flow rate of 0.75 $mL \cdot h^{-1}$ and needle-to-collector distance of 18 cm. ES was performed at 21°C and the relative humidity was determined by a hygrometer which was present in the ES cabinet. The homogeneous polymer solution (stirred overnight) was transferred into a 20 mL syringe that was clamped into the syringe pumping system. The ES needle (inner diameter: 0.580 mm for the AUP PCL530 blend and 0.495 mm for the AUP PCL2k blend) was placed at a variable height above the collector. First, a flat plate collector was used to generate sheets and the quality of the fibers was assessed. Secondly, a mandrel rotating around its axis (180 rpm, Inox stainless steel, 4-6 mm diameter) was applied during the process of ES to produce tubular constructs. For an easy release of the electrospun tubes from the mandrel, preheated mandrels were dip coated in molten poly(ethylene glycol) 8000 $g \cdot mol^{-1}$ (PEG8k) and, after performing ES, were submerged in ultrapure water to dissolve the water-soluble PEG-coating and allow an easy release of the developed tubular constructs.

(c) Design of the repair construct

The design of the tubular constructs in the present study is based on multiple layers. The inner layer and outer layer of the construct were electrospun PCL (reference) or AUP layers (i.e. AUP PCL530 or AUP PCL2k blended with PCL, as described above). The latter included anti-adhesion and anti-inflammatory drugs, i.e. hyaluronic acid (HA) and Naproxen (Nap). The middle layer acts as a reinforcement layer in between the two electrospun layers.

This reinforcement is based on the Chinese finger trap mechanism and is composed of a polypropylene tubular braid. The proposed reinforced, drug-loaded electrospun construct design is depicted in Figure 4.2.

4.4.3 Post-processing photo-crosslinking step

After ES, the AUP PCL530:PCL or AUP PCL2k:PCL mats and tubular constructs were transferred into a UV-transparent plastic bag and subsequently flushed with argon to remove oxygen that could interfere with the crosslinking process. The UV-treatment (both above and below the construct) was performed by UV-A irradiation (λ = 365 nm, at 10 mW·cm^{-2})(Philips TL 0W/08 P8 T5/ BLB lamps in the holder of Bi-Sonic Technology Corp.; model 8B-230 HB; 250-450 nm range) for 30 minutes.

4.4.4 Mechanical evaluation of the developed repair construct

(a) Tensile testing of reinforced, drug-loaded electrospun tubes on ex vivo sheep tendons

First, an *ex vivo* tensile test on the non-reinforced, drug-loaded constructs was performed and the obtained data were compared to those of reinforced, drug-loaded constructs (PCL as a reference, compared to AUP PCL530:PCL and AUP PCL2k:PCL) applied in cadaveric sheep tendon. An overview of the used materials with and without reinforcement, and the corresponding abbreviations is shown in Table 4.1. An example of the applied tensile testing setup is shown in Figure 4.1C.

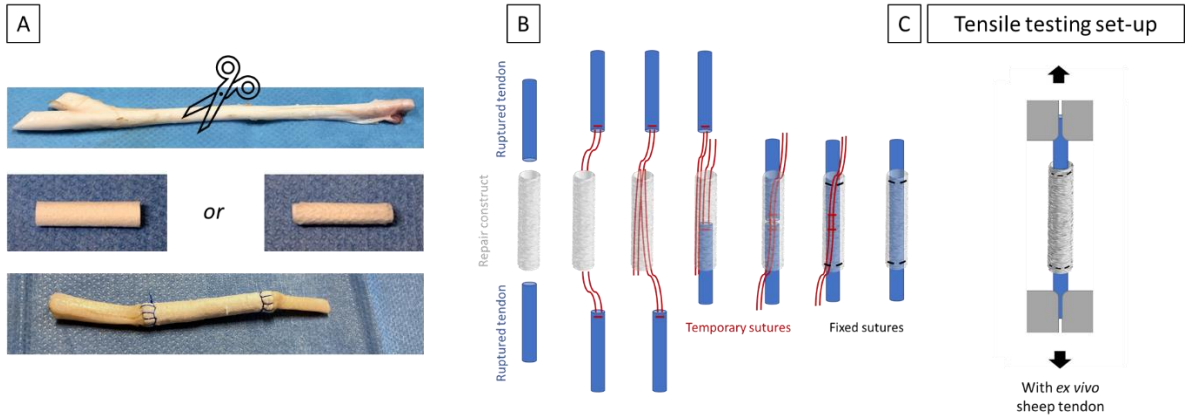

Figure 4.1. (A) Induction of a complete transection in the middle of the tendon, and final repaired tendon using the proposed repair construct, (B) application method of the repair construct on the damaged tendons (C) Set-up of the tensile testing set-up of the repair construct on the ex vivo sheep tendon.

Hind limbs of sheep were collected in a local abattoir. The flexor digitorum profundus tendons were immediately dissected from the sheep's hind leg and frozen at −18°C. Sheep tendons were chosen as a model because their tensile forces correspond mostly to those of human deep flexor tendons [336]. After thawing, a complete transection was induced in the middle of the tendons (Figure 4.1A). Both ends of the transected tendon were pulled in the construct with a temporary suture at both ends (Figure 4.1B). Subsequently, either the non-reinforced constructs or the reinforced constructs were fixed at their outer ends to the tendon by a circumferential interlocking suture, again using a polydioxanone suture (PDS size 4-0, Ethicon Inc., Piscataway, NJ). The samples were

mounted in a tensile testing machine (Lloyd Ametek C2S, software Nexygen Plus) with a clamp distance of 5 cm. After a preload of 1 N, an elongation test at a speed of 20 mm·min^{-1} was performed until failure. Each condition was tested in triplicate.

Table 4.1. Overview of materials tested for the development of a (reinforced) repair construct.

	PCL	**AUP PCL530:PCL**	**AUP PCL2k:PCL**
Non-reinforced	PCL	AUP PCL530	AUP PCL2k
Reinforced with tubular braid	rPCL	rAUP PCL530	rAUP PCL2k

(b) Degradation study in aqueous environment

Tubular constructs (thickness = 1 mm, inner diameter = 5 mm and length = 0.5 cm) were electrospun, the initial mass of each sample was registered, and the samples were subsequently incubated (T = 37°C, phosphate-buffered saline (PBS), pH = 7.4). Three samples were each time (every 2 weeks) removed and washed with ultrapure water to eliminate possible PBS salts. Samples were weighed and compared to their original mass. This ratio describes the percentage of mass loss and can thus be used as an indication of degradation. The degradation was studied for a time period of 17 weeks. The degradation study of the samples was performed every 2 weeks.

(c) Suture retention strength of the developed tubular repair constructs

The suture retention strength of the PCL and AUP PCL2k:PCL electrospun constructs was measured as described by Schaner *et al*. [337]. In brief: a tensile testing machine (Lloyd Ametek C2S, software Nexygen Plus) with a load cell of 100 N was used. One end of the tubular constructs was fixed on one side in a clamp while the opposite end was connected to another clamp by a polydioxanone suture (PDS size 4-0, Ethicon Inc., Piscataway, NJ) with a round needle to avoid any cutting effect. The sutures were placed in the four corners (0°-90°-180°-270°) at 2 mm from the edge of the constructs (diameter 5 mm). After a preload of 0.05 N, the constructs were pulled at a crosshead speed of 10 mm·min^{-1} until the suture pulled through the constructs. The suture retention strength, which was defined as the fracture strength, was obtained. Each test was performed 5 times.

4.4.5 Biological evaluation of the developed repair construct

(a) Cytotoxicity assay using human fibroblasts

In vitro (in)direct cell tests, using commercial human fibroblasts (hFBs) (primary foreskin fibroblasts, purchased from ATCC), were executed during this study to determine the biocompatibility of the materials. The electrospun materials (PCL, AUP PCL530:PCL blends, and AUP PCL2k:PCL), as described in Table 4.2, were first evaluated without additional compounds (reference) and subsequently with the addition of Nap or HA. The effect of Nap and HA concentrations on cellular response and cell viability was evaluated. Samples were sterilized by incubation in 70% (v/v%) ethanol for 24 hours (with a refreshing of ethanol after 12 hours) and subsequent UV-C irradiation (100-250 nm, 15 mW·cm^{-2}) for 2 hours.

Table 4.2. Overview of electrospun materials (PCL, AUP PCL530:PCL blend, AUP PCL2k:PCL blend) with or without additional components applied in in vitro (in)direct cell tests.

Function	Component	PCL	AUP PCL530:PCL	AUP PCL2k:PCL
Reference	/	PCL Ref	AUP PCL530 Ref	AUP PCL2k Ref
Anti-inflammatory	Nap	PCL Nap	AUP PCL530 Nap	AUP PCL2k Nap
Anti-adhesion	HA	PCL HA	AUP PCL530 HA	AUP PCL2k HA
			Positive control	

Human fibroblasts were cultured in culture medium, consisting of Dulbecco's Modified Eagle Medium (DMEM) high glucose, 10 v% nutritional fetal bovine serum and 1 v% antibacterial penicillin/streptomycin (P/S), at 37°C in 5% CO_2 until a desired number of cells was reached. Culture medium was refreshed every 2-3 days, and cells were passaged when 80-90% confluency was reached. Passage 13 human fibroblasts were used in these experiments. As positive control group, hFBs not having contact with the electrospun materials were included.

- *Indirect cell test*

The developed repair constructs were incubated during 1, 3 and 7 days to assess the effect of potential leachables using a cell proliferation and viability assay. These experiments were performed in triplicate. To this end, 10 000 hFBs were seeded onto a 96 well plate until 80% confluence.

The metabolic activity of the hFBs was assessed through an 3-(4,5-dimethylthiazol-2-yl)-5-(3-carboxy-methoxyphenyl)-2-(4-sulfophenyl)-^{2}H-tetrazolium (MTS) assay. A mixture of 16 v/v% of MTS in culture medium was prepared and added to the hFBs. Next, the MTS was bioreduced into the colored formazan by incubation at 37°C for 2 hours in the dark (wrapped with aluminum foil) under continuous shaking. Thereafter, a spectrophotometer (BioTek Instruments; EL800 Universal Micropate Reader, with GEN5 software) was used to measure the absorbance of formazan at 490 nm.

Furthermore, a live-dead viability assay was carried out using calcein-acetoxymethyl/propidium iodide (Ca-AM/PI). A mixture of 0.2 v/v% Ca-AM and 0.2 v/v% PI in PBS was added to the hFBs and incubated in the dark by covering them with aluminum foil for 15 minutes at room temperature. Visualization of the HFBs was performed by fluorescence microscopy (Olympus IX 81 with software Xcellence Pro), using a fluorescent protein (GFP) filter and a Texas Red (TxRed) filter, which led to the distinction of green living cells and red dead cells.

- *Direct cell test*

A biocompatibility assay was conducted on cells which were in direct contact with the electrospun material. After sterilization (*vide supra*), the materials were added to a confluent monolayer of hFBs in a 48-well plate (30 000 cells/well) supplemented with 400 µL culture medium. Cell viability was assessed in triplicate by a live-dead Ca-AM/PI fluorescence staining as well as a cell proliferation assay using MTS after 1, 3 and 7 days.

(b) Indirect co-culture (tenocytes and MSCs) assay to evaluate collagen production

To quantify the total collagen production, a Sirius Red/Fast Green Collagen staining kit (Chondrex) was used in mono-cultures (equine tenocytes or MSCs, respectively) and compared to direct co-cultures (equine tenocytes and MSCs). This was tested on electrospun materials (PCL and AUP PCL530:PCL) without additional components (reference) as well as supplemented with Nap or HA (Table 4.2).

Both tenocytes and MSCs were harvested from a 15-year-old Arabian horse. Equine tenocytes were isolated from the superficial digital flexor tendon using 0.1% collagenase type Ia digestion in high glucose DMEM [338]. MSCs were collected from abdominal adipose tissue using 0.1% liberase digestion in low glucose DMEM. Both cell types were cultured until passage 4 and were then seeded in 12-transwell plates at a density of 25000 cells·cm^{-2} in tenocyte medium (consisting of HG-DMEM, 10% FBS, 1% L-glutamine, 1% P/S/Amphotericin B(A)) or MSC culture medium (consisting of LG-DMEM, 30% FBS, 1% L-glutamine, 1% P/S/A), respectively. In addition, a co-culture with a ratio of 50% tenocytes and 50% MSCs was included in this study, cultured in a 50:50 ratio of the corresponding media, as well as a tissue culture plastic (TCP) control.

ES discs (D: 8 mm) were punched out and sterilized (*vide supra*) before cell seeding. ES discs were placed on a transparent insert with a pore size of 0.4 µm. Cells (i.e. tenocytes and/or MSCs) were located at the bottom of the well in order to have an indirect contact between the disk and the cells. All experiments were performed in triplicate. The Sirius Red staining kit was used to quantify collagen production. In brief, medium was discarded after 7 days, and cells were washed with PBS. An amount of 0.5 mL of Kahle fixative (i.e. 60 v% distilled water, 28 v% 97% ethanol, 10 v% 37% formaldehyde and 2 v% glacial acetic acid) was added and subsequently incubated for 10 minutes at room temperature. After removing the fixative and washing the cells again with PBS, 250 µL of dye solution was added and incubated at room temperature for 30 minutes. The stained cell layers were rinsed three times with distilled water followed by dehydration in ethanol from 70% to 96% (1 min per step). After visualization, 1 mL of dye extraction buffer was loaded in each well and carefully mixed by pipetting until the color was eluted from the sample. Finally, 100 µL was compiled of the eluted dye solution and transferred into a 96-well plate. The optical density (OD) was measured by a spectrophotometer (Infinite F50 Tecan) at 550 nm and 595 nm. The total collagen and non-collagenous protein production were determined by Equations (4.1) and (4.2).

$$Total\ collagen\ \left[\frac{\mu g}{section}\right] = \frac{OD550\ value - (OD595\ value\ x\ 0.291)}{Col.Eq} \quad (4.1)$$

$$Non - collagenous\ proteins\ \left[\frac{\mu g}{section}\right] = \frac{OD595}{Col.Eq} \quad (4.2)$$

With:

OD550 value = optical density of Fast Green (550 nm)

Contribution of Fast Green at 550 nm is 29.1% → OD595 value is multiplied by 0.291

OD595 value = optical density of Sirius Red (595 nm)

Col. Eq (total collagen) = color equivalence of total collagen = 0.0378
Col. Eq (non-collagenous proteins) = color equivalence of non-collagenous proteins = 0.00204

4.4.6 *In vivo* study in rabbit model

(a) Surgical techniques

Technique 1: "Reinforced, drug-loaded construct": The design of the electrospun repair construct has been described in section 4.4.2. The material used was AUP PCL2k blended with PCL in a 1:3 ratio.

Technique 2: "Drug-loaded construct": In this technique, the same protocol and processing parameters were used as described for technique 1, but without the incorporation of a reinforcement tubular braid. This construct did not have sufficient intrinsic strength (see results section 4.5.2) and was therefore combined with a modified Kessler suture. Using this construct without reinforcement allows the evaluation of possible biological advantages of the AUP PCL2k:PCL-drug-loaded polymers without interference from the braid.

Technique 3: "Tubular braid": In this technique, a tubular braid without any drug-loaded electrospun polymers was used. This braid is made of polypropylene strands of 0.18 mm, has a length of 15 mm, and a diameter of 2.5 mm. Using this construct without drug-loaded polymers allows the evaluation of the mechanical strength of the braid without medication interference.

Technique 4: "Modified Kessler": The modified Kessler was used as a gold standard / control technique. In brief, the Kessler repair is based on a suture that is anchored to the tendon in all 4 corners with a knot. This knot prevents the suture from moving within the tendon substance. In the modified Kessler, a loop is used at each corner instead of a knot. The suture is therefore not anchored in the tendon and can move freely [339].

(b) Animals

Forty 18-24-weeks-old female New Zealand White rabbits with an average weight of 4.6 ± 0.3 kg were used (Cegav S.S.C., France). The ethics committee of the Faculty of Veterinary Medicine of Ghent University, Merelbeke, Belgium, approved the study (2019-60). All animals received humane care in compliance with the Guide for Care and Use of Laboratory Animals published by the National Institutes of Health (NIH publication No. 85-23).

Before surgery, all rabbits were housed individually in standard rabbit cages for a minimum of 7 days. An overview of the grouping details is presented in Figure S4.1. The rabbits were randomly divided into two groups of 20 rabbits for evaluation at 3 and 8 weeks after surgery to assess the early and late stages of tendon healing. Surgery was performed in the second and fourth deep flexor tendons of one hind paw using one of the four repair techniques described above. Techniques 1 and 2 were always used in the same paw because the constructs used for these techniques both release the same medication. Therefore, other combinations were not possible because undesired

dispersion of medication could potentially influence the results. Whether a technique was used in the second or fourth tendons was randomly determined. This implies that 10 samples were available for analysis at 3 weeks and 10 at 8 weeks for each technique. Of these 10 samples, eight were used for mechanical testing, and two were used for histological analysis.

(c) Premedication and anaesthesia

All rabbits were sedated with intramuscular (IM) injection of medetomidine (0.2-0.3 $mg \cdot kg^{-1}$) and buprenorphine (0.03-0.05 $mg \cdot kg^{-1}$). Subsequently, IM ketamine (10 $mg \cdot kg^{-1}$) was used to induce anesthesia and a laryngeal mask (V-gel®) was placed to administer isoflurane. An intravenous (IV) catheter was inserted into the marginal ear vein (after applying EMLA® crème) to administer doxapram 5 $mg \cdot kg^{-1}$ IV in case of apnea. No antibiotic prophylaxis was administered.

(d) Injury induction and surgical reconstruction

After positioning the rabbit in dorsal decubitus, the operative site on the right hind paw was clipped and surgically prepared (chlorhexidine scrub and alcoholic disinfection). A proximal unloading tenotomy of the common deep digital flexor was performed proximal to the heel, as described by Berglund et al. [340]. Next, the flexor digitorum profundus (FDP) tendon rupture model described by Chou et al. [341] was used. Briefly, a longitudinal midline incision was made on the plantar side between the second and third metatarsi. After subcutaneous dissection, flexor digitorum superficialis (FDS) tendons were identified, and the second and fourth FDS were removed over a length of 2 cm to expose the underlying FDP tendons. A full transverse section was then performed midway through the second and fourth FDP tendons, which were subsequently repaired using one of the four techniques described above. The skin was closed using subcutaneous (vicryl 4-0 Ethicon) and intradermal sutures (monocryl 3-0 Ethicon). Finally, a custom-made splint using a thermoplastic strip was applied to immobilize the phalanges.

(e) Operative protocol for tendon repair with the proposed surgical techniques

Technique 1. Reinforced, drug-loaded construct: During surgery, the two ends of the transected tendon were pulled through the construct using a temporary simple suture (polydioxanone suture [PDS] 4-0, Ethicon). As a result, the tendon ends were pulled together to achieve an overlap of the tendon ends of 3 mm. The construct was then fixed to the tendon surface at the periphery of the construct using three simple surgical knots (PDS 4-0).

Technique 2. Drug-loaded construct: During surgery, the first part of the modified Kessler suture (PDS 4-0) was placed on the proximal tendon end. Next, the suture threads were pulled through the polymer structure, which was then glided halfway over the proximal tendon end. Finally, the modified Kessler suture was completed at the distal end of the tendon. To complete the suture and tighten the knot, the tubular polymer was divided longitudinally until midway through the construct. The cut was closed after completion with a simple surgical knot using a PDS 4-0.

Technique 3. Tubular braid: During surgery, the same surgical steps as in technique 1 were used, including the insertion of the two ends of the tendon in the tubular construct with temporary sutures and fixation of the braided construct to the tendon surface with three simple surgical knots on both ends.

Technique 4. Modified Kessler: In this control group, the sectioned tendon was reconstructed using a two-stranded modified Kessler suture with PDS 4-0.

(f) Post-operative protocol

During the first 3 weeks, the rabbits were housed individually. Subsequently, they were transferred to group housing to improve animal welfare. With no lack of access to food and water, a standard rabbit diet was provided in both housing conditions.

During the first 5 days, a daily dose of meloxicam 1 $mg \cdot kg^{-1}$ was administered. During the first week, eating, drinking, production of fecal pellets and cecotropes, weight, and temperature were monitored daily. From the second week onwards, weight and temperature were measured twice per week. An inspection for swelling and wound or bandage problems was conducted daily.

(g) Euthanasia

All rabbits were anesthetized using xylazine 5 $mg \cdot kg^{-1}$ IM and ketamine 10 $mg \cdot kg^{-1}$ IM. The animals were then euthanized by injecting sodium-pentobarbital (0.5 $g \cdot kg^{-1}$) IV in the lateral ear vein. Immediately after euthanasia, the hind legs were transected. Within 1 h, dissection of the tendons was performed with either immediate macroscopic evaluation, tensile testing, or preservation for further histological analysis.

(h) Biomechanical testing

Tensile testing was performed using a hydraulic tensile testing machine (LRX Plus with a 100N load cell, Lloyd Instruments, Bognor Regis, UK) using custom-made clamps with serrated teeth. Each tendon was secured between the clamps using sandpaper to prevent slippage. During testing, the tendons were kept moist by spraying them with a saline solution. The repaired tendons were first pre-tensioned at 0.5 N, and then a distraction was performed at a rate of 5 $mm \cdot min^{-1}$ until complete failure [331]. Ultimate load, extension from preload at maximum load, and stiffness were recorded using Nexygen Plus software. As planned, 32/32 tendons available for tensile testing were evaluated.

(i) Macroscopic evaluation

A macroscopic evaluation of the repaired tendons (32/32) was performed immediately after euthanasia. The presence of adhesions around the repair site was evaluated using a frequently used visual scale [342]: grade 1, no adhesions; grade 2, adhesion area requiring blunt dissection alone for separation; grade 3, adhesion area less

than or equal to 50% requiring sharp dissection for separation; grade 4, 51–97.5% adhesion area requiring sharp dissection for separation; grade 5, >97.5% adhesion area requiring sharp dissection for separation. One adaptation was made; instead of grading adhesion only centrally, a second grading was also applied more peripherally at 7.5 mm from the center on each side.

(j) Histological analysis

After dissection, the tendons used for histological examination were retrieved and immersed in 10% formaldehyde. Because of an infected hind paw in one rabbit, two tendons, treated with two different techniques, were excluded from further analysis. A transverse cut immediately adjacent to the repair zone was performed, and the remainder of the sample was cut longitudinally. After technical and qualitative evaluation of the sections, one sample of each technique at each period was selected for further analysis (8/16 tendons available for histology). The samples were then serially dehydrated in ethanol and embedded in paraffin wax to produce tissue sections of 5-µm thickness on positively charged glass slides. The slides were further heated in a 70°C oven followed by immersion in xylene solution for 5 min, and the process was repeated three times. The deparaffinized samples were then rehydrated and subjected to hematoxylin and eosin (H&E) and Masson's trichrome staining to analyze connective tissue, and immunohistochemical CD31 staining (Agilent, JC70A, 1/5 dilution) to analyze the number of blood vessels. The tissue sections were examined under an upright light microscope (Olympus BX3 microscope, Tokyo, Japan), and pictures were taken using an Olympus U-TVO.5XC-3 camera. Because of the limited number of samples available for histology, only a qualitative evaluation could be performed.

Tendon repair quality was examined on longitudinal histologic sections using a four-point grading scale based on Tang by a blinded observer [343]. The following four parameters were considered: the size of gap formation, newly formed collagen fibers, type of inflammation, and vascularization. The quality of tendon repair was classified as follows: (1) excellent - perfect continuity of the repaired zone, presence of collagen fibers, few inflammatory cells, and vascularization; (2) good - small gap formation, presence of newly formed collagen fibers, inflammatory cells, and vascularization; (3) fair - the presence of gap formation, minor presence of newly formed collagen fibers, a moderate amount of inflammatory cells, and vascularization, (4) poor - large gap formation, no presence of newly formed collagen fibers, numerous inflammatory cells, and vascularization.

To estimate the influence of the different repair techniques on vascularization, the total number of blood vessels per mm² was counted manually by two independent observers (at 10x magnification) on transverse CD31-immunohistochemical staining sections at 3 and 8 weeks for each technique using LAS V4.1 software (Leica Microsystems).

4.4.7 Statistical analysis

The mean and standard deviation (SD) on the samples (at least triplicate) were calculated using GraphPad Prism 7 software and all data were expressed as mean ± SD. Statistical evaluation was carried out by performing a one-way or two-way ANOVA, with a post Tukey multiple comparison test. Differences were considered statistically significant at $p < 0.05$ and were annotated with *.

For the biomechanical tests in the *in vivo* study, a total of 32 rabbits were chosen based on power analysis with a power of 0.80, an effect size of 0.65, and a significance level (alpha) of 0.05 for the biomechanical testing [122]. Furthermore, eight additional rabbits were added for histological analysis. Because normality (Shapiro-Wilk test) and equality of variances (Levene's test) could be assumed, parametric testing was performed. For each dependent factor (ultimate load, extension from preload, stiffness), a two-way analysis of variance (ANOVA, tests of between-subjects effects) was conducted to investigate the effects of both postsurgical periods, techniques, and possible interactions. Further pairwise comparisons were conducted to determine the significance. Pearson's chi-square (Fisher's exact) test was conducted to investigate the significance of the macroscopic evaluation of adhesion formation. For histological evaluation, only qualitative descriptions were provided. All statistical analyses were performed using SPSS version 26.0 (SPSS Inc., Chicago, IL, USA).

4.5 Results and discussion

The goal of this chapter was to design an electrospun tubular polymeric repair construct able to withstand mechanical stresses and to enable the controlled release of anti-adhesion and anti-inflammatory compounds, resulting in a mechanically and biologically improved flexor tendon healing. To this end, the polymer was first synthesized and characterized for its physico-chemical properties (Chapter 2). Subsequently, PCL (reference) and the developed AUP PCL530 and AUP PCL2k polymers were processed into a tubular repair construct using electrospinning. The mechanical, degradation and *in vitro* biological properties of the developed repair constructs were evaluated. In addition, the repair constructs were tested using *ex vivo* sheep tendons. Finally, the AUP PCL2k repair construct was tested in an *in vivo* rabbit model.

4.5.1 Design of the repair construct

The design of the tubular constructs in the present study is based on multiple layers. The inner layer and outer layer of the construct were electrospun PCL or AUP layers, i.e. AUP PCL530 and AUP PCL2k (as described in section 4.4.2). The average fiber diameter ranges between [3-4.5] µm for AUP PCL530 and AUP PCL2k, and was around 8 µm for the PCL-based electrospun constructs. The electrospun layer includes anti-adhesion and anti-inflammatory drugs, i.e. hyaluronic acid (HA) and Naproxen (Nap). These drugs should counter post-surgical peritendinous inflammatory responses and adhesion formation with surrounding tissues, which are known to induce pain and impede a proper healing and poor (re-)functionality of the tendon [333]. The middle layer acts as a reinforcement layer in between the two electrospun layers. This reinforcement is based on the Chinese finger

trap mechanism and is composed of a polypropylene tubular braid. This type of tubular braid tightens and grasps the tendon upon elongation, mimicking the stress-strain behavior of tendons [121]. The proposed reinforced, drug-loaded electrospun construct design is depicted in Figure 4.2. The dimensions of the repair constructs are: An internal diameter of 2.5 to 4 mm, a thickness of approx. 1 mm, and a length of approx. 15 to 35 mm (depending on their use in *ex vivo* sheep tendon testing or *in vivo* rabbit model).

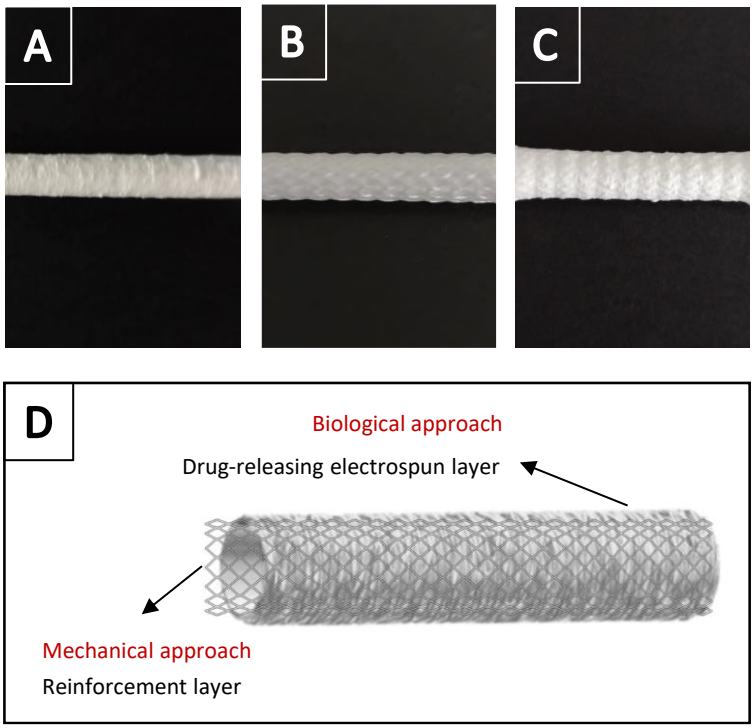

Figure 4.2. Visualization of a reinforced, drug-loaded ES construct. (A) Inner layer with no additional drugs that serves at enclosing the tubular braid in between two electrospun PCL or AUP (AUP PCL530 or AUP PCL2k) layers. (B) Tubular braid with a Chinese finger trap mechanism that acts as a mechanical support. (C) Outer electrospun PCL or AUP layer with incorporated anti-adhesion and anti-inflammatory components. (D) Schematic visualization of the reinforced ES repair construct. The dimensions of the repair constructs are: An internal diameter of 2.5 to 4 mm, a thickness of approx. 1 mm, and a length of approx. 15 to 35 mm (depending on their use in ex vivo *sheep tendon tests or in an in* vivo *rabbit model).*

4.5.2 Mechanical evaluation of the developed repair construct

One of the main goals was to develop a material with sufficient mechanical properties to support the tendon in the first stages of its recovery process in order to improve healing. The mechanical properties of the repair construct were evaluated using *ex vivo* sheep tendons. The developed PCL-based AUP repair constructs were compared to PCL constructs (as a reference). The minimal stress the construct should be able to bear in order to obtain an optimal repair, is approximately 4 MPa in hand tendons [82].

Two PCL-based AUPs with a varying backbone MM were expected to lead to differences in mechanical properties. The AUP precursor with a MM 530 $g \cdot mol^{-1}$ PCL backbone is expected to attain superior mechanical properties when compared to AUPs with higher MM PCL backbones. Herein, the AUP PCL530 will be compared to the AUP PCL2k. It is expected that shorter polymer chains lead to a more densely crosslinked network, increasing the stiffness. When comparing the mechanical properties of the pure (not processed) materials (evaluated as

crosslinked films), as discussed in Chapter 2, a Young's modulus of 8.72 ± 0.55 MPa and 5.68 ± 0.23 MPa was obtained for the AUP PCL530 and AUP PCL2k, respectively. These materials were processed using electrospinning into tubular constructs (as discussed in section 4.5.1). In the upcoming sections, the mechanical properties of the tubular electrospun repair constructs were evaluated.

(a) Tensile testing of (reinforced) drug-loaded electrospun tubes on ex vivo sheep tendons

Ex vivo tensile tests were performed on cadaveric sheep tendons. The tensile testing set-up is shown in Figure 4.3. Both the AUP PCL530 and AUP PCL2k were evaluated using *ex vivo* sheep tendon.

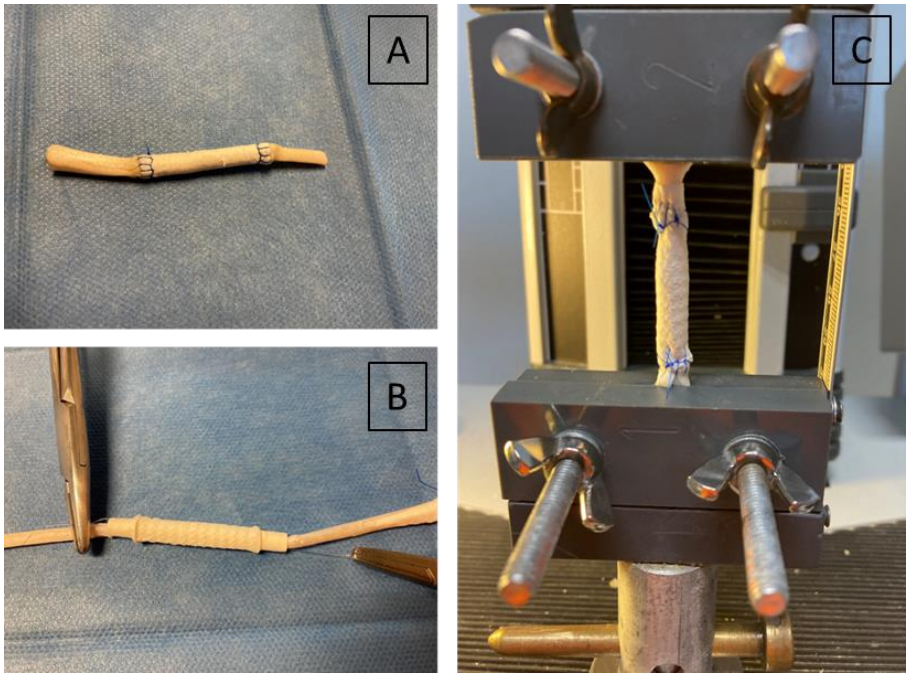

Figure 4.3. Ex vivo tensile testing of the repair constructs using cadaveric sheep tendons. (A) Repair construct without reinforcement; (B-C) Reinforced repair construct. The dimensions of the repair constructs are: An internal diameter of 2.5 to 4 mm, a thickness of approx. 1 mm, and a length of approx. 15 to 35 mm (depending on their use in ex vivo *sheep tendon tests or in an in* vivo *rabbit model).*

Both non-reinforced and reinforced repair constructs were tested (Figure 4.3). The non-reinforced repair constructs failed at an average ultimate stress of 0.4 ± 0.1 MPa, 0.8 ± 0.4 MPa and 0.8 ± 0.0 MPa for the PCL, AUP PCL530 and AUP PCL2k, respectively. These ultimate stress values are not sufficient for the intended tendon repair application, as a minimum of 4 MPa should be aimed at [82]. However, the developed reinforced repair constructs attained ultimate stresses of 4.8 ± 1.0 MPa, 6.4 ± 0.6 MPa and 8.4 ± 0.6 MPa for PCL, AUP PCL530 and AUP PCL2k, respectively. The difference in ultimate stress values between AUP PCL530 and AUP PCL2k can be attributed to the difference in crystallinity. The higher initial acrylate concentration in the lower MM AUP should result in a formation of a more densely crosslinked network, and thereby also in a higher stiffness. The higher Young's modulus obtained for the AUP PCL530 repair constructs (9.4 ± 2.5 MPa) compared to the AUP PCL2k repair constructs (3.7 ± 0.5 MPa) confirmed this statement.

For all materials, there was a significant difference ($p < 0.05$) when comparing the non-reinforced to the reinforced repair constructs, both with regard to the Young's moduli and the ultimate stresses (Table 4.3). Haussman et al. [336]. studied two different surgical suturing techniques on human flexor tendons and on sheep, pig and calf tendons. They reported a ultimate stress of 2.05 ± 0.32 MPa for a Modified Kessler suture and 3.47 ± 0.58 MPa for a deep running suture, on the repair of sheep tendons (with a surface value of 19 mm²) [336]. Two other suturing techniques (i.e. Adelaide and Modified Adelaide) were evaluated by Tahmassebi et al.[344], and led to ultimate stresses of 2.56 ± 0.31 MPa and 2.73 ± 0.16 MPa respectively. Considering the average maximum failure stresses in the current study of 6.4 ± 0.6 MPa and 8.4 ± 0.6 MPa for AUP PCL530 and AUP PCL2k respectively, the repair constructs reached superior ultimate stresses compared to most standard surgical suturing techniques. This suggests that the proposed repair technique might allow faster active rehabilitation, which is also beneficial in the prevention of adhesion formation.

Table 4.3. Overview of the tensile testing data of the non-reinforced, drug-loaded versus reinforced, drug-loaded repair constructs (AUP compared to PCL as a reference) on ex vivo sheep tendons.

Non-reinforced vs reinforced	Material	Young's modulus [MPa]	Ultimate stress [MPa]
Non-reinforced drug-loaded	PCL	0.3 ± 0.2	0.4 ± 0.1
Reinforced drug-loaded	PCL	5.7 ± 1.2	4.8 ± 1.0
Non-reinforced drug-loaded	AUP PCL530	2.5 ± 0.9	0.8 ± 0.4
Reinforced drug-loaded	AUP PCL530	9.4 ± 2.5	6.4 ± 0.6
Non-reinforced drug-loaded	AUP PCL2k	0.6 ± 0.2	0.8 ± 0.0
Reinforced drug-loaded	AUP PCL2k	3.7 ± 0.5	8.4 ± 0.6

(b) Degradation study in aqueous environment

The body-implanted construct should encourage a healing process (ideally within 6-8 weeks) in order to resume and stimulate the normal properties of a tendon [58]. Also, the tendon itself should be mechanically strong enough to perform its function before the repair construct starts degrading and the healed tendon is strong enough to bear loads again. This implies that the repair construct should not start to degrade before a period of at least 8 weeks. Moreover, it has been reported that the degradation of PCL occurs through hydrolysis of its ester linkages when in contact with physiological conditions (such as the human body) [345]. This is associated with a reduction in strength and a decrease in mass as a result of fiber rupture. Therefore, a degradation study in phosphate buffered saline (PBS) of more than 8 weeks was proposed to investigate whether premature mass loss of the electrospun repair construct (AUP PCL530, AUP PCL2k and PCL as reference) would occur.

Figure 4.4 demonstrates the degradation of the electrospun AUP PCL530 and the AUP PCL2k repair constructs. The high standard variations may be due to the limitation of accurate weighing of the light massed electrospun tubes (i.e. mg range). Only after 10 weeks, a decrease in remaining mass was observed, more in the PCL repair constructs than the AUP PCL530 constructs. For the AUP PCL2k repair constructs, no significant decrease in remaining mass was observed over the measured 9 weeks.

Importantly, the mass of the AUP (PCL530 and PCL2k) repair constructs did not significantly ($p > 0.05$) decrease in the crucial period up to 9 weeks, and thus would give the tendon enough time to pass to an advanced healing stage.

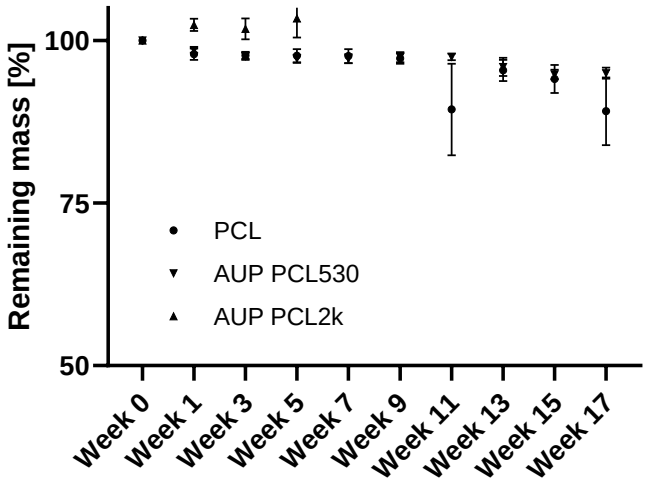

Figure 4.4. Degradation study of the electrospun AUP PCL530, AUP PCL2k and PCL repair constructs in aqueous medium.

(c) Suture retention strength

The non-reinforced PCL repair construct showed an average suture retention strength of 0.50 ± 0.09 MPa while the non-reinforced AUP PCL2k reached a significantly higher average strength of 0.79 ± 0.17 MPa ($p < 0.05$). The AUP PCL2k construct was thus better at holding sutures in place in comparison with the PCL. This can be attributed to the more densely covalently crosslinked structure obtained with AUP. The suture retention strength is a crucial and invaluable characteristic and is generally underestimated in literature concerning electrospinning specifically in tendon repair. This is in contrast with research in electrospun constructs in vascular surgery, where constructs are always attached with sutures and the aspect of suture retention strength receives more attention. In the field of tendon repair, no literature was found on sutures used for tubular electrospun constructs around a tendon. They are mostly used as a carrier for drugs or stem cells and are considered as an additive in addition to the normal repair techniques. Because in the current application, the construct will be used as a complete repair technique in itself and not only as a carrier, the suture retention strength becomes one of the vital characteristics of repair.

4.5.3 Biological evaluation of the developed repair construct

In tendon repair, adhesion is one of the main complications of the currently used surgical techniques and refers to the abnormal adherence of soft tissue to the surrounding structures [346]. In addition, during the repair period, large numbers of inflammatory cells are attracted to the injury site [333]. As a result, recurrent injury or loss of function are often observed.

The main goal of this research was to develop a mechanically and biologically relevant tubular construct for tendon repair. Within the biological approach, the main aim was to incorporate drugs, i.e. naproxen and hyaluronic acid,

in the electrospun construct to counter these adhesion and inflammatory processes. It has been reported in literature that Nap prevents adhesions by inhibiting the inflammatory response [334]. HA on the other hand is a natural polymer, ubiquitously present in the human body which has the ability to interfere with pro-inflammatory factors such as prostaglandins and cytokines [122]. Therefore, both drugs indirectly influence each other while no adverse effects on biocompatibility are expected [333].

(a) In vitro biocompatibility evaluation of the developed material

Potential cytotoxicity of the developed drug-loaded electrospun constructs was assessed using both an indirect and direct contact test. Evaluation of the biocompatibility of the materials was performed by Ca-AM/PI staining and an MTS assay at three different time points (i.e. day 1, day 3 and day 7) both in indirect and direct contact with human fibroblasts (hFBs).

Using the Ca-AM/PI staining, it was demonstrated that cell viability for all materials in both contact tests exceeded 70% after 7 days (Figure 4.5). Moreover, viability data for these materials was non-significantly different when compared to the tissue culture plastic positive control. Hence, the developed AUP material, and the incorporation of both an anti-inflammatory and an anti-adhesion component (i.e. Nap and HA) showed excellent biocompatibility, both in terms of the material on its own (direct contact) as well as leachable compounds derived from it (indirect contact) [317]. The live/dead staining images are shown in Figure S4.2 and S4.3 for AUP PCL530 and AUP PCL2k, respectively. The same trend was observed for the metabolic activity, used as a marker of cell proliferation (Figure S4.4 and S4.5, for AUP PCL530 and AUP PCL2k, respectively).

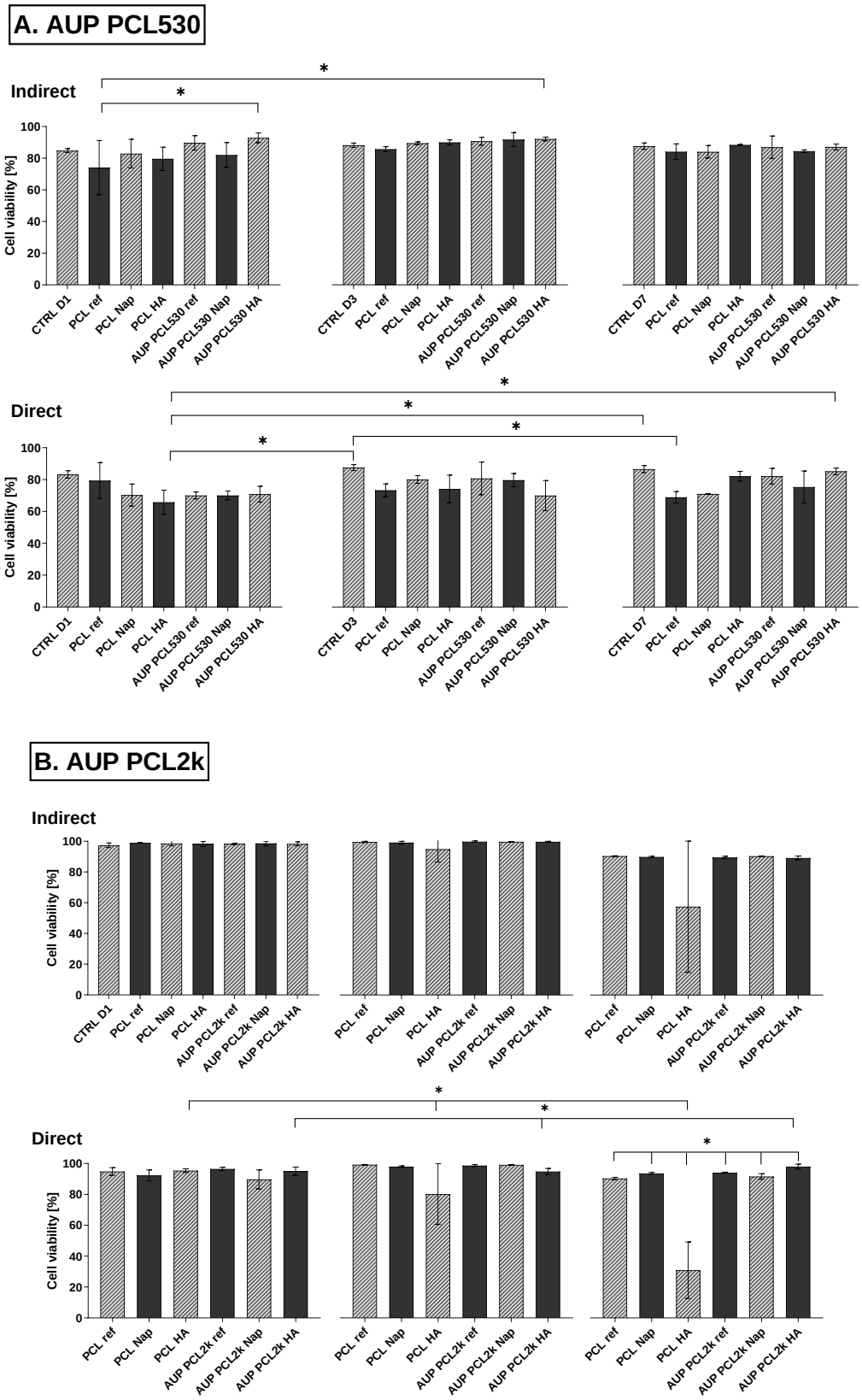

Figure 4.5. hFBs cell viability of indirect (top) and direct (bottom) assay using hFBs, by a Ca-AM/PI staining at day 1, 3 and 7. (= $p < 0.05$). Tissue culture plastic was used as a positive control. (A) AUP PCL530, (B) AUP PCL2k.*

(b) Quantification of the total collagen production in mono- or co-culture of mesenchymal stem cells and tenocytes

In vivo, tenocytes, which are the terminally differentiated cells of a tendon, maintain extracellular matrix (ECM) homeostasis and increase the production of collagen type I during the tendon healing process [32,35]. MSCs represent a promising regenerative treatment for tendon injuries, as they are known to promote tissue regeneration, prevent pathological scar formation, modulate immune responses and regulate inflammation [103,347]. As such, it has recently been demonstrated that direct co-culture of MSCs and tenocytes resulted an increased proliferation and collagen type I production when compared with mono-culture controls [103]. Additionally, non-collagenous proteins, such as glycoproteins, play an important role in modulating collagen fibrillogenesis during tendon development and healing [85]. Therefore, a co-culture with a ratio of 50% equine tenocytes and 50% equine MSCs was included in this study.

After 7 days, the main collagen production was significantly higher ($p < 0.05$) in the co-culture system (tenocytes & MSCs) when compared to mono-culture systems (tenocytes or MSCs) (Figure 4.6). When considering only the mono-cultures, a significantly higher ($p < 0.05$) collagen production was observed in tenocytes when compared to MSCs (Figure 4.6.A). Additionally, a high amount of non-collagenous proteins was detected in all cell conditions when compared to the total collagen production, and this production was significantly higher ($p < 0.05$) in the co-culture system when compared to MSC mono-culture, indicating that both collagen and non-collagenous protein production are higher in the co-culture system (Figure 4.6.C). These results illustrate the potential of MSCs to promote flexor tendon repair [103]. The Sirius Red/Fast Green staining images are depicted in Figure S4.6.

In the MSC mono-culture system, collagen production was significantly increased when MSCs were cultured on PCL Nap and PCL HA ($p < 0.05$) when compared to TCP. As it is known that the micro-environment regulates stem cell function [348], the increased collagen production might be a result of the different biochemical micro-environment with the presence of Nap and HA, and a differing mechanical strength [349]. It should be mentioned however that the Sirius Red/Fast Green Collagen staining kit cannot distinguish between different types of collagen. In the co-culture system, collagen production was significantly higher in PCL HA when compared to AUP PCL530 Nap ($p < 0.05$).

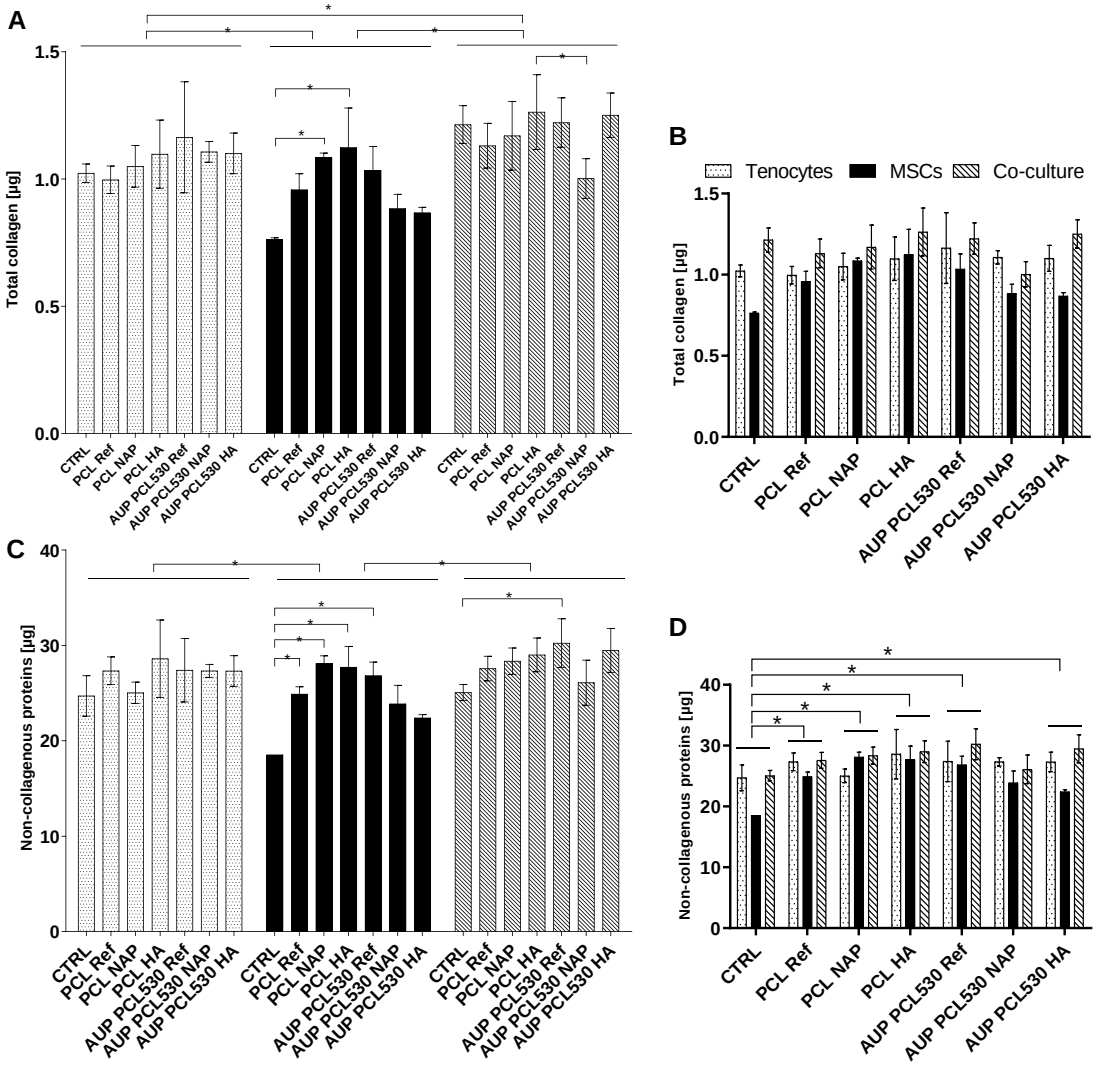

Figure 4.6. Production of total collagen (A&B) and non-collagenous proteins (C&D) illustrated in mono-cultures (tenocytes or mesenchymal stem cells, MSCs) and co-culture (tenocytes & MSCs) after an incubation of 7 days, including overall effects (B&D). Cells were cultured in direct contact with the electrospun constructs (PCL and AUP PCL530:PCL). Tissue culture plastic was used as a positive control. (= $p < 0.05$).*

Regardless of the cell type, the collagen production did not significantly differ between the materials evaluated in this study (Figure 4.6B). In almost all materials, except for AUP PCL530 Nap, however, an overall significantly higher ($p < 0.05$) production of non-collagenous proteins was observed when compared to TCP (Figure 4.6D). These findings were confirmed in the MSC mono-culture, except for AUP PCL530 HA (Figure 4.6C). In the co-culture, only AUP PCL530 ref showed a significantly higher non-collagenous protein production when compared to TCP ($p < 0.05$).

In conclusion, in both materials (PCL and AUP PCL530) evaluated in this study, an overall increased production of collagen and non-collagenous proteins was observed when tenocytes were directly co-cultured with MSCs. These findings illustrate that patients suffering from tendon injuries may benefit from MSC therapy as these proteins play a key role in tendon repair.

4.5.4 *In vivo* evaluation of the developed tendon repair constructs

In this *in vivo* study, biomechanical, macroscopic, and histological analyses were performed on four different techniques to repair flexor tendons. Based on previous studies, a rabbit tendon model was used as a model for human flexor tendons [122,350]. The modified Kessler suture was used as the control group because it is the most used technique in biomechanical studies both in hand surgery and regenerative medicine studies using rabbit tendon models [350]. Only AUP PCL2k repair constructs were tested in this *in vivo* study.

(a) Biomechanical testing

For the ultimate load at failure, the two-way ANOVA showed statistically significant differences between the postsurgical periods ($p = 0.05$) and the interaction between the postsurgical periods and techniques ($p = 0.018$). There was no statistically significant difference between the techniques ($p = 0.551$). Subsequently, a pairwise comparison was conducted for the interaction between the postsurgical periods and techniques, showing a statistically significant difference only for the drug-loaded construct between 3 and 8 weeks ($p = 0.001$).

For the extension from preload at maximum load, the two-way ANOVA showed a significant difference between the techniques ($p = 0.008$). There was no statistically significant difference between the postsurgical periods ($p = 0.498$) and the interaction between the postsurgical periods and techniques ($p = 0.184$). Subsequently, a pairwise comparison was conducted to compare the techniques showing statistically significant difference only between techniques using the drug-loaded construct and the tubular braid ($p = 0.006$). For stiffness, the two-way ANOVA showed no statistically significant difference between the postsurgical periods ($p = 0.094$), techniques ($p = 0.221$), and their interaction ($p = 0.054$).

In these biomechanical tests, the ultimate load to failure showed no statistically significant differences between the experimental techniques and the control group. This demonstrated that using a tubular braid as a repair strategy for tendon rupture has a strength comparable to that of the modified Kessler suture. Notably, the tubular braid with a smaller filament size (0.09 mm) used as a mechanical support in the reinforced drug-loaded construct showed similar strength as that of the tubular braid in technique 3 (0.18 mm). Furthermore, the techniques constituting the AUP/PCL polymers containing hyaluronic acid and naproxen also exhibited comparable strength, which indicates that the medication release does not adversely influence the strength of the repair.

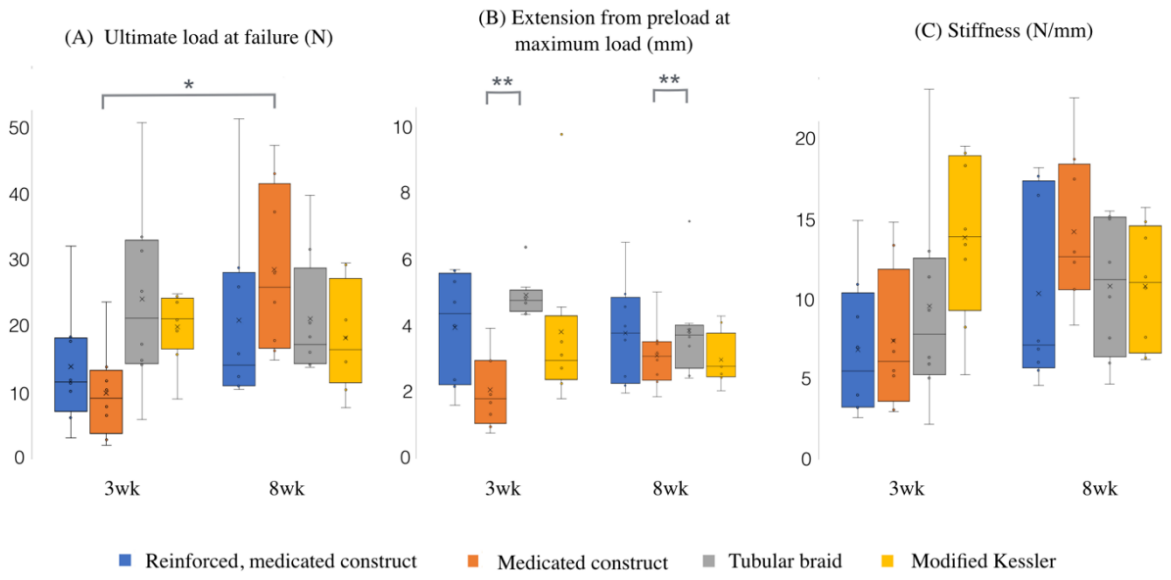

*Figure 4.7. Results of biomechanical testing of the four techniques at 3 and 8 weeks. (A) Ultimate load at failure, (B) extension from preload at maximum load, (C) stiffness. The data are shown as the mean ± standard deviation (SD). Asterisks indicate statistically significant differences after pairwise comparisons: * p=0.001, ** p=0.006. Blue: reinforced, drug-loaded AUP PCL2k construct, orange: drug-loaded AUP PCL2k construct, grey: tubular braid, yellow: modified Kessler.*

A significant difference was observed between the ultimate load to failure at 3 and 8 weeks. Evaluation of the graphs and post-hoc analysis indicates that the increase in strength of the drug-loaded construct between 3 and 8 weeks may have caused this group difference. The reinforced drug-loaded construct also increased in strength but failed to reach significance. Although one would expect the tendon repair complexes to become stronger over time, a previous study similar to ours failed to show significant differences between the postoperative periods [351].

(b) Macroscopic evaluation

Macroscopic samples of each technique are shown in Figure 4.8, and the results of the macroscopic evaluation are shown in Figure 4.9. All techniques showed a slight decrease in adhesion formation between 3 and 8 weeks postoperatively. A significantly different pattern can be distinguished with the techniques using the tubular braid (reinforced, drug-loaded construct and tubular braid as such), which predominantly showed peripheral adhesions, whereas the techniques using the Kessler suture (drug-loaded construct and modified Kessler) mainly showed central adhesions.

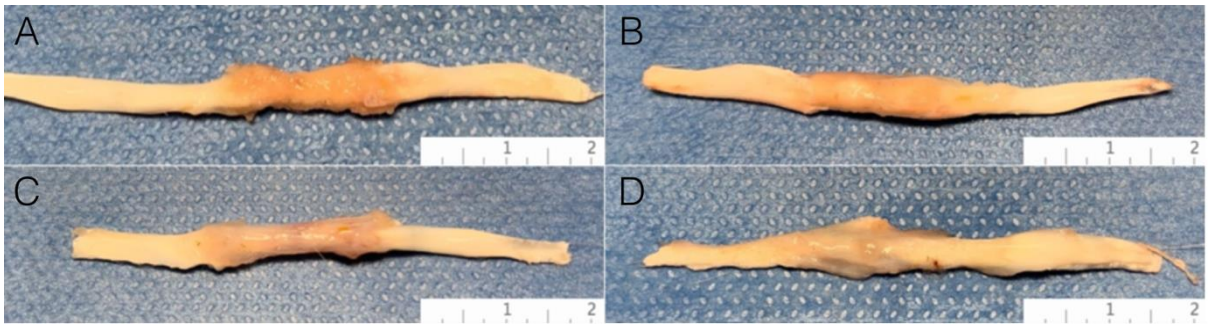

Figure 4.8. Macroscopic samples. (A) Reinforced, drug-loaded AUP PCL2k construct (B) Drug-loaded AUP PCL2k construct (C) Tubular braid (D) Modified Kessler.

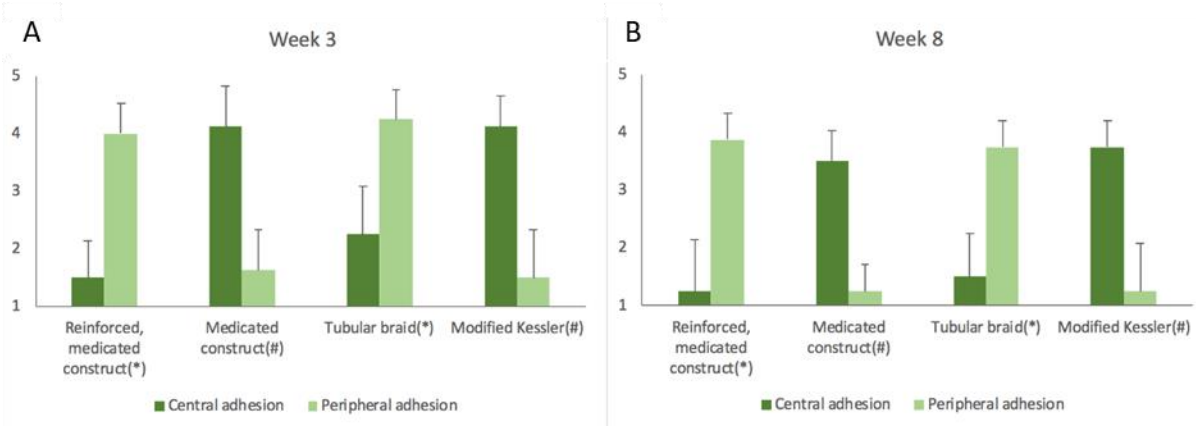

Figure 4.9. (A) Mean total scores on adhesion formation at 3 weeks postoperatively. (B) Mean total scores on adhesion formation at 8 weeks postoperatively. Techniques with (*) are each individually significantly different ($p < 0.05$) from those with (#). The (reinforced) drug-loaded constructs were based on AUP PCL2k.

Adhesion formation is one of the main causes of unsatisfactory postoperative results after flexor tendon surgery. It can lead to stiffness and pain, and sometimes necessitates a second surgery to release the repaired tendon. In this study, there were two distinct patterns of adhesion (Figure 4.9). In the reinforced, drug-loaded construct and the tubular braid techniques, adhesions were observed at the constructs' peripheral ends and not centrally where the actual repair zone was located. This is illustrated in Figure 4.10. It can be hypothesized that these adhesions were provoked by multiple exposed interrupted suture knots, rather than by the construct itself. Conversely, in the drug-loaded construct and the modified Kessler techniques, adhesions were observed more centrally, again at the suture knot. It is known that monofilament sutures require additional half-hitches compared to that with braided sutures because of their poorer loop-holding capability and inherently low coefficient of friction [352]. This creates longer and sharper knots that promote adhesion. In hindsight, an adaptation in the protocol using a continuous suture technique with only one suture knot or a (thin) multifilament suture that requires fewer half-hitches could potentially lead to a better evaluation of the anti-adhesion and anti-inflammatory effects of the drug-loaded electrospun constructs.

Figure 4.10. Image showing adhesion peripherally (black arrowhead) and no adhesion centrally (white arrowhead) when using a reinforced tubular, drug-loaded electrospun construct.

Although the anti-adhesion and anti-inflammatory effects of the drug-loaded electrospun constructs (techniques 1 and 2) were unfortunately confounded by the adhesion reaction on the suture knots, a trend towards a positive effect could still be assumed when comparing the complete absence of adhesions centrally in the reinforced drug-loaded construct compared to the presence of some adhesions in the tubular braided technique.

(c) Histological analysis

Qualitative measurements of the tendon repair quality grading are shown in Table 4.4. Histological images of the longitudinal sections stained with H&E and Masson's staining are shown in Figures 4.11 and 4.12, respectively. The reinforced, drug-loaded construct showed good healing with a gap of 0.25 mm at 3 weeks and excellent healing with continuity of the repaired zone at 8 weeks. The drug-loaded construct showed good healing with a gap of 0.75 mm at both 3 and 8 weeks, respectively. Less inflammatory cells and vascularization were observed with the drug-loaded construct compared to that with the reinforced, drug-loaded construct. The tubular braid showed fair healing with a gap of 1.5 mm at 3 weeks and excellent healing with continuity of the repaired zone at 8 weeks. The modified Kessler suture showed good healing with a gap of 0.75 mm at 3 weeks and excellent healing with continuity of the repaired zone at 8 weeks.

The connective tissue surrounding the repair site was also investigated histologically. In the techniques using the AUP PCL-based polymers with hyaluronic acid/naproxen, a larger number of macrophages and multinucleated foreign body giant cells were observed (Figure 4.13.A) compared to that with the tubular braid and modified Kessler techniques (Figure 4.13.B). Additional pan-macrophage CD 68 – immunohistochemical staining (Dako, clone KP1, 1/200 dilution) demonstrated stronger cytoplasmic granular staining in the macrophages and multinucleated giant cells in the technique using AUP PCL-based polymers with hyaluronic acid/naproxen (Figure 4.13.C) compared to the modified Kessler (Figure 4.13.D).

Table 4.4. Grading scales qualitative histological examination of the repaired region

	Week 3	**Week 8**
Reinforced, drug-loaded construct	Good	Excellent
Drug-loaded construct	Good	Good
Tubular braid	Fair	Excellent
Modified Kessler	Good	Excellent

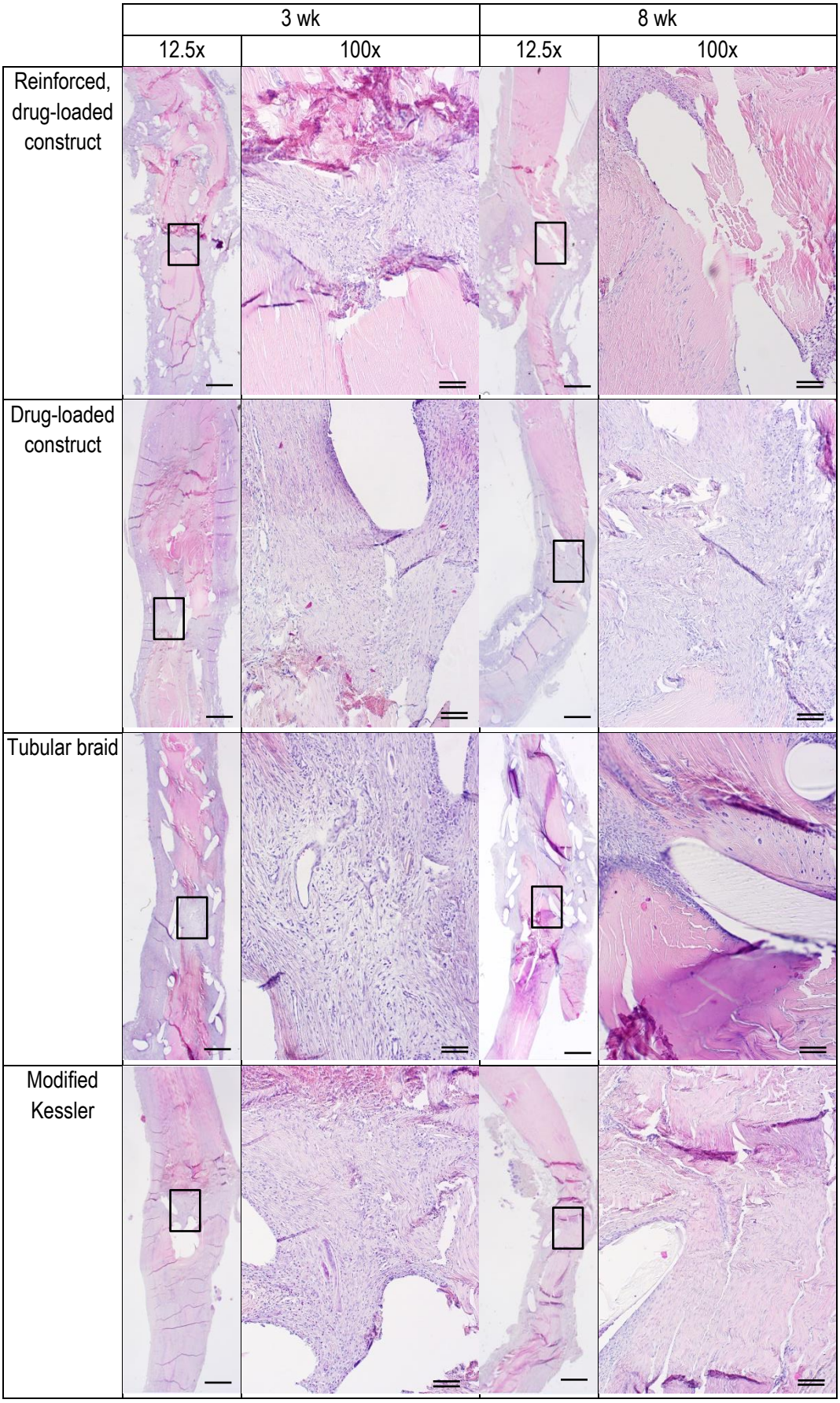

Figure 4.11. Longitudinal histologic sections of all four techniques at 3- and 8 weeks postoperatively. H&E staining. The region of interest is indicated at 12.5x magnification and enlarged at a 100x magnification. Single scalebar, 800 micron; double scalebar, 100 micron.

	3 wk		8 wk	
	12.5 x	100 x	12.5 x	100 x
Reinforced, drug-loaded construct	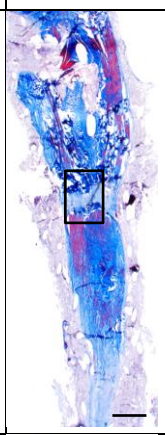	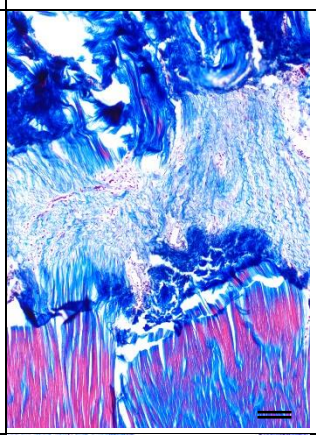	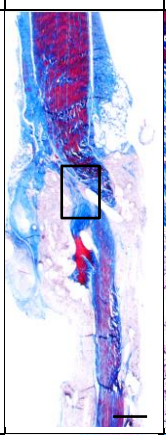	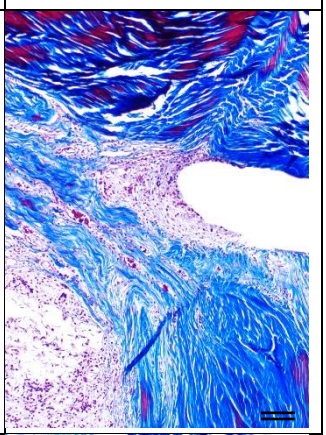
Drug-loaded construct	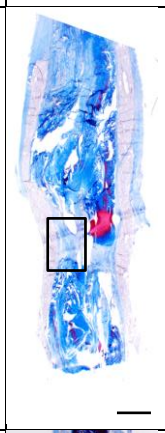	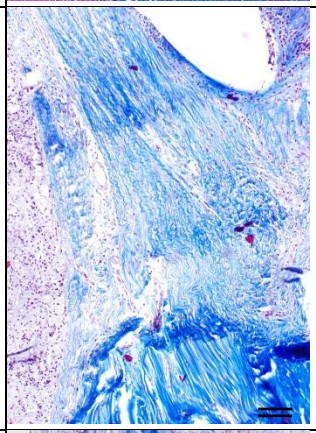		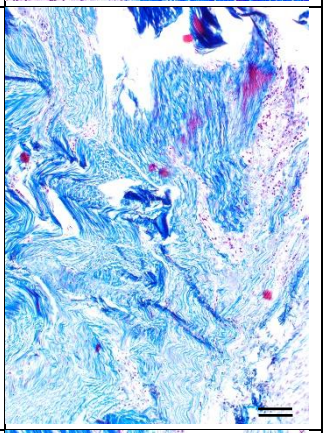
Tubular braid	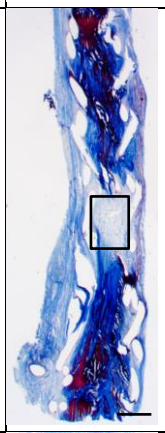	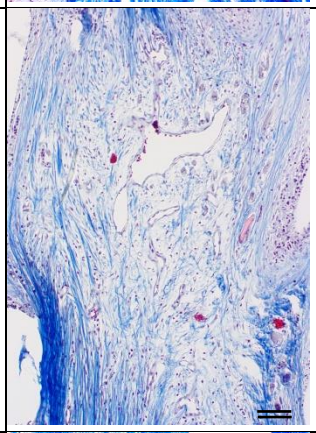	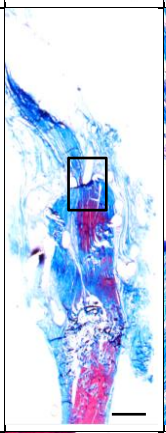	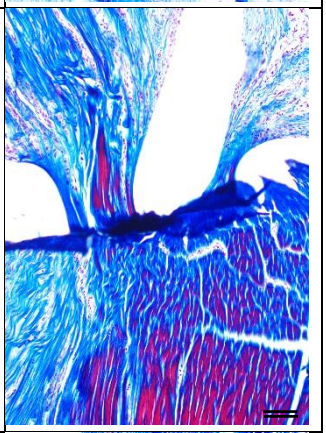
Modified Kessler	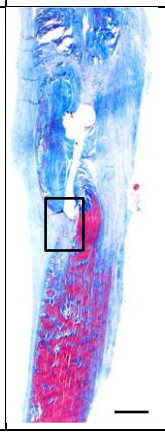	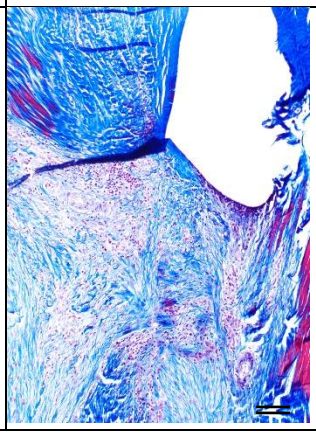	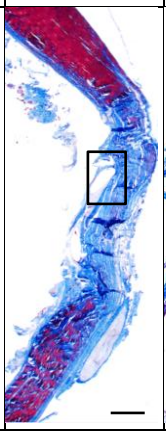	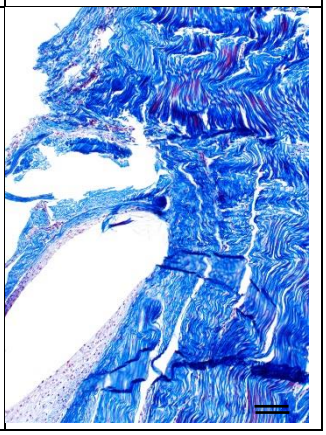

Figure 4.12. Longitudinal histological sections of all four techniques at 3- and 8 weeks postoperatively. Masson's trichome staining. Region of interest is indicated at 12.5x magnification and enlarged at a 100x magnification. Single scalebar, 800 micron; double scalebar, 100 micron.

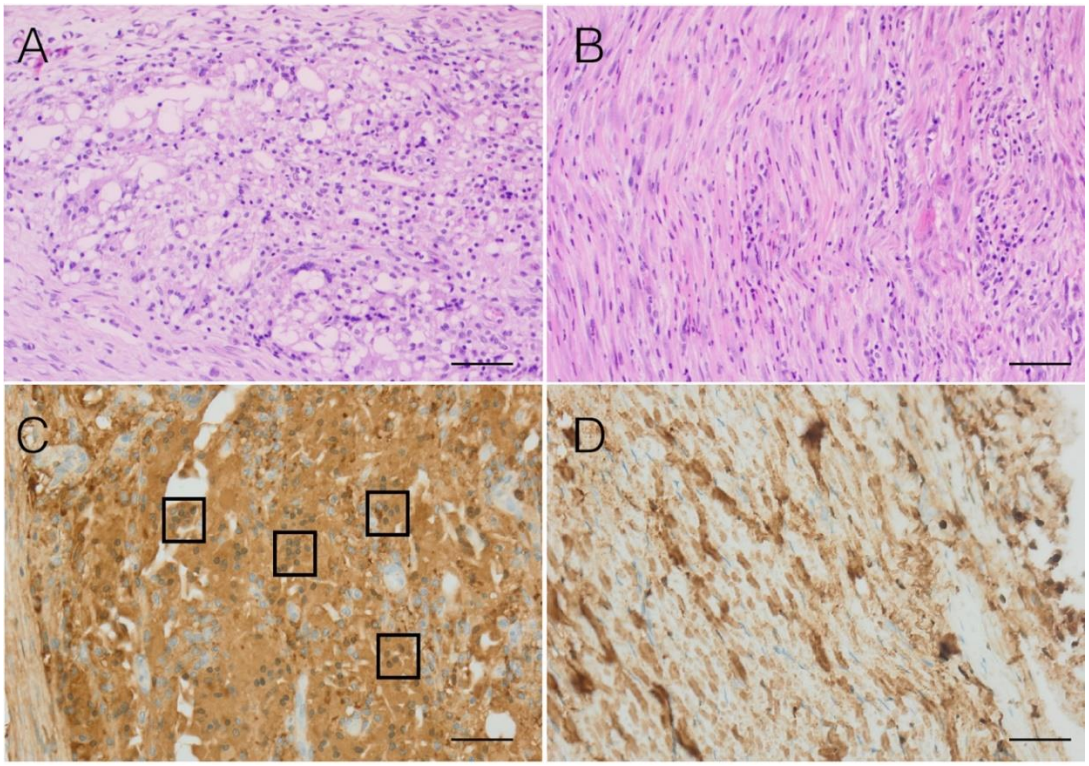

Figure 4.13. Illustration of the stronger macrophagic reaction in the connective tissue surrounding the repair in the drug-loaded constructs compared to that in the modified Kessler control group (A) H&E staining, drug-loaded construct demonstrating larger presence of macrophages and multinucleated foreign body giant cells (B) H&E staining, modified Kessler showing fewer macrophages and no multinucleated foreign body giant cells (C) CD 68 staining, drug-loaded construct: strong granular cytoplasmic CD68 staining in macrophages and multinucleated foreign body giant cells (multinucleated foreign body cells are marked in boxes) (D) CD 68 staining, modified Kessler with only punctate presence of macrophages. Magnification 200x, scalebar 50 micron.

For the reinforced drug-loaded construct, the mean number of blood vessels on a transverse section was 16.9/mm² at 3 weeks and 41.8/mm² at 8 weeks. For the drug-loaded construct (Figure 4.14), the mean number of blood vessels was 14.3/mm² at 3 weeks and 23.7/mm² at 8 weeks. For the tubular braid, the mean number of blood vessels was 18.1/mm² at 3 weeks and 22.9/mm² at 8 weeks. For the modified Kessler, the mean number of blood vessels was 28.1/mm² at 3 weeks and 14.4/mm² at 8 weeks.

The histological qualitative estimation of the repair using the four different techniques was graded from excellent to fair healing. Using a semi-quantitative scale is difficult because within a grade, some variation remains between the results due to the four evaluation criteria (gap formation, inflammation, vascularization, and the presence of newly formed collagen fibers). Inevitably, for example, between the samples of techniques 1, 2, and 4, all of which scored grade 2 at week 3, some variation was still observed in gap formation and the amount of inflammation.

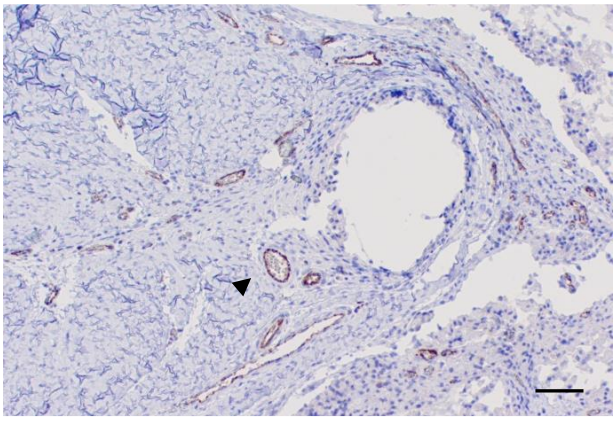

Figure 4.14. Example of transverse histologic section (drug-loaded construct) stained with CD31 immunohistochemical staining. Black arrowhead illustrating one blood vessel. Scalebar 20 micron.

In general, there seems to be an evolution from good/fair tendon healing at 3 weeks to excellent/good healing at 8 weeks. All repairs showed small to limited gap formation with the largest gap of 1.5 mm. This is smaller than the 2-mm limit for gap formation in human flexor tendon repair. In humans, a gap larger than 2 mm is considered a clinical failure and has been shown to result in inferior postoperative outcomes [353,354]. Extrapolation must be executed carefully because of the difference in the diameters of the tendons.

Notably, a noticeable increase in macrophages and giant cells was observed in the techniques using electrospun polymers. Because it is unlikely that there would be an inflammatory reaction against naproxen, either the AUP PCL-based polymers or hyaluronic acid must be the causative agents. According to Zimmermann et al., a literature search revealed that in plastic surgery, where hyaluronic acid is commonly used, a foreign body reaction with macrophages and a few multinucleated giant cells is a physiological rather than pathological reaction after hyaluronic acid injections [355].

Another important consideration is the influence of tubular braids on vascularization. The braid exerts a grasping effect, which could theoretically have a negative influence on vascularization. On the other hand, when the braid relaxes, it may also cause a pumping effect that could stimulate blood circulation. Therefore, a vessel analysis was performed. Healthy vessels were found in all four techniques, including those using a braid. Moreover, techniques using a braid did not show the lowest number of vessels at 3 or 8 weeks. Although this does not suffice to predict long-term results and the analysis was done only on one section per technique, it is reassuring that after 8 weeks, vascularization did not seem to be affected.

4.6 Conclusions

In this chapter, both a mechanical and a biological approach were combined to develop a tubular electrospun repair construct for flexor tendon. In order to improve the healing process, an optimal and controlled healing environment should be provided to minimize inflammation and adhesion processes. To this end, acrylate-

endcapped urethane-based polymers (AUP) with a poly(ε-caprolactone) (PCL) backbone of 530 and 2000 $g \cdot mol^{-1}$ were synthesized. The PCL-based AUP materials were electrospun into a tubular repair construct and benchmarked against PCL (reference). On a side note, the AUP PCL530 material was developed with the aim to overcome the need to use a reinforcement layer in the design of the AUP PCL2k repair construct.

The repair constructs were mechanically tested using *ex vivo* sheep tendons. The non-reinforced AUP PCL530 showed superior mechanical properties compared to the AUP PCL2k repair constructs (Young's moduli of 2.5 ± 0.9 versus 0.6 ± 0.2 MPa, respectively), but still insufficient to be applied for tendon repair without the reinforcement layer. However, the reinforced AUP PCL530 and AUP PCL2k repair constructs showed a Young's modulus of 9.4 ± 2.5 MPa and 3.7 ± 0.5 MPa, and an ultimate stress of 6.4 ± 0.6 MPa and 8.4 ± 0.6, respectively. In comparison, the reinforced PCL repair constructs (reference) showed a lower Young's modulus of 5.7 ± 1.2 MPa compared to AUP PCL530 and a lower ultimate stress of 4.8 ± 1.0 MPa compared to both reinforced AUP repair constructs. Thus, the reinforced repair constructs have proven to fulfill the required mechanical properties for flexor tendon repair (i.e. minimal ultimate stress of 4 MPa). In addition, the developed PCL and AUP repair constructs did not show any significant degradation before min. 8 weeks, which covers the initial healing period of an injured tendon to resume its normal properties and function.

Moreover, anti-inflammatory and anti-adhesion components were incorporated to further optimize the repair construct, i.e. hyaluronic acid and naproxen, respectively. *In vitro* biological evaluation using human fibroblasts indicated that the developed PCL-based AUP repair constructs, including the bio-active components, were non-cytotoxic (viability > 70%). Additionally, a direct co-culture of equine tenocytes and mesenchymal stem cells in the presence of the AUP PCL530 construct resulted in an increased production of both collagen and non-collagenous proteins, which play an important role in the tendon healing process.

In the *in vivo* study, the developed AUP PCL2k repair construct showed similar strength as the Modified Kessler (gold standard). However, macroscopically, a significantly different adhesion pattern was observed at the suture knots, either centrally or peripherally, depending on the applied technique. This observation indicated that the addition of bio-active compounds had a beneficial effect on the healing (adhesion limitation within the repair zone). Histologically, a qualitative assessment showed good to excellent repair at the tendon repair site.

In conclusion, the developed PCL-based AUP repair construct design combining a mechanical and biological approach shows potential for application in flexor tendon repair when designed with a reinforcement layer. However, as future perspective, it would be interesting to alter the building blocks of the AUP material in order to attain sufficient mechanical properties of the electrospun repair construct without the need of the reinforcement layer, e.g. multi-acrylate endcaps instead of mono-acrylate endcaps.

Chapter 5: Design and development of a reinforced vascular wall model

This chapter describes the application of synthetic polymers processed into tubular constructs for the development of a reinforced collagen-based vascular wall model. Three different processing techniques were used for the fabrication of the tubular constructs, i.e. solution electrospinning, 3D printing and melt electrowriting. The MEW processing was performed by N. Pien during a research stay in the fmz lab at Würzbürg University (Germany) under the supervision of Dr. T. Jüngst. The 3DP processing was conducted by V. Calbet at Biomechanics and Tissue Engineering group at Universitat Politècnica de Catalunya (Spain) under the supervision of Prof. M. Pegueroles. The mechanical and biological experiments were performed in collaboration with D. Di Francesco during a research stay at the LBB lab at ULaval (Canada) under the supervision of Dr. F. Copes and Prof. D. Mantovani. The SEM imaging was conducted by Dr. P. Chevallier (LBB lab). The data reported in this chapter will be submitted as an article which is in preparation:

N. Pien, D. Di Francesco, F. Copes, M. Bartolf-Kopp, V. Chausse Calbet, P. Chevallier, M. Pegueroles, T. Jüngst, S. Van Vlierberghe, P. Dubruel, D. Mantovani. Polymeric reinforcements for collagen-based vascular wall models: Influence of the processing technique on the final mechanical and biological properties. In preparation.

5.1 Résumé

Dans ce chapitre, nous visons à améliorer un modèle de paroi vasculaire tubulaire à base de collagène précédemment développé en le renforçant à l'aide d'un échafaudage polymérique tubulaire. Les échafaudages polymères tubulaires ont été fabriqués en poly(ε-caprolactone) (PCL) commercial, un polymère déjà utilisé pour fabriquer d'autres dispositifs approuvés par la FDA et disponibles dans le commerce pour des applications médicales, par (i) électrospinning en solution (SES), (ii) impression 3D (3DP) et (iii) électrowriting en fusion (MEW). Le modèle non renforcé à base de collagène a été utilisé comme référence (COL). L'effet de la technique de traitement (c'est-à-dire SES, 3DP et MEW) et de l'architecture correspondante de l'échafaudage sur les propriétés mécaniques et biologiques du modèle à base de collagène renforcé a été évalué.

5.2 Abstract

In this chapter, we aim to improve a previously developed tubular collagen-based vascular wall model by reinforcing it using a tubular polymeric scaffold. The tubular polymeric scaffolds were fabricated in commercial, poly(ε-caprolactone) (PCL), a polymer already used to fabricate other FDA-approved and commercially available devices for medical applications, by (i) solution electrospinning (SES), (ii) 3D printing (3DP) and (iii) melt electrowriting (MEW). The non-reinforced collagen-based model was used as a reference (COL). The effect of the processing technique (i.e. SES, 3DP and MEW) and the corresponding scaffold architecture on the resulting mechanical and biological properties of the reinforced collagen-based model were evaluated. SEM imaging showed the influence of the processing technique on the scaffold's architecture at both the micro- and the macrolevel. The polymeric scaffold led to significantly improved mechanical properties of the reinforced collagen-based model (initial elastic moduli of 382.05 ± 132.01 kPa, 100.59 ± 31.15 kPa and 245.78 ± 33.54 kPa, respectively for SES, 3DP and MEW at day 7 of maturation) compared to the non-reinforced collagen-based model (16.63 ± 5.69 kPa). Moreover, on day 7, the developed collagen gels showed stresses (for strains between 20-55%) in the range of [5-10] kPa for COL, [80-350] kPa for SES, [20-70] kPa for 3DP and [100-190] kPa for MEW. In addition to the effect on the resulting mechanical properties, the different processing techniques and polymeric tubes' architecture influenced the cell behavior, in terms of proliferation and attachment, along with collagen gel compaction. The MEW reinforcement led to a collagen gel compaction like the COL reference, whereas 3DP and SES led to thinner and longer collagen gels. Overall, it can be concluded that (i) the selected processing technique strongly influences the resulting mechanical and biological properties, and (ii) the incorporation of a polymeric reinforcement leads to mechanical properties more closely resembling those of the native arteries. In a follow-up study, it would be interesting to evaluate the effect of the reinforcement scaffold on a co-culture (i.e. endothelial cells, smooth muscle cells and fibroblasts, mimicking the three layers of the vascular wall) collagen-based model under dynamic maturation.

5.3 Introduction

Although tissue engineered blood vessels (TEBV) as living arterial substitutes have been studied extensively throughout the last 25 years, clinical translation has not yet occurred [93,94,356,357]. Strategies for vascular tissue engineering (vTE), and more specifically, for the fabrication of TEBV, differ from each other in terms of materials used, fabrication techniques, applied cell sources or the approach to statically/dynamically or biochemically stimulate constructs towards tissue formation [63,358]. During the past years, the potential of TEBV as living models in *in vitro* cardiovascular research has been explored with the aim to bridge the gap between 2D cultures and *in vivo* models [359], to advance the current knowledge of pathophysiological processes and to support the development of clinical therapies [358,360]. More precisely, an *in vitro* vascular wall model that is capable of recapitulating the cellular and mechanical environment of native vessels represents a valuable platform to study cellular interactions and signaling cascades, test drugs and medical devices under (patho)physiological conditions, and could reduce the number of animals required for preclinical testing [358,360].

Two of the most important elements when bioengineering a blood vessel or modelling the vascular wall are (1) the scaffold, an artificial structure that should possess mechanical stability, sustain biological functions and exhibit biocompatibility and biodegradability, and that is expected to support the formation of the three-dimensional (3D) tissue, and (2) vascular cells populating the scaffold and remodelling its structure, that should enable biological functioning similar to that in the native blood vessel [11,361].

With respect to the development of the *ideal* scaffold, the material selection plays an important role. Collagen, being one of the main components of the vascular extracellular matrix (ECM), is currently the most commonly used natural polymer for vTE applications [91,362], and more specifically, for the development of vascular wall models [109,181,363–365]. The use of collagen is prompted by several favorable characteristics including weak antigenicity and robust biocompatibility along with promotion of cell adhesion, and biodegradability [181,366,367]. However, one of the most important limitations of collagen-based materials includes their mechanical properties. In particular, their viscoelastic properties are often unsatisfactory, limiting their use in TE applications [181,368]. For vascular TE, this implies that the mechanical properties of collagen-based constructs are unable to withstand the high pressures and stresses encountered in the blood vessel [181,369]. Human coronary arteries have a compliance of 4.5 - 6.2% change in diameter for a pressure increase from 80 to 120 mmHg, a burst pressure of 2031 - 4225 mmHg, a maximum stress of 1.44 ± 0.87 MPa, a maximum strain of 0.54 ± 0.25 and a physiological elastic modulus of 1.48 ± 0.87 MPa [64,73–79]. Conversely, the extracted collagen that is used in vascular TE applications shows a poor burst pressure of 18 ± 1 mm Hg and elastic moduli of maximum 30 kPa [370–373].

Therefore, research has focused on different approaches to overcome this limitation, including (i) maintaining the construct's structural integrity by chemical, physical or enzymatic crosslinking [181,368], (ii) blending with other natural biomaterials, e.g. fibronectin [374] or elastin [372], or (iii) combining natural materials with synthetic biomaterials by developing multi-material scaffolds [181,363,367]. The latter includes blending before processing

[375], co-extrusion or layer-by-layer processing methods [376], post-processing steps including dipcoating [377], or using synthetic polymer scaffolds as a reinforcement for collagen-based models [378,379].

A plethora of synthetic materials as such (i.e. without blending with natural materials) have already been studied for vTE including poly(urethane) (PU) [380,381], poly(lactic-co-glycolic acid) (PLGA) [382,383], poly(ε-caprolactone) (PCL) [160,198,384–386], poly(lactic acid) (PLA) [161,387–389], poly(L-lactide-co-ε-caprolactone) (PLCL) [388,390] and, poly(vinyl alcohol) (PVA) [168,391]. The main advantages of synthetic polymers include their excellent reproducibility, mechanical properties' tunability and control over shape, architecture and chemistry [72,127–129]. PCL is a semi-crystalline, bioresorbable polymer that is approved by the U.S. Food and Drug Administration (FDA) for certain clinical purposes [287]. Compared to PGA and PLA, PCL exhibits a lower tensile strength yet increased elasticity (i.e. an initial tensile strength of 50 MPa versus 890 and 900 MPa for PGA and PLA, respectively; and an elongation at break of 70% compared to 30 and 25% for PGA and PLA, respectively) [392,393]. In addition, PCL grafts have shown improved patency and endothelialisation compared to commercially available non-degradable grafts such as expanded poly(tetrafluoroethylene) (ePTFE) [394].

The scaffolds' properties not only depend on the selected material, but are also strongly influenced by the architectural design of the matrix structure, which is mainly defined by the processing technique [66,187]. In turn, the architectural design affects prominently the cell behavior in terms of adhesion, migration, proliferation and differentiation [66,187]. Therefore, the processing technique has an important influence on the resulting mechanical and biological properties of the developed scaffold.

To process biomaterials into tubular constructs, multiple processing techniques have been proposed and evaluated. These processing techniques can be grouped into conventional and advanced techniques. Some examples of conventional techniques include gas foaming, moulding, solvent casting, dip coating amongst others [26]. More advanced techniques, include solution electrospinning (SES), three-dimensional (bio)printing (3D(B)P) and melt electrowriting (MEW) [9,216,242]. Each one of them has its own pros and cons, and will influence the resulting properties of the fabricated tubular construct [300]. SES and MEW are techniques that enable the production of nano- and micro-scale fibers, respectively, constituting an advantage with regard to mimicking the natural ECM in terms of hierarchical organization and properties [225,287]. 3D(B)P allows control of material deposition down to the micron level (45-1600 μm) [25,214,395]. Both 3D(B)P and MEW offer the possibility to design complex geometries through computer aided design [242,396]. All three techniques present unique advantages to process materials serving tissue engineering applications, including vTE [300].

The aim of this research was to improve a previously developed collagen-based model [372,397,398] by reinforcing the model using a tubular polymeric reinforcement composed of PCL. In doing so, we aimed at recapitulating the mechanical properties of the wall of the vascular medium diameter vessel (3-5 mm). The effect of the processing technique (i.e. SES, 3DP and MEW) and the corresponding scaffold architecture, were evaluated on the resulting

mechanical and biological properties of the reinforced collagen-based model. As a reference, a fibroblast-cellularized collagen-based model without PCL reinforcement layer was used. Cell viability and - proliferation, immunofluorescence staining, ECM production through gene expression analysis (ongoing experiments) and histology, and the viscoelastic properties were evaluated after 3 and 7 days of maturation.

5.4 Materials and methods

5.4.1 Development of reinforcement scaffold using solution electrospinning

Solution electrospun scaffolds were produced within the Polymer Chemistry and Biomaterials research group at Ghent University (Belgium). The in-house manufactured electrospinning set-up is composed of a high voltage source (Glassman High Voltage, Inc.; model series EL50P00, high voltage DC power), a motion controller (CWFW Ghent University) and a motor-driven syringe pumping system (New Era Pump Systems, Inc.; model Single Syringe Pump NE-300). The applied processing parameters were varied within the ES process (voltage 15-20 kV, flow rate 1.0-2.0 $mL \cdot h^{-1}$ and needle-to-collector distance from 16-18 cm) and an optimal set of parameters was selected subsequently (i.e. voltage of 18 kV, flow rate of 1.4 $mL \cdot h^{-1}$ and needle-to-collector distance of 18 cm). ES was performed at 21°C and the relative humidity (i.e. ranging between 25-35%) was determined by a hygrometer which was present in the ES cabinet.

The homogeneous polymer solution (23.3 (w/v)% PCL (Medical grade PCL, Purasorb PC 12) in chloroform, stirred overnight; optimized concentration from the tested range between 16 and 25 (w/v)%) was transferred into a 20 mL syringe that was clamped into the syringe pumping system. The ES needle (inner diameter: 0.58 mm) was placed above the collector. A mandrel rotating around its axis (180 rpm, Inox stainless steel, 2 mm diameter) was applied during the process of ES to produce tubular constructs. For an easy release of the electrospun tubes from the mandrel, preheated mandrels (T=80°C) were dipcoated in molten poly(ethylene glycol) 8000 $g \cdot mol^{-1}$ (PEG8k) (T=80°C). After performing ES, the mandrels were submerged in ddH_20 to dissolve the water-soluble PEG8k-coating (approx. 1 mm thickness) and allow an easy release of the developed tubular PCL constructs.

5.4.2 Development of reinforcement scaffold using melt electrowriting

Melt electrowritten scaffolds were produced at the fmz lab, Department for Functional Materials in Medicine and Dentistry, University of Würzburg (Germany). Tubular constructs of PCL (Medical grade PCL, Purasorb PC 12) were processed with a custom-made melt electrostatic writing device with a cylindrical and interchangeable collector. The motorization is based on an Aerotech axis system (PRO115) and uses the A3200 (Aerotech) software suite as coding and machine operating interface. A modified code has been developed similar to previous work [245] to move the collector in translational as well as rotational directions to allow precise fiber placement onto a steel mandrel in predetermined winding angles. For the extrusion of materials, polypropylene cartridges and 22G flat tipped needles (Nordson EFD) were used in all experiments. The printing temperature and pressure were set to 89°C and 0.65 bar, respectively [399]. Based on the dimension of the collagen-based model as previously

described [372] and based on earlier findings on evaluating MEW tubes for vascular TE [399], the following predefined specifications were chosen for tubular construct generation: the length of the construct was set to 11.56 mm, the number of fiber layers on top of each other was set to 20, the angle at which the fibers are aligned in relation to the longitudinal axis (winding angle) was 70°, and the number of turning points (pivot points) of the construct was 8. Further description of the printing variables can be found in previous work from McColl *et al.* [245].

5.4.3 Development of reinforcement scaffold using three-dimensional printing

3D printed scaffolds were produced at the Biomaterials, Biomechanics and Tissue Engineering group, Department of Materials Science and Engineering, Universitat Politècnica de Catalunya, (Spain). 3D printed tubular PCL constructs were fabricated by a solvent-casting direct-write technique using a BCN 3D+ printer (BCN 3D technologies) as explained previously [400]. In brief, the printer was modified to solvent cast inks through a syringe micro-nozzle with a 250 mm inner diameter (Nordson®). Moreover, the printer's Y-axis was modified by introducing a carbon fiber rotating mandrel to print cylindrical structures.

PCL inks were prepared by dissolution of PCL pellets (Medical grade PCL, Purasorb PC 12) in chloroform (Sigma-Aldrich) at a 62.5% ratio (w/v) using a centrifuge (SpeedMixer™, AC 150.1 FVZ, FlackTek). The tubular shape was inspired by the Igaki-Tamai stent (Kyoto Medical Planning, Japan) design structure composed of rhombic cells and its dimensions were 3 mm in diameter and 20 mm in length with 10 peaks. The software Fusion 360™ (Autodesk) was used for the tubular construct design and the resulting Computer-Aided Design was exported to STL format. Finally, Slic3r (open source) was used to translate STL to G-code, which was needed for the 3D printer. PCL tubes were printed at 4 $mm \cdot s^{-1}$ velocity.

5.4.4 Morphological characterization of the developed tubular constructs

Microstructural characterization of surfaces and cross-sections of the developed tubular constructs were conducted by scanning electron microscopy (SEM) performed with a FEI Quanta250 SEM system (Thermo-Fisher) using a secondary electron detector. The SEM images were acquired with an acceleration voltage of 15 kV. Calculations of the fiber diameter and pore size were performed using ImageJ software.

5.4.5 Cells and cell culture

Neonatal human dermal fibroblasts (HDFs, C0045C, Gibco, Thermo Fisher Scientific) were cultured in an incubator at 37°C under constant supply of 5% CO_2 in Dulbecco's Modified Eagle Medium (DMEM, Gibco) supplemented with 10% fetal bovine serum (FBS, Gibco) and 1% Penicillin-Streptomycin solution (Pen-Strep, Gibco). Cells were cultured up to 90% confluency, then enzymatically detached and counted for sub-culturing or experimental use. For the presented experiments, cells at passage 7 were used.

5.4.6 Preparation of reinforced cellularized collagen-constructs

Type I collagen was extracted from rat tail tendons, solubilized in 0.02 N acetic acid at a concentration of 4 $g \cdot L^{-1}$, sterilized and processed according to a previously reported protocol [401]. The collagen solution was mixed with a neutralizing buffer solution (3.5× DMEM supplemented with 10 mM HEPES and 60 mM NaOH) and a suspension of HDFs in culture medium (DMEM supplemented with 10% of FBS and 1% of Pen-Strep) at 4°C in a ratio of 2:1:1, respectively. The final collagen concentration in the gel was 2 $g \cdot L^{-1}$ (pH 7.2) and the cell density was 1.5×10^6 $cells \cdot ml^{-1}$. The final solution was poured in a 48-well custom-made plate containing a central PEEK mandrel (Ø = 2.985 mm), in 4 different conditions: (1) no reinforcement (COL, reference), (2) a solution electrospun (SES), (3) a three-dimensionally printed (3DP) or (4) a melt electrowritten (MEW) reinforcement (i.e. tubular reinforcement construct placed around the mandrel before adding the final solution). The tubular gel was gently detached from the wall and medium was added to fill the well. The plate was incubated at 37°C and 5% CO_2 for 3 and 7 days. Culture medium was changed every day. Four samples for each condition and time point were prepared.

5.4.7 Mechanical characterization of tubular constructs

(a) Evaluation of gel compaction

The length and the outer diameter of the developed constructs (gel and reinforcement layer) were measured to evaluate gel compaction after 3 and 7 days of culture. A calliper was used for measuring the length while a scanning laser interferometer (LaserMike 136, Series 183B, NDC Technologies) was applied to determine the external diameter. The inner diameter was known and equal to the diameter of the central polyether ether ketone (PEEK) mandrel (Ø = 2.985 mm), which allowed calculating the volume of each sample. Length and wall thickness were calculated for each sample at both time points. Data are expressed as mean ± standard error of mean (n=3).

(b) Evaluation of visco-elastic properties (Instron)

The viscoelastic properties were evaluated by tensile stress relaxation tests using an Instron E1000 (Instron Corporation) equipped with a 5 N load cell. Ring-shaped samples (length approx. 4 mm) were placed on *ad hoc* made L-shape grips and tested in a phosphate-buffered saline (PBS) bath at 37°C to mimic physiological conditions. A pre-strain of 5% was applied to the samples followed by 5 progressive stress relaxation cycles each consisting of 10% strain ramps ($5\% \cdot s^{-1}$ strain rate) and 10 minutes of relaxation. After the 5th cycle (55% of deformation), the test continued with the same strain rate up to sample failure. The measured load was divided by the initial cross-sectional area of the sample to obtain engineering stresses. Strain was determined as the variation of the distance between the grips (l-l_0) divided by the initial distance (l_0), the point of zero force calculated with the sample's original circumference. E_E is defined as the equilibrium elastic modulus, and E_0 as the initial (instantaneous) elastic modulus. Data are expressed as mean ± standard error of mean (n=3).

5.4.8 Biological characterization of tubular constructs

(a) Evaluation of cell viability (Resazurin)

AlamarBlue Cell Viability assay (Thermo Fisher Scientific) was performed according to the manufacturer's instructions. Briefly, the culture medium was removed from each well and replaced by 850 µL of resazurin solution in DMEM (1X) at each time point (i.e. day 3 and 7). The plate was then incubated for 4 hours at 37°C and in 5% CO_2 to allow the reduction of resazurin into the pink and highly fluorescent resorufin. Aliquots (100 µL, n=4) from each sample (n=3) were transferred to a 96-well plate and fluorescence was measured (λ_{ex} = 560 nm; λ_{em} = 590 nm) in a multi-well plate spectrophotometer (SpectraMax i3x, Molecular Devices). Results were normalized over the non-reinforced collagen-based model (COL) at day 3. Data are expressed as mean ± standard error of mean (n=4).

(b) Immunofluorescence staining (Phalloidin for actin / DAPI) and histochemistry

After 3 and 7 days of maturation, the constructs were fixed with 3.7% formaldehyde (Sigma) for 60 min, washed with PBS 1X (1x 20 min, 2x 2 min), and treated with 0.5% Triton X-100 in PBS1X for 5 min at room temperature (r.t.) to permeabilize the cells. Thereafter, the constructs were rinsed two times with PBS 1X. Afterwards, the samples were blocked in a 3% bovine serum albumin (BSA) in PBS solution for 20 minutes at r.t.. Then, the blocking solution was removed and the samples were incubated at r.t. for 2 h with Collagen I primary antibody (mouse) (1:1000, Novus Biologicals) in blocking solution. The samples were then rinsed with PBS 1X and incubated for 1 h with a goat anti-mouse Alexa Fluor 488 secondary antibody (1:200, Life Technologies) and with Rhodamine-conjugated phalloidin (1:200, Sigma), both prepared in blocking solution. The samples were then rinsed with PBS 1X and 4',6-diamidino-2-phenylindole (DAPI, 1:3000, Thermo Fisher Scientific) was used to stain cell nuclei. Images were obtained using an LSM 700 confocal laser scanning microscope (Zeiss) controlled by ZEN 2009 software for image acquisition and further analysis.

Histochemistry (HC) was performed to observe collagen, cell distribution and compaction. Tubular samples were rinsed in PBS and fixed in 3.7% formaldehyde (Sigma-Aldrich) for 60 min. Fixed samples were then embedded in paraffin and cut into circumferential cross-sections of 5 µm. Sections were deparaffinized with toluene, rehydrated with successive washes with ethanol in deionized water (dH_2O) at decreasing concentrations (100%, 95%, 80% and 0%), refixed in Bouin solution overnight and stained with a modified Masson's trichrome procedure. The following dye solutions were added to stain the nucleus, the cytoplasm and collagen: Weigert's iron hematoxylin, acid fuchsin with xylidine ponceau and light green SF yellowish, respectively. Images were obtained by an Olympus BX51 microscope (Olympus Canada Inc.).

5.4.9 Statistical analysis

All data were analyzed using GraphPad Prism 8.0.2. An two-way ANOVA test was performed followed by a Tukey post-test. The symbols representing the different significant levels are indicated on the graphs, and/or defined in the captions (i.e. ns = $p > 0.05$; * = $p \leq 0.05$; ** = $p \leq 0.01$; *** = $p \leq 0.001$).

5.5 Results and discussion

Tubular polymeric scaffolds were fabricated in PCL by (i) solution electrospinning (SES), (ii) 3D printing (3DP) and (iii) melt electrowriting (MEW). These PCL tubes were then used as reinforcement for the previously developed collagen-based model [372,397,398]. The non-reinforced collagen-based model was used as a reference throughout this chapter. The effect of the processing technique (i.e. SES, 3DP and MEW) and the corresponding scaffold architecture, on the resulting mechanical and biological properties of the reinforced collagen-based model were evaluated. In order to be able to compare this reinforcement approach to previous research done in the LBB lab by Camasao *et al.* [372], who studied the influence of elastin in the collagen-based model, fibroblasts were selected for this study.

5.5.1 Morphological analyses

As a first step in the evaluation of the effect of the selected processing technique on the scaffold's architecture, SEM was performed to visualize the fibers' alignment and diameter. Figure 5.1 shows the fibers of the developed scaffolds using SES, 3DP and MEW at different magnifications. The SES tubes showed a randomly oriented fiber distribution, closely resembling the native ECM. SES scaffolds (fabricated on rotating mandrels at low rpm) are known for such fiber arrangements, representing one of the main advantages of this processing technique [232]. The average diameter of the SES fibers was 6.58 ± 0.30 µm, the smallest of the three techniques compared in this chapter. The largest fiber diameters were measured in the 3DP structure, with an average fiber diameter of 237.04 ± 12.51 µm. The visualization of the 3DP structure also confirmed the predefined design and controlled deposition of the fibers down to 100 µm level. MEW is known to be a technique that allows the deposition of micrometer (up to ± 10 µm) scale fibers in a predefined design. This was confirmed by SEM images, which indicated that the average fiber diameter of MEW constructs was 13.16 ± 0.67 µm. The multiple layers of the MEW fibers were perfectly deposited onto each other, leading to a precisely defined scaffold architecture.

Next, the SEM images were analysed to assess the pore size of the different tubular scaffolds. The tightly packed fibers of the SES tubes showed the smallest pores, with widths (i.e. shortest distance between 2 struts) ranging from a minimum of 8 ± 1 µm up to a maximum of 37 ± 5 µm. Conversely, the 3DP tubes showed the largest pore sizes, being 800 ± 100 µm in width and 1800 ± 110 µm in length (i.e. greatest distance between 2 struts). Lastly, the MEW tubes showed pore sizes of 512 ± 4 µm in width and 736 ± 3 µm in length (see Figure 5.1).

The different PCL tubular scaffolds were also characterized in terms of their thickness. The 3D printed tubes, which constituted only a single fiber monolayer, exhibited a thickness of 216.43 ± 49.27 µm. This value was similar to the average fiber diameter shown in the SEM images (i.e. 237.04 ± 12.51 µm), confirming that the scaffold's structure is based on one single strut. For SES and MEW, a thickness of 613.07 ± 138.01 µm and 191.7 ± 5.50 µm were obtained, respectively. The small standard deviation obtained for the MEW tube, compared to SES, also evidences the excellent reproducibility and precision regarding fiber deposition of the MEW technique. All developed tubular scaffolds were fabricated with an inner diameter of 3 mm, aiming at small-diameter (i.e. < 6 mm) vTE [402].

It is hypothesized that differences in fiber alignment, diameter, pore size and hence scaffold architecture, will have an influence on collagen compaction, and on both mechanical and biological properties. These properties will be evaluated in the upcoming sections.

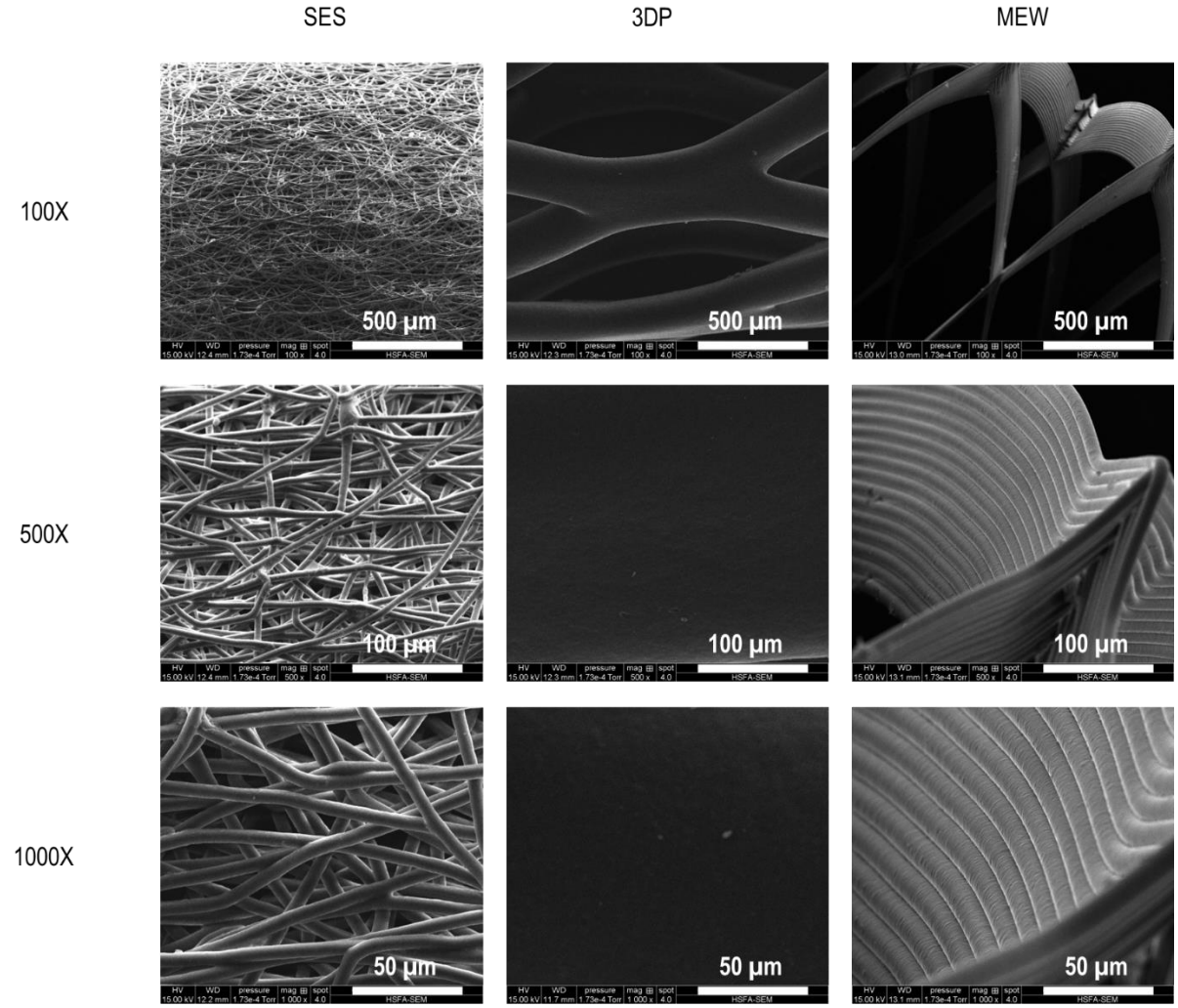

Figure 5.1. Visualization of the reinforcement tubes using SEM imaging, processed by SES, 3DP and MEW. Fiber diameters of SES, 3DP and MEW amounted 6.58 ± 0.30 µm, 237.04 ± 12.51 µm and 13.16 ± 0.67 µm, respectively.

5.5.2 Mechanical characterization

(a) Evaluation of gel compaction

Upon visual inspection, differences in gel compaction (both in length and thickness) could be observed at day 3 and day 7 when comparing the tubular gels reinforced by the three different processing techniques. In case of a SES reinforcement layer, the collagen gel compacted as an outer layer around the SES scaffold. For the 3DP scaffold, the collagen gel compacted thereby filling the large holes of the tubular structure. After maturation during 3 and 7 days, the collagen gels of COL (reference) and MEW were visually very similar in thickness and length (Figure 5.2). Seemingly, the HDFs-mediated collagen compaction was not influenced by the presence of the MEW scaffold. This is probably due to the predefined architecture and the resulting nicely stacked, thin PCL fibers that lead to a flexible structure. The flexible structure is anticipated to enable the deformation of the MEW tube, and therefore, the MEW scaffold shrunk in length upon compaction of the collagen gel (to the same length and thickness as the COL condition). When comparing COL to 3DP and SES, the cellularized collagen gel was more spread out in length over the 3DP and SES tube and was thinner in wall thickness.

The differences in scaffold architecture along with flexibility of the developed tubular reinforcements exhibit an important influence on the collagen gel compaction. The 3DP tubes showed the largest pores within the 3 developed tubular scaffolds (i.e. SES, 3DP and MEW), but had a less deformable, less flexible structure due to the presence of 1 thick strut (i.e. average diameter of 237.04 ± 12.51 µm). The MEW tube showed smaller pores and a much more flexible structure compared to the 3DP tube. The SES tube exhibited a high surface area-to-volume ratio, yet small pores and was less deformable compared to the MEW construct, but more deformable compared to the 3DP tube (*vide infra,* 3.2.b). When comparing the collagen compaction for the 3DP and SES tubes, the collagen gel did not seem to be compacted in the same way as in COL and MEW. For 3DP and SES, the collagen gel was found to be more spread out over almost the full length of the reinforcement tube. An overview of the measured wall thicknesses and lengths is shown in Figures 5.2.A and B, respectively. No statistically significant differences were found when comparing the wall thickness and the length of the different models between day 3 and day 7, with the exception of the wall thickness of the collagen model ($p = 0.0074$). The significant differences in between the groups (per day) are indicted in Figure 5.2.

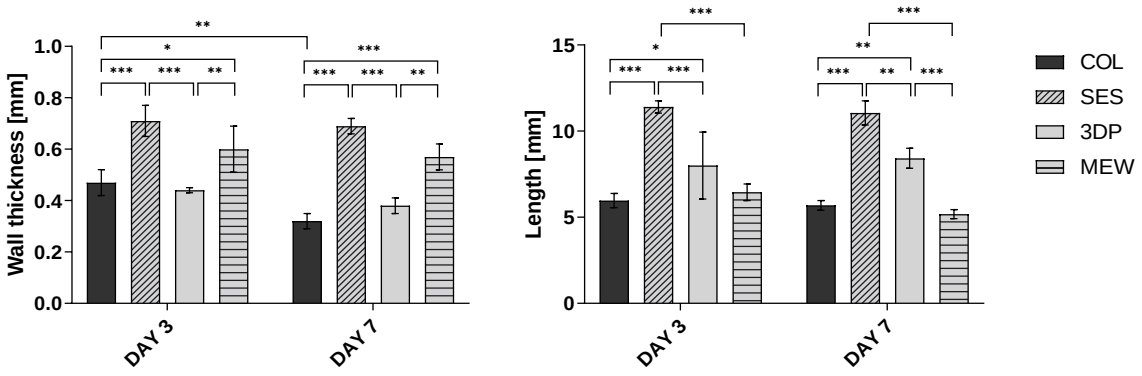

Figure 5.2. Compaction of the cellularized tubular gels without reinforcement (COL), and with the different types of reinforcement (SES, 3DP and MEW) at day 3 and day 7 of maturation. (A) Wall thickness of the tubular gel. (B) Length of the collagen gel. (= p ≤ 0.05; ** = p ≤ 0.01; *** = p ≤ 0.001).*

(b) Evaluation of visco-elastic properties

As shown by SEM imaging, the selected processing technique affects the developed scaffold's architecture on both the micro- and the macro level, thereby influencing the resulting mechanical properties. The effect of the reinforcement scaffold on the viscoelastic properties of the collagen-based model was evaluated by stress-relaxation testing. An example of the stress response of a collagen gel (COL, day 3) after five cycles of 10% deformation followed by 10 minutes relaxation is shown in Figure 5.3.A. The initial elastic modulus (E_0, Figure 5.3.B) corresponds to the data obtained right after the deformation, while the equilibrium elastic modulus (E_e, Figure 5.3.C) corresponds to data obtained just before a new deformation (i.e. at the end of the 10 minutes deformation) or cycle was initiated. Figure 5.3.D represents the ratio between E_e and E_0 and gives information on the predominance of the viscous or the elastic component. A higher ratio E_e / E_0 implies that the viscous component becomes less representative, and that there is a predominance of the elastic behavior [372].

No statistical differences were found when comparing E_e and E_0 of COL, 3DP and MEW ($p > 0.05$) on day 3 and day 7. For SES, a significant increase in elastic moduli was observed at day 7 ($p < 0.05$). The incorporation of a reinforcement scaffold (i.e. SES, 3DP or MEW) in the cellularized collagen-based model (COL) resulted in a significant increase in both E_0 and E_e, at both time points ($p < 0.05$). On day 3, the SES, 3DP and MEW reinforcement led to an equilibrium elastic modulus of 288.01 ± 37.81 kPa, 111.15 ± 28.27 kPa and 282.48 ± 89.68 kPa, respectively, compared to 7.23 ± 2.46 kPa for COL. This implies that the E_0 of SES and MEW is quite similar at day 3. However, at day 7, SES showed a higher E_0 than the MEW reinforcement, albeit not statistically significant. A similar trend was observed for E_e (Figure 5.3.C). On day 7, the developed collagen gels showed stresses (for strains between 20-55%) in the range of [5-10] kPa for COL, [80-350] kPa for SES, [20-70] kPa for 3DP and [100-190] kPa for MEW.

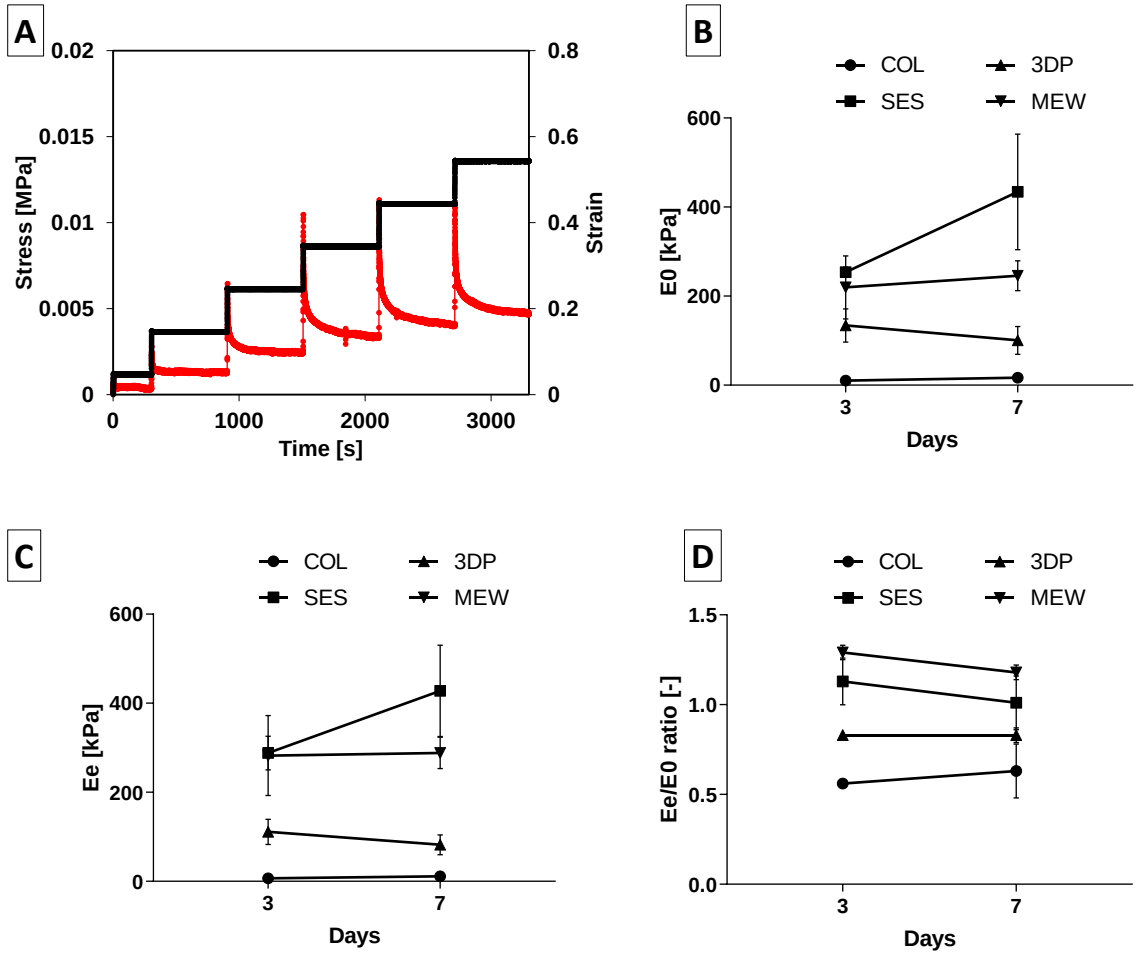

Figure 5.3. Mechanical evaluation of fibroblast-cellularized COL (reference), SES, 3DP and MEW reinforced collagen-based models (day 3 and day 7 of maturation). (A) Example of a stress-strain curve, obtained from stress-relaxation testing using Instron. Example represents a COL sample on day 3. (B) E0, initial (instantaneous) elastic modulus. (C) Ee, equilibrium elastic modulus. (D) Ratio of Ee / E0.

When considering the ratio of E_e and E_0 (at day 3), the highest ratio was found for MEW (1.29 ± 0.04), followed by SES (1.13 ± 0.13), 3DP (0.83 ± 0.02) and COL (0.56 ± 0.01). No significant differences were found when comparing values at day 3 or day 7 of the same group (i.e. COL, SES, 3DP, MEW). The ratio E_e / E_0 of the reinforced gels was significantly higher compared to the COL reference ($p < 0.05$) at both time points, with the exception of the 3DP reinforced gel at 7 days of maturation ($p > 0.05$). The predefined architecture of the MEW reinforcement scaffold, including the angle at which the fibers were aligned in relation to the longitudinal axis (winding angle of 70°) and the number of turning points of the scaffold (8 pivot points), enabled a flexibility and elasticity that neither the 3DP nor the SES tube showed. This already resulted in differences in gel compaction when comparing the MEW reinforced collagen gel with the 3DP and SES reinforced gels (Section 5.5.2.a), and was here confirmed by the high E_e / E_0 ratio, implying a predominantly elastic behavior.

These data highlight that, apart from material selection, also the selected processing technique has an important influence on the resulting mechanical properties of the developed tubular scaffold. The randomly deposited SES fibers showed the best mimicry compared to the native ECM, and also resulted in a significant increase of the elastic modulus compared to COL (reference). The collagen gel spread out over the full length of the SES

reinforcement tube. This implies that the less deformable structure of the randomly oriented SES fibers did not enable a change in the reinforcement tube's architecture (such as reduction in length) upon collagen compaction. A similar observation was seen for the 3DP reinforcement scaffold. Conversely, the MEW tube also showed a significant increase in elastic modulus compared to COL, but still enabled the HFDs to compact the collagen as they would do without the presence of a reinforcement scaffold (by "shrinking" upon collagen compaction). This is also thanks to the predominance of the elastic behavior in the MEW reinforcement tube, as was also shown by the E_e / E_0 ratio (Figure 5.3.D).

In literature, collagen-based models have already been described, referring to elastic moduli of maximum 30 kPa for a (non-reinforced) collagen-based model [370–372]. Different approaches have been evaluated in an attempt to increase the mechanical properties of collagen-based models, including increasing cell density [397] or addition of elastin-like recombinamers [372]. Camasao *et al.* [372] have reported a significant increase between initial and equilibrium elastic moduli of 40 and 50%, respectively for their developed elastin/collagen-based model (30% elastin) compared to the collagen-based model (reference). However, the initial elastic modulus E_0 did not exceed 30 versus 50 kPa after 3 and 7 days, respectively and the equilibrium elastic moduli E_e did not exceed 20 kPa after 7 days for any of the tested conditions. Compared to these results, the polymeric tubular reinforcements used herein greatly improved the mechanical properties of the collagen-based model with an E_0 of 382.05 ± 132.01 kPa, 100.59 ± 31.15 kPa and 245.78 ± 33.54 kPa, respectively for SES, 3DP and MEW at day 7 of maturation, respectively.

In the work of "Mc Donald's Blood Flow in Arteries", reported values on the pressure-strain elastic (Peterson) modulus (E_p) of human arteries range between [0.52-1.18] · 10^6 dynes·cm^{-2} or [52-118] kPa, depending on the type of artery and the age of the patient [78]. This can be translated into an incremental (~ Young's) elastic modulus by taken into account the diameter and the thickness of the blood vessel. As an example, for the abdominal aorta of a human aged 27 years old (diameter of 13.2 mm and thickness of 1.59 mm) [78], an E_p of 52 kPa corresponds to an incremental elastic modulus of 216 kPa.

In conclusion, the tubular, polymeric reinforcement scaffolds significantly improved the mechanical properties of the collagen-based model, reaching values closer to the mechanical properties of native arteries [78]. The three processing techniques have also resulted in different mechanical properties, which can be linked to differences in the scaffolds' architectures.

5.5.3 Biological performances

(a) Evaluation of cell viability

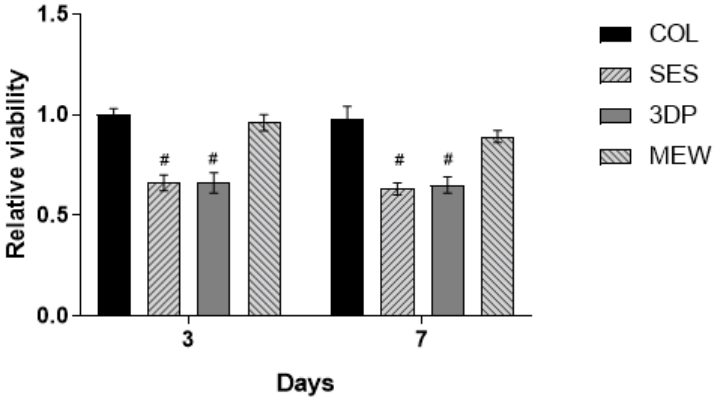

Figure 5.4. Relative viability based on a Resazurin assay at day 3 and day 7 on COL (reference), and on the reinforced collagen-based model using a SES, 3DP and MEW scaffold. (# = statistically significant difference at $p < 0.0001$ from the other groups in the same day)

HDFs metabolic activity was evaluated between groups at 3 and 7 days and the results were normalized towards the day 3 COL condition (as the non-reinforced collagen gel acts as reference in this study). The results (Figure 5.4) showed no significant difference in the cell metabolic function amongst the two time points irrespective of the processing technique applied. A significant decrease in cell metabolic function was found between the SES and 3DP conditions at both time points. However, no significant differences were observed between the COL control and the MEW condition, suggesting that cell viability was not affected by the presence of the MEW scaffold.

The lower metabolic activity observed in the SES and 3DP reinforced model, compared to COL and MEW, can be linked to the differences in materials' architecture (Section 5.5.1). The architecture of polymeric scaffolds, and more specifically, the scaffold properties such as fiber diameter and pore size, can greatly impact cell infiltration, - attachment, - proliferation and - differentiation [403]. Chen *et al.* [404] have demonstrated how the fiber diameter of electrospun PCL scaffolds can affect cell adhesion and proliferation. In their work, it was suggested that an increasing fiber diameter, from nanoscale to microscale, negatively impacts cell adhesion and growth kinetics of fibroblasts. This could explain why a significantly lower cell metabolic activity was observed for the SES condition, as the SES fibers of these scaffolds were situated within the microscale range (Section 5.5.1). Moreover, the tightly packed fibers seen in the SES scaffolds give rise to the small pores 8–37 µm (Section 5.5.1), which have been demonstrated to affect cell metabolic activity, i.e. decreasing it when compared to electrospun scaffolds with a lower fiber density and larger pore size (i.e. 44–64 µm) [405]. 3DP scaffolds showed the largest pore sizes (800 ± 100 µm in width; 1800 ± 110 µm in length, Section 5.5.1), which also seemed to negatively affect the fibroblasts' metabolic activity. It has already been suggested that fibroblasts exhibit a superior cell attachment and growth on scaffolds presenting pore sizes smaller than 160 - 200 µm [406]. Thus, the larger pores found in the 3DP tubes did not support cell attachment to the same extent as in the COL condition and led to a decreased cell viability. However, the pore size of the MEW scaffolds did not seem to affect HDFs' metabolic activity. This was possibly

due to the deformability of the MEW scaffold (Section 5.5.2.a), which allowed the MEW structure to be compressed and shrunk with the collagen upon its compaction, thereby changing the architecture and decreasing the pore size.

(b) Evaluation by immunofluorescent staining and histochemistry

The samples' cross-sections were stained to evaluate collagen thickness, cell distribution and alignment in the four different conditions at day 3 and day 7 via immunofluorescence and histochemistry. Figure 5.5 shows immunofluorescence staining of collagen (green), F-actin (red) and cell nuclei (blue), highlighting the differences in cell morphology between the conditions.

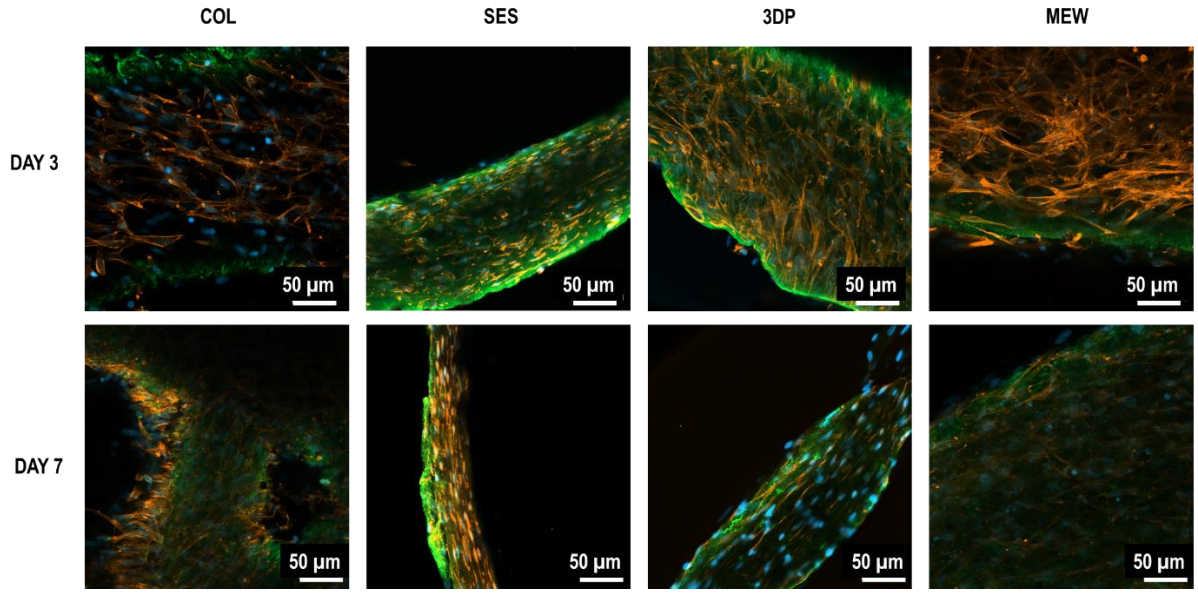

Figure 5.5. Immunofluorescence staining 2D images of fibroblast-celullarized tubular collagen-based gels, without (COL, reference) and with reinforcement (SES, 3DP and MEW) at day 3 and day 7 of maturation: Collagen I (green), F-actin (red), and cell nuclei (blue).

The 2D images of COL and MEW reinforced gels showed a thicker cross-section of the non-reinforced collagen gel (reference, COL), with HDFs being uniformly distributed within the gel. The SES and 3DP conditions showed thinner collagen gels with fewer cells. The 3D images (Supplementary Information, Figure S5.1) of COL and MEW reinforced gels showed that the cells were nicely distributed within the gel, forming a cellular network, with no significant differences between day 3 and day 7. Moreover, no particular cell alignment was displayed. The same was observed at day 3 in the 3DP samples. However, at day 7, the 3DP samples showed no cell network formation. The SES condition did not show a cellular network at any time point. Differences can also be observed in cell morphology, as HDFs in the COL and MEW conditions showed elongated actin, compared to the smaller and less extended actin cytoskeleton of HDFs in the SES and 3DP conditions. It would be interesting in a follow-up study, to evaluate the reinforced models in a SMC-cellularized collagen model in order to gain more insight in the dynamic interplay between the cellular properties and mechanobiology, which is more limited when using HDF.

Histological images (Figure 5.6) showed the cellularized collagen gel, its compaction and the cell distribution at day 3 and 7. The COL condition showed a thick gel at day 3, with a decrease in thickness by day 7, confirming the observations described in section 5.5.2.a regarding the gel compaction. For the SES condition, a very thin collagen gel was observed, lining the SES tube as an outer layer. The 3DP sample displayed the collagen gel filling the pores of the reinforcement scaffold's structure, surrounding the one single thick fiber (as indicated by the black arrows in Figure 5.6). A thicker collagen gel can be observed in the MEW condition, filling the structure completely.

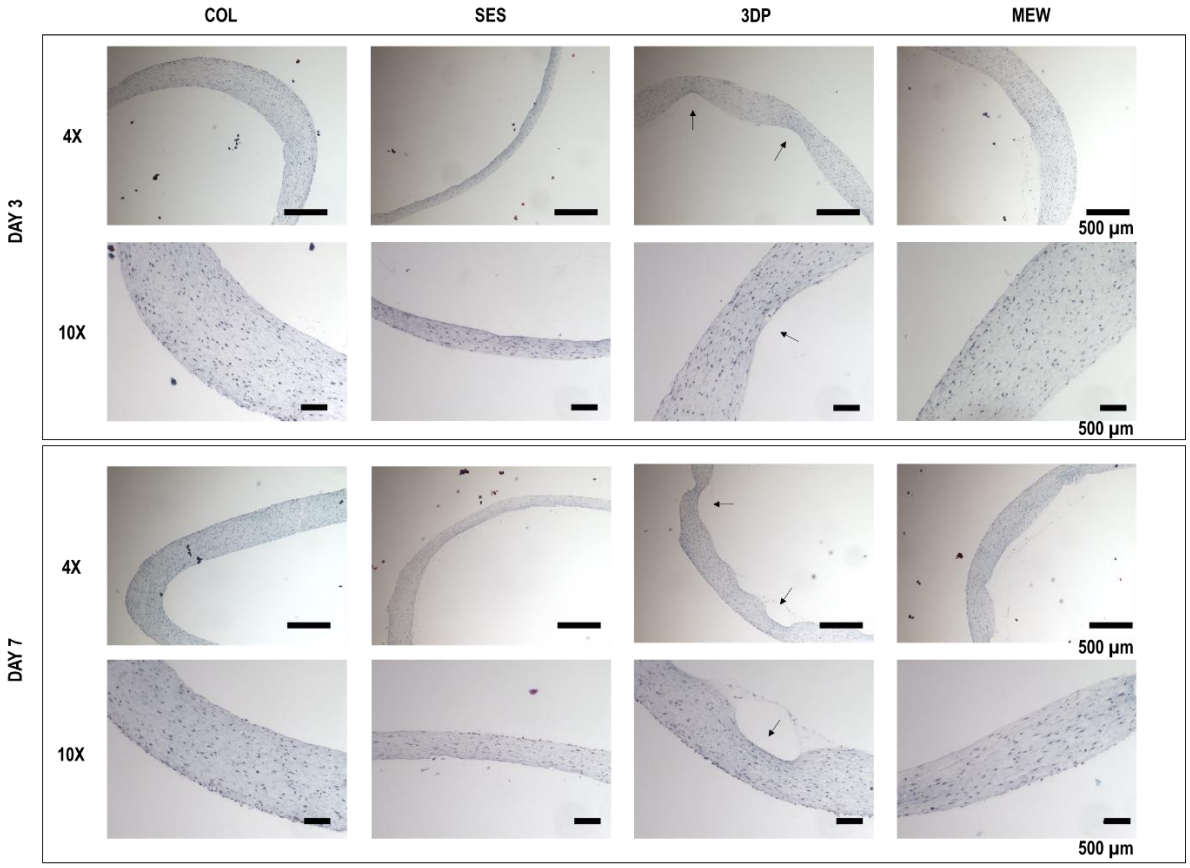

Figure 5.6. Histological analysis: Masson Trichrome staining of the fibroblast-cellularized tubular collagen-based gels, without (COL, reference) and with reinforcement (SES, 3DP and MEW) at day 3 and day 7 of maturation. The black arrows indicate the original location of the 3D printed scaffold. Scale bars represent 500 µm at 4X and 10X magnification.

With both imaging techniques, the similarities between the COL and the MEW conditions can be appreciated. Both showed a thick and highly cellularized collagen gel, supporting the hypothesis that the collagen gel's compaction nor the biological activity were impacted by the presence of the MEW reinforcement scaffold (Section 5.5.2.a and 5.3.3.a). In the SES condition, the small pores and dense structure (Section 5.5.1) did not allow the collagen and cells to penetrate, hence resulting in a sharp contrast between the reinforcement scaffold and the collagen gel. The 3DP scaffold showed to be even less deformable (Section 5.5.1 and 5.5.2.b), and the large pores that make up its structure were filled with the collagen gel, which resulted in a slender construct. Consequently, both SES and 3DP conditions showed thinner collagen gels, spread out in length throughout the scaffold. This difference in collagen gel thickness is hypothesized to be due to the architecture and lower deformability of these tubes, dictated by the different processing techniques. The collagen gel compaction is driven by the cells' contractile ability [407].

However, the architecture of SES and 3DP scaffolds led to a lower number of attached cells, which also resulted in decreased metabolic activity (Section 5.5.3.a) and different cell morphologies, finally affecting collagen gel compaction.

In conclusion, it is clear that the different processing techniques and tubes' architecture influenced the cell behavior, in terms of proliferation and attachment, as well as collagen gel compaction. Moreover, differences were also seen in the cells' morphology when comparing the conditions, varying from a dense network of randomly dispersed fibroblasts, with elongated actin cytoskeleton, within the thicker collagen gel of COL and MEW samples, to fewer fibroblasts presenting smaller cytoskeletons, which were found to be compressed together within the thinner collagen gel for the SES and 3DP conditions.

5.6 Conclusions

In this chapter, the aim was to improve a previously developed collagen-based vascular wall model by reinforcing this model using a tubular polymeric scaffold in PCL. Three different processing techniques were compared (i.e. SES, 3DP and MEW), and benchmarked against the non-reinforced collagen-based model (COL). As shown by SEM imaging, the selected processing technique affects the developed scaffold's architecture on micro- and macro-level. In turn, the scaffold's architecture (fiber diameter, fiber alignment, pore size) has shown to influence the resulting mechanical and biological properties of the collagen-based model. The tubular, polymeric reinforcements significantly improved the mechanical properties of the reinforced collagen-based model (i.e. initial elastic moduli of 382.05 ± 132.01 kPa, 100.59 ± 31.15 kPa and 245.78 ± 33.54 kPa, respectively for SES, 3DP and MEW at day 7 of maturation) compared to the non-reinforced collagen-based model (i.e. 16.63 ± 5.69 kPa). A difference in viscous to elastic behavior was also observed, showing the highest predominance in elastic behavior for the MEW reinforced model (E_0/ E_e ratio of 1.29 ± 0.04). Moreover, the different processing techniques and polymeric tubes' architecture influenced the cell behavior, in terms of proliferation and attachment, along with collagen gel compaction. A dense network of fibroblasts randomly dispersed within the thick collagen matrix was found in COL and MEW samples, to fewer fibroblasts presenting smaller cytoskeletons, which were found to be compressed together in the thinner collagen gel for the SES and 3DP conditions. Overall, it can be concluded that (i) the selected processing technique strongly influences the resulting mechanical and biological properties, and (ii) the incorporation of a polymeric reinforcement leads to mechanical properties more closely resembling those of the native arteries. In a follow-up study, it would be interesting to evaluate the effect of the reinforcement scaffold on a co-culture (i.e. endothelial cells, smooth muscle cells and fibroblasts, mimicking the three layers of the vascular wall) collagen-based model under dynamic maturation.

Chapter 6: Design and development of photo-crosslinkable biopolymers with tuneable mechanical properties

This chapter describes the methacrylamide modification of collagen bovine skin. The amino acid composition analysis was performed in collaboration with M. Vansteenland, under the supervision of Prof. B. De Meulenaer (Department of Food Safety and Food Quality, UGent). The *in vitro* assays were conducted by N. Pien during a research stay at the LBB lab (ULaval, Canada), under the supervision of Dr. D. Pezzoli. This chapter has been published as:

N. Pien, D. Pezzoli, J. Van Hoorick, F. Copes, M. Vansteenland, M. Albu, B. De Meulenaer, D. Mantovani, S. Van Vlierberghe, P. Dubruel. Development of photo-crosslinkable collagen hydrogel building blocks for vascular tissue engineering applications: a superior alternative to methacrylated gelatin? Materials Science and Engineering: C, Volume 130, 112460, DOI: 10.1016/j.msec.2021.112460, Published: OCT 2021, Impact Factor: 7.328. Peer reviewed.

6.1 Résumé

Le présent chapitre décrit le développement de précurseurs d'hydrogels à base de collagène, fonctionnalisés avec des fragments de méthacrylamide photoréticulables (COL-MA), pour des applications d'ingénierie tissulaire vasculaire (vTE). Les matériaux développés ont été caractérisés physico-chimiquement en termes de cinétique de réticulation, de degré de modification/conversion, de comportement de gonflement, de propriétés mécaniques et de cytocompatibilité *in vitro*. Les dérivés du collagène ont été comparés à la gélatine modifiée par le méthacrylamide (GEL-MA), en raison de ses antécédents dans le domaine de l'ingénierie tissulaire.

6.2 Abstract

The present chapter describes the development of collagen-based hydrogel precursors, functionalized with photo-crosslinkable methacrylamide moieties (COL-MA), for vascular tissue engineering (vTE) applications. The developed materials were physico-chemically characterized in terms of crosslinking kinetics, degree of modification/conversion, swelling behavior, mechanical properties and *in vitro* cytocompatibility. The collagen derivatives were benchmarked to methacrylamide-modified gelatin (GEL-MA), due to its proven track record in the field of tissue engineering. To the best of our knowledge, this is the first research in its kind comparing these two methacrylated biopolymers for vTE applications. For both gelatin and collagen, two derivatives with varying degrees of substitutions (DS) were developed by altering the added amount of methacrylic anhydride (MeAnH). This led to photo-crosslinkable derivatives with a DS of 74 and 96% for collagen, and a DS of 73 and 99% for gelatin. The developed derivatives showed high gel fractions (i.e. 74% and 84%, for the gelatin derivatives; 87 and 83%, for the collagen derivatives) and an excellent crosslinking efficiency. Furthermore, the results indicated that the functionalization of collagen led to hydrogels with tunable mechanical properties (i.e. storage moduli of [4.8 – 9.4 kPa] for the developed COL-MAs versus [3.9 – 8.4 kPa] for the developed GEL-MAs) along with superior cell-biomaterial interactions when compared to GEL-MA. Moreover, the developed photo-crosslinkable collagens showed superior mechanical properties compared to extracted native collagen. Therefore, the developed photo-crosslinkable collagens demonstrate great potential as biomaterials for vTE applications.

6.3 Introduction

Cardiovascular diseases (CVDs) are the leading cause of mortality worldwide, being responsible for over 17.9 million deaths annually [2]. An increasing number of people suffer from coronary artery diseases while the number of coronary interventions is predicted to increase considerably owing to the rapid growth of the elderly population [2,90,408]. The treatments for CVDs vary according to the affected body part and the medical history of the patient. Specific examples include coronary artery bypass grafting (CABG) or major arterial reconstruction procedures with autogenous, allogenic or synthetic materials [62]. Given the limitations in available and suitable allogenic or autologous vascular grafts (i.e. due to the lack of tissue donors, previous harvesting or anatomical variability) and the higher complication rate associated with synthetic materials (i.e. due to rejection, compliance mismatch), the search for a truly ideal conduit continues [62–65]. In this context, tissue engineering (TE) and biomaterial design have gained increasing interest with the final aim to repair, replace or regenerate injured tissues based on the development of scaffold structures that are able to (temporary) replace the natural extracellular matrix (ECM) until the host cells can (re)generate a new natural matrix [66].

In this respect, a wide variety of natural polymers have been proposed to date [11,133,152,409]. Generally, natural polymers are highly recognized biomaterials because they are accepted and easily integrated within the human body upon implantation. However, they present limited processability and often lack mechanical strength [410,411]. Nevertheless, promising work has been performed on natural polymers and ECM components (i.e. gelatin, collagen) for producing biomimetic scaffolds for TE and regenerative medicine (RM) applications [174]. Gelatin and its derivatives have been used as biomaterials because of their biocompatibility and excellent cell-interactive properties, due to the presence of Arginine-Glycine-Aspartic acid (Arg-Gly-Asp) (RGD) tripeptides in the protein structure [209,412]. The RGD motif is known for its cell adhesion properties as the cell surface integrins can interact with it. Collagen is one of the main components of the ECM of blood vessels making it a very interesting protein for vascular TE applications [181,401,413]. Beneficial properties of collagen include its low antigenicity, its excellent biocompatibility and the fact that a collagen network can be remodeled by vascular cells [63,191,192]. One of the most important challenges associated with using (extracted) natural polymers in vascular TE however remains their inferior mechanical strength (because of the high pressures and stresses encountered in blood vessels) [181,414–417]. Human coronary arteries have a compliance of 4.5 - 6.2% change in diameter for a pressure increase from 80 to 120 mmHg, a burst pressure of 2031 - 4225 mmHg, a maximum stress of 1.44 ± 0.87 MPa, a maximum strain of 0.54 ± 0.25 and a physiological elastic modulus of 1.48 ± 0.87 MPa [64,73–79]. However, it should be noted that these characteristics depend on the applied mechanical testing set-up and protocols. Therefore, some variation on data can be found in literature. The extracted collagen that is used in vascular TE applications shows insufficient mechanical properties, mainly regarding elasticity and also shows a poor burst pressure of 18 ± 1 mmHg [373]. Therefore, crosslinking of these biopolymers is indispensable in order to maintain the structural integrity of vascular tissue engineered scaffolds, especially upon hydration [415]. Various crosslinking methods (e.g. carbodiimide crosslinking, enzymatic crosslinking, photo-oxidation, etc.) [209] have

already been established, however, these often result in undesirable toxicity issues [181,411,418,419] or long reaction times (i.e. minutes to hours) [209,420].

Photo-crosslinking of methacrylamide functionalities is an interesting approach to provide the structural integrity to the natural scaffolds without the need of additional potentially toxic crosslinking agents (e.g. glutaraldehyde, formaldehyde and epoxy compounds) [415]. Furthermore, this approach enables a straightforward material handling, consisting of material dissolution and subsequent crosslinking via ultraviolet (UV)-irradiation [209]. To this extent, photo-crosslinkable moieties (i.e. (meth)acrylamide functionalities) have to be introduced onto some of the biopolymer side groups, more specifically the primary amines including (hydroxy)lysine. The crosslinking reaction occurs via UV irradiation in the presence of a suitable photo-initiator which leads to the polymerization of the introduced methacrylamides following a chain growth polymerization mechanism resulting in the formation of oligomethacrylamide kinetic chains, thereby resulting in a crosslinked network [209].

In the present chapter, the potential of photo-crosslinkable moieties incorporated on the side groups of bovine skin collagen was investigated. Methacrylamide-modified collagen (COL-MA) has not yet been evaluated in depth in terms of its physico-chemical properties in the field of vTE. In this study, the developed collagen derivatives have been benchmarked to methacrylamide-modified gelatin (GEL-MA), one of the gold standards in different biofabrication and tissue engineering and regenerative medicine (TERM) applications [209,395,421–423]. To the best of our knowledge, a comparative study of this type is unprecedented.

In brief, bovine skin gelatin and collagen have been functionalized with methacrylamide functionalities via the reaction of the primary amines with methacrylic anhydride. We hypothesize that the mechanical properties of the developed photo-crosslinkable materials can be tuned by varying the degree of substitution (i.e. 70 – 100% of the total amount of primary amines present in the gelatin/collagen protein structure) [412,421,423]. In addition, since gelatin is a denatured protein [209] derived from collagen, we anticipate that the functionalized collagen derivatives outperform currently reported gelatin derivatives [174,424] in terms of both the mechanical and the biological properties.

Therefore, the aim of the present study was to develop a cyto-compatible, photo-crosslinkable collagen hydrogel building block with tunable mechanical properties that can be used as an ECM-mimic for biomedical applications, and more specifically, to serve vTE applications.

6.4 Materials and Methods

6.4.1 Materials

Collagen type I, extracted from bovine skin, was kindly supplied by the Department of Collagen Research (National Research & Development Institute for Textiles and Leather, Romania). Gelatin type B, isolated from bovine hides via an alkaline process, was kindly supplied by Rousselot (Ghent, Belgium). Methacrylic anhydride (MeAnH), 2-mercaptoethanol, ortho-phthalic dialdehyde (OPA), sodium hydroxide (NaOH) and potassium chloride (KCl) were obtained from Sigma-Aldrich (Diegem, Belgium). Potassium phosphate monobasic (KH_2PO_4) and sodium phosphate dibasic (Na_2HPO_4) were obtained from Acros Organics (Geel, Belgium). All ^{1}H-NMR spectra were recorded in deuterium oxide (D_2O) obtained from Euriso-top (Saint-Aubin Cedex, France). Spectra/Por7 dialysis membranes (Molecular weight cut-off (MWCO) of 12,000-14,000 Da) were obtained from Polylab (Antwerp, Belgium). SpeedCure TPO-L (ethyl (2,4,6-trimethylbenzoyl) phenyl phosphinate) was purchased from Lambson (West Yorkshire, UK). The photoinitiator lithium(2,4,6-trimethylbenzoyl)phenylphosphinate (Li-TPO) was prepared according to the protocol reported by Markovic *et al.* [425].

Human umbilical vein endothelial cells (HUVECs) were isolated from human umbilical cord samples, as previously reported [109]. The cells were cultured with 5% CO_2 at 37°C in serum-free phenol red-free Dulbecco's Modified Eagle's Medium (DMEM, Gibco), supplemented with 1% Penicillin/Streptomycin (PenStrep) (G1146 Sigma), 5% Fetal Bovine Serum (FBS, Life Technologies, 12483-020), 2 ng·mL^{-1} basic Fibroblast Growth Factor (0.1%) (FGFb, Gibco), 0.5 ng·mL^{-1} Epidermal Growth Factor (0.2%) (EGF, Invitrogen, Life Technologies), 1 µg·mL^{-1} L-ascorbic acid (0.1%) (Sigma, St Louis, MO, USA), 1 µg·mL^{-1} hydrocortisone (0.1%) and 90 µg·mL^{-1} porcine heparin sodium salt (1%) (Grade I-A, Sigma). This complete medium is hereafter referred to as DMEM+. Serum-free phenol red-free DMEM (Gibco), supplemented with 1% Penicillin/Streptomycin (PenStrep, Gibco 15140-122), 1% Sodium Pyruvate (Gibco 11360-070) and 1% Glutamine (Sigma G7513) was used for cell viability tests and is referred as sDMEM.

6.4.2 Amino acid analysis of biopolymers

The amino acid (AA) composition of the biopolymers was analyzed as described by Kerkaert *et al.* [426]. In brief, proteins were first hydrolyzed to their amino acids (6 N HCl, 12 h, 105°C). Subsequently they were automatically derivatized with respectively 9-fluorenylmethylchloroformate (FMOC) (for proline and hydroxyproline) and ortho-phthalic dialdehyde (OPA) (all the other amino acids) just before injection and separation on HPLC (Agilent ZORBAX Eclipse plus C18 P.N. 959963-902 and pre-column P.N. 820950-936) followed by fluorometric detection. Due to the acid hydrolysis, some amino acids (i.e. tryptophan and cysteine) are lost and cannot be detected in the amino acid analysis and were thus not reported. Aspartate and asparagine are converted during the procedure to aspartic acid. Glutamate and glutamine are converted during the procedure to glutamic acid. All samples were analyzed in duplicate. The results were reported as an average of both analyses.

6.4.3 Functionalization of biopolymers

The methacrylation of bovine skin gelatin (GEL BS) and bovine skin collagen (COL BS) was performed according to the protocol of Van Den Bulcke *et al.* [421]. In brief, methacrylated gelatin (GEL-MA) and methacrylated collagen (COL-MA) were prepared by reaction of the primary amines with MeAnH (Figure 6.1).

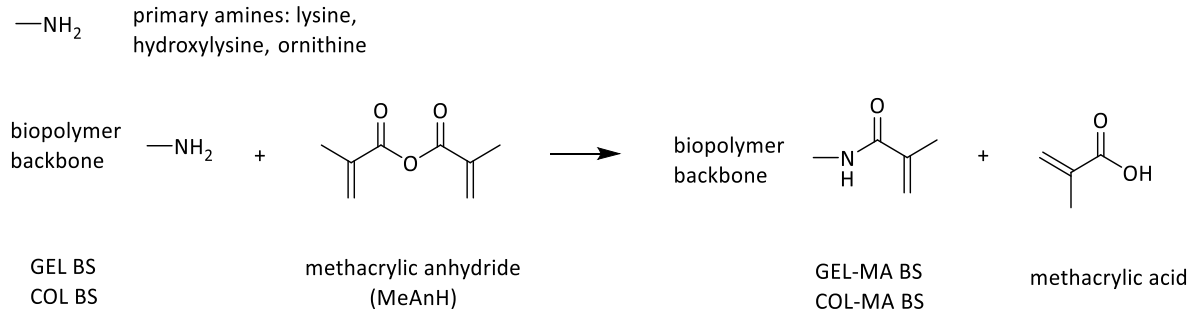

Figure 6.1. Synthesis of methacrylamide-modified gelatin and methacrylamide-modified collagen.

First, the biopolymer (10 w/v%) was dissolved in phosphate buffer solution (PBS) (0.2 M, pH = 7.8) at 37°C. Next, 0.5, 1 or 2.5 equivalents (EQ) of MeAnH with respect to the primary amines were added followed by stirring for 1 hour. The number of primary amines can be determined using amino acid (AA) analysis or through an ortho-phthalic dialdehyde assay (OPA), as described in sections 6.4.2 and 6.4.5 respectively. Next, the reaction mixture was dialyzed (MWCO 12-14 kDa) against distilled water (37°C, 24 h), followed by freeze-drying for 24 h (Christ Freeze-dryer alpha I-5). For both gelatin and collagen, a higher and a lower amount of MeAnH was added in order to aim at a target degree of substitution (DS) of 70% and 100%, respectively (for the determination of the DS, see 6.2.4 and 6.2.5). An overview of the developed gelatin and collagen derivatives can be found in Table 6.1.

Table 6.1. Overview of the four functionalized bovine skin gelatin- and collagen-based materials used in this study, the added equivalents of methacrylic anhydride (with respect to the primary amines), and their corresponding code after modification.

Material	Equivalents MeAnH	Code after modification
Bovine skin gelatin	1	GEL-MA BS 1 EQ
Bovine skin gelatin	2.5	GEL-MA BS 2.5 EQ
Bovine skin collagen	0.5	COL-MA BS 0.5 EQ
Bovine skin collagen	1	COL-MA BS 1 EQ

6.4.4 ^{1}H-NMR spectroscopy and ortho-phthalic dialdehyde (OPA) assay

The degrees of substitution for the gelatin and collagen derivatives were quantified via proton nuclear magnetic resonance (^{1}H-NMR) spectroscopy (Bruker WH 500 MHz) using D_2O as solvent at elevated temperature (40°C). The calculation of the DS was performed following the procedure as described earlier by Van Vlierberghe *et al.* [262] and based on the amino acid composition as determined by the analysis as described higher.

An OPA assay was also applied as a quantitative tool to evaluate the functionalization degree of the natural polymers. To this end, 20 mg of OPA was dissolved in 10 mL ethanol. Next, the mixture was diluted to 50 mL with

double distilled water (deionized water). A second stock solution containing 25 µL 2-mercaptoethanol in 50 mL borate buffer (pH = 10) was prepared. For 50 µL of heated (T = 37°C) gelatin or collagen solution (1 g / 40 mL deionized water), 950 µL deionized water, 1500 µL 2-mercaptoethanol solution and 500 µL of the OPA stock solution were added subsequently, followed by vigorously mixing. Finally, the absorbance at 335 nm was measured compared to a blank (i.e. mixture with deionized water instead of gelatin/collagen) at 37°C. All measurements were performed in triplicate.

Analogous measurements were performed with n-butylamine (0.002 M to 0.01 M) standards to obtain a calibration curve. Calculation of the amount of unreacted amine groups, remaining after the modification, enabled the determination of the degree of substitution.

6.4.5 Physical gelation study via differential scanning calorimetry (DSC)

For the DSC analysis, hydrogel building block solutions (10 w/v% in distilled water, 50 mg each dissolved at 37°C in 500 µL) were placed into a hermetic T_{zero} pan with a T_{zero} hermetic lid (TA Instruments, Zellik, Belgium). As a reference, an empty hermetic T_{zero} pan was applied. All measurements were performed on a TA Instruments Q 2000 with an RSC 500 cooler (Zellik, Belgium). The results were analyzed using Q series software.

The samples were subjected to a preparatory program as described earlier by Van Hoorick *et al.* [412]. First, a temperature ramp of 20°C·min^{-1} was applied to reach a temperature of 60°C. The sample was stabilized for 20 min. Next, a ramp of 1°C·min^{-1} was applied to cool the sample to a temperature of 5°C followed by stabilizing the samples at 5°C for 360 min. Then, a temperature ramp of 5°C·min^{-1} was applied until a temperature of 60°C was reached.

6.4.6 Photoinitiator (Lithium (2,4,6-trimethylbenzoyl)phenylphosphinate (LAP)) synthesis

The photoinitiator Li-TPO or LAP was synthesized according to a previously reported protocol [425]. Briefly, 8.60 g (27.2 mmol) of (2,4,6-trimethylbenzoyl)-phenyl-phosphinic acid ethyl ester (i.e. speedcure TPO-L by Lambson) was dissolved in 150 ml butanone followed by the addition of 9.45 g (109 mmol) lithium bromide. The mixture was allowed to react for 24 hours at 65°C under reflux conditions. The formed precipitate was isolated via filtration, washed with petroleum ether and dried under vacuum at room temperature.

6.4.7 Determination of mechanical properties via rheology

For rheological characterization a rheometer was used with a parallel plate geometry (Anton Paar Physica 501) with a top plate diameter of 25 mm. Hydrogel building block solutions (10 w/v%, 50 mg each in 500 µL) were prepared in deionized water. To monitor the crosslinking reaction, 300 µL of each solution containing 2 mol% Li-TPO, relative to the number of crosslinkable functionalities, was placed between the plates using a gap setting of 0.35 mm. The edges were trimmed and sealed using silicone grease (Bayer, mittelviskös, Sigma-Aldrich, Diegem,

Belgium) to prevent sample drying. An oscillation frequency of 1 Hz and a strain of 0.1% were applied as these values were within the linear viscoelastic range as determined by isothermal measurements (37°C) of the storage (G') and loss moduli (G") as a function of deformation at a constant frequency (1 Hz) and varying strain (0.01 – 10%). The solutions were irradiated at 37°C using UV-A light (10 min, EXFO Novacure 2000 UV light source at 365 nm using a fluence of 500 mW·cm^{-2}), followed by 2 min of post-curing monitoring in the absence of UV-A irradiation.

6.4.8 Photo-crosslinking of functionalized gelatin and collagen derivatives

The obtained gelatin (GEL-MA) and collagen (COL-MA) derivatives were dissolved in phosphate buffered saline (pH = 7.8) at 37°C to obtain a concentration of 10 w/v%. After complete dissolution, 2 mol% (relative to the amount of double bonds) of an 8 mg·mL^{-1} stock solution of Li-TPO in deionized water was added to the mixture followed by degassing for at least 30 s. Next, the heated solution was injected between two parallel glass plates covered with release foil and separated by a 1 mm thick silicone spacer. Finally, the hydrogel building block solution was irradiated from both sides with UV-A light (λ = 365 nm, 2 × 4 mW·cm^{-2}) for 30 min.

6.4.9 Determination of gel fraction, mass swelling ratio and crosslinking efficiency

The gel fraction was determined by freeze-drying films with a diameter of 0.8 cm immediately after crosslinking. Next, the dry mass of these films was determined ($m_{d,1}$), and the films were incubated in 20 mL deionized water at 37°C for 48 h to allow leaching of the sol fraction. After equilibrium swelling, the films were freeze-dried, and the dry mass was determined again ($m_{d,2}$). The gel fraction was determined by comparing the final dry mass to the original one resulting in the following equation (Equation 6.1):

$$\text{Gel fraction } [\%] = \frac{m_{d,2}}{m_{d,1}} \tag{6.1}$$

All measurements were performed in triplicate and the standard deviation was calculated.

The equilibrium swelling ratio was determined using films with a diameter of 0.8 cm punched from equilibrium swollen sheets. Before determining the swollen mass (m_s) of the films, the excess water on the surface was gently removed using tissue paper. Afterwards, the samples were freeze-dried to determine the dry mass (m_d).
The swelling ratio was then calculated using the following formula (Equation 6.2):

$$\text{Mass swelling ratio } [\text{Q}] = \frac{m_s}{m_d} \tag{6.2}$$

The crosslinking efficiency (CE) was assessed by high resolution magic angle spinning (HR-MAS) ^{1}H-NMR spectroscopy on a Bruker Avance II 700 spectrometer. The spectrometer contains a HR-MAS probe which was equipped with a ^{1}H, ^{13}C, ^{119}Sn and gradient channel. The spinning rate was set at 6 kHz. The freeze-dried samples were placed in a 4 mm zirconium oxide MAS rotor (50 µL). Next, 30 µL D_2O was added to let the samples swell.

Finally, the samples were homogenized prior to the measurement. A Teflon® coated cap was used to close the rotor. The crosslinking efficiency was calculated following the procedure as described earlier [427].

6.4.10 *In vitro* cytocompatibility study using human umbilical vein endothelial cells

Flat circular samples (D=0.86 cm, A=0.58 cm^2) were cut from equilibrium swollen hydrogel (i.e. GEL-MA BS 73%, GEL-MA BS 99%, COL-MA BS 74% and COL-MA BS 96%) in PBS in the presence of 1% PenStrep. Samples were placed in a 50 mL Falcon tube and incubated for 2 x 12 h in 70% EtOH for sterilization and thoroughly washed during 4 cycles of incubation in PBS+1% PenStrep for 24 h. The cytotoxicity and the cell adhesion on the GEL-MA and COL-MA films were assessed by indirect and direct cell assays.

Indirect Material Extraction Assay. Samples were placed in 24 well plates and incubated with 380 µL (0.33 $mL \cdot cm^{-2}$, considering the area of the two surfaces) of sDMEM for 1 day at 37°C in an incubator. Aliquots (100 µL) from culture medium (extracts) were collected and stored at 4°C. HUVECs were seeded in 96-well plates at a density of 20,000 $cells \cdot cm^{-2}$ in 100 µL of DMEM+. 24 hours after seeding, the culture medium was removed and 100 µL of the extracts was added and supplemented with 10 µL/well of 5% FBS, 2 $ng \cdot mL^{-1}$ of FGF, 1 $ng \cdot mL^{-1}$ of EGF, 1 $\mu g \cdot mL^{-1}$ of ascorbic acid, 1 $\mu g \cdot mL^{-1}$ of hydrocortisone and 90 $\mu g \cdot mL^{-1}$ of heparin. Cells were incubated at 37°C for 1 day. Cells cultured in DMEM+ for HUVEC, and seeded in a TCP, were used as controls (non-conditioned extraction medium supplemented with 10 µL of supplement). 1 day after incubation with the extracts, the medium was changed with 100 µL fresh DMEM+ containing 1X resazurin and cells were incubated for 4 hours at 37°C. The medium extracted from the 4 developed derivatives (i.e. GEL-MA BS 73%, GEL-MA BS 99%, COL-MA BS 74% and COL-MA BS 96%) was tested against non-conditioned extraction medium (as a control). The fluorescence of the medium was measured at λ_{Ex} = 545 nm, λ_{Em}= 590 nm using a SpectraMax i3x microplate reader (Molecular Devices, Sunnyvale CA, USA). The tests were performed in eight-fold.

Direct Cell Viability Test and Immunofluorescence Imaging. HUVECs were seeded on samples of the 4 developed derivatives (i.e. GEL-MA BS 73%, GEL-MA BS 99%, COL-MA BS 74% and COL-MA BS 96%) at a density of 15,000 $cells \cdot cm^{-2}$ in 400 µL complete DMEM+. Next, the cells were incubated at 37°C. For the direct cell viability assay, each time point had 4 replicates, and 2 replicates were used at each time point for immunofluorescence imaging.

A resazurin assay was performed at 1, 3 and 7 days after seeding to evaluate cell viability (200 µL of 1X resazurin solution in phenol red-free complete medium, incubation for 5 hours). Non-seeded samples were used as controls by incubating them with the fresh resazurin solution (negative control) and with resazurin solution already processed by cells (positive control). The fluorescence of the medium was measured at λ_{Ex} = 545 nm, λ_{Em}= 590 nm using a SpectraMax i3x microplate reader (Molecular Devices, Sunnyvale CA, USA). In addition to the cell

viability, the relative cell growth rate (RGR) was determined. The RGR was assessed by using the formula reported earlier by Nonkumwong *et al.* [428] with FU defined as the mean fluorescence unit.

$$relative\ cell\ growth\ rate\ (RGR) = \frac{FU_{test\ sample}}{FU_{negative\ control}} \tag{6.3}$$

At day 1, 3 and 7, after the resazurin test, two samples per material type were moved to another plate, washed once in 1 mL PBS and then fixed by 3.7% formaldehyde (0.5 mL) for 30 minutes at r.t. Then, formaldehyde was removed, and PBS was added. 24 hours later PBS was refreshed (1 mL).

After 1, 3, or 7 days of culture, the constructs were washed twice with PBS, fixed with 3.7% formaldehyde (Sigma) for 20 min, and treated with 0.5% Triton X-100 in PBS for 30 min at r.t. to permeabilize the cells. Thereafter, the constructs were incubated with mouse monoclonal antibodies against VE-cadherin (Abcam, Ab7047, dilution 1:50) for 1 h at r.t., washed twice with 0.05% Tween 20 in PBS, and finally incubated at r.t. for 1 h with the anti-mouse Alexa Fluor 488 antibody (Life Technologies). Rhodamine-phalloidin (Sigma, 1:200) and 4',6-diamidino-2-phenylindole (DAPI, 1:3000, Thermo Fischer Scientific) were used to stain F-actin and nuclei, respectively. Images were obtained using an Olympus BX51 fluorescence microscope and an LSM 700 confocal laser scanning microscope (Zeiss) controlled by ZEN 2009 software for image acquisition and further analysis. The cytoskeleton area (n = 12) was calculated using ImageJ software.

6.4.11 Statistical analysis

All data were analyzed using GraphPad Prism 8.0.2. An ordinary one-way ANOVA test was performed followed by a Tukey post-test. The symbols representing the different significant levels are indicated on the graphs (i.e. ns = $p > 0.05$; * = $p \leq 0.05$; ** = $p \leq 0.01$; *** = $p \leq 0.001$).

6.5 Results and discussion

In this chapter, the aim was to develop a photo-crosslinkable collagen-based hydrogel precursor for vascular TE applications that combines a better match with the mechanical properties of human arteries, while maintaining the intrinsic cell-interactive properties.

Several strategies exist to make natural (bio)polymers photo-crosslinkable. One of the most reported strategies in various TE and biofabrication applications is the modification of gelatin with methacrylamides [209,395,411,412,424,429]. The introduction of photo-crosslinkable groups (i.e. methacrylamide functionalities) onto gelatin via the reaction of the primary amines with methacrylic anhydride has successfully enabled the development of a crosslinkable gelatin derivative with superior mechanical (i.e. elastic modulus) and tunable physico-chemical properties (i.e. swelling properties, gel fraction) compared to unmodified gelatin [209,421,424].

In an attempt increasing the mechanical strength of collagen for TE purposes, research on the functionalization of collagen using methacrylic anhydride [369,430], 4-vinylbenzylchloride [416], glycidyl methacrylate [416], unsaturated cyclic anhydrides [431], along with strategies to introduce thiols was performed to date [181,432]. Because research on the functionalization of collagen with methacrylamides is however scarce (to the best of our knowledge non-existing for vTE applications), and due to the structural similarity of gelatin to collagen, a similar strategy was pursued for the functionalization of collagen, while GEL-MA was applied as a benchmark throughout this chapter. The physico-chemical and the biological properties of the developed photo-crosslinkable derivatives were studied in order to evaluate if the developed COL-MAs could be used as a superior alternative biomaterial for vTE applications compared to GEL-MA, the gold standard in various biofabrication and TE applications.

6.5.1 Functionalization of gelatin and collagen

In a first step, the amino acid composition of the applied proteins was analyzed. This enables the exact calculation of the number of primary amines prone to functionalization, required to determine the reaction conditions (e.g. equivalents of MeAnH). The results are summarized in Table S6.1.

The amino acid composition is dominated by glycine and proline, confirming literature reports [433,434]. This is intuitive as proline and hydroxyproline are responsible for the characteristic triple helix formation [209]. Ornithine, obtained through alkaline hydrolysis of arginine, is only present in gelatin type B as consequence of the alkaline isolation strategy. As a result, the applied collagen in this study possesses a lower number of primary amine groups available for the introduction of photo-crosslinkable moieties as compared to gelatin (i.e. 0.248 $mmol \cdot g^{-1}$ bovine skin collagen vs 0.304 $mmol \cdot g^{-1}$ bovine skin gelatin).

Based on the amino acid composition analysis, both bovine skin gelatin and bovine skin collagen were modified with methacrylamide functionalities via the modification of the primary amines present in the side chains of (hydroxy)lysine in collagen, and (hydroxy)lysine and ornithine in gelatin. These primary amines were reacted with MeAnH to introduce crosslinkable functionalities. The photo-crosslinkable groups enable the subsequent crosslinking in the presence of a suitable photo-initiator (i.e. Li-TPO or LAP) upon applying UV irradiation.

The number of primary amines available prior and after functionalization was determined using an OPA amine detection assay. This assay enables the determination of the amount of introduced crosslinkable groups (i.e. the so-called degree of substitution, DS) (Figure 6.2).

For both gelatin and collagen, derivatives with a lower (estimated to 70%) and a higher (estimated to 100%) DS were developed. Development of a derivative with a full substitution of the primary amines (DS 100%) was selected to evaluate the upper limit of functionalization, whereas a derivative with a significantly lower DS (DS 70%) would allow to evaluate the effect of the differences in DS on both the biological and the mechanical properties, and at

the same time still enable sufficient superior mechanical properties compared to extracted, non-functionalized collagen (i.e. a storage modulus of 1070 - 3333 Pa reported in literature) [412,431]. The number of introduced photo-crosslinkable functionalities onto collagen was lower in comparison to gelatin upon functionalization using 1 eq MeAnH (i.e. 0.242 mmol·g^{-1} for a DS of 96% for COL-MA BS 1 EQ vs 0.276 mmol·g^{-1} for a DS of 73% for GEL-MA 1 EQ). We anticipate that the observed differences can be attributed to differences in the location of the primary amine functions in both biopolymers. At present, we are investigating these phenomena through modeling approaches. Furthermore, the degree of substitution for both gelatin and collagen was found to be proportional to the added amount of MeAnH (i.e. the more eq MeAnH added, the higher the DS), as shown in Figure 6.2. These data correspond to literature reports [422].

Next to the OPA assay, the DS of the developed crosslinkable biopolymers was also determined using ^{1}H-NMR spectroscopy. In addition to enabling an efficient way of calculating the DS, ^{1}H-NMR spectroscopy also enables the exact chemical identification of the introduced photo-crosslinkable groups and proves that these are methacrylamide groups. The ^{1}H-NMR spectra of the modified proteins showed characteristic peaks at 5.75 and 5.55 ppm which correspond to the vinyl protons of the introduced methacrylamides (Supplementary information, Figure S6.1). Because the exact amino acid composition of gelatin and collagen is known, the protocol established by Van Vlierberghe *et al.* [262] to calculate the DS of methacrylated gelatin can thus be extended to collagen. Following this protocol, the DS was quantified by comparing the integration of these characteristic peaks (i.e. 5.75 and 5.55 ppm) to the integration of the methyl protons present in Val, Leu and Ile, (i.e. at 1.01 ppm) which are inert during modification [429].

For GEL-MA, applying 1 and 2.5 equivalents MeAnH with respect to the primary amines of the lysine, hydroxylysine and ornithine moieties resulted in a DS of 70% (0.213 mmol·g^{-1} gelatin) and 92% (0.280 mmol·g^{-1} gelatin) respectively. These NMR results were in line with previously reported results [412,435]. Importantly, the results agreed with those obtained via the OPA assay (i.e. 73% and 99%, respectively).

Optimization of the bovine skin collagen functionalization was performed by addition of 0.5, 1 and 2.5 equivalents MeAnH with respect to the primary amines of lysine. The functionalization of bovine skin collagen with 0.5 and 1 equivalents MeAnH with respect to the primary amines resulted in DS of 76% (0.188 mmol·g^{-1} BS collagen) and 100% (0.247 mmol·g^{-1} BS collagen), respectively. Because a DS of approx. 100% was already obtained by using 1 equivalent of MeAnH for the collagen derivatives, higher equivalents of MeAnH were omitted from further analysis. Like gelatin, the DS obtained for the COL-MA derivatives using ^{1}H-NMR spectroscopy were in line with the DS observed using OPA (i.e. 74% and 96% for COL-MA 0.5 and 1 EQ, respectively).

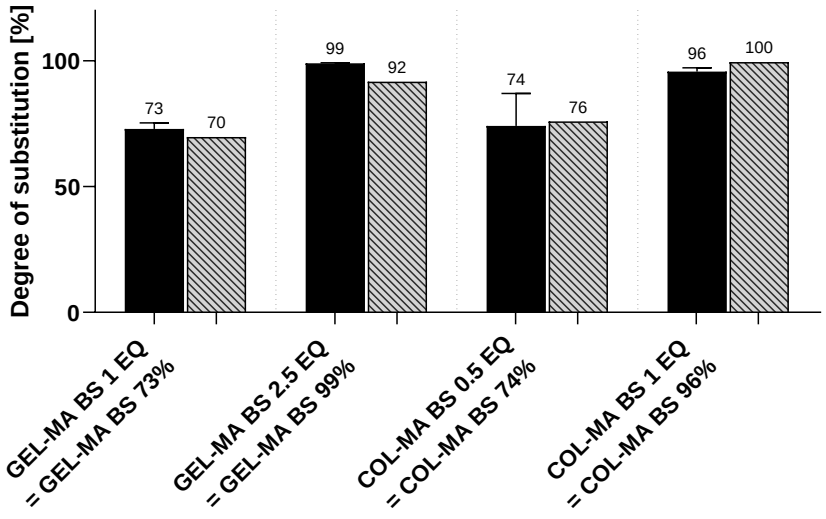

Figure 6.2. Degree of substitution of functionalized gelatin and collagen derivatives determined by OPA analysis (full bars) and 1H-NMR spectroscopy (dashed bars, one measurement was performed). The nomenclature for the developed materials will be based on type of material and their corresponding degree of substitution (i.e. GEL-MA BS 73%, GEL-MA BS 99%, COL-MA BS 74% and COL-MA BS 96%) and will be used as such in upcoming paragraphs.

Throughout the remaining part of this chapter, the developed photo-crosslinkable precursors will be referred to using their DS (as determined by OPA), as indicated in Figure 6.2.

6.5.2 Physical gelation study via differential scanning calorimetry (DSC)

Both collagen and gelatin are characterized by a dissociation temperature (T_d). Below this temperature, the materials form a hydrogel due to triple helix formation whereas a solution is obtained at elevated temperatures [209,436,437]. From literature, it is known that several factors including the molar mass, the hydrophilicity/hydrophobicity balance and the number of introduced photo-crosslinkable moieties can influence the thermo-responsive behavior of a material [421]. Therefore, DSC experiments were performed to evaluate the thermal characteristics of the developed gelatin and collagen derivatives. Upon heating above the T_d, the dissociation of collagen and gelatin is initiated with the separation of the alpha chains followed by the rupture of the inter-chain hydrogen bonds between the crystalline triple helices resulting in the formation of random coils [431,438].

The method applied was adapted from a previously reported protocol [412]. However, due to the added complexity of the physical interactions present in collagen and the lower chain mobility due to covalent interactions (i.e. disulfide bonds) [438], collagen is characterized by a longer gelation time in comparison to gelatin. As shown in Figure S6.2, the optimization of the gelation time (t = 1, 3, 6, 9 and 12 h) indicated a plateau for the obtained enthalpy values was reached at a gelation time of 6 h or 360 min. Therefore, this gelation time was selected for the DSC measurements in order to enable sufficient collagen restructuring.

Previous literature reports have shown that the dissociation enthalpy (i.e. the enthalpy corresponding to the endothermal peak at T_d) is proportional to the number of hydrogen bonds, which are responsible for the triple helix formation [412,435]. This statement is confirmed when comparing the dissociation enthalpy of the COL BS applied in our study (i.e. 2.031 $J \cdot g^{-1}$) to the value for its gelatin counterpart (i.e. 1.457 $J \cdot g^{-1}$). The observed difference can be ascribed to gelatin being denatured collagen [209,439].

Upon gelatin functionalization, the dissociation enthalpy for bovine skin gelatin was found to be 1.416 $J \cdot g^{-1}$ and 1.398 $J \cdot g^{-1}$ for GEL-MA BS 73% and GEL-MA BS 99% respectively. The results indicated that GEL-MA BS 73% showed a 2.8% decrease in number of hydrogen bonds, whereas GEL-MA BS 99% showed a 4.1% decrease due to the introduction of the photo-crosslinkable moieties. The small difference in hydrogen bond reduction between both derivatives can be explained by a small distortion of the triple helix formation due to the introduced photo-crosslinkable functionalities as compared to non-functionalized gelatin [209]. Van Hoorick *et al.* [412] reported a 7% decrease in intra-molecular interactions including hydrogen bonds for GEL-MA DS 97% vs unmodified gelatin, whereas Tytgat *et al.* [440] showed a decrease of 5% for GEL-MA 97%. These observations are thus in line with the results obtained in our study.

When looking at the trend for the collagens, it can be observed that almost no hydrogen bond reduction was obtained in case of the lower DS collagen (i.e. 2.004 $J \cdot g^{-1}$ for COL-MA BS 74%, 1.3% decrease), whereas a large drop in the number of hydrogen bonds was observed in case of the high DS collagen (i.e. 1.537 $J \cdot g^{-1}$, 24.3% decrease), as compared to native collagen (i.e. 2.031 $J \cdot g^{-1}$). Even though the exact dissociation enthalpy depends on the type of collagen (i.e. the origin), its exact amino acid composition (and thus the molar mass) and on the protocol used for DSC (i.e. in acid solution or PBS, temperature regime, gelation time, etc.), similar trends could be found in literature [431]. The study of Brinkman *et al.* [441] showed that the functionalization of collagen did not alter the triple helical content (within a certain range of functionalization degrees [39 – 86%]), confirming the observed low reduction (i.e. 1.3%) in dissociation enthalpy in our study for COL-MA BS with a DS of 74% compared to the unmodified COL BS [441].

Knowing that the structural conformation impacts the final material properties, the developed materials will be further investigated by physico-chemical characterization and biological evaluation.

Table 6.2. Effect of functionalization on the physical gelation of gelatin and collagen as studied using DSC, described by the dissociation enthalpy and the peak dissociation temperature.

	Dissociation enthalpy [$J \cdot g^{-1}$]	**Dissociation temperature (peak) [°C]**
GEL BS	1.457	30.27
GEL-MA BS 73%	1.416	28.53
GEL-MA BS 99%	1.398	28.99

COL BS	2.031	28.81
COL-MA BS 74%	2.004	29.63
COL-MA BS 96%	1.537	28.28

The dissociation temperatures for gelatin, collagen and their derivatives were recorded and are also shown in Table 6.2. The observed dissociation temperatures for gelatin (~ 30°C) and its derivatives are in accordance with previous results reported [412]. Collagen and two different types of anhydride derivatives (i.e. maleic anhydride and itaconic anhydride) were studied by Potorac *et al.* [431]. In their study, unmodified collagen showed an endothermic peak at 34°C, whereas an increase in T_d of 6 and 5°C was found for maleic anhydride and itaconic anhydride, respectively. Depending on the amino acid composition, differences in between collagens from other origins or even from the same origins but slightly different extraction protocols could result in differences in dissociation temperature. Next to this, also differences in the applied DSC protocols affect the reported dissociation enthalpy and temperature. From our study, the T_d was found to be lower than the values reported in literature [417,431,442,443]. This can be attributed to a slower heating rate (i.e. 0.5-2°C·min^{-1}) compared to the heating rate in our study (i.e. 5°C·min^{-1}).

6.5.3 Physico-chemical characterization of crosslinked hydrogels

(a) Determination of gel fraction, crosslinking efficiency and swelling ratio

In a next step, the developed materials were physico-chemically characterized via gel fraction determination, HR-MAS ^{1}H-NMR spectroscopy and swelling experiments. As indicated in Figure 6.3, the gel fractions of the functionalized bovine skin gelatins and bovine skin collagens exceeded 74% and 83%, respectively. No statistically significant differences were observed between the different crosslinked materials ($p > 0.05$). Hoch *et al.* [444] reported on gel fractions between 70-85% for bovine type B methacrylamide gelatins having a DS of around 68%, which is in line the results obtained in our study (i.e. 74% for GEL-MA BS 73%). The gel fractions obtained for GEL-MA BS 99% were also in accordance with previous reported data [412,433,440]. It should be noted that the higher DS derivatives did not lead to a significant difference in the obtained gel fractions (Figure 6.3, left panel). The gel fraction data of both the COL-MA and the GEL-MA derivatives provided a first indication of the successful hydrogel formation and an efficient crosslinking process.

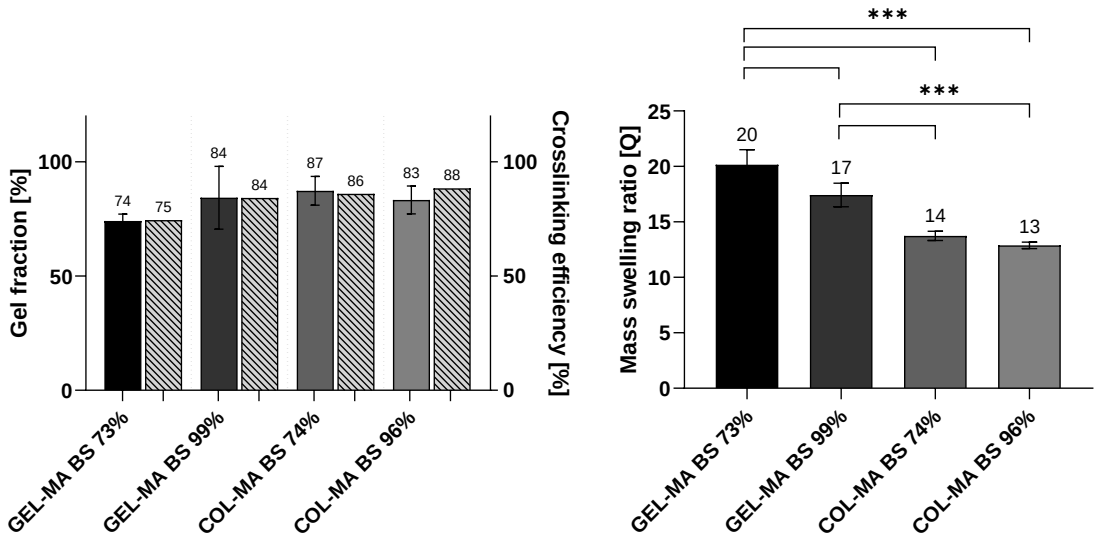

*Figure 6.3. Left panel: Gel fraction (left y-axis, full bars), crosslinking efficiency by HR-MAS (right y-axis, striped bars). Right panel: Mass swelling ratio for the functionalized gelatin and collagen derivatives with different degrees of substitution. (*** = p ≤ 0.001).*

With the aim to further study the crosslinked hydrogels, HR-MAS ^{1}H-NMR spectroscopy was performed to gain more information on the actual double bond conversion in the developed hydrogels. This was realized according to the protocol reported by Van Vlierberghe *et al.* [262]. The results indicated that 75 and 84% of the double bonds were reacted for the GEL-MA BS 73% and GEL-MA BS 99%, respectively. These results agreed with previously reported data [440,445]. The degree of conversion of the developed bovine skin collagen precursors was found to be 86% and 88% for the COL-MA BS 74% and 96%, respectively. It can thus be concluded that, irrespective of the type of hydrogel, the crosslinking reaction was successful (confirming our gel fraction data), without consuming all available double bonds (Table S6.2).

Several studies have shown that the water content of arteries is increased in hypertension, and that this may be associated with an increase in wall thickness [446,447]. Hydrogels are considered excellent candidates for TE applications given the close mimic of the aqueous environment of the ECM. Therefore, the capability to retain water and thus the water content is an important characteristic [183]. The percentage of wet tissue for a coronary artery is reported to be 63.2 ± 1.0% whereas other arteries have wet tissue percentages up to 73.8 ± 0.6% [448] which thus shows the potential of hydrogels for vascular TE applications. The equilibrium mass swelling ratio (Q) of the GEL-MA was 20 and 17, corresponding to a water content of 94.7 and 93.8%, for the GEL-MA BS 73% and 99% DS derivatives, respectively. These values are in accordance with previously reported data by Billiet *et al.* [433] and Tytgat *et al.* [440]. On the other hand, the swelling ratio for the functionalized bovine skin collagen was found to be 14 and 13 (corresponding to a water content of 92.3 and 91.7%) for COL-MA BS 74% and 96%, respectively. The water uptake capacity of the developed photo-crosslinkable collagens was significantly lower compared to GEL-MA ($p \leq 0.001$), but still quite high compared to the 73.8 ± 0.6% of wet tissue of arteries.

Due to their lower amount of introduced photo-crosslinkable groups (Table S6.2), the swelling ratio of the collagen derivatives was expected to be higher than their gelatin counterparts. The lower swelling ratio of the COL-MA derivatives can be attributed to more intra-molecular interactions and the triple helix formation. The higher swelling ratio of all developed derivatives compared to the % swelling for wet tissue of arteries might among other be due to the difference in swelling equilibrium conditions (i.e. deionized water versus human body fluid), because the absence of hydrated ions and ionic atmospheres results in higher swelling ratios [449]. In addition, all other constituents (i.e. enzymes, cells, etc.) present in the human body and in the blood also influence the swelling behavior. A physiologically relevant study on the interaction of these human body fluid constituents and the hydrogel material (after processing into a tubular structure with or without a cell-based model) by using e.g. a bioreactor, will enable a more accurate view and might reduce the discrepancy between the obtained results in this study and the *in vivo* situation.

(b) Determination of mechanical properties via rheology

The mechanical properties of the gelatin and collagen derivatives were studied through rheology experiments to study the influence of the biopolymer type and the DS on the hydrogel's mechanical properties. The mechanical properties of a biomaterial play an important role in their potential use in TERM applications. Not only because sufficient mechanical stability is required for a positive outcome, but also because the mechanical properties directly influence the biological properties (i.e. cell-biomaterial interactions) (*vide infra*). Because the aim of this study is to develop a material with superior mechanical properties compared to non-functionalized collagen (used in vTE but with insufficient mechanical properties)[20] a higher storage modulus, which is a measure for the elasticity of a material, was envisaged for the COL-MA derivatives. In addition, the obtained mechanical properties were compared to the reference material GEL-MA (used as the gold standard in a plethora of other TE applications).

During photo-rheology measurements, the storage modulus G' was monitored as a function of time during UV-irradiation (Figure 6.4). This measurement provides information about the elastic behavior of a material which in turn relates to the number of crosslinks present in a material [450]. First, the modified biopolymers are monitored prior UV-irradiation. At a certain time point (i.e. 120 seconds), the sample is irradiated with UV-light resulting in photo-crosslinking. Upon UV-irradiation, rheological monitoring shows an increase in the storage modulus, until a certain plateau value is obtained.

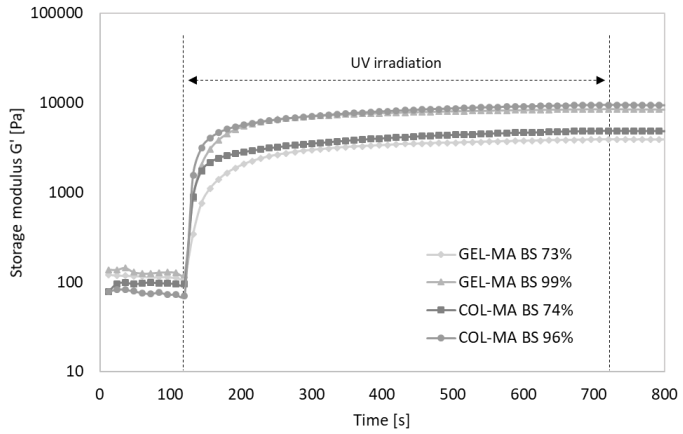

	G' [kPa] – plateau value
GEL-MA BS 73%	3.861 ± 0.017
GEL-MA BS 99%	8.399 ± 0.031
COL-MA BS 74%	4.831 ± 0.024
COL-MA BS 96%	9.385 ± 0.052

Figure 6.4. Left panel: Rheological measurements on the functionalized gelatin and collagen (10 w/v% and 2 mol% Li-TPO, relative to the number of crosslinkable functionalities) and the effect of the degree of substitution on the storage modulus G' as a function of time, and upon applying UV irradiation. Right panel: Plateau values of the storage moduli in kPa for each of the developed materials.

The measurements indicate a storage modulus of 3.861 ± 0.017 kPa for GEL-MA BS 73% in the relaxed state whereas a higher G' value (i.e. 8.399 ± 0.031 kPa) was observed for GEL-MA BS 99%. The functionalized collagens exhibited a similar behavior, with storage moduli of 4.831 ± 0.024 and 9.385 ± 0.052 kPa for the COL-MA BS 85% and 96%, respectively.

Irrespective of the biopolymer type, the storage modulus G' (at relaxed state) increased with a higher DS. This can be explained by a higher amount of introduced photo-crosslinkable groups and thus the formation of a more densely crosslinked network.

In addition to the effect of the DS, the nature of the biopolymer also affects the hydrogel mechanical properties. Indeed, the COL-MA derivatives reveal higher G' values compared to their GEL-MA counterparts. The effect is however less pronounced compared to the effect of the DS (Figure 6.4). At first sight, this effect is counter-intuitive when considering the number of introduced and reacted photo-crosslinkable functionalities on both biopolymers (summarized in Table S6.2). Considering the higher number of introduced and reacted photo-crosslinkable groups present in the gelatin derivatives, a stronger crosslinked network was expected for the GEL-MA-based hydrogels. However, based on the photo-rheology measurements, the opposite effect was observed with storage moduli for the collagen derivatives of 4.831 and 9.385 kPa as compared to those of the gelatin derivates being 3.861 and 8.399 kPa. As for the swelling properties of the developed gels, this can again (at least partly) be ascribed to structural differences between collagen and gelatin (as described above), more precisely the higher number of triple helices present in collagen (Table 6.2) [451].

It can thus be concluded that superior mechanical properties were obtained for the photo-crosslinkable collagen derivatives as compared to (i) native collagen (i.e. a storage modulus of 1070 - 3333 Pa reported in literature) [412,431], and (ii) GEL-MA, despite the lower number of photo-crosslinkable functionalities.

6.5.4 *In vitro* cytocompatibility study using human umbilical vein endothelial cells

In addition to the higher described biomaterial properties, cell-biomaterial interactions are crucial when developing a material for TE purposes. Because the collagen-based derivatives were developed with the final aim to be used as material for vascular TE applications, HUVECs (i.e. one of the vascular cell types) were selected for the biological assays. Indeed, implanted materials always contact the endothelium, directly or indirectly via possible degradation products [452]. To this end, both indirect and direct biological assays were performed.

First, the cytocompatibility of the developed materials was evaluated via an indirect cytotoxicity assay using HUVECs. The viability of the HUVECs after contact with the material extracts of the modified gelatin- or collagen-based materials is shown in Figure S6.3. Based on the indirect assay, a high HUVEC cell viability was obtained for all materials (i.e. > 93%). It can be concluded that all developed materials in this study (i.e. modified gelatin and collagen with different degrees of modification) are non-cytotoxic as the assessed materials exhibited cell viabilities well above 70% (referring to the definition of a "non-cytotoxic material" by ISO 10993-5) [317].

In addition to the indirect cytotoxicity assay, the cell-biomaterial interactions were evaluated by a viability test over a 7-day period using HUVECs. The cell viability of the HUVECs seeded onto the functionalized gelatin and collagen hydrogels was evaluated after 1, 3 and 7 days in culture.

The results of the resazurin assay using HUVECs (Figure 6.5) showed a statistically significant increase in cell viability for COL-MA BS 74% in comparison to GEL-MA BS 73% ($p \leq 0.05$) at day 1. The same trend was observed at day 3 and 7, where the COL-MA BS 74% also exhibited a significantly higher cell viability in comparison to GEL-MA BS 99% ($p \leq 0.01$). It can thus be concluded that after 1 week, the COL-MA BS 74% revealed a higher cell viability compared to both gelatin derivatives. This agrees with Ryglova *et al.* [451] who stated that the superior biological features of collagen compared to gelatin, are mainly the result of the integrity of the triple helical structure of collagen (which is generally not altered upon functionalization) [441]. In addition to the cell viability, the relative cell growth rate (RGR) was evaluated. The RGR data have indicated that HUVECs have a statistically significant higher growth rate on COL-MA BS 96% when comparing day 1 to day 3 ($p \leq 0.0001$) and day 1 to day 7 ($p \leq 0.01$) (Figure S6.4).

For the developed COL-MA BS 96% derivative, a significantly lower HUVEC viability was obtained at day 3 ($p \leq 0.05$) and day 7 ($p \leq 0.001$) as compared to COL-MA BS 74%. This could indicate a significant preference of the HUVECs for the developed COL-MA BS 74%. It is known that both mechanical and biochemical properties of the ECM are critical for the control of cell and tissue morphology and function [453]. Furthermore, as stated by Chen *et al.* [454], both chemical and topographical properties influence cellular responses. The difference in mechanical properties between COL-MA BS 74% and 96% (i.e. 4.831 ± 0.024 and 9.385 ± 0.052 kPa), depending on the degree of substitution, could thus explain in part the difference in HUVEC viability between both collagen derivatives. A lower DS implies a smaller alteration of the original collagen backbone and hence a closer

resemblance to the non-functionalized collagen [109]. This together with other effects could explain why the HUVECs show a preference towards the lower degree functionalized collagen (i.e. COL-MA BS 74%).

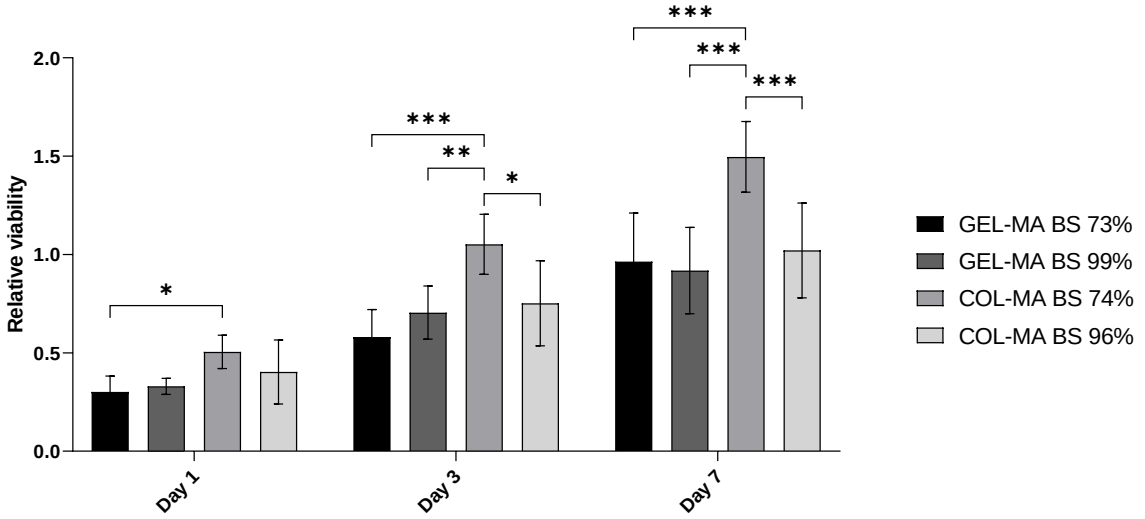

Figure 6.5. Viability of HUVECs evaluated via a direct assay at days 1, 3 and 7 after cell seeding. (= p ≤ 0.05; ** = p ≤ 0.01; *** = p ≤ 0.001).*

To further study the behavior of HUVEC in contact with our biomaterials, DAPI and VE-cadherin staining were performed in order to visualize the cell nuclei, the cytoskeleton and the intercellular junctions (Figure 6.6). The data supports the above-described observations. Indeed, a preference of the HUVECs towards the COL-MAs is observed as HUVECs were well attached and homogeneously spread on COL-MA films. For GEL-MA films, the cells were more rounded (i.e. cell circularity is also a factor to track cell growth [455]) and some clusters were observed, which is a sign of anomalous growth of HUVECs [456]. The intercellular junctions were also highlighted by VE-cadherin staining at day 7 (Figure S6.5). VE-cadherin is an endothelial-specific component that emerged as a regulator of endothelial cell-cell adhesive properties. Next to this, VE-cadherin is known to organize the opening and closing of the endothelial barrier, but also plays an important role in permeability changes [457]. Based on the images (Figure 6.6), it can be concluded that the VE-cadherin is present at the endothelial cell junctions irrespective of the developed material. Moreover, Loy *et al.* [109] stated that a polygonal shape of the EC marker VE-cadherin confirms the adhesion and proliferation of HUVECs on the underlying hydrogel.

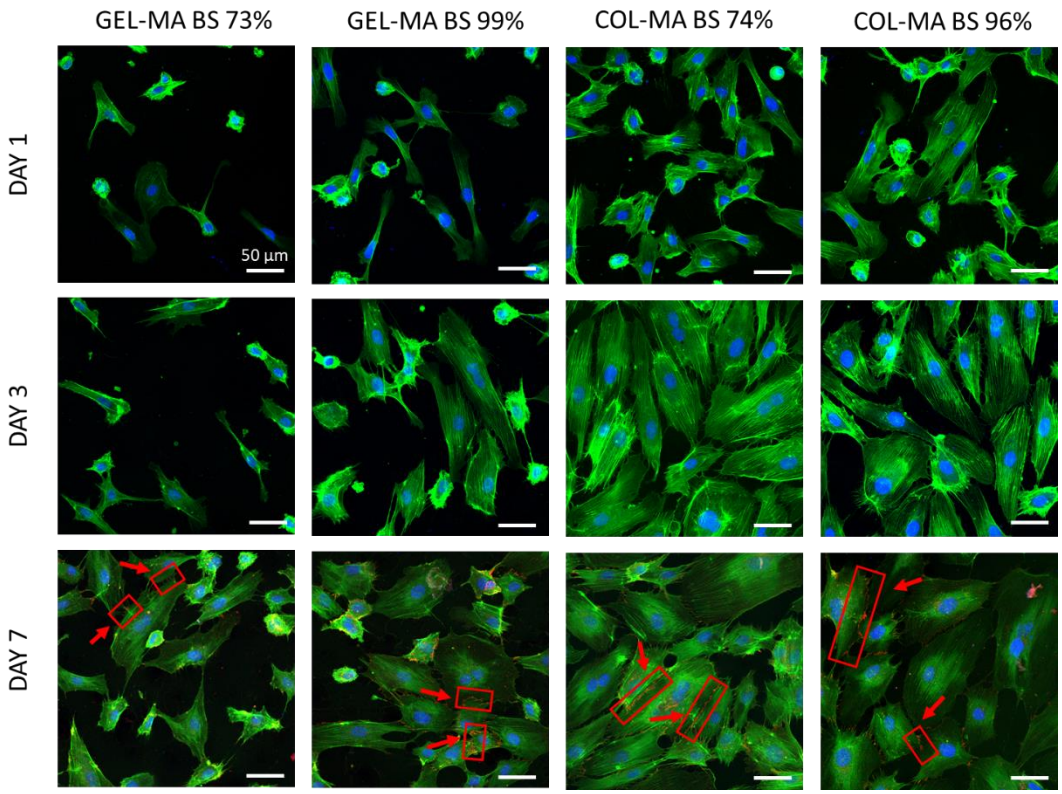

Figure 6.6. Nuclei (blue), cytoskeleton (green) and VE-cadherin (red) of HUVEC cells seeded on GEL-MA BS and COL-MA BS derivatives at day 1, 3 and 7. HUVECs were seeded at a density of 15,000 cells·cm^{-2} in 400 µL complete DMEM+. The red arrows and boxes indicate some VE-cadherin stained intercellular junctions, larger images of day 7 can be found in Fig. S6.5.

The endothelial cytoskeleton is a dynamic network that defines the cell shape, withstands external forces and effectively responds to mechanical stimuli. Moreover, it has a structural responsibility and plays a key role in cell migration, cell-cell adhesion, cell-substrate adhesion, and molecular transport between the plasma membrane and the nucleus [458]. When a cell contacts a surface (a biopolymer in this case), the cell spreads, exerts traction forces against the surface and forms new bonds with the surface as its contact area expands [459]. This can be examined by the changes in cell shape and actin polymerization. Upon rearranging its cytoskeleton, actin bundles and focal adhesions are formed [459]. Actin filaments anchor to the plasma membrane and reinforce it [460]. The cell cytoskeleton areas were quantified on day 1, 3 and 7 (reported in Figure 6.7). After 1 day, no statistically significant differences were observed ($p > 0.05$). However, at day 3, the developed collagen-based materials showed a significant increase in cytoskeleton area compared to GEL-MA BS 73% ($p \leq 0.01$) and GEL-MA BS 99% ($p \leq 0.001$). Interestingly, COL-MA BS 74% showed a significant increase in cytoskeleton area compared to both gelatin derivatives ($p \leq 0.01$) at day 7. This could imply a preference of HUVECs towards this material type, as they also show a more natural morphology and nicely spread cytoskeleton area on the COL-MA surface (Figure 6.7).

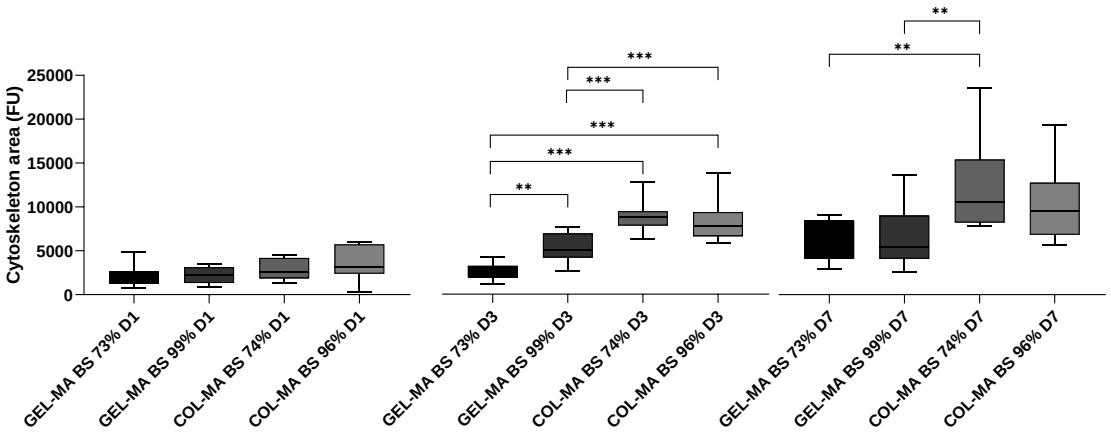

Figure 6.7. Cytoskeleton area of HUVECs seeded onto GEL-MA BS and COL-MA BS, calculated using ImageJ software on the DAPI and VE-cadherin stained images. (= p ≤ 0.05; ** = p ≤ 0.01; *** = p ≤ 0.001).*

According to the results of the biological evaluation using HUVECs, the cell-biomaterial interaction was shown to be superior for COL-MAs compared to GEL-MAs. Based on the direct cell assay, COL-MA BS 74% showed a statistically significant increase in HUVECs viability compared to the gelatin derivatives after 3 ($p \leq 0.01$) and 7 days ($p \leq 0.001$) compared to both types of gelatin (i.e. GEL-MA 73% and GEL-MA 99%), and compared to COL-MA 96% ($p \leq 0.05$ on day 3, $p \leq 0.001$ on day 7). Cell visualization revealed a preference of HUVECs towards the collagen derivatives compared to the gelatin derivatives. The cytoskeleton area of COL-MA BS 74% was found to be significantly higher compared to both gelatin derivatives at day 3 ($p \leq 0.001$) and day 7 ($p \leq 0.01$).

6.6 Conclusions

The methacrylamide functionalization of collagen (COL-MA) proves to be an interesting alternative for the gold standard GEL-MA used in TE and RM applications. The introduction of the photo-crosslinkable groups was confirmed both qualitatively and quantitatively. The hydrogels produced starting from the functionalized collagens exhibited a high gel fraction (> 83%) and a high conversion of the photo-crosslinkable groups (> 86%), being indicative for a stable hydrogel and an efficient crosslinking. Depending on the degree of substitution, materials with tunable mechanical properties were obtained. An increase in degree of substitution led to increasing storage moduli. The developed collagen derivatives showed superior mechanical properties compared to (i) native collagen, and (ii) the gold standard GEL-MA and showed a lower swelling degree, more closely mimicking the water content of natural tissue. *In vitro* biological assays showed that HUVECs have a preference towards the developed bovine skin COL-MAs and a significantly better cell-biomaterial interaction (i.e. cell shape, cell cytoskeleton area) when compared to bovine skin GEL-MAs. Given these findings, the functionalized collagens will be the subject of follow-up research in which the processing potential of the developed photo-crosslinkable collagens into tubular constructs for vTE applications will be studied. The most prominent challenges in the field, burst pressure and compliance will be tackled for these constructs.

Chapter 7: Proteomics as a tool to gain next level insights into photo-crosslinkable biopolymer modifications

This chapter describes proteomics as a tool to identify and localize photo-crosslinkable moieties in the biopolymer's amino acid sequence and within its 3D structure. The proteomics analysis was conducted in collaboration with MSAP (Université de Lille, France) by Dr. F. Bray. The 3D modeling was performed by Dr. T. Gheysens. This chapter has been published as:

N. Pien, F. Bray, T. Gheysens, L. Tygat, C. Rolando, D. Mantovani, P. Dubruel, S. Van Vlierberghe. Proteomics as a tool to gain next level insights into photo-crosslinkable biopolymer modifications. Bioactive Materials, DOI: 10.1016/j.bioactmat.2022.01.023. Published: JAN 2022, Impact Factor: 14.593. Peer reviewed.

7.1 Résumé

La répartition des groupements photoréticulables sur un squelette protéique peut affecter le comportement de réticulation d'un biomatériau, et donc aussi ses propriétés mécaniques et biologiques. Une connaissance approfondie à cet égard est essentielle pour les biomatériaux exploités en ingénierie tissulaire et en médecine régénérative. Dans le présent travail, des groupements photoréticulables ont été introduits sur les groupes amine primaire de: (i) d'un peptide de collagène recombinant (RCPhC1) avec une séquence d'acides aminés (AA) connue, et (ii) de collagène de peau bovine (COL BS) avec une séquence AA inconnue. Le degré de substitution (DS) a été quantifié à l'aide de deux techniques conventionnelles: un test au dialdéhyde ortho-phtalique (OPA) et la spectroscopie ^{1}H-NMR. Cependant, aucune de ces deux techniques ne fournit d'informations sur le type et l'emplacement exacts des AA modifiés. Par conséquent, pour la première fois, l'analyse protéomique a été évaluée ici comme un outil pour identifier les AA fonctionnalisés ainsi que la position exacte des parties photoréticulables le long de la séquence AA.

7.2 Abstract

The distribution of photo-crosslinkable moieties onto a protein backbone can affect a biomaterial's crosslinking behavior, and therefore also its mechanical and biological properties. A profound insight in this respect is essential for biomaterials exploited in tissue engineering and regenerative medicine. In the present work, photo-crosslinkable moieties have been introduced on the primary amine groups of: (i) a recombinant collagen peptide (RCPhC1) with a known amino acid (AA) sequence, and (ii) bovine skin collagen (COL BS) with an unknown AA sequence. The degree of substitution (DS) was quantified with two conventional techniques: an ortho-phthalic dialdehyde (OPA) assay and ^{1}H-NMR spectroscopy. However, neither of both provides information on the exact type and location of the modified AAs. Therefore, for the first time, proteomic analysis was evaluated herein as a tool to identify functionalized AAs as well as the exact position of photo-crosslinkable moieties along the AA sequence, thereby enabling an in-depth, unprecedented characterization of functionalized photo-crosslinkable biopolymers. Moreover, our strategy enabled to visualize the spatial distribution of the modifications within the overall structure of the protein. Proteomics has proven to provide unprecedented insight in the distribution of photo-crosslinkable moieties along the protein backbone, undoubtedly contributing to superior functional biomaterial design to serve regenerative medicine.

7.3 Introduction

Proteins are large, complex biomolecules composed of amino acid residues linked together into one or more chains. Depending on the amino acids present, combinations of hydrophobic, hydrophilic, polar and apolar regions can be present within a protein chain. Proteins differ from one another primarily in their sequence and composition of amino acids. Depending on this amino acid sequence, the protein usually folds into a specific three-dimensional (3D) structure. The structure and possible conformations of a protein affect a protein's function and bioactivity. For example, structural proteins like collagen, elastin, keratin, etc. maintain tissue shape and constitute structural elements in connective tissue like cartilage and bone[461].

Collagen is the most abundant structural protein, both in animals and humans. In the human body, collagen accounts for one third of the total protein content. Moreover, it forms the main component of the extracellular matrix (ECM) in various connective tissues in the body [462]. Collagen provides structural support and strength, and mediates local biological responses [187]. It is composed of three α-chains (i.e. two α1 and one α2) that are arranged in a triple helix. The sequence of this protein is characterized by the regular occurrence of glycine, proline and hydroxyproline [463].

In tissue engineering (TE) and regenerative medicine (RM), the aim is to regenerate, reconstruct or repair native tissue. Because connective tissue is mainly composed of fibrous ECM components, researchers have been exploiting ECM components as materials for TERM applications [464]. Due to the abundance of collagen in the ECM of human tissue, collagen has been studied frequently as a biomaterial for tissue engineering applications [465]. The main advantages of collagen include low antigenicity, biocompatibility, bioactivity, biodegradability and the capability to promote cell adhesion through cell receptors that recognize a specific peptide sequence (such as RGD (R: arginine; G: glycine; D: aspartic acid)) within collagen [4,181,466].

One of the most important limitations related to the use of extracted collagen for TERM applications is its mechanical properties, mainly at the viscoelastic level, such as the insufficient burst strength of collagen-based materials when exposed to the high stresses and pressures encountered in vascular tissue engineering (i.e. compliance of 4.5 - 6.2% change in diameter for a pressure increase from 80 to 120 mmHg, a burst pressure of 2031 - 4225 mmHg, a maximum stress of 1.44 ± 0.87 MPa, a maximum strain of 0.54 ± 0.25 and a physiological elastic modulus of 1.48 ± 0.24 MPa, for a human coronary artery) [64,73–77,79,181,416]. Therefore, research has focused on various approaches to control the polymerization and the stability in solution and to reduce enzymatic sensitivity, in an attempt to improve the mechanical strength. Another approach involves chemical, physical or enzymatic crosslinking of the individual collagen chains [439,451,461,467]. Therefore, crosslinkable moieties (introduced upon reaction with e.g. methacrylic anhydride, 4-vinylbenzyl chloride, glycidyl methacrylate, 2-iminothiolane, maleic anhydride, itaconic anhydride, etc.) have already been introduced on the protein backbone to obtain a stable, crosslinked network [181]. A frequently applied approach in this respect is to exploit the primary amines present in the biopolymer backbone (i.e. hydroxylysine, lysine and ornithine) for functionalization purposes.

Moreover, the type of modification, the corresponding crosslinking mechanism along with the crosslinking kinetics influence the processability of biomaterials into scaffolds along with their mechanical and biological properties (including the material's bioactivity) [264,468].

In order to engineer the structure reasonably allowing to achieve the targeted mechanical properties - and thus to mimic those of native tissue - one should obtain information on the molar mass (MM), the degree of functionalization, the location of the modified amino acids as well as the location of these functionalities within a protein's 3D structure (i.e. towards inner or outer side of the protein's 3D structure).

Conventional characterization techniques applied as quantitative tool to evaluate the degree of substitution (DS) of functionalized proteins include an ortho-phthalic dialdehyde (OPA) assay and proton nuclear magnetic resonance (^{1}H-NMR) spectroscopy [411,469]. However, these techniques only provide a quantitative evaluation of the amount of introduced functional groups but do not provide further insight in the distribution and the location of these modifications along the protein backbone.

In order to gain additional insight in biopolymer functionalization, proteomics can be a valuable tool. Proteomics involves the systematic, large-scale analysis of proteins. It is based on the study of the proteome, which is defined as a complete set of proteins produced by a given cell or organism under a defined set of conditions [470]. Proteomics is currently used to quantify and identify naturally occuring modifications present on a peptide/protein but more importantly, it enables to localize these modifications along the protein sequence [471,472].

During the past decade, mass spectrometry has become the method of choice in proteomics for the identification, quantification and study of post-translational modifications (PTMs) on proteins. It is a very sensitive (i.e. fmol·µL^{-1} peptide), accurate and efficient method for sequencing proteins. Shotgun proteomics refers to the use of bottom-up proteomics techniques to study complex protein mixtures [472]. It utilizes the technology of high-performance liquid chromatography (HPLC) hyphenated with mass spectrometry (MS). The most distinct feature of shotgun proteomics is that it enables the identification and comparative quantification of a wide range of proteins at the same time while only requiring minimal separation between the LC peaks of the peptides. This technique is based on the extraction of proteins followed by their denaturation, reduction and alkylation. Next, the proteins are digested by an enzyme like trypsin. The cleaved, released peptides are separated with HPLC, followed by tandem MS/MS analysis to identify the amino acid sequence of each peptide. The identified peptide mass sequences are then compared with a protein database such as Swiss-Prot, which enables the identification of the proteins [472–474].

In other words, proteomics can show exactly where functional groups are located on the amino acid sequence, which has already been studied for naturally occurring modifications (e.g. proline hydroxylation, phosphorylation, etc.) in a biopolymer, and in the field of modifications with drug conjugates [475] but has not yet been investigated for introduced chemical modifications aiming at developing photo-crosslinkable biomaterials for TE purposes (e.g.

methacrylamide modification). The latter could provide unprecedented insight in the distribution of introduced photo-crosslinkable functionalities along the chain. Moreover, proteomics can enable further unravelling of the efficiency of a biopolymer modification along with its potency to create a crosslinked network. This know-how is crucial to enable translation of novel, functionalized biomaterials from bench to bedside, given regulatory constraints and the need for perfectly defined and reproducible biomaterials.

In this chapter, proteomic analysis was used to determine the position and to quantify the number of photo-crosslinkable groups (i.e. introduced methacrylamide groups) in comparison with conventional characterization techniques (i.e. OPA and ^{1}H-NMR spectroscopy). To the best of our knowledge, this is the first time that photo-crosslinkable biomaterials serving TE applications are fully characterized with respect to their MM, DS, location of functionalities along the protein backbone as well as their accessibility within the protein's primary, secondary and tertiary structure.

In this chapter, proteomics was assessed for its potential to elucidate a known peptide sequence, i.e. a recombinant peptide based on collagen type I (RCPhC1) as well as its derivatives, containing photo-crosslinkable methacrylamides (MA). Afterwards, the proteomics technique was applied on a material with an unknown amino acid sequence, i.e. bovine skin collagen (COL BS).

7.4 Materials and methods

7.4.1 Materials

Recombinant peptide based on collagen I, commercially available as Cellnest™, was kindly provided by Fujifilm Manufacturing (Europe B.V.). Collagen type I, extracted from bovine skin [476], was supplied by the Department of Collagen Research (National Research & Development Institute for Textiles and Leather, Romania). Methacrylic anhydride (MeAnH), sodium hydroxide (NaOH) and potassium chloride (KCl) were obtained from Sigma-Aldrich (Diegem, Belgium). Potassium phosphate monobasic (KH_2PO_4) and sodium phosphate dibasic (Na_2HPO_4) were obtained from Acros Organics (Geel, Belgium). All ^{1}H-NMR spectra were recorded in deuterium oxide (D_2O) provided by Euriso-top (Saint-Aubin Cedex, France). Spectra/Por7 dialysis membranes (MWCO of 12000-14000 kDa) were obtained from Polylab (Antwerp, Belgium). UF filters were obtained from Amicon® units (10 kDa cutoff limit; Millipore, Billerica, MA) and the chemical products for proteomics were obtained from Sigma-Aldrich.

7.4.2 Derivatization of biopolymers

The methacrylation of biopolymers (Figure 7.1) was performed according to the protocol of Tytgat *et al.* [440]. In brief, methacrylamide-modified recombinant collagen (RCPhC1-MA) and methacrylamide-modified bovine skin collagen (COL-MA) were prepared through reaction of the primary amines with methacrylic anhydride (MeAnH). First, the biopolymer (10 w/v%) was dissolved in a phosphate buffer (pH = 7.8) at 37°C. Next, 0.5 or 1 equivalents MeAnH with respect to the primary amines were calculated and added, followed by stirring during 1 hour. Next,

the reaction mixture was dialyzed (MWCO 12-14 kDa) against distilled water (37°C, 24 h), followed by freeze-drying.

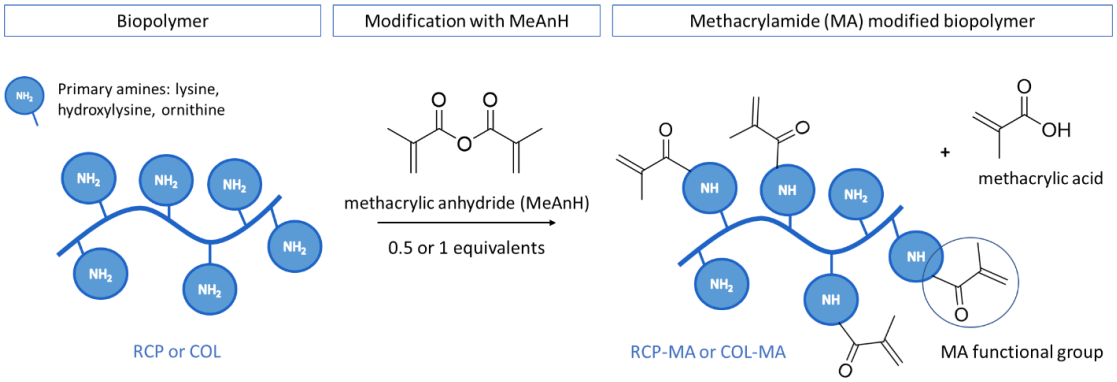

Figure 7.1. Development of methacrylamide-modified RCPhC1 (RCPhC1-MA) and methacrylamide-modified collagen (COL-MA) by introduction of methacrylamide moieties on the primary amines of the biopolymer (i.e. lysine, hydroxylysine and ornithine).

7.4.3 ^{1}H-NMR spectroscopy

The degree of substitution of the RCPhC1 and collagen derivatives was quantified via ^{1}H-NMR spectroscopy (Bruker WH 500 MHz) using D_2O as solvent at elevated temperature (40°C). The calculation of the DS was performed following the procedure as described earlier by Van Vlierberghe *et al.* [262] and using the MestReNova software. A Whittaker Smoother baseline correction was performed before analyzing the obtained spectra and integrating the peaks of interest. The ^{1}H-NMR spectra of the modified proteins show characteristic peaks at 5.75 and 5.55 ppm which correspond to the vinyl protons of the introduced MA functional groups (Figure S1). The DS was quantified by comparing the integration of these characteristic peaks (i.e. 5.75 and 5.55 ppm) to the integration of the signal corresponding with the methyl protons present in Val, Leu and Ile (i.e. at 1.01 ppm) which are inert during the modification [262].

7.4.4 Ortho-phthalic dialdehyde assay

An OPA assay was applied as a quantitative tool to evaluate the DS of the functionalized polymers. To this end, 20 mg OPA was dissolved in 10 mL ethanol. Next, the mixture was diluted to 50 mL with double distilled water (deionized water). A second stock solution containing 25 µL 2-mercaptoethanol in a 50 mL borate buffer (pH = 10) was prepared. For 50 µL of heated (T = 37°C) collagen solution (1 g / 40 mL deionized water), 950 µL deionized water, 1500 µL 2-mercaptoethanol solution and 500 µL of the OPA stock solution were added, followed by vigorously mixing. Finally, the absorbance (Uvikon XL, BioTek Instruments) at 335 nm was measured compared to a blank (i.e. mixture with deionized water instead of collagen) at 37°C. All measurements were performed in triplicate. Analogous measurements were performed with n-butylamine (0.002 M to 0.01 M) standards to obtain a calibration curve. Calculation of the amount of unreacted amine groups remaining after the modification, enabled the determination of the DS.

7.4.5 Sample preparation for proteomic analysis

The sample preparation via the enhanced filter aided sample preparation (eFASP) tryptic digestion workflow is illustrated in Figure 7.2. First, different collagens were dissolved in ultrapure water at 1 $mg \cdot mL^{-1}$ in an Eppendorf® microtube (Eppendorf, Hamburg, Germany). The solutions were heated at 90°C for 5 min to dissolve RCPhC1 or COL BS. The samples were prepared using a modified eFASP [477]. Before their use, 0.5 mL Amicon® ultra centrifugal filters equipped with a cut-off of 10 kDa (EMD Millipore, Darmstadt, Germany) were incubated overnight in a passivation solution containing 5% (v/v) Tween®-20 and then rinsed with ultrapure water. Next, 100 µg of protein was incubated in a 100 µL lysis buffer (8 M urea, 0.2% deoxycholic acid, 25 mM DTT, 100 mM ammonium bicarbonate pH 8.8). The solutions were transferred to an Amicon® filter and 100 µL of exchange buffer was added (8 M urea, 0.2% deoxycholic acid, 100 mM ammonium bicarbonate pH 8.8). After a centrifugation step of 20 min at 20817 g, the filtrates were removed and 200 µL of exchange buffer was added to the Amicon® filters, which were consecutively centrifuged. This operation was repeated twice. The proteins were alkylated for 1 h at room temperature (20°C) in the dark using 100 µL of alkylation buffer (8 M urea, 50 mM iodoacetamide and 100 mM ammonium bicarbonate, pH 8.8). The Amicon® filters were centrifuged again for 20 min at 20817 g and the filtrates were discarded. After this alkylation step, 200 µL of exchange buffer was added to the Amicon® filters, which were again centrifuged for 20 min at 20817 g and the filtrates were discarded. An aliquot (200 µL) of digestion buffer (0.2% deoxycholic acid, 50 mM ammonium bicarbonate, pH 8.8) was added to the Amicon® filters, prior to another centrifugation step (20 min at 20817 g). This operation was repeated twice, with the filtrate being removed and discarded. The Amicon® filters were transferred to a new 2 mL concentrator collection tube. Next, 100 µL of digestion buffer containing 40 µL of endoproteinases Trypsin/LysC or GluC (Promega, Madison, WI) was added at 1/50 ratio enzyme/protein (w/w) and incubated in the Amicon® filters under continuous shaking in a heating block tube (MHR23, Hettich, Netherlands) during 16 h at 37°C.

Thereafter, the peptides present in the Amicon® filters were recovered in the tube by centrifugation for 15 min at 20817 g. To maximize the peptide recovery, two washing steps were implemented with 50 µL of ammonium bicarbonate solution (50 mM pH 8.8). The filtrates containing all peptides were transferred to a 1.5 mL Eppendorf® microtube. Next, 200 µL of ethyl acetate with 2.5 µL of trifluoroacetic acid (TFA) was added, to precipitate the peptide (white color). Again, 800 µL of ethyl acetate was added, the resulting solutions were centrifuged for 10 min at 10681 g and the organic phases were eliminated. This operation was repeated twice. The Eppendorf® microtubes were placed for 5 min at 60°C in a heating block (SBH130, Stuart, Staffordshire, UK) to enable evaporation of the remaining ethyl acetate. The samples were dried at room temperature in a SpeedVac™ Concentrator (EppendorfTM Concentrator Plus, Eppendorf). Next, 100 µL of a methanol/water (50/50) mixture was added to the resulting solid phase and let to evaporate.

For MS analysis, the samples were dissolved in 10 µL of ultrapure water supplemented with 0.1% of formic acid (FA). The sample concentration was estimated by measuring the optical density (OD) at 215 nm of 1 µL of the solution using a droplet UV spectrometer (DS-11+, Denovix, Wilmington, USA). Finally, the concentration of the

samples was adjusted to 1 µg·µL^{-1} by dilution with ultrapure water containing 0.1% FA before analysis. Each sample was analyzed in triplicate.

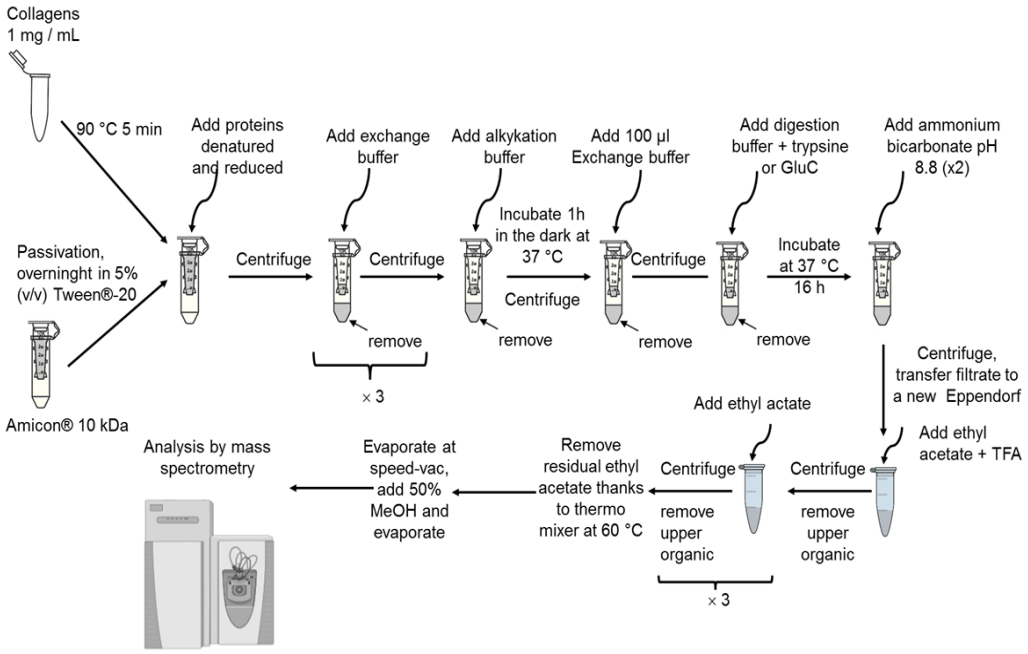

Figure 7.2. Workflow of the sample preparation (for proteomic analysis) by enhanced Filter Aided Sample Preparation (eFASP) digestion.

7.4.6 Proteomic analysis using LC-MS/MS Orbitrap

Liquid chromatography tandem mass spectrometry (LC-MS/MS) protein analyses were performed on an Orbitrap Q Exactive plus Mass Spectrometer hyphenated to a U3000 RSLC Microfluidic high-performance liquid chromatography (HPLC) System (ThermoFisher Scientific, Waltham, MA). An aliquot of the peptide mixture (1 µL) at a concentration of 1 µg·µL^{-1} was injected with a solution A (5% acetonitrile, 94.9% H_2O and 0.1% FA) for 3 min at an isocratic flow rate of 5 µL·min^{-1} of solution A on an Acclaim PepMap100 C18 pre-column (5 µm, 300 µm i.d. × 5 mm) (ThermoFisher Scientific). Next, the peptides were separated on a C18 Acclaim PepMap100 C18 reversed phase column (3 µm, 75 mm i.d. × 500 mm) (ThermoFisher Scientific), using a linear gradient (5-40%) from solution A to solution B (75% ACN, 24.9% H_2O and 0.1% FA) and a flow rate of 250 nL·min^{-1} in 160 min followed by 100% solution B for 5 min, to clean the column and then re-equilibrated with solution A during 10 min. The column and the pre-column were placed in a column oven at a temperature of 45°C. The total duration of the analysis of one sample was 180 min. The LC runs were acquired in positive ion mode. MS scans for DDA (data dependent acquisition) were acquired from m/z 350 to 1500 in the Orbitrap mass analyzer with a 70000 resolution with maximum injection time of 80 ms and AGC target of 1×10^6. MS/MS scans were sequentially acquired in the high-energy collision dissociation cell for the 10 most-intense ions detected in the full MS survey scan. For MS/MS, the resolution was set to 35000 with maximum injection time of 120 ms and AGC target of 5×10^5 and the normalized collision energy was set to 28 eV. Dynamic exclusion was set at 90 s and ions with 1 and more than 8 charges were excluded. The workflow of the proteomics approach for the identification and quantification is shown in Figure 7.3.

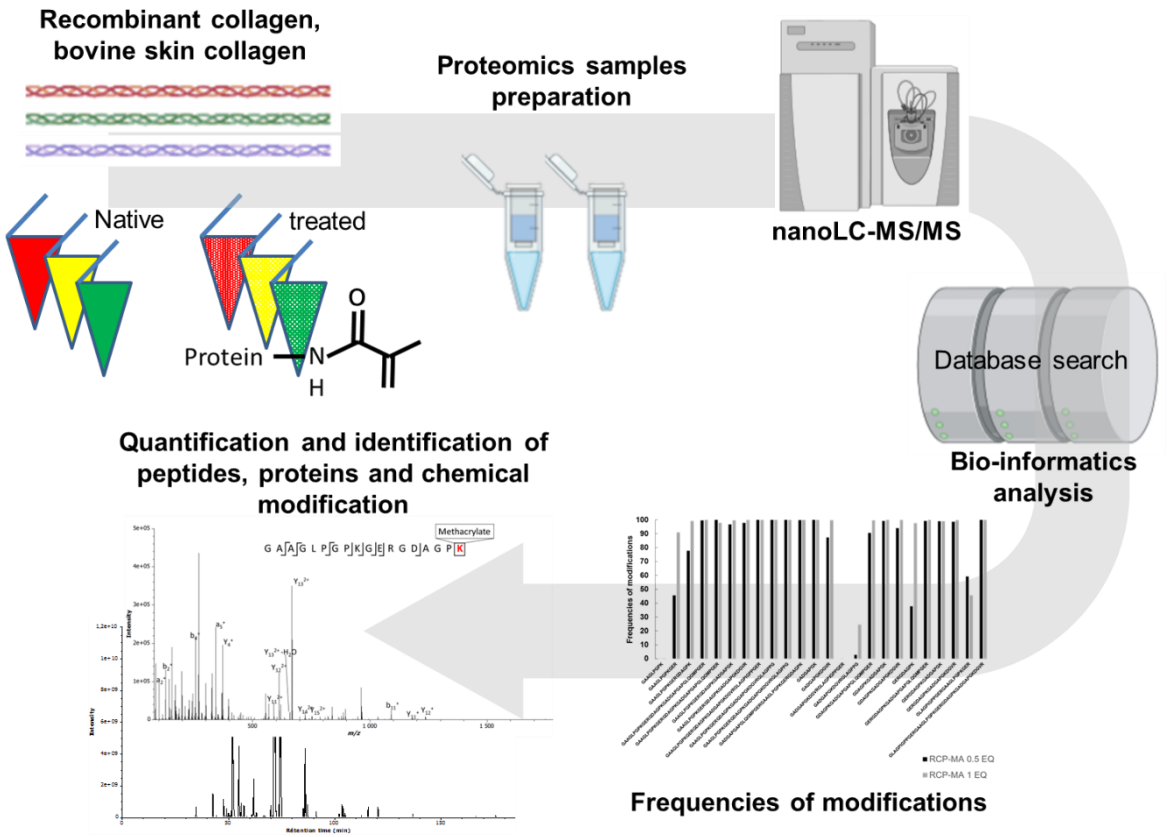

Figure 7.3. Workflow of proteomics approach for identification and quantification of (modified) biopolymers.

7.4.7 Label-free quantification of modified peptides

The raw data from LC-MS/MS were processed by Proteome Discoverer version 2.2 (ThermoFisher Scientific) with a SEQUEST search engine against all entries of Swiss-Prot database (563552 sequences, version UniProtKB 2020_05) or Bos taurus database from Swiss-Prot (37512 sequences, version June 29, 2020) or home-made collagen sequences containing 3 sequences (i.e. recombinant collagen, collagen α1(I) chain P02453, collagen α2(I) chain P02465). The quantification was done with Minora node. The MS error was set to 10 ppm and 0.05 Da for MS/MS mass tolerance error. Trypsin with specific cleavage site (K, R) and GluC with specific cleavage site (E, D) were selected, together with variable modifications of the MA functionalities on lysine with a specific delta mass (+ 68.026 Da), oxidation of methionine (+ 15.994 Da), and/or deamidation of glutamine and asparagine (+ 0.984 Da). Oxidation of proline (+ 15.994 Da) was added for collagen. The fixed modification of carbamidomethyl cysteine (+ 57.021 Da) was also selected. The minimal peptide length of amino acids and the maximum number of missed cleavages were both set to six. The false discovery rate (FDR) threshold was set to 0.05 using the Percolator node. Relative abundances of peptides were calculated by integration of the area under the curve of the MS1 peaks using Minora LFQ node. The peptides were filtered on posterior error probability (PEP) score, q-value, Xcorr score. The PEP score and q-value threshold was set to less than 0.05 and Xcorr score greater than 1.

The percentage of the MA modified peptides (i.e. the degree of modification/substitution) is calculated using Equation 7.1. An example of the calculation of the degree of modification using proteomics can be found in Supplementary Information, Annex 4 – Chapter 7.

$$DS\ [\%] = 100 \cdot \left(\frac{Intensity_{MA\ modified\ peptide}}{Intensity_{MA\ modified\ peptide} + Intensity_{control\ peptide}} \right) \quad (7.1)$$

With;

DS = degree of substitution

$Intensity_{MA\ modified\ peptide}$ = intensity of all MA modified peptides in the MA modified sample

$Intensity_{control\ peptide}$ = intensity of the MA modifiable peptides without modification in the MA modified sample

7.4.8 Intact mass analysis using MALDI-TOF

The RCPhC1 and its derivatives were analyzed by matrix-assisted laser desorption/ionization (MALDI) time-of-flight (TOF) (MALDI TOF/TOF) 4800+ (Sciex, Framingham, MA). Five µg of the RCPhC1 collagens were mixed with 1 µL of CHCA (α-cyano-4-hydroxycinnamic acid) matrix (70% ACN, 30% H_2O, 0.1% TFA). The RCPhC1 collagens were acquired in linear positive ion mode. The mass range was set to 40000 until 60000 m/z and 2000 spectra were accumulated.

7.4.9 SDS-PAGE analysis on RCPhC1 and COL BS

Different collagens were dissolved in water at 5 mg·mL^{-1} in Eppendorf. The solutions were heated at 90°C during 5 min to dissolve the collagen. 50 µg of collagens samples were dissolved in 30 µl of laemmli buffer (4% SDS, 20% glycerol, 50 mM DTT, 0.004% bromophenol blue and 0.125 M Tris HCl, pH approx. 6.8) and heated 5 min at 90°C. Collagens were separated on one-dimensional SDS-polyacrylamide gel electrophoresis. SDS-polyacrylamide gel was performed using standard methods on the Invitrogen SureCast™ system (10 cm × 10.5 cm minigels). The SDS–PAGE was carried out with 4% stacking gel and 12% resolving gel for the separation of recombinant collagen and the 10% polyacrylamide gels was used for the separation of bovine skin collagen. Dextran 500 kDa was incorporated in SDS–PAGE to improve the separation [478]. The voltage of power supply was set at 200 V for 60 min. The gel was stained with Coomassie Brilliant Blue R-250 for 120 min, then the stained gel was destained using a destaining solution (water/ethanol/acetic acid, 7:2:1, v/v/v). PageRuler Plus prestained protein ladder (Themoscientific, Baltics, UAB) was used to determinate the molar mass of proteins.

7.4.10 In gel tryptic digestion

The protein bands were excised from the gel and the gel slices were rinsed with a mixture of acetonitrile/ammonium bicarbonate (50 mM, pH 8.8) (50/50, v/v), then dehydrated with 100% acetonitrile. The gel slices were subjected to reduction of disulfide bonds by 10 mM DTT, 50 mM ammonium bicarbonate (pH 8.8) at 56°C at 45°C for 1 h.

Alkylation step was then performed with 55 mM iodoacetamide, 50 mM ammonium bicarbonate (pH 8.8) at room temperature for 1 h in the dark. Before trypsin digestion, the gel slices were washed tree times with a mixture of acetonitrile: 50 mM ammonium bicarbonate (v/v) and dehydrated with acetonitrile. The gel slices were dried for 30 min at room temperature. Trypsin digestion was finally performed by incubating the gel slices with 25 µL of trypsin solution (20 µg of Trypsin Gold; Promega with 1 mL of 50 mM ammonium bicarbonate pH 8.8) during 15 min at 4°C. The excess of solution was discarded and 50 µL of 50 mM ammonium bicarbonate pH 8.8 were added on gel slices and incubated 16 h with shaking in a heating block tube (MHR23, Hettich, Netherlands) overnight at 37°C. Following digestion, the tryptic digested fragments present in the supernatant were collected. The gel slices were dehydrated with 100% acetonitrile containing 0.1% TFA for 30 min and the solution was added in the supernatant. The extracts were finally dried in a SpeedVac™ Concentrator (EppendorfTM Concentrator Plus, Eppendorf) and dissolved in a solution of 0.1% FA for mass spectrometric analysis.

7.4.11 LC-MS/MS of in gel tryptic digestion

LC-MS/MS protein analysis was performed on an Orbitrap Q Exactive plus Mass Spectrometer hyphenated to a U3000 RSLC Microfluidic HPLC System (ThermoFisher Scientific). 1 µL of the peptide mixture was injected with a solution A (5% acetonitrile, 94.9% H_2O and 0.1% FA) for 3 min at a flow rate of 5 $\mu L \cdot min^{-1}$ on an Acclaim PepMap100 C18 pre-column (5 µm, 300 µm i.d.×5 mm) (ThermoFisher Scientific). The peptides were next separated on a C18 Acclaim PepMap100 C18 reversed phase column (3 µm, 75 mm i.d. × 500 mm) (ThermoFisher Scientific), using a linear gradient (5-40%) from solution A to solution B (75% ACN and 0.1% formic acid) using a flow rate of 250 $mL \cdot min^{-1}$ in 50 min followed by 100% solution B for 5 min and then re-equilibrated with solution A during 10 min. The column and the pre-column were placed in an oven at a temperature of 45°C. The total duration of the analysis was 70 min. The LC runs were acquired in positive ion mode. MS scans for DDA were acquired from m/z 350 to 1500 in the Orbitrap mass analyzer with a 70000 resolution with maximum injection time of 100 ms and AGC target of 1×10^6. MS/MS scans were sequentially acquired in the high-energy collision dissociation cell for the 15 most-intense ions detected in the full MS survey scan. For MS/MS the resolution was set to 35000 with maximum injection time of 140 ms and AGC target of 5×10^5 and the normalized collision energy was set to 28 eV. Dynamic exclusion was set at 30 s and ions with 1 and more than 8 charges were excluded.

Identification of protein in SDS-PAGE. The raw data from LC-MS/MS were processed by Proteome Discoverer version 2.2 (Thermo Scientific) with a SEQUEST search engine against Bos taurus database from Swiss-Prot (37512 sequences, version june 29, 2020) and the sequence of the recombinant collagen. Proteins and peptides were identified and quantified with the same parameters than section 7.4.7.

7.4.12 Structural 3D-prediction of proteins via I-TASSER

For the 3D protein structure prediction of the proteins, the online I-TASSER platform was used (https://zhanglab.ccmb.med.umich.edu/I-TASSER/). The I-TASSER procedure follows the sequence-to-structure-

to-function paradigm and involves four steps: (1) retrieving template proteins of similar folds from the protein data bank (PDB) library by LOMETS, (2) fragment structure reassembly by replica-exchange Monte Carlo simulations, (3) atomic level structure refinement using REMO and FG-MD, and 4) structure-based function interpretations using COFACTOR [479–481].

The primary amino acid sequences of our proteins RCPhC1, COL1α1 and COL1α2 were submitted to the I-TASSER server, which each took 2-4 months to model. The sequences were submitted as such and thus no advanced options were used like specifying distance constraints nor structure templates to assist in modeling, excluding some templates from the I-TASSER template library and specifying secondary structure for specific residues.

The results from the I-TASSER simulation that are relevant to us in this paper include:

- Up to five full-length atomic predicted models ranked based on cluster density via SPICKER. The confidence of each model is quantitatively measured by a C-score, a confidence score for estimating the quality of the predicted models by I-TASSER, in the range of 2 to -5, with higher values signifying high model confidence. It is calculated based on the significance of threading template alignments and the convergence parameters of the structure assembly simulations.
- Predicted secondary structures
- Predicted solvent accessibility
- Top 10 threading templates from LOMETS
- Top 10 proteins in PDB which are structurally the closest to the predicted models with a TM-score for the first model. The TM-score is a scale for measuring the structural similarity between two structures [482] with a value > 0.5 indicating a model of correct topology and a value of < 0.17 meaning a random similarity.

Our simulation data have been uploaded and can be accessed through the RSCB PDB protein bank (https://www.rcsb.org/#Category-deposit).

The generated PDB models from each protein were then visualized with Pymol 2.4 (Version 2.4.1). Each model is presented in cartoon and solvent surface accessibility view, and a consistent color code is implemented on all 3D-protein representations showing helices (red), sheets (yellow), loops (green (cartoon view)), RGD sequences at the surface (orange), protein surface (green (surface view)), lysine residues in the structure (magenta) and modified lysines (cyan). RCPhC1 is considered not to possess immunogenicity [483], and the 3D structural conformation of RCPhC1 as presented by this 3D model does not raise antibodies.

7.5 Results and discussion

In a first part, RCPhC1 and its derivative (i.e. methacrylamide-modified RCPhC1, RCPhC1-MA) were investigated. In proteomic analysis, the identification of the proteins is based on a partial sequence analysis with the aid of databank matching tools, or with the aid of an exactly known amino acid sequence as is the case for RCPhC1 [471]. Therefore, RCPhC1(-MA) acted as a proof-of-concept for evaluating proteomic analysis as characterization tool to study functionalized biopolymers. In a next step, the same protocol was used to analyze COL BS and its derivative (i.e. methacrylamide-modified COL BS, COL-MA BS) to prove that the proteomic analysis is also applicable to more complex samples with an unknown amino acid sequence.

7.5.1 Recombinant collagen (RCPhC1)

The potential of RCPhC1 as a source of hydrogel-based material for tissue engineering and regenerative medicine applications has already been shown by Tytgat *et al.* [440] and Fushimi *et al.* [483]. In this study, RCPhC1 was functionalized with methacrylamide moieties which enable UV-induced crosslinking to form networks in the presence of a photo-initiator. Two RCPhC1 derivatives were targeted namely with a lower and a higher degree of substitution (DS), based on literature [440]. Herein, 0.5 and 1 equivalents of MeAnH were added with respect to the number of lysine groups present. Because there are no available hydroxylysine nor ornithine groups in RCPhC1, only lysine groups were taken into consideration for functionalization (Table 7.1). A total of 33 lysine groups are present in RCPhC1 and could thus potentially be modified.

Table 7.1. Overview of the amino acid composition of RCPhC1.

AA	Number	%	mmol·g^{-1}
Ala	88	15.4	1.72
Cys	0	0.0	0.00
Asp	33	5.8	0.64
Glu	24	4.2	0.47
Phe	0	0.0	0.00
Gly	191	33.5	3.73
His	0	0.0	0.00
Ile	6	1.1	0.12
Lys	33	5.8	0.64
Leu	33	5.8	0.64
Met	9	1.6	0.18
Asn	0	0.0	0.00
Pro	100	17.5	1.95
Gln	12	2.1	0.23
Arg	33	5.8	0.64

Ser	0	0.0	0.00
Thr	0	0.0	0.00
Val	9	1.6	0.18
Trp	0	0.0	0.00
Tyr	0	0.00	0.00
hydroxyLys	0	0.00	0.00
Ornithine	0	0.00	0.00

(a) Determination of the molar mass (MM) of RCPhC1 and its derivative

^{1}H-NMR spectroscopy and OPA do not allow the determination of the MM of RCPhC1. For polymers with a MM > 25 kDa [484], the determination of the MM by ^{1}H-NMR spectroscopy can be intractable because the resolution is diminished and the NMR spectra are too complex for natural biopolymers [484,485]. The OPA assay is used to measure the amount of primary amines in a sample, and is thus not appropriate for the determination of the MM.

Based on the known amino acid sequence of RCPhC1 (Table 7.1), the theoretical MM could be calculated. The unmodified RCPhC1 shows a MM of 51185 Da (Table 7.2). MALDI-TOF analysis was used in order to confirm the theoretical MM and (the type of) PTMs (possibly) present in the analyzed samples (e.g. phosphorylations, glycolysations, etc.). This technique can be used on RCPhC1 because the MM of RCPhC1 is less than 150 kDa [486]. The intact protein analysis of the recombinant collagen showed a measured MM of 51188 Da (Figure S7.2), closely matching the theoretical MM of 51185 Da. The number of modified lysines is zero for the unmodified RCPhC1. Additionally, the analysis showed that the recombinant protein does not have any naturally occurring PTMs (e.g. oxidations, deaminations). Analysis of the RCPhC1 protein modified with MA photo-crosslinkable groups (RCPhC1-MA) targeting a low and a high DS (i.e. by addition of 0.5 and 1 EQ MeAnH) showed higher MM of 52280 Da and 53380 Da, respectively. One MA modification increases the mass of the protein with +68.0 Da, corresponding to the incorporation of one $C_4H_4O_1$ moiety on one lysine entity. RCPhC1 (unmodified) has 33 lysines in its amino acid sequence, whereas the intact mass analysis of the RCPhC1 derivatives (RCPhC1-MA) showed the presence of 16 and 32 modified lysines upon adding respectively 0.5 and 1 EQ MeAnH. The measured and theoretical MM of RCPhC1 are shown in Table 7.2.

Table 7.2. Theoretical and measured molar mass of RCPhC1 obtained by MALDI-TOF. The theoretical molar mass of RCPhC1 is calculated from the sequence of its amino acids (https://web.expasy.org/protparam/).

	Theoretical MM [Da]	Measured MM [Da]	Number of modified primary amines [n]
Unmodified RCPhC1	51185	51188	0
RCPhC1-MA 0.5 EQ	52205	52280	16
RCPhC1-MA 1 EQ	53429	53380	32

Polyacrylamide SDS-PAGE gel analysis showed a MM for the RCPhC1 protein of roughly 50 kDa (Figure S7.3). This is in agreement with literature [483]. The MM of the protein increases with an increase in the number of methacrylamides incorporated. These SDS-PAGE data are thus in correlation with the data obtained by MALDI-TOF. The digestion of the gel bands allowed the identification of the RCPhC1 protein in the gel bands (Supplementary Data Table 1). Peptides carrying a methacrylamide were identified in the gel bands corresponding to RCPhC1-MA 0.5EQ and RCPhC1-MA 1EQ.

In conclusion, MALDI-TOF analysis is the only suitable technique (of the techniques discussed in this chapter: ^{1}H-NMR, OPA, MALDI-TOF and SDS PAGE) for the accurate determination of the MM of (functionalized) RCPhC1. Other suitable techniques that would allow the determination of the MM include (1) gel permeation chromatography (GPC), which are used rather for qualitative than for quantitative analysis [487,488], (2) membrane osmometry [488,489], (3) intrinsic viscosimetry in combination with static/dynamic light scattering (can be further combined with ultracentrifugation) [489–496], and (4) a top-down method in proteomics using high resolution mass spectrometry [497,498]. Although all these techniques would allow the determination of the MM, herein, we have selected the most commonly applied methods in the state-of-the-art [264,468].

(b) Identification and localization of the modified groups in the amino acid sequence of RCPhC1-MA

The RCPhC1 was digested by two different enzymes (that cut collagen at different sites) to improve the coverage, identification of the sequence and quantification of the modification [499]. Trypsin cuts after lysine (K) and arginine (R), while endoproteinases GluC cut after glutamic (E) and aspartic acid (D). The shotgun proteomic analysis identified 100% of the RCPhC1 sequence that contained 571 amino acids and provided a theoretical MM of 51185 Da. The coverage of the sequence of RCPhC1-MA was found to be 100% for both types of digestions (Table 7.3). However, the proteomics approach identified more peptides in unmodified RCPhC1 compared to RCPhC1-MA 0.5 EQ and RCPhC1-MA 1 EQ, for both types of digestion. This difference may be explained by steric hindrance due to the introduced MA groups or unreachable sites in the protein structure (see section 7.5.1 (d)). The number of identified peptides (Table 7.3) corresponds to the number of digested peptides with and without chemically introduced modifications, showing a high coverage percentage.

Table 7.3. Number of identified peptides and percentage of coverage for RCPhC1 from trypsin and GluC digestion by LC-MS/MS.

		RCPhC1	RCPhC1-MA 0.5 EQ	RCPhC1-MA 1 EQ
Trypsin digestion	Peptides	40	30	26
	Coverage (%)	100	100	100
GluC digestion	Peptides	56	37	39
	Coverage (%)	100	100	100

The number of missed cleavages observed is between 0 to 5 sites for trypsin and 0 to 6 for GluC (Figure 7.4). The average size of the peptides after digestion with trypsin is 2,340 Da and 3,550 Da for GluC. This result was anticipated because the number of lysine and arginine is higher than the number of glutamic acids, which induces a longer peptide size for GluC.

Figure 7.4 shows a slight increase in the percentage of missed cleavages (3, 4, 5) for trypsin digestion, and (3,4) for GluC, when comparing the MA-modified RCPhC1 to unmodified RCPhC1 protein. This could be explained by the steric hindrance of the MA groups present near the trypsin cleavage site (after the lysine groups), and the fact that the size of the MA group can also hinder the cleavage by GluC.

The analysis indicated the presence of peptides containing 1 up to 3 MA moieties. An increase in missed cleavages makes the peptides (to be identified) larger in size and therefore these larger peptides can contain more than one lysine. Moreover, a trend was seen between the number of missed cleavage sites and the number of MAs introduced onto lysines (Figure S7.4). When more MA groups were present in the sequence, an increase in the number of missed cleavages was detected. Both trypsin and GluC digestion showed a clear linear correlation with a higher missed cleavage with increasing modification, most likely due to steric hindrance of the enzyme.

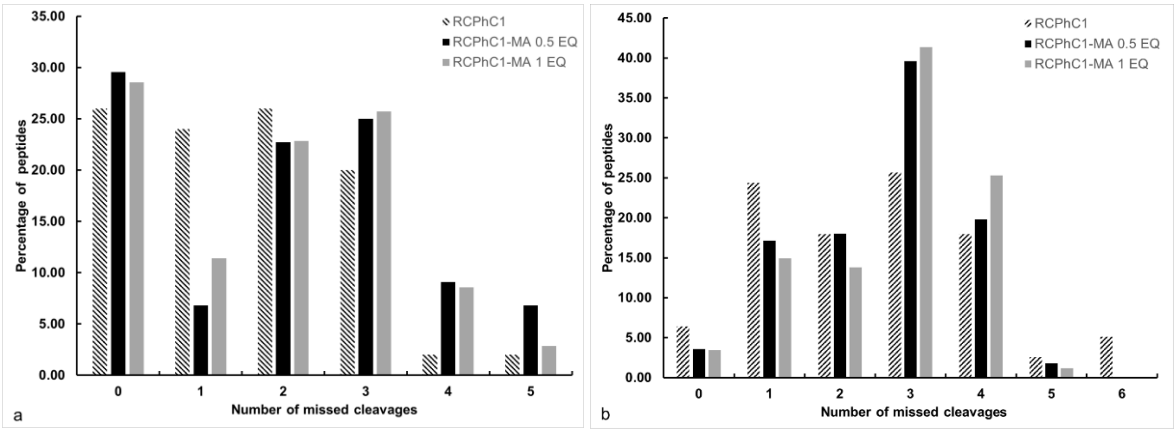

Figure 7.4. Histogram of the percentage of missed cleavages of peptides for RCPhC1 and its derivatives by trypsin digestion (a) and GluC digestion (b). The percentage of missed cleavages is obtained based on the ratio of the peptides with a missed cleavage identified by LC-MS/MS over the total number of identified peptides.

The LC-MS/MS analysis confirmed that there are no identified MA sites in the unmodified RCPhC1. The analysis of RCPhC1-MA 0.5 EQ and RCPhC1-MA 1 EQ indicated that all lysine groups were MA modified lysines for both digestions, but at a different modification frequency (*vide infra*, section 7.5.1 (c)). Correlating these results with MALDI TOF indicates that on average 16 lysines are modified in case of RCPhC1-MA 0.5 EQ. This means that there are isoforms possible of RCPhC1-MA 0.5 EQ with 16 modified lysines, but at variable positions (see Figure 7.8, c-d; section 7.5.1 (d)). In case of RCPhC1-MA 1 EQ, LC-MS/MS showed that all lysines groups were modified.

LC-MS/MS analysis also enables to determine the position of the MA functional groups. Figure 7.5 shows the fragmentation of the peptide GAAGLPGPKGERGDAGPK. It is possible to localize the modification by observing a

specific fragment obtained by MS/MS corresponding to the amino acid carrying the modification. Herein, HCD fragmentation (see section 7.4.6) leads to the formation of b (N-terminal) and y (C-terminal) charged fragment ions. The MS/MS spectrum from the peptide GAAGLPGPKGERGDAGPK with one or two MAs can be compared with the MS/MS spectrum of the unmodified peptide (Figure 7.5, red spectrum). The MS/MS spectrum with one MA in Figure 7.5 (a, blue spectrum) allowed the localization of the modifications at the C-terminal due to the series of b and y ions, because there is no fragment corresponding to lysine at position 9 with a MA group. The b11 and y11 ions made it possible to show that the lysine at position 9 did not carry a MA group. The MS/MS spectrum in Figure 7.5 (b, green spectrum), showed that all available lysines in the peptide were modified. The spectrum allowed the identification of the MA on lysine in positions 9 and 18 on the sequence peptide GAAGLPGPKGERGDAGPK because the y11 ion at *m/z* 1150.5847 corresponds to the MA group on the lysines.

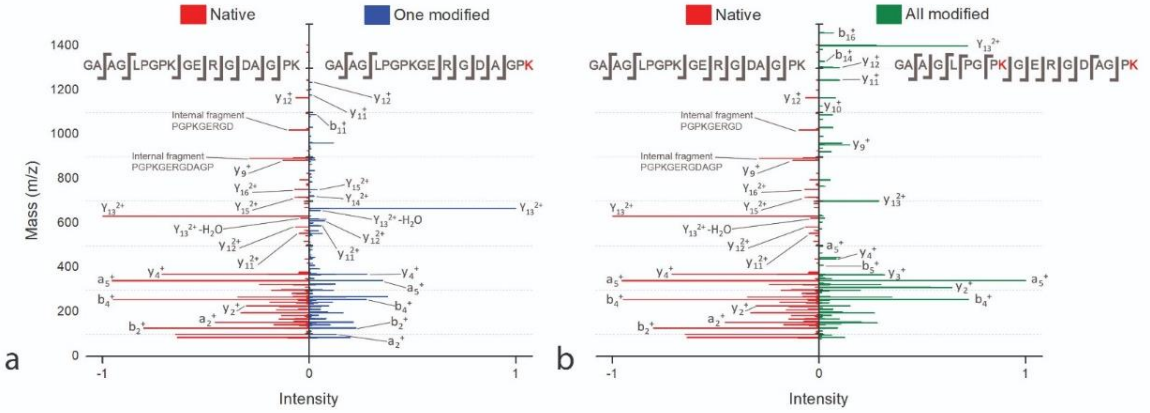

Figure 7.5. MS/MS of peptide GAAGLPGPKGERGDAGPK. Panel (a) shows the fragmentation of native peptide (red) and the modified peptide with 1 methacrylate on lysine in C-terminal position (blue). Panel (b) shows the fragmentation of native peptides (red) and peptides with all methacrylated lysines (green).

On the one hand, the shotgun proteomic analysis highlights that there are isoforms of the RCPhC1 with different positions of the MA groups. On the other hand, the results showed that there are redundant (or repetitive) peptide sequences in the complete RCPhC1 sequence. This presents an additional challenge when identifying the exact position of the MA groups in the sequence. For example, the LC-MS/MS analysis identified the peptide GAAGLPGPKGERGDAGPK with a modified lysine (after trypsin digestion) but this peptide was identified at different positions in the RCPhC1 sequence, namely positions [22-39]; [58-75]; [100-117]; [157-174]; [211-228]; [247-264]; [289-306]; [346-363]; [400-417]; [436-453]; [478-495]; [535-552].

Furthermore, the incorporated MA groups might influence the ionization of the peptides, that can in turn lead to a decrease in sensitivity. Nevertheless, even though the number of identified peptides decreased (upon increasing the number of incorporated MA groups), the sensitivity remained sufficiently high to reach a sequence coverage of 100%, for all analyzed samples (i.e. RCPhC1, RCPhC1-MA 0.5 EQ and RCPhC1-MA 1 EQ) [500].

In conclusion, the shotgun proteomic analysis is the only technique that enables: (1) the identification of the fragmented peptides, and (2) the determination of the exact location of the MA-modified amino acids in the amino acid sequence. In case of RCPhC1 however, one major challenge was identified using the shotgun proteomic analysis, namely the occurrence of redundant peptides.

(c) Determination of the degree of substitution (DS) of modified RCPhC1

The DS of the developed RCPhC1 derivatives can be determined via ^{1}H-NMR spectroscopy [440]. The ^{1}H-NMR spectra of modified RCPhC1 showed characteristic peaks at 5.75 and 5.55 ppm which correspond to the vinyl protons of the introduced MA functional groups. The DS was quantified by comparing the integration of these characteristic peaks (i.e. 5.75 and 5.55 ppm) to the integration of the methyl protons present in Val, Leu and Ile, (i.e. at 1.01 ppm) which are chemically inert during modification (Figure S7.1, a-b) [262]. Based on ^{1}H-NMR spectroscopy, the addition of 0.5 and 1 equivalents MeAnH (i.e. RCPhC1-MA 0.5 EQ and RCPhC1-MA 1 EQ) resulted in a DS of 53.7% [0.346 mmol·g^{-1} of available photo-crosslinkable MA groups] and 93.3% [0.597 mmol·g^{-1}], respectively.

In addition to ^{1}H-NMR spectroscopy, an OPA amine quantification assay was performed on RCPhC1 and its derivatives to determine the number of primary amines available prior to and after functionalization. By comparing those two values, the DS and thus the number of introduced crosslinkable groups can be determined. Based on the OPA assay, the DS values of RCPhC1-MA 0.5 EQ and RCPhC1-MA 1 EQ were 51.9 ± 1.6% and 99.2 ± 0.2%, respectively. The result of RCPhC1-MA 0.5 EQ are comparable to those obtained via NMR (i.e. 53.7%). For the 1 EQ derivative, there is a minor discrepancy between both techniques. Compared to ^{1}H-NMR spectroscopy, the OPA assay is based on the difference of the number of primary amines available before and after functionalization, and may therefore be seen as the most accurate technique for the determination of the DS [501,502].

Based on MALDI-TOF analysis, the measured MM could be determined for the original (unmodified) RCPhC1 showing 33 unmodified lysines, versus the modified RCPhC1 (Table 7.2) showing 16 and 32 modified lysines for RCPhC1-MA 0.5 EQ and 1 EQ respectively. The latter corresponds to a DS of 50.0% and 97.0% for RCPhC1-MA 0.5 EQ and 1 EQ, respectively.

When performing the proteomic analysis, the quantification method (LC-MS/MS) is based on a label-free method, that aims at determining the relative amount of proteins and peptides in two or more biological samples. In other words, the quantification by LC-MS/MS was performed by carrying out the ion extraction of the modified and unmodified peptides in the samples (Figure 7.6).

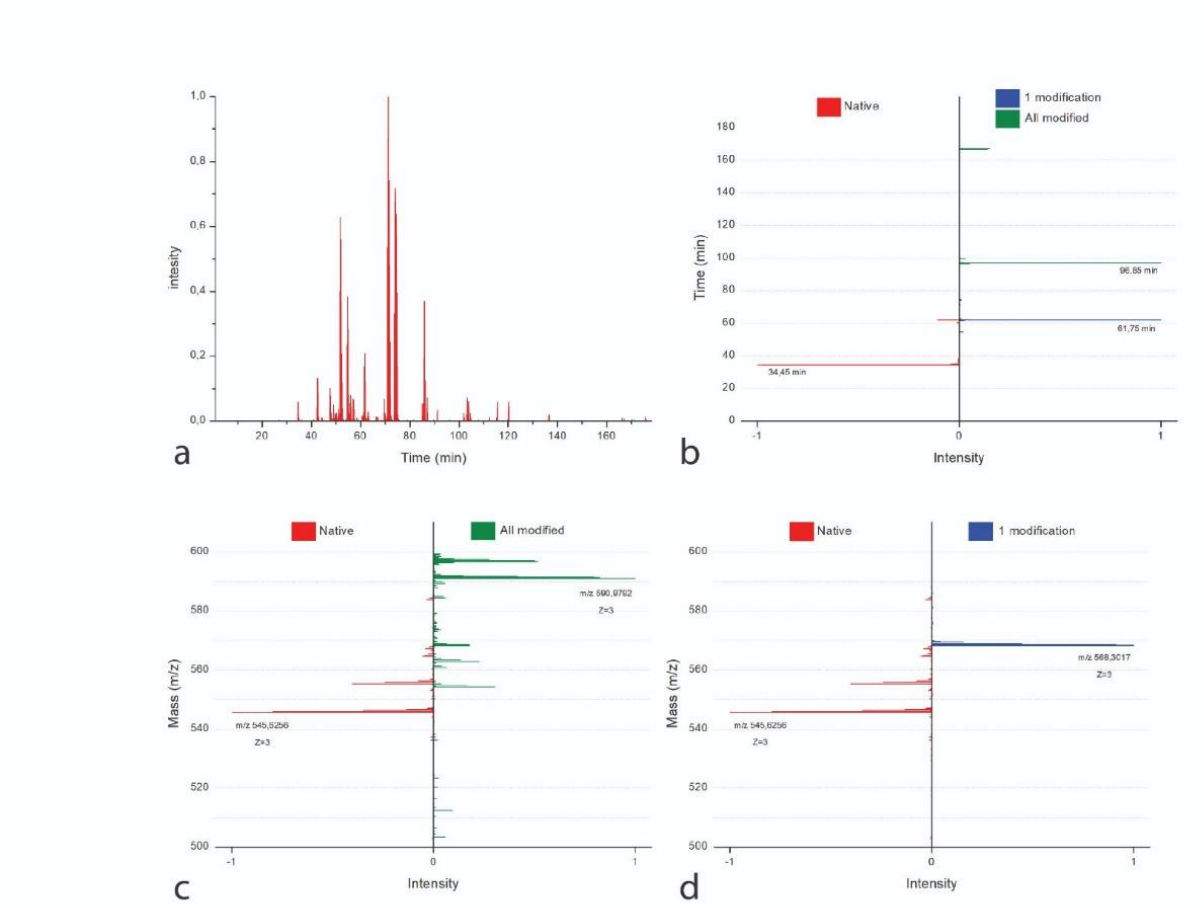

Figure 7.6. Ion extraction chromatogram of the peptide GAAGLPGPKGERGDAGPK (as an example) with and without MA groups in RCPhC1-MA 1 EQ. Panel (a) shows the total ion extraction chromatogram. Panel (b) shows the retention time (RT) and corresponding signal intensity of the unmodified peptide (red, RT 34.45 min) versus 1 lysine modification (blue, 61.75 min) and all lysines modified (green, 96.85 min). Panel (c) and Panel (d) show mass (m/z) with z = 3 and the corresponding signal intensity of the unmodified peptide (red, m/z 545.6256) versus all lysines modified (c, green, m/z 590.9792) and versus 1 lysine modification (d, blue m/z 568.3017), respectively.

Figure 7.6 shows the signal intensity of the unmodified peptide (red), the peptide functionalized with one MA (blue) and the peptide with all lysines functionalized with MAs extracted from the total ion extraction spectrum of the RCPhC1-MA 1 EQ sample. This analysis showed a different retention time depending on the peptide containing one MA, the maximum amount of MAs or no MA (i.e. unmodified). This difference was caused by the introduction of MA groups, modifying the physico-chemical properties of the peptide thereby leading to a shift in retention time (Figure 7.6, a-d).

Using both the Proteome Discoverer 2.2 software and the Minora quantification node, the peptides of the samples were quantified for the RCPhC1, RCPhC1-MA 0.5 EQ and RCPhC1-MA 1 EQ samples. The software extracted the intensity of the peptides, allowing the comparison between samples. The number of quantified peptides with one or more MA modifications was determined to be 34 for the trypsin digestions and 66 for the GluC digestions. These numbers included the peptides with oxidations on methionine, deamination of asparagine and glutamine and peptides with missed cleavages. Supplementary Data Table 2 provides a list of all quantified peptides.

In addition, quantitative proteomic analysis provides information on the frequency of the modifications at one specific location (i.e. one specific AA in the AA sequence). The modification frequency can be defined as the probability that a certain peptide can be modified and is calculated with Equation 7.1 (section 7.4.7). In general, the quantification by LC-MS/MS showed a higher frequency of modification for RCPhC1-MA 1 EQ than for RCPhC1-MA 0.5 EQ. This can be deduced from the peptide frequency histogram (Figure 7.7). The majority of peptides in RCPhC1-MA 1 EQ have shown a modification frequency close to 100%, indicating that all lysine groups present in RCPhC1-MA 1 EQ were almost completely modified (i.e. a DS close to 100%). The latter is in excellent agreement with the data obtained from MALDI-TOF (i.e. DS of 97.0%), OPA (i.e. DS of 99.2%) and NMR spectroscopy (i.e. DS of 93.3%). For RCPhC1-MA 0.5 EQ, the modification frequency of the modified lysines was lower. For example, the peptide GAAGLPGPKGER containing one MA identified on the lysine group after trypsin digestion, exhibited a modification frequency of 45% for RCPhC1-MA 0.5 EQ and 90% for the RCPhC1-MA 1 EQ (Figure 7.7, a). The co-elution of the peptides can affect the quantification of the chemical modification independently of the quantification methods used, therefore, proteomics analysis as a stand-alone technique is not ideal for the exact quantification of the DS [503].

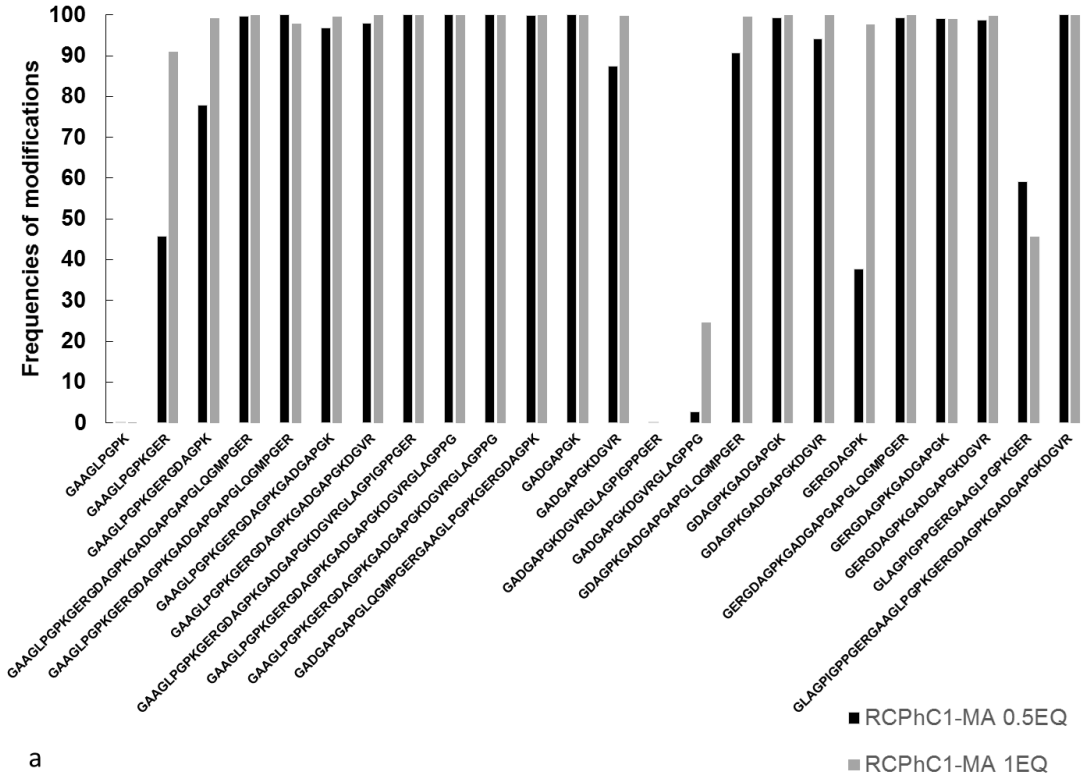

a

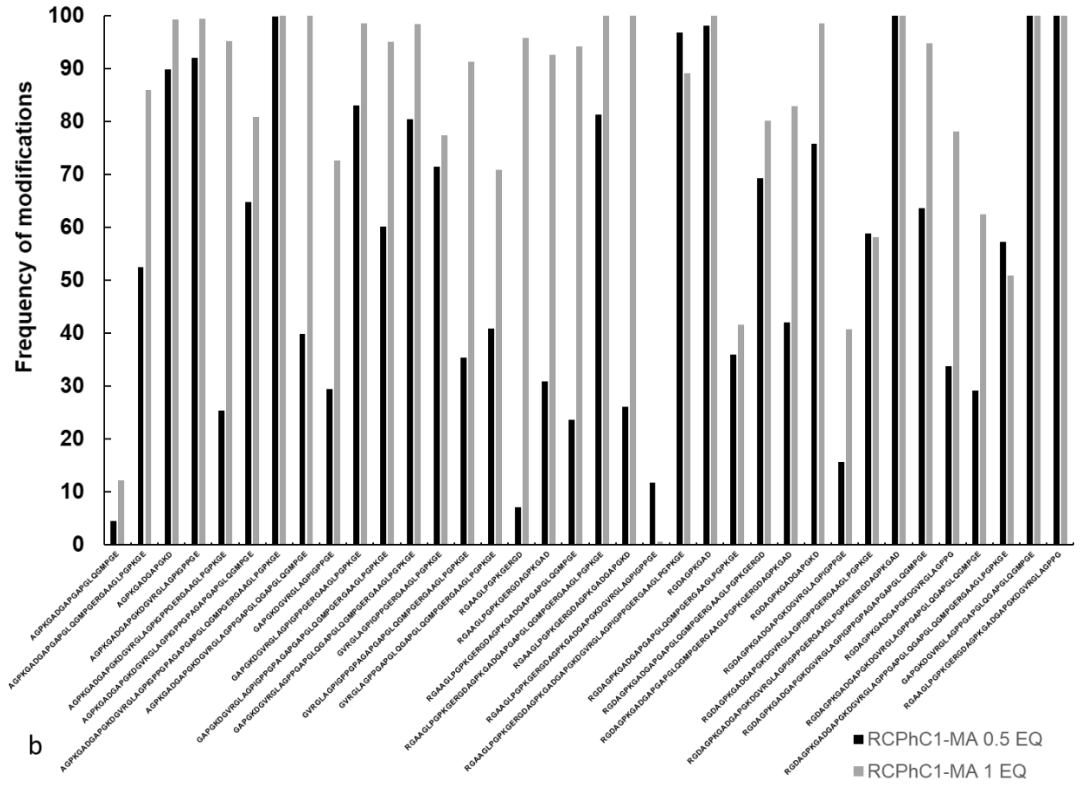

Figure 7.7. Histogram of frequency of MA modification (on lysines) for peptides resulting from cleavage with enzyme Trypsin (a) and GluC (b). Black bars correspond to RCPhC1-MA 0.5 EQ and grey bars to RCPhC1-MA 1 EQ.

On the one hand, some peptides contained certain lysine positions that had a 100% modification frequency in both the low and high DS RCPhC1-MA (i.e. RCPhC1-MA 0.5 and 1 EQ). On the other hand, some peptides were not modified in either of the RCPhC1-MA derivatives. An example is the peptide GAAGLPGPK, that did not constitute a modified lysine in either of the derivatives. An explanation could be that this peptide was frequently found to have 1 or 2 missed cleavages, indicating that either the MA modification or the position of the lysine in the overall structure of RCPhC1 (i.e. inner versus outer side of the protein's structural conformation, *vide infra*) interferes with the function of the enzyme. A similar result was observed for the frequency of MA upon GluC digestion (Figure 7.7, b). The majority of peptides in RCPhC1-MA 1 EQ showed a modification frequency close to 100%, which shows that the lysine groups in RCPhC1-MA 1 EQ were almost completely modified.

Using shotgun proteomic analysis for the calculation of the DS of RCPhC1-MA is more challenging as the identification is complex due to the presence of redundant peptides (i.e. more challenging to identify them in the AA sequence because of repeating units) and because a higher DS results in more steric hindrance interfering with the enzyme function. Casey *et al.* [504] have already shown that chemical derivatization can modify the charge state distribution and the ionization. In one case, chemical derivatization was even shown to enhance the ionization of the peptide [505]. It can be concluded that for a protein of this size (i.e. RCPhC1, MM of 53 kDa), MALDI-TOF is the most sensitive and thus preferred technique to determine the DS.

As described above, proteomic analysis enabled to determine the modification frequency at one specific position in the sequence. Based on these modification frequencies, an estimation of the DS becomes possible. In order to increase the accuracy of the identification and quantification using proteomic analysis, the results of the analyses using two different types of digestion enzymes (trypsin and GluC) were combined. The average of the DS obtained by shotgun proteomics was 66.2% for RCPhC1-MA 0.5 EQ and 81.7% for RCPhC1-MA 1 EQ. Table 7.4 shows the DS based on the different techniques applied.

In conclusion, proteomics is not an accurate technique to determine the exact DS, but only enables to determine an average DS, based on the modification frequencies. However, as stated in section 7.5.1 (b), one of the aforementioned „conventional" techniques (i.e. MALDI-TOF, OPA or ^{1}H-NMR) combined together with proteomic analysis makes it possible to fully characterize RCPhC1 and its derivatives.

Table 7.4. Overview of the obtained data for RCPhC1-MA 0.5 and 1 EQ: Determination of the molar mass using MALDI-TOF and determination of the degree of substitutions (DS) using MALDI-TOF, 1H-NMR spectroscopy (based on the known amino acid composition), OPA assay and shotgun proteomic analysis.

	MM obtained by MALDI-TOF [kDa]	DS obtained by MALDI-TOF [%]	DS obtained via ^{1}H-NMR (based on known AA composition) [%]	DS obtained via OPA [%]	DS obtained by shotgun analysis [%]
RCPhC1-MA 0.5 EQ	52.28	50.0	53.7	51.9 ± 1.6	66.2
RCPhC1-MA 1 EQ	53.38	97.0	93.3	99.2 ± 0.2	81.7

(d) Localization of modified amino acids in the 3D-structure of RCPhC1 modified biopolymers

To gain insight in the 3D-conformation of RCPhC1 and its derivatives, the I-TASSER server was used to model the 3D structure of RCPhC1 (see section 7.4.12). These 3D-models cannot be confirmed by X-ray studies and should be treated as possible folding configurations. However, the I-TASSER has a strong history of predicting simulation models close to X-ray confirmed models. The I-TASSER provides different models that are ranked according to a c-score (i.e. a confidence score for estimating the quality of the predicted models) with the first ranked model being the most reliable. The first model of RCPhC1 had a c-score of 0.44 and the estimated TM-score and root mean square deviation (RMSD) were 0.77 (± 0.10) and 6.6 (± 4.02Å) respectively, signifying a high confidence in the model.

For RCPhC1, the obtained 3D-model is presented in Figure 7.8 (a), showing the occurrence of helices (red) and sheets (yellow) in the main structure of the protein. In contrast to native COL1α1 (Figure 7.8, a-b), the RCPhC1 derivative consists of considerably higher amounts of sheets and less helices. This is in accordance with the study of Fushimi *et al.* [483] in which the secondary structure of RCPhC1 was characterized by circular dichroism and based on a sequence-derived *in silico* model. This could be due to (i) the introduction of multiple RGD sequences

in the sequence causing repetition (Figure S7.5), (ii) its high content in alanine, glycine and proline, and/or (iii) the absence of hydroxyprolines in RCPhC1. This also explains why the second model that is predicted by I-TASSER has the same c-score as the first model and only contains β-sheets (Figure S7.6, a and b). This second model will not be discussed herein as it resembled to a lesser extent the structure of COL1α1.

The predicted model for RCPhC1 showed a good spatial distribution of the introduced RGD sequences in the protein, favoring optimal cell interaction [466,506], which is important for TE applications (Figure 7.8, b, orange). More importantly, a good spatial distribution was observed for the lysines present in the amino acid sequence of the protein (Figure 7.8, b, magenta), which is vital for the network formation of the functionalized proteins into crosslinkable materials after modification. This assumption is strengthened by the ability to form a solid and strong crosslinked biomaterial exploiting these protein derivatives as starting materials [440].

For RCPhC1-MA 1 EQ, it was shown that all lysines were modified (DS 100%), meaning that all magenta colored lysines can be colored in cyan in Figure 7.8 (b). For RCPhC1 EQ 0.5, however, only 50% (based on MALDI-TOF, Table 7.4) of the lysines have been modified and obtaining a detailed insight into the modification is extremely challenging. In this respect, two possible isoforms of RCPhC1-MA 0.5 EQ are shown in Figure 7.8 (c and d), as derived from the sequences shown in Figure S7.8.

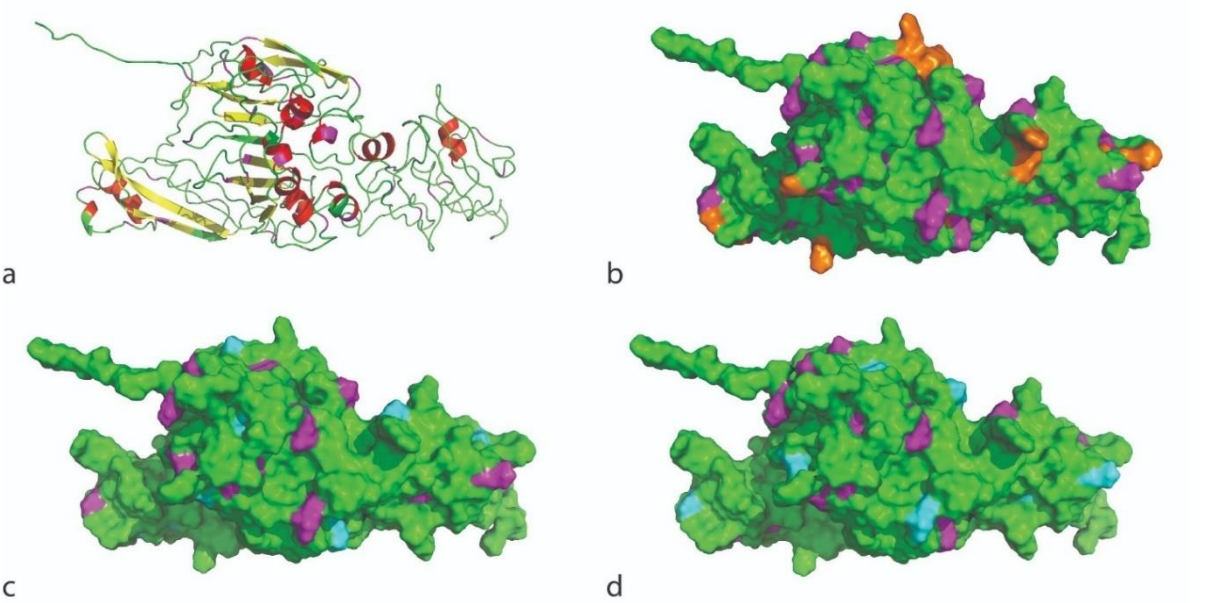

Figure 7.8. The protein 3D-conformation of the sequence of RCPhC1 modelled with I-TASSER; (a) in the cartoon view, showing helices (red), sheets (yellow), loops (green) and lysine residues in the structure (magenta), (b) in the solvent surface accessibility view, showing the protein accessibility surface (green), all lysines on the surface (magenta) and the RGD sequences at the surface (orange). The model in b is also the same as for RCPhC1-MA 1 EQ of which all lysines are modified (magenta = cyan) (Figure S7.7). (c-d) 3D-conformation showing the modified lysines in two RCPhC1-MA 0.5 EQ isomorphs, and the corresponding RCP sequences in Supplementary Information: (c) the first isomorph (Figure S7.8, blue) and (d) the second isomorph (Figure S7.8, yellow), showing the unmodified lysines (magenta) and the modified lysines (cyan).

The two isoforms indicate that the spatial distribution of the modified lysines is somewhat reduced compared to RCPhC1-MA 1 EQ which might imply that the crosslinking efficiency may be reduced. Overall, it seems that all

lysines are accessible in the solvent accessibility view in the protein's pristine condition, meaning that they have almost equal chances of being modified with MA or being cleaved by the enzymes. This also supports the observation that complete modification of the lysines was realized for RCPhC1-MA 1 EQ, along with a successful protein identification (i.e. 100% coverage of identification).

7.5.2 Collagen bovine skin (COL BS)

Exploiting proteomic analysis to quantify and localize the chemical modifications introduced on a recombinant protein RCPhC1 with a known amino acid sequence, was shown to be a successful tool in the study of modified biopolymers. In a next step, the potential of the elaborated proteomics approach was evaluated on "more complex" protein-based biopolymers [465] with an unknown amino acid composition and/or sequence. The main difference between natural proteins and RCPhC1 is that PTMs and amino acid substitutions can occur in natural proteins. Herein, collagen from bovine skin origin (COL BS) was modified with MA-functional groups, resulting in different degrees of substitution (through addition of 0.5 and 1 EQ MeAnH).

(a) Determination of the molar mass (MM) of COL BS and its derivative

The determination of the MM of COL BS by the three aforementioned techniques for RCPhC1 is not possible for several reasons:

- As described in section 7.5.1 (a) for RCPhC1, and keeping in mind that the size of collagen is approx. 6 times larger than RCPhC1, ^{1}H-NMR spectroscopy and OPA do not enable determining the MM of collagen.
- MALDI-TOF is not able to determine the MM of collagen because the MM of collagen is around 300 kDa and the practical limit of conventional MALDI-TOF is around 80 kDa upon ensuring excellent resolution (theoretically to 150 kDa, yet resulting in low resolution) [486]. The MALDI-TOF used in this study only allowed screening of masses of modified proteins in the range of 2 up to 100 kDa approximately [440,507]. It would however be possible to determine the mass of large proteins more precisely with the use of very high resolution mass spectrometers such as FT-ICR [508,509] and the use of fragmentation techniques, making it possible to identify the protein sequence as well as the PTMs [510], by a technique called Top Down [511]. In case of complex proteins, this technique only gives the stoichiometry but not the individual MM.

Polyacrylamide SDS-PAGE gel analysis revealed the typical pattern for type I collagen, with bands corresponding to the MM for COL BS pointing to β (215 kDa), α1 (130 kDa), and α2 (115 kDa) chains [512,513] (Figure S7.9). The collagen contains numerous PTMs such as oxidations and deamidations that increase the MM. Three bands were observed in COL BS which correspond to COL1α1 and COL1α2 while the bands corresponding with a higher MM indicated a mixture of two collagens. The MM of the collagen protein increases with an increase in MeAnH equivalents. The digestion of the gel bands allowed identification of COL1α1, COL1α2, COL3α1, COL2α1. The

mass spectrometry results showed that COL1α2 was the most abundant protein in the band corresponding with the lowest MM (Supplementary Data Table 1). COL1α1 was the most abundant protein in the next band. A band of a high MM compound (± 200 kDa) was observed on the SDS-PAGE gel. The LC-MS/MS analysis of the digested bands corresponding with higher MM showed the presence of COL1α1, COL1α2, COL3α1, COL2α1. The COL1α1 and the COL1α2 were the most abundant proteins. It is hypothesized that this identification showed the crosslinks between collagens. Previous research showed the presence of the crosslinks on the collagen protein and were mainly derived from the allysine route [514,515]. Mass spectrometry analysis showed the presence of peptides with methacrylamides in the gel bands corresponding to COL-MA BS 0.5EQ and COL-MA BS 1EQ.

The shotgun proteomic analysis does not allow the determination of the MM of COL BS directly. However, the theoretical MM of COL BS can be estimated based on the identified proteins (*vide infra*, cfr. 3.2.2) using the Swiss-Prot database (COL1α1 and COL1α2), resulting in an estimated MM of 94673.0 Da for the COL1α1 chain precursor (amino acid 162 until 1217) and 93415.3 Da for the COL1α2 chain precursor (amino acid 80 until 1117). Collagen is constituted of two α1 chains and one α2 chain, thus resulting in an approximate theoretical MM of 282761.3 Da.

(b) Identification and localization of the modified groups in the amino acid sequence of COL-MA BS

The shotgun proteomic analysis enabled the study of more complex samples such as COL BS. By using LC, it became possible to separate the peptides resulting from the tryptic or GluC digestion of the protein. After digestion, a larger number of peptides was cleaved compared to the digestion of RCPhC1 because of the higher MM of COL BS (Figure S7.10). The identification of the most abundant proteins present in COL BS was carried out by querying the total Swiss-Prot database containing 563082 sequences and 13936 taxons. The first identified protein is the collagen α1(I) chain from *Bos taurus,* conforming with the origin of the sample. Then, the identification of the most abundant proteins in COL BS was carried out by querying the *Bos taurus* database of Swiss-Prot. The results indicated that the most abundant proteins are the COL1α1 and COL1α2, amounting for 57% and 28% respectively (Supplementary Data Table 3). The sample also contained low quantities of other proteins like collagen α1(III) chain, collagen α1(II) chain and keratin. LC-MS/MS analysis showed that the *N*- and *C*-terminal pro-peptides are not present in COL1α1 and COL1α2. This indicated that it was the matured protein of COL1α1 and COL1α2 without its pro-peptides ends. Therefore, the LC-MS/MS analysis was carried out on the sequences of the proteins COL1α1 and COL1α2 of *Bos taurus* without the pro-peptides. Table 7.5 shows the number of identified peptides, the percentage of coverage for the COL BS samples from COL1α1 and COL1α2 (*Bos taurus*) for both types of digestion (trypsin and GluC). The number of identified peptides decreased with an increasing number of introduced MA moieties, as was also observed for RCPhC1 (Figure S7.10).

Table 7.5. Overview of the number of identified peptides and the percentage of coverage for trypsin and Gluc digestion from the bovine skin collagen samples. The information is given for the 2 major proteins which are COL1α1 and COL1α2.

		Peptides		Coverage [%]	
		COL1α1	COL1α2	COL1α1	COL1α2
Trypsin digestion	COL BS	127	103	91	92
	COL-MA BS 0.5EQ	119	89	88	81
	COL-MA BS 1EQ	79	75	75	76
GluC digestion	COL BS	92	59	65	54
	COL MA BS 0.5EQ	77	49	60	48
	COL MA BS 1EQ	73	49	56	48

The shotgun proteomics approach allows identifying 91 and 92% of the sequence of COL1α1 and COL1α2 for the unmodified COL BS by trypsin digestion (Figure 7.9) thereby providing very good coverage [516]. However, the coverage decreased upon higher degrees of modification (i.e. COL MA BS 0.5EQ and COL MA BS 1EQ). A similar trend was observed for the GluC digested proteins with an overall coverage (i.e. 65 and 54%) that is lower than for trypsin. However, by combining the two digestions it is possible to obtain more than 90% of coverage for COL BS with and without MA functional groups [517].

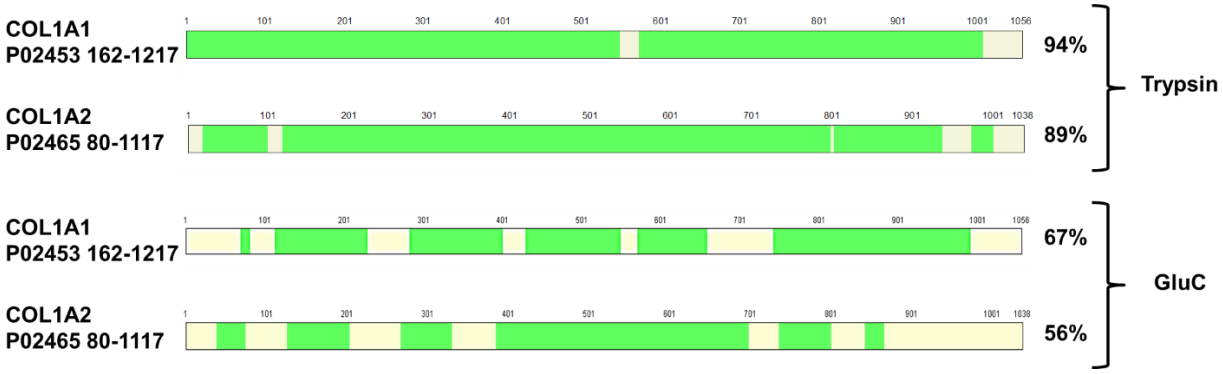

Figure 7.9. Coverage of the identified and quantified peptides on the sequence of COL1α1 and COL1α2 for the samples of COL BS from both digestions. Green areas show the protein sequence coverage. Yellow areas show the non-covered parts of the protein.

The identified peptides (green) were distributed homogeneously along the sequence as shown in Figure 7.9. The number of identified peptides decreases with increasing equivalents of MeAnH addition, thus increasing protein modification (i.e. higher DS). This was also observed for RCPhC1 for which we hypothesized that this was due to steric hindrance of the enzyme and a decrease in ionization. Therefore, we can assume that the MA modifications influence the identification of all types of collagen-based biomaterials. For collagen with trypsin or GluC digestion, the number of missed cleavages varied between 1 and 6 (Figure S7.11-S7.14). The data showed that the longer the peptides were, the larger the number of MAs on the peptide.

This is also visualized in Figure S7.4 where a clear positive trend is visible between the number of missed cleavages and the number of MA's for the three peptides RCPhC1, COL1α1 and COL1α2. This was logical because increasing the number of missed cleavages increased the number of lysines present in the peptide.

Moreover, we have observed a slight increase in the percentage of peptides with 1 and 2 missed cleavages for COL1α1 in the modified collagens (i.e. COL-MA BS 0.5EQ and COL-MA BS 1EQ) compared to COL BS (Figure S7.11 and S7.13), for both digestions. For COL1α2 with trypsin digestion (Figure S7.12), a slight increase in the percentage of peptides with 1, 2, 3 missed cleavages was observed. But for the digestion with GluC (Figure S7.14), a slight increase in the percentage of peptides with 0 missed cleavages has been noticed. We also saw a high percentage of peptides with 0 and 1 missed cleavages.

The results were not identical to those from the analysis of the RCPhC1 protein. COL1α1 (94673.0 Da) and COL1α2 (93415.3 Da) were composed of 38 and 31 lysines respectively, compared to the RCPhC1 protein (51185 Da) which has 33 lysines. The RCPhC1 protein had more lysines compared to collagen COL1α1 or COL1α2 considering the size, which may allow a better action of the enzymes on COL1α1 and COL1α2.

In addition to MA modification, PTMs were observed such as the oxidation of methionine and the deamidation of asparagine and glutamine. These modifications are common in shotgun proteomics approaches on "complex" natural biopolymers [473]. As an example, hydroxyproline was also observed in the analysis of COL BS. These PTMs are common for collagen because they are involved in the structure of the protein, and thus inherently present [463].

Next, the sequence of the different α strands (i.e. COL1α1 and COL1α2) in COL BS was studied, together with the number of modified lysines. The COL1α1 sequence contains a total of 38 lysines, whereas COL1α2 contains a total of 31 lysines (based on Swiss-Prot databases). Table 7.6 shows the numbers of MA-modified lysines identified by LC-MS/MS with trypsin and Gluc digestion.

Table 7.6. The numbers of MA-modified lysines identified by LC-MS/MS with trypsin and Gluc digestion. The MA sites are identified on COL1α1 and COL1α2 from Bos taurus. Based on the AA sequences from the Swiss-Prot database, the total number of lysines for COL1α1 and COL1α2 were 38 and 31, respectively.

		Trypsin digestion	GluC digestion
COL-MA BS 0.5 EQ	COL1α1	30	17
	COL1α2	23	16
COL-MA BS 1 EQ	COL1α1	26	19
	COL1α2	21	15

This enabled the identification of the MA sites on COL1α1 and COL1α2. The sequences of COL1α1 and COL1α2 were reconstructed from the digested peptides and the MA modifications were localized in these sequences. The sequences of COL1α1 and COL1α2 together with the modified lysines for the trypsin and GluC digestion can be found in Supplementary Info (Figure S7.15 and S7.16, Figure S7.17 and S7.18, respectively). The digestion with trypsin and GluC makes it possible to identify a total of 4 unmodified lysines and 34 modified lysines (with MA) in the COL1α1 sequence. For the COL1α2 sequence, digestion with trypsin and GluC resulted in an identification of a total of 6 unmodified lysines and 25 modified lysines. These modifications will be further discussed and shown in the next section 7.5.2 (d), "Localization of modified amino acids in the 3D-structure of the modified biopolymer".

To conclude, proteomic analysis showed that MA modifications were present over the entire sequence of COL BS, determined by using both types of digestion. Moreover, the proteomic analysis identified that the modifications were present on lysine groups, and that the MA-modified lysines were distributed homogeneously over the sequence. This is key in the development of biomaterials with an intentional use for TERM applications, because the distribution of the modified, photo-crosslinkable MA groups affects the crosslinking behavior of the biomaterial. A homogeneously spreading of the modified groups will result in a better crosslinked network (due to the homogeneously spread crosslinks), which will influence the mechanical properties of the biomaterial. In turn, these mechanical properties influence the biological properties (i.e. cell-biomaterial interaction). This highlights the importance of the insights given by proteomic analysis. However, although homogeneous spreading of the lysines over the primary amino acid composition is positive for their distribution, it does not ensure that they will be homogeneously spread in their 3D conformation, hence the study in section 7.5.2 (d).

(c) Determination of the degree of substitution (DS) of modified COL BS

Similar to the analysis of RCPhC1, the COL BS and its derivatives (i.e. COL-MA BS) were analyzed using ^{1}H-NMR spectroscopy (Figure S7.1, c-d). Based on ^{1}H-NMR data, the MA-modification of collagen led to a DS of 76.6 and 103.7% for the COL-MA BS 0.5 EQ and 1 EQ, respectively. The degree of substitution higher than 100% (for the higher DS) can be explained by the fact that the calculations are based on the amino acid composition as found in the Swiss-Prot and NCBi database (which do not give the exact amino acid composition as the COL BS used in this chapter) and the fact that the NMR data might overestimate the DS due to hydroxyl groups that could be modified as well and/or integration errors. Instead of using a database, the amino acid composition can be analyzed in order to know the exact AA composition [368]. Calculating the DS of the COL-MA derivatives using the results from the AA analysis, a DS of 75.9% and 99.6% were obtained for COL-MA 0.5 EQ and COL-MA 1 EQ, respectively.

Based on the OPA assay, the amount of primary amines available for functionalization was found to be 0.252 $mmol \cdot g^{-1}$ in COL BS. For the COL-MA BS 0.5 and 1 EQ, a DS of 74.1% and 95.8% was obtained. An overview of the obtained DS values via the different methods is provided in Table 7.8.

Because it was not possible to perform MALDI-TOF analysis on the COL BS and its derivatives, due to their high MM (> 150 kDa), it was also not possible to determine the DS using our currently available MALDI-TOF.

In addition to the conventional characterization techniques, proteomic analysis was performed on COL BS and its derivatives. The percentage of coverage for COL BS by trypsin digestion was found to be very high (i.e. 91% and 92%), which is important for enabling superior identification and quantification of the modified groups in the AA sequence (Table 7.5, cfr. 7.3.2(b)). Moreover, this method makes it possible to identify almost the entire sequence [518,519].

The numbers of quantified peptides after trypsin digestion of COL-MA BS was 195 for COL1α1 and 106 for COL1α2. LC-MS/MS analysis quantified 32 lysines with a MA on COL1α1 and 24 lysines with a MA on COL1α2. The numbers of quantified peptides after GluC digestion of COL-MA BS was 115 for COL1α1 and 68 for COL1α2. LC-MS/MS analysis quantified 20 lysines with a MA, on COL1α1 and 18 lysines with a MA on COL1α2 (Table 7.7).

Table 7.7. The numbers of MA-modified lysines quantified by LC-MS/MS with trypsin and Gluc digestion. The MA sites are identified on COL1α1 and COL1α2.

	Trypsin digestion		GluC digestion	
	Quantified peptides	Quantified modified lysines	Quantified peptides	Quantified modified lysines
COL1α1	195	32	115	20
COL1α2	106	24	62	18

For the COL1α1, the first and last lysines were not modified with MA. However, for the COL1α2, the last lysine (Figure S7.16) was modified. The position of this lysine within the collagen 3D structure could have an influence on the accessibility of the lysine and thus on the potential modification. Also, as shown in Figure 7.9, the coverage of the identified and quantified peptides from both digestions showed non-covered parts of the protein at the end of the sequence, implying that the last lysine might not be detected using proteomics analysis (which can be due to the length of the last peptide in this sequence).

The LC-MS/MS analysis identified a few lysines without modification but the NMR and OPA showed a modification percentage close to 100% for COL-MA BS 1 EQ. Proteomic analysis indicated that the two chains α1 and α2 were modified and it was possible to locate the preferential positions of these modifications. The quantitative analysis of the modifications showed a higher MA modification frequency in the COL-MA BS 1 EQ than in the COL-MA BS 0.5 EQ samples. The results using the trypsin digestion indicated that COL-MA BS 1 EQ had an overall frequency of MA modification higher than COL-MA BS 0.5 EQ (Figure S7.19 and S7.20), for both sequences of COL1α1 and COL1α2. The results were similar for GluC digestion (Figure S7.21 and S7.22). Based on the modification frequency, an average DS could be calculated of 74.9 and 80.4% for COL-MA BS 0.5 and 1 EQ respectively. This

trend (increase in DS when increasing eq MeAnH) correlates with the OPA and NMR data on the COL BS derivatives. An overview of the data is shown in Table 7.8.

To conclude, unlike ^{1}H-NMR and OPA, proteomic analysis does not allow to calculate the exact DS of a modified protein. Proteomic analysis gives information on the modification frequency (in %) of a specific amino acid, meaning that an average can be calculated to get an estimation on the DS. It is thus possible to identify which positions are easily modified (i.e. modification frequency of 100% in both COL-MA BS 0.5 EQ and 1 EQ) and thus to determine the preferential (lysine) sites for MA modification. It can be hypothesized that the location of the lysine groups in the 3D-structure of COL BS (i.e. inner or outer side of the 3D conformation, easy or difficult to access) is (partly) responsible for the ease of modification of specific positions in the sequence (section 7.5.2 (d)).

Table 7.8. Determination of the degree of substitution (DS) of COL-MA BS 0.5 and 1 EQ using 1H-NMR spectroscopy (based on the amino acid sequence from the Swiss-Prot database, and the analyzed amino acid composition), OPA assay and shotgun proteomic analysis.

	DS obtained via ^{1}H-NMR (based on database Swiss-Prot) [%]	DS obtained via ^{1}H-NMR (based on known AA composition) [%]	DS obtained via OPA [%]	DS obtained via shotgun analysis [%]
COL-MA BS 0.5 EQ	76.6	75.9	74.1	74.9
COL-MA BS 1 EQ	103.7	99.6	95.8	80.4

(d) Localization of modified amino acids in the 3D-structure of COL BS modified biopolymers

Similarly to RCPhC1, the more complex sequences of COL1α1 and COL1α2 (P02453 and P02465 in Swiss-Prot DB respectively) were modelled using the I-TASSER server to obtain an idea of the 3D-conformation of the protein. The two COL BS sequences were a lot longer (i.e. 1463 and 1364 AA for the COL1α1 and COL1α2 respectively) than the RCPhC1 sequence (i.e. 571 AA), taking about 2-3 months per sequence to calculate a model (based on the protein data bank). Again, these 3D-models could not be confirmed by X-ray studies (not possible yet for such large proteins) and should be treated as possible folding configurations of the proteins studied. Moreover, the longer the protein sequence being modelled, the more possible degrees of freedom resulting in a decreasing confidence in the final protein model. However, even though the two sequences, COL1α1 and COL1α2, were separately submitted and ran on the I-TASSER, they resulted in remarkably similar models. Both models exhibited the same U-shape morphology and had similar amounts and positions of helices and sheets. Moreover, they resembled the model for RCPhC1, a derivative of collagen type I. These observations suggest that these models could be very close to the native protein configuration.

The best predicted model with I-TASSER for COL1α1 had a c-score of 0.22, which is excellent for such a large protein sequence. The estimated TM-score and RMSD were 0.74 (± 0.11) and 9.3 (± 4.6 Å) respectively, signifying a high confidence in the model. The best predicted model with I-TASSER for COL1α2 had a c-score of 0.63, which

is extremely high for such a large protein sequence. The estimated TM-score and RMSD were 0.8 (± 0.09 Å) and 8.2 (± 4.4 Å) respectively, signifying the highest confidence in the model of all three modelled protein sequences in this paper. For COL1α1 and COL1α2, the obtained 3D-models are shown in Figure 7.10 in a and b respectively, showing the occurrence of the helices (red), sheets (yellow), lysines (magenta) in the main structure of the protein.

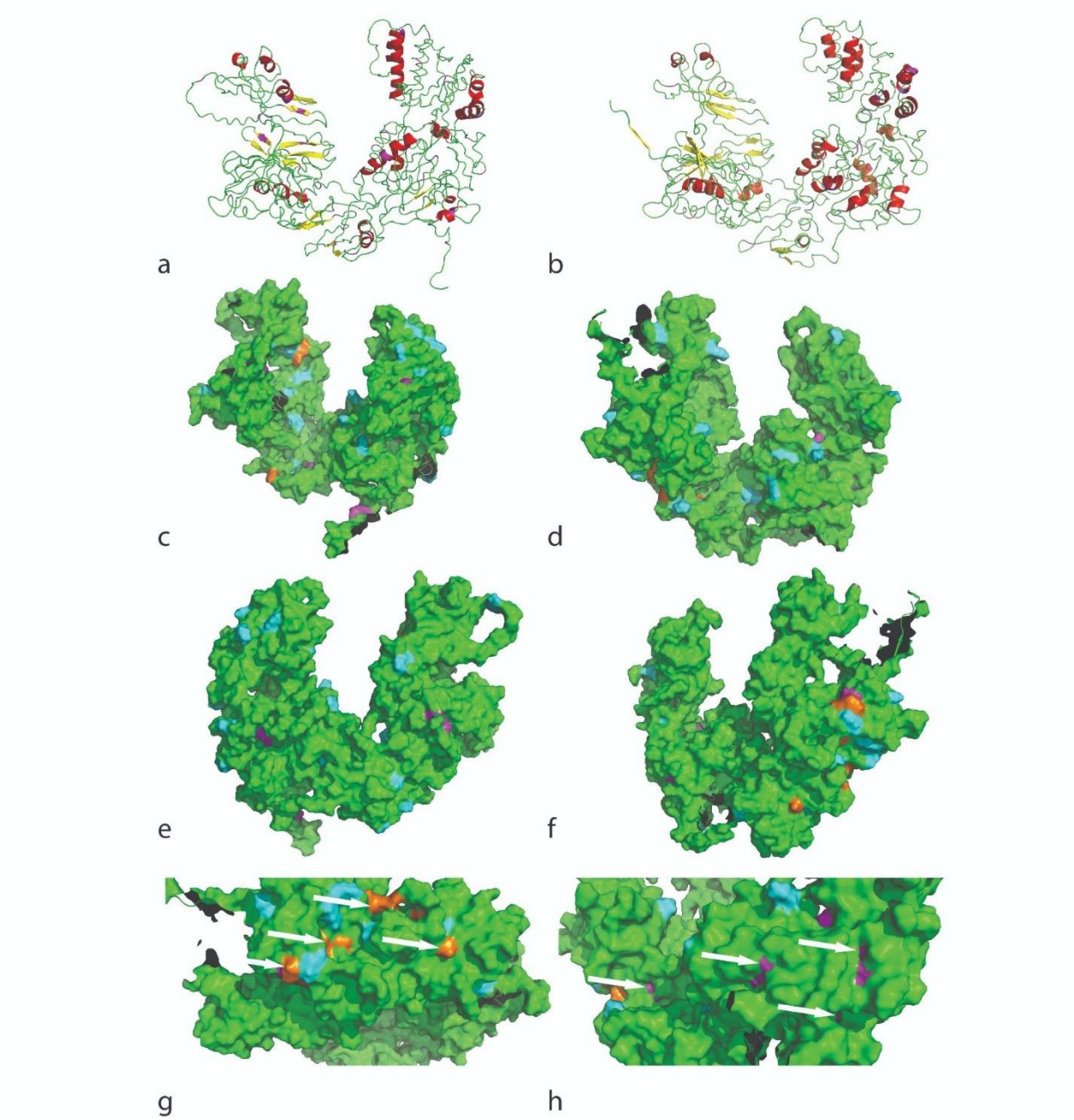

Figure 7.10. The protein 3D-conformation of the COL1α1 (a) and COL1α2 (b) proteins modelled with I-TASSER in the cartoon view showing helices (red), sheets (yellow), loops (green), and lysine residues in the structure (magenta). The same models shown in the solvent surface accessibility view for COL1α1for one side (c) and 180° turn around Y-axis site (e), and COL1α2 for one side (d) and 180° turn around Y-axis site (f), showing the protein accessibility surface (green), unmodified lysines on the surface (magenta), modified lysine (cyan) and the RGD sequences at the surface (orange). Close-ups of the protein COL1α2 showing (g) the grouped RGD sequences (orange, indicated with arrow) and proximity of the modified lysines (cyan) and (h) the buried unmodified lysines (magenta, indicated with arrow).

The predicted models for COL1α1 and COL1α2 show that they only have 2 and 4 RGD sequences, respectively, in contrast to RCPhC1 that has 12 RGD sites for a shorter overall sequence. Moreover, unlike RCPhC1, these

RGD sites were not homogeneously distributed over both proteins COL1α1 and COL1α2 and even were aggregated into one location for COL1α2 (Figure 7.10, c-f, orange). Moreover, these RGD sites were very closely positioned to modified lysines (cyan), meaning that cell accessibility may be limited once crosslinked into networks (Figure 7.10, c-g, orange-cyan). This should be tested and confirmed in future work.

The spatial distribution of modified lysines in COL1α1 (Figure 7.10, c and e) occurred to be better than in COL1α2 (Figure 7.10, d and f), with the latter having large areas on the protein surface without any modified lysines present. As discussed above, the homogeneous distribution of the modified lysines is vital for the network formation of the proteins into usable biomaterials, important for TERM applications.

Although many lysines were modified (cyan), some were not modified (magenta) (Figure 7.10, c-f). Whereas most modified lysines seem to be very accessible in the solvent accessibility view, some of the non-modified lysines occurred to be less accessible/more buried in the protein structure (Figure 7.10, h (arrows)). This was certainly true for COL1α2, where some residues even barely reached the surface, possibly influencing their modification efficiency (Figure 7.10, h). This also holds true for enzymes, making it more difficult to cut them due to steric hindrance caused by the natural protein shape and induced hindrance due to lysine modifications.

7.6 Conclusion

In this chapter, photo-crosslinkable moieties have been introduced onto RCPhC1 and COL BS, followed by applying different characterization techniques to determine the most important properties: the MM, the DS, the location of the modifications introduced in the AA sequence and the location of these modifications in the protein's 3D structure (exposed at the surface or less exposed and deeper within the protein's conformation). An overview of these properties in relation to the characterization techniques can be found in Table 7.9, and will also be used as a guideline in this conclusion.

Table 7.9. Summary of the characterization techniques discussed in this chapter, and what information these techniques can reveal on modified biopolymers.

	Molar mass (MM)	Localization of modified group	Degree of substitution (DS)	Localization in 3D model possible
MALDI-TOF	+*	-	+*	-
^{1}H-NMR	-	-	+	-
OPA	-	-	+	-
PROTEOMICS	±	+	±	+

(*) MALDI-TOF: only possible if MM < 150 kDa

In general, the molar mass could not be determined by ^{1}H-NMR spectroscopy, nor by OPA. In case of low MM proteins (< 150 kDa) such as RCPhC1, MALDI-TOF is very useful for the determination of the MM. However, in case of high MM proteins (> 150 kDa), the MM could only be estimated using the sequences (found in the Swiss-Prot database) of the abundant proteins as determined by proteomic analysis.

Besides the molar mass, the identification and localization of the modified peptides is important information to optimize the biopolymer modification procedure and/or to control the resulting physico-chemical properties. Neither MALDI-TOF, ^{1}H-NMR spectroscopy, nor OPA enabled the identification and the localization of the introduced functionalities. Conversely, proteomic analysis enabled: (i) the identification of the peptides and modified AAs, and (ii) the localization of the introduced photo-crosslinkable groups. This is vital information when pursuing the development of a biomaterial for TERM applications because it provides insight in the distribution of these photo-crosslinkable groups throughout a biopolymer chain. It is hypothesized that this distribution directly affects the crosslinking behavior of a biopolymer and hence the mechanical properties, that in turn influence the biological properties (i.e. cell-biomaterial interactions and bioactivity).

Whereas the identification and localization of the modified peptides is important, the quantification of modifications present along the protein backbone is as essential. The degree of substitution/functionalization (DS) could be determined by MALDI-TOF (for MM < 150 kDa), ^{1}H-NMR spectroscopy and OPA. However, with proteomic analysis, some challenges were encountered when quantifying the photo-crosslinkable moieties: (i) the presence of redundant peptide sequences, and (ii) a higher DS (corresponding with more photo-crosslinkable moieties) resulting in more steric hindrance. Despite these challenges, proteomic analysis was able to provide insight in the modification frequency of specific modification sites, enabling the calculation of an average DS. Obtaining modification frequencies is exciting as they also indicated that some positions were more accessible towards modification compared to others, resulting in additional information which was absent upon applying the other techniques. Based on the proteomic analysis and the obtained information on the localization of the modified groups, it was possible to 3D model the biopolymers. Moreover, it permitted the identification, localization and distribution of each unmodified and modified AA in its 3D structural conformation, providing crucial insight in the overall distribution of the modified sites along the protein backbone.

In conclusion, proteomic analysis cannot (yet) be used as a stand-alone technique to fully characterize a modified (photo-crosslinkable) biopolymer because it only provides an average DS based on the modification frequencies. However, it is the only technique that enables the identification and localization of the functionalized AA along with supplying the required information for establishing the 3D model. This enabled to gain unprecedented insight in the distribution of the introduced functionalities along the protein backbone which is crucial with respect to reproducibility and regulatory aspects for its use as a biomaterial for TERM applications, and further unravelling of the efficiency of the biopolymer modification process and the effect on the crosslinked network.

Conclusions and future perspectives

General conclusions

The current PhD research aimed at addressing the challenges currently encountered in tissue engineering and regenerative medicine, and more specifically, in tendon repair and vascular wall modeling. To this end, specific biomaterials were designed and characterized, and multiple biomaterial processing techniques were evaluated for the development of tubular scaffolds.

An introduction to the anatomical structure and physiological functions of tubular organs, as well as their diseases and malfunctions were described in **Chapter 1**. Next, current treatments, and tissue engineering and regenerative medicine as a viable solution were discussed. In particular, the state-of-the-art on currently studied biological models, (bio)materials and manufacturing processes for the fabrication of tubular constructs for tendon repair and vascular wall modeling were discussed in detail.

In a first part of this PhD thesis, novel versatile photo-crosslinkable urethane-based polymers were developed, along with their implementation as starting materials for the development of tubular scaffolds. Because each tissue has its own mechanical and biological requirements, and because each processing technique has its own specific challenges, a toolbox of AUPs was proposed, taken into account the challenges and requirements while synthesizing and formulating the AUPs.

In **Chapter 2**, the synthesis and characterization of photo-crosslinkable acrylate-endcapped urethane-based polymer precursors (AUPs) were described. In order to obtain a series of AUPs with a broad range of physical properties, AUPs based on a poly(ethylene glycol) (PEG) backbone versus a poly(ε-caprolactone) (PCL) backbone with different molar masses were synthesized (i.e. AUP PEG2k, 20k; AUP PCL530, 2k, 10k and 20k). By varying the constituting building blocks, polymers with tunable properties were developed. The PEG-based AUPs showed water uptake capacities ranging from 1.9 ± 0.1 up to 23.1 ± 0.3, ultimate stresses from 0.09 ± 0.01 up to 0.40 ± 0.07, elongations at break from 14.13 ± 2.28 up to 59.75 ± 7.16%, and Young's moduli from 0.22 ± 0.05 to 2.99 ± 0.23 MPa for AUP PEG2k and AUP PEG20k, respectively. By applying PCL as backbone for AUPs rather than PEG, hydrophobic biodegradable polymers were obtained. These PCL-based AUPs showed negligible water uptake capacities, and mechanical testing resulted in ultimate stresses ranging from 1.28 ± 0.23 up to 13.23 ± 1.17 MPa, Young's moduli from 5.68 ± 0.23 up to 321.44 ± 21.23 MPa and elongations at break from 5.67 ± 1.16 up to 17.75 ± 3.13%. Thus, the developed PEG- and PCL-based AUPs showed a broad range in physical and mechanical properties, covering the properties of many tissues and rendering them ideal for regenerative medicine from a mechanical perspective. Moreover, the developed AUPs enabled efficient UV-crosslinking in the solid state,

paving the way towards various processing opportunities, including solution electrospinning, extrusion-based 3D printing and melt electrowriting.

One of the above-mentioned processing opportunities can be found in melt electrowriting. At present, one of the challenges associated with the use of MEW is the limited availability of compatible materials. Therefore, in **Chapter 3**, melt electrowriting was investigated as an emerging fabrication technique to process the developed AUPs into tubular constructs with a predefined architecture and exhibiting tunable mechanical properties. Some key requirements to consider when designing a material for MEW include the material's processability above its melting temperature due to reduced melt viscosity, lack of pronounced thermal degradation and rapid solidification after processing. These properties can be achieved by sufficiently high molar masses to ensure that sufficient chain entanglements are present which result in viscoelastic melt properties that improve processing via MEW. For these reasons, the developed PCL-based AUP with a backbone of 20k was selected (i.e. AUP PCL20k). Processing with MEW did not result in degradation of the material while the photo-crosslinking capacity was preserved. Blending with commercially available PCL helped improving fiber morphology and homogeneity. At the same time, altering the mechanical properties of the created tubular constructs by adjusting the blend ratios was possible. This enabled tailor-made construct characteristics for different applications and their corresponding specific mechanical requirements. *In vitro* assays using HUVECs revealed non-cytotoxic behavior of the AUP PCL20k material demonstrating its relevance in biomedical applications.

A second processing technique that was selected to evaluate the processing potential of the developed AUPs is solution electrospinning. One possible biomedical application of tubular constructs in regenerative medicine can be found in tendon repair. In order to overcome the challenges currently encountered in tendon repair (i.e. insufficient mechanical properties along with adhesion and anti-inflammatory issues), a combination of a mechanical (by material and scaffold design) and biological approach (by anti-adhesion and anti-inflammatory drugs) was proposed in **Chapter 4**. To this end, PCL-based AUPs with a backbone of 530 versus 2000 $g \cdot mol^{-1}$ (i.e. AUP PCL530 and 2k) were synthesized and processed into tubular, electrospun repair constructs. The repair constructs were mechanically tested exploiting *ex vivo* sheep tendons. The non-reinforced AUP PCL530 showed superior mechanical properties compared to the AUP PCL2k repair constructs (Young's moduli of 2.5 ± 0.9 versus 0.6 ± 0.2 MPa, respectively), but still insufficient to be applied for tendon repair without the reinforcement layer. The reinforced AUP PCL530 and AUP PCL2k repair constructs showed a Young's modulus of 9.4 ± 2.5 MPa and 3.7 ± 0.5 MPa, and an ultimate stress of 6.4 ± 0.6 MPa and 8.4 ± 0.6, respectively. In comparison, the reinforced PCL repair constructs (reference) showed a lower Young's modulus of 5.7 ± 1.2 MPa compared to AUP PCL530 and a lower ultimate stress of 4.8 ± 1.0 MPa compared to both reinforced AUP repair constructs. The reinforced repair constructs have proven to fulfill the required mechanical properties for flexor tendon repair (i.e. minimal ultimate stress of 4 MPa). In addition, the developed PCL and AUP repair constructs did not show any significant degradation occurring before min. 8 weeks, which covers the initial healing period of an injured tendon to resume its normal properties and function. Moreover, anti-inflammatory and anti-adhesion components were incorporated

to further optimize the repair constructs, i.e. hyaluronic acid and naproxen, respectively. *In vitro* biological evaluation using human fibroblasts indicated that the developed PCL-based AUP repair constructs, including the bio-active components, were non-cytotoxic (viability > 70%). In the *in vivo* study, the developed AUP PCL2k repair construct showed similar strength as the Modified Kessler (gold standard). However, macroscopically, a significantly different adhesion pattern was observed at the suture knots, either centrally or peripherally, depending on the applied technique. This observation indicated that the addition of bio-active compounds had a beneficial effect on the healing (adhesion limitation within the repair zone). Histologically, a qualitative assessment showed good to excellent repair at the tendon repair site. In conclusion, the developed PCL-based AUP repair construct design combining a mechanical and biological approach shows potential for application in flexor tendon repair when designed with a reinforcement layer.

Another possible application of tubular constructs in regenerative medicine can be found in the field of vascular tissue engineering. Collagen, being one of the main components of the vascular extracellular matrix (ECM), is currently the most commonly applied natural polymer for vTE applications, and more specifically, for the development of vascular wall models. However, one of the most important limitations of collagen-based materials is their mechanical properties. In particular, their viscoelastic properties are often unsatisfactory, limiting their use in TE applications. For example, in vascular TE, the mechanical properties of collagen-based constructs are unable to withstand the high pressures and stresses encountered in the blood vessel.

Therefore, in **Chapter 5**, the use of a tubular, synthetic scaffold as reinforcement for collagen-based models was exploited with the aim to achieve the required mechanical properties for vascular wall modeling. Three different processing techniques (i.e. solution electrospinning SES, extrusion three dimensional printing 3DP, and melt electrowriting MEW) were evaluated for the development of the tubular, polymeric reinforcement. The reinforced collagen-based models were benchmarked against a non-reinforced collagen-based model (COL). As shown by SEM imaging, the selected processing technique affects the developed scaffold's architecture on micro- and macro level. In turn, the scaffold's architecture (fiber diameter, fiber alignment, pore size) has shown to influence the resulting mechanical and biological properties of the collagen-based model. The tubular, polymeric reinforcements significantly improved the mechanical properties of the collagen-based model (initial elastic moduli of 382.05 ± 132.01 kPa, 100.59 ± 31.15 kPa and 245.78 ± 33.54 kPa, respectively for SES, 3DP and MEW at day 7 of maturation) compared to the non-reinforced collagen-based model (16.63 ± 5.69 kPa). A difference in visco-elastic behavior was also observed, showing the highest predominance in elastic behavior in the MEW reinforced model (E_0/E_e ratio of 1.29 ± 0.04). Moreover, the different processing techniques and polymeric tubes' architecture influenced the cell behavior, in terms of proliferation and attachment, as well as collagen gel compaction. A dense network of fibroblasts randomly dispersed in the thick collagen matrix was found in COL (reference) and MEW samples, while fewer fibroblasts presenting smaller cytoskeletons, were found to be compressed together in the thinner collagen gel observed for the SES and 3DP conditions. Overall, it can be concluded that the selected processing technique strongly influences the resulting mechanical and biological properties.

Apart from using a synthetic reinforcement scaffold to achieve superior mechanical properties in collagen-based vascular wall models, another approach includes maintaining the construct's structural integrity by chemical, physical or enzymatic crosslinking. In **Chapter 6,** a photo-crosslinkable collagen (COL-MA) with tunable properties was developed and benchmarked against the gold standard in TE, being methacrylamide-modified gelatin (GEL-MA). For both gelatin and collagen, two derivatives with varying degrees of substitutions (DS) were developed by altering the added amount of methacrylic anhydride. This led to photo-crosslinkable derivatives with a DS of 74 and 96% for collagen, and a DS of 73 and 99% for gelatin. The developed derivatives showed high gel fractions (i.e. 74% and 84%, for the gelatin derivatives; 87 and 83%, for the collagen derivatives, respectively) and an excellent crosslinking efficiency. Furthermore, the results indicated that the functionalization of collagen led to hydrogels with tunable mechanical properties (i.e. storage moduli of [4.8 – 9.4 kPa] for the developed COL-MAs versus [3.9 – 8.4 kPa] for the developed GEL-MAs) along with superior cell-biomaterial interactions when compared to GEL-MA. Moreover, the developed photo-crosslinkable collagens showed superior mechanical properties compared to extracted native collagen. *In vitro* biological assays showed that HUVECs have a preference towards the developed bovine skin COL-MAs and a significantly superior cell-biomaterial interaction (i.e. cell shape, cell cytoskeleton area) when compared to bovine skin GEL-MAs. Therefore, the developed photo-crosslinkable collagens demonstrate great potential as biomaterials for vTE applications.

The distribution of photo-crosslinkable moieties onto a protein backbone can affect a biomaterial's crosslinking behavior, and therefore also its mechanical and biological properties. A profound insight in this respect is essential for biomaterials exploited in tissue engineering and regenerative medicine to enable translation of novel, functionalized biomaterials from bench to bedside, given regulatory constraints and the need for perfectly defined and reproducible biomaterials. In order to gain additional insight in biopolymer functionalization, proteomics can be a valuable tool. Therefore, in **Chapter 7**, proteomic analysis was evaluated as a tool to gain next level insights in photo-crosslinkable biopolymer modifications. ^{1}H-NMR spectroscopy and a colorimetric assay (i.e. OPA assay) were used as conventional techniques for the analysis of modified biopolymers. Proteomic analysis cannot (yet) be used as a stand-alone technique to fully characterize a modified (photo-crosslinkable) biopolymer because it only provides an estimate on the average degree of substitution based on the modification frequencies. However, it is the only technique that enables the identification and localization of the functionalized amino acids along with supplying the required information for establishing a 3D model. This enabled unprecedented insights in the distribution of the introduced functionalities along the protein backbone which is crucial with respect to reproducibility and regulatory aspects for its use as a biomaterial for TERM applications, and further unravelling the efficiency of the biopolymer modification process and the effect on the crosslinked network.

Future perspectives

The versatile chemistry, biocompatibility and unique solid-state reactivity of AUPs render these polymers suitable for a wide range of tissue engineering and regenerative medicine applications. The developed AUPs showed great potential as starting materials for processing techniques including solution electrospinning and melt electrowriting. Besides these two techniques, the AUPs also hold great promise to be exploited in other processing techniques such as selective laser sintering, digital light processing, and fused deposition modelling. These techniques can be further investigated in future research with the aim to extend the processing capabilities of the AUPs for the fabrication of (tubular) scaffolds for a variety of TE applications.

Regarding the emerging melt electrowriting technique, only AUP PCL20k was evaluated for its processing potential. In this study, it was shown that the AUP PCL20 precursor could be printed but that the developed tubular constructs showed high brittleness. For this reason, AUP PCL20k was blended with commercially available PCL in various blending ratios with the aim to tune the mechanical properties of the developed tubular constructs. Next steps in this research could entail blending of AUP PCL20k with a lower molar mass backbone AUP such as AUP PCL2k. Other options include the development of AUP precursors with other building blocks (i.e. variation in backbone, and/or in endcaps) in order to reduce the brittleness, but at the same time, fulfilling the requirements for MEW processing (as described above in section “General conclusions”, and in detail in Chapter 3).

With respect to tendon repair, two PCL-based AUPs were evaluated (i.e. AUP PCL530 and AUP PCL2k) using solution electrospinning. Two different molar masses were evaluated with the aim to achieve sufficient mechanical properties for the electrospun repair construct without the need for a tubular braid as reinforcement (i.e. minimal ultimate stress of 4 MPa). Even though the AUP PCL530 repair construct showed improved mechanical properties compared to AUP PCL2k repair constructs, it was still not sufficiently high for the intended application being tendon repair. In a follow-up study, the AUP building blocks could be varied to develop an AUP with superior mechanical properties so that no additional reinforcement structure (under the form of a poly(propylene) braid) within the electrospun repair construct is required. An option could be to vary the diisocyanate block within the AUP structure. The implementation of aromatic isocyanates within the AUP structure is expected to lead to AUPs with superior mechanical properties.

Overall, the proposed toolbox of AUP materials could be further finetuned towards tendon repair by varying the AUP building blocks and/or processing techniques, but the developed AUPs and their wide range of physical properties could also be evaluated for other applications in the field of regenerative medicine and tissue engineering including muscle TE, muscle-to-tendon TE, wound dressings, etc.

For vascular tissue engineering, the three different processing techniques evaluated for the development of tubular scaffolds showed the importance and the effect of the processing technique on the resulting mechanical and

biological properties. However, in this study, only PCL tubular constructs were developed and compared. It is known that not only the processing technique, but also the material itself plays an important role in the resulting properties. Therefore, next steps could include the evaluation of other materials than PCL. In particular, the developed AUPs could offer finetuning of the resulting properties aiming at a maximum stress of 1.44 ± 0.87 MPa, a maximum strain of 0.54 ± 0.25 and a physiological elastic modulus of 1.48 ± 0.24 MPa, a compliance of 4.5 - 6.2% change in diameter for a pressure increase from 80 to 120 mmHg and a burst pressure of 2031 - 4225 mmHg for human coronary arteries [64,73–79]. Moreover, herein, the developed synthetic tubular scaffolds were only evaluated in a static, mono-culture, mono-layered collagen-based model of the vascular wall, hence, a follow-up study should include the development of a co-culture (i.e. endothelial cells, smooth muscle cells and fibroblasts), multi-layered model in a bioreactor set-up. This could lead to important insights in the cell-cell interactions and on the effect of the synthetic scaffold and its corresponding architecture on the final properties of the reinforced collagen-based model.

The development of photo-crosslinkable collagen was intended for its use in vascular TE. The evaluation of the physico-chemical properties of the (crosslinked) collagens evidenced great potential to serve as biomaterial for vascular TE applications. Given these findings, the functionalized collagens should be the subject of follow-up research in which the processing potential of the developed photo-crosslinkable collagens into tubular constructs for vTE applications will be studied. The most prominent challenges in the field, including burst pressure and compliance, should be tackled for these constructs.

It the final chapter of this PhD thesis, it has been shown that proteomics can offer unprecedented insights into biomaterial modifications. The study was performed on recombinant collagen-based peptide (with a known amino acid sequence) and on bovine skin collagen (with an unknown amino acid sequence). As described in Chapter 7, both materials lead to challenges in the proof-of-concept using proteomics (i.e. repetitive units in the AA sequence in recombinant peptide, and the very large AA sequence in collagen). Therefore, the next steps in this research should include the full characterization of a small peptide with a known amino acid sequence (without repetitive units) and with a known structural conformation. This implies that the 3D model will not only be based on a theoretical model, but can also be based on x-ray diffraction. In this case, not only the physico-chemical properties could be linked to the peptide's structural conformation, but also a more precise 3D model could be linked to the obtained results in proteomics analysis. This way, the 3D modeling can also be evaluated with respect to solvent accessibility and the probability for a specific AA to be modified based on their position and accessibility within the (more precise) 3D model. In addition to this, future perspectives also include the evaluation of proteomics analysis as a tool to study other biomaterial modifications apart from methacrylamide functionalities as well as other proteins beyond collagen (e.g. gelatin, albumin, …).

Bibliography

[1] M.E. Gomes, R.L. Reis, M.T. Rodrigues, Tendon Regeneration: Understanding Tissue Physiology and Development to Engineer Functional Substitutes, 2015.

[2] World Health Organisation, Cardiovascular Diseases, (2017). http://www.who.int/cardiovascular_diseases/en/.

[3] A. Góra, D. Pliszka, S. Mukherjee, S. Ramakrishna, Tubular tissues and organs of human body-challenges in regenerative medicine, J. Nanosci. Nanotechnol. 16 (2016) 19–39. https://doi.org/10.1166/jnn.2016.11604.

[4] F.M. Chen, X. Liu, Advancing biomaterials of human origin for tissue engineering, Prog. Polym. Sci. 53 (2016) 86–168. https://doi.org/10.1016/j.progpolymsci.2015.02.004.

[5] C. Del Gaudio, S. Baiguera, F. Ajalloueian, A. Bianco, P. Macchiarini, Are synthetic scaffolds suitable for the development of clinical tissue-engineered tubular organs?, J. Biomed. Mater. Res. - Part A. 102 (2014) 2427–2447. https://doi.org/10.1002/jbm.a.34883.

[6] C. Mandrycky, Z. Wang, K. Kim, D.H. Kim, 3D bioprinting for engineering complex tissues, Biotechnol. Adv. 34 (2015) 422–434. https://doi.org/10.1016/j.biotechadv.2015.12.011.

[7] A.N. Leberfinger, S. Dinda, Y. Wu, S. V. Koduru, V. Ozbolat, D.J. Ravnic, I.T. Ozbolat, S. V Koduru, V. Ozbolat, D.J. Ravnic, I.T. Ozbolat, Bioprinting functional tissues, Acta Biomater. 95 (2019) 32–49. https://doi.org/10.1016/j.actbio.2019.01.009.

[8] S.J. Hodges, A. Atala, Tissue-Engineered Organs, 4th ed, Elsevier, 2014. https://doi.org/10.1016/B978-0-12-398358-9.00085-9.

[9] I. Holland, J. Logan, J. Shi, C. McCormick, D. Liu, W. Shu, 3D biofabrication for tubular tissue engineering, Bio-Design Manuf. 1 (2018) 89–100. https://doi.org/10.1007/s42242-018-0013-2.

[10] A. Atala, Tissue engineering, stem cells and cloning: current concepts and changing trends, Expert Opin. Biol. Ther. 5 (2005) 879–892. https://doi.org/10.1517/14712598.5.7.879.

[11] B.D. Ratner, A.S. Hoffman, F.J. Schoen, J.E. Lemons, Biomaterial Science - An Introduction to Materials in Medicine, 2nd ed, Elsevier Academic Press, 2004. http://ilkerpolatoglu.cbu.edu.tr/docs/Introduction to Materials.pdf.

[12] U.A. Stock, J.P. Vacanti, Tissue engineering : Current State and Prospects, Annu Rev Med. 52 (2001) 443–451. https://doi.org/10.1146/annurev.med.52.1.443.

[13] J.P. Vacanti, C.A. Vacanti, Chapter 1 - The History and Scope of Tissue Engineering, in: R. Lanza, R. Langer, J. Vacanti (Eds.), Princ. Tissue Eng. (Fourth Ed., Fourth Edi, Academic Press, Boston, 2014: pp. 3–8. https://doi.org/https://doi.org/10.1016/B978-0-12-398358-9.00001-X.

[14] M. Mozafari, F. Sefat, A. Atala, Handbook of tissue engineering scaffolds: Volume one, Woodhead Publishing, 2019. https://doi.org/10.1016/C2017-0-00858-3.

[15] A. Shafiee, A. Atala, Tissue Engineering: Toward a New Era of Medicine, Annu. Rev. Med. 68 (2017) 29–40. https://doi.org/10.1146/annurev-med-102715-092331.

[16] M.E. Furth, A. Atala, Tissue Engineering: Future Perspectives, 4th ed, Elsevier, 2013. https://doi.org/10.1016/B978-0-12-398358-9.00006-9.

[17] M.A. Barbosa, M.C.L. Martins, eds., Peptides and Proteins as Biomaterials for Tissue Regeneration and Repair, Woodhead Publishing, 2018.

[18] R.M. Nerem, S.C. Schutte, The Challenge of Imitating Nature, 4th ed, Elsevier, 2014. https://doi.org/10.1016/B978-0-12-398358-9.00002-1.

[19] K.L. Moffat, R.A. Neal, L.E. Freed, F. Guilak, Engineering Functional Tissues: In Vitro Culture Parameters, 4th ed, Elsevier, 2014. https://doi.org/10.1016/B978-0-12-398358-9.00013-6.

[20] J.W. Nichol, A. Khademhosseini, Modular tissue engineering: engineering biological tissues from the bottom up, Soft Matters. 5 (2010) 1312–1319. https://doi.org/10.1039/b814285h.Modular.

[21] B.Y.V. Marx, Organs from the lab, Nature. (2015).

[22] A. Atala, F.K. Kasper, A.G. Mikos, Engineering Complex Tissues, Sci. Transl. Med. 4 (2012) 1–11.

[23] E. Bayrak, P. Yilgor Huri, Engineering musculoskeletal tissue interfaces, Front. Mater. 5 (2018). https://doi.org/10.3389/fmats.2018.00024.

[24] A. Moriscot, E.H. Miyabara, B. Langeani, A. Belli, S. Egginton, T.S. Bowen, Firearms-related skeletal muscle trauma: pathophysiology and novel approaches for regeneration, Npj Regen. Med. 6 (2021). https://doi.org/10.1038/s41536-021-00127-1.

[25] R.D. Pedde, B. Mirani, A. Navaei, T. Styan, S. Wong, M. Mehrali, A. Thakur, N.K. Mohtaram, A. Bayati, A. Dolatshahi-Pirouz, M. Nikkhah, S.M. Willerth, M. Akbari, Emerging Biofabrication Strategies for Engineering Complex Tissue Constructs, Adv. Mater. 29 (2017) 1606061. https://doi.org/10.1002/adma.201606061.

[26] R.C. Dutta, M. Dey, A.K. Dutta, B. Basu, Competent processing techniques for scaffolds in tissue engineering, Biotechnol. Adv. 35 (2017) 240–250. https://doi.org/10.1016/j.biotechadv.2017.01.001.

[27] J. Buschmann, G.M. Bürgisser, Biomechanics of Tendons and Ligaments: Tissue Reconstruction and Regeneration, 2017.

[28] A. Shojaee, A. Parham, Strategies of tenogenic differentiation of equine stem cells for tendon repair: Current status and challenges, Stem Cell Res. Ther. 10 (2019). https://doi.org/10.1186/s13287-019-1291-0.

[29] M.L. Osborn, J.L. Cornille, U. Blas-Machado, E.W. Uhl, The equine navicular apparatus as a premier enthesis organ: Functional implications, Vet. Surg. 50 (2021). https://doi.org/10.1111/vsu.13620.

[30] M.N. Doral, M. Alam, M. Bozkurt, E. Turhan, O.A. Atay, G. Dönmez, N. Maffulli, Functional anatomy of the Achilles tendon, Knee Surgery, Sport. Traumatol. Arthrosc. 18 (2010) 638–643. https://doi.org/10.1007/s00167-010-1083-7.

[31] P.W. Ackermann, P. Salo, D.A. Hart, Tendon innervation, Adv. Exp. Med. Biol. 920 (2016). https://doi.org/10.1007/978-3-319-33943-6_4.

[32] C. Myer, J.R. Fowler, Flexor Tendon Repair. Healing, Biomechanics, and Suture Configurations, Orthop. Clin. North Am. 47 (2016). https://doi.org/10.1016/j.ocl.2015.08.019.

[33] A.A. Salgado, ed., Essentials of Hand Surgery, InTech, 2018. https://doi.org/10.5772/intechopen.69751.

[34] M. Kaya, N. Karahan, B. Yılmaz, Tendon Structure and Classification, Tendons. (2019) 1–9. https://doi.org/10.5772/intechopen.84622.

[35] J. Zabrzyński, Łapaj, Paczesny, A. Zabrzyńska, D. Grzanka, Tendon — function-related structure, simple healing process and mysterious ageing, Folia Morphol. 77 (2018). https://doi.org/10.5603/FM.a2018.0006.

[36] M. Benjamin, E. Kaiser, S. Milz, Structure-function relationships in tendons: A review, J. Anat. 212 (2008) 211–228. https://doi.org/10.1111/j.1469-7580.2008.00864.x.

[37] J.A.G. Rhodin, Architecture of the Vessel Wall, in: Compr. Physiol., John Wiley & Sons, Inc., Hoboken, NJ, USA, 1980: pp. 1–31. https://doi.org/10.1002/cphy.cp020201.

[38] D.D. Gutterman, Adventitia-dependent influences on vascular function, Am. J. Physiol. Circ. Physiol. 277 (1999) H1265–H1272. https://doi.org/10.1152/ajpheart.1999.277.4.H1265.

[39] K.J. Ottenbacher, M.A. Short, Vestibular processing dysfunction in children, Routledge, 2013. https://doi.org/10.4324/9780203708170.

[40] C. Burton, Relation of Structure of the Wall, Physiol. Rev. 34 (1954) 619–642.

[41] H. Ait-Oufella, E. Maury, S. Lehoux, B. Guidet, G. Offenstadt, The endothelium: Physiological functions and role in microcirculatory failure during severe sepsis, in: Appl. Physiol. Intensive Care Med. 2 Physiol. Rev. Ed., 2012: pp. 237–249. https://doi.org/10.1007/978-3-642-28233-1_24.

[42] H.R. Schelbert, Anatomy and physiology of coronary blood flow, J. Nucl. Cardiol. 17 (2010) 545–554. https://doi.org/10.1007/s12350-010-9255-x.

[43] L.A. Martinez-Lemus, M.A. Hill, G.A. Meininger, The Plastic Nature of the Vascular Wall: A Continuum of Remodeling Events Contributing to Control of Arteriolar Diameter and Structure, Physiology. 24 (2009) 45–57. https://doi.org/10.1152/physiol.00029.2008.

[44] J.E. Wagenseil, R.P. Mecham, Vascular Extracellular Matrix and Arterial Mechanics, Physiol. Rev. 89 (2009) 957–989. https://doi.org/10.1152/physrev.00041.2008.

[45] K.R. Stenmark, M.E. Yeager, K.C. El Kasmi, E. Nozik-Grayck, E. V. Gerasimovskaya, M. Li, S.R. Riddle, M.G. Frid, K.C. El Kasmi, E. Nozik-Grayck, E. V. Gerasimovskaya, M. Li, S.R. Riddle, M.G. Frid, K.C. El Kasmi, E. Nozik-Grayck, E. V. Gerasimovskaya, M. Li, S.R. Riddle, M.G. Frid, The Adventitia: Essential Regulator of Vascular Wall Structure and Function, Annu. Rev. Physiol. 75 (2013) 23–47. https://doi.org/10.1146/annurev-physiol-030212-183802.

[46] P. Chelladurai, W. Seeger, S.S. Pullamsetti, Series “matrix metalloproteinases in lung health and disease”: Matrix metalloproteinases and their inhibitors in pulmonary hypertension, Eur. Respir. J. 40 (2012) 766–782. https://doi.org/10.1183/09031936.00209911.

[47] J.D. Raffetto, C.M. Niswender, P.J. Conn, M.A. Sommer, R.H. Wurtz, Matrix Metalloproteinases and their Inhibitors in Vascular Remodeling and Vascular Disease, Biochem Pharmacol. 75 (2008) 346–359.

[48] P. Theobald, M. Benjamin, L. Nokes, N. Pugh, Review of the vascularisation of the human Achilles tendon,

Injury. 36 (2005) 1267–1272. https://doi.org/10.1016/j.injury.2005.02.012.

[49] G.L. Canata, P. D'Hooghe, K.J. Hunt, Muscle and tendon injuries: Evaluation and management, 2017. https://doi.org/10.1007/978-3-662-54184-5.

[50] A.L. Titan, D.S. Foster, J. Chang, M.T. Longaker, Flexor Tendon: Development, Healing, Adhesion Formation, and Contributing Growth Factors, Plast. Reconstr. Surg. 144 (2019). https://doi.org/10.1097/PRS.0000000000006048.

[51] B.L. Banik, G.S. Lewis, J.L. Brown, Multiscale Poly-(ϵ-caprolactone) Scaffold Mimicking Non-linearity in Tendon Tissue Mechanics, Regen. Eng. Transl. Med. 2 (2016) 1–9. https://doi.org/10.1007/s40883-016-0008-5.

[52] W.L. Lim, L.L. Liau, M.H. Ng, S.R. Chowdhury, J.X. Law, Current Progress in Tendon and Ligament Tissue Engineering, Tissue Eng. Regen. Med. 16 (2019). https://doi.org/10.1007/s13770-019-00196-w.

[53] V. Schöffl, A. Heid, T. Küpper, Tendon injuries of the hand, World J. Orthop. 3 (2012) 62–69. https://doi.org/10.5312/wjo.v3.i6.62.

[54] D.M. Avery, C.M. Rodner, C.M. Edgar, Sports-related wrist and hand injuries: A review, J. Orthop. Surg. Res. 11 (2016). https://doi.org/10.1186/s13018-016-0432-8.

[55] E.N. Marieb, K. Hoehn, Human Anatomy & Physiology, 8th ed, Pearson, 2010. https://doi.org/10.1007/BF00845519.

[56] E. Feigl, Coronary Physiology, Physiol. Rev. 63 (1983) 1–205. https://doi.org/10.1242/jeb.053124.

[57] D. Docheva, S.A. Müller, M. Majewski, C.H. Evans, Biologics for tendon repair, Adv. Drug Deliv. Rev. 84 (2015). https://doi.org/10.1016/j.addr.2014.11.015.

[58] F. Wu, M. Nerlich, D. Docheva, Tendon injuries: Basic science and new repair proposals, EFORT Open Rev. 2 (2017) 332–342. https://doi.org/10.1302/2058-5241.2.160075.

[59] C. Lebled, L.M. Grover, J.Z. Paxton, Combined decellularisation and dehydration improves the mechanical properties of tissue-engineered sinews, J. Tissue Eng. 5 (2014). https://doi.org/10.1177/2041731414536720.

[60] C. Liu, S. Tian, J. Bai, K. Yu, L. Liu, G. Liu, R. Dong, D. Tian, Regulation of ERK1/2 and SMAD2/3 pathways by using multi-layered electrospun PCL–amnion nanofibrous membranes for the prevention of post-surgical tendon adhesion, Int. J. Nanomedicine. 15 (2020). https://doi.org/10.2147/IJN.S231538.

[61] S. Kokubu, R. Inaki, K. Hoshi, A. Hikita, Adipose-derived stem cells improve tendon repair and prevent ectopic ossification in tendinopathy by inhibiting inflammation and inducing neovascularization in the early stage of tendon healing, Regen. Ther. 14 (2020) 103–110. https://doi.org/10.1016/j.reth.2019.12.003.

[62] E. Benrashid, C.C. McCoy, L.M. Youngwirth, J. Kim, R.J. Manson, J.C. Otto, J.H. Lawson, Tissue engineered vascular grafts: Origins, development, and current strategies for clinical application, Methods. 99 (2016) 13–19. https://doi.org/10.1016/j.ymeth.2015.07.014.

[63] D.G. Seifu, A. Purnama, K. Mequanint, D. Mantovani, Small-diameter vascular tissue engineering, Nat. Rev. Cardiol. 10 (2013) 410–421. https://doi.org/10.1038/nrcardio.2013.77.

[64] N. L'Heureux, N. Dusserre, G. Konig, B. Victor, P. Keire, T.N. Wight, N.A.F. Chronos, A.E. Kyles, C.R.

Gregory, G. Hoyt, R.C. Robbins, T.N. McAllister, Human tissue-engineered blood vessels for adult arterial revascularization, Nat. Med. 12 (2006) 361–5. https://doi.org/10.1038/nm1364.

[65] A. Hasan, A. Memic, N. Annabi, M. Hossain, A. Paul, M.R. Dokmeci, F. Dehghani, A. Khademhosseini, Electrospun scaffolds for tissue engineering of vascular grafts, Acta Biomater. 10 (2014) 11–25. https://doi.org/10.1016/j.actbio.2013.08.022.

[66] R. Erdem, M. Yüksek, E. Sancak, O. Atak, M. Erginer, L. Kabasakal, A. Beyit, Electrospinning of single and multilayered scaffolds for tissue engineering applications, J. Text. Inst. 108 (2017) 935–946. https://doi.org/10.1080/00405000.2016.1204900.

[67] W. Balestri, R.H. Morris, J.A. Hunt, Y. Reinwald, Current Advances on the Regeneration of Musculoskeletal Interfaces, Tissue Eng. Part B Rev. (2021). https://doi.org/10.1089/ten.teb.2020.0112.

[68] R. López-Cebral, J. Silva-Correia, R.L. Reis, T.H. Silva, J.M. Oliveira, Peripheral Nerve Injury: Current Challenges, Conventional Treatment Approaches, and New Trends in Biomaterials-Based Regenerative Strategies, ACS Biomater. Sci. Eng. 3 (2017). https://doi.org/10.1021/acsbiomaterials.7b00655.

[69] J.J. Paredes, N. Andarawis-Puri, Therapeutics for tendon regeneration: a multidisciplinary review of tendon research for improved healing, Ann. N. Y. Acad. Sci. 1383 (2016) 125–138. https://doi.org/10.1111/nyas.13228.

[70] E. Bianchi, M. Ruggeri, S. Rossi, B. Vigani, D. Miele, M.C. Bonferoni, G. Sandri, F. Ferrari, Innovative strategies in tendon tissue engineering, Pharmaceutics. 13 (2021) 1–24. https://doi.org/10.3390/pharmaceutics13010089.

[71] H. Liao, G.Q. Zhou, Development and progress of engineering of skeletal muscle tissue, Tissue Eng. - Part B Rev. 15 (2009). https://doi.org/10.1089/ten.teb.2009.0092.

[72] T. Fortunato, P.A. De Bank, G. Pula, D.B. P, G. Pula, Vascular Regenerative Surgery : Promised Land for Tissue Engineers ? Cell Sources for Vascular Tissue Engineering, Int. J. Stem Cell Res. Transplant. 5 (2017) 268–276. https://doi.org/10.19070/2328-3548-1700041.

[73] H. Chen, G.S. Kassab, Microstructure-based biomechanics of coronary arteries in health and disease, J. Biomech. 49 (2016) 2548–2559. https://doi.org/10.1016/j.jbiomech.2016.03.023.

[74] S. Sarkar, H.J. Salacinski, G. Hamilton, A.M. Seifalian, The Mechanical Properties of Infrainguinal Vascular Bypass Grafts: Their Role in Influencing Patency, Eur. J. Vasc. Endovasc. Surg. 31 (2006) 627–636. https://doi.org/10.1016/j.ejvs.2006.01.006.

[75] F. Montini-Ballarin, D. Calvo, P.C. Caracciolo, F. Rojo, P.M. Frontini, G.A. Abraham, G. V. Guinea, Mechanical behavior of bilayered small-diameter nanofibrous structures as biomimetic vascular grafts, J. Mech. Behav. Biomed. Mater. 60 (2016) 220–233. https://doi.org/10.1016/j.jmbbm.2016.01.025.

[76] A. Karimi, M. Navidbakhsh, A. Shojaei, S. Faghihi, Measurement of the uniaxial mechanical properties of healthy and atherosclerotic human coronary arteries, Mater. Sci. Eng. C. 33 (2013) 2550–2554. https://doi.org/10.1016/j.msec.2013.02.016.

[77] A. Goins, A.R. Webb, J.B. Allen, Multi-layer approaches to scaffold-based small diameter vessel engineering: A review, Mater. Sci. Eng. C. 97 (2019) 896–912. https://doi.org/10.1016/j.msec.2018.12.067.

[78] W. Nichols, M. O'Rourke, C. Vlachopoulos, McDonald's Blood Flow in Arteries Theoretical, Experimental and Clinical Principles, Sixth edit, Hodder Arnold, 2011.

[79] D.B. Camasão, D. Mantovani, The mechanical characterization of blood vessels and their substitutes in the continuous quest for physiological-relevant performances. A critical review, Mater. Today Bio. 10 (2021). https://doi.org/10.1016/j.mtbio.2021.100106.

[80] N.K. Awad, H. Niu, U. Ali, Y.S. Morsi, T. Lin, Electrospun Fibrous Scaffolds for Small-Diameter Blood Vessels: A Review, Membranes (Basel). 8 (2018) 15. https://doi.org/10.3390/membranes8010015.

[81] G. Bentley, Repair and Regeneration of Ligaments, Tendons and Joint Capsule, Ann. R. Coll. Surg. Engl. 89 (2007) 329–330. https://doi.org/10.1308/rcsann.2007.89.3.329b.

[82] J.B. Tang, Y.T. Gu, K. Rice, F. Chen, C.Z. Pan, Evaluation of four methods of flexor tendon repair for postoperative active mobilization, Plast. Reconstr. Surg. 107 (2001) 742–749. https://doi.org/10.1097/00006534-200103000-00014.

[83] A. Sensini, G. Massafra, C. Gotti, A. Zucchelli, L. Cristofolini, Tissue Engineering for the Insertions of Tendons and Ligaments: An Overview of Electrospun Biomaterials and Structures, Front. Bioeng. Biotechnol. 9 (2021). https://doi.org/10.3389/fbioe.2021.645544.

[84] C.T. Thorpe, H.L. Birch, P.D. Clegg, H.R.C. Screen, Tendon Physiology and Mechanical Behavior: Structure-Function Relationships, Elsevier Inc., 2015. https://doi.org/10.1016/B978-0-12-801590-2.00001-6.

[85] C.T. Thorpe, H.L. Birch, P.D. Clegg, H.R.C. Screen, The role of the non-collagenous matrix in tendon function, Int. J. Exp. Pathol. 94 (2013). https://doi.org/10.1111/iep.12027.

[86] J. Bojsen-Møller, S. Peter Magnusson, Mechanical properties, physiological behavior, and function of aponeurosis and tendon, J. Appl. Physiol. 126 (2019) 1800–1807. https://doi.org/10.1152/japplphysiol.00671.2018.

[87] C.N. Maganaris, M. V. Narici, Mechanical properties of tendons, in: Tendon Inj. Basic Sci. Clin. Med., 2005. https://doi.org/10.1007/1-84628-050-8_2.

[88] C.N. Maganaris, P. Chatzistergos, N.D. Reeves, M. V. Narici, Quantification of internal stress-strain fields in human tendon: Unraveling the mechanisms that underlie regional tendon adaptations and mal-adaptations to mechanical loading and the effectiveness of therapeutic eccentric exercise, Front. Physiol. 8 (2017). https://doi.org/10.3389/fphys.2017.00091.

[89] M.B. Elliott, S. Gerecht, Three-dimensional culture of small-diameter vascular grafts, J. Mater. Chem. B. 4 (2016) 3443–3453. https://doi.org/10.1039/c6tb00024j.

[90] J. Xu, G.-P.P. Shi, Vascular wall extracellular matrix proteins and vascular diseases., Biochim. Biophys. Acta. 1842 (2014) 2106–2119. https://doi.org/10.1016/j.bbadis.2014.07.008.

[91] W.J. Zhang, W. Liu, L. Cui, Y. Cao, Tissue engineering of blood vessel: Tissue Engineering Review Series, J. Cell. Mol. Med. 11 (2007) 945–957. https://doi.org/10.1111/j.1582-4934.2007.00099.x.

[92] T.B. Wissing, V. Bonito, C.V.C. Bouten, A.I.P.M. Smits, Biomaterial-driven in situ cardiovascular tissue engineering—a multi-disciplinary perspective, Npj Regen. Med. 2 (2017) 18.

https://doi.org/10.1038/s41536-017-0023-2.

[93] J.G. Nemeno-Guanzon, S. Lee, J.R. Berg, Y.H. Jo, J.E. Yeo, B.M. Nam, Y.-G. Koh, J.I. Lee, Trends in Tissue Engineering for Blood Vessels, J. Biomed. Biotechnol. 2012 (2012) 1–14. https://doi.org/10.1155/2012/956345.

[94] V. Catto, S. Farè, G. Freddi, M.C. Tanzi, Vascular Tissue Engineering: Recent Advances in Small Diameter Blood Vessel Regeneration, ISRN Vasc. Med. 2014 (2014) 1–27. https://doi.org/10.1155/2014/923030.

[95] S. Pashneh-Tala, S. MacNeil, F. Claeyssens, The Tissue-Engineered Vascular Graft—Past, Present, and Future, Tissue Eng. Part B Rev. 22 (2016) 68–100. https://doi.org/10.1089/ten.teb.2015.0100.

[96] M.A. Cleary, E. Geiger, C. Grady, C. Best, Y. Naito, C. Breuer, Vascular tissue engineering: The next generation, Trends Mol. Med. 18 (2012) 394–404. https://doi.org/10.1016/j.molmed.2012.04.013.

[97] C.E. Fernandez, H.E. Achneck, W.M. Reichert, G.A. Truskey, Biological and engineering design considerations for vascular tissue engineered blood vessels (TEBVs), Curr. Opin. Chem. Eng. 3 (2014) 83–90. https://doi.org/10.1016/j.coche.2013.12.001.

[98] Y. Naito, T. Shinoka, D. Duncan, N. Hibino, D. Solomon, M. Cleary, A. Rathore, C. Fein, S. Church, C. Breuer, Vascular tissue engineering: Towards the next generation vascular grafts, Adv. Drug Deliv. Rev. 63 (2011) 312–323. https://doi.org/10.1016/j.addr.2011.03.001.

[99] H.H.G. Song, R.T. Rumma, C.K. Ozaki, E.R. Edelman, C.S. Chen, Vascular Tissue Engineering: Progress, Challenges, and Clinical Promise, Cell Stem Cell. 22 (2018) 340–354. https://doi.org/10.1016/j.stem.2018.02.009.

[100] H.Y. Tuan-Mu, P.C. Lu, P.Y. Lee, C.C. Lin, C.J. Chen, L.L.H. Huang, J.H. Lin, J.J. Hu, Rapid Fabrication of a Cell-Seeded Collagen Gel-Based Tubular Construct that Withstands Arterial Pressure: Rapid Fabrication of a Gel-Based Media Equivalent, Ann. Biomed. Eng. 44 (2016) 3384–3397. https://doi.org/10.1007/s10439-016-1645-z.

[101] P.B. Dobrin, STRESS GRADIENTS IN THE WALLS OF LARGE ARTERIES * t, 16 (1973) 631–639.

[102] G.A. Holzapfel, R.W. Ogden, T. Rectors, M.G.V.- Madrid, T.S. General, F.S. General, E. Editor, C.T.-Udine, C. Science, M.L.T. Cossio, L.F. Giesen, G. Araya, M.L.S. Pérez-Cotapos, R.L. VERGARA, M. Manca, R.A. Tohme, S.D. Holmberg, T. Bressmann, D.R. Lirio, J.S. Román, R.G. Solís, S. Thakur, S.N. Rao, E.L. Modelado, A.D.E. La, C. Durante, U.N.A. Tradición, M. En, E.L. Espejo, D.E.L.A.S. Fuentes, U.A. De Yucatán, C.M. Lenin, L.F. Cian, M.J. Douglas, L. Plata, F. Héritier, Biomechanics of Soft Tissue in Cardiovascular Systems, Springer-Verlag Wien GmbH, 2003. https://doi.org/10.1007/978-3-7091-2736-0.

[103] C. Long, Z. Wang, A. Legrand, A. Chattopadhyay, J. Chang, P.M. Fox, Tendon Tissue Engineering: Mechanism and Effects of Human Tenocyte Coculture With Adipose-Derived Stem Cells, J. Hand Surg. Am. 43 (2018). https://doi.org/10.1016/j.jhsa.2017.07.031.

[104] A.H. Huang, J.L. Balestrini, B. V. Udelsman, K.C. Zhou, L. Zhao, J. Ferruzzi, B.C. Starcher, M.J. Levene, J.D. Humphrey, L.E. Niklason, Biaxial Stretch Improves Elastic Fiber Maturation, Collagen Arrangement, and Mechanical Properties in Engineered Arteries, Tissue Eng. Part C Methods. 22 (2016) 524–533.

https://doi.org/10.1089/ten.tec.2015.0309.

[105] L. V. Thomas, V. Lekshmi, P.D. Nair, Tissue engineered vascular grafts - Preclinical aspects, Int. J. Cardiol. 167 (2013) 1091–1100. https://doi.org/10.1016/j.ijcard.2012.09.069.

[106] J. Lowenthal, S. Gerecht, Stem cell-derived vasculature: A potent and multidimensional technology for basic research, disease modeling, and tissue engineering, Biochem. Biophys. Res. Commun. 473 (2016) 733–742. https://doi.org/10.1016/j.bbrc.2015.09.127.

[107] M. Rabionet, A.J. Guerra, T. Puig, J. Ciurana, 3D-printed Tubular Scaffolds for Vascular Tissue Engineering, Procedia CIRP. 68 (2018) 352–357. https://doi.org/10.1016/j.procir.2017.12.094.

[108] Z. Tan, H. Wang, X. Gao, T. Liu, Y. Tan, Composite vascular grafts with high cell infiltration by co-electrospinning, Mater. Sci. Eng. C. 67 (2016) 369–377. https://doi.org/10.1016/j.msec.2016.05.067.

[109] C. Loy, S.S. Meghezi, L. Lévesque, D. Pezzoli, H. Kumra, D. Reinhardt, J.N. Kizhakkedathu, D. Mantovani, L. Levesque, D. Pezzoli, H. Kumra, D. Reinhardt, J.N. Kizhakkedathu, D. Mantovani, A planar model of the vessel wall from cellularized-collagen scaffolds: Focus on cell-matrix interactions in mono-, bi- and tri-culture models, Biomater. Sci. 5 (2017) 153–162. https://doi.org/10.1039/c6bm00643d.

[110] S. Chung, R. Sudo, P.J. MacK, C.R. Wan, V. Vickerman, R.D. Kamm, Cell migration into scaffolds under co-culture conditions in a microfluidic platform, Lab Chip. 9 (2009) 269–275. https://doi.org/10.1039/b807585a.

[111] C.J. Kirkpatrick, S. Fuchs, R.E. Unger, Co-culture systems for vascularization - Learning from nature, Adv. Drug Deliv. Rev. 63 (2011) 291–299. https://doi.org/10.1016/j.addr.2011.01.009.

[112] H. Kaji, G. Camci-Unal, R. Langer, A. Khademhosseini, Engineering systems for the generation of patterned co-cultures for controlling cell-cell interactions, Biochim. Biophys. Acta - Gen. Subj. 1810 (2011) 239–250. https://doi.org/10.1016/j.bbagen.2010.07.002.

[113] A. Prabhath, V.N. Vernekar, E. Sanchez, C.T. Laurencin, Growth factor delivery strategies for rotator cuff repair and regeneration, Int. J. Pharm. 544 (2018). https://doi.org/10.1016/j.ijpharm.2018.01.006.

[114] D. Tsekes, G. Konstantopoulos, W.S. Khan, D. Rossouw, M. Elvey, J. Singh, Use of stem cells and growth factors in rotator cuff tendon repair, Eur. J. Orthop. Surg. Traumatol. 29 (2019). https://doi.org/10.1007/s00590-019-02366-x.

[115] P. Randelli, A. Menon, V. Ragone, R. D'Ambrosi, F. Randelli, P. Cabitza, G. Banfi, The Role of Growth Factors in Tendon Stimulation, Elsevier Inc., 2015. https://doi.org/10.1016/B978-0-12-801590-2.00007-7.

[116] G.D. Yancopoulos, S. Davis, N.W. Gale, J.S. Rudge, S.J. Wiegand, J. Holash, Vascular-specific growth factors and blood vessel formation, Nature. 407 (2000). https://doi.org/10.1038/35025215.

[117] M. Beldjilali-Labro, A.G. Garcia, F. Farhat, F. Bedoui, J.F. Grosset, M. Dufresne, C. Legallais, Biomaterials in tendon and skeletal muscle tissue engineering: Current trends and challenges, Materials (Basel). 11 (2018). https://doi.org/10.3390/ma11071116.

[118] C. Akduman, I. Özgüney, E.P.A. Kumbasar, Preparation and characterization of naproxen-loaded electrospun thermoplastic polyurethane nanofibers as a drug delivery system, Mater. Sci. Eng. C. 64 (2016) 383–390. https://doi.org/10.1016/j.msec.2016.04.005.

[119] C.-H. Chen, S.-H. Chen, K.T.T. Shalumon, J.-P. Chen, Dual functional core–sheath electrospun hyaluronic acid/polycaprolactone nanofibrous membranes embedded with silver nanoparticles for prevention of peritendinous adhesion, Acta Biomater. 26 (2015) 225–235. https://doi.org/https://doi.org/10.1016/j.actbio.2015.07.041.

[120] N. Pien, I. Peeters, L. Deconinck, L. Van Damme, L. De Wilde, A. Martens, S. Van Vlierberghe, P. Dubruel, A. Mignon, Design and development of a reinforced tubular electrospun construct for the repair of ruptures of deep flexor tendons, Mater. Sci. Eng. C. 119 (2021) 111504. https://doi.org/https://doi.org/10.1016/j.msec.2020.111504.

[121] I. Peeters, N. Pien, A. Mignon, L. Van Damme, P. Dubruel, S. Van Vlierberghe, D. Mantovani, V. Vermeulen, D. Creytens, A. Van Tongel, S. Schauvliege, K. Hermans, L. De Wilde, A. Martens, Flexor tendon repair using a reinforced tubular, medicated electrospun construct, J. Orthop. Res. (2021). https://doi.org/10.1002/jor.25103.

[122] K.T.T. Shalumon, C. Sheu, C.-H. Chen, S.-H. Chen, G. Jose, C.-Y. Kuo, J.-P. Chen, Multi-functional electrospun antibacterial core-shell nanofibrous membranes for prolonged prevention of post-surgical tendon adhesion and inflammation, Acta Biomater. 72 (2018) 121–136. https://doi.org/https://doi.org/10.1016/j.actbio.2018.03.044.

[123] K.L. Christman, Regenerative medicine: Biomaterials for tissue repair, Science (80-.). 363 (2019) 340–341. https://doi.org/10.1126/science.aar2955.

[124] S.I. Stupp, Biomaterials for regenerative medicine, MRS Bull. 30 (2005) 546–553. https://doi.org/10.1557/mrs2005.148.

[125] M. Kitsara, O. Agbulut, D. Kontziampasis, Y. Chen, P. Menasché, Fibers for hearts: A critical review on electrospinning for cardiac tissue engineering, Acta Biomater. 48 (2016) 20–40. https://doi.org/10.1016/j.actbio.2016.11.014.

[126] P. Kim, A. Yuan, K.-H. Nam, A. Jiao, D.-H. Kim, Fabrication of poly(ethylene glycol): gelatin methacrylate composite nanostructures with tunable stiffness and degradation for vascular tissue engineering., Biofabrication. 6 (2014) 024112. https://doi.org/10.1088/1758-5082/6/2/024112.

[127] F. Askari, M. Shafieian, A. Solouk, A. Hashemi, A comparison of the material properties of natural and synthetic vascular walls, J. Mech. Behav. Biomed. Mater. 71 (2017) 209–215. https://doi.org/10.1016/j.jmbbm.2017.03.016.

[128] C.E.T. Stowell, Y. Wang, Quickening: Translational design of resorbable synthetic vascular grafts, Biomaterials. 173 (2018) 71–86. https://doi.org/10.1016/j.biomaterials.2018.05.006.

[129] D. Hielscher, C. Kaebisch, B.J.V. Braun, K. Gray, E. Tobiasch, Stem Cell Sources and Graft Material for Vascular Tissue Engineering, Stem Cell Rev. Reports. 14 (2018) 642–667. https://doi.org/10.1007/s12015-018-9825-x.

[130] J. Malda, J. Visser, F.P. Melchels, T. Jüngst, W.E. Hennink, W.J.A. Dhert, J. Groll, D.W. Hutmacher, 25th anniversary article: Engineering hydrogels for biofabrication, Adv. Mater. 25 (2013) 5011–5028. https://doi.org/10.1002/adma.201302042.

[131] N. Pien, S. Van Vlierberghe, P. Dubruel, D. Mantovani, Chapter 8. Hydrogel Processing Techniques and Vascular Tissue Engineering, in: 2021. https://doi.org/10.1039/9781839163975-00207.

[132] C. Archer, J. Ralphs, Regenerative medicine and biomaterials for the repair of connective tissues, 2010. https://doi.org/10.1533/9781845697792.

[133] J.L. Drury, D.J. Mooney, Hydrogels for tissue engineering: Scaffold design variables and applications, Biomaterials. 24 (2003) 4337–4351. https://doi.org/10.1016/S0142-9612(03)00340-5.

[134] N.A. Peppas, J.Z. Hilt, A. Khademhosseini, R. Langer, Hydrogels in biology and medicine: From molecular principles to bionanotechnology, Adv. Mater. 18 (2006) 1345–1360. https://doi.org/10.1002/adma.200501612.

[135] G.D. Nicodemus, S.J. Bryant, Cell Encapsulation in Biodegradable Hydrogels for Tissue Engineering Applications, Tissue Eng. Part B Rev. 14 (2008) 149–165. https://doi.org/10.1089/ten.teb.2007.0332.

[136] H. Gregory, J.B. Phillips, Materials for peripheral nerve repair constructs: Natural proteins or synthetic polymers?, Neurochem. Int. 143 (2021). https://doi.org/10.1016/j.neuint.2020.104953.

[137] R. Boni, A. Ali, A. Shavandi, A.N. Clarkson, Current and novel polymeric biomaterials for neural tissue engineering, J. Biomed. Sci. 25 (2018) 1–21. https://doi.org/10.1186/s12929-018-0491-8.

[138] E. Alarcin, A. Bal-Öztürk, H. Avci, H. Ghorbanpoor, F. Dogan Guzel, A. Akpek, G. Yesiltas, T. Canak-Ipek, M. Avci-Adali, Current Strategies for the Regeneration of Skeletal Muscle Tissue, Int. J. Mol. Sci. 22 (2021) 5929. https://doi.org/10.3390/ijms22115929.

[139] P. Zhuang, J. An, C.K. Chua, L.P. Tan, Bioprinting of 3D in vitro skeletal muscle models: A review, Mater. Des. 193 (2020) 108794. https://doi.org/10.1016/j.matdes.2020.108794.

[140] A. Houben, Intelligent Hydrogel Design : towards more Performing Hydrogel Processing, (2017) 2016–2017.

[141] M. Martina, D.W. Hutmacher, Biodegradable polymers applied in tissue engineering research: A review, Polym. Int. 56 (2007). https://doi.org/10.1002/pi.2108.

[142] G.-J. Graulus, T. Billiet, S. Van Vlierberghe, H. Thienpont, H. Ottevaere, P. Dubruel, Biodegradable Polyesters: From Monomer to Application, 2015.

[143] S.P. Lyu, D. Untereker, Degradability of polymers for implantable biomedical devices, Int. J. Mol. Sci. 10 (2009). https://doi.org/10.3390/ijms10094033.

[144] E. Tamariz, A. Rios-Ramrez, Biodegradation of Medical Purpose Polymeric Materials and Their Impact on Biocompatibility, in: Biodegrad. - Life Sci., 2013. https://doi.org/10.5772/56220.

[145] S. Teixeira, K.M. Eblagon, F. Miranda, M.F. R. Pereira, J.L. Figueiredo, Towards Controlled Degradation of Poly(lactic) Acid in Technical Applications, C. 7 (2021). https://doi.org/10.3390/c7020042.

[146] I. Vroman, L. Tighzert, Biodegradable Polymers, Materials (Basel). 2 (2009) 307–344. https://doi.org/10.3390/ma2020307.

[147] S. Farah, D.G. Anderson, R. Langer, Physical and mechanical properties of PLA, and their functions in widespread applications — A comprehensive review, Adv. Drug Deliv. Rev. 107 (2016). https://doi.org/10.1016/j.addr.2016.06.012.

[148] A.A. Konta, M. García-Piña, D.R. Serrano, Personalised 3D printed medicines: Which techniques and polymers are more successful?, Bioengineering. 4 (2017). https://doi.org/10.3390/bioengineering4040079.

[149] E. Göktürk, H. Erdal, Biomedical applications of polyglycolic acid (PGA), SAÜ Fen Bilim. Enstitüsü Derg. (2017) 1–1. https://doi.org/10.16984/saufenbilder.283156.

[150] H. Sun, L. Mei, C. Song, X. Cui, P. Wang, The in vivo degradation, absorption and excretion of PCL-based implant, Biomaterials. 27 (2006). https://doi.org/10.1016/j.biomaterials.2005.09.019.

[151] M. Hakkarainen, A.C. Albertsson, Degradation products of aliphatic and aliphatic-aromatic polyesters, Adv. Polym. Sci. 211 (2008). https://doi.org/10.1007/12_2007_128.

[152] I. Manavitehrani, A. Fathi, H. Badr, S. Daly, A.N. Shirazi, F. Dehghani, Biomedical applications of biodegradable polyesters, Polymers (Basel). 8 (2016). https://doi.org/10.3390/polym8010020.

[153] C. Zhang, X. Wen, N.R. Vyavahare, T. Boland, Biomaterials Synthesis and characterization of biodegradable elastomeric polyurethane scaffolds fabricated by the inkjet technique, 29 (2008) 3781–3791. https://doi.org/10.1016/j.biomaterials.2008.06.009.

[154] P.A. Gunatillake, R. Adhikari, Biodegradable synthetic polymers for tissue engineering, 5 (2003) 1–16.

[155] J.P. Santerre, K. Woodhouse, G. Laroche, R.S. Labow, Understanding the biodegradation of polyurethanes : From classical implants to tissue engineering materials, 26 (2005) 7457–7470. https://doi.org/10.1016/j.biomaterials.2005.05.079.

[156] G.T. Howard, Biodegradation of polyurethane: A review, Int. Biodeterior. Biodegrad. 49 (2002) 245–252. https://doi.org/10.1016/S0964-8305(02)00051-3.

[157] O. Figovsky, L. Shapovalov, A. Leykin, O. Birukova, R. Potashnikova, Recent advances in the development of non-isocyanate polyurethanes based on, 10 (2013).

[158] H. Blattmann, M. Fleischer, M. Bähr, R. Mülhaupt, Isocyanate- and phosgene-free routes to polyfunctional cyclic carbonates and green polyurethanes by fixation of carbon dioxide, Macromol. Rapid Commun. 35 (2014) 1238–1254. https://doi.org/10.1002/marc.201400209.

[159] L.S. Nair, C.T. Laurencin, Biodegradable polymers as biomaterials, Prog. Polym. Sci. 32 (2007) 762–798. https://doi.org/10.1016/j.progpolymsci.2007.05.017.

[160] Y. Pan, X. Zhou, Y. Wei, Q. Zhang, T. Wang, M. Zhu, W. Li, R. Huang, R. Liu, J. Chen, G. Fan, K. Wang, D. Kong, Q. Zhao, Small-diameter hybrid vascular grafts composed of polycaprolactone and polydioxanone fibers, Sci. Rep. 7 (2017) 1–11. https://doi.org/10.1038/s41598-017-03851-1.

[161] C. Li, F. Wang, P. Chen, Z. Zhang, R. Guidoin, L. Wang, Preventing collapsing of vascular scaffolds: The mechanical behavior of PLA/PCL composite structure prostheses during in vitro degradation, J. Mech. Behav. Biomed. Mater. 75 (2017) 455–462. https://doi.org/10.1016/j.jmbbm.2017.08.015.

[162] F.M. Veronese, G. Pasut, PEGylation, successful approach to drug delivery, Drug Discov. Today. 10 (2005) 1451–1458. https://doi.org/10.1016/S1359-6446(05)03575-0.

[163] P. Bailon, C.-Y. Won, PEG-modified biopharmaceuticals, Expert Opin. Drug Deliv. 6 (2009) 1–16. https://doi.org/10.1517/17425240802650568.

[164] M.C. Lensen, V. a. Schulte, M. Diez, Cell Adhesion and Spreading on an Intrinsically Anti-Adhesive PEG

Biomaterial, in: R. Pignatello (Ed.), Biomater. - Phys. Chem., InTech, 2011: pp. 397–414. https://doi.org/10.5772/24273.

[165] B.D. Ulery, L.S. Nair, C.T. Laurencin, Biomedical Applications of Biodegradable Polymers., J. Polym. Sci. Part B-Polymer Phys. 49 (2011) 832–864. https://doi.org/10.3390/polym8010020.

[166] K.L. Spiller, S.A. Maher, A.M. Lowman, Hydrogels for the Repair of Articular Cartilage Defects, Tissue Eng. Part B Rev. 17 (2011) 281–299. https://doi.org/10.1089/ten.teb.2011.0077.

[167] M.W. Tibbitt, K.S. Anseth, Hydrogels as extracellular matrix mimics for 3D cell culture, Biotechnol. Bioeng. 103 (2009) 655–663. https://doi.org/10.1002/bit.22361.

[168] J.L. Holloway, A.M. Lowman, G.R. Palmese, Mechanical evaluation of poly(vinyl alcohol)-based fibrous composites as biomaterials for meniscal tissue replacement, Acta Biomater. 6 (2010) 4716–4724. https://doi.org/10.1016/j.actbio.2010.06.025.

[169] I. Gibas, H. Janik, Review: Synthetic Polymer Hydrogels for Biomedical Applications, Chem. Chem. Technol. 4 (2010) 297–304. https://doi.org/10.23939/chcht04.04.297.

[170] M. Suzuki, S. Itoh, I. Yamaguchi, K. Takakuda, H. Kobayashi, K. Shinomiya, J. Tanaka, Tendon chitosan tubes covalently coupled with synthesized laminin peptides facilitate nerve regeneration in vivo, J. Neurosci. Res. 72 (2003). https://doi.org/10.1002/jnr.10589.

[171] M. Mir, N. Ahmed, A. ur Rehman, Recent applications of PLGA based nanostructures in drug delivery, Colloids Surfaces B Biointerfaces. 159 (2017). https://doi.org/10.1016/j.colsurfb.2017.07.038.

[172] H. Amani, H. Kazerooni, H. Hassanpoor, A. Akbarzadeh, H. Pazoki-Toroudi, Tailoring synthetic polymeric biomaterials towards nerve tissue engineering: a review, Artif. Cells, Nanomedicine Biotechnol. 47 (2019). https://doi.org/10.1080/21691401.2019.1639723.

[173] H.Y. Cheung, K.T. Lau, T.P. Lu, D. Hui, A critical review on polymer-based bio-engineered materials for scaffold development, Compos. Part B Eng. 38 (2007) 291–300. https://doi.org/10.1016/j.compositesb.2006.06.014.

[174] S. Van Vlierberghe, P. Dubruel, E. Schacht, Biopolymer-based hydrogels as scaffolds for tissue engineering applications: A review, Biomacromolecules. 12 (2011) 1387–1408. https://doi.org/10.1021/bm200083n.

[175] N.C. Hunt, L.M. Grover, Cell encapsulation using biopolymer gels for regenerative medicine, Biotechnol. Lett. 32 (2010) 733–742. https://doi.org/10.1007/s10529-010-0221-0.

[176] R.A.A. Muzzarelli, F. Greco, A. Busilacchi, V. Sollazzo, A. Gigante, Chitosan, hyaluronan and chondroitin sulfate in tissue engineering for cartilage regeneration: A review, Carbohydr. Polym. 89 (2012) 723–739. https://doi.org/10.1016/j.carbpol.2012.04.057.

[177] M.D. Brigham, A. Bick, E. Lo, A. Bendali, J. a Burdick, A. Khademhosseini, Mechanically robust and bioadhesive collagen and photocrosslinkable hyaluronic acid semi-interpenetrating networks., Tissue Eng. Part A. 15 (2009) 1645–53. https://doi.org/10.1089/ten.tea.2008.0441.

[178] D.B. Johns, T.C. Kiorpes, K.E. Rodgers, G.S. Dizerega, W.D. Donahue, Reduction of adhesion formation by postoperative administration of ionically cross-linked hyaluronic acid, Fertil. Steril. 68 (1997) 37–42.

https://doi.org/10.1016/S0015-0282(97)81472-0.

[179] C.B. Highley, G.D. Prestwich, J.A. Burdick, Recent advances in hyaluronic acid hydrogels for biomedical applications, Curr. Opin. Biotechnol. 40 (2016) 35–40. https://doi.org/10.1016/j.copbio.2016.02.008.

[180] S. Van Vlierberghe, Cell-Interactive Biopolymer-based Hydrogels designed for Tissue Engineering (PhD), (2007).

[181] F. Copes, N. Pien, S. Van Vlierberghe, F. Boccafoschi, D. Mantovani, Collagen-Based Tissue Engineering Strategies for Vascular Medicine, Front. Bioeng. Biotechnol. 7 (2019) 1–15. https://doi.org/10.3389/fbioe.2019.00166.

[182] K. Weadock, R.M. Olson, F.H. Silver, Evaluation of Collagen Crosslinking Techniques, Biomater. Med. Devices. Artif. Organs. 11 (1983) 293–318. https://doi.org/10.3109/10731198309118815.

[183] S. Van Vlierberghe, E. Schacht, P. Dubruel, Reversible gelatin-based hydrogels: Finetuning of material properties, Eur. Polym. J. 47 (2011) 1039–1047. https://doi.org/10.1016/j.eurpolymj.2011.02.015.

[184] A. Ethirajan, K. Schoeller, A. Musyanovych, U. Ziener, K. Landfester, Synthesis and optimization of gelatin nanoparticles using the miniemulsion process, Biomacromolecules. 9 (2008) 2383–2389. https://doi.org/10.1021/bm800377w.

[185] P. Aramwit, N. Jaichawa, J. Ratanavaraporn, T. Srichana, A comparative study of type A and type B gelatin nanoparticles as the controlled release carriers for different model compounds, Mater. Express. 5 (2015) 241–248. https://doi.org/10.1166/mex.2015.1233.

[186] F. Costa, R. Silva, A.R. Boccaccini, Fibrous protein-based biomaterials (silk, keratin, elastin, and resilin proteins) for tissue regeneration and repair, 2018. https://doi.org/10.1016/B978-0-08-100803-4.00007-3.

[187] D. Miranda-Nieves, E.L. Chaikof, Collagen and Elastin Biomaterials for the Fabrication of Engineered Living Tissues, ACS Biomater. Sci. Eng. 3 (2017) 694–711. https://doi.org/10.1021/acsbiomaterials.6b00250.

[188] M.R. Falvo, O. V. Gorkun, S.T. Lord, The molecular origins of the mechanical properties of fibrin, Biophys. Chem. 152 (2010) 15–20. https://doi.org/10.1016/j.bpc.2010.08.009.

[189] J.W. Weisel, The mechanical properties of fibrin for basic scientists and clinicians, Biophys. Chem. 112 (2004) 267–276. https://doi.org/10.1016/j.bpc.2004.07.029.

[190] P.X. Ma, Biomimetic materials for tissue engineering, Adv. Drug Deliv. Rev. 60 (2008) 184–198. https://doi.org/10.1016/j.addr.2007.08.041.

[191] F. Boccafoschi, J. Habermehl, S. Vesentini, D. Mantovani, Biological performances of collagen-based scaffolds for vascular tissue engineering, Biomaterials. 26 (2005) 7410–7417. https://doi.org/10.1016/j.biomaterials.2005.05.052.

[192] K.M. Pawelec, S.M. Best, R.E. Cameron, Collagen: a network for regenerative medicine, J. Mater. Chem. B. 4 (2016) 6484–6496. https://doi.org/10.1039/C6TB00807K.

[193] A.M.J. Coenen, K. V. Bernaerts, J.A.W. Harings, S. Jockenhoevel, S. Ghazanfari, Elastic materials for tissue engineering applications: natural, synthetic, and hybrid polymers, Acta Biomater. 79 (2018) 60–82. https://doi.org/10.1016/J.ACTBIO.2018.08.027.

[194] A. Patel, B. Fine, M. Sandig, K. Mequanint, Elastin biosynthesis: The missing link in tissue-engineered blood vessels, Cardiovasc. Res. 71 (2006) 40–49. https://doi.org/10.1016/j.cardiores.2006.02.021.

[195] J. Araujo, J. Padrão, J.P. Silva, F. Dourado, D.M. Correia, G. Botelho, J.L. Gomez Ribelles, S. Lanceros-Méndez, V. Sencadas, Processing and characterization of α-elastin electrospun membranes, Appl. Phys. A Mater. Sci. Process. 115 (2014) 1291–1298. https://doi.org/10.1007/s00339-013-7984-9.

[196] B. Shiroud Heidari, R. Ruan, E.M. De-Juan-Pardo, M. Zheng, B. Doyle, Biofabrication and Signaling Strategies for Tendon/Ligament Interfacial Tissue Engineering, ACS Biomater. Sci. Eng. 7 (2021) 383–399. https://doi.org/10.1021/acsbiomaterials.0c00731.

[197] H. Ahn, Y.M. Ju, H. Takahashi, D.F. Williams, J.J. Yoo, S.J. Lee, T. Okano, A. Atala, Engineered small diameter vascular grafts by combining cell sheet engineering and electrospinning technology, Acta Biomater. 16 (2015) 14–22. https://doi.org/10.1016/j.actbio.2015.01.030.

[198] Y.M. Ju, H. Ahn, J. Arenas-Herrera, C. Kim, M. Abolbashari, A. Atala, J.J. Yoo, S.J. Lee, Electrospun vascular scaffold for cellularized small diameter blood vessels: A preclinical large animal study, Acta Biomater. 59 (2017) 58–67. https://doi.org/10.1016/j.actbio.2017.06.027.

[199] M.J. McClure, S.A. Sell, D.G. Simpson, B.H. Walpoth, G.L. Bowlin, A three-layered electrospun matrix to mimic native arterial architecture using polycaprolactone, elastin, and collagen: A preliminary study, Acta Biomater. 6 (2010) 2422–2433. https://doi.org/10.1016/j.actbio.2009.12.029.

[200] E. Vatankhah, D. Semnani, M.P. Prabhakaran, M. Tadayon, S. Razavi, S. Ramakrishna, Artificial neural network for modeling the elastic modulus of electrospun polycaprolactone/gelatin scaffolds, Acta Biomater. 10 (2014) 709–721. https://doi.org/10.1016/j.actbio.2013.09.015.

[201] P. Ferreira, P. Santos, P. Alves, M.P. Carvalho, K.D. de Sá, S.P. Miguel, I.J. Correia, P. Coimbra, Photocrosslinkable electrospun fiber meshes for tissue engineering applications, Eur. Polym. J. 97 (2017) 210–219. https://doi.org/10.1016/j.eurpolymj.2017.10.018.

[202] P. Coimbra, P. Santos, P. Alves, S.P. Miguel, M.P. Carvalho, K.D. de Sá, I.J. Correia, P. Ferreira, Coaxial electrospun PCL/Gelatin-MA fibers as scaffolds for vascular tissue engineering, Colloids Surfaces B Biointerfaces. 159 (2017) 7–15. https://doi.org/10.1016/j.colsurfb.2017.07.065.

[203] N. Corrigan, J. Yeow, P. Judzewitsch, J. Xu, C. Boyer, Seeing the Light: Advancing Materials Chemistry through Photopolymerization, Angew. Chemie. 131 (2019). https://doi.org/10.1002/ange.201805473.

[204] J. Wu, Z. Zhao, C.M. Hamel, X. Mu, X. Kuang, Z. Guo, H.J. Qi, Evolution of material properties during free radical photopolymerization, J. Mech. Phys. Solids. 112 (2018). https://doi.org/10.1016/j.jmps.2017.11.018.

[205] K.S. Lim, J.H. Galarraga, X. Cui, G.C.J. Lindberg, J.A. Burdick, T.B.F. Woodfield, Fundamentals and Applications of Photo-Cross-Linking in Bioprinting, Chem. Rev. 120 (2020) 10662–10694. https://doi.org/10.1021/acs.chemrev.9b00812.

[206] A. GhavamiNejad, N. Ashammakhi, X.Y. Wu, A. Khademhosseini, Crosslinking Strategies for 3D Bioprinting of Polymeric Hydrogels, Small. 16 (2020) 2002931. https://doi.org/10.1002/smll.202002931.

[207] Z. Zheng, D. Eglin, M. Alini, G.R. Richards, L. Qin, Y. Lai, Visible Light-Induced 3D Bioprinting

Technologies and Corresponding Bioink Materials for Tissue Engineering: A Review, Engineering. 7 (2021) 966–978. https://doi.org/10.1016/j.eng.2020.05.021.

[208] B. van Bochove, D.W. Grijpma, Photo-crosslinked synthetic biodegradable polymer networks for biomedical applications, J. Biomater. Sci. Polym. Ed. 30 (2019) 77–106. https://doi.org/10.1080/09205063.2018.1553105.

[209] J. Van Hoorick, L. Tytgat, A. Dobos, H. Ottevaere, J. Van Erps, H. Thienpont, A. Ovsianikov, P. Dubruel, S. Van Vlierberghe, (Photo-)crosslinkable Gelatin Derivatives for Biofabrication applications, Acta Biomater. 97 (2019) 46–73. https://doi.org/10.1016/j.actbio.2019.07.035.

[210] W. Hu, Z. Wang, Y. Xiao, S. Zhang, J. Wang, Advances in crosslinking strategies of biomedical hydrogels, Biomater. Sci. 7 (2019) 843–855. https://doi.org/10.1039/C8BM01246F.

[211] R.F. Pereira, P.J. Bártolo, R. F. Pereira, P. J. Bártolo, R.F. Pereira, P.J. Bártolo, 3D Photo-Fabrication for Tissue Engineering and Drug Delivery, Engineering. 1 (2015) 090–112. https://doi.org/10.15302/J-ENG-2015015.

[212] J.R. Choi, K.W. Yong, J.Y. Choi, A.C. Cowie, Recent advances in photo-crosslinkable hydrogels for biomedical applications, Biotechniques. 66 (2019) 40–53. https://doi.org/10.2144/btn-2018-0083.

[213] H. Xu, J. Casillas, S. Krishnamoorthy, C. Xu, Effects of Irgacure 2959 and lithium phenyl-2,4,6-trimethylbenzoylphosphinate on cell viability, physical properties, and microstructure in 3D bioprinting of vascular-like constructs, Biomed. Mater. 15 (2020) 055021. https://doi.org/10.1088/1748-605X/ab954e.

[214] S. V Murphy, A. Atala, 3D bioprinting of tissues and organs, Nat. Publ. Gr. 32 (2014) 773–785. https://doi.org/10.1038/nbt.2958.

[215] L. Moroni, T. Boland, J.A. Burdick, C. De Maria, B. Derby, G. Forgacs, J. Groll, Q. Li, J. Malda, V.A. Mironov, C. Mota, M. Nakamura, W. Shu, S. Takeuchi, T.B.F. Woodfield, T. Xu, J.J. Yoo, G. Vozzi, Biofabrication: A Guide to Technology and Terminology, Trends Biotechnol. 36 (2018) 384–402. https://doi.org/10.1016/j.tibtech.2017.10.015.

[216] H.J. Jeong, H. Nam, J. Jang, S.J. Lee, 3D bioprinting strategies for the regeneration of functional tubular tissues and organs, Bioengineering. 7 (2020) 1–24. https://doi.org/10.3390/bioengineering7020032.

[217] J. Li, M. Chen, X. Fan, H. Zhou, Recent advances in bioprinting techniques: approaches, applications and future prospects, J. Transl. Med. 14 (2016) 271. https://doi.org/10.1186/s12967-016-1028-0.

[218] N. Sahai, M. Gogoi, 3D tissue scaffold library development form medical images for bioprinting application, Mater. Today Proc. 26 (2020) 399–404. https://doi.org/10.1016/j.matpr.2019.12.063.

[219] A. Panwar, L.P. Tan, Current status of bioinks for micro-extrusion-based 3D bioprinting, Molecules. 21 (2016). https://doi.org/10.3390/molecules21060685.

[220] L.A. Bosworth, S. Downes, eds., Electrospinning for tissue regeneration, 1st ed, Woodhead Publishing, 2011.

[221] H.M. Ibrahim, A. Klingner, A review on electrospun polymeric nanofibers : Production parameters and potential applications, Polym. Test. 90 (2020) 106647. https://doi.org/10.1016/j.polymertesting.2020.106647.

[222] X. Mo, B. Sun, T. Wu, D. Li, Chapter 24 - Electrospun Nanofibers for Tissue Engineering, Elsevier Inc., 2019. https://doi.org/10.1016/B978-0-323-51270-1.00024-8.

[223] A.E. Oprea, A. Ficai, E. Andronescu, Chapter 4. Electrospun nanofibers for tissue engineering applications, Elsevier Inc., 2019. https://doi.org/10.1016/B978-0-12-816909-4.00004-X.

[224] T.J. Sill, H.A. von Recum, Electrospinning: Applications in drug delivery and tissue engineering, Biomaterials. 29 (2008) 1989–2006. https://doi.org/10.1016/j.biomaterials.2008.01.011.

[225] N. Bhardwaj, S.C. Kundu, Electrospinning: A fascinating fiber fabrication technique, Biotechnol. Adv. 28 (2010) 325–347. https://doi.org/10.1016/j.biotechadv.2010.01.004.

[226] T. Subbiah, G.S. Bhat, R.W. Tock, S. Parameswaran, S.S. Ramkumar, Electrospinning of Nanofibers, J. Appl. Polym. Sci. 96 (2005) 557–569. https://doi.org/10.1002/app.21481.

[227] A.K. Moghe, B.S. Gupta, Co-axial electrospinning for nanofiber structures: Preparation and applications, Polym. Rev. 48 (2008) 353–377. https://doi.org/10.1080/15583720802022257.

[228] S.A. Sell, P.S. Wolfe, K. Garg, J.M. McCool, I.A. Rodriguez, G.L. Bowlin, The use of natural polymers in tissue engineering: A focus on electrospun extracellular matrix analogues, Polymers (Basel). 2 (2010) 522–553. https://doi.org/10.3390/polym2040522.

[229] P. Lelkens, M. Li, A. Perets, L. Lin, J. Han, D. Woerdeman, Electrospinning of natural proteins for tissue engineering scaffolding, in: R.L. Reis, N.M. Neves, J.F. Mano, M.E. Gomes, A.P. Marques, H.S. Azevedo (Eds.), Nat. Polym. Biomed. Appl., Woodhead Publishing, 2008: pp. 446–482. https://doi.org/https://doi.org/10.1533/9781845694814.3.446.

[230] K.M. Kennedy, A. Bhaw-Luximon, D. Jhurry, Cell-matrix mechanical interaction in electrospun polymeric scaffolds for tissue engineering: implications for scaffold design and performance, Acta Biomater. 50 (2016) 41–55. https://doi.org/10.1016/j.actbio.2016.12.034.

[231] L. Jin, T. Wang, M.L. Zhu, M.K. Leach, Y.I. Naim, J.M. Corey, Z.Q. Feng, Q. Jiang, Electrospun fibers and tissue engineering, J. Biomed. Nanotechnol. 8 (2012) 1–9. https://doi.org/10.1166/jbn.2012.1360.

[232] T. Jiang, E.J. Carbone, K.W.-H. Lo, C.T. Laurencin, Electrospinning of Polymer Nanofibers for Tissue Regeneration, Prog. Polym. Sci. 46 (2014) 1–24. https://doi.org/10.1016/j.progpolymsci.2014.12.001.

[233] S.M. Willerth, Melt electrospinning in tissue engineering, Elsevier Ltd., 2017. https://doi.org/10.1016/B978-0-08-101022-8.00009-0.

[234] W. Yang, H. Li, X. Chen, Melt electrospinning, in: Electrospinning Nanofabrication Appl., Elsevier Inc., 2018: pp. 339–361. https://doi.org/10.1016/B978-0-323-51270-1.00011-X.

[235] Y. Jin, Q. Gao, C. Xie, G. Li, J. Du, J. Fu, Fabrication of heterogeneous scaffolds using melt electrospinning writing : Design and optimization, Mater. Des. 185 (2020) 108274. https://doi.org/10.1016/j.matdes.2019.108274.

[236] G. Hochleitner, T. Jüngst, T.D. Brown, K. Hahn, C. Moseke, F. Jakob, P.D. Dalton, J. Groll, Additive manufacturing of scaffolds with sub-micron filaments via melt electrospinning writing, Biofabrication. 7 (2015) 35002. https://doi.org/10.1088/1758-5090/7/3/035002.

[237] M.L. Muerza-cascante, D. Haylock, D.W. Hutmacher, P.D. Dalton, Melt Electrospinning and Its

Technologization in Tissue Engineering, Tissue Eng. Part B. 21 (2015) 187–202. https://doi.org/10.1089/ten.teb.2014.0347.

[238] T.D. Brown, P.D. Dalton, D.W. Hutmacher, Melt electrospinning today: An opportune time for an emerging polymer process, Prog. Polym. Sci. 56 (2015) 116–166. https://doi.org/10.1016/j.progpolymsci.2016.01.001.

[239] P.D. Dalton, M.L. Muerza-Cascante, D.W. Hutmacher, Design and Fabrication of Scaffolds via Melt Electrospinning for Applications, in: Tissue Eng. Princ. Pract. Possibilities, The Royal Society of Chemistry, 2015: pp. 100–120.

[240] F. Afghah, C. Dikyol, M. Altunbek, B. Koc, Biomimicry in bio-manufacturing: Developments in melt electrospinning writing technology towards hybrid biomanufacturing, Appl. Sci. 9 (2019). https://doi.org/10.3390/app9173540.

[241] P.D. Dalton, C. Vaquette, B.L. Farrugia, T.R. Dargaville, T.D. Brown, D.W. Hutmacher, Electrospinning and additive manufacturing: Converging technologies, Biomater. Sci. 1 (2013) 171–185. https://doi.org/10.1039/c2bm00039c.

[242] T.M. Robinson, D.W. Hutmacher, P.D. Dalton, The Next Frontier in Melt Electrospinning: Taming the Jet, Adv. Funct. Mater. 29 (2019). https://doi.org/10.1002/adfm.201904664.

[243] Y.S. Ibrahim, E.A. Hussein, M.M. Zagho, G.G. Abdo, A.A. Elzatahry, Melt Electrospinning Designs for Nanofiber Fabrication for Different Applications, Int. J. Mol. Sci. 20 (2019) 1–17. https://doi.org/10.3390/ijms20102455.

[244] T. Jungst, M.L. Muerza-Cascante, T.D. Brown, M. Standfest, D.W. Hutmacher, J. Groll, P.D. Dalton, Melt electrospinning onto cylinders: Effects of rotational velocity and collector diameter on morphology of tubular structures, Polym. Int. 64 (2015) 1086–1095. https://doi.org/10.1002/pi.4948.

[245] E. McColl, J. Groll, T. Jungst, P.D. Dalton, Design and fabrication of melt electrowritten tubes using intuitive software, Mater. Des. 155 (2018) 46–58. https://doi.org/10.1016/j.matdes.2018.05.036.

[246] N.C. Paxton, M. Lanaro, A. Bo, N. Crooks, M.T. Ross, N. Green, K. Tetsworth, M.C. Allenby, Y. Gu, C.S. Wong, S.K. Powell, M.A. Woodruff, Design tools for patient specific and highly controlled melt electrowritten scaffolds, J. Mech. Behav. Biomed. Mater. 105 (2020) 103695. https://doi.org/10.1016/j.jmbbm.2020.103695.

[247] I. Gherghescu, M.B. Delgado-Charro, The Biosimilar Landscape: An Overview of Regulatory Approvals by the EMA and FDA, Pharmaceutics. 13 (2020) 48. https://doi.org/10.3390/pharmaceutics13010048.

[248] G.A. Van Norman, Drugs and Devices, JACC Basic to Transl. Sci. 1 (2016) 399–412. https://doi.org/10.1016/j.jacbts.2016.06.003.

[249] U.S. Food and Drug Administration., The Device Development Process., (n.d.). https://www.fda.gov/patients/learn-about-drug-and-device-approvals/device-development-process (accessed October 31, 2020).

[250] J. Hunsberger, J. Neubert, J.A. Wertheim, J. Allickson, A. Atala, Bioengineering Priorities on a Path to Ending Organ Shortage, Curr. Stem Cell Reports. 2 (2016) 118–127. https://doi.org/10.1007/s40778-016-

0038-4.

[251] J. Mason, S. Visintini, T. Quay, An Overview of Clinical Applications of 3-D Printing and Bioprinting, CADTH Issues Emerg. Heal. Technol. 175 (2016). http://www.ncbi.nlm.nih.gov/pubmed/31211545.

[252] J.A. Arcidiacono, S.R. Bauer, D.S. Kaplan, C.M. Allocca, S. Sarkar, S. Lin-Gibson, FDA and NIST collaboration on standards development activities supporting innovation and translation of regenerative medicine products, Cytotherapy. 20 (2018) 779–784. https://doi.org/10.1016/j.jcyt.2018.03.039.

[253] R. Song, M. Murphy, C. Li, K. Ting, C. Soo, Z. Zheng, Current development of biodegradable polymeric materials for biomedical applications, Drug Des. Devel. Ther. 12 (2018). https://doi.org/10.2147/DDDT.S165440.

[254] E.P. Ivanova, K. Bazaka, R.J. Crawford, Natural polymer biomaterials: advanced applications, 2014. https://doi.org/10.1533/9781782422662.32.

[255] M.C. Catoira, L. Fusaro, D. Di Francesco, M. Ramella, F. Boccafoschi, Overview of natural hydrogels for regenerative medicine applications, J. Mater. Sci. Mater. Med. 30 (2019). https://doi.org/10.1007/s10856-019-6318-7.

[256] S. Kumbar, Natural and Synthetic Biomedical Polymers, Else, 2014. https://www.elsevier.com/books/natural-and-synthetic-biomedical-polymers/kumbar/978-0-12-396983-5.

[257] E. Andrzejewska, Photopolymerization kinetics of multifunctional monomers, Prog. Polym. Sci. 26 (2001) 605–665. https://doi.org/10.1016/S0079-6700(01)00004-1.

[258] C.G. Williams, A.N. Malik, T.K. Kim, P.N. Manson, J.H. Elisseeff, Variable cytocompatibility of six cell lines with photoinitiators used for polymerizing hydrogels and cell encapsulation, Biomaterials. 26 (2005). https://doi.org/10.1016/j.biomaterials.2004.04.024.

[259] H.R. Kricheldorf, Syntheses of Biodegradable and Biocompatible Polymers by Means of Bismuth Catalysts, Chem. Rev. 109 (2009). https://doi.org/10.1021/cr900029e.

[260] R.H. Schmedlen, K.S. Masters, J.L. West, Photocrosslinkable polyvinyl alcohol hydrogels that can be modified with cell adhesion peptides for use in tissue engineering, Biomaterials. 23 (2002). https://doi.org/10.1016/S0142-9612(02)00177-1.

[261] A. Houben, P. Roose, H. Van den Bergen, H. Declercq, J. Van Hoorick, P. Gruber, A. Ovsianikov, D. Bontinck, S. Van Vlierberghe, P. Dubruel, H. Van den Bergen, H. Declercq, J. Van Hoorick, P. Gruber, A. Ovsianikov, D. Bontinck, P. Van Vlierberghe, S. Dubruel, Flexible oligomer spacers as the key to solid-state photopolymerization of hydrogel precursors, 2017. https://doi.org/10.1016/j.mtchem.2017.01.005.

[262] S. Van Vlierberghe, B. Fritzinger, J.C. Martins, P. Dubruel, Hydrogel network formation revised: High-resolution magic angle spinning nuclear magnetic resonance as a powerful tool for measuring absolute hydrogel cross-link efficiencies, Appl. Spectrosc. 64 (2010) 1176–1180. https://doi.org/10.1366/000370210792973550.

[263] M. Szycher, Szycher's handbook of polyurethanes: Second edition, 2012. https://doi.org/10.1201/b12343.

[264] A. Arslan, W. Steiger, P. Roose, H. Van den Bergen, P. Gruber, E. Zerobin, F. Gantner, O. Guillaume, A. Ovsianikov, S. Van Vlierberghe, P. Dubruel, Polymer architecture as key to unprecedented high-resolution

3D-printing performance: The case of biodegradable hexa-functional telechelic urethane-based poly-ε-caprolactone, Mater. Today. 44 (2021) 25–39. https://doi.org/10.1016/j.mattod.2020.10.005.

[265] R. Lomölder, F. Plogmann, P. Speier, Selectivity of isophorone diisocyanate in the urethane reaction influence of temperature, catalysis, and reaction partners, J. Coatings Technol. 69 (1997) 51–57. https://doi.org/10.1007/bf02696250.

[266] P. Roose, E. Vermoesen, S. Van Vlierberghe, Non-steady scaling model for the kinetics of the photo-induced free radical polymerization of crosslinking networks, Polym. Chem. 11 (2020). https://doi.org/10.1039/d0py00106f.

[267] I. Cerkez, A. Sezer, S.K. Bhullar, Fabrication and characterization of electrospun poly(e-caprolactone) fibrous membrane with antibacterial functionality, R. Soc. Open Sci. 4 (2017). https://doi.org/10.1098/rsos.160911.

[268] K. Pielichowski, K. Flejtuch, Differential scanning calorimetry studies on poly(ethylene glycol) with different molecular weights for thermal energy storage materials, Polym. Adv. Technol. 13 (2002). https://doi.org/10.1002/pat.276.

[269] J.G. Fatou, L. Mandelkern, The Effect of Molecular Weight on the Melting Temperature and Fusion of Polyethylene 1, J. Phys. Chem. 69 (1965) 417–428. https://doi.org/10.1021/j100886a010.

[270] B. Bogdanov, V. Toncheva, E. Schacht, L. Finelli, B. Sarti, M. Scandola, Physical properties of poly(ester-urethanes) prepared from different molar mass polycaprolactone-diols, Polymer (Guildf). 40 (1999). https://doi.org/10.1016/S0032-3861(98)00552-7.

[271] V.R. Sinha, K. Bansal, R. Kaushik, R. Kumria, A. Trehan, Poly-ε-caprolactone microspheres and nanospheres: An overview, Int. J. Pharm. 278 (2004). https://doi.org/10.1016/j.ijpharm.2004.01.044.

[272] H. Wang, M. Domingos, F. Scenini, Advanced mechanical and thermal characterization of 3D bioextruded poly(e-caprolactone)-based composites, Rapid Prototyp. J. 24 (2018). https://doi.org/10.1108/RPJ-10-2016-0165.

[273] H. Park, X. Guo, J.S. Temenoff, Y. Tabata, A.I. Caplan, F.K. Kasper, A.G. Mikos, Effect of Swelling Ratio of Injectable Hydrogel Composites on Chondrogenic Differentiation of Encapsulated Rabbit Marrow Mesenchymal Stem Cells In Vitro, Biomacromolecules. 10 (2009) 541–546. https://doi.org/10.1021/bm801197m.

[274] S. Adamczak, J. Bochnia, C. Kundera, Stress and strain measurements in static tensile tests, Metrol. Meas. Syst. 19 (2012). https://doi.org/10.2478/v10178-012-0046-3.

[275] M. Grosvenor, The effect of molecular weight on the rheological and tensile properties of poly(ε-caprolactone), Int. J. Pharm. 135 (1996) 103–109. https://doi.org/10.1016/0378-5173(95)04404-3.

[276] Y. Kong, J.N. Hay, The enthalpy of fusion and degree of crystallinity of polymers as measured by DSC, Eur. Polym. J. 39 (2003). https://doi.org/10.1016/S0014-3057(03)00054-5.

[277] W.R. Frontera, J. Ochala, Skeletal Muscle: A Brief Review of Structure and Function, Behav. Genet. 45 (2015) 183–195. https://doi.org/10.1007/s00223-014-9915-y.

[278] A. Tits, D. Ruffoni, Joining soft tissues to bone: Insights from modeling and simulations, Bone Reports. 14

(2021). https://doi.org/10.1016/j.bonr.2020.100742.

[279] T.D. Brown, P.D. Dalton, D.W. Hutmacher, Direct Writing By Way of Melt Electrospinning, Adv. Mater. 23 (2011) 5651–5657. https://doi.org/10.1002/adma.201103482.

[280] A. Hrynevich, B. Elçi, J.N. Haigh, R. McMaster, A. Youssef, C. Blum, T. Blunk, G. Hochleitner, J. Groll, P.D. Dalton, Dimension-Based Design of Melt Electrowritten Scaffolds, Small. 14 (2018). https://doi.org/10.1002/smll.201800232.

[281] J. Kim, E. Bakirci, K.L. O'Neill, A. Hrynevich, P.D. Dalton, Fiber Bridging during Melt Electrowriting of Poly(ε-Caprolactone) and the Influence of Fiber Diameter and Wall Height, Macromol. Mater. Eng. 306 (2021). https://doi.org/10.1002/mame.202000685.

[282] G. Hochleitner, E. Fürsattel, R. Giesa, J. Groll, H.W. Schmidt, P.D. Dalton, Melt Electrowriting of Thermoplastic Elastomers, Macromol. Rapid Commun. 39 (2018). https://doi.org/10.1002/marc.201800055.

[283] D. Belotti, C. Foglieni, A. Resovi, R. Giavazzi, G. Taraboletti, Targeting angiogenesis with compounds from the extracellular matrix, Int. J. Biochem. Cell Biol. 43 (2011) 1674–1685. https://doi.org/10.1016/j.biocel.2011.08.012.

[284] K. Klimek, G. Ginalska, Proteins and peptides as important modifiers of the polymer scaffolds for tissue engineering applications-A review, Polymers (Basel). 12 (2020). https://doi.org/10.3390/POLYM12040844.

[285] A. Nadernezhad, M. Ryma, H. Genç, I. Cicha, T. Jüngst, J. Groll, Melt Electrowriting of Isomalt for High-Resolution Templating of Embedded Microchannels, Adv. Mater. Technol. 6 (2021). https://doi.org/10.1002/admt.202100221.

[286] F.M. Wunner, P. Mieszczanek, O. Bas, S. Eggert, J. Maartens, P.D. Dalton, E.M. De-Juan-Pardo, D.W. Hutmacher, Printomics: The high-throughput analysis of printing parameters applied to melt electrowriting, Biofabrication. 11 (2019). https://doi.org/10.1088/1758-5090/aafc41.

[287] J.C. Kade, P.D. Dalton, Polymers for Melt Electrowriting, Adv. Healthc. Mater. 10 (2021) 2001232. https://doi.org/10.1002/adhm.202001232.

[288] S. Shafiei Sabet, A.A. Katbab, Interfacially compatibilized poly(lactic acid) and poly(lactic acid)/polycaprolactone/organoclay nanocomposites with improved biodegradability and barrier properties: Effects of the compatibilizer structural parameters and feeding route, J. Appl. Polym. Sci. 111 (2009). https://doi.org/10.1002/app.29210.

[289] M.A. Woodruff, D.W. Hutmacher, The return of a forgotten polymer—Polycaprolactone in the 21st century, Prog. Polym. Sci. 35 (2010) 1217–1256. https://doi.org/10.1016/j.progpolymsci.2010.04.002.

[290] F. Chen, G. Hochleitner, T. Woodfield, J. Groll, P.D. Dalton, B.G. Amsden, Additive Manufacturing of a Photo-Cross-Linkable Polymer via Direct Melt Electrospinning Writing for Producing High Strength Structures, Biomacromolecules. 17 (2016) 208–214. https://doi.org/10.1021/acs.biomac.5b01316.

[291] M. Abedalwafa, F. Wang, L. Wang, C. Li, Biodegradable poly-epsilon-caprolactone (PCL) for tissue engineering applications: A review, Rev. Adv. Mater. Sci. 34 (2013).

[292] S. Wachirahuttapong, C. Thongpin, N. Sombatsompop, Effect of PCL and Compatibility Contents on the Morphology, Crystallization and Mechanical Properties of PLA/PCL Blends, in: Energy Procedia, 2016. https://doi.org/10.1016/j.egypro.2016.05.026.

[293] S. Florczak, T. Lorson, T. Zheng, M. Mrlik, D.W. Hutmacher, M.J. Higgins, R. Luxenhofer, P.D. Dalton, Melt electrowriting of electroactive poly(vinylidene difluoride) fibers, Polym. Int. 68 (2019). https://doi.org/10.1002/pi.5759.

[294] A. Arslan, H. Van Den Bergen, P. Roose, D. Bontinck, S. Van Vlierberghe, P. Dubruel, Acrylate end-capped urethane- or urea-based polymers, WO2020/094621 A1, 2020.

[295] P. Dubruel, S. Van Vlierberghe, A. Houben, H. Van den Bergen, P. Roose, D. Bontinck, Patent WO 2017/005613. Novel urethane based materials, derivatives, methods of their preparation and uses, 2017. https://www.google.com/patents/WO2017005613A1?cl=en.

[296] A. Houben, N. Pien, X.X. Lu, F. Bisi, J. Van Hoorick, M.N. Boone, P. Roose, H. Van den Bergen, D. Bontinck, T. Bowden, P. Dubruel, S. Van Vlierberghe, Indirect Solid Freeform Fabrication of an Initiator-Free Photocrosslinkable Hydrogel Precursor for the Creation of Porous Scaffolds, Macromol. Biosci. 16 (2016) 1883–1894. https://doi.org/10.1002/mabi.201600289.

[297] M. Minsart, A. Mignon, A. Arslan, I.U. Allan, S. Van Vlierberghe, P. Dubruel, Activated Carbon Containing PEG-Based Hydrogels as Novel Candidate Dressings for the Treatment of Malodorous Wounds, Macromol. Mater. Eng. 306 (2021) 2000529. https://doi.org/10.1002/mame.202000529.

[298] A. Mignon, D. Pezzoli, E. Prouvé, L. Lévesque, A. Arslan, N. Pien, D. Schaubroeck, J. Van Hoorick, D. Mantovani, S. Van Vlierberghe, P. Dubruel, Combined effect of Laponite and polymer molecular weight on the cell-interactive properties of synthetic PEO-based hydrogels. submitted., React. Funct. Polym. 136 (2019) 95–106. https://doi.org/10.1016/j.reactfunctpolym.2018.12.017.

[299] T.D. Brown, A. Slotosch, L. Thibaudeau, A. Taubenberger, D. Loessner, C. Vaquette, P.D. Dalton, D.W. Hutmacher, Design and Fabrication of Tubular Scaffolds via Direct Writing in a Melt Electrospinning Mode, Biointerphases. 7 (2012) 13. https://doi.org/10.1007/s13758-011-0013-7.

[300] N. Pien, S. Palladino, F. Copes, G. Candiani, P. Dubruel, S. Van Vlierberghe, D. Mantovani, Tubular bioartificial organs: From physiological requirements to fabrication processes and resulting properties. A critical review., Cells Tissues Organs. (2021). https://doi.org/10.1159/000519207.

[301] A. Youssef, A. Hrynevich, L. Fladeland, A. Balles, J. Groll, P.D. Dalton, S. Zabler, The Impact of Melt Electrowritten Scaffold Design on Porosity Determined by X-Ray Microtomography, Tissue Eng. - Part C Methods. 25 (2019). https://doi.org/10.1089/ten.tec.2018.0373.

[302] A. Daneshfar, S.L. Edwards, L.F. Dumée, L. Kong, T.C. Hughes, Predicting Operating Rules for Successful Melt Electrowriting, ACS Appl. Polym. Mater. 3 (2021) 1890–1898. https://doi.org/10.1021/acsapm.0c01421.

[303] G. Hochleitner, F. Chen, C. Blum, P.D. Dalton, B. Amsden, J. Groll, Melt electrowriting below the critical translation speed to fabricate crimped elastomer scaffolds with non-linear extension behaviour mimicking that of ligaments and tendons, Acta Biomater. 72 (2018). https://doi.org/10.1016/j.actbio.2018.03.023.

[304] G. Hochleitner, M. Kessler, M. Schmitz, A.R. Boccaccini, J. Teβmar, J. Groll, Melt electrospinning writing of defined scaffolds using polylactide-poly(ethylene glycol) blends with 45S5 bioactive glass particles, Mater. Lett. 205 (2017). https://doi.org/10.1016/j.matlet.2017.06.096.

[305] G. Hochleitner, A. Youssef, A. Hrynevich, J.N. Haigh, T. Jungst, J. Groll, P.D. Dalton, Fibre pulsing during melt electrospinning writing, Biofabrication. 17 (2016) 159–171. https://doi.org/10.1515/bnm-2015-0022.

[306] P. Zilla, D. Bezuidenhout, P. Human, Prosthetic vascular grafts: Wrong models, wrong questions and no healing, Biomaterials. 28 (2007). https://doi.org/10.1016/j.biomaterials.2007.07.017.

[307] N.R. Tai, H.J. Salacinski, A. Edwards, G. Hamilton, A.M. Seifalian, Compliance properties of conduits used in vascular reconstruction, Br. J. Surg. 87 (2000). https://doi.org/10.1046/j.1365-2168.2000.01566.x.

[308] G. Konig, T.N. McAllister, N. Dusserre, S.A. Garrido, C. Iyican, A. Marini, A. Fiorillo, H. Avila, W. Wystrychowski, K. Zagalski, M. Maruszewski, A.L. Jones, L. Cierpka, L.M. de la Fuente, N. L'Heureux, Mechanical properties of completely autologous human tissue engineered blood vessels compared to human saphenous vein and mammary artery, Biomaterials. 30 (2009). https://doi.org/10.1016/j.biomaterials.2008.11.011.

[309] X. Li, H. Zhao, Mechanical and degradation properties of small-diameter vascular grafts in an in vitro biomimetic environment, J. Biomater. Appl. 33 (2019). https://doi.org/10.1177/0885328218820751.

[310] F. Fazal, S. Raghav, A. Callanan, V. Koutsos, N. Radacsi, Recent advancements in the bioprinting of vascular grafts, Biofabrication. 13 (2021). https://doi.org/10.1088/1758-5090/ac0963.

[311] X. Gu, Flat-Cladding Fiber Bragg Grating Sensors for Large Strain Amplitude Fatigue Tests, in: Opto-Mechanical Fiber Opt. Sensors Res. Technol. Appl. Mech. Sens., 2018. https://doi.org/10.1016/B978-0-12-803131-5.00003-9.

[312] Y.C. Fung, S.C. Cowin, Biomechanics: Mechanical Properties of Living Tissues, 2nd ed., J. Appl. Mech. 61 (1994). https://doi.org/10.1115/1.2901550.

[313] J.P. Trotignon, J. Verdu, C. Martin, E. Morel, Fatigue behaviour of some temperature-resistant polymers, J. Mater. Sci. 28 (1993). https://doi.org/10.1007/BF00367585.

[314] J.J. Green, J. Shi, E. Chiu, E.S. Leshchiner, R. Langer, D.G. Anderson, Biodegradable polymeric vectors for gene delivery to human endothelial cells, Bioconjug. Chem. 17 (2006). https://doi.org/10.1021/bc0600968.

[315] Y. Cao, Y. Gong, L. Liu, Y. Zhou, X. Fang, C. Zhang, Y. Li, J. Li, The use of human umbilical vein endothelial cells (HUVECs) as an in vitro model to assess the toxicity of nanoparticles to endothelium: a review, J. Appl. Toxicol. 37 (2017). https://doi.org/10.1002/jat.3470.

[316] L. OPIE, D.I. Abramson and P.B. Dobrin, Editors, Blood vessels and Lymphatics in Organ Systems, Academic Press, Orlando (May 1984)., J. Mol. Cell. Cardiol. 18 (1986) 335–336. https://doi.org/10.1016/S0022-2828(86)80418-7.

[317] ISO 10993-5:2009(en) Biological evaluation of medical devices – Part 5: Tests for in vitro cytotoxicity., 2009.

[318] L.C. Mozdzen, R. Rodgers, J.M. Banks, R.C. Bailey, B.A.C. Harley, Increasing the strength and bioactivity

of collagen scaffolds using customizable arrays of 3D-printed polymer fibers, Acta Biomater. 33 (2016). https://doi.org/10.1016/j.actbio.2016.02.004.

[319] J.B. Tang, P.C. Amadio, J.C. Guimberteau, J.C. Chang, Tendon Surgery of the Hand, 1st ed., Elsevier Inc., 2012. https://doi.org/10.1097/00006534-198008000-00029.

[320] A.K.S. Chong, J. Riboh, R.L. Smith, D.P. Lindsey, H.M. Pham, J. Chang, Flexor tendon tissue engineering: Acellularized and reseeded tendon constructs, Plast. Reconstr. Surg. 123 (2009) 1759–1766. https://doi.org/10.1097/PRS.0b013e3181a65ae7.

[321] T.W. Lin, L. Cardenas, L.J. Soslowsky, Biomechanics of tendon injury and repair, J. Biomech. 37 (2004) 865–877. https://doi.org/10.1016/j.jbiomech.2003.11.005.

[322] S. Eggli, A. Dietsche, S. Eggli, E. Vögelin, Tenolysis after combined digital injuries in zone II, Ann. Plast. Surg. 55 (2005). https://doi.org/10.1097/01.sap.0000174357.03839.2a.

[323] L. Woythal, P. Hølmer, S. Brorson, Splints, with or without wrist immobilization, following surgical repair of flexor tendon lesions of the hand: A systematic review, Hand Surg. Rehabil. 38 (2019). https://doi.org/10.1016/j.hansur.2019.05.004.

[324] J.W. Howell, F. Peck, Rehabilitation of flexor and extensor tendon injuries in the hand: Current updates, Injury. 44 (2013). https://doi.org/10.1016/j.injury.2013.01.022.

[325] C.Y. Leon-Valdivieso, A. Garcia-Garcia, C. Legallais, F. Bedoui, Electrospinning of biomedically relevant multi-region scaffolds: From honeycomb to randomly-oriented microstructure, Polymer (Guildf). 202 (2020). https://doi.org/10.1016/j.polymer.2020.122606.

[326] O. Hakimi, P.A. Mouthuy, N. Zargar, E. Lostis, M. Morrey, A. Carr, A layered electrospun and woven surgical scaffold to enhance endogenous tendon repair, Acta Biomater. 26 (2015). https://doi.org/10.1016/j.actbio.2015.08.007.

[327] S. Guo, L. He, R. Yang, B. Chen, X. Xie, B. Jiang, T. Weidong, Y. Ding, Enhanced effects of electrospun collagen-chitosan nanofiber membranes on guided bone regeneration, J. Biomater. Sci. Polym. Ed. 31 (2020) 155–168. https://doi.org/10.1080/09205063.2019.1680927.

[328] S.J. Lee, H.J. Kim, M. Heo, H.R. Lee, E.J. Choi, H. Kim, D. Lee, R.L. Reis, S.H. Do, I.K. Kwon, In vitro and in vivo assessments of an optimal polyblend composition of polycaprolactone/gelatin nanofibrous scaffolds for Achilles tendon tissue engineering, J. Ind. Eng. Chem. 76 (2019). https://doi.org/10.1016/j.jiec.2019.03.036.

[329] B.P. Roßbach, M.F. Gülecyüz, L. Kempfert, M.F. Pietschmann, T. Ullamann, A. Ficklscherer, T.R. Niethammer, A. Zhang, R.M. Klar, P.E. Müller, Rotator Cuff Repair With Autologous Tenocytes and Biodegradable Collagen Scaffold: A Histological and Biomechanical Study in Sheep, Am. J. Sports Med. 48 (2020). https://doi.org/10.1177/0363546519892580.

[330] S.Y. Tong, Z. Wang, P.N. Lim, W. Wang, E.S. Thian, Uniformly-dispersed nanohydroxapatite-reinforced poly(ε-caprolactone) composite films for tendon tissue engineering application, Mater. Sci. Eng. C. 70 (2017) 1149–1155. https://doi.org/10.1016/j.msec.2016.03.051.

[331] S.-H.H. Chen, C.-H.H. Chen, Y.T. Fong, J.-P.P. Chen, Prevention of peritendinous adhesions with

electrospun chitosan-grafted polycaprolactone nanofibrous membranes, Acta Biomater. 10 (2014) 4971–4982. https://doi.org/10.1016/j.actbio.2014.08.030.

[332] C.-H. Chen, S.-H. Chen, K.T. Shalumon, J.-P. Chen, Prevention of peritendinous adhesions with electrospun polyethylene glycol/polycaprolactone nanofibrous membranes, Colloids Surfaces B Biointerfaces. 133 (2015) 221–230. https://doi.org/https://doi.org/10.1016/j.colsurfb.2015.06.012.

[333] J.A. Miller, R.L. Ferguson, D.L. Powers, J.W. Burns, S.W. Shalaby, Efficacy of hyaluronic acid/nonsteroidal anti-inflammatory drug systems in preventing postsurgical tendon adhesions, J. Biomed. Mater. Res. 38 (1997). https://doi.org/10.1002/(SICI)1097-4636(199721)38:1<25::AID-JBM4>3.0.CO;2-J.

[334] Y.S. Lui, M.P. Lewis, S.C.J. Loo, Sustained-release of naproxen sodium from electrospun-aligned PLLA-PCL scaffolds: Naproxen sodium release for tendon tissue regeneration, J. Tissue Eng. Regen. Med. 11 (2017) 1011–1021. https://doi.org/10.1002/term.2000.

[335] S.-J. Kim, J.-M. Shin, E.J. Lee, I.-H. Park, H.-M. Lee, K.-S. Kim, Efficacy of hyaluronic acid and hydroxyethyl starch in preventing adhesion following endoscopic sinus surgery, Eur. Arch. Oto-Rhino-Laryngology. 274 (2017) 3643–3649. https://doi.org/10.1007/s00405-017-4669-6.

[336] J.T. Hausmann, G. Vekszler, M. Bijak, T. Benesch, V. Vécsei, C. Gäbler, Biomechanical Comparison of Modified Kessler and Running Suture Repair in 3 Different Animal Tendons and in Human Flexor Tendons, J. Hand Surg. Am. 34 (2009) 93–101. https://doi.org/10.1016/j.jhsa.2008.09.015.

[337] P.J. Schaner, N.D. Martin, T.N. Tulenko, I.M. Shapiro, N.A. Tarola, R.F. Leichter, R.A. Carabasi, P.J. DiMuzio, Decellularized vein as a potential scaffold for vascular tissue engineering, J. Vasc. Surg. 40 (2004) 146–153. https://doi.org/10.1016/j.jvs.2004.03.033.

[338] M. Meeremans, L. Van Damme, W. De Spiegelaere, S. Van Vlierberghe, C. De Schauwer, Equine tenocyte seeding on gelatin hydrogels improves elongated morphology, Polymers (Basel). 13 (2021). https://doi.org/10.3390/polym13050747.

[339] S.J. Sebastin, A. Ho, T. Karjalainen, K.C. Chung, History and Evolution of the Kessler Repair, J. Hand Surg. Am. 38 (2013) 552–561. https://doi.org/10.1016/j.jhsa.2012.11.033.

[340] M. Berglund, D.A. Hart, M. Wiig, The inflammatory response and hyaluronan synthases in the rabbit flexor tendon and tendon sheath following injury, J. Hand Surg. Eur. Vol. 32 (2007) 581–587. https://doi.org/10.1016/j.jhse.2007.05.017.

[341] P.Y. Chou, S.H. Chen, C.H. Chen, S.H. Chen, Y.T. Fong, J.P. Chen, Thermo-responsive in-situ forming hydrogels as barriers to prevent post-operative peritendinous adhesion, Acta Biomater. 63 (2017) 85–95. https://doi.org/10.1016/j.actbio.2017.09.010.

[342] S. Jiang, H. Yan, D. Fan, J. Song, C. Fan, Multi-layer electrospun membrane mimicking tendon sheath for prevention of tendon adhesions, Int. J. Mol. Sci. 16 (2015) 6932–6944. https://doi.org/10.3390/ijms16046932.

[343] J. bo Tang, S. Ishii, U. Masamichi, M. Aoki, Dorsal and circumferential sheath reconstructions for flexor sheath defect with concomitant bony injury, J. Hand Surg. Am. 19 (1994) 61–69. https://doi.org/10.1016/0363-5023(94)90225-9.

[344] R. Tahmassebi, T. Peltz, R. Haddad, P. Scougall, M. Gianoutsos, W. Walsh, The Interlocking Modification of the Cross Locked Cruciate Tendon Repair (Modified Adelaide Repair): A Static and Dynamic Biomechanical Assessment, J. Hand Microsurg. 07 (2016) 6–12. https://doi.org/10.1007/s12593-014-0144-4.

[345] X. Zhang, Science and Principles of Biodegradable and Bioresorbable Medical Polymers: Materials and Properties, 2016.

[346] Y.S. Lui, M.P. Lewis, S.C.J. Loo, Sustained-release of naproxen sodium from electrospun-aligned PLLA–PCL scaffolds, J. Tissue Eng. Regen. Med. 11 (2017) 1011–1021. https://doi.org/10.1002/term.2000.

[347] C. De Schauwer, G.R. Van de Walle, A. Van Soom, E. Meyer, Mesenchymal stem cell therapy in horses: Useful beyond orthopedic injuries?, Vet. Q. 33 (2013). https://doi.org/10.1080/01652176.2013.800250.

[348] P.P.Y. Lui, C.M. Wong, Biology of Tendon Stem Cells and Tendon in Aging, Front. Genet. 10 (2020). https://doi.org/10.3389/fgene.2019.01338.

[349] W.L. Murphy, T.C. McDevitt, A.J. Engler, Materials as stem cell regulators, Nat. Mater. 13 (2014). https://doi.org/10.1038/nmat3937.

[350] S.H. Chen, P.Y. Chou, Z.Y. Chen, F.H. Lin, Electrospun water-borne polyurethane nanofibrous membrane as a barrier for preventing postoperative peritendinous adhesion, Int. J. Mol. Sci. 20 (2019). https://doi.org/10.3390/ijms20071625.

[351] J.C.Y. Liao, M. He, A.W.T. Gan, F. Wen, L.P. Tan, A.K.S. Chong, The effects of bi-functional anti-adhesion scaffolds on flexor tendon healing in a rabbit model, J. Biomed. Mater. Res. - Part B Appl. Biomater. 106 (2018) 2605–2614. https://doi.org/10.1002/jbm.b.34077.

[352] S.H. Kim, J.C. Yoo, J.H. Wang, K.W. Choi, T.S. Bae, C.Y. Lee, Arthroscopic sliding knot: How many additional half-hitches are really needed?, Arthrosc. - J. Arthrosc. Relat. Surg. 21 (2005) 405–411. https://doi.org/10.1016/j.arthro.2004.12.010.

[353] Y.R. Wong, I.S.M. Jais, M.K. Chang, B.H. Lim, S.C. Tay, An Exploratory Study Using Semi-Tabular Plate in Zone II Flexor Tendon Repair, J. Hand Surg. Asian-Pacific Vol. 23 (2018) 547–553. https://doi.org/10.1142/S242483551850056X.

[354] C. Zhao, P.C. Amadio, T. Tanaka, K. Kutsumi, T. Tsubone, M.E. Zobitz, K.N. An, Effect of gap size on gliding resistance after flexor tendon repair, J. Bone Jt. Surg. - Ser. A. 86 (2004) 2482–2488. https://doi.org/10.2106/00004623-200411000-00019.

[355] U.S. Zimmermann, T.J. Clerici, The histological aspects of fillers complications, Semin. Cutan. Med. Surg. 23 (2004) 241–250. https://doi.org/10.1016/j.sder.2004.09.004.

[356] W.J. Zhang, W. Liu, L. Cui, Y. Cao, Tissue engineering of blood vessel., J. Cell. Mol. Med. 11 (2007) 945–57. https://doi.org/10.1111/j.1582-4934.2007.00099.x.

[357] J. Laurence, E. Zakhem, K.N. Bitar, Translating Regenerative Medicine to the Clinic, 2016. https://doi.org/10.1016/B978-0-12-800548-4.00005-X.

[358] F. Wolf, F. Vogt, T. Schmitz-Rode, S. Jockenhoevel, P. Mela, Bioengineered vascular constructs as living models for in vitro cardiovascular research, Drug Discov. Today. 21 (2016) 1446–1455.

https://doi.org/10.1016/j.drudis.2016.04.017.

[359] A.J. Ryan, C.M. Brougham, C.D. Garciarena, S.W. Kerrigan, F.J. O'Brien, Towards 3D in vitro models for the study of cardiovascular tissues and disease, Drug Discov. Today. 21 (2016) 1437–1445. https://doi.org/10.1016/j.drudis.2016.04.014.

[360] J. Robert, B. Weber, L. Frese, M.Y. Emmert, D. Schmidt, A. von Eckardstein, L. Rohrer, S.P. Hoerstrup, A Three-Dimensional Engineered Artery Model for In Vitro Atherosclerosis Research, PLoS One. 8 (2013) e79821. https://doi.org/10.1371/journal.pone.0079821.

[361] J. Fu, D.A. Wang, In Situ Organ-Specific Vascularization in Tissue Engineering, Trends Biotechnol. 36 (2018) 834–849. https://doi.org/10.1016/j.tibtech.2018.02.012.

[362] A.H. Huang, L.E. Niklason, Engineering of arteries in vitro, Cell. Mol. Life Sci. 71 (2014) 2103–2118. https://doi.org/10.1007/s00018-013-1546-3.

[363] J.D. Berglund, M.M. Mohseni, R.M. Nerem, A. Sambanis, A biological hybrid model for collagen-based tissue engineered vascular constructs, Biomaterials. 24 (2003) 1241–1254. https://doi.org/10.1016/S0142-9612(02)00506-9.

[364] A. Rachev, T. Shazly, A structure-based constitutive model of arterial tissue considering individual natural configurations of elastin and collagen, J. Mech. Behav. Biomed. Mater. 90 (2019) 61–72. https://doi.org/10.1016/j.jmbbm.2018.09.047.

[365] K. Wolf, S. Alexander, V. Schacht, L.M. Coussens, U.H. von Andrian, J. van Rheenen, E. Deryugina, P. Friedl, Collagen-based cell migration models in vitro and in vivo, Semin. Cell Dev. Biol. 20 (2009) 931–941. https://doi.org/10.1016/j.semcdb.2009.08.005.

[366] S.H. Park, T. Song, T.S. Bae, G. Khang, B.H. Choi, S.R. Park, B.H. Min, Comparative analysis of collagens extracted from different animal sources for application of cartilage tissue engineering, Int. J. Precis. Eng. Manuf. 13 (2012) 2059–2066. https://doi.org/10.1007/s12541-012-0271-4.

[367] E.J. Sheehy, G.M. Cunniffe, F.J. O'Brien, Collagen-based biomaterials for tissue regeneration and repair, Pept. Proteins as Biomater. Tissue Regen. Repair. (2017) 127–150. https://doi.org/10.1016/B978-0-08-100803-4.00005-X.

[368] N. Pien, D. Pezzoli, J. Van Hoorick, F. Copes, M. Vansteenland, M. Albu, B. De Meulenaer, D. Mantovani, S. Van Vlierberghe, P. Dubruel, Development of photo-crosslinkable collagen hydrogel building blocks for vascular tissue engineering applications: A superior alternative to methacrylated gelatin?, Mater. Sci. Eng. C. 130 (2021) 112460. https://doi.org/10.1016/j.msec.2021.112460.

[369] I.D. Gaudet, D.I. Shreiber, Characterization of methacrylated Type-I collagen as a dynamic, photoactive hydrogel, Biointerphases. 7 (2012) 1–9. https://doi.org/10.1007/s13758-012-0025-y.

[370] S. Meghezi, F. Couet, P. Chevallier, D. Mantovani, Effects of a Pseudophysiological Environment on the Elastic and Viscoelastic Properties of Collagen Gels, Int. J. Biomater. 2012 (2012) 1–9. https://doi.org/10.1155/2012/319290.

[371] D.G. Seifu, S. Meghezi, L. Unsworth, K. Mequanint, D. Mantovani, Viscoelastic properties of multi-layered cellularized vascular tissues fabricated from collagen gel, J. Mech. Behav. Biomed. Mater. 80 (2018) 155–

163. https://doi.org/10.1016/j.jmbbm.2018.01.021.

[372] D.B. Camasão, M. González-Pérez, S. Palladino, M. Alonso, J.C. Rodríguez-Cabello, D. Mantovani, Elastin-like recombinamers in collagen-based tubular gels improve cell-mediated remodeling and viscoelastic properties, Biomater. Sci. 8 (2020). https://doi.org/10.1039/d0bm00292e.

[373] F. Boccafoschi, N. Rajan, J. Habermehl, D. Mantovani, Preparation and characterization of a scaffold for vascular tissue engineering by direct-assembling of collagen and cells in a cylindrical geometry, Macromol. Biosci. 7 (2007) 719–726. https://doi.org/10.1002/mabi.200600242.

[374] D. Pezzoli, J. Di Paolo, H. Kumra, G. Fois, G. Candiani, D.P. Reinhardt, D. Mantovani, Fibronectin promotes elastin deposition, elasticity and mechanical strength in cellularised collagen-based scaffolds, Biomaterials. 180 (2018) 130–142. https://doi.org/10.1016/j.biomaterials.2018.07.013.

[375] J. Joy, R. Aid-Launais, J. Pereira, G. Pavon-Djavid, A.R. Ray, D. Letourneur, A. Meddahi-Pellé, B. Gupta, Gelatin-polytrimethylene carbonate blend based electrospun tubular construct as a potential vascular biomaterial, Mater. Sci. Eng. C. 106 (2020) 110178. https://doi.org/10.1016/j.msec.2019.110178.

[376] S.G. Wise, M.J. Byrom, A. Waterhouse, P.G. Bannon, M.K.C. Ng, A.S. Weiss, A multilayered synthetic human elastin/polycaprolactone hybrid vascular graft with tailored mechanical properties, Acta Biomater. 7 (2011) 295–303. https://doi.org/10.1016/j.actbio.2010.07.022.

[377] J. Huling, I.K. Ko, A. Atala, J.J. Yoo, Fabrication of biomimetic vascular scaffolds for 3D tissue constructs using vascular corrosion casts, Acta Biomater. 32 (2016) 190–197. https://doi.org/10.1016/j.actbio.2016.01.005.

[378] M.B. Browning, D. Dempsey, V. Guiza, S. Becerra, J. Rivera, B. Russell, M. Höök, F. Clubb, M. Miller, T. Fossum, J.F. Dong, A.L. Bergeron, M. Hahn, E. Cosgriff-Hernandez, Multilayer vascular grafts based on collagen-mimetic proteins, Acta Biomater. 8 (2012) 1010–1021. https://doi.org/10.1016/j.actbio.2011.11.015.

[379] Y.E. Aguirre-Chagala, V. Altuzar, E. León-Sarabia, J.C. Tinoco-Magaña, J.M. Yañez-Limón, C. Mendoza-Barrera, Physicochemical properties of polycaprolactone/collagen/elastin nanofibers fabricated by electrospinning, Mater. Sci. Eng. C. 76 (2017) 897–907. https://doi.org/10.1016/j.msec.2017.03.118.

[380] J. Kucinska-Lipka, I. Gubanska, H. Janik, M. Sienkiewicz, Fabrication of polyurethane and polyurethane based composite fibres by the electrospinning technique for soft tissue engineering of cardiovascular system, Mater. Sci. Eng. C. 46 (2015) 166–176. https://doi.org/10.1016/j.msec.2014.10.027.

[381] H. Bergmeister, N. Seyidova, C. Schreiber, M. Strobl, C. Grasl, I. Walter, B. Messner, S. Baudis, S. Fröhlich, M. Marchetti-Deschmann, M. Griesser, M. Di Franco, M. Krssak, R. Liska, H. Schima, Biodegradable, thermoplastic polyurethane grafts for small diameter vascular replacements, Acta Biomater. 11 (2015) 104–113. https://doi.org/10.1016/j.actbio.2014.09.003.

[382] J. Han, P. Lazarovici, C. Pomerantz, X. Chen, Y. Wei, P.I. Lelkes, Co-electrospun blends of PLGA, gelatin, and elastin as potential nonthrombogenic scaffolds for vascular tissue engineering, Biomacromolecules. 12 (2011) 399–408. https://doi.org/10.1021/bm101149r.

[383] O. Chrzanowska, M.H. Struszczyk, I. Krucinska, M. Puchalski, L. Herczyńska, M. Chrzanowski,

Elaboration of small-diameter vascular prostheses - Selection of appropriate sterilisation method, J. Appl. Polym. Sci. 131 (2014) 9611–9620. https://doi.org/10.1002/app.40812.

[384] Y. Wu, Y. Qin, Z. Wang, J. Wang, C. Zhang, C. Li, D. Kong, The regeneration of macro-porous electrospun poly(ε-caprolactone) vascular graft during long-term in situ implantation, J. Biomed. Mater. Res. - Part B Appl. Biomater. 106 (2018) 1618–1627. https://doi.org/10.1002/jbm.b.33967.

[385] K. Wang, Q. Zhang, L. Zhao, Y. Pan, T. Wang, D. Zhi, S. Ma, P. Zhang, T. Zhao, S. Zhang, W. Li, M. Zhu, Y. Zhu, J. Zhang, M. Qiao, D. Kong, Functional Modification of Electrospun Poly(ε-caprolactone) Vascular Grafts with the Fusion Protein VEGF-HGFI Enhanced Vascular Regeneration, ACS Appl. Mater. Interfaces. 9 (2017) 11415–11427. https://doi.org/10.1021/acsami.6b16713.

[386] I. Pennings, E.E. van Haaften, T. Jungst, J.A. Bulsink, A.J.W.P. Rosenberg, J. Groll, C.V.C. Bouten, N.A. Kurniawan, A.I.P.M. Smits, D. Gawlitta, Layer-specific cell differentiation in bi-layered vascular grafts under flow perfusion, Biofabrication. 12 (2019) 015009. https://doi.org/10.1088/1758-5090/ab47f0.

[387] T. Sugiura, S. Tara, H. Nakayama, H. Kurobe, T. Yi, Y.U. Lee, A.Y. Lee, C.K. Breuer, T. Shinoka, Novel Bioresorbable Vascular Graft With Sponge-Type Scaffold as a Small-Diameter Arterial Graft, Ann. Thorac. Surg. 102 (2016) 720–727. https://doi.org/10.1016/j.athoracsur.2016.01.110.

[388] W. Wang, J. Hu, C. He, W. Nie, W. Feng, K. Qiu, X. Zhou, Y. Gao, G. Wang, Heparinized PLLA/PLCL nanofibrous scaffold for potential engineering of small-diameter blood vessel: Tunable elasticity and anticoagulation property, J. Biomed. Mater. Res. - Part A. 103 (2015) 1784–1797. https://doi.org/10.1002/jbm.a.35315.

[389] I.P. Dobrovolskaya, G.I. Popov, E.M. Ivan'kova, G.Y. Yukina, V.N. Vavilov, V.E. Yudin, P. V. Popryadukhin, Tissue-Engineered Vascular Graft of Small Diameter Based on Electrospun Polylactide Microfibers, Int. J. Biomater. 2017 (2017) 1–10. https://doi.org/10.1155/2017/9034186.

[390] A.I. Pangesty, T. Arahira, M. Todo, Development and characterization of hybrid tubular structure of PLCL porous scaffold with hMSCs/ECs cell sheet, J. Mater. Sci. Mater. Med. 28 (2017). https://doi.org/10.1007/s10856-017-5985-5.

[391] V.M. Merkle, P.L. Tran, M. Hutchinson, K.R. Ammann, K. Decook, X. Wu, M.J. Slepian, Core-shell PVA/gelatin electrospun nanofibers promote human umbilical vein endothelial cell and smooth muscle cell proliferation and migration, Acta Biomater. 27 (2015) 77–87. https://doi.org/10.1016/j.actbio.2015.08.044.

[392] R.H. Liu, C.S. Ong, T. Fukunishi, K. Ong, N. Hibino, Review of Vascular Graft Studies in Large Animal Models, Tissue Eng. Part B Rev. 24 (2017) 133–143. https://doi.org/10.1089/ten.teb.2017.0350.

[393] T. Fukunishi, T. Shoji, T. Shinoka, Nanofiber composites in vascular tissue engineering, in: Nanofiber Compos. Biomed. Appl., 2017. https://doi.org/10.1016/B978-0-08-100173-8.00018-1.

[394] W. Mrówczyński, D. Mugnai, S. De Valence, J.C. Tille, E. Khabiri, M. Cikirikcioglu, M. Möller, B.H. Walpoth, Porcine carotid artery replacement with biodegradable electrospun poly-e-caprolactone vascular prosthesis, J. Vasc. Surg. 59 (2014). https://doi.org/10.1016/j.jvs.2013.03.004.

[395] T. Billiet, E. Gevaert, T. De Schryver, M. Cornelissen, P. Dubruel, The 3D printing of gelatin methacrylamide cell-laden tissue-engineered constructs with high cell viability, Biomaterials. 35 (2014) 49–

62. https://doi.org/10.1016/j.biomaterials.2013.09.078.

[396] N.A. Sears, D.R. Seshadri, P.S. Dhavalikar, E. Cosgriff-Hernandez, A Review of Three-Dimensional Printing in Tissue Engineering, Tissue Eng. - Part B Rev. 22 (2016) 298–310. https://doi.org/10.1089/ten.teb.2015.0464.

[397] D.B. Camasão, D. Pezzoli, C. Loy, H. Kumra, L. Levesque, D.P. Reinhardt, G. Candiani, D. Mantovani, Increasing Cell Seeding Density Improves Elastin Expression and Mechanical Properties in Collagen Gel-Based Scaffolds Cellularized with Smooth Muscle Cells, Biotechnol. J. 1700768 (2018) 1700768. https://doi.org/10.1002/biot.201700768.

[398] C. Loy, D. Pezzoli, G. Candiani, D. Mantovani, A Cost-Effective Culture System for the In Vitro Assembly, Maturation, and Stimulation of Advanced Multilayered Multiculture Tubular Tissue Models, Biotechnol. J. 13 (2018) 1–9. https://doi.org/10.1002/biot.201700359.

[399] T. Jungst, I. Pennings, M. Schmitz, A.J.W.P.W.P. Rosenberg, J. Groll, D. Gawlitta, Heterotypic Scaffold Design Orchestrates Primary Cell Organization and Phenotypes in Cocultured Small Diameter Vascular Grafts, Adv. Funct. Mater. 29 (2019). https://doi.org/10.1002/adfm.201905987.

[400] V. Chausse, R. Schieber, Y. Raymond, B. Ségry, R. Sabaté, K. Kolandaivelu, M.P. Ginebra, M. Pegueroles, Solvent-cast direct-writing as a fabrication strategy for radiopaque stents, Addit. Manuf. 48 (2021). https://doi.org/10.1016/j.addma.2021.102392.

[401] N. Rajan, J. Habermehl, M.-F.F. Coté, C.J. Doillon, D. Mantovani, Preparation of ready-to-use, storable and reconstituted type I collagen from rat tail tendon for tissue engineering applications, Nat. Protoc. 1 (2007) 2753–2758. https://doi.org/10.1038/nprot.2006.430.

[402] D. Wang, Y. Xu, Q. Li, L.S. Turng, Artificial small-diameter blood vessels: Materials, fabrication, surface modification, mechanical properties, and bioactive functionalities, J. Mater. Chem. B. 8 (2020) 1801–1822. https://doi.org/10.1039/c9tb01849b.

[403] Q.P. Pham, U. Sharma, A.G. Mikos, Electrospun poly (ε-caprolactone) microfiber and multilayer nanofiber/microfiber scaffolds: Characterization of scaffolds and measurement of cellular infiltration, Biomacromolecules. 7 (2006). https://doi.org/10.1021/bm060680j.

[404] M. Chen, P.K. Patra, S.B. Warner, S. Bhowmick, Role of fiber diameter in adhesion and proliferation of NIH 3T3 fibroblast on electrospun polycaprolactone scaffolds, Tissue Eng. 13 (2007). https://doi.org/10.1089/ten.2006.0205.

[405] S. Soliman, S. Sant, J.W. Nichol, M. Khabiry, E. Traversa, A. Khademhosseini, Controlling the porosity of fibrous scaffolds by modulating the fiber diameter and packing density, J. Biomed. Mater. Res. - Part A. 96 A (2011). https://doi.org/10.1002/jbm.a.33010.

[406] I. Bružauskaitė, D. Bironaitė, E. Bagdonas, E. Bernotienė, Scaffolds and cells for tissue regeneration: different scaffold pore sizes—different cell effects, Cytotechnology. 68 (2016). https://doi.org/10.1007/s10616-015-9895-4.

[407] P. Fernandez, A.R. Bausch, The compaction of gels by cells: A case of collective mechanical activity, Integr. Biol. 1 (2009). https://doi.org/10.1039/b822897c.

[408] A. Mathur, Z. Ma, P. Loskill, S. Jeeawoody, K.E. Healy, In vitro cardiac tissue models: Current status and future prospects, Adv. Drug Deliv. Rev. 96 (2016) 203–213. https://doi.org/10.1016/j.addr.2015.09.011.

[409] A.S. Hoffman, Hydrogels for biomedical applications, Adv. Drug Deliv. Rev. 64 (2012) 18–23. https://doi.org/10.1016/j.addr.2012.09.010.

[410] S. Heydarkhan-Hagvall, K. Schenke-Layland, A.P. Dhanasopon, F. Rofail, H. Smith, B.M. Wu, R. Shemin, R.E. Beygui, W.R. MacLellan, Three-dimensional electrospun ECM-based hybrid scaffolds for cardiovascular tissue engineering, Biomaterials. 29 (2008) 2907–2914. https://doi.org/10.1016/j.biomaterials.2008.03.034.

[411] R. Ravichandran, M.M. Islam, E.I. Alarcon, A. Samanta, S. Wang, P. Lundström, J. Hilborn, M. Griffith, J. Phopase, Functionalised type-I collagen as a hydrogel building block for bio-orthogonal tissue engineering applications, J. Mater. Chem. B. 4 (2016) 318–326. https://doi.org/10.1039/C5TB02035B.

[412] J. Van Hoorick, P. Gruber, M. Markovic, M. Tromayer, J. Van Erps, H. Thienpont, R. Liska, A. Ovsianikov, P. Dubruel, S. Van Vlierberghe, Cross-Linkable Gelatins with Superior Mechanical Properties Through Carboxylic Acid Modification: Increasing the Two-Photon Polymerization Potential, Biomacromolecules. 18 (2017) 3260–3272. https://doi.org/10.1021/acs.biomac.7b00905.

[413] J. Hackethal, S. Mühleder, A. Hofer, K.H. Schneider, J. Prüller, S. Hennerbichler, H. Redl, A. Teuschl, An Effective Method of *Atelocollagen* Type 1/3 Isolation from Human Placenta and Its *In Vitro* Characterization in Two-Dimensional and Three-Dimensional Cell Culture Applications, Tissue Eng. Part C Methods. 23 (2017) 274–285. https://doi.org/10.1089/ten.tec.2017.0016.

[414] M. Achilli, J. Lagueux, D. Mantovani, On the effects of UV-C and pH on the mechanical behavior, molecular conformation and cell viability of collagen-based scaffold for vascular tissue engineering, Macromol. Biosci. 10 (2010) 307–316. https://doi.org/10.1002/mabi.200900248.

[415] C.P. Barnes, C.W. Pemble, D.D. Brand, D.G. Simpson, G.L. Bowlin, Cross-Linking Electrospun Type II Collagen Tissue Engineering Scaffolds with Carbodiimide in Ethanol, Tissue Eng. 13 (2007) 1593–1605. https://doi.org/10.1089/ten.2006.0292.

[416] G. Tronci, S.J. Russell, D.J. Wood, Photo-active collagen systems with controlled triple helix architecture, J. Mater. Chem. B. 1 (2013) 3705–3715. https://doi.org/10.1039/c3tb20720j.

[417] E. Leikina, M. V. Mertts, N. Kuznetsova, S. Leikin, Type I collagen is thermally unstable at body temperature, Proc. Natl. Acad. Sci. U. S. A. 99 (2002) 1314–1318. https://doi.org/10.1073/pnas.032307099.

[418] W.E. Hennink, C.F. van Nostrum, Novel crosslinking methods to design hydrogels, Adv. Drug Deliv. Rev. 64 (2012) 223–236. https://doi.org/10.1016/j.addr.2012.09.009.

[419] L. Gu, T. Shan, Y. xuan Ma, F.R. Tay, L. Niu, Novel Biomedical Applications of Crosslinked Collagen, Trends Biotechnol. xx (2018). https://doi.org/10.1016/j.tibtech.2018.10.007.

[420] L. Tytgat, M. Vagenende, H. Declercq, J.C. Martins, H. Thienpont, H. Ottevaere, P. Dubruel, S. Van Vlierberghe, Synergistic effect of κ-carrageenan and gelatin blends towards adipose tissue engineering, Carbohydr. Polym. 189 (2018) 1–9. https://doi.org/10.1016/j.carbpol.2018.02.002.

[421] A.I. Van Den Bulcke, B. Bogdanov, N. De Rooze, E.H. Schacht, M. Cornelissen, H. Berghmans, Structural and rheological properties of methacrylamide modified gelatin hydrogels., Biomacromolecules. 1 (2000) 31–38. https://doi.org/10.1021/bm990017d.

[422] K. Yue, G. Trujillo-de Santiago, M.M. Alvarez, A. Tamayol, N. Annabi, A. Khademhosseini, Synthesis, properties, and biomedical applications of gelatin methacryloyl (GelMA) hydrogels, Biomaterials. 73 (2015) 254–271. https://doi.org/10.1016/j.biomaterials.2015.08.045.

[423] E. Hoch, T. Hirth, G.E.M.M. Tovar, K. Borchers, Chemical tailoring of gelatin to adjust its chemical and physical properties for functional bioprinting, J. Mater. Chem. B. 1 (2013) 5675–5685. https://doi.org/10.1039/c3tb20745e.

[424] B.J. Klotz, D. Gawlitta, A.J.W.P. Rosenberg, J. Malda, F.P.W. Melchels, Gelatin-Methacryloyl Hydrogels: Towards Biofabrication-Based Tissue Repair, Trends Biotechnol. 34 (2016) 394–407. https://doi.org/10.1016/j.tibtech.2016.01.002.

[425] M. Markovic, J. Van Hoorick, K. Hölzl, M. Tromayer, P. Gruber, Hybrid tissue engineering scaffolds by combination of 3D printing and cell photoencapsulation Hybrid Tissue Engineering Scaffolds by Combination of Three-Dimensional Printing and Cell Photoencapsulation, J. Nanotechnol. Eng. Med. 6 (2015). https://doi.org/10.1115/1.4031466.

[426] B. Kerkaert, F. Mestdagh, T. Cucu, P.R. Aedo, S.Y. Ling, B. De Meulenaer, Hypochlorous and peracetic acid induced oxidation of dairy proteins, J. Agric. Food Chem. 59 (2011) 907–914. https://doi.org/10.1021/jf1037807.

[427] J. Van Hoorick, P. Gruber, M. Markovic, M. Rollot, G.J. Graulus, M. Vagenende, M. Tromayer, J. Van Erps, H. Thienpont, J.C. Martins, S. Baudis, A. Ovsianikov, P. Dubruel, S. Van Vlierberghe, Highly Reactive Thiol-Norbornene Photo-Click Hydrogels: Toward Improved Processability, Macromol. Rapid Commun. 39 (2018) 1–7. https://doi.org/10.1002/marc.201800181.

[428] J. Nonkumwong, P. Pakawanit, A. Wipatanawin, P. Jantaratana, S. Ananta, L. Srisombat, Synthesis and cytotoxicity study of magnesium ferrite-gold core-shell nanoparticles, Mater. Sci. Eng. C. 61 (2016) 123–132. https://doi.org/10.1016/j.msec.2015.12.021.

[429] D. Loessner, C. Meinert, E. Kaemmerer, L.C. Martine, K. Yue, P.A. Levett, T.J. Klein, F.P.W. Melchels, A. Khademhosseini, D.W. Hutmacher, Functionalization, preparation and use of cell-laden gelatin methacryloyl-based hydrogels as modular tissue culture platforms., Nat. Protoc. 11 (2016) 727–46. https://doi.org/10.1038/nprot.2016.037.

[430] J. Pupkaite, M. Ahumada, S. Mclaughlin, M. Temkit, S. Alaziz, R. Seymour, M. Ruel, I. Kochevar, M. Griffith, E.J. Suuronen, E.I. Alarcon, Collagen-Based Photoactive Agent for Tissue Bonding, ACS Appl. Mater. Interfaces. 9 (2017) 9265–9270. https://doi.org/10.1021/acsami.7b01984.

[431] S. Potorac, M. Popa, L. Picton, V. Dulong, L. Verestiuc, D. Le Cerf, Collagen functionalized with unsaturated cyclic anhydrides - Interactions in solution and solid state, Biopolymers. 101 (2014) 228–236. https://doi.org/10.1002/bip.22319.

[432] R. Holmes, X. Bin Yang, A. Dunne, L. Florea, D. Wood, G. Tronci, Thiol-ene photo-click collagen-PEG

hydrogels: Impact of water-soluble photoinitiators on cell viability, gelation kinetics and rheological properties, Polymers (Basel). 9 (2017). https://doi.org/10.3390/polym9060226.

[433] T. Billiet, Gelatin Functionalizations for Cell Embedding in 3D Geometries Using Rapid Prototyping Technology, Ghent University, 2014.

[434] M. Gauza-Włodarczyk, L. Kubisz, D. Włodarczyk, Amino acid composition in determination of collagen origin and assessment of physical factors effects, Int. J. Biol. Macromol. 104 (2017) 987–991. https://doi.org/10.1016/j.ijbiomac.2017.07.013.

[435] A. Bigi, S. Panzavolta, K. Rubini, Relationship between triple-helix content and mechanical properties of gelatin films, Biomaterials. 25 (2004) 5675–5680. https://doi.org/10.1016/j.biomaterials.2004.01.033.

[436] L. Altomare, L. Bonetti, C.E. Campiglio, L. De Nardo, L. Draghi, F. Tana, S. Farè, Biopolymer-based strategies in the design of smart medical devices and artificial organs, Int. J. Artif. Organs. (2018). https://doi.org/10.1177/0391398818765323.

[437] M. Taylor, P. Tomlins, T. Sahota, Thermoresponsive Gels, Gels. 3 (2017) 4. https://doi.org/10.3390/gels3010004.

[438] H. Capella-Monsonís, J.Q. Coentro, V. Graceffa, Z. Wu, D.I. Zeugolis, An experimental toolbox for characterization of mammalian collagen type I in biological specimens, Nat. Protoc. 13 (2018) 507–529. https://doi.org/10.1038/nprot.2017.117.

[439] N. Davidenko, C.F. Schuster, D. V. Bax, N. Raynal, R.W. Farndale, S.M. Best, R.E. Cameron, Control of crosslinking for tailoring collagen-based scaffolds stability and mechanics, Acta Biomater. 25 (2015) 131–142. https://doi.org/10.1016/j.actbio.2015.07.034.

[440] L. Tytgat, M. Markovic, T.H. Qazi, M. Vagenende, F. Bray, J.C. Martins, C. Rolando, H. Thienpont, H. Ottevaere, A. Ovsianikov, P. Dubruel, S. Van Vlierberghe, Photo-crosslinkable recombinant collagen mimics for tissue engineering applications, J. Mater. Chem. B. 7 (2019) 3100–3108. https://doi.org/10.1039/c8tb03308k.

[441] W.T. Brinkman, K. Nagapudi, B.S. Thomas, E.L. Chaikof, Photo-cross-linking of type I collagen gels in the presence of smooth muscle cells: Mechanical properties, cell viability, and function, Biomacromolecules. 4 (2003) 890–895. https://doi.org/10.1021/bm0257412.

[442] L. He, C. Mu, D. Li, W. Lin, Revisit the pre-transition of type I collagen denaturation in dilute solution by ultrasensitive differential scanning calorimetry, Thermochim. Acta. 548 (2012) 1–5. https://doi.org/10.1016/j.tca.2012.08.024.

[443] C.A. Miles, T. V. Burjanadze, A.J. Bailey, The kinetics of the thermal denaturation of collagen in unrestrained rat tail tendon determined by differential scanning calorimetry, J. Mol. Biol. 245 (1995) 437–446. https://doi.org/10.1006/jmbi.1994.0035.

[444] E. Hoch, C. Schuh, T. Hirth, G.E.M. Tovar, K. Borchers, Stiff gelatin hydrogels can be photo-chemically synthesized from low viscous gelatin solutions using molecularly functionalized gelatin with a high degree of methacrylation., J. Mater. Sci. Mater. Med. 23 (2012) 2607–17. https://doi.org/10.1007/s10856-012-4731-2.

[445] I. Van Nieuwenhove, A. Salamon, K. Peters, G.J. Graulus, J.C. Martins, D. Frankel, K. Kersemans, F. De Vos, S. Van Vlierberghe, P. Dubruel, Gelatin- and starch-based hydrogels. Part A: Hydrogel development, characterization and coating, Carbohydr. Polym. 152 (2016) 129–139. https://doi.org/10.1016/j.carbpol.2016.06.098.

[446] L.H. PETERSON, Systems behavior, feed-back loops, and high blood pressure research., Circ. Res. 2 (1963) 585–596. https://doi.org/10.1161/01.res.12.5.585.

[447] L. TOBIAN, Interrelationship of electrolytes, juxtaglomerular cells and hypertension, Physiol. Rev. 40 (1960) 280–312. https://doi.org/10.1152/physrev.1960.40.2.280.

[448] J. Black, G. Hastings, Handbook of Biomaterial Properties, Chapman & Hall, 1998. https://doi.org/10.1007/978-1-4615-5801-9.

[449] S.S. Choi, S.H. Ha, Water swelling behaviors of silica-reinforced NBR composites in deionized water and salt solution, J. Ind. Eng. Chem. 16 (2010) 238–242. https://doi.org/10.1016/j.jiec.2010.01.052.

[450] G.J. Graulus, A. Mignon, S. Van Vlierberghe, H. Declercq, K. Fehér, M. Cornelissen, J.C. Martins, P. Dubruel, Cross-linkable alginate-graft-gelatin copolymers for tissue engineering applications, Eur. Polym. J. 72 (2015) 494–506. https://doi.org/10.1016/j.eurpolymj.2015.06.033.

[451] Š. Rýglová, M. Braun, T. Suchý, Collagen and Its Modifications—Crucial Aspects with Concern to Its Processing and Analysis, Macromol. Mater. Eng. 302 (2017) 1–29. https://doi.org/10.1002/mame.201600460.

[452] D.J. Medina-Leyte, M. Domínguez-Pérez, I. Mercado, M.T. Villarreal-Molina, L. Jacobo-Albavera, Use of Human Umbilical Vein Endothelial Cells (HUVEC) as a Model to Study Cardiovascular Disease : A Review, Appl. Sci. 10 (2020). https://doi.org/10.3390/app10030938.

[453] N. Yamamura, R. Sudo, M. Ikeda, K. Tanishita, Effects of the mechanical properties of collagen gel on the in vitro formation of microvessel networks by endothelial cells, Tissue Eng. 13 (2007) 1443–1453. https://doi.org/10.1089/ten.2006.0333.

[454] Y.M. Chen, J.J. Yang, J.P. Gong, Adhesion, spreading, and proliferation of endothelial cells on charged hydrogels, J. Adhes. 85 (2009) 839–868. https://doi.org/10.1080/00218460903291486.

[455] J. Ramon-Azcon, S. Ahadian, R. Obregon, G. Camci-Unal, S. Ostrovidov, V. Hosseini, H. Kaji, K. Ino, H. Shiku, A. Khademhosseini, T. Matsue, Gelatin methacrylate as a promising hydrogel for 3D microscale organization and proliferation of dielectrophoretically patterned cells, Lab Chip. 12 (2012) 2959–2969. https://doi.org/10.1039/c2lc40213k.

[456] E. Seo, K.W. Seo, J.E. Gil, Y.R. Ha, E. Yeom, S. Lee, S.J. Lee, Biophysiochemical properties of endothelial cells cultured on bio-inspired collagen films, BMC Biotechnol. 14 (2014) 1–16. https://doi.org/10.1186/1472-6750-14-61.

[457] J. Gavard, Endothelial permeability and VE-cadherin, Cell Adh. Migr. 8 (2014) 158–164. https://doi.org/10.4161/cam.29026.

[458] M. Janmaleki, M. Pachenari, S.M. Seyedpour, R. Shahghadami, A. Sanati-Nezhad, Impact of Simulated Microgravity on Cytoskeleton and Viscoelastic Properties of Endothelial Cell, Sci. Rep. 6 (2016) 1–11.

https://doi.org/10.1038/srep32418.

[459] C.A. Reinhart-King, M. Dembo, D.A. Hammer, The dynamics and mechanics of endothelial cell spreading, Biophys. J. 89 (2005) 676–689. https://doi.org/10.1529/biophysj.104.054320.

[460] C. Jia, J. Shi, T. Han, F. Li, P. Cai, A.C.H. Yu, P. Qin, New Insights in the Actin Cytoskeleton Dynamics of the Sonoporated Human Umbilical Vein Endothelial Cells, in: 2018 IEEE Int. Ultrason. Symp., 2018: pp. 1–4. https://doi.org/10.1109/ULTSYM.2018.8579686.

[461] X. Liu, C. Zheng, X. Luo, X. Wang, H. Jiang, Recent advances of collagen-based biomaterials: Multi-hierarchical structure, modification and biomedical applications, Mater. Sci. Eng. C. 99 (2019) 1509–1522. https://doi.org/10.1016/j.msec.2019.02.070.

[462] T. Wang, J. Lew, J. Premkumar, C.L. Poh, M. Win Naing, Production of recombinant collagen: state of the art and challenges, Eng. Biol. 1 (2017) 18–23. https://doi.org/10.1049/enb.2017.0003.

[463] M.D. Shoulders, R.T. Raines, Collagen Structure and Stability, Annu Rev Biochem. 78 (2009) 929–958. https://doi.org/10.1146/annurev.biochem.77.032207.120833.COLLAGEN.

[464] S. Hinderer, S.L. Layland, K. Schenke-Layland, ECM and ECM-like materials - Biomaterials for applications in regenerative medicine and cancer therapy, Adv. Drug Deliv. Rev. 97 (2016) 260–269. https://doi.org/10.1016/j.addr.2015.11.019.

[465] M. Meyer, Processing of collagen based biomaterials and the resulting materials properties, Biomed. Eng. Online. 18 (2019) 1–74. https://doi.org/10.1186/s12938-019-0647-0.

[466] U. Hersel, C. Dahmen, H. Kessler, RGD modified polymers: Biomaterials for stimulated cell adhesion and beyond, Biomaterials. 24 (2003) 4385–4415. https://doi.org/10.1016/S0142-9612(03)00343-0.

[467] P.M. Gallop, M. a Paz, Posttranslational protein modifications, with special attention to collagen and elastin., Physiol. Rev. 55 (1975) 418–87. http://www.ncbi.nlm.nih.gov/pubmed/50603.

[468] J. Van Hoorick, A. Dobos, M. Markovic, T. Gheysens, L. Van Damme, P. Gruber, L. Tytgat, J. Van Erps, H. Thienpont, P. Dubruel, A. Ovsianikov, S. Van Vlierberghe, J. Van Hoorick, Thiol-Norbornene gelatin hydrogels: influence of thiolated crosslinker on network properties and high definition 3D printing, Biofabrication. (2020). http://iopscience.iop.org/article/10.1088/1758-5090/abc95f.

[469] L. Tytgat, L. Van Damme, J. Van Hoorick, H. Declercq, H. Thienpont, H. Ottevaere, P. Blondeel, P. Dubruel, S. Van Vlierberghe, Additive manufacturing of photo-crosslinked gelatin scaffolds for adipose tissue engineering, Acta Biomater. 94 (2019) 340–350. https://doi.org/10.1016/j.actbio.2019.05.062.

[470] R.M. Twyman, Priciples of Proteomics, BIOS Scientific Publishers, 2004.

[471] D.C. Liebler, Introduction to Proteomics, Tools for the New Biology, Humana Press Inc., 2002.

[472] R. Aebersold, M. Mann, Mass spectrometry-based proteomics, Nature. 422 (2003). https://doi.org/10.1038/nature01511.

[473] Y. Zhang, B.R. Fonslow, B. Shan, M.C. Baek, J.R. Yates, Protein analysis by shotgun/bottom-up proteomics, Chem. Rev. 113 (2013) 2343–2394. https://doi.org/10.1021/cr3003533.

[474] M.R. Larsen, M.B. Trelle, T.E. Thingholm, O.N. Jensen, Analysis of posttranslational modifications of proteins by tandem mass spectrometry, Biotechniques. 40 (2006) 790–798.

https://doi.org/10.2144/000112201.

[475] R. Gahoual, G. Bolbach, I. Ould-Melha, G. Clodic, Y.N. François, D. Scherman, N. Mignet, P. Houzé, Kinetic and structural characterization of therapeutic albumin chemical functionalization using complementary mass spectrometry techniques, J. Pharm. Biomed. Anal. 185 (2020). https://doi.org/10.1016/j.jpba.2020.113242.

[476] M.G. Albu, Collagen Gels and Matrices for Biomedical Applications, Lambert Academic Publishing, 2011. https://books.google.be/books?id=9WyWZwEACAAJ.

[477] S. Helle, F. Bray, J. Verbeke, S. Devassine, A. Courseaux, M. Facon, C. Tokarski, C. Rolando, N. Szydlowski, Proteome analysis of potato starch reveals the presence of new starch metabolic proteins as well as multiple protease inhibitors, Front. Plant Sci. 9 (2018) 1–14. https://doi.org/10.3389/fpls.2018.00746.

[478] N. Ainseba-Chirani, Z. Dembahri, C. Tokarski, C. Rolando, M. Benmouna, Newly designed polyacrylamide/dextran gels for electrophoresis protein separation: Synthesis and characterization, Polym. Int. 60 (2011) 1024–1029. https://doi.org/10.1002/pi.3035.

[479] J. Yang, R. Yan, A. Roy, D. Xu, J. Poisson, Y. Zhang, The I-TASSER Suite : protein structure and function prediction, Nat. Publ. Gr. 12 (2015) 7–8. https://doi.org/10.1038/nmeth.3213.

[480] A. Roy, A. Kucukural, Y. Zhang, I-TASSER: A unified platform for automated protein structure and function prediction, Nat. Protoc. 5 (2010) 725–738. https://doi.org/10.1038/nprot.2010.5.

[481] J. Yang, Y. Zhang, Protein Structure and Function Prediction Using I-TASSER, Curr. Protoc. Bioinforma. 52 (2015) 5.8.1-5.8.15. https://doi.org/10.1002/0471250953.bi0508s52.

[482] Y. Zhang, J. Skolnick, TM-align: A protein structure alignment algorithm based on the TM-score, Nucleic Acids Res. 33 (2005) 2302–2309. https://doi.org/10.1093/nar/gki524.

[483] H. Fushimi, T. Hiratsuka, A. Okamura, Y. Ono, I. Ogura, I. Nishimura, Recombinant collagen polypeptide as a versatile bone graft biomaterial, Commun. Mater. 1 (2020) 1–13. https://doi.org/10.1038/s43246-020-00089-9.

[484] J.U. Izunobi, C.L. Higginbotham, Polymer Molecular Weight Analysis by 1H NMR Spectroscopy, J. Chem. Educ. 88 (2011) 1098–1104. https://doi.org/10.1021/ed100461v.

[485] F.M. Arrabal-Campos, L.M. Aguilera-Sáez, I. Fernández, A diffusion NMR method for the prediction of the weight-average molecular weight of globular proteins in aqueous media of different viscosities, Anal. Methods. 11 (2019) 142–147. https://doi.org/10.1039/C8AY01817K.

[486] L. Signor, E.B. Erba, Matrix-assisted laser desorption/ionization time of flight (MALDI-TOF) mass spectrometric analysis of intact proteins larger than 100 kDa, J. Vis. Exp. (2013) 1–7. https://doi.org/10.3791/50635.

[487] A. Martinsen, G. Skjåk-Bræk, O. Smidsrød, F. Zanetti, S. Paoletti, Comparison of different methods for determination of molecular weight and molecular weight distribution of alginates, Carbohydr. Polym. 15 (1991). https://doi.org/10.1016/0144-8617(91)90031-7.

[488] R.K. Mohammad, Molecular Weight Distribution for Biopolymers: A Review, J. Polym. Biopolym. Phys.

Chem. 6 (2018).

[489] M.R. Kasaai, J. Arul, G. Charlet, Intrinsic viscosity-molecular weight relationship for chitosan, J. Polym. Sci. Part B Polym. Phys. 38 (2000). https://doi.org/10.1002/1099-0488(20001001)38:19<2591::AID-POLB110>3.0.CO;2-6.

[490] Garth W. Hastings, C. Chem, Paul Ducheyne, Macromolecular Materials, CRC Press, 2018. https://doi.org/10.1201/9781351074223.

[491] U. Nobbmann, M. Connah, B. Fish, P. Varley, C. Gee, S. Mulot, J. Chen, L. Zhou, Y. Lu, F. Sheng, J. Yi, S.E. Harding, Dynamic light scattering as a relative tool for assessing the molecular integrity and stability of monoclonal antibodies, Biotechnol. Genet. Eng. Rev. 24 (2007). https://doi.org/10.1080/02648725.2007.10648095.

[492] W. Burchard, Static and dynamic light scattering from branched polymers and biopolymers, in: Light Scatt. from Polym., 2007. https://doi.org/10.1007/3-540-12030-0_1.

[493] R.S. Langer, N.A. Peppas, Present and future applications of biomaterials in controlled drug delivery systems, Biomaterials. 2 (1981). https://doi.org/10.1016/0142-9612(81)90059-4.

[494] A.T. Metters, C.-C. Lin, Biodegradable Hydrogels: Tailoring Properties and Function through Chemistry and Structure, in: Biomaterials, CRC Press, 2007: pp. 5-1-5–44. https://doi.org/10.1201/9780849378898-5.

[495] J. Stetefeld, S.A. McKenna, T.R. Patel, Dynamic light scattering: a practical guide and applications in biomedical sciences, Biophys. Rev. 8 (2016). https://doi.org/10.1007/s12551-016-0218-6.

[496] H.B. Wineinger, J.L. Shamshina, A. Kelly, C. King, R.D. Rogers, A method for determining the uniquely high molecular weight of chitin extracted from raw shrimp shells using ionic iquids, Green Chem. 22 (2020). https://doi.org/10.1039/d0gc00753f.

[497] N.L. Kelleher, Peer Reviewed: Top-Down Proteomics, Anal. Chem. 76 (2004). https://doi.org/10.1021/ac0415657.

[498] W. Cai, T. Tucholski, B. Chen, A.J. Alpert, S. McIlwain, T. Kohmoto, S. Jin, Y. Ge, Top-Down Proteomics of Large Proteins up to 223 kDa Enabled by Serial Size Exclusion Chromatography Strategy, Anal. Chem. 89 (2017). https://doi.org/10.1021/acs.analchem.7b00380.

[499] P. Giansanti, L. Tsiatsiani, T.Y. Low, A.J.R. Heck, Six alternative proteases for mass spectrometry-based proteomics beyond trypsin, Nat. Protoc. 11 (2016) 993–1006. https://doi.org/10.1038/nprot.2016.057.

[500] J. V Olsen, M. Mann, Status of Large-scale Analysis of Post- translational Modifications by Mass Spectrometry *, Mol. Cell. Proteomics. 12 (2013) 3444–3452. https://doi.org/10.1074/mcp.O113.034181.

[501] S.K. Bharti, R. Roy, Quantitative 1H NMR spectroscopy, TrAC - Trends Anal. Chem. 35 (2012) 5–26. https://doi.org/10.1016/j.trac.2012.02.007.

[502] J.R. Benson, P.E. Hare, o-Phthalaldehyde : Fluorogenic Detection of Primary Amines in the Picomole, Proc. Natl. Acad. Sci. U. S. A. 72 (1975) 619–622.

[503] M.-S. Kim, J. Zhong, A. Pandey, Common errors in mass spectrometry-based analysis of post-translational modifications, Proteomics. 16 (2016) 700–714. https://doi.org/10.1002/pmic.201500355.

[504] C.J. Krusemark, B.L. Frey, P.J. Belshaw, L.M. Smith, Modifying the charge state distribution of proteins in electrospray ionization mass spectrometry by chemical derivatization, J. Am. Soc. Mass Spectrom. 20 (2009) 1617–1625. https://doi.org/10.1016/j.jasms.2009.04.017.

[505] B.-L. Qi, P. Liu, Q.-Y. Wang, W.-J. Cai, B.-F. Yuan, Y.-Q. Feng, Derivatization for liquid chromatography-mass spectrometry, TrAC Trends Anal. Chem. 59 (2014) 121–132. https://doi.org/https://doi.org/10.1016/j.trac.2014.03.013.

[506] S.L. Bellis, Advantages of RGD peptides for directing cell association with biomaterials, Biomaterials. 32 (2011) 4205–4210. https://doi.org/10.1016/j.biomaterials.2011.02.029.Advantages.

[507] M. Kubala, J. Geleticova, M. Huliciak, M. Zatloukalova, J. Vacek, M. Sebela, Na+/K+-ATPase inhibition by cisplatin and consequences for cisplatin nephrotoxicity, Biomed. Pap. 158 (2014) 194–200. https://doi.org/10.5507/bp.2014.018.

[508] A. V. Tolmachev, E.W. Robinson, S. Wu, L. Paša-Tolić, R.D. Smith, FT-ICR MS optimization for the analysis of intact proteins, Int. J. Mass Spectrom. 287 (2009) 32–38. https://doi.org/10.1016/j.ijms.2008.10.010.

[509] S.G. Valeja, N.K. Kaiser, F. Xian, C.L. Hendrickson, J.C. Rouse, A.G. Marshall, Unit mass baseline resolution for an intact 148 kDa therapeutic monoclonal antibody by fourier transform ion cyclotron resonance mass spectrometry, Anal. Chem. 83 (2011) 8391–8395. https://doi.org/10.1021/ac202429c.

[510] B. Bogdanov, R.D. Smith, Proteomics by fticr mass spectrometry: TOP down and bottom up, Mass Spectrom. Rev. 24 (2005) 168–200. https://doi.org/10.1002/mas.20015.

[511] A.D. Catherman, O.S. Skinner, N.L. Kelleher, Top Down proteomics: Facts and perspectives, Biochem. Biophys. Res. Commun. 445 (2014) 683–693. https://doi.org/10.1016/j.bbrc.2014.02.041.

[512] S. Techatanawat, R. Surarit, T. Suddhasthira, S.O.P. Khovidhunkit, Type I collagen extracted from rat-tail and bovine Achilles tendon for dental application: A comparative study, Asian Biomed. 5 (2011) 787–798. https://doi.org/10.5372/1905-7415.0506.111.

[513] L.C. Abraham, E. Zuena, B. Perez-Ramirez, D.L. Kaplan, Guide to collagen characterization for biomaterial studies, J. Biomed. Mater. Res. - Part B Appl. Biomater. 87 (2008) 264–285. https://doi.org/10.1002/jbm.b.31078.

[514] D.R. Eyre, T.J. Koob, K.P. Van Ness, Quantitation of hydroxypyridinium crosslinks in collagen by high-performance liquid chromatography, Anal. Biochem. 137 (1984) 380–388. https://doi.org/10.1016/0003-2697(84)90101-5.

[515] A.J. Van Der Slot-Verhoeven, E.A. Van Dura, J. Attema, B. Blauw, J. DeGroot, T.W.J. Huizinga, A.M. Zuurmond, R.A. Bank, The type of collagen cross-link determines the reversibility of experimental skin fibrosis, Biochim. Biophys. Acta - Mol. Basis Dis. 1740 (2005) 60–67. https://doi.org/10.1016/j.bbadis.2005.02.007.

[516] Q. Li, B.E. Uygun, S. Geerts, S. Ozer, M. Scalf, S.E. Gilpin, H.C. Ott, M.L. Yarmush, L.M. Smith, N. V. Welham, B.L. Frey, Proteomic analysis of naturally-sourced biological scaffolds, Biomaterials. 75 (2016) 37–46. https://doi.org/10.1016/j.biomaterials.2015.10.011.

[517] T. Dau, G. Bartolomucci, J. Rappsilber, Proteomics Using Protease Alternatives to Trypsin Benefits from Sequential Digestion with Trypsin, Anal. Chem. 92 (2020) 9523–9527. https://doi.org/10.1021/acs.analchem.0c00478.

[518] M. Buckley, Species identification of bovine, ovine and porcine type 1 collagen; comparing peptide mass fingerprinting and LC-based proteomics methods, Int. J. Mol. Sci. 17 (2016). https://doi.org/10.3390/ijms17040445.

[519] C.T. Yang, D. Ghosh, F. Beaudry, Detection of gelatin adulteration using bio-informatics, proteomics and high-resolution mass spectrometry, Food Addit. Contam. - Part A Chem. Anal. Control. Expo. Risk Assess. 35 (2018) 599–608. https://doi.org/10.1080/19440049.2017.1416680.

Annex A. Supplementary Information

Annex 1. Chapter 3 - Supplementary Information

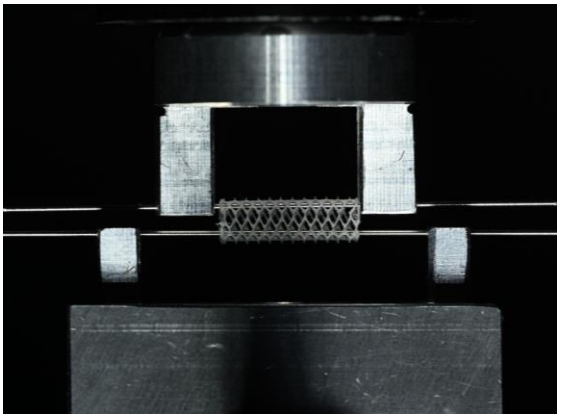

Figure S3.1. Set-up of the mechanical testing device.

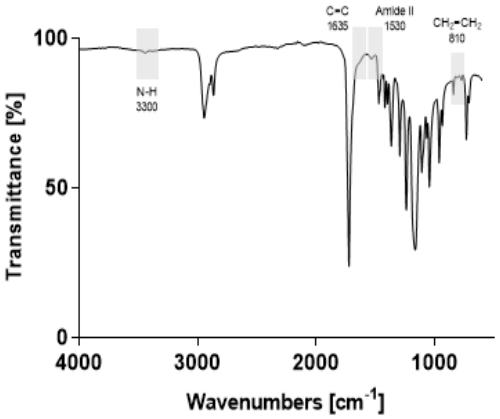

Figure S3.2. FT-IR spectrum of the developed acrylate-endcapped urethane-based PCL material.

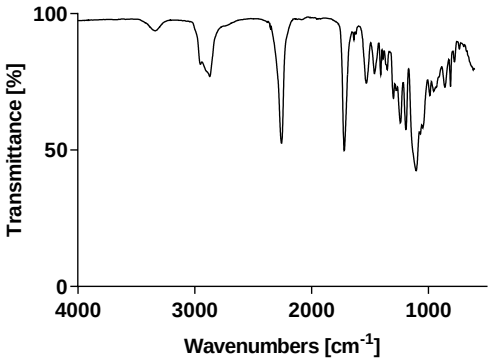

Figure S3.3. FT-IR spectrum of the endcap for the AUP PCL20k synthesis.

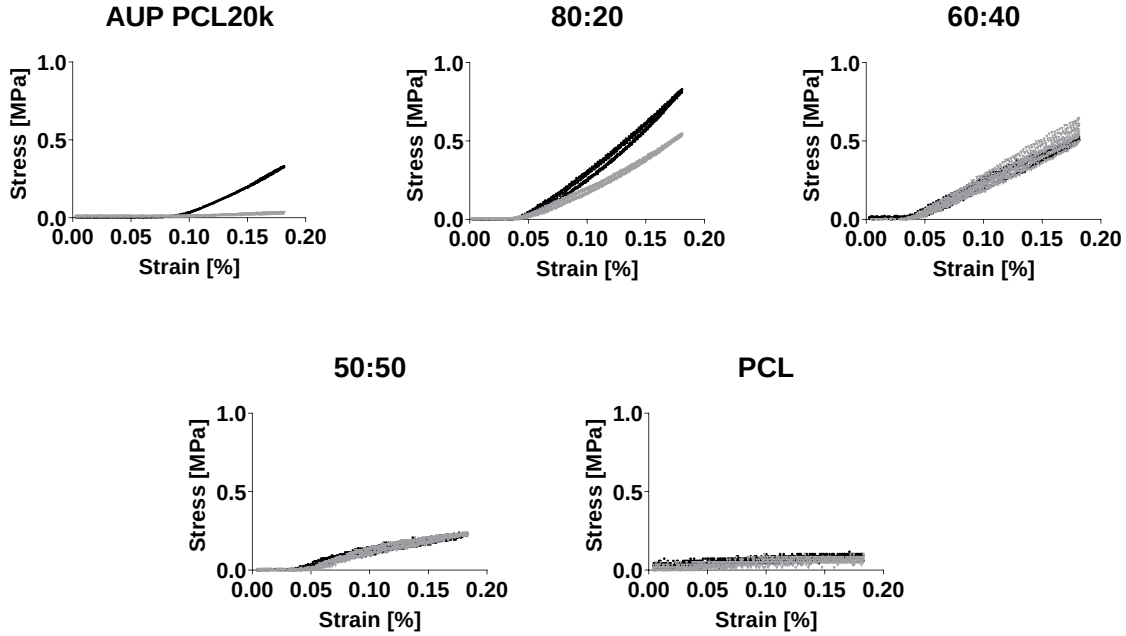

Figure S3.4. Stress [MPa versus strain [%] data obtained by uniaxial tensile testing on MEW processed tubes (AUP PCL20k, AUP PCL20k:PCL ratios of 80:20, 60:40 and 50:50, and PCL) with (black) and without (grey) post-processing UV-irradiation.

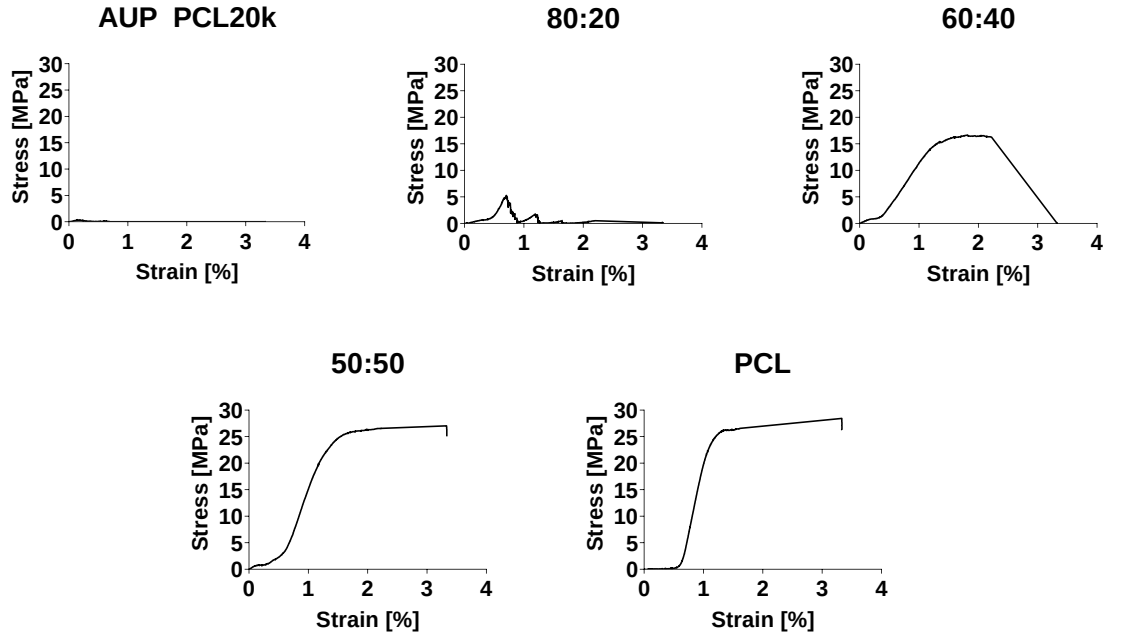

Figure S3.5. Representative graphs of pull to failure testing. Constructs were pulled to 330 % strain to elucidate their failure point. Data obtained by uniaxial tensile testing on MEW processed tubes (AUP PCL20k, AUP PCL20k:PCL ratios of 80:20, 60:40 and 50:50, and PCL) with (black) and without (grey) post-processing UV-irradiation.

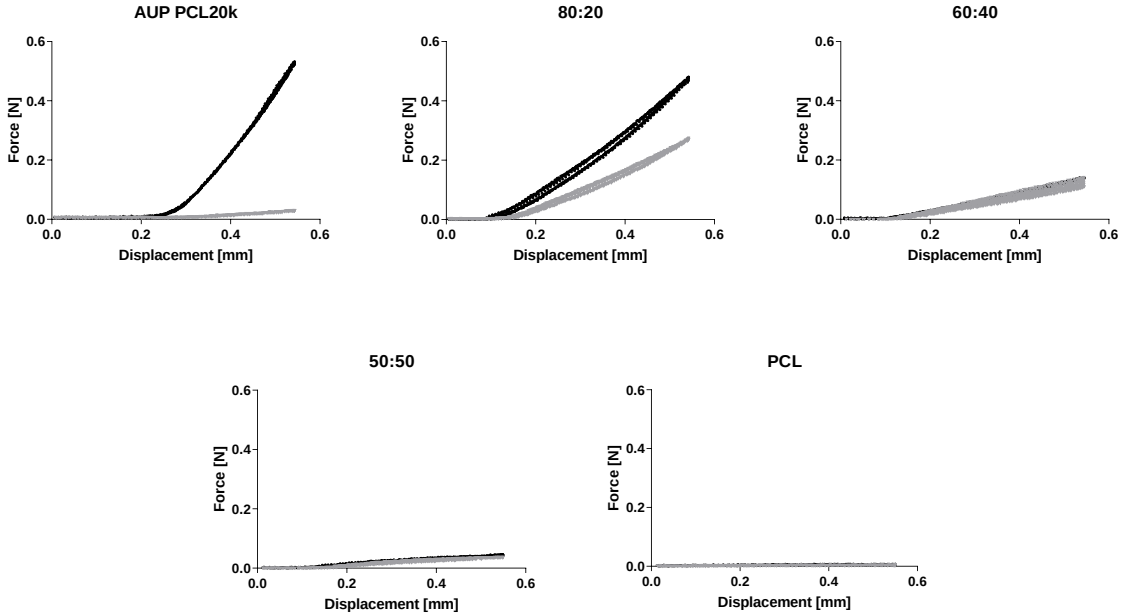

Figure S3.6. Force [N] versus displacement [mm] data obtained by uniaxial tensile testing on MEW processed tubes (AUP PCL20k, AUP PCL20k:PCL ratios of 80:20, 60:40 and 50:50, and PCL) with (black) and without (grey) post-processing UV-irradiation.

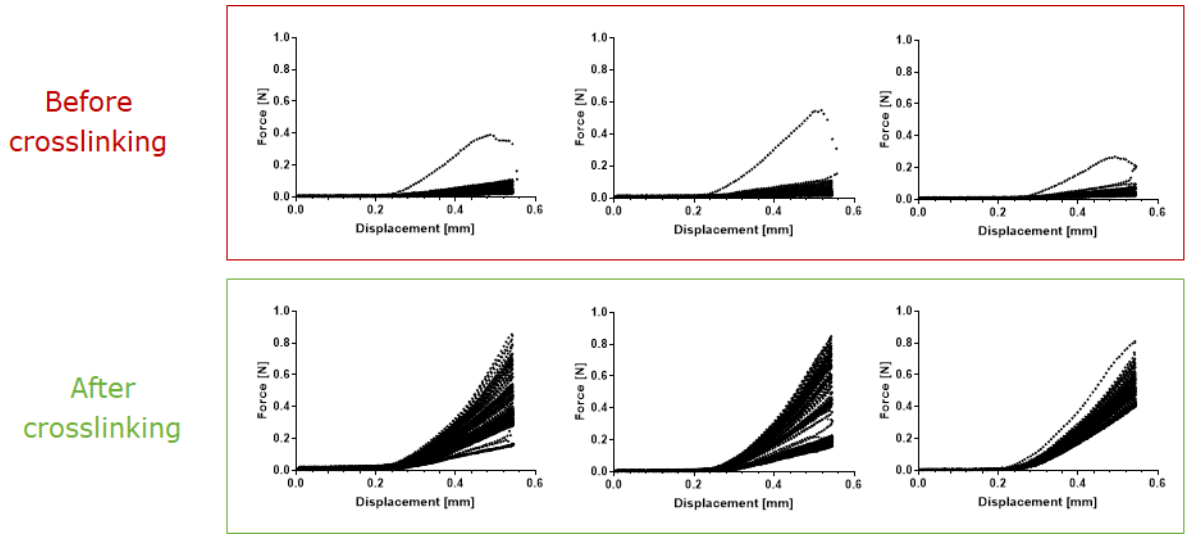

Figure S3.7. Mechanical testing on non-crosslinked versus crosslinked AUP PCL20k tubes.

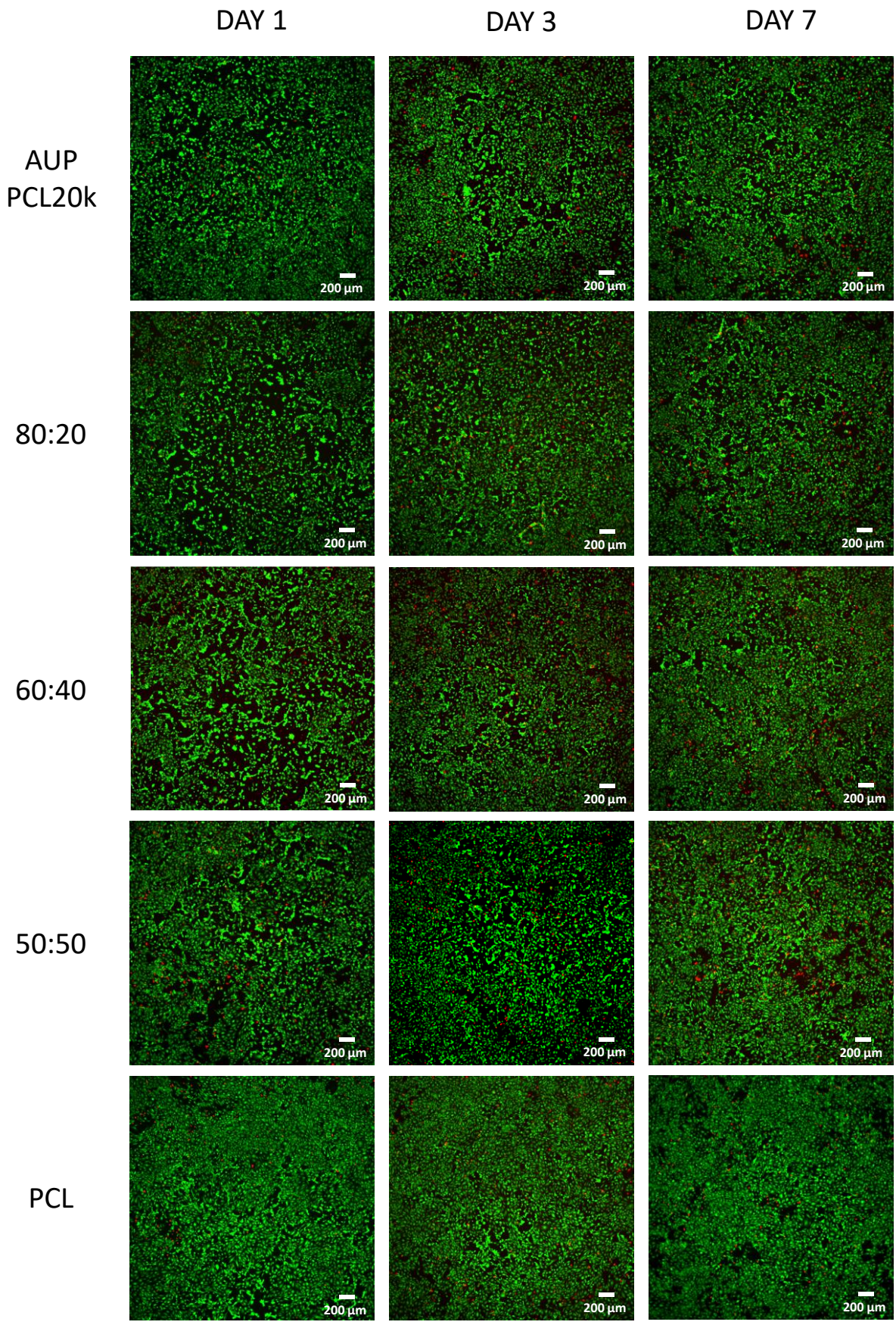

Figure S3.8. Live/dead (Ca-AM/PI) staining images of HUVECs in an indirect contact assay for AUP PCL20k, PCL and their blends at day 1, day 3 and day 7.

Annex 2. Chapter 4 - Supplementary Information

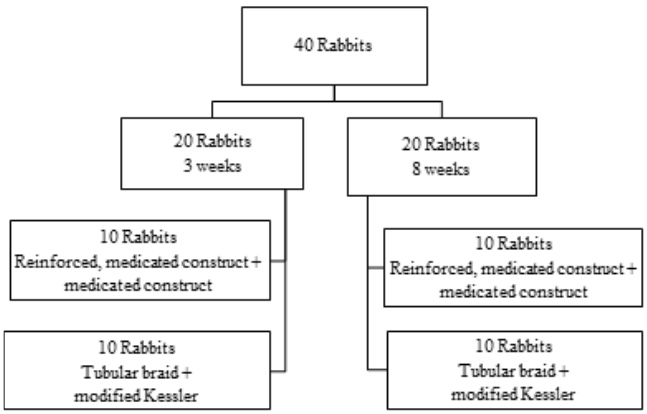

Figure S4.1. Overview of grouping details.

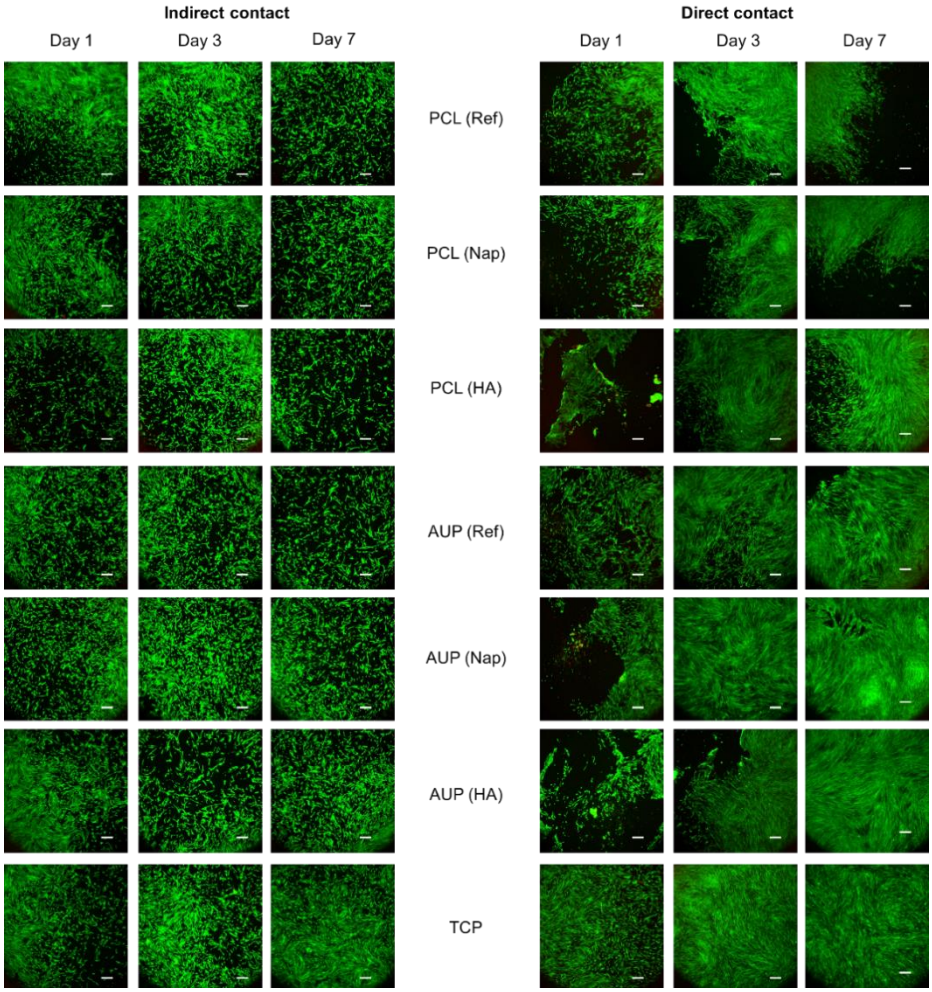

Figure S4.2. Live/Dead assay of the AUP PCL530 and PCL (reference) materials with or without naproxen or hyaluronic acid in presence of human fibroblast cells (hFBs) after 1, 3 and 7 days. This was performed in indirect contact (i.e. materials incubated in culture medium) as well as direct contact (i.e. materials placed on top of the cells). Tissue culture plastic (TCP) was used as a positive control.

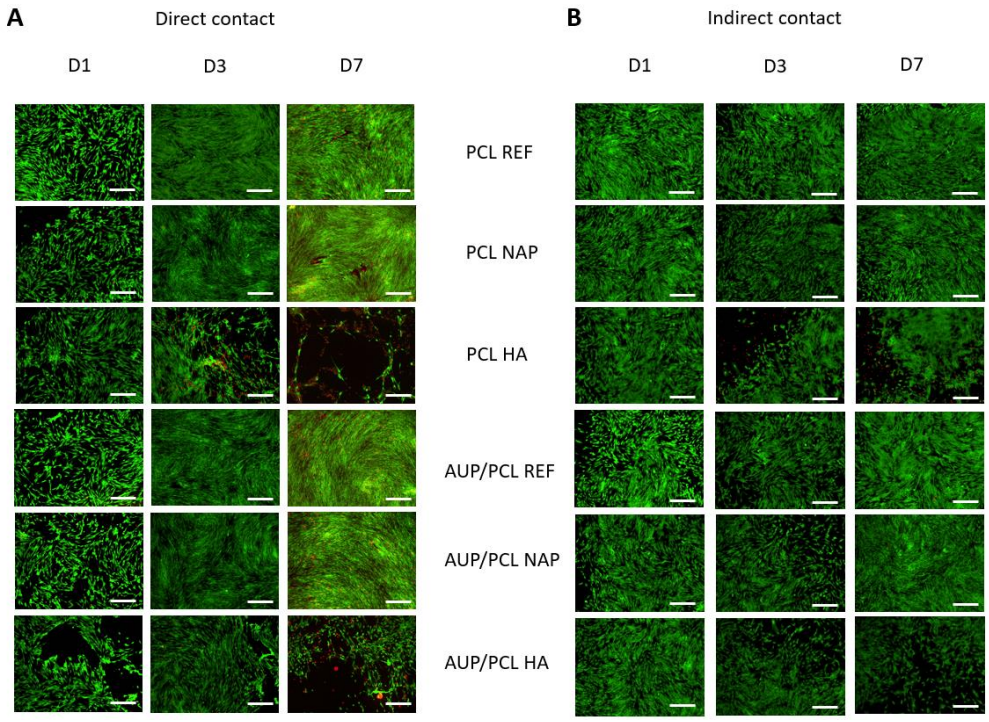

Figure S4.3. Live/Dead assay of the AUP PCL2k and PCL (reference) materials with or without naproxen or hyaluronic acid in the presence of HFF cells. (A) After 24h, the materials were placed on top of the seeded cells to assess the response of the HFF' in direct contact. Ca-AM/PI staining was done on days 1, 3 and 7. (B) Materials were incubated in culture medium for 1, 3 and 7 days before adding the medium to HFF cells seeded in a well plate. The scalebar indicates 500 µm.

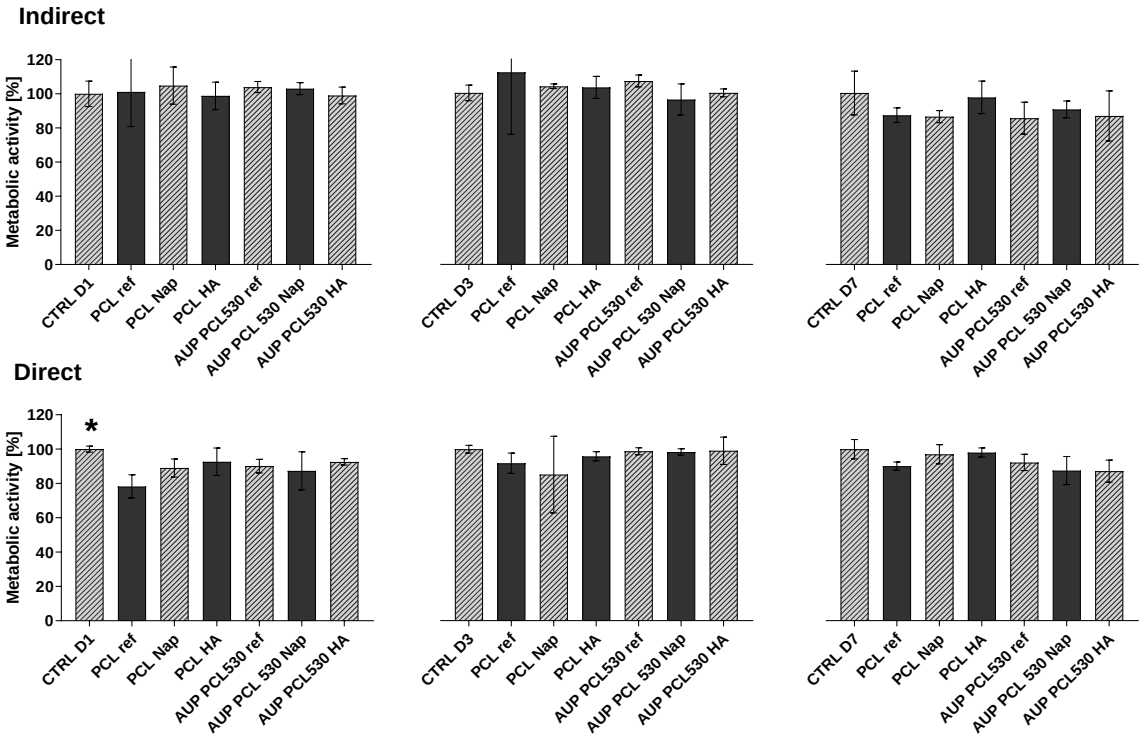

Figure S4.4. AUP PCL530. Metabolic activity of indirect (top) and direct (bottom) in vitro testing using human fibroblast cells (hFBs), by an MTS assay at day 1, 3 and 7. Tissue culture plastic was used as a positive control.

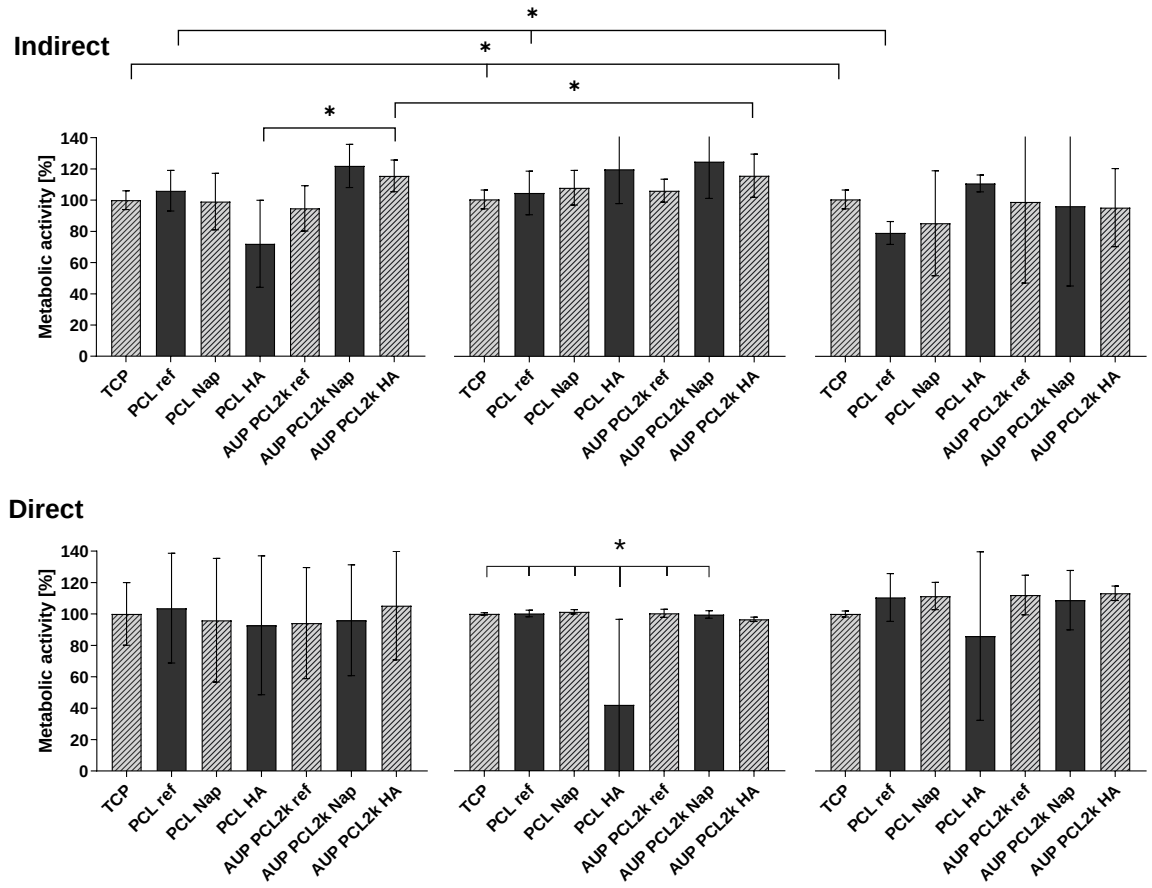

Figure S4.5. AUP PCL2k. Metabolic activity of indirect (top) and direct (bottom) in vitro testing using human fibroblast cells (hFBs), by an MTS assay at day 1, 3 and 7. Tissue culture plastic was used as a positive control.

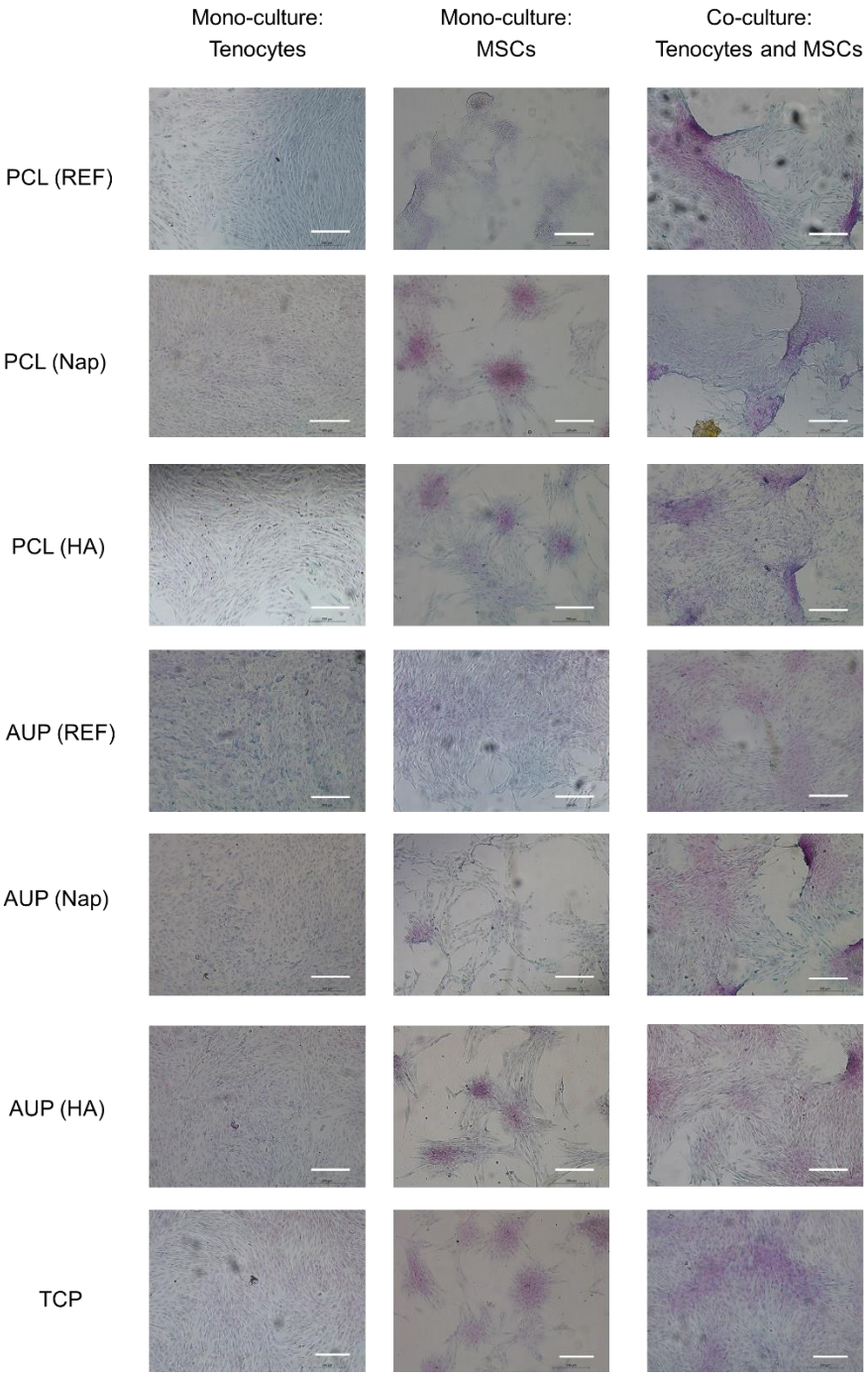

Figure S4.6. Mono-cultures (tenocytes or MSCs) and co-culture (tenocytes and MSCs) stained with Sirius Red/Fast Green to quantify production of total collagen and non-collagenous proteins. The scalebar indicates 200 µm. Tissue culture plastic (TCP) was used as a positive control.

Annex 3. Chapter 5 - Supplementary Information

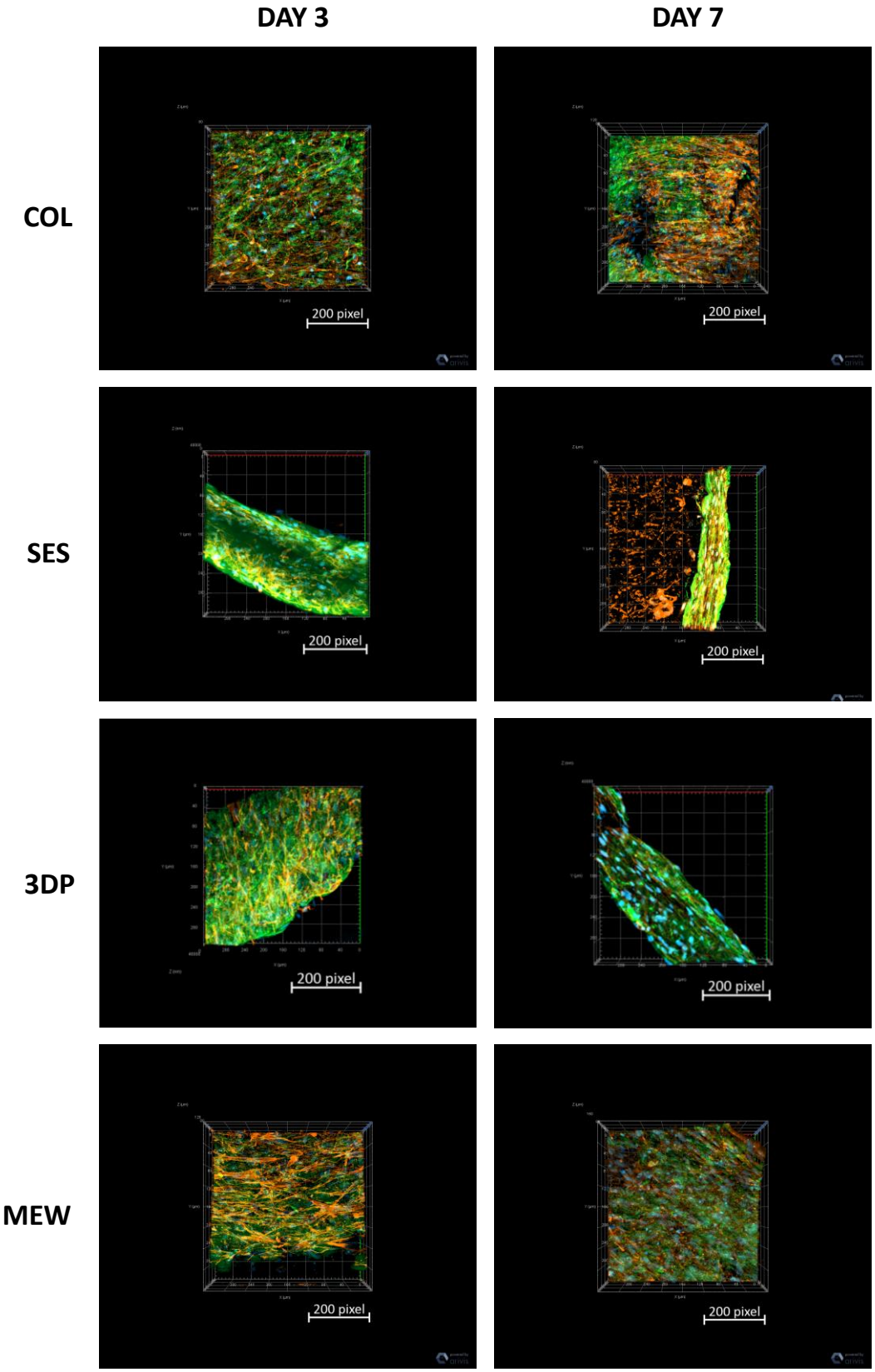

Figure S5.1. Immunofluorescence staining 3D images of fibroblast-celullarized tubular collagen-based gels, without (COL, reference) and with reinforcement (SES, 3DP and MEW) at day 3 and day 7 of maturation: Collagen I (green), F-actin (red), and cell nuclei (blue).

Annex 4. Chapter 6 - Supplementary Information

The ^{1}H-NMR spectra of the developed methacrylamide modified, photo-crosslinkable hydrogel precursors are shown in Figure S6.1, (i) GEL-MA BS 1 EQ, (ii) GEL-MA BS 2.5 EQ, (iii) COL-MA BS 0.5 EQ, and (iv) COL-MA BS 1 EQ. These spectra enabled the determination of the degree of substitution (DS), following a protocol described earlier by Van Vlierberghe et al.[262].

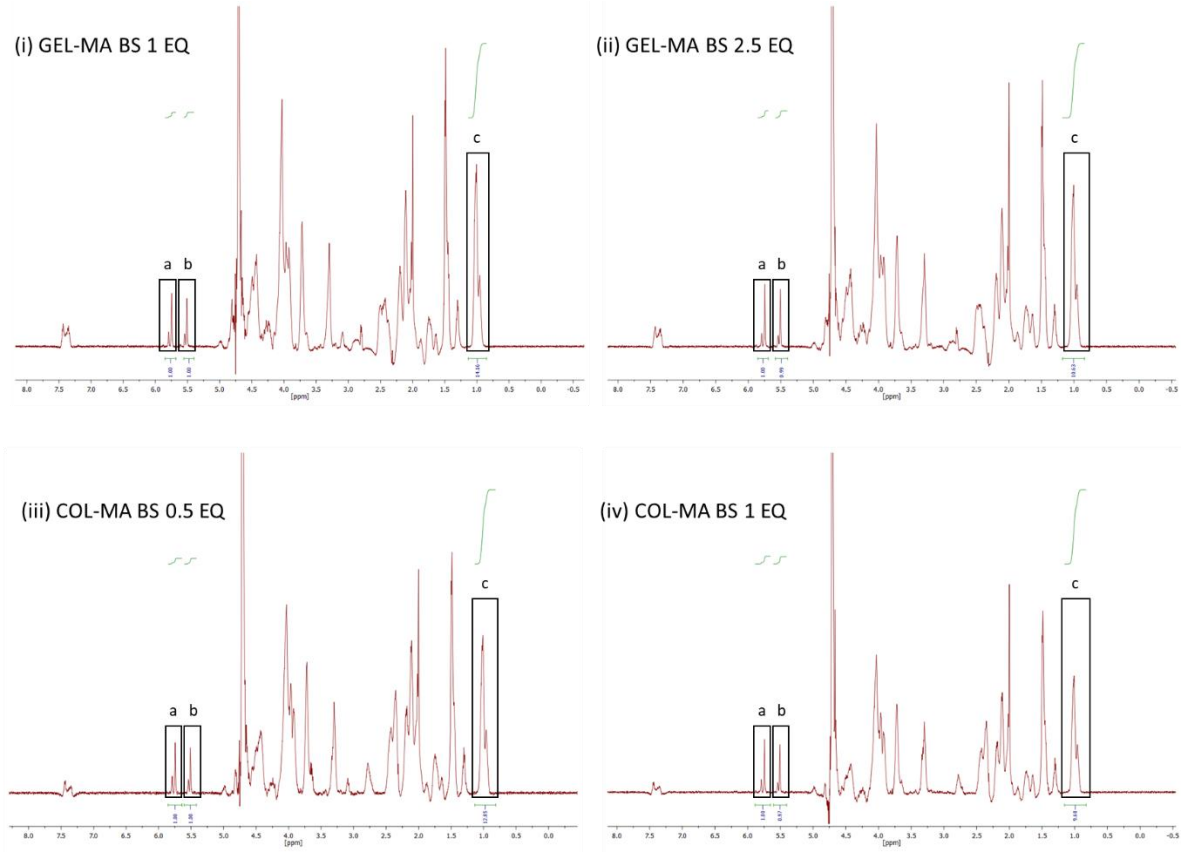

Figure S6.1. 1H-NMR spectra of the developed methacrylamide modified, photo-crosslinkable hydrogel precursors: (i) GEL-MA BS 1 EQ, (ii) GEL-MA BS 2.5 EQ, (iii) COL-MA BS 0.5 EQ, and (iv) COL-MA BS 1 EQ. The characteristic peaks of the vinyl protons are indicated at 5.75 ppm (a) and 5.55 ppm (b), the characteristic peak of the methyl protons is indicated at 1.01 ppm (c).

Table S6.1. Amino acid (AA) composition of bovine skin gelatin and bovine skin collagen as determined using standard AA analysis techniques as described in the Materials and Methods section.

Amino Acid	BOVINE SKIN GELATIN		BOVINE SKIN COLLAGEN	
	g/100g	± STDEV	g/100g	± STDEV
Aspartic acid	5.16	0.00	4.49	0.04
Glutamic acid	9.45	0.03	8.02	0.10
Asparagine	N.D	N.D	N.D	N.D
Serine	3.16	0.00	2.85	0.03
Glutamine	N.D	N.D	N.D	N.D
Histidine	0.60	0.00	0.58	0.01
Glycine	23.08	0.00	19.93	0.00
Threonine	1.85	0.00	1.56	0.01
Arginine	7.51	0.04	6.52	0.01
Alanine	8.90	0.04	7.36	0.06
Tyrosine	0.28	0.01	< LOD	< LOD
Valine	2.05	0.00	1.66	0.00
Methionine	0.61	0.01	0.68	0.03
Hydroxylysine	2.00	0.00	1.91	0.02
Phenylalanine	1.86	0.01	1.52	0.00
Isoleucine	1.36	0.00	1.17	0.01
Ornithine	0.32	0.01	< LOD	< LOD
Leucine	2.85	0.01	2.29	0.02
Lysine	3.36	0.02	2.78	0.01
Hydroxyproline	3.06	0.59	2.38	0.01
Proline	13.06	0.14	11.76	0.16
Total	90.50	0.43	77.46	0.44

(N.D.= not detected) (LOD histidine: 0.00054 mg·ml^{-1})

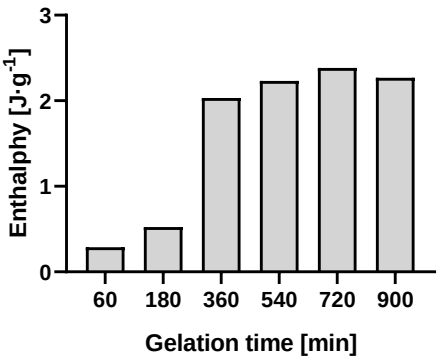

Figure S6.2. Dissociation enthalpy as a function of the collagen gelation time as studied using DSC.

Table S6.2. Overview of the amount of (i) primary amines available for introduction of photo-crosslinkable functionalities, (ii) introduced photo-crosslinkable functionalities, and (iii) consumed photo-crosslinkable functionalities by crosslinking (determined by HR-MAS).

	Primary amines available for functionalization [mmol·g^{-1}]	Introduced photo-crosslinkable functionalities [mmol·g^{-1}]	Reacted photo-crosslinkable functionalities by crosslinking [mmol·g^{-1}]
GEL BS	0.304		
GEL-MA BS 73%		0.276	0.207
GEL-MA BS 99%		0.374	0.314
COL BS	0.248		
COL-MA BS 74%		0.186	0.160
COL-MA BS 96%		0.242	0.213

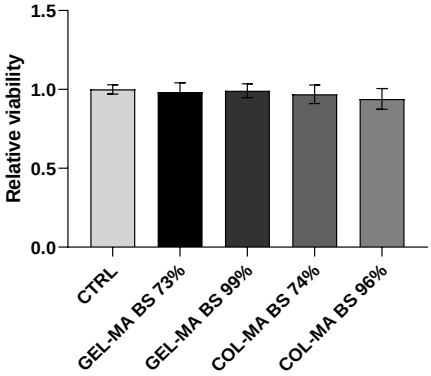

Figure S6.3. Viability of HUVECs evaluated via an indirect cytotoxicity assay. No significant differences were found between the different groups (ns = p > 0.05).

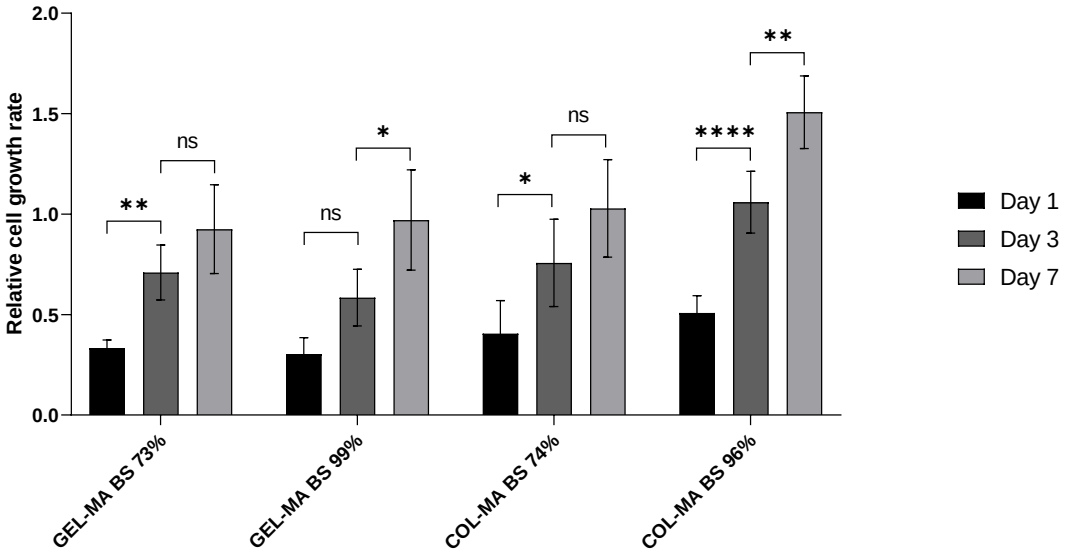

*Figure S6.4. Relative cell growth rate (RGR) of HUVECs on the developed materials at day 1, day 3 and day 7 after cell seeding (ns = not significant; * = p ≤ 0.05; ** = p ≤ 0.01; *** = p ≤ 0.001; **** = p ≤ 0.0001).*

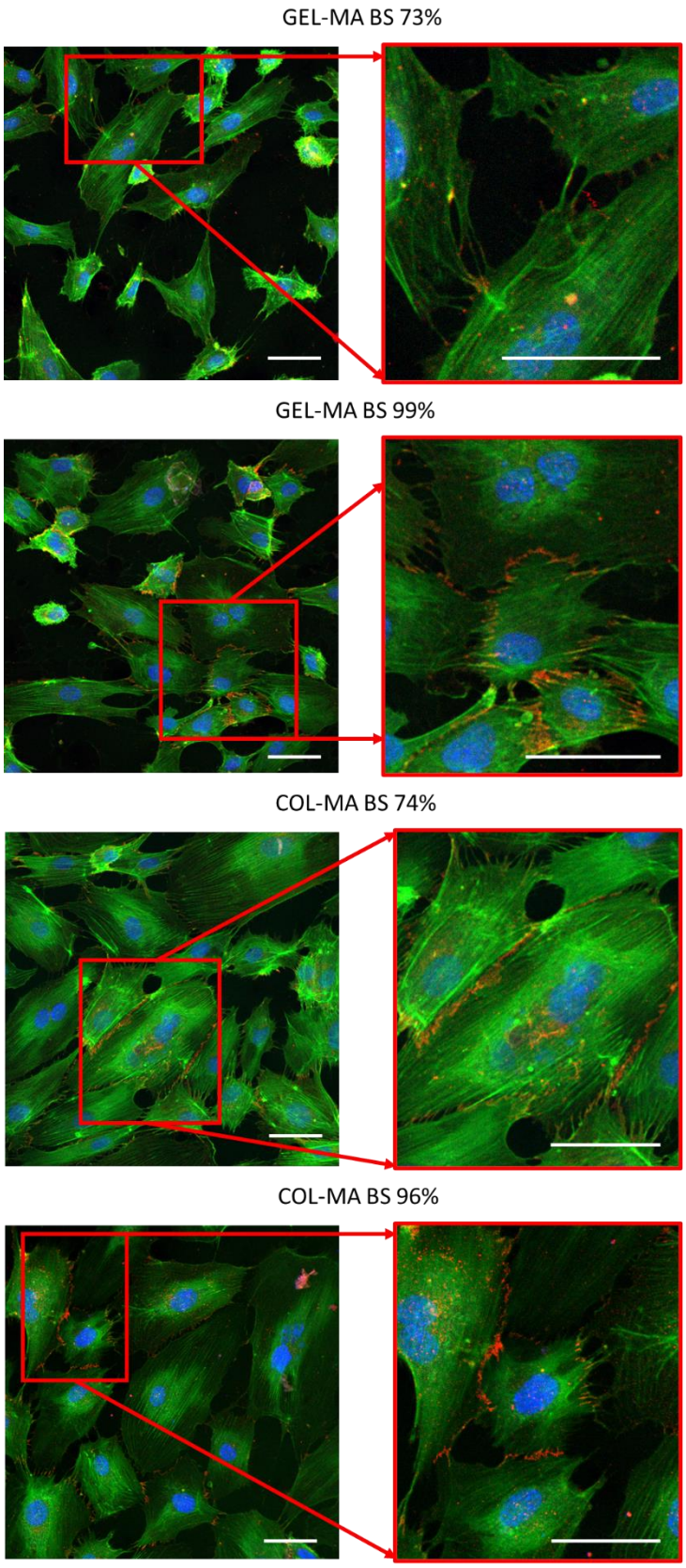

Figure S6.5. Nuclei (blue), cytoskeleton (green) and VE-cadherin (red) of HUVEC cells seeded on GEL-MA BS and COL-MA BS derivatives at day 7. HUVECs were seeded at a density of 15,000 cells·cm-2 in 400 µL complete DMEM+. The red boxes show a zoom of the VE-cadherin staining (at day 7) and thus the intercellular junctions. White scalebars are 50 µm.

Annex 5. Chapter 7 - Supplementary Information

The mass spectrometry proteomics data have been deposited to the ProteomeXchange Consortium via the PRIDE partner repository with the data set identifier PXD024622.

The additional Supporting Information documents include:

(i) Supplementary Information Figures contain graphs and figures (see below).

(ii) Supplementary Data Table 1 corresponds to the identification of the SDS PAGE analysis on RCPhC1 and its derivatives and COL BS and its derivatives.

(iii) Supplementary Data Table 2 contains the identification and quantification of peptides from RCPhC1. The first sheet corresponds to the information in each column of the following sheets.

(iv) Supplementary Data Table 3 corresponds to the identification of proteins of the SDS PAGE analysis on COL BS and its derivatives.

(v) Supplementary Data Table 4 corresponds to the identification of peptides of the SDS PAGE analysis on COL MA BS 0.5EQ and COL MA BS 1EQ.

(vi) Supplementary Data Table 5 corresponds to the protein identification on bovine skin. The first sheet is the protein identification against all entries of Swiss-Prot database, the second sheet is the protein identification against the *Bos taurus* database, and the third sheet is the protein quantification results of bovine skin sample against *Bos taurus* database

(vii) Supplementary Data Table 6 contains the identification and quantification of peptides from COL1α1 and COL1α2. The first sheet corresponds to the information in each column of the following sheets.

Chapter 7, Materials & Methods, Section 7.2.7: An example of the calculation of the degree of modification using proteomics is explained below.

To determine the frequency of modification, we quantified the same peptide with and without methacrylamide. We did an ion extraction for a given peptide with and without modification which allows to determine the effect of the modification, e.g. GAAGLPPKGERGDAGPK and GAAGLPGPKGERGDAGPK (K modified lysine). Equation 7.1 (Section 7.2.7) gives an estimate of the degree of substitution for one peptide GAAGLPGPKGERGDAGPK (COL1α1) with 1 methacrylamide.

For the peptide sequence EGAPGAEGSPGRDGSPGAKGDR from COL1α1 with 1 methacrylamide, we have identified 3 peptides with 1 methacrylamide on position 19 with 1, 2 and 3 hydroxyprolines (see Table S7.1). From these data, we can calculate the percentage of modifications for each peptide modified using Equation 7.1. We can also calculate the average of the percentage modification for lysine on this peptide.

Red = position of lysine with methacrylate, blue = hydroxyproline

Table S7.1. Example of peptides used for the calculation of the degree of subsitution.

Number	Peptides sequence	Modifications	Position K	% modification for each peptide	% modification for peptide
1	EGAPGAEGSPGRDGSPGAKGDR	1xOxidation [P16]	871		
2	EGAPGAEGSPGRDGSPGAKGDR	2xOxidation [P10; P16]	871		
3	EGAPGAEGSPGRDGSPGAKGDR	3xOxidation [P4; P10; P16]	871		
4	EGAPGAEGSPGRDGSPGAKGDR	1xOxidation [P16]; 1xmethacrylate [K19]	871	4/(1+4) * 100	(4+5+6)/(1+2+3+4 +5+6) * 100
5	EGAPGAEGSPGRDGSPGAKGDR	2xOxidation [P10; P16]; 1xmethacrylate [K19]	871	5/(2+5) * 100	
6	EGAPGAEGSPGRDGSPGAKGDR	3xOxidation [P4; P10; P16]; 1xmethacrylate [K19]	871	6/(3+6) * 100	

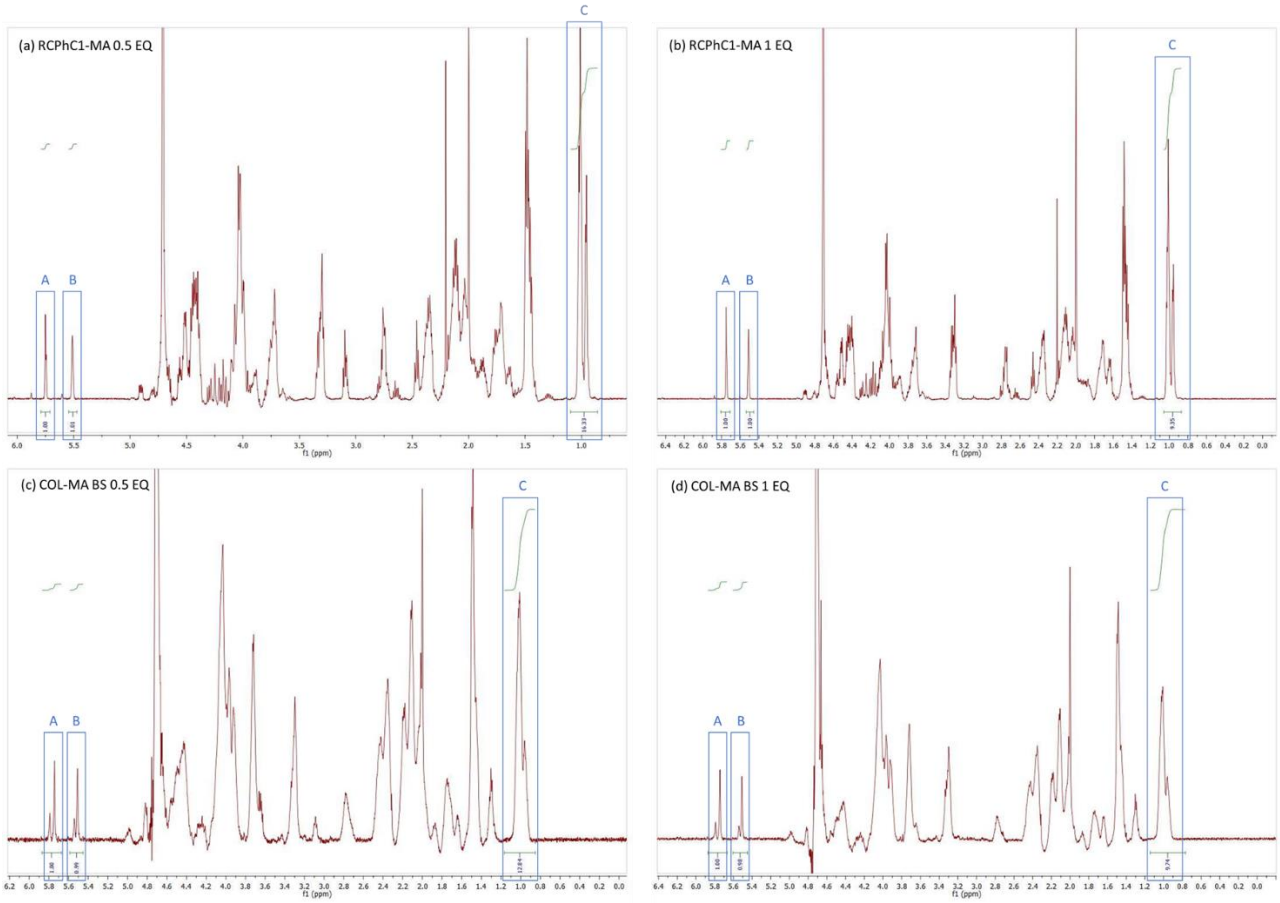

Figure S7.1. 1H-NMR spectrum of (a) RCPhC1-MA 0.5 EQ, (b) RCPhC1-MA 1 EQ, (c) COL-MA BS 0.5 EQ and (d) COL-MA BS 1 EQ, with the characteristic peaks of the vinyl protons at 5.75 (A) and 5.55 ppm (B) and the characteristic peak of the methyl protons at 1.01 ppm (C).

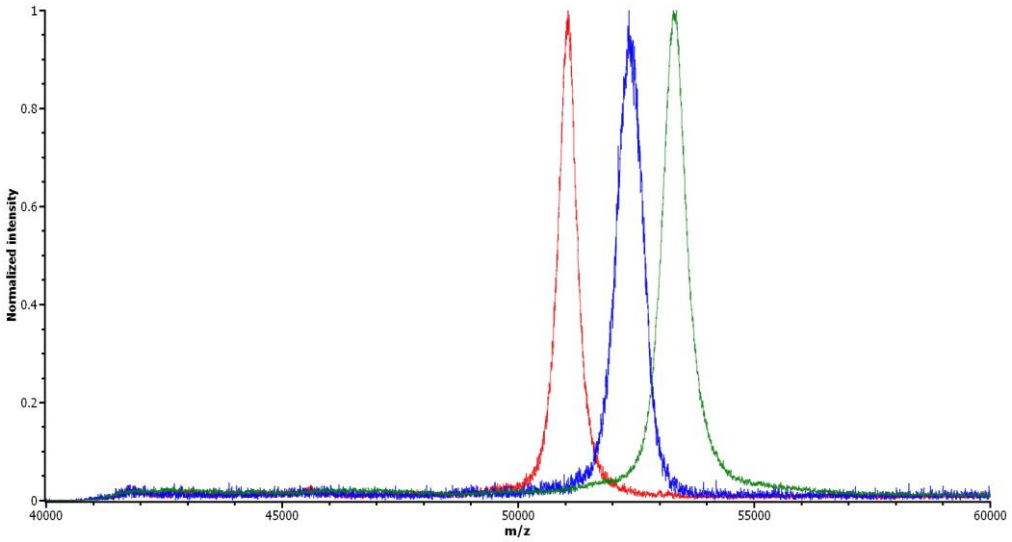

Figure S7.2. MALDI TOF analysis of 3 recombinant collagens. Red line is the intact mass of non-modified RCPhC1 collagen. The m/z observed was 51,188. Blue line is the RCPhC1-MA 0.5 EQ at m/z 52,280 with 16 modified lysines. Green line is the RCPhC1-MA 1 EQ at m/z 53,380 with 32 modified lysines.

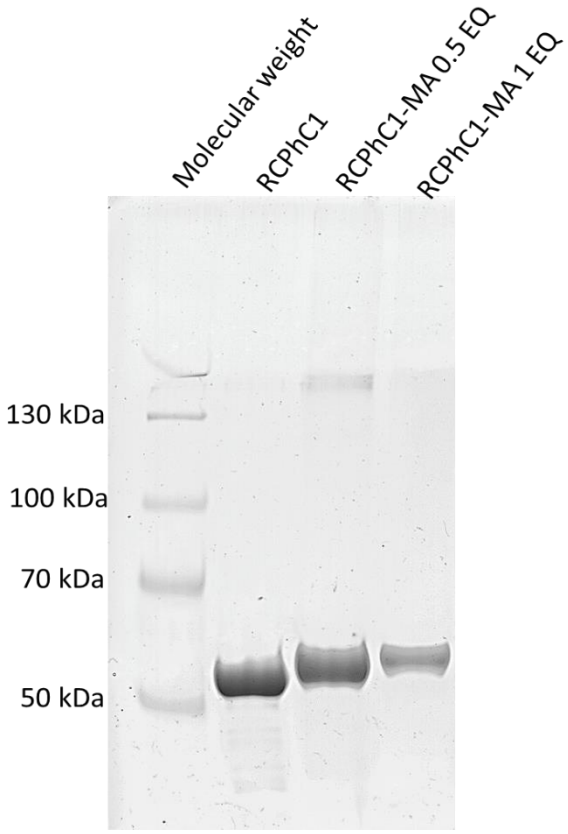

Figure S7.3. Polyacrylamide SDS-PAGE gel of RCPhC1 and its derivatives. The first lane corresponds to protein ladder, the second lane corresponds to native RCPhC1, the third lane corresponds to RCPhC1-MA 0.5EQ and the last corresponds to RCPhC1-MA 1EQ.

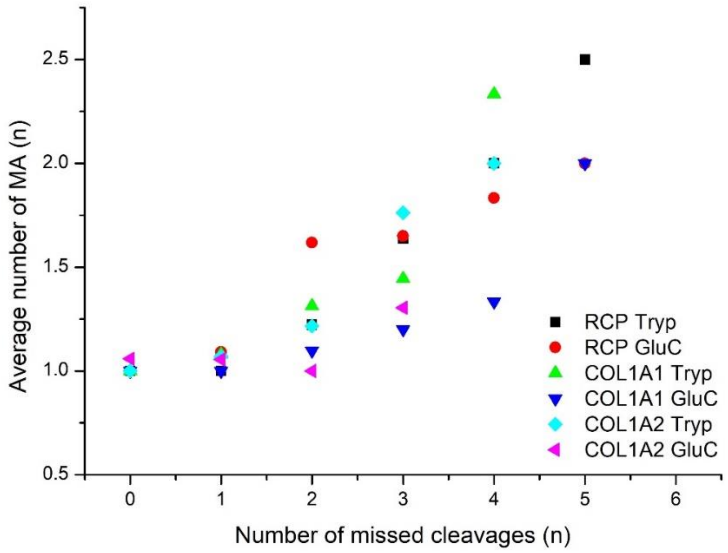

Figure S7.4. Correlation between missed cleavages and number of modified MAs on RCPhC1 and COL BS, both for trypsin and Glu-C digestion.

>RCP
GAPGAPGLQGAPGLQGMPGERGAAGLPGPKGERGDAGPKGADGAPGAPGLQGMPGERGAA
GLPGPKGERGDAGPKGADGAPGKDGVRGLAGPIGPPGERGAAGLPGPKGERGDAGPKGAD
GAPGKDGVRGLAGPIGPPGPAGAPGAPGLQGMPGERGAAGLPGPKGERGDAGPKGADGAP
GKDGVRGLAGPPGAPGLQGAPGLQGMPGERGAAGLPGPKGERGDAGPKGADGAPGAPGLQ
GMPGERGAAGLPGPKGERGDAGPKGADGAPGKDGVRGLAGPIGPPGERGAAGLPGPKGER
GDAGPKGADGAPGKDGVRGLAGPIGPPGPAGAPGAPGLQGMPGERGAAGLPGPKGERGDA
GPKGADGAPGKDGVRGLAGPPGAPGLQGAPGLQGMPGERGAAGLPGPKGERGDAGPKGAD
GAPGAPGLQGMPGERGAAGLPGPKGERGDAGPKGADGAPGKDGVRGLAGPIGPPGERGAA
GLPGPKGERGDAGPKGADGAPGKDGVRGLAGPIGPPGPAGAPGAPGLQGMPGERGAAGLP
GPKGERGDAGPKGADGAPGKDGVRGLAGPPG

Figure S7.5. Amino acid sequence of RCPhC1 with redundant peptides GDAGPK (green), GADGAPGK (blue) and GAAGLPGPK (red).

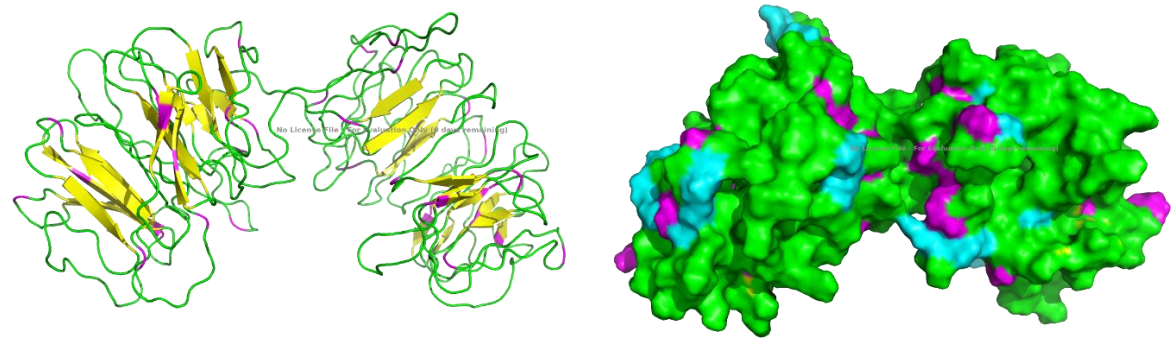

a b

Figure S7.6. The second model for the protein 3D-conformation of the sequence of RCPhC1 modelled with I-TASSER; (a) in the cartoon view showing sheets (yellow), loops (green) and lysine residues in the structure (magenta), (b) in the solvent surface accessibility view showing the protein accessibility surface (green), all lysines on the surface (magenta) and the RGD sequences at the surface (orange). The model in b is also the same as for RCPhC1-MA 1 EQ where all lysines are modified (magenta = cyan).

GAPGAPGLQGAPGLQGMPGERGAAGLPGPKGERGDAGPKGADGAPGAPGLQGMPGERGAAGLPGPKGERG
DAGPKGADGAPGKDGVRGLAGPIGPPGERGAAGLPGPKGERGDAGPKGADGAPGKDGVRGLAGPIGPPGPAG
APGAPGLQGMPGERGAAGLPGPKGERGDAGPKGADGAPGKDGVRGLAGPPGAPGLQGAPGLQGMPGERGA
AGLPGPKGERGDAGPKGADGAPGAPGLQGMPGERGAAGLPGPKGERGDAGPKGADGAPGKDGVRGLAGPIG
PPGERGAAGLPGPKGERGDAGPKGADGAPGKDGVRGLAGPIGPPGPAGAPGAPGLQGMPGERGAAGLPGPKG
ERGDAGPKGADGAPGKDGVRGLAGPPGAPGLQGAPGLQGMPGERGAAGLPGPKGERGDAGPKGADGAPGAP
GLQGMPGERGAAGLPGPKGERGDAGPKGADGAPGKDGVRGLAGPIGPPGERGAAGLPGPKGERGDAGPKGA
DGAPGKDGVRGLAGPIGPPGPAGAPGAPGLQGMPGERGAAGLPGPKGERGDAGPKGADGAPGKDGVRGLAG
PPG

Figure S7.7. Amino acid sequence of RCPhC1-MA 1 EQ with the identification of lysine modified with a methacrylamide group (yellow K).

GAPGAPGLQGAPGLQGMPGERGAAGLPGPKGERGDAGPKGADGAPGAPGLQGMPGERGAAGLPGPKGERG
DAGPKGADGAPGKDGVRGLAGPIGPPGERGAAGLPGPKGERGDAGPKGADGAPGKDGVRGLAGPIGPPGPAG
APGAPGLQGMPGERGAAGLPGPKGERGDAGPKGADGAPGKDGVRGLAGPPGAPGLQGAPGLQGMPGERGA
AGLPGPKGERGDAGPKGADGAPGAPGLQGMPGERGAAGLPGPKGERGDAGPKGADGAPGKDGVRGLAGPIG
PPGERGAAGLPGPKGERGDAGPKGADGAPGKDGVRGLAGPIGPPGPAGAPGAPGLQGMPGERGAAGLPGPKG
ERGDAGPKGADGAPGKDGVRGLAGPPGAPGLQGAPGLQGMPGERGAAGLPGPKGERGDAGPKGADGAPGAP
GLQGMPGERGAAGLPGPKGERGDAGPKGADGAPGKDGVRGLAGPIGPPGERGAAGLPGPKGERGDAGPKGA
DGAPGKDGVRGLAGPIGPPGPAGAPGAPGLQGMPGERGAAGLPGPKGERGDAGPKGADGAPGKDGVRGLAG
PPG

Figure S7.8. Amino acid sequence of RCPhC1-MA 0.5 EQ with indication of lysine modified with 100% modification frequency (red K), lysine modified with 50% modification frequencies from peptide GAAGLPGPKGER (blue K) and lysine modified with 50% modification frequency from peptide GAAGLPGPKGERGDAGPK (yellow K).

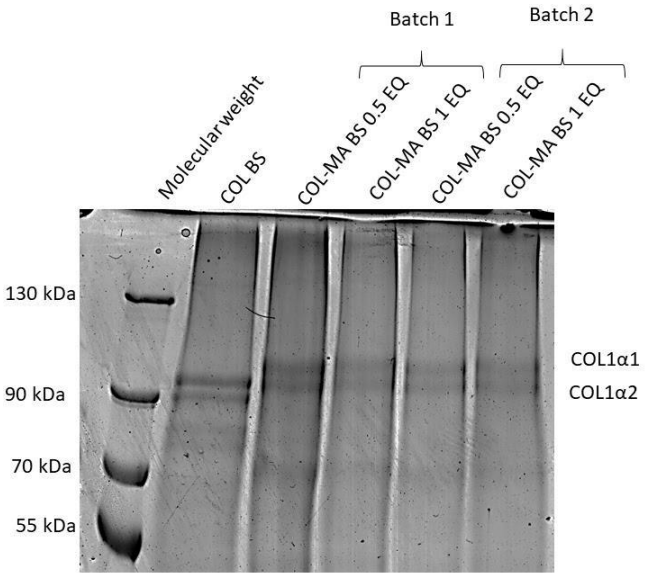

Figure S7.9. Polyacrylamide SDS-PAGE gel of collagen bovine skin and its derivatives. The first lane corresponds to protein ladder, the second lane corresponds to native collagen bovine COL BS, the third lane corresponds to COL-MA BS 0.5EQ and the last corresponds to COL-MA BS 1EQ.

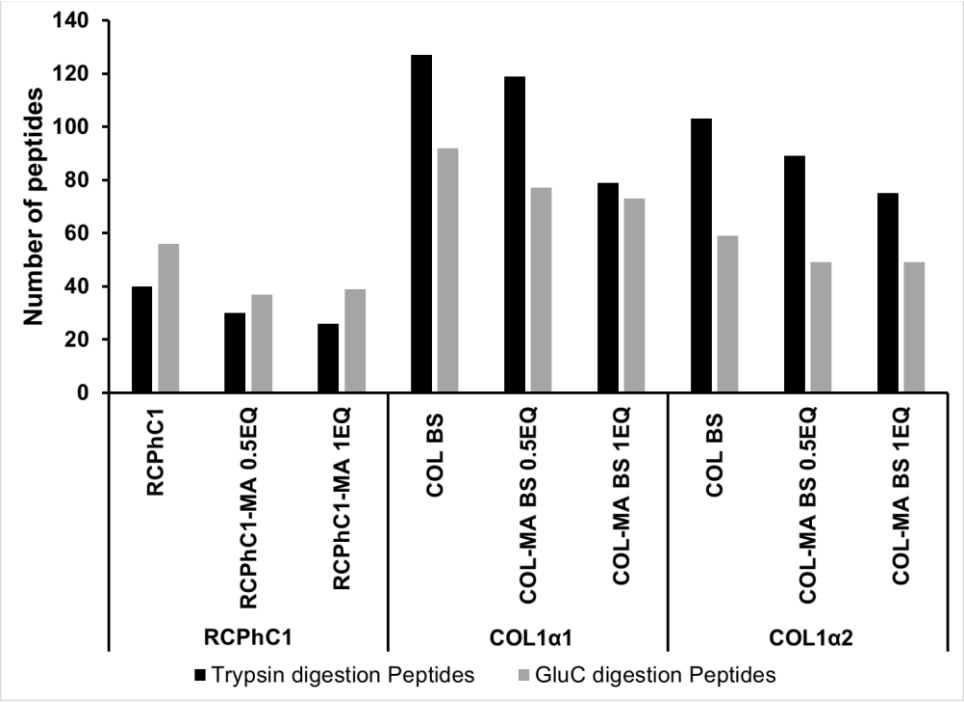

Figure S7.10. Histogram of number of peptides and PSMs identified for RCPhC1 and collagen bovine skin. The black bar corresponds to number of peptides and grey diamond corresponds to PSMs.

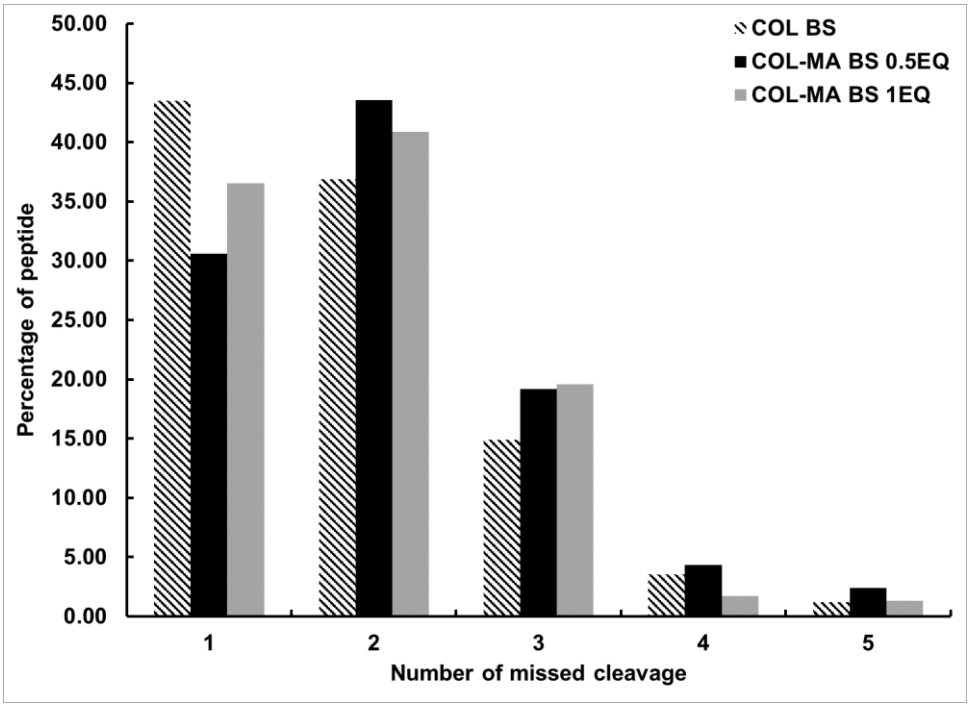

Figure S7.11. Histogram of the percentage of missed cleavage of peptide for COL1α1 from collagen bovine skin for trypsin digestion. The percentage of missed cleavages is calculated by making the ratio of the peptides with a missed cleavage identified by LC-MS / MS over the totality of the identified peptides. Hasted bar corresponding to COL BS, black bar to COL-MA BS 0.5EQ and grey bar to COL-MA BS 1EQ.

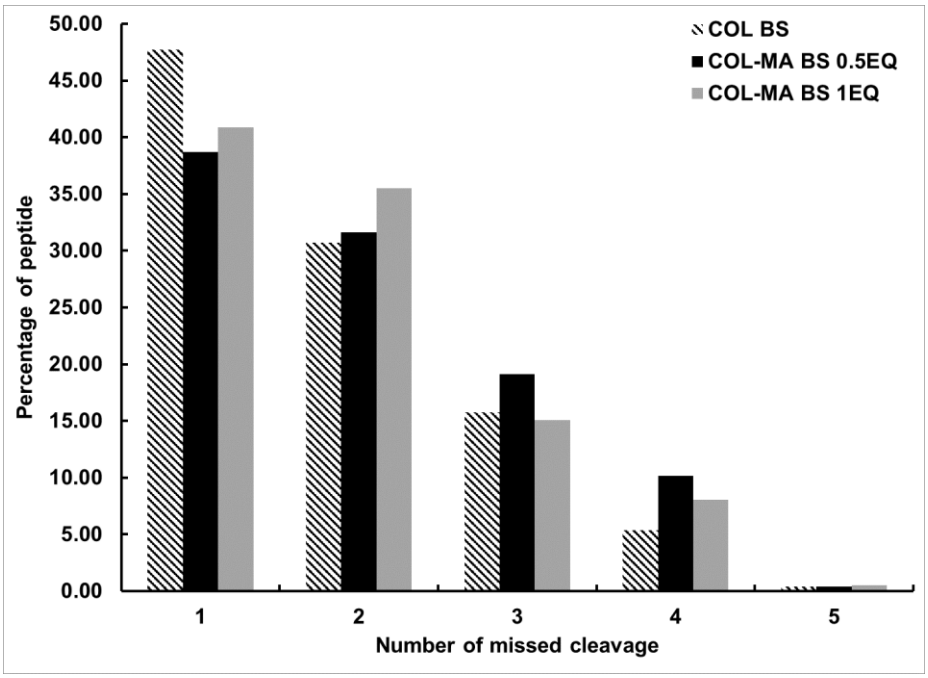

Figure S7.12. Histogram of the percentage of missed cleavage of peptide for COL1α2 from collagen bovine skin for trypsin digestion. The percentage of missed cleavages is calculated by making the ratio of the peptides with a missed cleavage identified by LC-MS / MS over the totality of the identified peptides. Hasted bar corresponding to COL BS, black bar to COL-MA BS 0.5EQ and grey bar to COL-MA BS 1EQ.

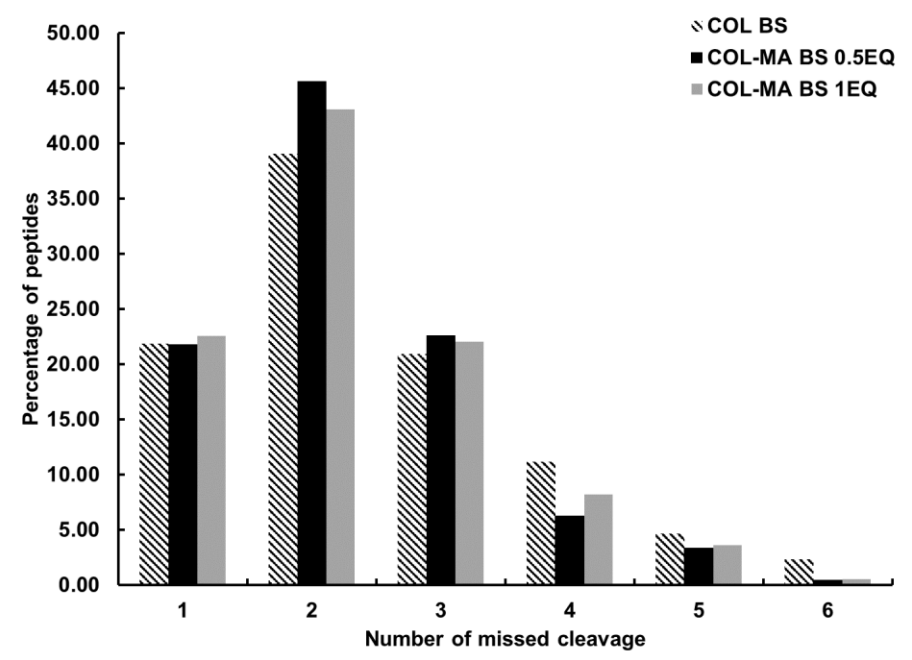

Figure S7.13. Histogram of the percentage of missed cleavage of peptide for COL1α1 from collagen bovine skin for Gluc digestion. The percentage of missed cleavages is calculated by making the ratio of the peptides with a missed cleavage identified by LC-MS / MS over the totality of the identified peptides. Hasted bar corresponding to COL BS, black bar to COL-MA BS 0.5EQ and grey bar to COL-MA BS 1EQ.

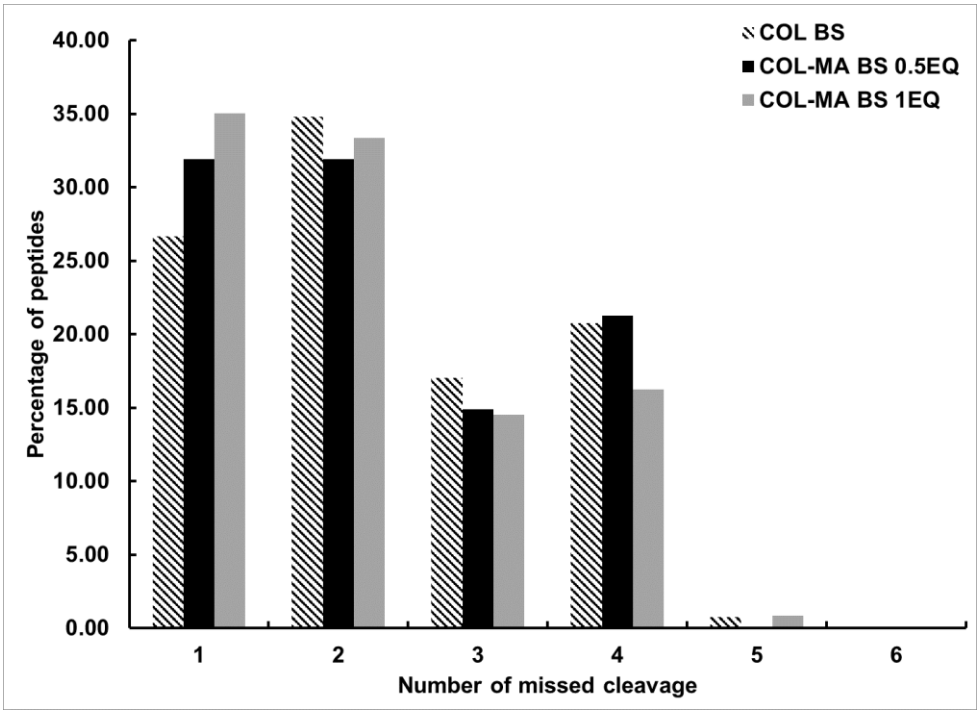

Figure S7.14. Histogram of the percentage of missed cleavage of peptide for COL1α2 from collagen bovine skin for GluC digestion. The percentage of missed cleavages is calculated by making the ratio of the peptides with a missed cleavage identified by LC-MS / MS over the totality of the identified peptides. Hasted bar corresponding to COL BS, black bar to COL-MA BS 0.5EQ and grey bar to COL-MA BS 1EQ.

>sp|P02453|COL1A1|162-1217
QLSYGYDEKSTGISVPGPMGPSGPRGLPGPPGAPGPQGFQGPPGEPGEPGASGPMGPRGPPG
PPGKNGDDGEAGKPGRPGERGPPGPQGARGLPGTAGLPGMKGHRGFSGLDGAKGDAGPAGPK
GEPGSPGENGAPGQMGPRGLPGERGRPGAPGPAGARGNDGATGAAGPPGPTGPAGPPGFPGA
VGAKGEGGPQGPRGSEGPQGVRGEPGPPGPAGAAGPAGNPGADGQPGAKGANGAPGIAGAPG
FPGARGPSGPQGPSGPPGPKGNSGEPGAPGSKGDTGAKGEPGPTGIQGPPGPAGEEGKRGAR
GEPGPAGLPGPPGERGGPGSRGFPGADGVAGPKGPAGERGAPGPAGPKGSPGEAGRPGEAGL
PGAKGLTGSPGSPGPDGKTGPPGPAGQDGRPGPPGPPGARGQAGVMGFPGPKGAAGEPGKAG
ERGVPGPPGAVGPAGKDGEAGAQGPPGPAGPAGERGEQGPAGSPGFQGLPGPAGPPGEAGKP
GEQGVPGDLGAPGPSGARGERGFPGERGVQGPPGPAGPRGANGAPGNDGAKGDAGAPGAPG
SQGAPGLQGMPGERGAAGLPGPKGDRGDAGPKGADGAPGKDGVRGLTGPIGPPGPAGAPGDK
GEAGPSGPAGPTGARGAPGDRGEPGPPGPAGFAGPPGADGQPGAKGEPGDAGAKGDAGPPGP
AGPAGPPGPIGNVGAPGPKGARGSAGPPGATGFPGAAGRVGPPGPSGNAGPPGPPGPAGKEGS
KGPRGETGPAGRPGEVGPPGPPGPAGEKGAPGADGPAGAPGTPGPQGIAGQRGVVGLPGQRG
ERGFPGLPGPSGEPGKQGPSGASGERGPPGPMGPPGLAGPPGESGREGAPGAEGSPGRDGSP
GAKGDRGETGPAGPPGAPGAPGAPGPVGPAGKSGDRGETGPAGPAGPIGPVGARGPAGPQGPR
GDKGETGEQGDRGIKGHRGFSGLQGPPGPPGSPGEQGPSGASGPAGPRGPPGSAGSPGKDGL
NGLPGPIGPPGPRGRTGDAGPAGPPGPPGPPGPPGPPSGGYDLSFLPQPPQEKAHDGGRYYRA

Figure S7.15. Sequence of COL1α1 quantified by LC-MS/MS for bovine collagen with trypsin digestion. Red lysine is identified and quantified with methacrylation. Green lysine corresponds to identified and quantified without methacrylate.

>sp|P02465|COL1A2|80-1117
QFDAKGGGPGPMGLMGPRGPPGASGAPGPQGFQGPPGEPGEPGQTGPAGARGPPGPPGKAGE
DGHPGKPGRPGERGVVGPQGARGFPGTPGLPGFKGIRGHNGLDGLKGQPGAPGVKGEPGAPGE
NGTPGQTGARGLPGERGRVGAPGPAGARGSDGSVGPVGPAGPIGSAGPPGFPGAPGPKGELGP
VGNPGPAGPAGPRGEVGLPGLSGPVGPPGNPGANGLPGAKGAAGLPGVAGAPGLPGPRGIPGPV
GAAGATGARGLVGEPGPAGSKGESGNKGEPGAVGQPGPPGPSGEEGKRGSTGEIGPAGPPGPP
GLRGNPGSRGLPGADGRAGVMGPAGSRGATGPAGVRGPNGDSGRPGEPGLMGPRGFPGSPGNI
GPAGKEGPVGLPGIDGRPGPIGPAGARGEPGNIGFPGPKGPSGDPGKAGEKGHAGLAGARGAPG
PDGNNGAQGPPGLQGVQGGKGEQGPAGPPGFQGLPGPAGTAGEAGKPGERGIPGEFGLPGPAG
ARGERGPPGESGAAGPTGPIGSRGPSGPPGPDGNKGEPGVVGAPGTAGPSGPSGLPGERGAAGI
PGGKGEKGETGLRGDIGSPGRDGARGAPGAIGAPGPAGANGDRGEAGPAGPAGPAGPRGSPGE
RGEVGPAGPNGFAGPAGAAGQPGAKGERGTKGPKGENGPVGPTGPVGAAGPSGPNGPPGPAG
SRGDGGPPGATGFPGAAGRTGPPGPSGISGPPGPPGPAGKEGLRGPRGDQGPVGRSGETGASG
PPGFVGEKGPSGEPGTAGPPGTPGPQGLLGAPGFLGLPGSRGERGLPGVAGSVGEPGPLGIAGP
PGARGPPGNVGNPGVNGAPGEAGRDGNPGNDGPPGRDGQPGHKGERGYPGNAGPVGAAGAP
GPQGPVGPVGKHGNRGEPGPAGAVGPAGAVGPRGPSGPQGIRGDKGEPGDKGPRGLPGLKGHN
GLQGLPGLAGHHGDQGAPGAVGPAGPRGPAGPSGPAGKDGRIGQPGAVGPAGIRGSQGSQGPA
GPPGPPGPPGPPGPSGGGYEFGFDGDFYRA

Figure S7.16. Sequence of COL1α2 quantified by LC-MS/MS for bovine collagen with trypsin digestion. Red lysine is identified and quantified with methacrylation. Green lysine corresponds to identified and quantified without methacrylate.

>sp|P02453|COL1A1|162-1217
QLSYGYDEKSTGISVPGPMGPSGPRGLPGPPGAPGPQGFQGPPGEPGEPGASGPMGPRGPPG
PPGKNGDDGEAGKPGRPGERGPPGPQGARGLPGTAGLPGMKGHRGFSGLDGAKGDAGPAGPK
GEPGSPGENGAPGQMGPRGLPGERGRPGAPGPAGARGNDGATGAAGPPGPTGPAGPPGFPGA
VGAKGEGGPQGPRGSEGPQGVRGEPGPPGPAGAAGPAGNPGADGQPGAKGANGAPGIAGAPG
FPGARGPSGPQGPSGPPGPKGNSGEPGAPGSKGDTGAKGEPGPTGIQGPPGPAGEEGKRGAR
GEPGPAGLPGPPGERGGPGSRGFPGADGVAGPKGPAGERGAPGPAGPKGSPGEAGRPGEAGL
PGAKGLTGSPGSPGPDGKTGPPGPAGQDGRPGPPGPPGARGQAGVMGFPGPKGAAGEPGKAG
ERGVPGPPGAVGPAGKDGEAGAQGPPGPAGPAGERGEQGPAGSPGFQGLPGPAGPPGEAGKP
GEQGVPGDLGAPGPSGARGERGFPGERGVQGPPGPAGPRGANGAPGNDGAKGDAGAPGAPG
SQGAPGLQGMPGERGAAGLPGPKGDRGDAGPKGADGAPGKDGVRGLTGPIGPPGPAGAPGDK
GEAGPSGPAGPTGARGAPGDRGEPGPPGPAGFAGPPGADGQPGAKGEPGDAGAKGDAGPPGP
AGPAGPPGPIGNVGAPGPKGARGSAGPPGATGFPGAAGRVGPPGPSGNAGPPGPPGPAGKEGS
KGPRGETGPAGRPGEVGPPGPPGPAGEKGAPGADGPAGAPGTPGPQGIAGQRGVVGLPGQRG
ERGFPGLPGPSGEPGKQGPSGASGERGPPGPMGPPGLAGPPGESGREGAPGAEGSPGRDGSP
GAKGDRGETGPAGPPGAPGAPGAPGPVGPAGKSGDRGETGPAGPAGPIGPVGARGPAGPQGPR
GDKGETGEQGDRGIKGHRGFSGLQGPPGPPGSPGEQGPSGASGPAGPRGPPGSAGSPGKDGL
NGLPGPIGPPGPRGRTGDAGPAGPPGPPGPPGPPGPPSGGYDLSFLPQPPQEKAHDGGRYYRA

Figure S7.17. Sequence of COL1α1 quantified by LC-MSMS from bovine collagen with GluC digestion. Red lysine is identified and quantified with methacrylation. Green lysine corresponds to identified and quantified without methacrylation.

>sp|P02465|COL1A2|80-1117
QFDAKGGGPGPMGLMGPRGPPGASGAPGPQGFQGPPGEPGEPGQTGPAGARGPPGPPGKAGE
DGHPGKPGRPGERGVVGPQGARGFPGTPGLPGFKGIRGHNGLDGLKGQPGAPGVKGEPGAPGE
NGTPGQTGARGLPGERGRVGAPGPAGARGSDGSVGPVGPAGPIGSAGPPGFPGAPGPKGELGP
VGNPGPAGPAGPRGEVGLPGLSGPVGPPGNPGANGLPGAKGAAGLPGVAGAPGLPGPRGIPGPV
GAAGATGARGLVGEPGPAGSKGESGNKGEPGAVGQPGPPGPSGEEGKRGSTGEIGPAGPPGPP
GLRGNPGSRGLPGADGRAGVMGPAGSRGATGPAGVRGPNGDSGRPGEPGLMGPRGFPGSPGNI
GPAGKEGPVGLPGIDGRPGPIGPAGARGEPGNIGFPGPKGPSGDPGKAGEKGHAGLAGARGAPG
PDGNNGAQGPPGLQGVQGGKGEQGPAGPPGFQGLPGPAGTAGEAGKPGERGIPGEFGLPGPAG
ARGERGPPGESGAAGPTGPIGSRGPSGPPGPDGNKGEPGVVGAPGTAGPSGPSGLPGERGAAGI
PGGKGEKGETGLRGDIGSPGRDGARGAPGAIGAPGPAGANGDRGEAGPAGPAGPAGPRGSPGE
RGEVGPAGPNGFAGPAGAAGQPGAKGERGTKGPKGENGPVGPTGPVGAAGPSGPNGPPGPAG
SRGDGGPPGATGFPGAAGRTGPPGPSGISGPPGPPGPAGKEGLRGPRGDQGPVGRSGETGASG
PPGFVGEKGPSGEPGTAGPPGTPGPQGLLGAPGFLGLPGSRGERGLPGVAGSVGEPGPLGIAGP
PGARGPPGNVGNPGVNGAPGEAGRDGNPGNDGPPGRDGQPGHKGERGYPGNAGPVGAAGAP
GPQGPVGPVGKHGNRGEPGPAGAVGPAGAVGPRGPSGPQGIRGDKGEPGDKGPRGLPGLKGHN
GLQGLPGLAGHHGDQGAPGAVGPAGPRGPAGPSGPAGKDGRIGQPGAVGPAGIRGSQGSQGPA
GPPGPPGPPGPPGPSGGGYEFGFDGDFYRA

Figure S7.18. Sequence of COL1α2 quantified by LC-MSMS from bovine collagen with GluC digestion. Red lysine is identified and quantified with methacrylation. Green lysine corresponds to identified and quantified without methacrylation.

Figure S7.19. Histogram of percentage of methacrylation for trypsin digested peptides from COL1α1 from COL-MA BS 0.5 EQ and 1 EQ. Black bars correspond to COL-MA BS 0.5 EQ and grey bars to COL-MA BS 1 EQ.

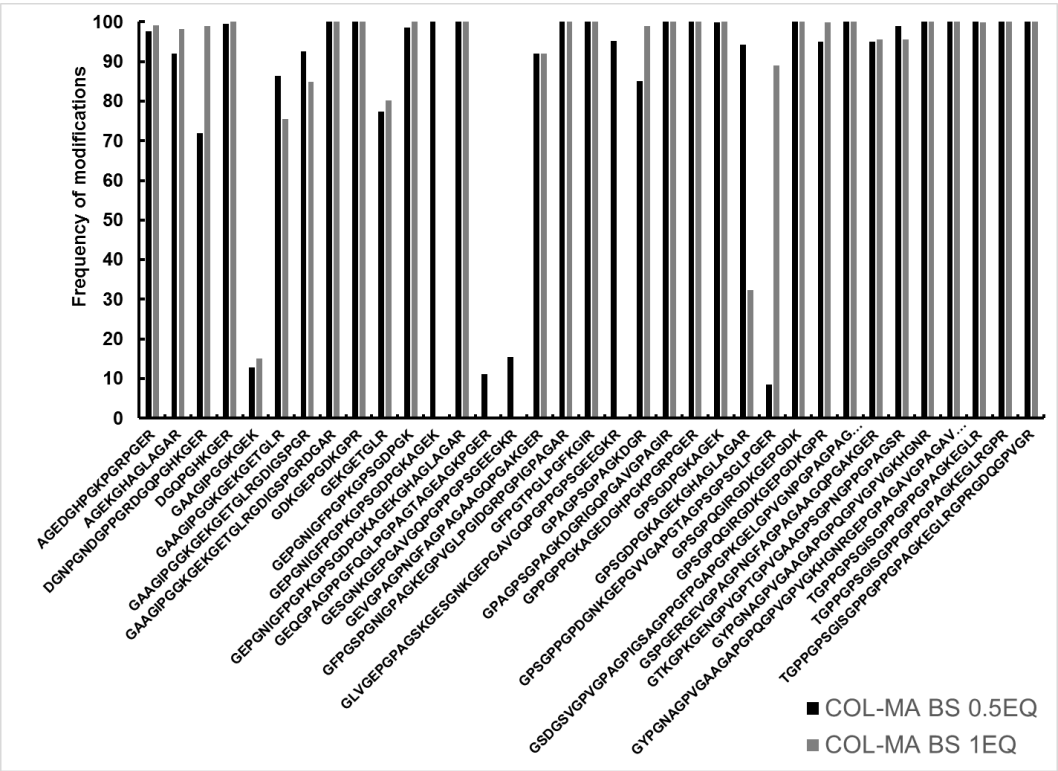

Figure S7.20. Histogram of percentage of methacrylation for trypsin digested peptides from COL1α2 from COL-MA BS 0.5 EQ and 1 EQ. Black bars correspond to COL-MA BS 0.5 EQ and grey bars to COL-MA BS 1 EQ.

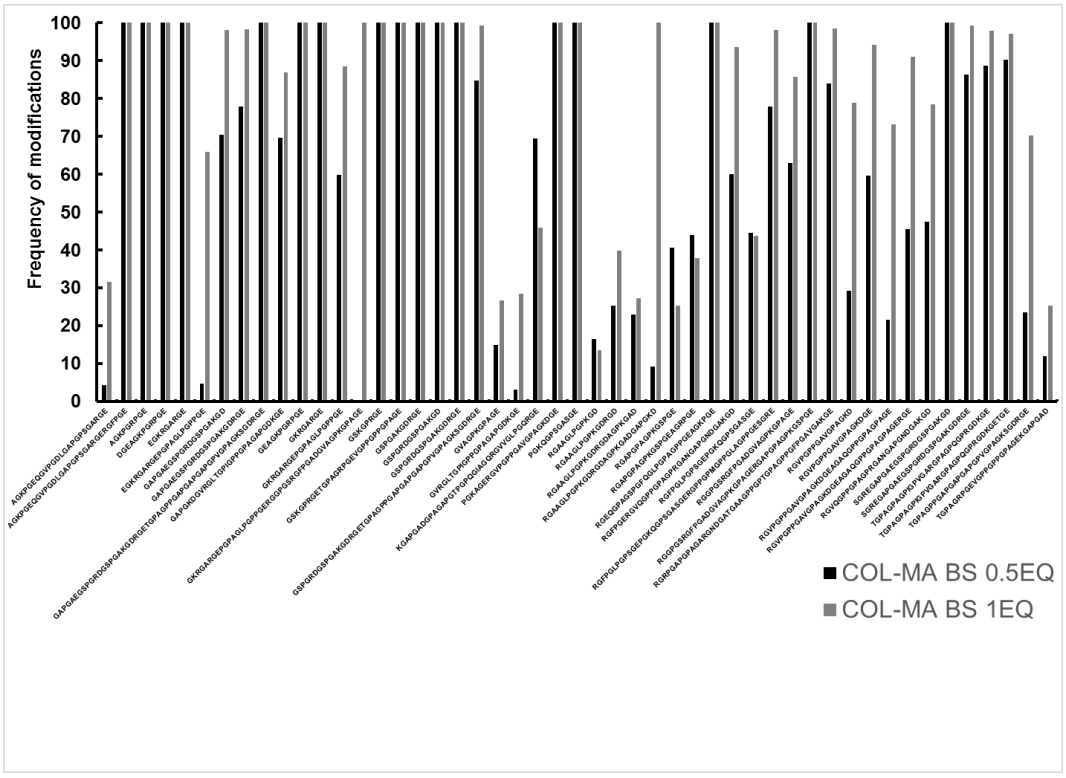

Figure S7.21. Histogram of percentage of methacrylation for GluC peptides from COL1α1 from COL-MA BS 0.5 EQ and 1 EQ. Black bars correspond to COL-MA BS 0.5 EQ and grey bars to COL-MA BS 1 EQ.

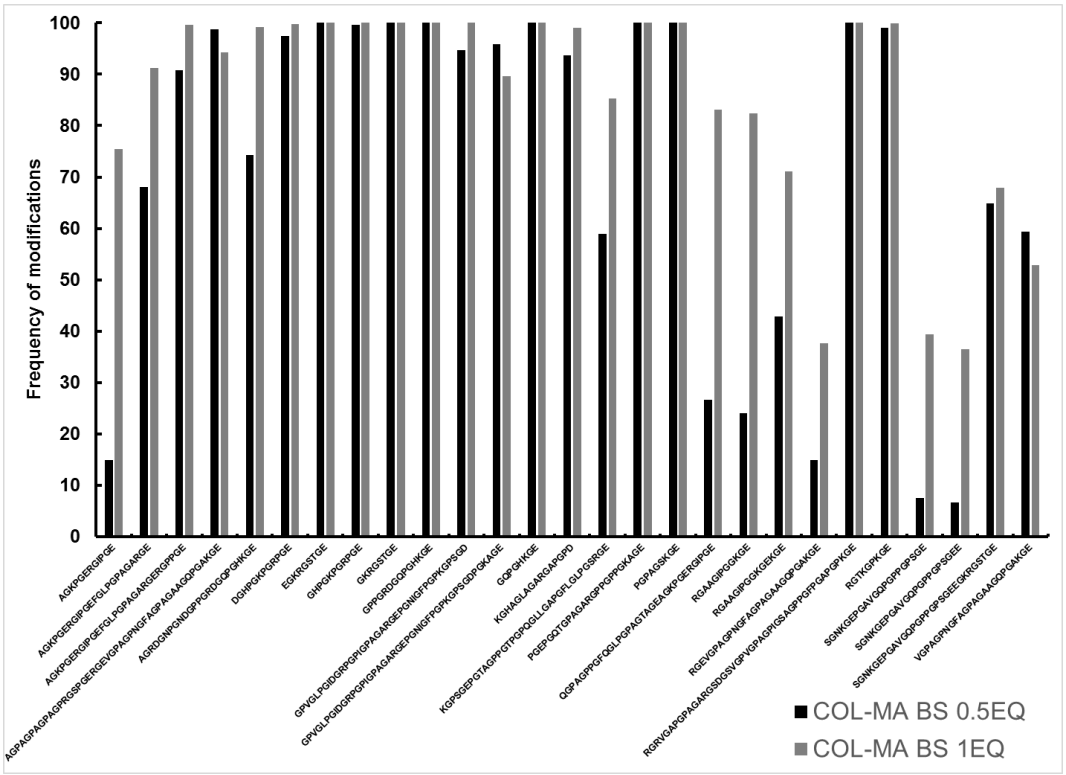

Figure S7.22. Histogram of percentage of methacrylation for GluC peptides from COL1α2 from COL-MA BS 0.5 EQ and 1 EQ. Black bars correspond to COL-MA BS 0.5 EQ and grey bars to COL-MA BS 1 EQ.

Table S7.2. Percentage of coverage, number of identified peptides and percentage of abundance of collagens identified after trypsin digestion by LC-MS/MS in the four bands for COL BS CTRL.

	Proteins	Coverage [%]	Peptides [n]	Abundance [%]
Band 1	Collagen alpha-1(I) chain	46	46	41.0
	Collagen alpha-2(I) chain	52	40	17.0
	Collagen alpha-1(III) chain	42	27	4.8
	Collagen alpha-1(II) chain	10	6	4.2
Band 2	Collagen alpha-1(I) chain	50	56	54.9
	Collagen alpha-2(I) chain	56	47	17.5
	Collagen alpha-1(III) chain	62	44	9.8
	Collagen alpha-1(II) chain	8	5	1.3
Band 3	Collagen alpha-1(I) chain	58	62	74.7
	Collagen alpha-2(I) chain	52	44	6.5
	Collagen alpha-1(III) chain	62	43	5.8
	Collagen alpha-1(II) chain	7	6	1.6
Band 4	Collagen alpha-1(I) chain	54	62	14.9
	Collagen alpha-2(I) chain	61	56	21.6
	Collagen alpha-1(III) chain	60	44	3.0
	Collagen alpha-1(II) chain	6	5	0.5